

Lecture Notes in Mechanical Engineering

G. S. V. L. Narasimham

A. Veeresh Babu

S. Sreenatha Reddy

Rajagopal Dhanasekaran *Editors*

Recent Trends in Mechanical Engineering

Select Proceedings of ICIME 2020

 Springer

Lecture Notes in Mechanical Engineering

Series Editors

Francisco Cavas-Martínez, Departamento de Estructuras, Universidad Politécnica de Cartagena, Cartagena, Murcia, Spain

Fakher Chaari, National School of Engineers, University of Sfax, Sfax, Tunisia

Francesco Gherardini, Dipartimento di Ingegneria, Università di Modena e Reggio Emilia, Modena, Italy

Mohamed Haddar, National School of Engineers of Sfax (ENIS), Sfax, Tunisia

Vitalii Ivanov, Department of Manufacturing Engineering Machine and Tools, Sumy State University, Sumy, Ukraine

Young W. Kwon, Department of Manufacturing Engineering and Aerospace Engineering, Graduate School of Engineering and Applied Science, Monterey, CA, USA

Justyna Trojanowska, Poznan University of Technology, Poznan, Poland

Lecture Notes in Mechanical Engineering (LNME) publishes the latest developments in Mechanical Engineering—quickly, informally and with high quality. Original research reported in proceedings and post-proceedings represents the core of LNME. Volumes published in LNME embrace all aspects, subfields and new challenges of mechanical engineering. Topics in the series include:

- Engineering Design
- Machinery and Machine Elements
- Mechanical Structures and Stress Analysis
- Automotive Engineering
- Engine Technology
- Aerospace Technology and Astronautics
- Nanotechnology and Microengineering
- Control, Robotics, Mechatronics
- MEMS
- Theoretical and Applied Mechanics
- Dynamical Systems, Control
- Fluid Mechanics
- Engineering Thermodynamics, Heat and Mass Transfer
- Manufacturing
- Precision Engineering, Instrumentation, Measurement
- Materials Engineering
- Tribology and Surface Technology

To submit a proposal or request further information, please contact the Springer Editor of your location:

China: Dr. Mengchu Huang at mengchu.huang@springer.com

India: Priya Vyas at priya.vyas@springer.com

Rest of Asia, Australia, New Zealand: Swati Meherishi at swati.meherishi@springer.com

All other countries: Dr. Leontina Di Cecco at Leontina.dicecco@springer.com

To submit a proposal for a monograph, please check our Springer Tracts in Mechanical Engineering at <http://www.springer.com/series/11693> or contact Leontina.dicecco@springer.com

Indexed by SCOPUS. The books of the series are submitted for indexing to Web of Science.

More information about this series at <http://www.springer.com/series/11236>

G. S. V. L. Narasimham · A. Veeresh Babu ·
S. Sreenatha Reddy · Rajagopal Dhanasekaran
Editors

Recent Trends in Mechanical Engineering

Select Proceedings of ICIME 2020

 Springer

Editors

G. S. V. L. Narasimham
Indian Institute of Science Bangalore
Bengaluru, Karnataka, India

A. Veeresh Babu
National Institute of Technology Warangal
Warangal, Telangana, India

S. Sreenatha Reddy
Guru Nanak Institute of Technology
Hyderabad, Telangana, India

Rajagopal Dhanasekaran
Guru Nanak Institute of Technology
Ibrahimpatnam, Telangana, India

ISSN 2195-4356

ISSN 2195-4364 (electronic)

Lecture Notes in Mechanical Engineering

ISBN 978-981-15-7556-3

ISBN 978-981-15-7557-0 (eBook)

<https://doi.org/10.1007/978-981-15-7557-0>

© Springer Nature Singapore Pte Ltd. 2021

This work is subject to copyright. All rights are reserved by the Publisher, whether the whole or part of the material is concerned, specifically the rights of translation, reprinting, reuse of illustrations, recitation, broadcasting, reproduction on microfilms or in any other physical way, and transmission or information storage and retrieval, electronic adaptation, computer software, or by similar or dissimilar methodology now known or hereafter developed.

The use of general descriptive names, registered names, trademarks, service marks, etc. in this publication does not imply, even in the absence of a specific statement, that such names are exempt from the relevant protective laws and regulations and therefore free for general use.

The publisher, the authors and the editors are safe to assume that the advice and information in this book are believed to be true and accurate at the date of publication. Neither the publisher nor the authors or the editors give a warranty, expressed or implied, with respect to the material contained herein or for any errors or omissions that may have been made. The publisher remains neutral with regard to jurisdictional claims in published maps and institutional affiliations.

This Springer imprint is published by the registered company Springer Nature Singapore Pte Ltd. The registered company address is: 152 Beach Road, #21-01/04 Gateway East, Singapore 189721, Singapore

Contents

Analysis of Hybrid Green Fuel Blended with Diesel as Fuel for Conventional Engine	1
N. S. Senthur, S. Shafquath ibn sulthan, H. Ram Ganesh, and K. Arun	
Experimental Investigation of Direct Evaporative Cooler with Sisal, Hemp, and Abaca Cooling Pad Material	13
Manojkumar Udgire	
Mitigation of Carbon Dioxide Gas from a DI Diesel Engine Fuelled with Honge Biodiesel for Agriculture	25
K. Muralidharan, K. Senthil Kumar, K. Shanmugavel, S. Lakshmana Kumar, and S. Rajkumar	
Reduction of Greenhouse Gases from a Coated Diesel Engine Fuelled with Honge Biodiesel for Sustainable Environment	37
K. Muralidharan, V. L. Raja, S. Lakshmana Kumar, K. Shanmugavel, and R. Dhanasekaran	
Thermal Barrier Coating on IC Engines; A Review	47
Anoop. R. Chattarki and K. G. Basavakumar	
Modeling and Analysis of Compression Ignition Engine Performance and Emissions of Biodiesel	69
V. Nageswar Reddy, G. Sreenivasarao, and K. Thirupati Reddy	
Simulation of Performance of Boiler System for a Bagasse Unit Using LabVIEW	79
Mahesh G. Emmi, Aravindrao M. Yadwad, Vinay V. Kuppast, B. S. Talikoti, and M. Sampanna	

Experimental Investigation of Performance, Emission and Combustion Characteristics of a Di-diesel Engine Fuelled with Aqueous Cerium Oxide and Aqueous Aluminium Oxide Nanoparticle Additives	85
P. Ravichandra Ganesh, K. Hemachandra Reddy, J. M. Babu, and M. Sarath Chandra	
Emission Characteristics of CSOME in CRDI Diesel Engine with Multiple Injection Strategy	97
Ramesh Babu Nallamotheu, Anantha Kamal Nallamotheu, and Seshu Kishan Nallamotheu	
Impact of Process Parameters on Peak Temperature Inside the Workpiece During Friction Stir Welding of AA5083 Aluminum Alloys	109
M. Shiva Chander, M. Ramakrishna, and B. Durgaprasad	
Optimization of Friction Welding Process Parameters for Weldment of Aluminium–Copper Electrical Connector	121
Balkeshwar Singh, Worku Mamuye, and Moera Gutu Jiru	
A Study on Effect of Cutting Fluids on Surface Roughness of EN 8 Steel Turning Using Taguchi Method	139
V. Kumar, P. Surendernath, and K. Amarnath	
Study on Mechanical Behavior of Friction Stir Welded Nylon-6 Sheets	151
Santosh K. Sahu, Kamal Pal, Susmita Das, and Avissek Tripathy	
Optimization and Characterization Study on Deposition of Aluminium 6063 Over IS 2062 Low Carbon Steel by Friction Surfacing	161
Dillip Kumar Sahoo, Bhulok Sundar Mohanty, A. Jaswanth, and D. Abhinay Varma	
Determination of Bending Force and Bend Angle of Sheet Metal Welds	177
R. Uday Kumar	
A Novel Approach for Reducing Delamination During Drilling of CFRP by Response Surface Methodology (RSM) Integrated with the Taguchi Method	185
Tarakeswar Barik, Sourav Kumar Jena, Avissek Tripathy, Kamal Pal, and Suchismita Parida	
Application of MCDM Methods for Process Parameter Optimization in Turning Process—A Review	199
Ch. Divya, L. Suvarna Raju, and B. Singaravel	

Effect of Hybridization, Influence of Surface Modification on the Properties and Optimization of bio fiber Composites 209
 G. Venkatesha Prasanna, M. Nikhil, and A. Sai Kiran

Review on Processing and Characterization of Duplex Stainless Steels 219
 Rayappa Shrinivas Mahale, V. Shamanth, and P. C. Sharath

Prediction of Wear Characteristics of Polymer Composites by ANN Modified by GA 231
 V. L. Raja, K. Muralidharan, and R. Dhanasekaran

Experimental Investigation of Mohair Fibrous Composite Material on Mechanical Properties 239
 K. Amarnath, R. Venumadhav, and E. Sreedhar

FE Analysis of Superplastic Forming Complex Shapes in Aluminum-Coated Magnesium Alloys 247
 J. Kandasamy

Failure Analysis of GFRP Composite Reinforced with Semimetals for Marine Applications 261
 Pala Srinivasa Reddy, Inkulu Anil Kumar, Satuluri Sriikiran, and Dannana Suresh

Mechanical Behavior in Tungsten Carbide-Reinforced Aluminum Composites 281
 Yamuzala Sai Ratnakar and Allu Venkata Pradeep

Simulation of Bridge Deck Made-Up of Fibre Reinforced Polymer Composites Reinforced with ZrO₂ 295
 I. Anil Kumar, P. Srinivasa Reddy, M. Balajee, and R. Jagadeesh Kumar

Friction and Wear Characteristics of Austenitic Stainless Steel Against Ceramic Disc 311
 V. Sumalatha, P. Ravinder Reddy, A. Krishnaiah, and G. S. Reddy

Fiber Surface Treatment and Quantity, Impact on the Performance of Biocomposites 321
 Gowdagiri Venkatesha Prasanna, A. Nikhil Nihar, G. Lokesh, and N. Naga Sai

Compressive and Impact Behavior of Nanoscale Hybrid Composite Materials 333
 Mohd. Minhajuddin Saif, Dasari V. Ravi Shankar, and Mohd. Manzoor Husain

Study of Mechanical Properties of Coconut Coir Fiber-Reinforced Polymer Composites 341
 Gondi Konda Reddy and H. Madhusudhana Reddy

Processing and Characterization of 6061 Aluminium Alloy with Nickel (Ni) and Zirconium (Zr)	353
S. Arun Kumar and R. Raman Goud	
Static Structural Analysis of Hybrid Honeycomb Structures Using FEA	363
A. Chandrashekhar, Himam Saheb Shaik, S. Ranjan Mishra, Tushar Srivastava, and M. L. Pavan Kishore	
Design and Random Vibrational Analysis of Horizontal Impact Hammer Crusher	377
S. Naveen, P. Praveen Kumar Reddy, and S. L. N. Reddy	
Fault Diagnosis of Unbalanced Multirotor System	387
V. Hariharan, G. Rajeshkumar, and K. A. Ibrahim Sheriff	
Robust Design of Deterministically Synthesized Four-Bar Mechanism	397
Sanjay Matekar and Ajay Fulambarkar	
Analysis of Various Cooling Mechanisms for Plastic Gears Using Decision Tree Algorithms	407
Sam Cherian, Abu Bakr Azam, and Lokavarapu Bhaskara Rao	
Design and Analysis of Sedan Car B-Pillar Outer Panel Using Abirbara with S-Glass Fiber Hybrid Composites	419
Ramesh Babu Nallamothe and Melkamu Yigrem Yihunie	
Design and Analysis of Shock Absorber	433
N. Ankitha and M. R. S. Rupa Sri	
Design and Optimization of a Two-Stage Gearbox Using GearTrax	445
Kalyan Sekhar, Pradyumna Dharmadhikari, Shreyash Panchal, and Lokavarapu Bhaskara Rao	
Analysis of Composite Leaf Springs Using Finite Element Method	479
S. Geetha Satya Sai, Venigalla Sailesh, S. K. Mobin, T. Subash Chandra Bose, Y. Sai Krishna, and P. Phani Prasanthi	
Design of Gears Using Aluminium 6061-T6 Alloy for Formula SAE Steering System	489
Arnav Gupta, V. P. Yashvanth, and Lokavarapu Bhaskara Rao	
Design and Analysis of Helical Teeth Harmonic Drive	507
Sekar Anand, Arunachalam Dharmalingam Srikeshav, Baskar Sharran, and Lokavarapu Bhaskara Rao	
Design and Analysis of Permanent Magnetic Gears	521
Kolape Poonam Gujaba, Sharmila Parashar, and Lokavarapu Bhaskara Rao	

Design and Analysis of Swing Arm Using Carbon Fiber Composite by Using Creo 2.0 and ANSYS 531
 Pidaparthy Maheshbabu, R. Ramkumar, and Dasari Ajay

Comparison of Kinematic Analysis of Robot Made of Conventional Theo Jansen Mechanism, Modified Theo Jansen Mechanism of PLA and Modified Theo Jansen Mechanism of Mild Steel 545
 Keval Bhavsar, Pranav Darji, Dharmik Gohel, Jitendra Modi, and Umang Parmar

Modeling of a Warfield Autonomous Robot with GPS and Digital Compass 561
 P. V. Prasad Reddy, S. Madhava Reddy, and D. L. Tejaswini

Analysis of Enterprise Model Using System Dynamics: A Case of Production–Inventory System 575
 P. S. R. K. Nageswara Rao, P. Usha Sri, and K. Vizayakumar

Comparative Analysis of Small and Large Capacity Sized On-grid, Rooftop Solar PV Systems - An LCA Approach 587
 N. Leela Prasad, M. Shreyas, and P. Usha Sri

Automated Real-Time Software Based Forecasting of Climate Change Using Chlorophyll Content on Agriculture 599
 K. Sujatha, K. S. Thivya, S. Elakkiya, V. Srividhya, NPG. Bhavani, and Bhuvaneshwari Nagarajan

Studies on Drop Test of a Helmeted Head Form with and Without Chinstrap Using LS-Dyna 607
 Madipalli Manisha, Suresh Lonka, R. Dhanasekaran, and S. Sreenatha Reddy

Design and Implementation of SEPIC Converter Based Nine-Level MLI Fed IM with PI, FLC, and ANN Controller 621
 S. Karthikeyan, K. Lakshmi, and S. Gobhinath

Preparation and Experimental Evaluation of Membrane Electrode Assembly of Proton Exchange Membrane Fuel Cell 633
 Syed Aslam, Md. Masood, and Sudheer Prem Kumar

Relative Importance Analysis of Factors Influencing Sea Port Service Quality 641
 S. Hemalatha, Lingaraju Dumpala, and B. Balakrishna

Photovoltaic/Thermal (PV/T) System Performance Effects Using Conventional/Modern Cooling Techniques with and Without PCM 651
 D. Kameswara Rao, K. Sudhakar Reddy, and V. V. Subba Rao

Studies on Emergency Alert for Women with Smart Dollar	667
R. Dhanasekaran, S. Sreenatha Reddy, Mohammed Sirajuddin, Harisaiteja Nanaboina, and I. Jahnavi	
A Comparative Analysis of Multi-criteria Decision-Making Techniques to Optimize the Process Parameters in Electro Discharge Machine	675
J. Anitha and Raja Das	
Studies on Customized Compression Bandage Materials for Healing Injured Part	687
S. Sreenatha Reddy, R. Dhanasekaran, M. Srihari, Sirgiripet Sai Kiran, S. Kalyan, and T. Anvesh Kumar	
Investigation on Effect of Industrial Waste on Tribological Properties of Polymer Composites	695
V. L. Raja, K. Muralidharan, S. Lakshman Kumar, and K. Shanmugavel	
Computational Analysis of Concentrating Solar Boiler Uses with and Without Graphene Coating	705
Mohammad Arif Hussain, S. Nagakalyan, and M. Prakashbabu	

About the Editors

Dr. G. S. V. L. Narasimham is Chief Research Scientist in the Department of Mechanical Engineering. He received his M. Tech. from IIT, Madras, and Ph.D. from IISc, Bangalore, both in Mechanical Engineering. His research interests include Solar Thermal Engineering, HVAC, Refrigeration, Cryogenics, Heat and Mass Transfer, CFD, and Simulation of thermal systems. He has about three decades of experience in teaching, academic and sponsored research and guidance to masters and research students. He worked as an investigator in the projects sponsored by the Departments of non-conventional energy sources, atomic energy, space, power, science and technology and planning commission, as well as industrial research projects sponsored by IMI, GE, Mahindra and Mahindra. He also works as a consultant from IISc for various organizations and is a life member of professional bodies related to heat and mass transfer and cryogenics.

Dr. A. Veeresh Babu received B.Tech in Mechanical Engineering and M.Tech in Heat Power Refrigeration from JNTU, Andhra Pradesh in 1998 and 2000, respectively. He obtained Ph.D. from Andhra University in 2013. He had an experience of refrigerator design, clean room technology, cold room/freezer room design and construction while he was working with the industry. He erected and commissioned clean rooms at DRDE, Gwalior, RCI, Hyderabad and CRDI, Lucknow. He is having research experience of more than 12 years ever since he joined NIT Warangal as an Assistant Professor in the year 2006. At present, He is an Associate Professor in the Department of Mechanical Engineering, NIT Warangal. He has published more than 15 papers in SCI/SCOPUS/peer-reviewed journals. He has also presented his works in 10 international conferences. He has produced one Ph.D. student, and nearly seven students are working under him for the Ph.D. At present, he completed two minor research projects and two major projects are under review. He has also been appointed as a course writer for certificate in Power Plant Engineering offered by IGNOU, India.

Dr. S. Sreenatha Reddy is presently working as a Principal and Professor at Guru Nanak Institute of Technology under JNTU, Hyderabad. He obtained B.Tech in Mechanical Engineering from JNTU, Hyderabad, M. Tech in Heat power, Refrigeration & Air conditioning from JNTU, Hyderabad and Ph.D. from Faculty of Mechanical Engineering from JNTUA. Notable among his awards are National award for best research publication; Jawaharlal Nehru memorial prize issued Institution of Engineers on the occasion of inauguration of the 27th Indian Engineering Congress at New Delhi in the year 2012; Bharat Vidya Shiromani Award; and a Certificate of Education Excellence for outstanding achievements in the field of Education given by International Institute of Education & management on 22nd December 2014 at New Delhi; Glory of Education of Excellence Award is issued by IIEM on 4th March 2015 at New Delhi. He has also received award for being the best academic administrator for the Centre for Advanced Research and Design under Venus International Foundation on 5th July, 2015. He received National Award as an Eminent Educationist issued by the INDUS FOUNDATION on the occasion of Indo-American Education Summit 2016 at Hyderabad. He has received many more prestigious awards. He is a young and dynamic technical person and has been working for past 19 years teaching in mechanical and aeronautical fields and 3 years in thermal power plants. He worked in the fields of automotives, critical challenges in thermal field like propulsion, combustion, and heat transfer have been pioneering. He has rich experience in research and administrative area. He has published 141 international and national reputed Journals, and 26 international and national conference papers. He is a member of governing body in prestigious institution of GNIT. He has also served as an expert committee member of AICTE for scrutinizing project reports internally as well as the member in the board of reviewers for the Institution of Engineers journal. He is a fellow member of many professional bodies in the field of mechanical engineering and technical education.

Dr. Rajagopal Dhanasekaran received BE in Mechanical and Production Engineering from the Annamalai University in 2002, M.E, and Ph.D. from the Department of Mechanical Engineering, Anna University in 2007 and 2013, respectively. He has been working as a Professor in Mechanical Engineering, Guru Nanak Institute of Technology, Hyderabad, India since November 2015. He has published more than 40 research journal papers, 7 patent publications and received funds from AICTE. He is a member in ISTE and Tribology Society of India. His research interests include tribology, engineering failure, wear characterization and production engineering.

Analysis of Hybrid Green Fuel Blended with Diesel as Fuel for Conventional Engine



N. S. Senthur, S. Shafquath ibn sulthan, H. Ram Ganesh, and K. Arun

Abstract We are in a scenario where the fuel prices are increasing and the demand for fuel is on the rise but the resources are reducing. There is a big gap between the demand and supply of fuel resources. Green fuel is obtained from vegetable oils, which is the best alternative fuel. Several types of research have been done on using a blend of diesel and green fuel. Nonetheless, quite less research has been done on using a combination of two different green fuel blends with the diesel. This has given a lot of opportunities to analyze the usage of such fuel in an engine. In this research, an empirical study has been made by performing certain tests on two green fuels from Kanuga oil and Eucalyptus oil and they are mixed with diesel using varied mixing proportions. The impact of using dual green fuel on the engine effectiveness and release of toxic gas have been investigated on a single-cylinder, direct injection, air-cooled, and high-speed diesel engine at various engine loads with a steady engine speed of 3000 rpm. On conducting emission test, the impact on the release of CO, CO₂, HC, NO_x, and smoke opacity have been examined. The brake thermal efficiency of blend A is higher in contrast to that of diesel. The release of smoke, hydrocarbon, and nitrogen oxides from dual green fuel blends have been high in contrast to diesel. But the exhaust gas temperature of dual green fuel blends has been lesser in contrast to diesel.

Keywords Green fuel · Dual green fuel · Alternate fuel · Emission analysis

N. S. Senthur (✉) · S. Shafquath ibn sulthan · H. Ram Ganesh · K. Arun
Einstein College of Engineering, Tirunelveli, Tamil Nadu, India
e-mail: senthur.ns@gmail.com

S. Shafquath ibn sulthan
e-mail: sulthanibn96@gmail.com

H. Ram Ganesh
e-mail: ramganesh683@gmail.com

K. Arun
e-mail: arunkaradimuthu@gmail.com

1 Introduction

The energy is conserved less in the present days that causes energy demand. In the past few centuries, the focus on using alternative fuel is on the rise. A possible alternative fuel for diesel has been in the form of green that has ethyl ester of fatty acids generated by using transesterification reaction of triglycerides of vegetable oils and ethanol by using a catalyst. Green fuel has better efficiency in contrast to diesel as it has minimal sulfur content and also it has greater flash and fire point temperatures in contrast to diesel.

Many researchers have indicated that green fuel as the best alternative fuel. Green fuel and its blends with diesel have been utilized in operating diesel engines without modifying the engine parameter. The research on the generation of green fuel has raised in recent years as there is a tremendous need for an alternative as it is renewable, emits lesser toxic gas, and is biodegradable [1]. The green fuel generated by using transesterification indicated identical features properties as that of standard green fuel. The transesterification method lessens the stickiness of vegetable oil [2]. The prickly poppy methyl ester (PPME) mixed with diesel can be easily used instead of diesel in a diesel engine. The experiments further denoted that on using diesel the brake thermal efficiency, brake power increases whereas the specific fuel consumption for PPME lessens. The lower blends of green fuel raised brake thermal efficiency and lessened fuel consumption. Also, the green fuel blends emit lesser engine emissions in contrast to diesel [3].

The combination of diesel fuel is bioethanol and sunflower methyl ester in diesel engine. If we increase the proportions of bioethanol level in the blend, the CO releasing level as exhaust decreases i.e. the release of CO lessens with the increase of bioethanol level in the blend. This variation is because bioethanol has a lesser level of carbon in contrast to diesel [4]. Kanuga oil is using transesterification and used in C.I. engine. They have stated that blend B5 shows reduced release of un-burnt hydrocarbon, carbon monoxide, oxides of nitrogen, and carbon dioxide by applying full load [5].

Several literature have been studied on the details related to using green fuel and its blends in engines. Nevertheless, many literature concentrated on a single green fuel and its blends. The earlier studies indicate that a single green fuel offers satisfactory engine performance, and reduction in release of toxic gas in emissions while operating diesel engine.

Very few experiments have been conducted with the combination of dual green fuel and diesel as a fuel. Many write-ups have indicated Kanuga oil as an appropriate alternative for diesel and a few investigations were done by using eucalyptus oil. Hence in this paper, an investigative analysis on Kanuga oil and Eucalyptus oil has been performed as the oils are effortlessly available in the neighborhood. The initial phase of the experiments has been done to discover the features of the suggested oil for experiments. The investigations revealed that the calorific value of the dual green fuels and its blends along with diesel is higher in contrast to the single green fuel and its blends along with diesel. Therefore, it has been concluded to choose Kanuga

oil, eucalyptus oil, and diesel as the propellant for the present analysis. In the next phase of the investigations, we ascertain the impact of using dual green fuel and its blends on the engine effectiveness and release of exhaust gas from a diesel engine and the outcome of the investigations are contrasted by using diesel.

2 Materials and Methods

Transesterification method is used to prepare the two green fuels (Kanuga oil and Eucalyptus oil). The dual green fuel blends have been prepared by using varied proportions of green fuel such as Blend A-Diesel 90%, KEE 5%, and EEE 5% by volume basis; Blend B-Diesel 80%, KEE 10%, and EEE 10% by volume basis; Blend C-Diesel 60%, KEE 20%, and EEE 20% by volume basis; Blend D-Diesel 40%, KEE 30%, and EEE 30% by volume basis; Blend E-Diesel 20%, KEE 40%, and EEE 40% by volume basis, and Blend F-Diesel 0%, KEE 50%, and EEE 50% by volume basis.

Using the blends features of the engine such as kinematic viscosity, specific gravity, calorific value, flash point temperature, and fire point temperature of baseline fuel, raw oils, and two green fuel mixed blends have been ascertained by using ASTM methods [6]. The results have been contrasted with the properties of diesel. The investigations have been done on a stationary single-cylinder four-stroke air-cooled diesel engine with electrical loading. The features such as the engine effectiveness, release of toxic gas have been contrasted with baseline data of diesel. Tests have been done at a constant speed and at varying loads by using all dual green fuel blends. Engine speed has been sustained at 3000 rpm during all the experiments. Three experiments for each load have been done to check the correctness [7]. Fuel consumption and exhaust gas temperatures have also been ascertained. The smoke opacity of the exhaust gases has been ascertained using AVL-make smoke meter. Release of exhaust gas has been ascertained using Crypton-make five-gas analyzer. The experimental layout is illustrated using a diagram as seen in Fig. 1 and the details of the engine specifications are given in Table 1. Calorific value for various fuels is given in Table 2.

3 Results and Discussion

Various physical and thermal properties of dual green fuels of Kanuga oil and Eucalyptus oil and its blends were assessed. The engine effectiveness has been assessed by certain parameters such as thermal efficiency, specific fuel consumption, and exhaust gas temperature.

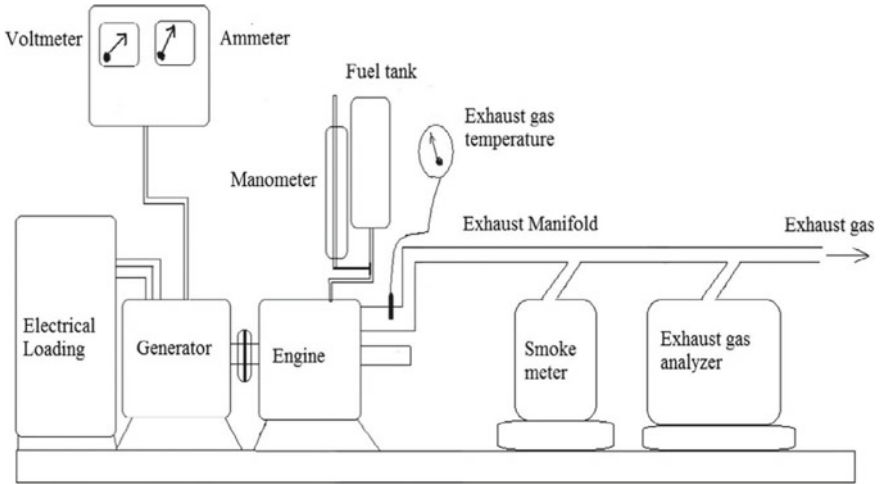


Fig. 1 Test engine setup

Table 1 Test engine specifications

Items	Specifications
Model	Kirloskar engine
Type	Single cylinder
Bore-stroke	68–76 mm
Compression ratio	18:1
Type of cooling	Air cooling
Speed	3000 rpm
BHP	4.5

Table 2 Calorific value for various fuels

Fuel	Calorific value (MJ/kg)	Fuel	Calorific value (MJ/kg)	Fuel	Calorific value (MJ/kg)
Diesel	46.2	Eucalyptus oil	41.73	Kanuga oil	40.75
Blend A	45.23	EB 10% blend	45.6	KB10% blend	45.2
Blend B	44.85	EB 20% blend	44.68	KB20% blend	44.46
Blend C	43.23	EB 30% blend	43.68	KB30% Blend	43.27
Blend D	42.67	EB 40% blend	42.84	KB40% blend	41.76
Blend E	41.46	EB 50% blend	42.24	KB50% blend	41.12
Blend F	40.34				

3.1 Calorific Value of Fuels

The digital bomb calorimeter has been utilized to check the calorific value of propellant. ASTM D420 procedure has been followed to study the calorific value of different test fuels. Diagrammatic representation of the calorific value of different fuels is shown in Fig. 1. Raw vegetable oil has less calorific value in contrast to diesel. After the transesterification process, the calorific value of green increases mildly in contrast to raw oil. The Kanuga ethyl ester has a low percentage of calorific value in contrast to Eucalyptus oil ethyl ester. By mixing the dual green fuels with diesel, the calorific values of Blend A and Blend B are nearer to the value of diesel that is more than a single green fuel blend. The calorific values of Blend C, Blend D, and Blend E are nearly the same as to that of a single green fuel blend. The calorific value of Blend F is lesser than the single green fuel blends because of the presence of pure green fuel blends without diesel. Hence, dual green fuel and its blends are used to analyze the engine effectiveness and release of toxic gas from the engine by performing certain experiments by using them in an engine.

3.2 Specific Gravity of Fuels

A precision hydrometer has been used to measure the specific gravity of various dual blends. The specific gravity of dual green fuel blends Blend A, Blend B, and Blend C is 0.818, 0.827, and 0.841, respectively, but for diesel it is 0.813. The other blends specific gravity values vary more than diesel.

3.3 Viscosity of Fuels

Calibrated Redwood viscometer has been utilized to determine the kinematic viscosity. ASTM D0445 method has been used to study the viscosity of fuels. The viscosity of the blends rises with the increase in blend ratio. These values are greater than the viscosity of diesel. The viscosity of the raw Kanuga oil and the Eucalyptus oils are more in contrast to diesel. Nonetheless, by using transesterification process the high viscosities of raw oils can be lessened. The viscosity of dual green fuel blends Blend A and Blend B is closer to that of diesel. The viscosity of diesel is 4 Cs, but the viscosity of Blend A and Blend B is 4.2 Cs and 4.4 Cs correspondingly.

3.4 Performance Analysis

Specific Fuel Consumption

The impact of brake power over specific fuel consumption is diagrammatically represented in Fig. 2. On increase in the brake power, the SFC lessens and this applies to all the dual green fuel blends. For the optimum load, the value of SFC of Blend A is 0.35 kg/kW h, Blend B is 0.38 kg/kW h, Blend C is 0.40 kg/kW h but for diesel it is 0.33 kg/kW h. Due to the lower calorific value of the blends, the SFC of the dual green fuel is high.

Brake Specific Energy Consumption

Brake specific energy consumption (BSEC) values have been used to compare the engine effectiveness on using varied blends of fuel with diverse calorific values. A diagrammatic representation of the brake specific energy consumption for dual green fuel, its blends and diesel is shown in Fig. 3. The diagram denotes that the BSEC of all dual green fuel blends is the highest in contrast to that of mineral diesel. BSEC is a perfect feature as it is reliant on the calorific value of the fuel. The high

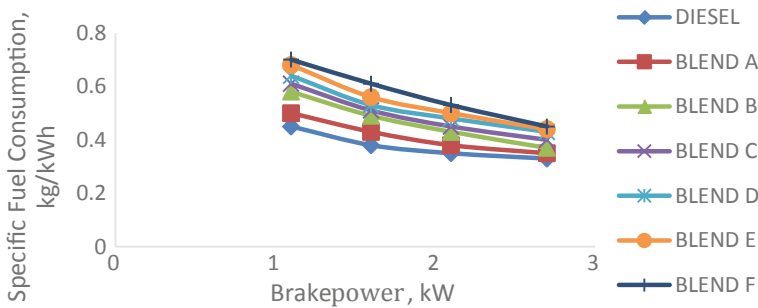


Fig. 2 Deviation in SFC versus brake power

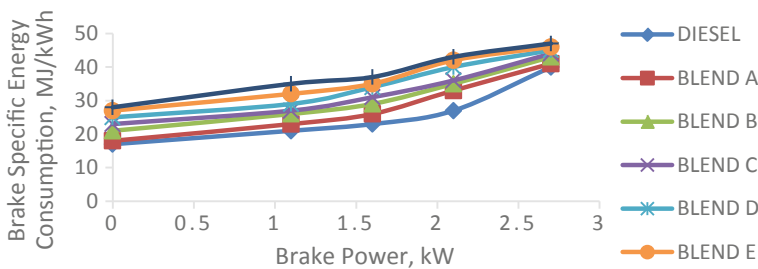


Fig. 3 Deviation in BSEC versus brake power

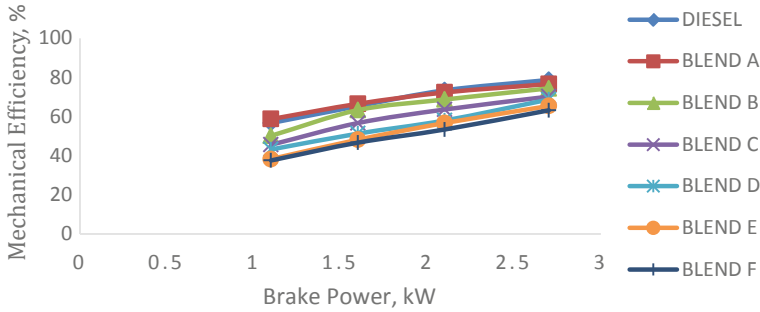


Fig. 4 Deviation in mechanical efficiency versus brake power

specific energy consumption is because of the lower energy content of the ester [8]. Therefore, the brake specific energy consumption of the dual green fuel blends rises in contrast to that of diesel.

Mechanical Efficiency

The impact of brake power on the mechanical efficiency of the engine is shown in Fig. 4. Designated power and engine friction are vital for calculating the mechanical efficiency of the engine. Efficiency is measured as a ratio of the measured performance to the performance of an ideal machine [9]. Mechanical efficiency measures the effectiveness of a machine in converting the energy and power which is provided as information to the device that turns out as force and movement. For this reason, the mechanical efficiency shows the efficiency of the engine in transforming the indicated power to useful power. Blend A provides the optimum mechanical efficiency of 76.6% for the optimum brake power, but on using diesel it gives 78.7% at the same brake power. The same is not the case while using other blends of fuel because mechanical efficiency is comparatively lesser than that of diesel.

Exhaust Gas Temperature

The deviations in brake power on exhaust gas temperature are shown diagrammatically in Fig. 5. The impact of applying more brake power is it increases the exhaust temperature [10]. Quality of ignition is a direct measure of the exhaust gas temperature. Extra fuel is used by the engine with engine load hence it increases the exhaust gas temperature, this parallelly increases on additional loads. Similarly, all the blends that have reduced exhaust temperature than that of diesel on any brake power is because of its lower heating value and the enhanced oxygen content of the green fuel that improves combustion. Therefore, the dual green fuel blends are superior to diesel while taking into account the impact of exhaust temperature.

Exhaust Smoke Emission

Figure 6 indicates that there is an increased level of smoke when there is a rise in the brake power. For the optimum load, the emission of smoke using diesel has been 58%, but the level of smoke emission using Blend A is 62% and Blend B is 65% by

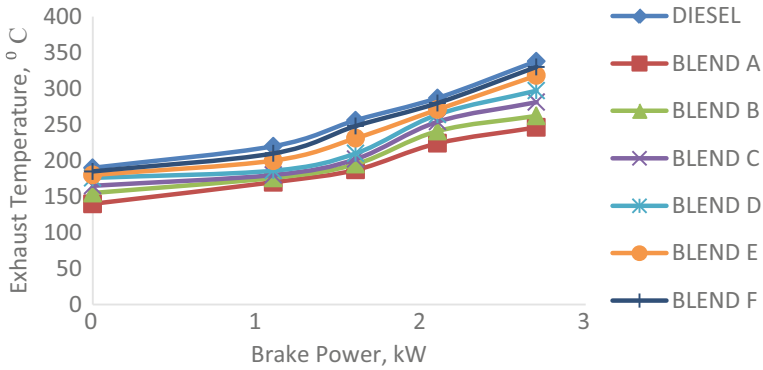


Fig. 5 Deviation in exhaust temperature versus brake power

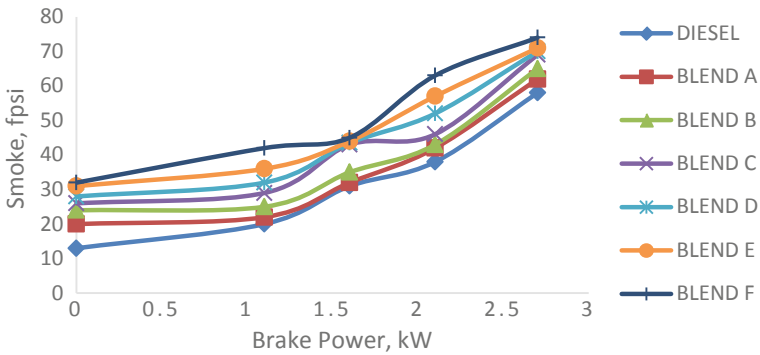


Fig. 6 Deviation in smoke versus brake power

applying the similar optimum load. Blend A has a nearer value of smoke emission as that of diesel. Using other blends, the smoke percentage was more than the diesel with the same brake power. The higher density and viscosity may be the reason for more smoke emissions as compared to diesel [11]. The high viscosity of pure green fuel deteriorates the fuel atomization and increases exhaust smoke.

Carbon Monoxide and Carbon Dioxide Emission

The deviations in brake power on the release of Carbon monoxide are illustrated in Fig. 7. Carbon monoxide’s (CO) content increases with increase in brake power. Blend A and Blend B emit lesser CO in contrast to diesel. A similar pattern is illustrated in Fig. 8 in the release of carbon dioxide (CO₂). Blend A and Blend B emit lesser CO and CO₂ in contrast to diesel at optimum load. This is because of the oxygen contents in the green fuel that enables burning of the fuel at a higher temperature in the cylinder [12]. The results of using other blends of fuel deviate from diesel. This is because of high viscosity; the air–fuel mixing process is impacted

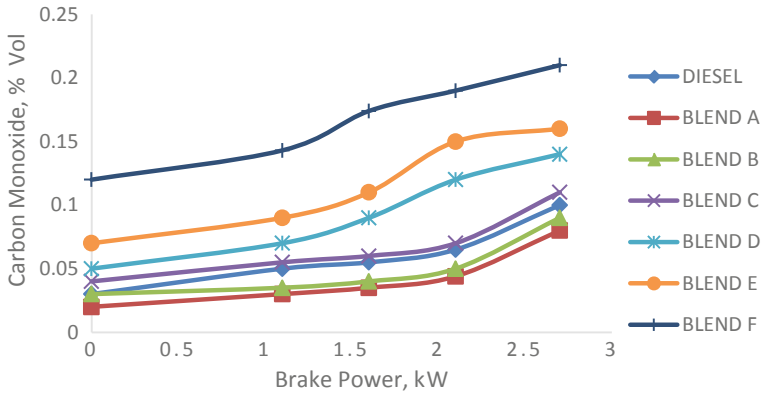


Fig. 7 Deviation in carbon monoxide versus brake power

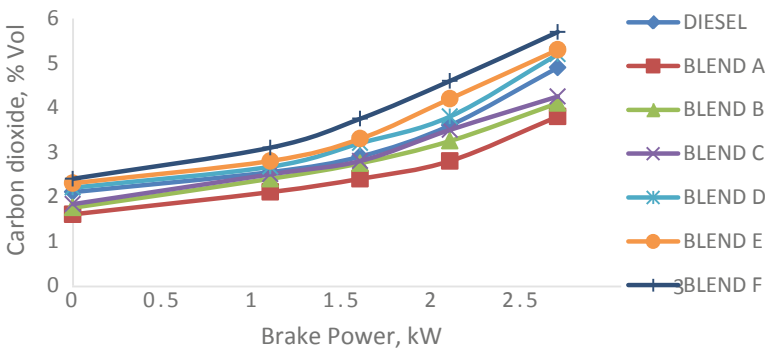


Fig. 8 Deviation in carbon dioxide versus brake power

by the difficulty in atomization and vaporization of dual green fuels. When the engine load is high, richer fuel–air mixture is burnt, and therefore high level of CO and CO₂ are generated.

Nitrogen Oxide Emission

Figure 9 shows the impact of brake power on nitrogen oxides. The nitrogen oxides (NO_x) rises on increase in the load for each blend. On the optimum load, Blend A gives 162 ppm while diesel gives 148 ppm, Blend B gives 174 ppm, Blend C gives 192 ppm. From the output, NO_x release is more on using dual green fuel blends in contrast to diesel. Nonetheless, Blend A releases reduced NO_x in contrast to dual green fuel blends. The vegetable oil based green fuel has a lesser amount of nitrogen [13]. This contributes to NO_x production. All the blends produces a higher level of NO_x in contrast to diesel. Reason for high-level release of NO_x is because of high average gas temperature, the availability of oxygen in the fuel and residence time at higher load conditions along with the blend combustion.

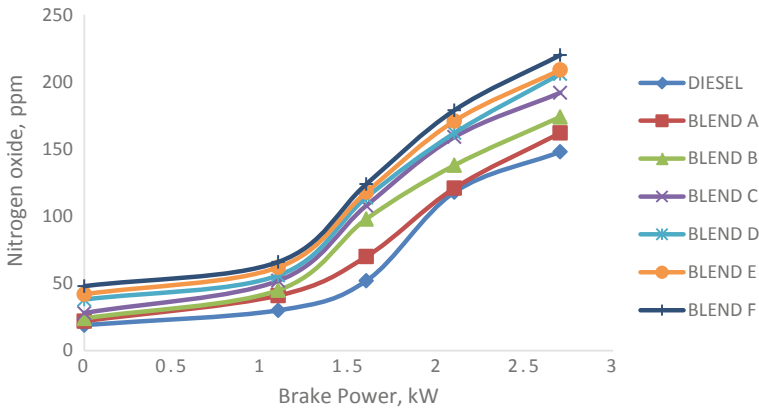


Fig. 9 Deviation in nitrogen oxide versus brake power

Hydrocarbon Emission

Figure 10 indicates the relation between brake power and hydrocarbon (HC). The release of hydrocarbon increases when the load increases on using each blend of fuel. The release of hydrocarbon is comparatively higher than diesel. The outcome of using blends of green fuel is Blend A releases reduced HC than other blends. The dual green fuels and blends generally emit lesser HC on lower engine loads and the reverse happens when the engine load is high. At high load, fuel injected in the cylinder is more and less oxygen will be available for the reaction [14]. The hydrocarbon release is high because of the lower calorific value and the higher viscosity of green fuel oil.

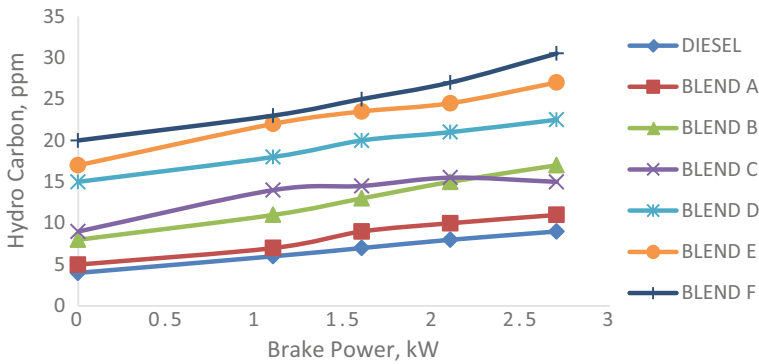


Fig. 10 Deviation in hydrocarbon versus brake power

4 Conclusion

Single-cylinder high-speed diesel engine ran successfully during tests on dual green fuels and its blends. The blends of diesel and the dual green fuels of Kanuga oil and Eucalyptus oil were characterized for their various physical, chemical, and thermal properties. From the experimental analysis results, the thermal efficiency and mechanical efficiency of Blend A and Blend B were closer to the diesel values. The specific fuel consumption values of dual green fuel blends were analogous to diesel. Blend A and Blend B produced slightly lower CO and CO₂ than diesel. This is a considerable advantage over diesel on using dual green fuel blends. The dual green fuel blends emits a higher level of smoke opacity, HC and NO_x in contrast to diesel. Nonetheless, the smoke opacity on using Blend A, Blend B, and Blend C was nearer to diesel. Therefore, it may be concluded that dual green fuel blends of Blend A, Blend B, and Blend C would be used as an alternative fuel instead of diesel in the diesel engine.

Acknowledgments The research work was supported by Einstein College of Engineering under Anna University, Tamil Nadu.

References

1. A. Demirba, Green fuel from vegetable oils via transesterification in supercritical methanol. *Energy Convers. Manage.* **43**, 2349–2356 (2002)
2. H.C. Ong, H.H. Masjuki, T.M.I. Mahlia, A.S. Silitonga, W.T. Chong, K.Y. Leong, Optimization of green fuel production and engine performance from high free fatty acid Calophyllum inophyllum oil in CI diesel engine. *Energy Convers. Manage.* **81**, 30–40 (2014)
3. F.K. Forson, E.K. Oduro, E. Hammond-Donkoh, Performance of jatropha oil blends in a diesel engine. *Renew. Energy* **29**, 1135–1145 (2004)
4. J. Van Gerpen, Green fuel processing and production. *Fuel Process. Technol.* **86**, 1097–1107 (2005)
5. M.S. Kumar, A. Ramesh, B. Nagalingam, An experimental comparison of methods to use methanol and jatropha oil in a compression ignition engine. *Biomass Bioenergy* **25**, 309–318 (2003)
6. H. Rahimi, B. Ghobadian, T. Yusuf, An environment-friendly IC engine fuel. *Renew. Energy* **34**, 335–342 (2009)
7. R. Dhanasekaran, A.S. Anirudh, C. Sai Kiran, S. Sreenatha Reddy, Review of acoustic enclosure for noise control in diesel generator. *Int. J. Adv. Trends Eng. Technol. Special Issue*, 117–120 (2018)
8. A.S. Ramadhas, S. Jayaraj, C. Muraleedharan, Dual fuel mode operation in diesel engines using renewable fuels: rubber seed oil and coir-pith producer gas. *Renew. Energy* **33**, 2077–2083 (2008)
9. R.A. Korus, J. Jaiduk, C.L. Peterson, A rapid engine test to measure injector fouling in diesel engines using vegetable oil fuels. *J. Am. Oil Chem. Soc.* **62**(11), 1563–1564 (1985)
10. C. Rewolinski, D.L. Shaffer, Sunflower oil diesel fuel: lubrication system contamination. *J. Am. Oil Chem. Soc.* **61**(7), 1120–1124 (1985)

11. K. Nanthagopal, B. Ashok, R. ThundilKaruppa Raj, Influence of fuel injection pressures on Calophyllum inophyllum methyl ester fuelled direct injection diesel engine. *Energy Convers. Manage.* **116**, 165–173 (2016)
12. A.K. Yadav, M.E. Khan, A.M. Dubey, A. Pal, Performance and emission characteristics of a transportation diesel engine operated with non-edible vegetable oils green fuel. *Case Stud. Therm. Eng.* **8**, 224–236 (2016)
13. E.H. Pryde, Vegetable oil as diesel fuels: overview. Papers from the symposium on vegetable oils as diesel fuels, presented at the 73rd AOCS annual meeting, Toronto, Canada. *J. Am. Oil Chem. Soc.* **60**(8), 345–352 (1983)
14. M.A. Fazal, A.S.M.A. Haseeb, H.H. Masjuki, Green fuel feasibility study: an evaluation of material compatibility; performance; emission and engine durability. *Renew. Sustain. Renew. Energy* **15**(2), 1314–1324 (2011)

Experimental Investigation of Direct Evaporative Cooler with Sisal, Hemp, and Abaca Cooling Pad Material



Manojkumar Udgire

Abstract Evaporative cooling is environmentally friendly and a more efficient air cooling method. The efficiency of evaporative cooling systems increases with an increase in temperature and decrease in humidity. Therefore in hot and dry climates, evaporative cooling can save a large amount of energy used for conventional air-conditioning systems. Direct Evaporative Cooler (DEC) uses a wetted pad with large air-water contact surface area through which air is passed at a uniform rate to make it saturated. However, this process is accompanied by an increase in humidity which is sometimes not desirable. Thus, it is seen that a variety of materials that can be used as cooling media in direct evaporative cooler is very large. Hence there is a need to analyze the performance of alternative materials in terms of saturation efficiency and cooling capacity. Further, the performance of a cooler using hemp and abaca as cooling media has not been analyzed. Hence, the attempt is made to fabricate and analyze the performance of such cooler in the present work. The efficiency of evaporative cooling systems increases with an increase in temperature and decrease in humidity. In the developed direct evaporative cooler, 15–20% effectiveness is more in case of hemp as cooling pad material as compared to the abaca and Sisal cooling pad material. Enhancement in effectiveness is 10–15% more in case water flow rate at 220 LPH in all cooling pad material as compared to 180 LPH and 200 LPH. Average outlet dry bulb temperature was varying between 240 and 280 °C. Cooling capacity can be improved by increasing the water flow rate through the cooling pad and the dry bulb temperature of incoming air can be reduced below its wet-bulb temperature.

Keywords Abaca cooling pad · Cooling efficiency · Cooling capacity · Effectiveness · Hemp cooling pad

M. Udgire (✉)

Department of Mechanical Engineering, Mukesh Patel School of Technology Management & Engineering, SVKM's NMIMS, Mumbai, Maharashtra, India

e-mail: udgiremanojkumar@gmail.com

© Springer Nature Singapore Pte Ltd. 2021

G. S. V. L. Narasimham et al. (eds.), *Recent Trends in Mechanical Engineering*,

Lecture Notes in Mechanical Engineering,

https://doi.org/10.1007/978-981-15-7557-0_2

1 Introduction

Nowadays, great attention is paid to the environment, energy saving, and energy efficiency. Energy production often adversely affects the environment and increases greenhouse gas emissions. Despite this, global energy consumption grows from year to year. That is why the question of the development of new, cleaner, and more efficient technologies has been raised acutely in recent years. A large part of the world's energy is consumed by ventilation and air-conditioning. Practically in each modern building, ventilation and air-conditioning systems are installed. Even many of the old buildings wherever possible are equipped with modern ventilation systems. Many building facilities, such as hospitals and industrial buildings, have specific requirements for ventilation and air-conditioning systems. One of the most energy-intensive processes in the ventilation and air-conditioning is the process of cooling. Traditional systems based on the compressor cycle consume a lot of energy. Refrigerants contained in compressor circuits are often very harmful to the environment. These factors led to the active development of evaporative coolers. Air coolers based on evaporative cooling of the air consume far less energy compared to traditional compressor systems.

They are also more ecological and environmental-friendly systems. However, the efficiency of evaporative air cooling systems is strongly dependent on the state of the air. The most suitable conditions for these systems are the areas with a hot and dry climate. Determining factor, in this case, is the air wet-bulb temperature. This is the theoretical minimum temperature to which air can be cooled. Adiabatic cooling is the use of an adiabatic process to cool the air passing through a wetted cooling media or a spray of water. The ancient Egyptians hung wet mats on their doors and windows, and the wind blowing through the mats cooled the air—the first attempt at air-conditioning. This basic idea was refined through the centuries: mechanical fans to provide air movement in the sixteenth century, cooling towers with fans that blew water cooler air inside factories in the early nineteenth century, swamp coolers in the twentieth century. Modern technology has dramatically increased the efficiency and effectiveness of adiabatic cooling. Adiabatic saturation is good for those who want cost-cutting budgets because it is designed without a refrigerant, condenser, pressurized pipes to provide comfort cooling, not only the materials are cheap but lesser energy consumption. Another is it uses 100% fresh air so it is healthy because it brings in outside air and exhausts stale air, smoke, odors, and germs. It helps to maintain natural humidity levels, which benefits both people and furniture and cuts static electricity. Lastly, it does not need an airtight structure for maximum efficiency, so building occupants can open doors and windows. The evaporative cooler works on one of the oldest principles of air-conditioning known to Man—cooling of air by the evaporation of water. It is the most common form of household cooling found in arid areas. The popularity of evaporative cooling in such areas is due to its relatively low initial and operational cost compared to refrigerated cooling. Conventional direct evaporative coolers consist of a large water reservoir, a pump that draws water from

the reservoir and discharges it through spray nozzles directly into air stream or through cooling pads.

The direct evaporative cooler cools the air when the air comes in contact with water in the wetted media (cooling pads). During evaporation of water in the air stream, the required heat is taken from air itself. At hot climate conditions, the inner ambient temperature of the closed agricultural production buildings, such as greenhouse, poultry house, stable, and barn may reach very high values. This situation causes heat stress at the produced livestock. Pad evaporative cooling systems are used in such closed production buildings to decrease the ambient temperature. The obtained decrease at the temperature of the air passing the pad and the cooling efficiency of the pad evaporative cooling systems, depends on structural features of the pad as well as the velocity of the air passing through the pad.

Problem Statement

- Time interval for cleaning pad frames and removal of old pads are less.
- Degradation of material is high.
- Moisture absorbing capacity is less.
- Cooling capacity and efficiency are less.
- Effectiveness is low.
- Odor and skin irritation is the main issue.

Scope

Developed evaporator cooler has been successfully tested and results are quite promising, still, there are some areas on which the same work can be further extended so that effectiveness and cooling capacity can be improved successfully. The details of which are follows:

1. Efforts can be made with modification in cooling pad system so that its use can be extended for a longer period in cooling process Controlled cooling environment can be maintained in the cabinet and its effect can be analyzed to improve the effectiveness.
2. Evaporative cooling is environmentally friendly and a more efficient air cooling method
3. The efficiency of evaporative cooling systems increases with an increase in temperature and decrease in humidity. Therefore, in hot and dry climates, evaporative cooling can save a large amount of energy used for conventional air-conditioning systems.
4. Direct Evaporative Cooler (DEC) uses a wetted pad with large air-water contact surface area through which air is passed at a uniform rate to make it saturated. However, this process is accompanied by an increase in humidity which is sometimes not desirable.

2 Constructions and Working of Direct Evaporative Cooling Setup

- Construction of DEC

The experimental setup consists of major components such as cooling pad material, inlet/outlet duct, water tanks, fan with motor, pump, and required instrumentation. The actual experimental setup is fabricated in a local workshop having all manufacturing facilities. Figure 1 shows the schematic of the experimental setup. It consists of the different components like cooling pad materials, inlet/outlet duct, water tanks, and fan with motor, pump, vane anemometer, and hygrometer.

On the basis of the criteria mentioned, the design of the individual component was prepared and the corresponding parameter (i.e., relative dimensions and material for all components) were calculated. The procedure of design and calculations for each component is mentioned below.

3 Materials and Methods

Hemp is a long, soft, shiny vegetable fiber that can be spun into coarse, strong threads. Advantages of hemp are high moisture retention capacity and ease of manufacture with no skin irritations. Hence, hemp fiber is chosen as media for evaporative cooler

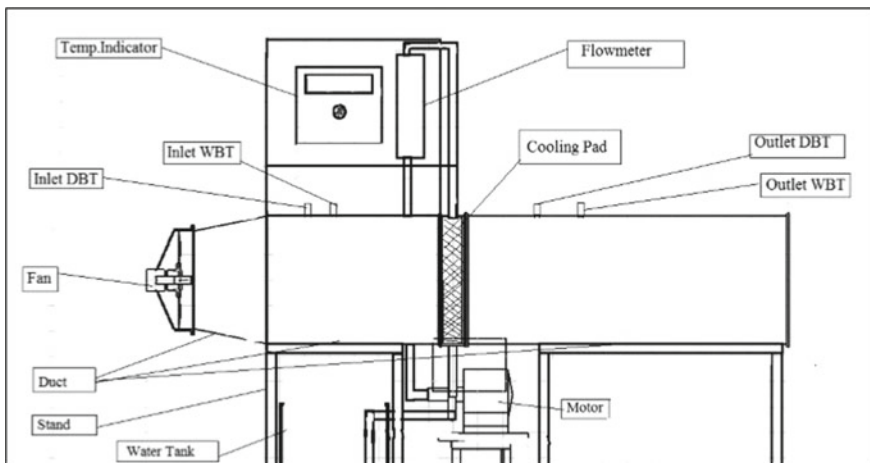


Fig. 1 Schematic of experimental setup

also abaca and sisal were tested under the same condition. Hemp fibers cannot be used in their normal shape because it is difficult to retain the shape after wetting. According to the theory of cooling pad material, either compact or widely spaced bank can be used for the purpose. But due to fabrication limitations of the fixing plate for the pad, widely spaced bank is chosen for the experimental setup. Surface area of pad forms the wetted surface for evaporation of water. Water pump is used to circulate water over the cooling pads. A fan draws hot and dry air over the ropes and water gets evaporated on the surface of the cooling pad. Heat required for evaporation is taken from air as well as water. Hence, air gets cooled and its moisture content gets increased. Makeup water is added in the tank if required after running the unit for a long time. The necessary instrumentation is done for the measurement of different parameters. In order to study the direct evaporative cooling, experimental setup will be fabricated with a facility for cooling efficiency measurement. In this work to compare the performance of DEC system different pad materials like hemp, abaca, and sisal are selected. The proposed pad materials are arranged in the setup to evaluate the performance of pad materials.

The purpose of the present study is to experimentally investigate the performance of direct evaporative cooling with hemp, abaca, and sisal as cooling pads materials. The block diagram of the experimental setup to be developed is given in Fig. 1 The setup includes a tunnel, a blower, rigid pad media, a recirculating pump, nozzles, and a water collecting tank. A connecting piece of the rectangular cross section connects the test section to the blower whereas another end of the test section connects the diffuser. Ambient air can be forced to circulate through the tunnel by a fan. Cooling water can be sprayed from above the test section by nozzles onto the top surface of the cooling pad. The falling water can be collected in the water collecting tank and can be re-circulated through the pump as shown in Fig. 2. A provision can be made for easy changing of the cooling pad of different materials and thicknesses. A number of calibrated thermocouples are fitted to measure dry bulb and wet-bulb temperatures at the inlet and outlet of the test section. The thermocouples are connected to data logger for recording various temperatures. Hotwire anemometer was used for measuring the air flow rate. In order to carry out the experimentation, the setup is validated with the help of cooling pads materials. By using the fabricated experimental setup and hemp, abaca and sisal evaporative cooling pad materials the experimentation was conducted under various mass flow rates. Figure 3 shows the cooling pad with cooling material.

4 Experimental Setup Details

• Duct

Duct selection consists of finding out two parameters:

- To decide dimensions of the duct,
- To find out cross-sectional area of the duct, and

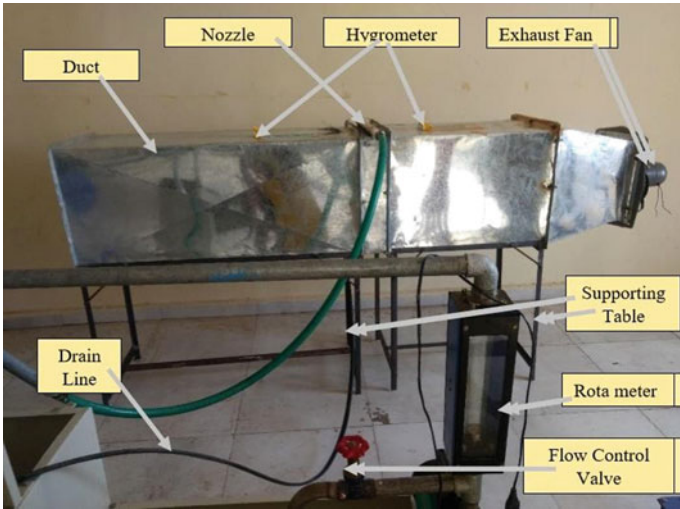


Fig. 2 Actual experimental setup



Fig. 3 Cooling pad material

- Duct height and width are considered to be 500 mm and 500 mm, respectively.

Duct Specifications:

1. To find out cross section area of duct:

$$\begin{aligned} \text{Cross sectional Area of Duct (A)} &= \text{Height (H) X Width (W)} \\ A &= 0.5 \times 0.5 \text{ m}^2 \\ A &= 0.25 \text{ m}^2. \end{aligned}$$

To find out Perimeter of duct:

$$\begin{aligned} &2 \times [(\text{Height}) + (\text{Width})] \\ &2 \times [(0.5) + (0.5)] \\ &2 \text{ m}. \end{aligned}$$

Cooling pads

- **Hemp**

Natural cooling material is hemp, but hemp lowers surface temperature through “evapotranspiration”, which is a process similar to that used by old-fashioned evaporative coolers (“swamp coolers”) for home air-conditioning. On a hot summer day, lawns will typically be 30° cooler than asphalt and a huge 35° cooler than artificial turf. Figure 4 shows the hemp material photograph.

- **Abaca**

The Evaporative Cooling Pad (ECP) is shown in Fig. 5, it is made of abaca from cross-sectional, specially treated flute media capable of absorbing and retaining water to provide the maximum cooling efficiencies. The cellulose media are treated with



Fig. 4 Hemp

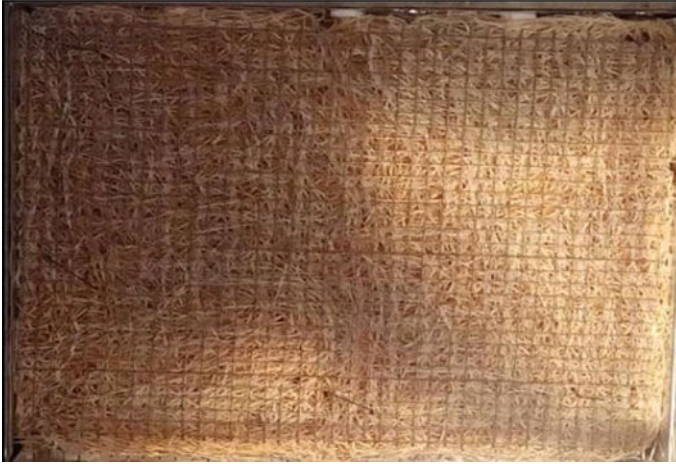


Fig. 5 Abaca

stiffening and wetting agents to provide the cooling without any water carryover. The pads are designed for tropical and subtropical countries, ensures the greatest performance during summer seasons. The abaca pad is crossing corrugated coated with anti-rot, rigidifying, and wetting resins. The pads are made for maximum efficiency, at minimum pressure drop.

- **Sisal**

As shown in Fig. 6, sisal is often considered an environmental “super fiber”. Sisal fabric is made from the fibers in the herbaceous plant of the species *Cannabis sativa*. It has a high-yield crop that produces significantly more fiber per acre than either cotton or flax.

5 Results and Discussion

The results obtained from the experimentations, carried out on the evaporator cooler by the mentioned testing methodology, are presented in the following section. Various graphs are plotted for the study of variation of cooling capacity, variation of cooling effectiveness, study of effect of mass flow rate on cooling capacity, variation in the inlet and outlet DBT, etc.

- **Variation of Effectiveness with Different Air Velocities**

The variation of effectiveness with air velocity is calculated at different mass flow rates of water and for different cooling pad materials. The graphs of effectiveness



Fig. 6 Sisal fibers

were plotted which is shown in Figs. 7 and 8 against air velocity for the study of the variation ineffectiveness for various air velocities.

The experiments were conducted for different cooling pad materials, so in accordance to study of effectiveness on air velocity is evaluated, the Figs. 7 and 8 shows the variation of effectiveness when the experiment was conducted using different air velocity from 1.1 to 2.5 m/s. From that sentence it is clear that among all results the effectiveness for any cooling pad material is more in case of water flow rate is 360 LPH. Especially, if we are considering cooling pad materials, then we get the effectiveness more in case of hemp material as compared to the other two materials.

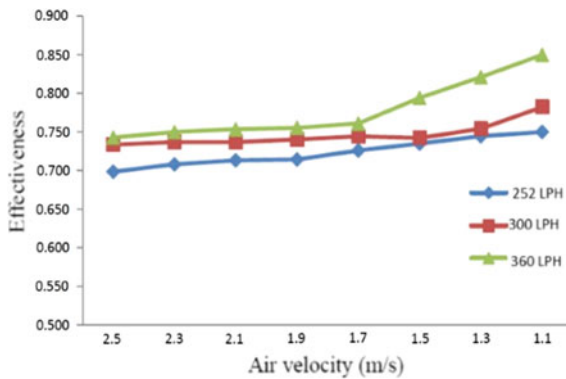


Fig. 7 Variation of effectiveness at different water flow rates for hemp

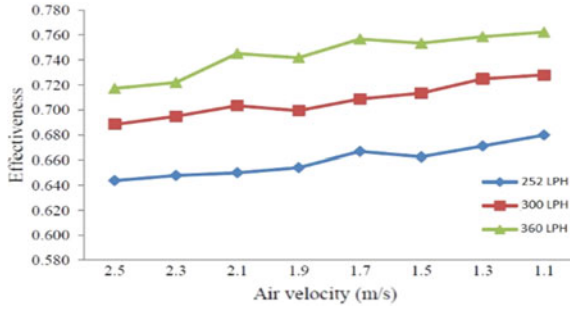


Fig. 8 Variation of effectiveness at different water flow rates for abaca

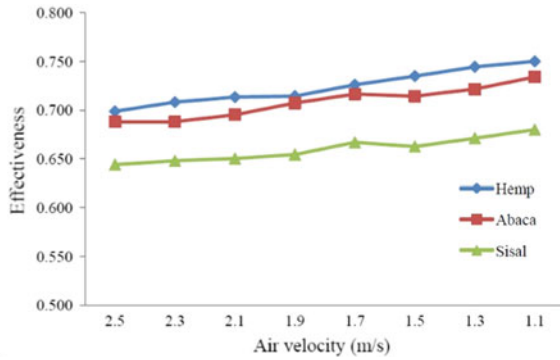


Fig. 9 Variation of effectiveness for different cooling pad material for 252 LPH

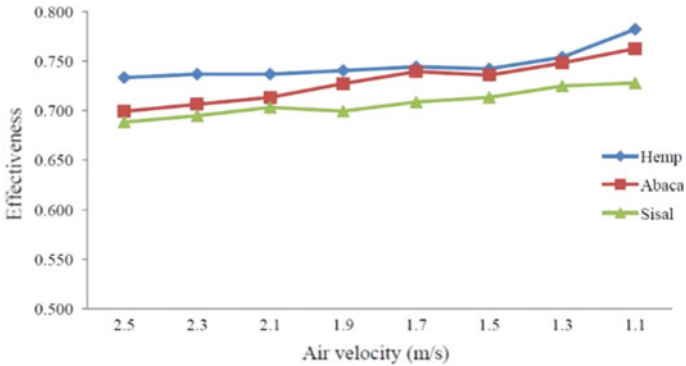


Fig. 10 Variation of effectiveness for different cooling pad materials for 300 LPH

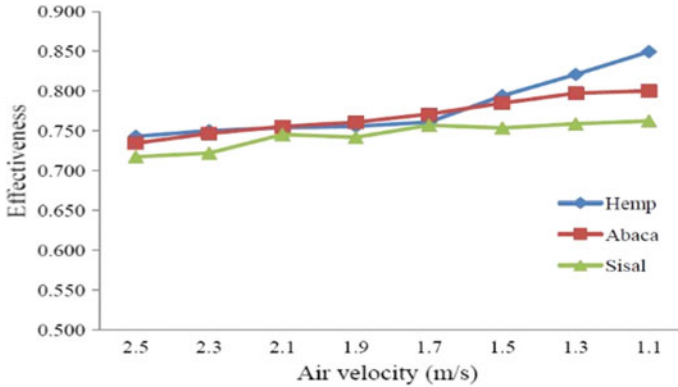


Fig. 11 Variation of effectiveness for different cooling pad materials for 360 LPH

The Figs. 9, 10, and 11 show the variation of effectiveness when the experiment was conducted using different air velocities from 1.1 to 2.5 m/s for the same material with different water flow rates 252 LPH, 300 LPH, and 360 LPH.

The experiments were conducted for different water flow rates, so in accordance to study of effectiveness on air velocity is evaluated, the Figs. 9, 10, and 11 show the variation of effectiveness when the experiment was conducted using different air velocities from 1.1 to 2.5 m/s for the same material with different water flow rates 252 LPH, 300 LPH, and 360 LPH. From the above graphs, it is clear that the effectiveness of hemp material for three different water flow rates is more as compared to two different materials.

6 Conclusion

In this work, direct evaporative cooler has been developed and tested experimentally. The effect of air velocity, water flow rate, different cooling pad material, on cooling capacity, and effectiveness has been evaluated different period of time. The following conclusions have been arrived at from the experimental investigation carried out in the present work on the direct evaporative cooler.

From Figs. 7, 8, 9 10, and 11, we conclude that in the developed direct evaporative cooler, 15–20% effectiveness is more in case of hemp as cooling pad material as compared to the abaca and sisal cooling pad material.

Enhancement in effectiveness is 10–15% more in case water flow rate at 360 LPH in all cooling pad materials as compared to 252 LPH and 300 LPH.

From appendix VII, we conclude the average outlet dry bulb temperature was varying between 240 and 280 °C.

Water consumption of the cooler varies between 252 LPH and 360 LPH depending on the mode of operation and the material used.

References

1. J.K. Jain, D.A. Hindoliya, Experimental performance of new evaporative cooling pad materials. *Sustain. Cities Soc. Mechanical Engineering Department, Ujjain Polytechnic College, Ujjain (M.P.)* 456010, India, pp. 252–256 (2011)
2. M. Malli, R.S. Hamid, et. al., Investigating the performance of cellulosic evaporative cooling pads. *Energy Convers. Manage.* 2598–2603 (2011)
3. D. Metin, K. Cengiz, Y.I. Yildiz, B. Ali, P. Omer, The effects of air velocity on the performance of pad evaporative cooling systems. *Afr. J. Agric. Res.* **6**(7), 1813–1822 (2011)
4. A. Osama et al., Performance evaluation of three different types of local evaporative cooling pads in greenhouses in Sudan. *King Saud University Saudi J. Biol. Sci.* **3**(18), 45–51 (2011)
5. R.S. Khurmi, J.K. Gupta, *Refrigeration and air conditioning*, 5th edn. (Eurasia Publishing House (P) LTD, Ram Nagar, New Delhi, 2011), pp. 467–725
6. I.M. Seth, O.O. Simon, Evaluation of pads and geometrical shapes for constructing evaporative cooling system. *Can. Center Sci. Educ.* **6**(6), 45–53 (2012)
7. T. Abdulrahman, B. Mohammada, B.M. Sohif, Experimental performance of a direct evaporative cooler operating in Kuala Lumpur. *Int. J. Thermal Environ. Eng.* **6**(1), 15–20 (2013)
8. R.K. Kulkarni, S.P.S. Rajput, S.A. Gutte, D.M. Patil, Laboratory performance of evaporative cooler using jute fiber ropes as cooling media. *Int. J. Eng. Res. Appl.* **4**(12), 60–66 (2014)

Mitigation of Carbon Dioxide Gas from a DI Diesel Engine Fuelled with Honge Biodiesel for Agriculture



K. Muralidharan, K. Senthil Kumar, K. Shanmugavel,
S. Lakshmana Kumar, and S. Rajkumar

Abstract This paper investigates the mitigation level of carbon dioxide (CO₂) gas released from a direct injection (DI) diesel engine fuelled with honge biodiesel fuel suitable for agriculture. This study involves the use of thermal barrier coating on diesel engine combustion chamber components so that heat loss through the coolant can be kept minimum thereby improving engine combustion and emission characteristics when honge biodiesel blends are used as an alternate fuel. Experimental results depicted lesser BSFC with a significant reduction of emissions CO, HC, smoke, and slight increase of NO_x and CO₂ gas for fuels tested in the coated engine. Of various biofuel blends tested, blend B15 showed a significant reduction in CO of about 50%, HC of 26.5%, smoke of 20% with slightly higher values of 2.37% NO_x, and 5.17% of CO₂ at 230 bar in the coated engine at full load condition compared with an uncoated engine. The presence of oxygen and high in-cylinder temperature condition prevailed in coated engine enhances the combustion process in biodiesel blend B15 resulting in improved combustion at this operating condition. A retrofit kit was developed to separate CO₂ gas from engine exhaust through chemical absorption technique. The separated CO₂ in gaseous form was stored in cylinders.

Keywords Honge oil · Blend · Coating · Combustion · CO₂ gas separation

Symbols and Abbreviations

NaOH Sodium hydroxide

KOH Potassium hydroxide

K. Muralidharan (✉) · K. Shanmugavel · S. Lakshmana Kumar · S. Rajkumar
Department of Mechanical Engineering, Sona College of Technology, Salem, Tamil Nadu
636005, India
e-mail: Muralidharan_dr@sonatech.ac.in

K. Senthil Kumar
Department of Mechanical Engineering, Adhiyamaan College of Engineering, Hosur, Tamil
Nadu, India

BSFC	Brake-specific fuel consumption
CO	Carbon monoxide
CO ₂	Carbon dioxide
NO _x	Oxides of nitrogen
HC	Hydrocarbon
D	Diesel
B5	[5% by volume of biodiesel + 95% by volume of diesel]
B10	[10% by volume of biodiesel + 90% by volume of diesel]
B15	[15% by volume of biodiesel + 85% by volume of diesel]
B20	[20% by volume of biodiesel + 80% by volume of diesel]
B25	[25% by volume of biodiesel + 75% by volume of diesel]
B30	[30% by volume of biodiesel + 70% by volume of diesel]
C	Coated engine
CA	Crank angle
DI	Direct injection
cSt	Centi stoke
MEA	Monoethanolamine
PZ	Piperazine

1 Introduction

Fuels derived from biomass seems to be the most promising solution to resolve the global energy demand, to avoid the dwindling of fossil fuels, fuel price hike, and to control the vehicular pollution growth. India is very rich in biomass besides having more forests and wastelands as indicated in Biomass energy magazine by Jain [1]. Ease of availability and more economy of honge vegetable oil makes it to choose as the alternative fuel for diesel. Oil content in honge seed is around 27–39% as specified by Murugesan et al. [2].

Biodiesel possesses higher viscosity compared with diesel fuel, so higher injection pressure causes better fuel–air mixing, improves atomization, and enhances combustion process. Many studies showed that the influence of injection pressure increases the amount of fuel delivered during the delay period due to its high injection rate. This tends to improve fuel and air mixing and causes better atomization resulting in improved combustion process at high injection pressures as observed by the authors Tashtoush et al. [3], Purushothaman and Nagarajan [4].

Hasimoglu et al. [5], Haldar [6] coated engine components with yttria-stabilized zirconia (YSZ) over nickel chromium aluminium alloy (NiCrAl) bond coat for a thickness of 500 μm and examined the behaviour of biodiesel and its blends as fuel supplements. They noticed slight improvements in engine performance and emission characteristics. Hejwowski and Weronki [7] in their research work recommended thermal barrier coating to a thickness of slightly below 500 μm for (YSZ) and bond coat for improvement of diesel engine performance.

Carbon Capture and Sequestration (CCS) is seen as a crucial climate protection technology for coal-rich countries like India having potential in massively reducing CO₂ emission as compared to any other existing technology. As third-largest producer of coal and fourth-largest greenhouse gas (GHG) emitter, India's total emissions are 7% of global emissions and is increasing at 4.5% per annum. India's current and expected future emissions are sufficiently massive to have an adverse effect on global mitigation efforts as observed by Gupta and Paul [8].

In this work, the thermal barrier coating is applied on combustion chamber components, namely, cylinder head, piston crown, inlet and exhaust valves of a Direct Injection (DI) diesel engine for an overall thickness of 200 μm to evaluate the behaviour of honge biodiesel with the influence of injection pressure over the engine combustion and emission characteristics.

2 Materials and Methods

2.1 Transesterification

The most efficient method of producing biodiesel is transesterification process, where triglyceride (oil) is made to react with methyl alcohol in the presence of alkyl catalyst (sodium, potassium carbonates, NaOH, KOH) to form methyl ester and glycerol. High yield of honge methyl ester or biodiesel can be obtained through the use of alkyl catalysts as specified by Murugesan et al. [2].

2.2 Test Fuel Properties

Viscosity is the major problem for the biodiesel, it imposes a lot of problems for engine, in comparison of diesel (2.87 cSt) the viscosity of biodiesel (38 cSt) is much higher, in raw oil it is found to be 58.54 cSt which is reduced to 38 cSt by transesterification process by virtue of removal of fats in the form of glycerol, viscosity of the esters up to 30% blends can be used in an unmodified engine. The honge methyl ester produced was blended with diesel in various proportions from 0 to 30% by volume (B5, B10, B15, B20, B25, and B30) with the help of a magnetic stirrer. The blends were mixed continuously to achieve stable property values.

2.3 Error Analysis

An uncertainty analysis was performed using the method described by Holman [9]. Using the calculation procedure, the total uncertainty for the whole experiment is obtained to be $\pm 2.28\%$.

2.4 Thermal Barrier Coating

Thermal barrier coating is usually laid by means of plasma spray coating technique using plasma gun Metco 3 MB in the presence of atmosphere. In this experimental study, the piston surface, cylinder head, inlet and exhaust valves of DI diesel engine were coated with yttria-stabilized Zirconia ($Y_2O_3ZrO_2$) ceramic material for over a thickness of 150 μm above the nickel chromium aluminium alloy (NiCrAl) as a bond coat with a total thickness of 200 μm .

2.5 Engine Operating Conditions

The experiments were conducted on twin-cylinder four-stroke, naturally aspirated, direct injection (DI) diesel engine of rated power 5 BHP. The engine was coupled to an eddy current dynamometer to control engine speed and load. The output shaft of eddy current dynamometer is fixed to electrical loading. Engine cooling water inlet temperature, cooling water outlet temperature, and engine exhaust temperature were measured using *K*-type thermocouples. The honge biofuel was blended with diesel in the range from 5 to 30% with an incremental step of 5% by volume were used to explore the engine performance under different fuel injection pressures (210, 220, 230, and 240 bar) in full load. Under these operating conditions, the engine performance is evaluated with thermal barrier coated diesel engine operated in constant engine speed of 1500 rpm and the test results acquired for honge biodiesel blends and diesel fuel have been compared against uncoated diesel engine. All test runs were conducted on the test-bench at various engine operating conditions. In each test, engine speed and load were recorded. The combination of all test is included engine setting at full load in rated speed were recorded for each injection pressure. Each test was repeated three times. The values given in this study are the average of these three results.

2.6 Chemical Absorption Technique for CO₂ Gas Separation

This project involves the separation and storage of carbon dioxide gas from the diesel engine exhaust through chemical absorption technique. The amine-based bi-solvent has the tendency to absorb CO₂ gas at 35 °C and desorbs CO₂ gas at 150 °C. Stainless steel material has been used to develop carbon capture and storage test rig in lab scale. A specially designed heat exchanger would be used as reboiler, which would improve the overall efficiency of the plant. A retrofit CO₂ separation system has been used in this research work to collect CO₂ gas from the engine as indicated in Fig. 1. The system includes an absorber column, waste heat recovery heat exchanger, amine tank, condenser, and gas storage facility.

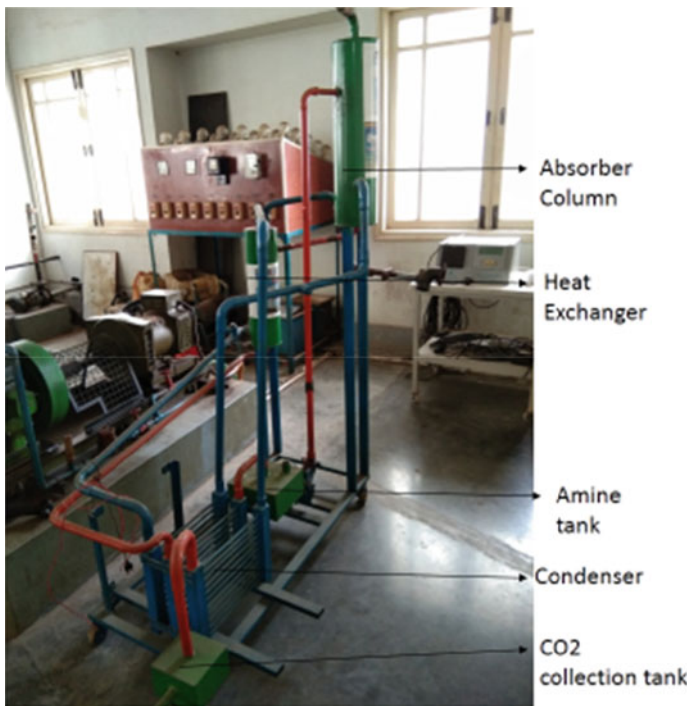


Fig. 1 Schematic of retrofit kit developed based on chemical absorption technique

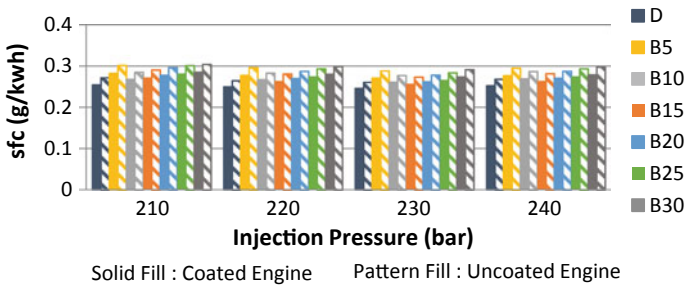


Fig. 2 Variation of BSFC versus injection pressure

3 Results and Discussion

3.1 Brake Specific Fuel Consumption (BSFC)

The increase of fuel injection pressure up to 230 bar enhances fuel spray characteristics forming finer spray and thereby improve atomization and combustion resulting in lesser BSFC as represented in Fig. 1 and agreed by authors Agarwal and Agarwal [10]. The high operating temperature condition prevailed in the coated engine promotes fuels to attain self-ignition temperature rapidly and makes the combustion complete resulting in lesser specific fuel consumption than the uncoated engine in the percentage of 5.63, 6.16, 5.91, 5.80, 5.87, 5.96, and 6.07 for fuels D, B5, B10, B15, B20, B25, and B30 at 230 bar under full load as represented in Fig. 2 pointed out by Hazar [11]. Blend B15 consumes slightly higher BSFC of about 4.47% compared with diesel at 230 bar injection pressure and shows a closer trend with diesel at full load.

3.2 Carbon Monoxide Emission (CO)

Coated engine exhibited lesser CO values in percentage of about 25% for D followed by 26.67% for B5, 36.36% for B10, 40% for B15, 28.57% for B20, 30.77% for B25, and 33.33% for B30 at 230 bar pressure. The high cylinder wall temperature prevailed in the coated engine increases the combustion temperature which enhances combustion process resulting in reduced emission values as compared with uncoated engine proposed by Purushothaman and Nagarajan [4], Agarwal and Agarwal [10], Hazar [11]. The lowest value of CO emission was observed at 230 bar pressure of about 0.06% for D and 0.03% for B15 in the coated engine as represented in Fig. 3.

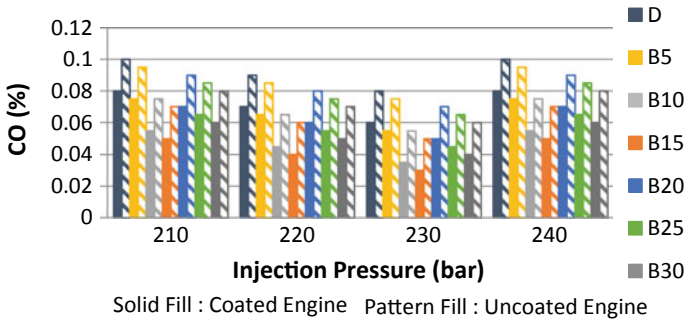


Fig. 3 Variation of CO emission versus injection pressure

3.3 Unburnt Hydrocarbon Emission (HC)

The HC emission level changes significantly with variation in fuel injection pressure as shown in Fig. 3. Increase of fuel injection pressure tends to emit relatively lesser values of HC emission up to 230 bar for all the fuels tested and shows slightly higher emission on further increase at full load. Relatively lesser emission values are observed in coated engine especially at 230 bar for all of the tested fuels in the percentage of 10.53% for *D* followed by blends 10.81, 12.5, 13.8, 11.43, 11.76, 12.12 for B5, B10, B15, B20, B25, B30 at full load since the high in-cylinder temperature of engine cylinder together with improved atomization at this injection pressure may be the cause for complete combustion for diesel and biodiesel blends. At 230 bar pressure, diesel and B15 exhibits the lowest HC emission of 34 and 25 ppm in full load condition. This is because at this pressure finer fuel spray characteristics may improve atomization process and the high cylinder temperature in coated engine offers slightly earlier peaking characteristics for biodiesel blends resulting in more heat release rate as shown in Fig. 4.

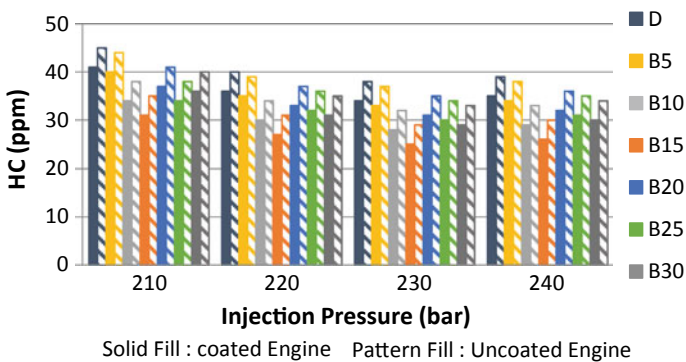


Fig. 4 Variation of HC emission versus injection pressure

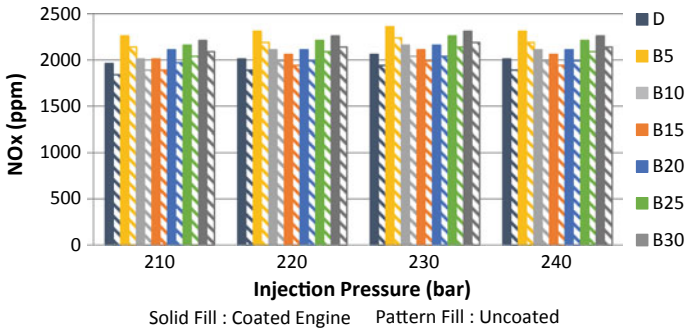


Fig. 5 Variation of NO_x emission versus injection pressure

3.4 Oxides of Nitrogen (NO_x)

Increase of fuel injection pressure increases NO_x emission up to 230 bar as shown in Fig. 5 and decreases thereafter. This may be due to the high injection rate of fuel, which forms more air–fuel mixture resulting in improved atomization and combustion at 230 bar pressure. Higher emission of NO_x in the percentage of 5.82%, 5.08, 5.56, 5.69, 5.56, 5.31, and 5.19 for fuels D, B5, B10, B15, B20, B25, and B30 compared with the uncoated engine due to the improved fuel spray characteristics and improved combustion phenomenon produced at 230 bar pressure as reported by Devan and Mahalakshmi [12].

3.5 Smoke Emission

The coated engine exhibits lesser smoke emission than the uncoated engine in the percentage of 9.09, 9.38, 10.71, 11.11, 9.68, 10.35, and 10.71 for fuels diesel and biodiesel blends B5, B10, B15, B20, B25, and B30. The high combustion chamber temperature in coated engine promotes complete combustion at this injection pressure compared with limited temperature condition in the uncoated engine. Diesel produces higher smoke emission than biodiesel blends due to the presence of oxygen in biodiesel blends in addition to air–fuel mixture improves the combustion process and forming comparatively lesser emission. B15 showed lower values of smoke at 230 bar than other blends because the slightly higher viscosity, density, and its oxygen content in fuel aid for better atomization and improved combustion. Compared with diesel at 230 bar blend B15 emits lesser smoke value of 20% at full load is shown in Fig. 6.

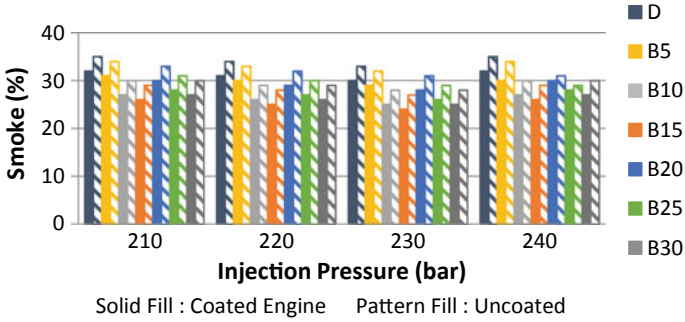


Fig. 6 Variation of smoke emission versus injection pressure

3.6 Carbon Dioxide Emission

The increase of fuel injection pressure from 210 to 230 bar caused increasing rate of CO₂ emission at all loads, which may be due to better fuel spray characteristics in all fuels tested as prescribed by Purushothaman and Nagarajan [4], Agarwal and Agarwal [10]. The coated engine at 230 bar produces an increased amount of CO₂ than the uncoated engine in the percentage of 7.27, 7.55, 7.02, 6.90, 7.02, 7.14, and 7.41 for fuels D, B5, B10, B15, B20, B25, and B30 at full load observed from Fig. 6 which may be due to the finer fuel droplets produced at this injection pressure and the high operating temperature condition prevailed in coated engine improves the atomization process resulting in better combustion. Blend B15 showed higher values of CO₂ emission at all loads than other fuels due to its inherent oxygen availability and slightly higher viscosity, which may enhance the combustion process as shown in Fig. 7.

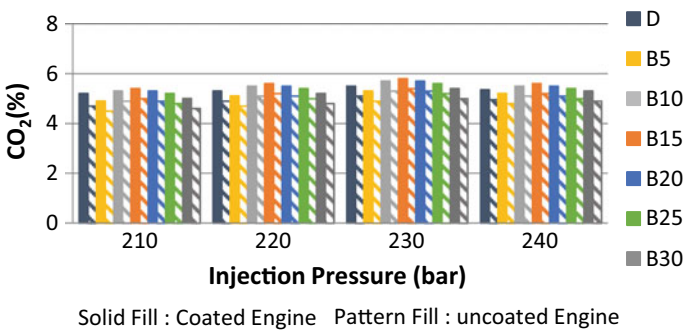


Fig. 7 Variation of CO₂ emission versus Injection pressure

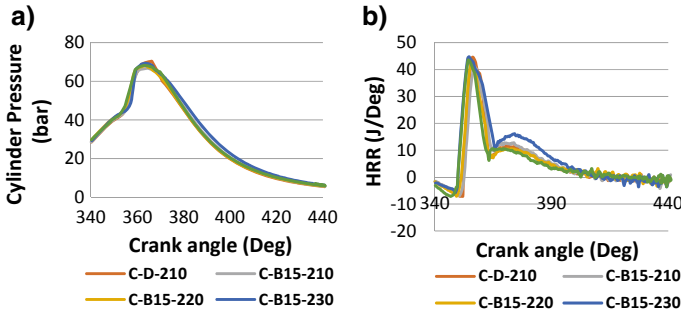


Fig. 8 a and b Variation of cylinder pressure and heat release rate versus crank angle

3.7 Cylinder Peak Pressure

It was noticed from Fig. 8a that the coated engine exhibits higher peak cylinder pressure for diesel and biodiesel blend B15 at full load in the percentage of 5.37 for diesel, 5.62, 5.83, 5.74, and 5.85 for B15 at 210, 220, 230, and 240 bar. Biodiesel blend B15 experiences an earlier start of combustion due to its shorter ignition delay than diesel and it may be due to the excess oxygen available in fuel along with higher working temperature in the coated engine.

Diesel exhibits higher HRR of about 6.76% than uncoated readings and biodiesel blend B15 shows higher HRR of 7.55% at 210 bar, 6.83% at 220 bar, 10.26% at 230 bar, 9.8% at 240 bar as represented in Fig. 8b. Biodiesel blend B15 at 230 bar injection pressure exhibits slightly lower peak cylinder pressure of about 1.41% than diesel fuel at an injection of 210 bar in the coated engine due to its lower calorific value. The occurrence of maximum heat release rate was about 2.5° CA BTDC for diesel at 210 bar and blend B15 at 230nbar experiences earlier heat release at 4° CA BTDC due to its rapid combustion process in the coated engine. The increase of fuel injection pressure in biodiesel blend from 210 to 230 bar caused an increase in the heat release rate of about 8% in the coated engine and 5.35% in the uncoated engine which may be the cause of fine fuel spray and increased spray angle causes impingement of fuel droplets on combustion chamber wall and the high cylinder temperature in insulated engine vaporizes the fuel quickly forming a homogeneous mixture for the initial stage of combustion followed by diffusion combustion as agreed by Purushothaman and Nagarajan [4].

4 Conclusion

In this study, a twin-cylinder diesel engine fuelled with honge biodiesel, a nonedible oil feedstock widely available in India and highly suitable for agriculture has been investigated. The piston top surface, cylinder head, and valves of a diesel engine were

coated with ceramic materials. The test results acquired for honge biodiesel blends and diesel fuel were compared with the uncoated engine. Biodiesel blend B15 seems to be better than diesel fuel at 230 bar pressure. Engine was coupled with the retrofit CO₂ gas separation unit and the following observations are made:

- Lesser BSFC values are attained for diesel of 3.15% and blend B15 of 5.76% in the coated engine.
- Drastic reduction in CO emission of 25% for diesel and 40% for biodiesel blend B15.
- Significant reduction in HC emission for diesel of 17.07 and 17.14% for biodiesel blend B15.
- Slightly higher CO₂ emission for diesel and biodiesel blend B15 of about 5.45, 6.90%.
- Significant reduction of smoke emission was achieved for diesel and biodiesel blend B15 of about 6.25, 7.69%.
- Improved peak heat release rate of 5.21, 4.65% for diesel and blend B15 in the coated engine and 3.53, 5% in the uncoated engine when compared with 210 bar injection pressure.
- The occurrence of peak HRR for B15 is earlier around 2° CA before diesel fuel in coated engine at 230 bar pressure.
- Of various biofuel blends tested, blend B15 showed a significant reduction in CO of about 50%, HC of 26.5%, smoke of 20%, and slightly higher values of 2.37% NO_x at 230 bar in the coated engine at full load condition.
- The novel 30% by weight of MEA-PZ bi-solvent study resulted in CO₂ gas absorption capacity of 85% at minimum gas velocity, high cyclic capacity, and high regeneration rate.

Acknowledgments I would like to acknowledge the Management, Secretary, Principal, and Head of Department of Mechanical Engineering, Sona College of Technology, Salem-636005 for providing all the institutional help and support for this research work.

References

1. V.K. Jain, Bioenergy India. Q. Mag. UNDP-GEF Biomass Power Proj. Minis. New Renew. Energy, Gov. India **9**(10), 1–40 (2011)
2. A. Murugesan, C. Umarani, T.R. Chinnusamy, M. Krishnan, R. Subramanian, N. Neduzchezain, Production and analysis of bio-diesel from non-edible oils-a review. Renew. Sustain. Energy Rev. **13**, 825–834 (2009)
3. M. Tashtoush, I. Mohamad, A. Widyan, M. Albatayneh, Factorial analysis of diesel engine performance using different types of biofuels. J. Env. Manag. **84**, 401–411 (2007)
4. K. Purushothaman, G. Nagarajan, Effect of injection pressure on heat release rate and emissions in CI engine using orange skin powder diesel solution. Energy Convers. Manag. **50**, 962–969 (2009)

5. C. Hasimoglu, M. Ciniviz, I. Ozsert, Y. Icingur, A. Parlak, M.S. Salman, Performance characteristics of a low heat rejection diesel engine operating with biodiesel. *Renew. Energy* **33**, 1709–1715 (2008)
6. S.K. Haldar, B.B. Ghosh, A. Nag, Utilization of unattended Putranjivaroxburghii non-edible oil as fuel in diesel engine. *Renew. Energy* **34**, 343–347 (2009)
7. T. Hejwowski, A. Weronki, The effects of thermal barrier coatings on diesel engine performance. *J. Vacuum* **65**, 427–432 (2002)
8. A. Gupta, A. Paul, Carbon capture and sequestration potential in India: a comprehensive review. *Energy Procedia* **160**, 848–855 (2019)
9. J.P. Holman, *Experimental Methods for Engineers*, 7th edn. McGraw-Hill International Edition (2001)
10. D. Agarwal, A.K. Agarwal, Performance and emissions characteristics of Jatropa oil (preheated and blends) in a direct injection compression ignition engine. *Appl. Therm. Eng.* **27**, 2314–2323 (2007)
11. H. Hazar, Cotton methyl ester usage in a diesel engine equipped with insulated combustion chamber. *Appl. Energy* **87**(1), 134–140 (2010)
12. P.K. Devan, N.V. Mahalakshmi, Performance, emission and combustion characteristics of poon oil and its blends in a DI diesel engine. *Fuel* **88**, 861–867 (2009)
13. T.M. Ghassan, M.I. Al-Widyan, A.M. Albatayneh, Factorial analysis of diesel engine performance using different types of biofuels. *J. Environ. Manage.* **84**, 401–411 (2007)

Reduction of Greenhouse Gases from a Coated Diesel Engine Fuelled with Honge Biodiesel for Sustainable Environment



K. Muralidharan, V. L. Raja, S. Lakshmana Kumar, K. Shanmugavel, and R. Dhanasekaran

Abstract In this research work, the impact of thermal barrier coating on combustion and gas emissions in a diesel engine fuelled with honge biodiesel fuel is examined. The engine combustion chamber components including inlet and exhaust valves, cylinder head, and piston crown were coated with YSZ ceramic material over nickel aluminium alloy bond coat for 250 μm thickness. Test results exhibited that in the coated engine, fuel blend B15 emitted significant reduction in carbon monoxide gas, unburnt hydrocarbon gas, smoke emission with a slight increase of NO_x and CO_2 gaseous emission than other fuels tested. At lower loads, honge fuel blend B15 showed a drastic reduction in CO gas emission of 18.65%, HC emission of 17.24%, smoke gas reduction of 29% with a slight increase in NO_x emission of 5.38% and CO_2 gas of 6.80% in injection advance of 27° crank angle BTDC. At higher loads, fuel B15 experienced emission reduction in CO of 10%, HC of 10.4%, smoke of 9.85% and slight increase in NO_x gas of 2.94% and CO_2 gas of 4.60%. Diesel posed higher HRR of 46.25 J/deg and higher cylinder peak pressure of 71.456 bar followed by B15 blend of HRR 43.25 J/deg, peak cylinder pressure 67.33 bar in an injection advance. Engine exhaust gases are passed into a retrofit CO_2 capture kit developed to separate CO_2 gas from vehicle exhaust through chemical absorption technique. Amine-based chemical solvent has been employed to separate CO_2 gas.

Keywords Honge biodiesel · Coating · Combustion

K. Muralidharan (✉) · S. Lakshmana Kumar · K. Shanmugavel
Department of Mechanical Engineering, Sona College of Technology, Salem, Tamil Nadu
636005, India
e-mail: Muralidharan_dr@sonatech.ac.in

V. L. Raja
Department of Mechanical Engineering, Muthyammal Engineering College, Rasipuram, Tamil
Nadu 637408, India

R. Dhanasekaran
Department of Mechanical Engineering, Guru Nanak Institute of Technology, Hyderabad,
Telangana, India

Symbols and Abbreviations

NaOH	Sodium hydroxide
KoH	Potassium hydroxide
BSFC	Brake-specific fuel consumption
CO	Carbon monoxide
CO ₂	Carbon dioxide
NO _x	Oxides of nitrogen
HC	Hydrocarbon
D	Diesel
B5	[5% by volume of biodiesel + 95% by volume of diesel]
B10	[10% by volume of biodiesel + 90% by volume of diesel]
B15	[15% by volume of biodiesel + 85% by volume of diesel]
B20	[20% by volume of biodiesel + 80% by volume of diesel]
B25	[25% by volume of biodiesel + 75% by volume of diesel]
B30	[30% by volume of biodiesel + 70% by volume of diesel]
C	Coated engine
CA	Crank angle
DI	Direct injection
cSt	Centi stoke
MEA	Monoethanolamine
PZ	Piperazine.

1 Introduction

Vegetable oils have been gained universal attention as an alternative energy source because they are environment friendly and renewable in nature. Use of non-edible plant oils seems to be technically feasible and more economic for developing countries [1]. Transesterified biofuel possesses lower viscosity, less flash and fire point, and improved fuel properties compared with unprocessed vegetable oil. The authors observed that lower blends of biodiesel say B20, 20% biodiesel along with 80% of diesel can be utilized as suitable biodiesel blend for diesel engine for improved performance and emission characteristics [2].

Many studies showed higher fuel injection rate tends to improve fuel and air mixing and causes better atomization resulting in improved combustion process at high injection pressures [3–5]. The effect of injection timing on performance and emission are analysed in diesel engine and revealed that injection retard causes reduced NO_x and CO₂ emissions for lower blends of biodiesel over the entire range of engine operation [4]. The influence of YSZ ceramic coating for a thickness of 300 μm over combustion chamber components revealed lesser BSFC with a significant reduction in emissions of CO, HC, smoke with a slight increase of NO_x and CO₂ for diesel and biodiesel fuels [6].

Post-combustion capture using amine-based chemical absorption can be a feasible approach for carbon capture in the cement plant. A 29% of reduction can be achieved in the specific energy consumption related to the solvent regeneration compared with the tests involving a conventional flue gas from fossil fuel power plants as studied by [7].

This research focuses to study the sole effect of injection timing period on the use of the fuel blend honge methyl ester and diesel in thermal barrier coated diesel engine.

2 Materials and Methods

2.1 Transesterification

Honge methyl ester was produced in lab practice by base-catalyzed transesterification process, where methanol reacts with NaOH and forms methyl ester and glycerol. Honge oil seeds were collected from local farmers in Tamil Nadu and the crude honge oil was extracted mechanically with a crushing machine.

2.2 Test Fuel Properties

Honge methyl ester poses high viscosity in comparison of diesel (2.87 cSt) the viscosity of bio-diesel (38 cSt) is much higher, in raw oil it is found to be 58.54 cSt which is reduced to the 38 cSt by transesterification process by virtue of removal of fats in the form of glycerol. The honge methyl ester produced was blended with diesel in various proportions from 0 to 30% by volume (B5, B10, B15, B20, B25, and B30) with the help of a magnetic stirrer.

2.3 Error Analysis

An uncertainty analysis was performed using the method described by Holman [8]. Using the calculation procedure, the total uncertainty for the whole experiment is obtained to be $\pm 2.28\%$.

2.4 Thermal Barrier Coating

In this experimental study, the piston surface, cylinder head, inlet and exhaust valves of DI diesel engine were coated with yttria-stabilized zirconia ($Y_2O_3ZrO_2$) ceramic material for over a thickness of 200 μm on nickel chromium aluminium alloy (NiCrAl) as a bond coat with a total thickness of 250 μm .

2.5 Engine Operating Conditions

The engine used in this experiment was a twin-cylinder four-stroke, naturally aspirated, direct injection (DI) diesel engine. The engine was coupled to an eddy current dynamometer to control engine speed and load. The dynamic fuel injection timing was tuned to 27° BTDC (before top dead centre) from standard injection timing of 23° CA BTDC. The engine speed was kept fixed at 1500 rpm. The emissions of HC, CO, NO_x and CO_2 were measured with a portable digital multi-gas analyser (NETEL).

2.6 Chemical Absorption Technique for CO_2 Gas Separation

This project involves the absorption and storage of carbon dioxide gas from the diesel engine exhaust through chemical absorption system. The amine-based bi-solvent has the tendency to absorb CO_2 gas at 35 °C and desorbs CO_2 gas at 150 °C. Stainless steel material has been used to develop carbon capture and storage test rig in lab scale. A specially designed heat exchanger would be used as reboiler, which would improve the overall efficiency of the plant by recovering waste heat from the engine exhaust gas. A retrofit CO_2 separation system has been used in this research work to collect CO_2 gas from engine as indicated in Fig. 1. The system includes an absorber column, waste heat recovery heat exchanger, amine tank, condenser, and gas storage facility.

3 Results and Discussion

3.1 Carbon Dioxide Emission (CO_2)

The influence of fuel injection advance of about 4° CA before 23° CA BTDC enhanced ignition delay period and forming more fuel–air accumulation for initial stages of combustion and resulting in more heat release rate than other injection timings and produces more amount of CO_2 [9, 10]. Compared with injection timing

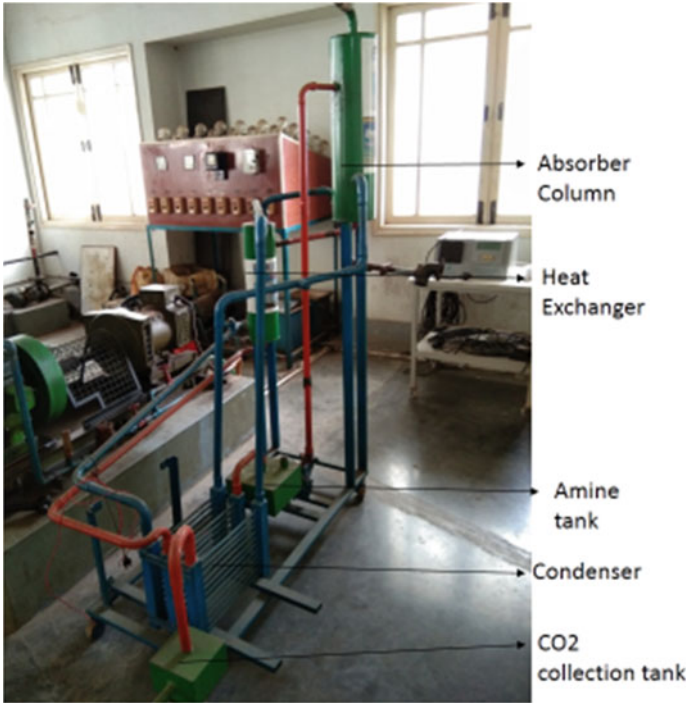


Fig. 1 Schematic of retrofit kit developed based on chemical absorption technique

of 23° CA BTDC, fuel injection at 27° CA BTDC imparts higher CO₂ emission in the percentage of 3.92 for diesel, 3.84 for B5, 3.64 for B10, 3.57 for B15, 3.64 for B20, 3.70 for B25, and 3.64 for B30 in full load. Fuels D, B15 exhibited CO₂ emission of 2.3, 2.8% at low load and 5.1, 5.6% at full load condition in injection timing of 27° CA BTDC as shown in Fig. 2.

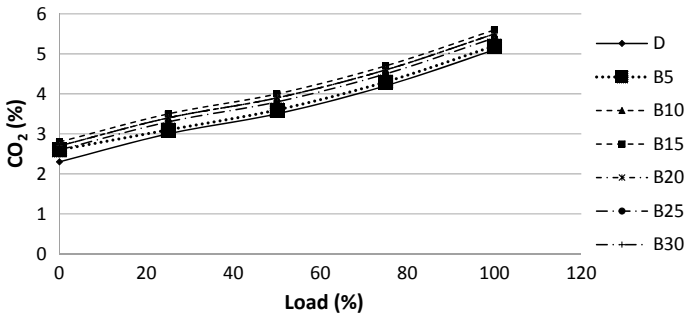
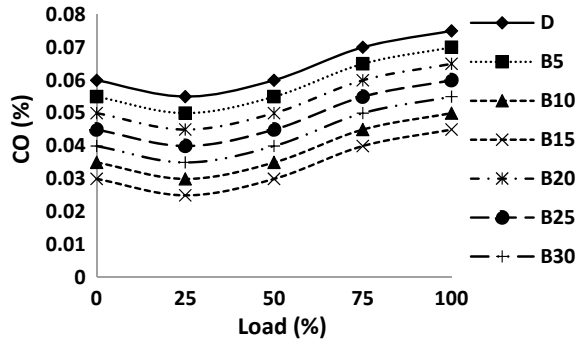


Fig. 2 CO₂ emission versus load at 27° CA BTDC

Fig. 3 CO emission versus load at 27° CA BTDC



3.2 Carbon Monoxide Emission (CO)

Lowest CO emission was observed for B15 in order of 0.03, 0.025, 0.03, 0.04, 0.045% at loads 0, 25, 50, 75, 100% for B15 than other fuels tested as shown in Fig. 3. The high operating temperature prevailing in the coated engine causes early peaking characteristics and increases the combustion process resulting in complete combustion than the uncoated engine. Injection advance resulted in reduced CO emission of 18.65% in part loads and 10% in peak loads for B15 compared with standard injection timing. This is because at part loads, the air–fuel mixture was lean since the availability of oxygen is more and hence the formation of CO is also low due to more complete oxidation of biodiesel as compared to diesel [11]. At higher loads, fuel–air mixture was rich since the presence of fuel is more in mixture causing incomplete combustion resulting in an increase of CO at high loads for all fuels [12].

3.3 Unburnt Hydrocarbon Emission (HC)

Compared with diesel, B15 shows HC reduction of the order of 40% at part loads and 30% in peak loads. Lowest value of HC emission was observed for B15 of the order of 11 ppm at 0% load, 15 ppm 25% load, 19 ppm at 50% load, 24 ppm at 75% load, and 28 ppm at 100% load as indicated in Fig. 4. Compared with 23° CA, 4° CA injection advance cause HC reduction for B15 in order of 21.43, 16.67, 13.63, 11.11, 9.68% in loads 0, 25, 50, 75, 100%. This injection timing offers additional time for fuel–air mixing rate due to earlier fuel injection thereby producing earlier high heat release rate before the TDC and ensures improved combustion resulting in lesser unburnt HC emission [9].

Fig. 4 HC emission versus load at 27° CA BTDC

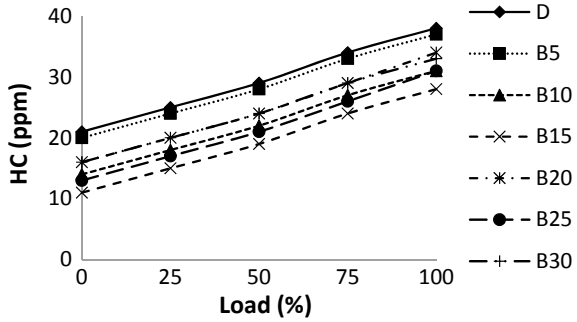
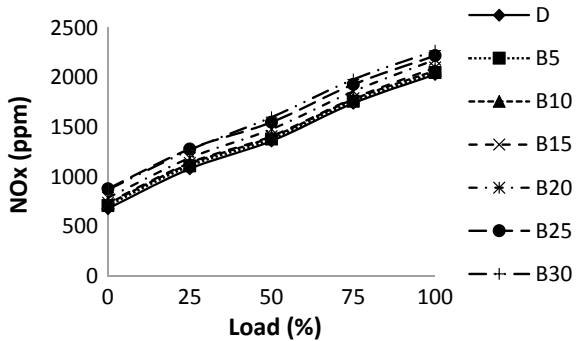


Fig. 5 Variation of NO_x emission versus injection pressure



3.4 Oxides of Nitrogen (NO_x)

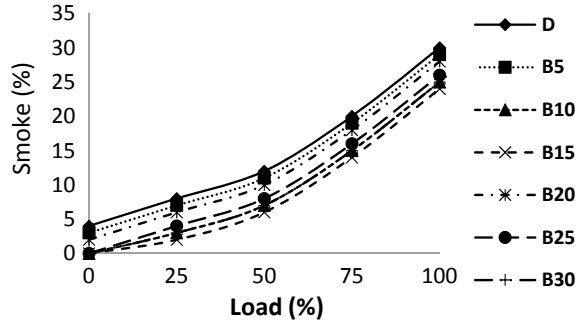
Compared with diesel, B15 shows higher NO_x of the order of 5.55% at part loads and 2.80% in peak loads.

Injection advance shows increase in NO_x at the rate of 7.43, 4.82, 3.9, 3.5, 2.38% in loads 0, 25, 50, 75, 100% for B15 as shown in Fig. 5. It was observed that earlier fuel injection caused an increase of ignition delay period allowing sufficient time for fuel–air mixing rate resulting in more heat release rate during earlier stages of combustion. This enhances the combustion process of all fuels [12]. Moreover, less heat rejection in the coated engine caused higher cylinder temperature resulting in more NO_x.

3.5 Smoke Emission

It was noticed from Fig. 6 that increase in engine load tends to increase smoke emission. Lowest value of smoke emission was observed in 4° CA injection advance for B15 of the order of 0, 2, 6, 14, 24% at loads 0, 25, 50, 75, 100%. Compared with 23° CA, 4° CA injection advance cause smoke reduction for B15 in order of 50, 25,

Fig. 6 Smoke versus load at 27° CA BTDC



12, 7.7% in loads 0, 25, 50, 75, 100%. Smoke formation mainly occurs in the fuel-rich zone of the engine cylinder especially at high temperature and pressure in the diffusive side of combustion. B15 compared with diesel, B15 shows a smoke reduction of the order of 75% at part loads and 33.33% in peak loads due to the increase of oxygen percentage in diesel resulting in more complete and stable combustion than diesel as shown in Fig. 6 [2].

3.6 Heat Release Rate (J/Degree)

It was found from Fig. 7 diesel experiences the maximum amount of heat release rate than biodiesel blend B15 due to its higher calorific value. The coated engine exhibits higher HRR of 46.25 J/deg for diesel, 43.25 J/deg for B15. The occurrence of Peak HRR was earlier around 1.5° CA for B15 than diesel at 27° CA BTDC. Compared with 23° CA, diesel posed higher HRR of 3.67%, B15 4.92% at injection advance of 4° CA in the coated engine. It can be seen that blend B15 experiences earlier peaking characteristics due to high combustion chamber wall temperature in the coated engine which vaporizes the fuel quickly and shortens the ignition delay

Fig. 7 HRR versus load at 27° CA BTDC

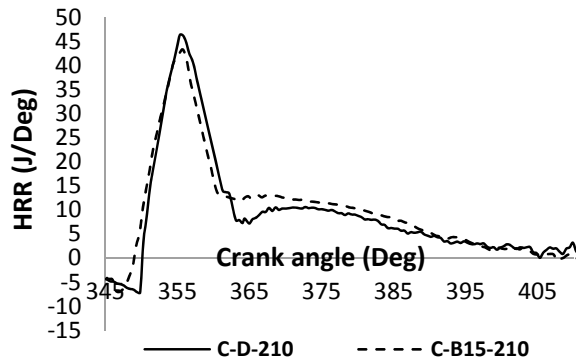
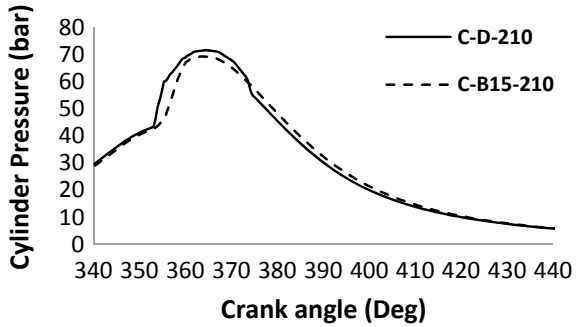


Fig. 8 Cylinder pressure versus load



forming more homogeneous mixture for premixed combustion followed by diffusion combustion resulting in improved heat release rate than uncoated engine [10].

3.7 Cylinder Peak Pressure

In coated engine at 27° CA BTDC, Diesel poses higher cylinder peak pressure of 71.456 bar at 364.96° CA and 69.2056 bar at 363.87° CA for B15. Figure 8 represents the attainment of cylinder peak pressure was earlier in B15 and later in Diesel. Maximum pressure occurs after TDC for both diesel and B15. Attainment of cylinder peak pressure was earlier in B15 around 1° CA than Diesel.

The advanced fuel injection at 27° CA BTDC generally lengthens ignition process and allows additional time for premixing fuel and air and generally increases the premix portion of diesel combustion resulting in more heat release rate and higher peak cylinder pressure as agreed by Sahoo and Das [13]. In coated engine at 23 CA BTDC, Diesel poses higher cylinder peak pressure of 70.34 bar at 366.23 CA and 67.33 bar at 364.59 CA for B15.

4 Conclusion

The measured values are compared with standard injection timing of 23° CA BTDC in the coated engine. Test results revealed better combustion and emission characteristics for blend B15 than other fuels. Diesel posed higher HRR of 46.25 J/deg and higher cylinder peak pressure of 71.456 bar followed by B15 blend of HRR 43.25 J/deg, peak cylinder pressure 67.33 bar in injection advance. The occurrence of Peak HRR was earlier around 1.5° CA for B15 than diesel at 27° CA BTDC.

Honge blend B15 showed a drastic reduction in CO emission of 18.65%, HC emission of 17.24%, smoke reduction of 29% with a slight increase in NO_x of 5.38% and CO₂ of 6.80% in injection advance of 27-degree crank angle BTDC at part loads.

At peak loads, B15 experienced emission reduction in CO of 10%, HC of 10.4%, Smoke of 9.85%, and slight increase in NO_x of 2.94% and CO₂ of 4.60%.

Engine was coupled with the retrofit CO₂ gas separation unit. The novel 30% by weight of MEA-PZ bi-solvent study resulted in CO₂ gas absorption capacity of 85% at minimum gas velocity, high cyclic capacity, and high regeneration rate.

Acknowledgments I would like to acknowledge the Management, Secretary, Principal, and Head of Department of Mechanical Engineering, Sona College of Technology, Salem-636005 for providing all the institutional help and support for this research work.

References

1. A. Kumar, S. Sharma, Potential non-edible oil resources as biodiesel feedstock: an Indian perspective. *Renew. Sustain. Energy Rev.* **15**–4, 1791–1800 (2011)
2. H. Aydin, H. Bayindir, Performance and emission analysis of cottonseed oil methyl ester in a diesel engine. *Renew. Energy* **35**(3), 588–592 (2010)
3. K. Muralidharan, P. Govindarajan, The effect of bio-fuel blends and fuel injection pressure on diesel engine emission for sustainable environment. *Am. J. Environ. Sci.* **7**(4), 377–382 (2011)
4. K. Muralidharan, P. Govindarajan, Influence of injection timing on the performance and emission characteristics of DI diesel engine using pongamia pinnata methyl ester. *Eur. J. Sci. Res.* **59**(3), 417–431 (2011)
5. K. Muralidharan, Effect of injection pressure on heat release rate and emissions in CI engine using honge bio-fuel. *Int. J. Appl. Eng. Res.* **10**(50) (2011/2015)
6. K. Muralidharan, D. Senthilkumar, Influence of fuel injection pressure on combustion and gas emissions in a TBC diesel engine fuelled with pongamia bio-fuel blends for sustainable environment. *Asian J. Res. Soc. Sci. Humanities* **6**(5), 1–17 (2016)
7. F. Vega, M. Cano, E. Portillo, S. Camino, J.A. Camino, B. Navarrete, Evaluation of MEA 5 M performance at different CO₂ concentrations of flue gas tested at a CO₂ capture lab-scale plant. *Energy Procedia* **114**, 6222–6228 (2017)
8. J.P. Holman, *Experimental Methods for Engineers*, 7th edn. McGraw-Hill International Edition (2001)
9. Sayincenk and Canakci Mustafa, Effects of injection timing on the engine performance and exhaust emissions of a dual-fuel diesel engine. *Energy Convers. Manag.* **50**, 203–213 (2009)
10. D.H. Qi, L.M. Geng, H. Chen, Y.Z. Bian, J. Liu, X.C. Ren, Combustion and performance evaluation of a diesel engine fuelled with biodiesel produced from soybean crude oil. *Renew. Energy* **34**, 2706–2713 (2009)
11. H. Raheman, S.V. Ghadge, Performance of compression ignition engine with mahua (*Madhuca indica*) biodiesel. *Fuel* **86**, 2568–2573 (2007)
12. M.N. Nabi, M.M. Rahman, M.S. Akhter, Biodiesel from cotton seed oil and its effect on engine performance and exhaust emissions. *Appl. Therm. Eng.* **29**, 2265–2270 (2009)
13. P.K. Sahoo, L.M. Das, Combustion analysis of Jatrpaha, karanja and polanga based biodiesel as fuel in a diesel engine. *Fuel* **88**, 994–999 (2009)

Thermal Barrier Coating on IC Engines; A Review



Anoop. R. Chattarki and K. G. Basavakumar

Abstract In the recent years, usage of fossil fuels had increased rapidly which negatively affects the environment like ozone depletion, hazardous emission content in atmosphere, etc., so in order to avoid this many technologies have been discovered, but among them Thermal Barrier Coating draws great attention because of its brilliant properties like reducing various toxic emissions like NO_x , CO, Smoke, SO_x , etc., and reducing thermal stresses, erosion, and corrosion on metallic surfaces of IC engines, so this process became the industrial standard for many automobile companies. TBCs are bi-form systems that consist of Top coat, Bond coat. These two layers are deposited on the metal (substrate) that needs to be coated. TBC's empower very high surface temperature due to this heating of charge during intake can be minimized which causes increase in engine efficiency. By adopting TBC's on engine, the in-cylinder temperature gets increased up to $1000\text{ }^\circ\text{C}$ compared to the uncoated engine, which helps in reducing emissions of IC engines. TBCs are not only used in IC engines, turbines but they are also used on the surface of disc brakes, which reduces heat dissipation on it due to huge braking conditions. Many of the automobile companies use coating with less than 0.2 mm in order to obtain high performance of engines. By introducing just TBC's cannot improve performance and emissions of engines there are few parameters that need to be observed like properties of coating materials (nano or micro), Deposition techniques, Implementation of nanomaterials, Exhaust characteristics, Coating construction (multilayer), etc. So this paper describes these parameters based on the colonial work of many researchers.

Keywords Thermal barrier coating · TBC materials · Deposition techniques · Nanostructures · Engine parameters · Multilayered coatings

Anoop. R. Chattarki (✉) · K. G. Basavakumar
Department of Mechanical Engineering, R.N.S. Institute of Technology, Bengaluru, India
e-mail: anoopchattarki1999@gmail.com

K. G. Basavakumar
e-mail: bkumarkg@gmail.com

© Springer Nature Singapore Pte Ltd. 2021
G. S. V. L. Narasimham et al. (eds.), *Recent Trends in Mechanical Engineering*,
Lecture Notes in Mechanical Engineering,
https://doi.org/10.1007/978-981-15-7557-0_5

1 Introduction

Ceramic coatings were introduced in the 1950s for the use in gas turbines. The first application of TBC's was found to be in the aerospace industry, which was developed by the National Advisory Committee for Aeronautics (NACA) and the National Bureau of Standards (NBS). In the case of IC engine, it was first used on Cummins V903 engine in the 1980s with YSZ as coating material with a thickness of 1.5 mm, NiCrAlY as bond coat material. Many authors had identified different TBC processes to improve performance and to reduce emissions of IC engines. Reviewing various research papers, it is observed that researchers had modified engine itself for improving performance and to reduce emissions instead of using Air Injection System (AIR), Exhaust Gas Recirculation System (EGR), Bio-fuels, Bio-oils, etc. In the case of IC engine, more than half of the heat generated during combustion is absorbed by the piston and walls of combustion chamber [1]. The loss of heat is mainly due to combustion temperature so in order to avoid this TBCs are used. The main aim of the TBC's is to provide thermal insulation, higher resistance to corrosion and erosion on the surface of the substrate material. TBC's are also used on turbocharged engines by many of the authors due to its higher mechanical efficiency, power, and also reduction in emission characteristics.

Residual stresses, combustion temperature, crack initiation mainly depend upon the thickness of the coating as this coating thickness increases it can provide better thermal insulation for substrate but it increases thermal stresses on it. Sometimes spallation of the top coat may also take place due to immoderate thickness of coating.

Important factors that affect failures of TBC's are Thermal mismatch between substrate and top coat, bond coat oxidation, phase transformation at high temperature. As coatings are subjected to rapid heating or cooling during the working of engines these factors may cause cracks on it and thus causes failure of TBC's, in order to avoid these failures CaO, MgO, etc., are added to TBC materials [2].

YSZ (Yttrium Stabilized Zirconia) with 7–8 wt% have the capability to withstand up to 1200 °C above then this sintering may take place. But Lanthanum Zirconate has more attractive properties than YSZ like higher thermal conductivity and phase stability up to 2000 °C so it is widely used, though it is costlier compared to YSZ [2]. Ceramic coating reduces soot, smoke and hazardous gases up to 50%. Sintering may take place to TBC material if the temperature of the material is greater than that of its operational temperature so this should be avoided by implementing multilayered coating, which has lower thermal conductivity, sintering capability compared to single-layered coating.

From many research papers, it has been surveyed that nanomaterials have excellent properties than micro-ceramic materials like toughening, resistance to crack initiation, corrosion and adhesion resistance between TBC and substrate, etc. Hardness and yield stress of these materials are 10 times higher than its counterpart (micro) due to the presence of porous nano zones. Performance of these materials are reviewed in the further section.

Materials	Coating	Function	
ZrO ₂ + (6-8%)Y ₂ O ₃	Ceramic top coat	Thermal insulation	TBC
Al ₂ O ₃	TGO	Oxidation barrier	
MCrAlY (20%Cr-12%Al) or Ni-aluminides	Bond coat	Bonding of TBC, oxidation protection	
Ni superalloys (8%Cr-5%Al)	Substrate	Thermo-mechanical loading	

Fig. 1 Scheme of coating structure obtained by TBC. Image courtesy Moskal [4]

2 Thermal Barrier Coating

Thermal barrier coatings are the widely used process for gas turbines, aero-engine parts, photo voltaic panels, solar cells, diesel engine components, etc., which are operating at high temperature. Commonly used TBC materials which have low thermal conductivity are Al₂O₃, BeO, Y₂O₃, CeO₂, ThO₂, In₂O₃, SnO₂, ZrO₂, mullite, titania, Si₃N₄, porcelain, diamond, etc. The application of TBCs for just 0.1 mm surface temperature got reduced up to 100–200 °C [3]. The main disadvantage possessed by TBCs is durability due to low coefficient of thermal expansion in comparison with the substrate material and due to this disadvantage cracking and spallation arise on the thermal barrier coated surface. Nanostructured materials with CTE more than that of substrate material are used to overcome this problem as shown in Fig. 1.

3 Topcoat

Topcoat is essential so as to maintain stress free, oxidation resistant, and stability under long-term exposure. YSZ is the most commonly used material because of its low cost, low thermal conductivity, thermal stability up to 1200 °C. As shown in Fig. 1, (6–8 wt%) Y₂O₃ + ZrO₂ is used as topcoat material because of lower thermal conductivity with 2.1 W/mk, thermal expansion coefficient of 11 × 10⁻⁶ C⁻¹, and high thermal insulation, which influences in reducing thermal stresses [4]. By using alternative materials like gadolinium (gd), europium (eu), samarium (sm), niobium (nb), etc., as topcoat material very low thermal conductivity of 1–1.7 W/mk can be obtained [3]. Usually topcoat layer has a thickness of 250–375 μm [4]. Young’s

modulus of topcoat material plays a vital role in thermal fatigue behaviour, thermal shock resistance, and stress distribution over TBC's [3]. Crack initiation on topcoat should be avoided because the transition of oxygen takes place through these cracks, which lead to the formation of sudden failures of TBC's.

Few other important properties for better topcoat material are

1. High phase stability.
2. High coefficient of thermal expansion.
3. High resistance to corrosion, etc.

Wang et al. [5] used lanthanum zirconate as topcoat material, and they observed that high melting point around 2280 °C, low thermal conductivity, and high thermal stability can be obtained.

4 Thermally Grown Oxide Layer (TGO)

Oxidation of bond coat at higher temperature leads to the formation of TGO on its surface. Flow of oxygen from coating takes place at a high temperature, which reacts with Al at bond coat leads to the formation of Al_2O_3 layer between top coat and bond coat which causes failure of TBC's by removing coated material [6]. These TGO increases huge compressive stress between substrate and coating material, which causes spallation, so the growth of these TGO layers should be avoided. Generally, it is having the thickness of 100 nm.

Nowadays, "Smart coatings" are used to avoid the formation of TGO with MCrAlY-type bond coat having functional gradient layers enriched with chromium and aluminium. Chromium helps in increasing resistance against hot corrosion and aluminium helps in protection of surface against oxidation [4]. Still, various research work is going on to find growth initiation of TGO either due to outward diffusion or inward diffusion of oxygen within the bond coat layer.

5 Bond Coat

Bond coat is used for protecting substrate material against oxidation, hot corrosion, and thermal shocks. It provides a better passage by giving good adhesion between ceramic coating and metallic substrate. Generally, it is having a thickness of 75–125 μm with an important role in the durability of TBC's. Clake et al. [7] observed that Columnar structured bond coat is necessary to avoid thermal fluctuations over bond coat.

In order to obtain Clake's observation; materials, deposition technique plays a very important role in the formation of bond coat. The materials used for the bond coat are Al_2O_3 , SiO_2 , MCrAlY alloys, etc. Among them, Al_2O_3 is widely used because of its

lower oxygen diffusivity, lower the oxygen diffusivity higher will be the resistance towards corrosion and erosion.

6 Substrate

Commonly used substrate materials are nickel-based superalloys, alumina, titanium-aluminium alloys, etc. Substrate materials should be capable of withstanding creep, thermal fatigue, mechanical loads, stresses produced during operations, etc. Residual stress concentration in the substrate leads to the formation of porosity, lower adhesiveness, hardness, and toughness, respectively. Subjecting substrate materials to heat treatment process can avoid stress concentrations [8].

In the case of diesel engines, titanium, titanium-aluminium, niobium alloys can also be used as substrate material which comprises nickel-based superalloys.

6.1 Materials Used for TBC's

TBC materials should have important properties like

- Low thermal conductivity.
- High hardness.
- High wear resistance.
- Excellent adhesive property.
- High thermal stability
- Low weight.
- Low sintering rate, etc.

Different materials used for TBCs are 7–8% YSZ, mullite, alumina, YSZ + CeO₂, La₂Zr₂O₇, silicates, spinel, forsterite, etc. Coating material should have the capability to withstand very high strains without any failure.

Among them 7–8% YSZ, lanthanum zirconate is most widely used because of its properties like Low thermal conductivity, high thermal stability, low cost, high thermal shock resistance, low sintering value, etc. However, there are few disadvantages with these materials but it can be overcome easily by using different processing methods. Due to continuous variation of the temperature inside the engine the thermal conductivity of materials changes abruptly. Until now, there is no theory which is going to explain the thermal conductivity of materials at high temperature.

According to Winter and Clarke [9], atomic number density, phonon spectrum is used to identify the materials which have lower thermal conductivity.

Soares et al. [10] depict that thermal conductivity of materials can also be determined by the equation $K = \alpha \rho C$, where α is thermal diffusivity, ρ is the specific mass of the material, and C is the heat capacity at constant pressure.

Different rare-earth materials like $Gd_2Zr_2O_7$, $La_2Zr_2O_7$, hafnia, ytterbium, etc., are used as modern TBC material because of its low thermal conductivity, high thermal stability compared to standard TBC materials. As dopants these materials also help in maintaining phase stability at a higher temperature, high resistance for corrosion and erosion compared to yttrium dopants.

Jianguo zhu [11] conducted an experiment by using 8% PSZ on Ni-based superalloy substrate, which is subjected to the high temperature of 1400 °C. They observed that Young's modulus and hardness of coated material increase with an increase in heat treatment time. Maximum Young's modulus of 180 GPa and maximum hardness of 90 GPa was obtained for 20 h heat treatment time and also porosity, cracks reduced by 5.8% at 10 h heat treatment time. From this experiment, it is concluded that important parameters of coating materials like Young's modulus, hardness, surface finish can be increased and porosity, cracks can be decreased to a greater extent by increasing heat treatment time.

7 Deposition Techniques

In order to obtain different microstructures, different surface finishes various deposition techniques are used for coating on IC engines. Generally, coating is deposited on piston, cylinder head, cylinder sleeve, and exhaust valves of IC engines as shown in Fig. 2.

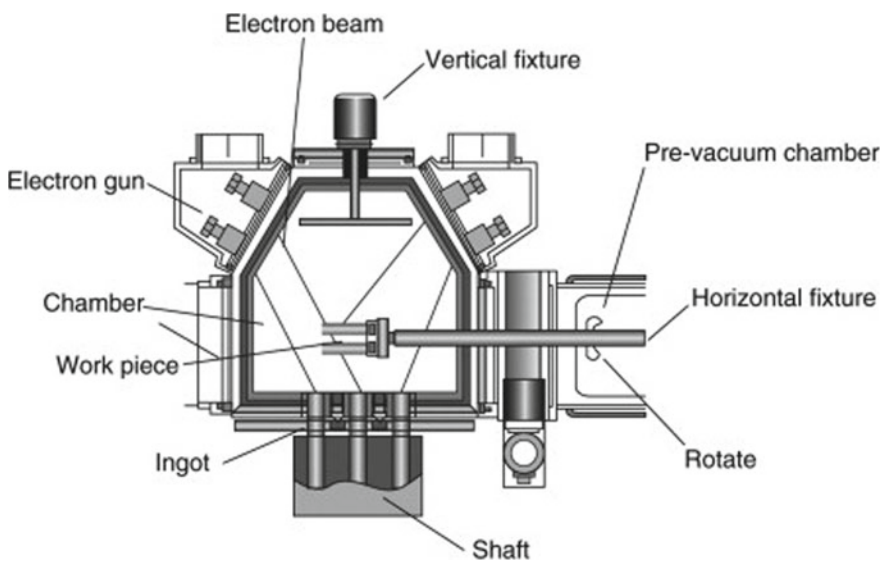


Fig. 2 EBPVD coating chamber. *Image courtesy* Zhang et al. [52]

Engines with thermal barrier coating are called Low Heat Rejection Engines [LHR].

The different deposition techniques are

- Electron Beam Physical Vapour Deposition (EBPVD),
- Air Plasma Spray Process (APS),
- Electrostatic Spray-Assisted Vapour Deposition Method (ESAVD),
- Direct Vapour Deposition,
- Plasma-Enhanced Chemical Vapour Deposition Method(PECVD),
- Electrostatic Spray-Assisted Vapour Deposition (ESAVD), etc.

Among them, EBPVD technique is widely used because of its columnar structured coating which has high strain tolerance, 10 times longer coating life compared to plasma spraying process. Besides materials used for TBCs, structure of coating obtained from various deposition process also plays very important role on performance of IC engines. Thermal conductivity obtained by EBPVD is 1.8 W/mk which is higher than that of APS with 1.1 Wm/K due to this it imparts high strain tolerance compared to APS so it is extensively used in aerospace industries [12]. This process also helps in reducing thermal mismatch between bond coat and top coat.

EBPVD coating chamber as shown in Fig. 2 consists of shaft, ingot, electron gun, horizontal fixture, vertical fixture and the workpiece that need to be coated. Horizontal and vertical fixtures are used to move workpiece easily. Electron beam gun produces electrons with high energy power directly impinges on the workpiece that needs to be coated due to this the temperature of workpiece increases. The evaporation of coating materials takes place at a high temperature, which gets condensed and forms a coating on the substrate. The substrate temperature (T_s) mainly depends upon electron beam gun, this substrate temperature plays an important role in coating thickness. Power, size, and orientation of electron beam can be controlled easily, so this process is used to produce uniform thickness. Since in this process, temperature is very high so almost all TBC materials get evaporated and forms a strong bond and complete deposition on substrate material compared to plasma spray coating method.

Keshavarz et al. [13] conducted a test on nano- and micro-indentation on stabilized zirconia which is deposited by EBPVD at 10,500 °C, it is observed that maximum hardness of 120 mN and improved adhesiveness can be obtained. The spallation resistance of TBC coatings obtained by EBPVD was also very high compared to the plasma spraying process.

Figure 3 shows columnar structured topcoat with a thickness of 120–200 μm , growth of TGO with a less thickness of 2–10 μm and bond coat of 30–100 μm is deposited on the substrate. From this figure, it is concluded that having the thickness of about 200 μm columnar structured topcoat obtained from EBPVD imparts high-strength coatings compared to the plasma spraying process.

The advantages of EBPVD is very high compared to the plasma spraying process and other deposition techniques, however, there are few disadvantages that could affect this process are the following:

1. It is a very expensive process.

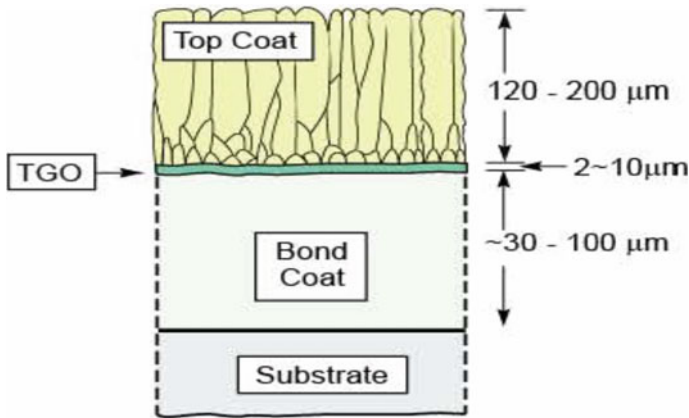


Fig. 3 Scheme of TBC's obtained by EBPVD process. *Image courtesy Karlsson [53]*

2. Brittleness of topcoat increases with sintering of coatings.
3. With increasing the brittleness of topcoat failure of TBC takes place very easily.
4. Residual stresses on TBC will be very high.

The major disadvantage which affects this deposition technique is thermal conductivity which is higher compared to that of the APS process as shown in Fig. 3. In order to overcome this defect, EBPVD coating with zig-zag morphology pores technique was introduced with thermal conductivity of 0.8 W/mk at room temperature was achieved which was much lower in compared with APS process [12]. So by implementing this technique thermal conductivity issues related to EBPVD can be solved.

8 Nanostructured TBC

Nanostructured materials grab a great attention in recent years on the application as TBC materials on IC engines due to its brilliant properties like high thermal stability, low sintering value, high tensile strength, high bonding strength, high thermal cyclic lifetime, etc.

Nanomaterials are classified into two types:

- Organic nanomaterials.
- Inorganic nanomaterials.

Chitosan, cationic polyelectrolytes, quaternary ammonia are some examples of organic nanomaterials.

Metal and its oxides like gold, silver, aluminium, copper, titanium, iron, zinc are some examples of inorganic nanomaterials.

But among them, inorganic nanomaterials are widely used as coating materials because of its properties like non-toxicity, high thermal stability, strong chemical bonding, etc. However, nanocoatings exhibit superior properties than its counterpart but phase transformation takes place at high temperatures so trivalent oxides like Al, B, Ga, etc., need to be added to these materials before coating.

9 Literature Survey of Nanoceramic Thermal Barrier Coating on IC Engines

Mustafa et al. [14] took Al_2O_3 nanomaterial with a coating thickness of 200 μm on engine combustion chamber using plasma spray coating technique in phase 1 and micro- Al_2O_3 material in phase 2. They observed that engine power shoots up with a very high rate in phase 1 and other parameters like specific fuel consumption, Exhaust gas emissions and smoke density also got reduced then compared with phase 2. But there was no reduction in NO_x emissions in both the phases.

Soltani et al. [15] observed that combination of both nano–microstructured zirconia ceramics exhibits good properties like high chemical and thermal stability, high refractive index, low thermal conductivity, etc.

Xianliang [16] conducted an experiment between nano- and micro-lanthanum zirconate, they observed that nano-lanthanum zirconate material exhibits better thermal cycling life with 6 times more than that of micro-lanthanum zirconate.

It is reported that with a similar composition of materials nanostructured coating reduces 2–10 times greater residual stresses when compared to its counterpart. Even the reduction of grain size of nanomaterials below 50 nm, thermal conductivity remains unaffected so this property plays a very important role in thermal barrier coating.

Ghasemi and Vakilifard [17] conducted experiments on YSZ coatings and they observed that nanostructured YSZ coating exhibits superior properties like adhesive strength, coating resistance, charge transfer resistance, reducing in the insulation of cylinder head and fuel intake when compared with the microstructured YSZ coating.

Gell et al. [18] used nanostructured $\text{Al}_2\text{O}_3\text{--TiO}_2$ as their coating material and they observed that increasing crack resistance, abrasive wear resistance was obtained. But they also observed a few disadvantages of this nanostructured coating like phase transformation, oxidation of bond coat at a higher temperature. So in order to avoid these, trivalent-oxide materials like cerium, vanadium, tantalum, erbium, etc., are used along with these nano-structured coating materials.

Hajizadeh-oghaz et al. [19] observed that nanostructured $\text{ZrO}_2\text{--Y}_2\text{O}_3\text{--CeO}_2$ ceramic material showed superior hot corrosion resistance when compared with conventional YSZ coatings.

Sathpathy et al. [20] used nanostructured bi-layer zirconate as their TBC material and from this paper it is reviewed that this material withstood high rapid thermal shocks with more than 30,000 nozzle actuations without any chipping or spallation

on them. It is also observed that nano-lanthanum zirconate has 6 times higher cyclic lifetime compared to that of micro-lanthanum zirconate.

Lima and Marple [21] conducted an experimental test on nano- and microstructure titania, alumina-titania coatings. They observed that bonding strength in titania was 2.4 times greater and in alumina-titania with 1.8 times greater than its counterpart, respectively.

Bahamiran et al. [22] used nano- $\text{Gd}_2\text{Zr}_2\text{O}_7/\text{GZ}$ as TBC topcoat material, which was synthesized by co-precipitation process and gets deposited by APS technique with CoNiCrAlY as a bond coat on Ni-based superalloy substrate (IN738LC). Co-precipitation method was used because of cost-effectiveness, low synthesis temperature, and controlling in chemical composition. It was observed that porous structure was reduced in nano-GZ coating with 7–10% because of ultra-fine nanoparticles. But in YSZ coating porous structure was very high with 12–15% on both inside and outer surface of the coating. The author also observed that nano $\text{Gd}_2\text{Zr}_2\text{O}_7$ (GZ) coating reduces the diffusion rate of oxygen from coated surface, thus increases the performance of the engine.

From Fig. 4, it is observed that nano-GZ coating consists of unmolten zones with nanostructures (nanozones), which increases hot corrosive resistance compared to that of conventional YSZ coating and also acts as a barrier for the corrosion of molten salts on TBC. At 950 °C with 4 h cycles, hot corrosion resistance of nano GZ and conventional YSZ was investigated. So by reviewing this paper it is concluded that

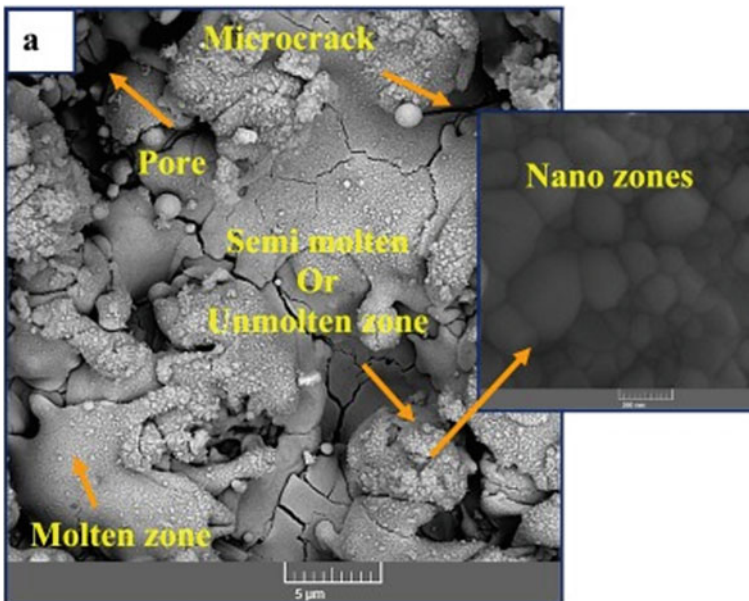


Fig. 4 FE-SEM image of the surface of nanostructured GZ coating. *Image courtesy* Bahamiran et al. [22]

Gd₂Zr₂O₇ nanomaterial plays a significant role in the protection of thermal barrier coating from oxidation. These GZ coating material has low thermal conductivity, high coefficient of thermal expansion compared to YSZ.

Wang and Zhou [23] conducted an experiment with nanostructured Gd₂O₃YSZ/2GdYSZ and nano YSZ coating using air plasma spraying technique. It is observed that the phase stability of nano Gd₂O₃YSZ was higher compared to that of nano YSZ coating. In nano 2GdYSZ % of m-ZrO₂ is very less due to this hot corrosion resistance is higher with Na₂SO₄ + V₂O₅ salt at 900 °C compared to that of nano YSZ.

Karthik et al. [24] used Al₂O₃-ZrO₂ nanomaterial as their TBC material with spray pyrolysis technique on EN₃ mild steel substrate. It was observed that this material has high toughness, bonding strength, surface damage resistance due to phase transformation of ZrO₂ from tetragonal to the monoclinic structure. To absorb a large amount of heat from combustion chamber, they advised using of 30-40% ZrO₂ content with Al₂O₃.

From Fig. 5, it is observed that Al₂O₃-ZrO₂ binary nanoparticle at 400 °C with 65% Al₂O₃ and 35% ZrO₂ (by mass) had uniform ratio throughout the experiment which reveals that there is no phase transformation of this binary nanoparticle, due to this it improves the life span of IC engine components.

Loghman-Estarki et al. [25] took two materials, namely nanostructured scandia and yttrium co-stabilized zirconia as their experimental materials. These two materials are sprayed on Ni-22Cr-10Al-Y (bond coat) and Inconel 738 Ni alloy (substrate) for preparation of specimens. These specimens were dipped in corrosive salts for 300hrs for hot corrosion test and they observed that hot corrosion resistance of nano-scandia was very high compared to that of yttrium-stabilized zirconia.

Jamali et al. [26] depicts that nano zones arrests crack propagation at boundaries and increases the bonding strength of coated material. The author took 4 TBC samples

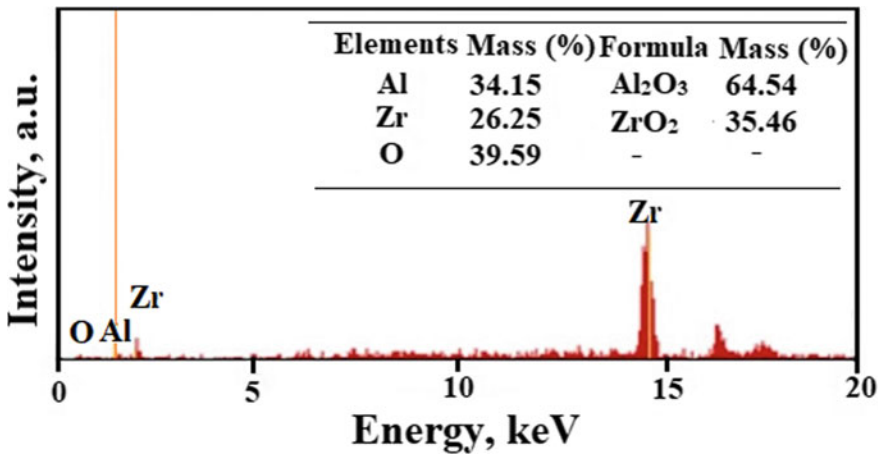


Fig. 5 XRF spectrum of Al₂O₃-ZrO₂ binary particle at 400 °C. Image courtesy Karthik et al. [24]

of nano- and micro-coated material and conducted a repetitive bonding strength test between them. They concluded that nanomaterials had average bonding strength of 42 MPa, which was 1.8 times higher compared with its counterpart. Thermal insulation capacity (TIC) plays a crucial role in the efficiencies of IC engine, so the author reveals that TIC of nanostructured coating was high with 145 °C compared to that of conventional coating with 119 °C.

Keyvani [27] conducted experiment of nanostructured Al_2O_3 -YSZ coating on Ni-based alloy substrate. They observed that higher hot corrosion resistance up to 1100 °C, oxidation resistance up to 1050 °C is obtained when compared to its conventional counterpart, respectively.

Tong et al. [28] conducted bonding strength, thermal shock resistance test on 3 different materials, i.e., MGO-stabilized zirconia, Y_2O_3 -stabilized zirconia, and nano-zirconia with a coating thickness of 150–200 μm . From Fig. 6a, it is observed that nano-zirconia has a higher bonding strength of 32 MPa, which is greater than that of the other two materials.

Similarly, from Fig. 6b, thermal shock resistance of nano zirconia was 38 which was also greater than that of the other two materials. This is because nano zirconia has closed packed structure, which enables high strength, high thermal shock resistance property than MGO, Y_2O_3 -stabilized zirconia.

10 TBC's Effect on Various Engine Parameters

At present, automobile industries are facing major challenges in order to control harmful emissions from engines as per zero-emission norms all over the world. So various research work is going on until today in order to control these emissions.

IC engines emit various toxic pollutants like nitrogen oxides (NO_x), unburnt hydrocarbons (UHBC), smoke, carbon monoxide (CO), sulphur oxides (SO_x), etc., which seriously affect environment like ozone layer depletion, acid rain, climatic changes, air pollution, etc. So in order to reduce this effect TBCs are used.

TBCs not only reduce emissions, fuel consumption but also increase efficiencies, power, components life, etc., of engines.

11 Literature Survey of TBC'S on Performance Characteristics of IC Engines

Kamo et al. [29] coated YSZ TBC material with a 100–500 μm thickness on IC engine, they observed that fuel efficiency of the engine increased by 6%, fuel consumption, heat rejection got reduced significantly by coating on cylinder bore, piston of the engine, respectively, instead of coating on other parts of the engine.

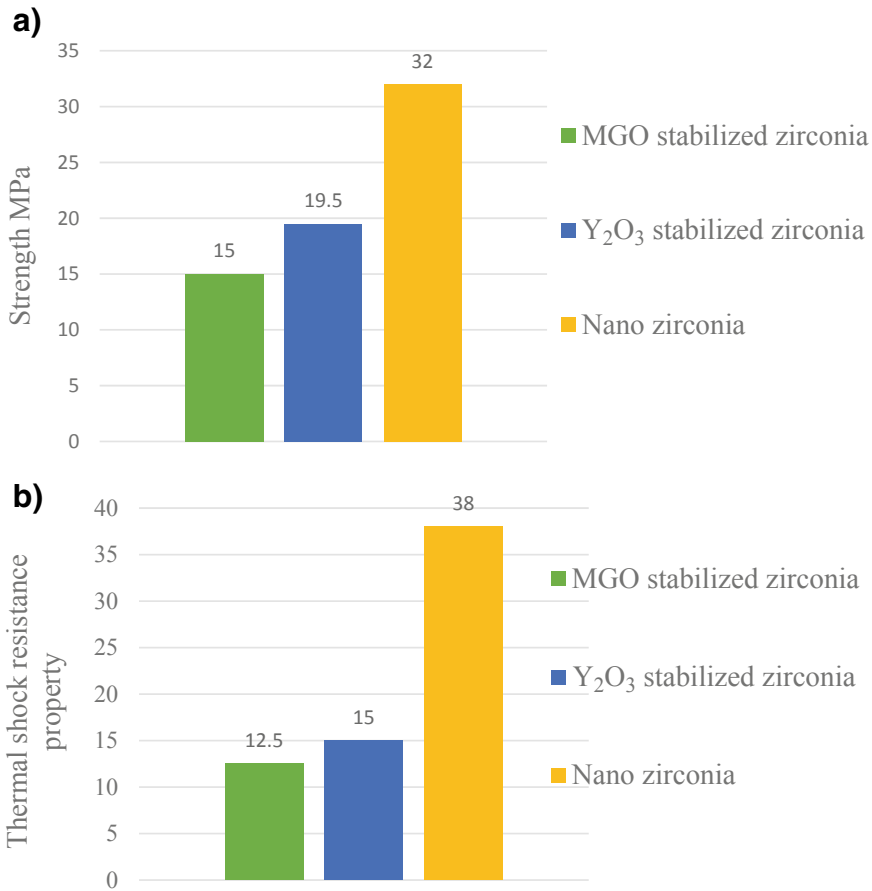


Fig. 6 **a** Bonding strength of TBC's. **b** Thermal shock resistance of TBC's. *Image courtesy Tong [28]*

Application of TBCs for the past one decade on IC engines fetched few modifications on engine parameters and they are engine lifetime, engine power, valve lifetime increased by 20,10,300 (in percentage), respectively. Similarly, fuel consumption, emissions, oil consumption, and engine noise reduced by 11%, 20–40%, 15%, 3db, respectively [30].

Krishnamani et al. [31] observed emission characteristics of ceramic coated engines and they concluded that CO and HC emissions from these engines were reduced by 10% and 18%, respectively.

Sivakumar and Senthil Kumar [32] used copper + nickel nanostructure as TBC material on engine piston they observed that smoke, nitrogen oxide (NO_x), and hydrocarbons were reduced by 21, 45, 64 (in percentage), respectively.

Taymaz et al. [33] used CaZrO_3 and MgZrO_3 as TBC material by using plasma spraying process on cylinder head, valves, combustion chamber, and piston and they observed engine parameters like thermal efficiency, engine power, durability got increased. But among them, thermal efficiency has a significant effect which was increased nearly up to 34% at all loads on the engine.

Assani's et al. [34] used YSZ as a coating material on engine piston with a thickness of 0.5–1 mm. The results depict that thermal efficiency increases by 10% at 0.5 mm thickness but hazardous emissions were reduced at 1.5 mm thickness. From this paper, they also concluded that has coating thickness of ceramic material increases may negatively effect on the performance characteristics of the IC engine.

Powell et al. [35] used YSZ coating with a coating thickness of 150 μm on HCCI engine they observed that by using this coating CO, unburned hydrocarbon emissions were reduced by 29, 37%, respectively. From this paper, it is observed that as the speed of the engine increases CO emissions reduces. Compared to uncoated HCCI engine, thermal efficiency of coated HCCI increases up to 2%.

Palaniswamy and Manohar [36] used partially stabilized zirconia with a coating thickness of 200 μm on the combustion chamber and piston crown of the IC engine. It is observed that CO, HC, smoke level from emissions got reduced up to 0.069%, 14 ppm, 4 mg/kg, respectively.

Sivakumar and Senthil Kumar et al. [32] used YSZ on piston crown with a thickness of 100 μm and investigated the diesel engine performance and emission characteristics. It was observed that thermal efficiency increased by 5%, brake-specific fuel consumption, HC emission was reduced by 28%, 35%, respectively.

Domakonda [37] used lanthanum zirconate as TBC material with biofuel (Pongamia Pinnata oil) obtained from transesterification process on the direct injection diesel engine. It was concluded that by using both BSFC reduced by 4.2% and CO by 18%.

Shrirao and Pawar [38] used Mullite as their TBC material on the turbocharged engine piston crown, cylinder head as well as on the valves. They observed that 12% increase in exhaust gas temperature due to this efficiency of engine increases, CO reduced by 28%, NO_x emission increased by 21%.

Praveen Raman [39] used YSZ as TBC material and algae oil as biofuel blend on Kirloskar single-cylinder water-cooled engine and they observed that heat release rate and peak pressure increased by 13%, 20%, respectively, at full load condition compared to that of the uncoated engine.

Zeng et al. [40] used platinum coating on the piston of HCCI engine and they observed that coating has a positive effect on engine performance, emission characteristics but NO_x emissions got increased significantly by using this coating.

Hejwowski and Weronki [41] conducted experiments by using different TBC materials like $\text{Al}_2\text{O}_3 + 40\% \text{TiO}_2$, $\text{ZrO}_2 + 8\% \text{Y}_2\text{O}_3$, $\text{Al}_2\text{O}_3 + 40\% \text{ZrO}_2$ with a coating thickness of 0.35 mm, 0.3 mm, 0.25 mm, respectively, along with NiCrAl alloy having a thickness of 0.15 mm on the piston of IC engine. They obtained the graph of specific fuel consumption versus engine speed and from this graph it is concluded that coated engine has a low specific fuel consumption of 330 g/kwh compared to a conventional engine with 420 g/kwh at 4225 rpm as shown in Fig. 7.

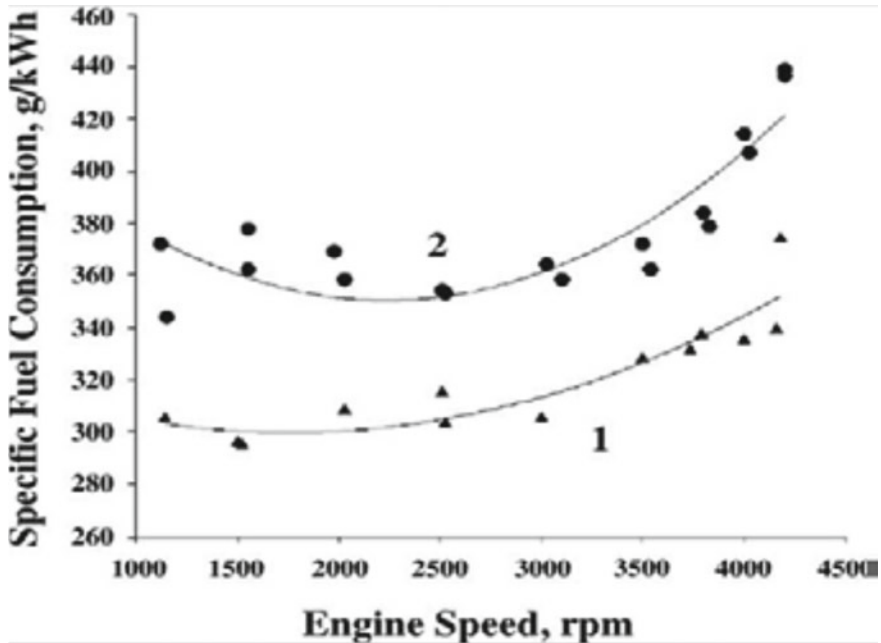


Fig. 7 Shows Specific fuel consumption characteristics. (1) Coated engine, (2) conventional engine. Image courtesy Hejwowski and Weronki [41]

Hasimoglu et al. [42] took CaZrO_3 material on turbocharged direct injection diesel engine and observed that BTE increased by 6.5% and heating of fuel reduced by 14%.

Assani's et al. [34] used $\text{ZrO}_2 + \text{Al}_2\text{O}_3$ coating material in phase 1 and SIC coatings in phase 2 for IC engine from experimental results they observed that NO_x emissions got reduced about 500 ppm in phase 1 and 800 ppm in phase 2, respectively, as shown in Fig. 8.

Sathiyagnanam et al. [43] used TBC + Fuel additive for Di Diesel engine and observed that NO_x emissions reduced up to 500 ppm for TBC engine but for TBC + Fuel additive engine it got reduced up to 600 ppm and by observing this it is concluded that using both TBC + fuel additives improves engine performance and emission characteristics rather than using only thermal barrier coatings.

NO_x emission for three different materials was investigated at 5 KW brake power, it is observed that NO_x emission reduces abruptly to 410 ppm for SIC-coated engine due to late combustion of fuel when compared to that of $\text{Al}_2\text{O}_3 + \text{ZrO}_2$ -coated, non-coated engines with approximately 760 ppm, 1200 ppm, respectively.

By using TBC's on piston top thermal stresses can be reduced to a greater extent because of reduction in thermal conductivity and increase in unburnt charge oxidation thereby increases the life of engine component. So Jose et al. [44] created the model of the piston by using SOLIDWORKS designing software.

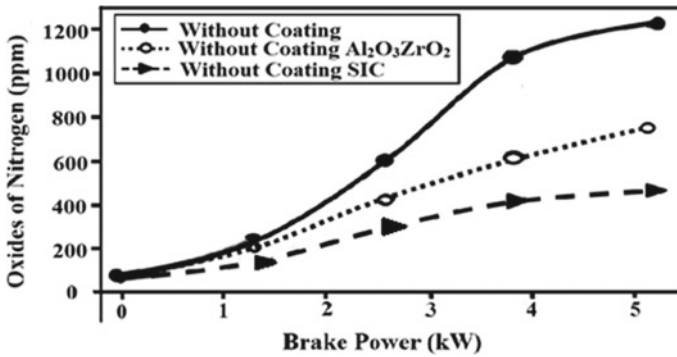


Fig. 8 Shows NO_x emission characteristics of Non-coated, Al₂O₃ + ZrO₂-coated, SiC-coated engines at constant brake power. *Image courtesy* Azadi et al. [54]

They make use of YSZ as TBC material on piston top because of its low thermal conductivity and higher Young's modulus. It was observed that the coating thickness of 0.6 mm reduced top land temperature up to 473 °C compare to the uncoated piston with 600 °C. Heat flux was also reduced to 0.467 W/mm² compared to uncoated piston with 0.95 W/mm².

By reviewing various research papers, it is observed that NO_x emission increases with the implementation of TBCs because NO_x emission reduces if combustion of fuel takes place with constant stoichiometric ratio and flame temperature but it doesn't due to diffusive mixing of air–fuel ratio, so in order to avoid this issue, many authors used biodiesel blends with fuel + TBC in order to reduce these hazardous emissions into the atmosphere. Few of the investigations are the following

Sadhik Bhasha and Anand [45], Kao and many more introduced nanocatalysts in diesel along with TBC material and due to this NO_x emissions reduced to a greater extent.

Kao et al. [46] used aqueous alumina nanoparticle blend with diesel and YSZ coating on engine, the results reveal that NO_x emissions and smoke reduced to a greater extent.

Srinivasan and Sivakumar [47] used the Exhaust Gas Recirculation (EGR) method by reducing combustion chamber temperature with exhaust residual present inside the cylinder.

They concluded that by using this method NO_x, smoke, soot can be reduced to a very high extent.

El-Seesya et al. [48] used multi-walled carbon nanotube additive blend with diesel fuel to determine emission characteristics of the engine. These characteristics were observed at a constant speed of 2000 rpm with different engine torques.

Emissions like NO_x, CO, and UHC were reduced by 45, 50, 60%, respectively, by using MWCNT additive blend with a dose level of 40 mg/l.

Intenan et al. [49] used jatropha, ethanol, diethyl ether as biofuel blends along with diesel in the light-duty diesel engine. The test was carried out at a constant speed

of 2200 rpm with ethanol and diethyl ether fuel blends, they observed that CO, NO_x emissions were reduced by 40, 13%, respectively, as shown in Table 1.

Table 1 Experimental results of coated engine compared with conventional engine

Investigator's	Test engine	Material and thickness of coating	Operational characteristics	Performance of coated engine compared to standard engine
Lakshmanan et al. [55]	Horizontal four-stroke single-cylinder water-cooled diesel engine	Partially stabilized zirconia (PSZ)	All parameters are with a constant load of 12 amps	HC, CO reduced to 7.5 ppm, 0.04%, respectively, but NO _x emission increased by 10 ppm
Balamurugan et al. [56]	Kirloskar TV-1, DI, Naturally aspirated, Water-cooled diesel engine	Nanostructured zirconium	All parameters are observed at 100% load (Full load condition)	BTE, exhaust gas temperature, NO _x increased to 25%, 410 °C, 1390 ppm. BSFC, CO, HC, smoke density reduced to 13 MJ/kwh, 0.215%, 80 ppm, and 52 HSU, respectively
Gnanamoorthi et al. [57]	Four-stroke, direct-injected, water-cooled single-cylinder diesel engine	Aluminium oxide (Al ₂ O ₃) + Molybdenum (Mo) + Titanium oxide with a thickness of 300 μm along with ethanol as a fuel blend	All parameters are observed with constant brake power of 4.8KW	BSFC, BTE, NO _x increased by 6.55 Kg/KW-hr, 4.90%, 28 ppm CO, HC, and smoke density was reduced by 4% of volume, 6 ppm, 50%, respectively
Taymaz et al. [33]	Four-stroke, direct-injected, water-cooled, six-cylinder, intercooled, turbocharged diesel engine	CaZrO ₃ with 0.35 mm thickness applied on cylinder head and valves and piston with 0.35 mm of MgZrO ₃	BSFC was observed at 1400 rpm, effective efficiency at 1800 rpm at high-load conditions	BSFC reduced to 285 g/KW-hr and effective efficiency increased to 38%

12 Discussions

As we observed earlier, due to various ill effects of TBC coatings like cracking, oxidation, spallation, high-temperature surface deterioration may cause failures of coating materials, which reduce efficiencies/performance of IC engines. So in order to overcome these failures, multilayered coatings are introduced within the structure.

Each layer in these coatings acts as heat dissipater so that coating delamination at higher temperatures can be avoided.

By introducing multilayered coating, thermal conductivity of material reduces linearly because of increase in the number of structural layers [24].

In a thick thermal barrier coating system it is desirable to obtain low TEC on hot surface metal components to minimize thermal shock and residual stresses on them, so these multilayered systems are used to resolve these issues.

Karthik et al. [24] used $\text{Al}_2\text{O}_3 + \text{ZrO}_2$ nano particle multilayered (6 layer) coating as their TBC material. It was observed that these coatings form a protective film on mild steel specimen without changing its actual surface. It was also observed that when specimen is subjected to high temperature these coatings improve compatibility and surface damage resistance in compared to single-layered coating.

Patnaik et al. [12] introduced a new high reflective multilayered coating consists of ceramic stacks which are designed to obtain low thermal conductivity, reflecting thermal radiations for the wavelength of 0.45–5 μm . Design parameters, number of stacks plays an important role in obtaining lower thermal conductivity.

To achieve low thermal conductivity, high reflectivity each stack should have multiple ceramic layers with alternating high and low refractivity. The stack with lower, higher wavelength reflectivity are arranged on top and bottom of multilayered stack, respectively.

They observed that high reflectance multilayered coating system of 250 μm thickness, irrespective of layer arrangement (either top or bottom on single layer) exhibits temperature reduction of 90 °C on a metallic substrate compared to mono-layered coatings with same thickness because of reduction in radiation which is entering into coating system.

In multilayered coatings thickness of individual layers plays a very important role in stress distribution during operating conditions.

Mahade et al. [50] conducted experiments between single-layer, double-layer, and triple-layered coating obtained from Suspension Plasma Spraying (SPS) process. As shown in Fig. 9, SL coating has YSZ with 300 μm , DL coating has GZ with 240 μm , and TL coating has dense GZ with 40 μm as topcoat materials. Thermal cyclic fatigue test reports that DL and TL coatings have better thermal cyclic life compared with SL coating.

As sintering may take place above 1200 °C for YSZ as topcoat material so they suggest that to use of DL and TL coating may reduce this sintering effect instead of using SL coating. Thermal conductivity of DL and TL coating was also very less when compared with coating. Schlegel et al. [51] conducted an experiment on double-layered system by using rare-earth perovskite $\text{La}(\text{Al}_{1/4}\text{Mg}_{1/2}\text{Ta}_{1/4})$

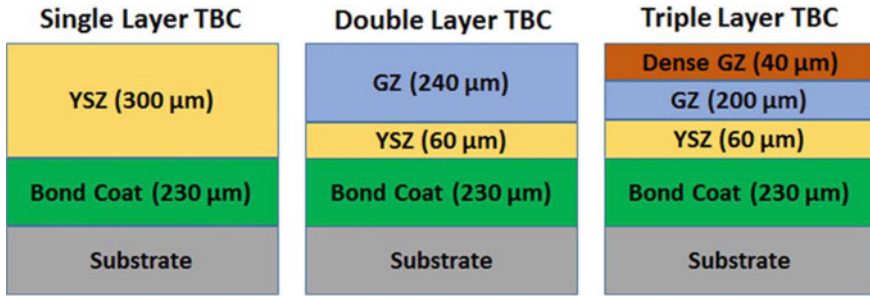


Fig. 9 Shows scheme of single-layered and multilayered (DL, TL) coatings obtained by SPS process. *Image courtesy* Mahade et al. [50]

O₃ (LAMT) as topcoat material because of its low thermal conductivity and good CMAS(calcium–magnesium–alumina–silicate) resistance. Thermal cycling test was carried out at 1390 °C, which shows that the DL system has more cyclic lifetime than SL system as shown in Fig. 9.

13 Conclusion

In this paper, various research work on thermal barrier coating on IC engines is reviewed. While reviewing this paper, many observations were made regarding materials, methods, etc., and these observations are discussed below:

- Many authors applied yttrium-stabilized zirconia as their TBC material on IC engines because of its most important property of low cost.
- Though lanthanum zirconate has more excellent properties than that of YSZ like less sintering effect, thermal stability up to 2000 °C, high corrosion resistance, 20% lower thermal conductivity compared to PSZ, etc. But it is used by only a few authors like Xianliang [16], etc., because of its high cost, high CTE so new processing methods need to be introduced for reducing the cost of these materials.
- Lanthanum zirconate-EBPVD method is also facing the same issue (high cost) even though coatings obtained by this method has superior characteristics like higher bonding strength, columnar grain structure, long durability, etc., so research work needs to be carried out to improve this process which reduces its cost.
- Regarding materials of TBCs until today there is no theory that explained about the selection of material having low thermal conductivity at high temperature, but this property plays a major role in the life span of TBCs.
- Some of the authors used perovskite, pyrochlores, GZ, and other rare-earth materials such as ceramic coating material and it was observed that brilliant properties can be obtained compared to YSZ so in future these materials can replace YSZ as standard TBC material.

- It is observed that by using nanostructured TBCs various engine parameters like bonding strength, efficiency, thermal shock resistance, etc., increase and emissions like CO, HC (hydrocarbons), fuel consumption, sintering of material at high temperature reduce to a greater extent than that of the microstructured coating.
- Many of the authors like Hejwowski and Weronki, Gell, Mohammed Mustafa, etc., used Al_2O_3 content in TBC material because it provides corrosion resistance at high temperature, low porosity, high hardness, etc.
- Multilayered coating will be the upcoming research topic in the field of TBCs because of its excellent properties.
- Various authors like W K Cheng, S. Furuham, D.W Dickey, and many more concluded that with the use of TBCs engine efficiency got reduced due to in-cylinder heat characteristics, deteriorated emissions, etc., which is still a discussion topic as of now.
- By using TBCs various hazardous emissions, fuel consumption also got reduced which prevents the environment from various negative effects like acid rain, ozone layer depletion (as discussed earlier), scarcity of fuel, etc. Last but not least by using TBC's on IC engine not only provides huge advantages for engines but also for human beings (in both economically, medically), etc.

References

1. S. Dhomme, A.M. Mahalle, Review article on thermal barrier coating materials for SI engine. *J. Mater. Res. Technol.* (2018). <https://doi.org/10.1016/j.jmrt.2018.08.002>
2. D. Elumalai, et al., A Review study on experimental investigation on improving thermal performance of IC engine by varying the piston coating. *J. Aerosp. Eng. Sci.* **2**(3) (2017)
3. A.K. Saini, et al., TBC applications, stability and longevity. *J. Elsevier* (2012). <https://doi.org/10.1016/j.proeng.2012.06.368>
4. G. Moskal, TBC characteristics of microstructure and properties, generation and directions of development of bond. *J. OCSCO* **37**(2) (2009)
5. C. Wang, Y. Wang, L. Wang, G. Hao, X. Sun, F. Shan et al., Nanocomposite lanthanum zirconate thermal barrier coating deposited by suspension plasma spray process. *J. Therm. Spray Technol.* **23**(7), 1030–1036 (2014)
6. S. Ghosh, Thermal barrier ceramic coatings. *J. Web Sci.* (2015). <https://doi.org/10.5772/61346>
7. D.R. Clake, et al., TBC materials. *J. Elsevier* (2005)
8. A. Naveen, et al. A review on TBC and its deposition techniques. *J. Eng. Sci.* (2016)
9. M.R. Winter, D.R. Clarke, Oxide Materials with low thermal conductivity. *J. Am. Ceram. Soc.* **90**(2), 533–540 (2007)
10. D.S. de Almeida, C.A.A. Cairo, C.R.M. Silva, M. do Carmo, A. Nono, Thermal barrier coating by electron beam-physical vapor deposition of zirconia co doped with yttrium and niobia. *J. Aerosp. Technol. Manage. São José dos Campos* **2**(2), 195–202 (2010)
11. K.M. Jianguo zhu, Microstructural and mechanical properties of thermal barrier coating at 1400 °C treatment. *Chin. Soc. Theor. Appl. Mech.* (2014). <https://doi.org/10.1063/2.1402108>
12. P.C. Patnaik, X. Huang, J. Singh, State of the art and future trends in the development of thermal barrier coating systems, in *Innovative Missile Systems. Meeting Proceedings RTO-MP-AVT-135, Paper 38* (Neuilly-sur-Seine, RTO, France, 2006), pp. 38–1–38–20

13. M. Keshavarz, M.H. Idris, N. Ahmad (2013) Mechanical properties of stabilized zirconia nano crystalline EB-PVD coating evaluated by micro and nano indentation. *J. Adv. Ceram.* **2**(4), 333–340
14. M. Mohamed Musthafa, S.P. Sivapirakasam, M. Udaykumar, Comparative studies on fly ash coated low heat rejection diesel engine on performance and emission characteristics fueled by rice bran and pangomia methyl ester and their blend with diesel. *Energy* **36**(5), 2343–2351 (2011)
15. Soltani R., et al., Development of alternative TBC for diesel engines. *J. SAE* (2005)
16. J. Xianliang, Overview on the development of Nano-structured thermal barrier coatings. *J. Mater. Sci. Technol.* **23**(4), 449–456 (2007)
17. R. Ghasemi, H. Vakilifard, Plasma-sprayed nanostructured YSZ thermal barrier coatings: thermal insulation capability and adhesion strength. *Ceram. Int.* **43**(12), 8556–8563 (2017)
18. M. Gell, E.H. Jordan, Y.H. Sohn, D. Goberman, L. Shaw, T.D. Xiao, Development and implementation of plasma sprayed nanostructured ceramic coatings. *J. Surf. Coat. Technol.* **146–147**, 48–54 (2001)
19. Hajizadeh-oghaz, et al., Nano structured TBC coating on IC engines
20. R.K. Satpathy, et al., Synthesis and application of nanostructured bi-layer YSZ-LZ thermal barrier coating. *Def. Sci. J.* (2019). <https://doi.org/10.14429/dsj.69.13212>
21. R.S. Lima, B.R. Marple, Enhanced ductility in thermally sprayed titania coating synthesized using a nanostructured feedstock. *A. Mater. Sci. Eng.* **395**, 269–280 (2005)
22. M. Bahamirian, et al., Enhancement of hot corrosion of TBC by using Nanostructured $Gd_2Zr_2O_7$ coating. *J. Elsevier* 1–12 (2019)
23. Y. Wang, *Prog. Nat. Sci.: Mater. Int.* (2017). <https://doi.org/10.1016/j.pnsc.2017.06.010>
24. A. Karthik, et al., Production of Al_2O_3 -stabilized tetragonal ZrO_2 Nanoparticles for thermal barrier coating. *Int. J. Appl. Ceram. Technol.* **10**(6) (2013). <https://doi.org/10.1111/ijac.12032>
25. M.R. Loghman-Estarkia, M. Nejati, H. Edris, R.S. Razavi, Hossein Jamali, A.H. Pakseresht, Evaluation of hot corrosion behavior of plasma sprayed scandia and yttria co-stabilized nanostructured thermal barrier coatings in the presence of molten sulfate and vanadate salt. *J. Eur. Ceram. Soc.* **35**, 693–702 (2015)
26. H. Jamali, et al., Fabrication and evaluation of plasma sprayed Nanostructured and conventional YSZ TBC's". *J. Benthem Sci.* (2012)
27. A. Keyvani, Microstructural stability oxidation and hot corrosion resistance of nano structured Al_2O_3/YSZ composite compared to conventional YSZ TBC coatings. *J. Alloy. Compd.* **623**, 229–237 (2015)
28. C.U.I. Tong, et al., Microstructural properties of plasma sprayed Nano structured zirconia. *J. Ironand Steel Res.* (2007)
29. R. Kamo, N.S. Mavinahally, L. Kamo, W. Bryzik, E.E. Schwartz, Injection characteristics that improve performance of ceramic coated diesel engines, in *SAE Paper No. 1999-01-0972*
30. N. Balaganesh, et al., Review on thermal barrier coating effects on diesel engine performance and emission characteristics. *J. Chem. Pharm. Sci.* (2015)
31. S. Krishnamani, T. Mohanraj, K. Murugumohan Kumar, Experimental investigation on performance, combustion and emission characteristics of a low heat rejection engine using rapeseed methyl ester and Diethyl ether. *Ind. J. Sci. Technol.* **9**(15), 1–9 (2016)
32. G. Sivakumar, S. Senthil Kumar, Investigation on effect of yttria stabilized zirconia coated piston crown on performance and emission characteristics of a diesel engine. *Alexandria Eng. J.* **53**, 787–794 (2014)
33. I. Taymaz, K. Cakir, A. Mimaroglu, Experimental study of effective efficiency in a ceramic coated diesel engine. *Surf. Coat. Technol.* **200**, 1182–1185 (2005)
34. D. Assini's, K. Wiese, E. Schwarz, W. Bryzik, The effects of ceramic coatings on diesel engine performance and exhaust emissions, in *SAE Technical Paper* (1991)
35. T. Powell, et al., Impact of yttrium-stabilized zirconia thermal barrier coating on HCCI engine combustion, emissions, and efficiency, vol. 139 (2017)
36. E. Palaniswamy, N. Manohar, Ceramic coated combustion chamber for improving IC engine performance. *Int. J. Des. Manuf. Technol.* **2**(1) (2008)

37. V.K. Domakonda*, R.K. Puli, Application of thermal barrier coatings on diesel engine; a review. *Energy Power* **2**(1), 9–17 (2012). <https://doi.org/10.5923/j.ep.20120201.02>
38. P.N. Shirrao, A.N. Pawar, Evaluation of performance and emission characteristics of turbocharged diesel engine with mullite as thermal barrier coating. *Int. J. Eng. Technol.* **3**, 256–262 (2011)
39. S. Praveen Raman, Influence of TBC on combustion characteristics in a biodiesel fueled Diesel Engine. *J. Adv. Res. Ideas Innov.* **4**(3) (2018)
40. W. Zeng, M. Xie, M. Jia, Numerical investigation on the application of catalytic combustion to HCCI engines. *Chem. Eng. J.* **127**, 81–93 (2007)
41. T. Hejwowski, A. Weronki, The effect of thermal barrier coatings on diesel engine performance. *Vacuum* **65** 427–432 (2002)
42. C. Hasimoglu et al., Performance characteristics of a low heat rejection diesel engine operating with biodiesel. *Renew Energy* (2007). <https://doi.org/10.1016/j.renene.2007.08.002>
43. A.P. Sathiyagnanam, S.C. Gand Dhandapani, Effect of thermal-barrier coating plus fuel additive for reducing emission from diesel engine, in *Proceedings of the World Congress on Engineering, WCE 2010*, vol. II, June 30–July 2, London (2010)
44. B. Jose, et al., Thermal barrier coating on IC engine piston to improve efficiency. *Int. J. Sci. Eng. Res.* **8**(3) (2017). ISSN 2229-5518
45. J. Sadhik Bhasha, R.B. Anand, Application of Nano particle or nano fluid in CI engine—A case study. *Int. J. Appl. Eng. Res.* **5**(4), 697–708 (2010). ISSN 0973-4562
46. M.-J. Kao, C.-C. Ting, B.-F. Lin, T.-T. Tsung (2008) Aqueous aluminium nanofluid combustion in diesel fuel. *J. Test. Eval.* **36**(2), PA 19428-2959
47. V. Srinivasan, Prof. G. Siva Kumar, Review on nano particles in CI engine with new and better proposal on stabilization. *Int. J. Innov. Res. Sci. Eng. Technol.* **5**(2) (2016). <https://doi.org/10.15680/ijirset.2016.0502093,2319-8753>
48. A.I. EL-Seesya, A.K. Abdel-Rahmana, M. Badya, S. Ookawarab, The Influence of multi-walled carbon nano tubes additives into non-edible biodiesel-diesel fuel blend on diesel engine performance and emissions, in *3rd International Conference on Power and Energy Systems Engineering, CPSE 2016*, 8–12 September 2016, Kitakyushu, Japan
49. S. Intenan, H.H. Masjuki, M. Varman, M.A. Kalam, M.I. Arbab, H. Sajjad, S.M. Ashrafur Rahman, Impact of oxygenated additives to palm and jatropa biodiesel blends in the context of performance and emissions characteristics of a light-duty diesel engine. *Energy Convers. Manage.* **83** 149–158 (2014)
50. S. Mahade, N. Curry, S. Bjorklund, N. Markocsan, P. Nysten, R. Vassen, Functional performances of Gd₂Zr₂O₇/YSZ multi-layered thermal barrier coatings deposited by suspension plasma spray. *Surf. Coat. Technol.* **318**, 208–216 (2017)
51. N. Schlegel, D. Sebold, Y.J. Sohn, G. Mauer, R. Vassen, Cycling performance of a columnar-structured complex perovskite in a temperature gradient test. *J. Therm. Spray Technol.* **24**, 1205–1212 (2015)
52. D. Zhang, et al., Thermal barrier Coatings prepared by EBPVD. *J. Sci. Direct* (2011)
53. A.M. Karlsson, Modeling failures of TBC's. *J. MSL Acad. Endeavors* 155–165 2007
54. M. Azadi, et al., A review of TBC effects on diesel engine performance and components lifetime. *J. Autom. Eng.* **3**(1) (2015)
55. S. Lakshmanan, et al., Investigation of thermal barrier coating on IC engine piston. *Int. J. Res. Appl. Sci. Technol.* **Special Issue-1**, (2014). SJ ISSN 2321-9653
56. T. Balamurugan, et al., Effect of TBC on piston in performance, combustion and emission characteristics of a diesel engine. *J. Curr. Res. Dev.* (2018)
57. V. Gnanamoorthi, et al., The effect of TBC material in CI engine. *J. Chem. Pharm. Res.* **7**(2) (2015)

Modeling and Analysis of Compression Ignition Engine Performance and Emissions of Biodiesel



V. Nageswar Reddy, G. Sreenivasarao, and K. Thirupati Reddy

Abstract Biodiesel is one of the most promising alternative fuels for diesel engines because they are potentially renewable, nontoxic, biodegradable, clean-burning, high lubricity, low environmental impact, derived from vegetable oils, and could be used directly in diesel engines without requiring extensive engine modifications. The major objective of the present work is to investigate the engine performance and exhaust emissions of variable compression ratio of a single cylinder, 4-stroke, and direct injection diesel engine with different blends of biodiesel, load, compression ratio, and injection pressure. Four parameters were considered to investigate the engine performance and emissions. Hence, to reduce the cost of experimentation, it is decided to conduct the experiments using Design of Experiments (DOE) technique, which in turn reduces the number of experiments. The significant parameters were determined using the Analysis of Variance (ANOVA) test. The adequacy of the developed models is verified by using coefficient of determination (R^2). The results are predicted by the response surface model. The engine performance and emissions were analyzed in detail.

Keywords Biodiesel · Compression ratio · Design of experiments (DOE) technique · Emissions · Injection pressure · Load

V. Nageswar Reddy (✉) · K. Thirupati Reddy
Department of Mechanical Engineering, Rajeev Gandhi Memorial College of Engineering and Technology, Nandyal, Andhra Pradesh, India
e-mail: vnreddy70@gmail.com

K. Thirupati Reddy
e-mail: gsraorvr@gmail.com

G. Sreenivasarao
Department of Mechanical Engineering, R.V.R & J.C. Engineering College, Guntur, Andhra Pradesh, India
e-mail: kotatreddy@gmail.com

1 Introduction

Schwab et al. [1] Fuel Properties of Eleven Vegetable oils. Pischinger and Siekmaam [2] Results of Engine and Vehicle Tests with Methyl Esters of Plant Oils as Alternative Diesel Fuels. Nagarajaiah and Giriprakash [3] Experimental investigation using alcohols and vegetable oils as fuels for CI engines Goering and Jindal [4] Experimental investigation of the effect of compression ratio and injection pressure in a DI diesel engine running on jatropha methyl ester. Jo-Han [5] Advances in biodiesel fuel for application in compression ignition engines. Karnwal et al. [6] Multiresponse optimization of diesel engine performance parameters using Thumba biodiesel—diesel blends by applying the Taguchi method and Grey relational analysis. Maheswari [7] A nonlinear regression based multi-objective optimization of parameters based on experimental data from an IC engine fueled with biodiesel blends. The software was released in its first version in 1968 as the Statistical Package for the Social Sciences (SPSS) after being developed by Norman, Dale H. Bent, and C. Hadlai Hull. SPSS is widely used in programming for statistical analysis in social science. It is also used by market researchers, health researchers, survey companies, government, education researchers, marketing organizations, data miners, and others.

2 Modeling

One of the important data mining techniques, regression analysis has been applied to develop the mathematical models for brake thermal efficiency, nitrogen oxide, and carbon dioxide in terms of input parameters: compression ratio, injection pressure (in bars), applied load (kg), and blend (%). It has been decided to use three levels for the control factors to capture nonlinearity. $L81 (3^4)$ orthogonal array (OA) has been used to perform the experimental combination involving engine parameters. The design resulted in a total of 81 experiments were conducted to analyze the influence of engine performance and emissions. Levels for Control Factors are shown in Table 1.

Based on the experimental data, the parameter estimates, ANOVA and model equations are given for each response. The R^2 values for the model equations of brake thermal efficiency, brake-specific fuel consumption, nitrogen oxide, carbon

Table 1 Level for control factors

Factor symbol	Factor Name	Level-(1)	Level-(2)	Level-(3)
<i>V</i>	Compression ratio	14	16	18
<i>P</i>	Injection pressure (In bars)	180	200	220
<i>L</i>	Applied load on the engine(kgf)	03	09	15
<i>B</i>	Blend (%)	10	20	30

dioxides, carbon monoxide, and hydrocarbons are 0.996, 0.963, and 0.981, respectively, which is very close to unity showing good correlation between input values and the responses are shown in Table 2.

$$\begin{aligned}
 \text{BTE} = & 19.459 - 0.266 * P + 2.675 * L \\
 & + 0.002 * V * V + 0.001 * P * P - 0.035 * L * L \\
 & - 0.002 * V * B - 0.002 * P * L + 0.003 * L * B.
 \end{aligned}
 \tag{1}$$

($R^2 = 0.996$).

From Eq. (1), it can be observed that load and pressure are most significant on brake thermal efficiency. Though the individual effect of compression ratio and blend is not identified as significant, their presence as interaction terms is also identified are shown in Table 3.

From the graph, it can be observed that the factor load is highly significance on BTE, followed by the factor pressure and blend. In addition to the individual

Table 2 Parameter estimates for brake thermal efficiency

Model	Unstandardized coefficients		Standardized coefficients	t	Significance	
Constant	19.459	14.029	–	2.029	0.046	
P	–0.266	0.140	–0.482	–1.855	0.068	
L	2.675	0.183	1.486	14.635	0.000	
VV	0.002	0.001	0.012	1.717	0.090	
PP	0.001	0.001	0.542	2.089	0.040	
LL	–0.035	0.004	–0.358	–9.031	0.000	
VB	–0.002	0.001	–0.037	–2.340	0.022	
PL	–0.002	0.001	–0.179	–1.929	0.058	
LB	0.003	0.002	0.049	2.074	0.042	
Model	Sum of squares		df	Mean square	F	Significance
<i>ANOVA</i>						
Regression	6279.045		8	784.881	2.221E3	0.000f
Residual	25.449		72	0.353	–	–
Total	6304.494		80	–	–	–

Table 3 Level means of brake thermal efficiency

	V	P	L	B
Level-1	23.81	23.56	12.65	23.89
Level-2	23.74	23.63	24.67	23.86
Level-3	23.92	23.78	34.95	23.72
Difference	0.11	0.22	22.30	0.16

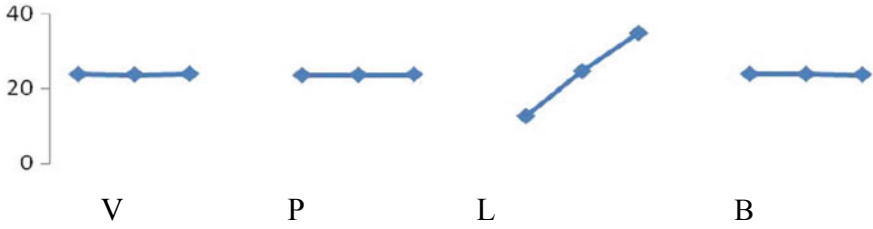


Fig. 1 Response graphs of BTE

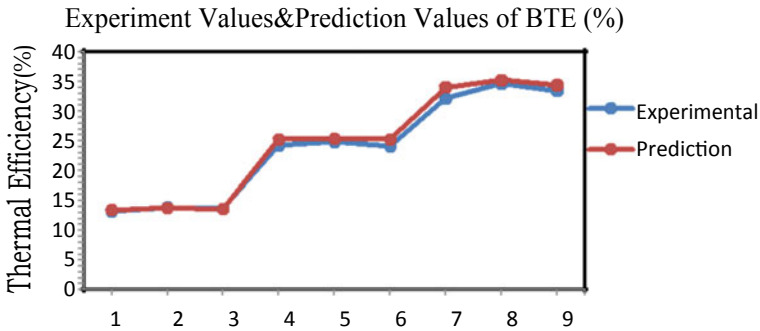


Fig. 2 Experimental and prediction values of BTE

effect of load and pressure interaction with compression ratio and blend its square term entering into the model are shown in Fig. 1. Though the individual effect of compression ratio and blend is not identified as significant, their interactions, i.e., *VV*, *PP*, *VB*, *PL*, and *LB* entering into the model are shown in Fig. 2.

$$\begin{aligned}
 NO_x = & 1145.159 - 14.562 * P + 65.073 * L \\
 & + 0.031 * P * P - 0.308 * L * L + 0.164 * V * P \\
 & - 1.043 * V * L - 0.101 * P * L + 0.013 * P * B. \quad (2)
 \end{aligned}$$

($R^2 = 0.961$).

From Eq. (2), it can be observed that load and pressure are most significant on nitrogen oxides. Though the individual effect of compression ratio and blend is not identified as significant, their presence as interaction terms is also identified shown in Table 4.

From the graph, it can be observed that the factor load is highly significance on nitrogen oxides, followed by the factor variable compression ratio and pressure shown in Table 5. In addition to the individual effect of load, pressure interaction with variable compression ratio and blend its square term entering into the model. Though the individual effect of blend is not identified as significant, their interactions, i.e., *VP*, *VL*, *PL*, and *PB* entering into the model are shown in Fig. 3.

Table 4 Parameter estimates for nitrogen oxides

Model	Un standardized coefficients		Standardized coefficients	t	Significance
Constant	1145.159	605.551	–	1.908	0.600
P	–14.562	6.059	–1.986	–2.458	0.160
L	65.073	9.600	2.606	6.778	0.000
PP	0.031	0.015	1.668	2.069	0.042
LL	–0.308	0.168	–0.226	–1.833	0.071
VP	0.164	0.018	0.560	9.029	0.000
VL	–1.043	0.353	–0.682	–2.959	0.004
PL	–0.101	0.036	–0.820	–2.837	0.006
PB	0.013	0.002	0.180	7.577	0.000
Model	Sum of squares	df	Mean square	F	Significance
<i>ANOVA</i>					
Regression	1,170,309.289	8	146,288.661	221.998	0.000f
Residual	47,445.329	72	658.963	–	–
Total	1,217,754.618	80	–	–	–

Table 5 Level means for nitrogen oxides

	V	P	L	B
Level-1	1.85E2	2.43E2	91.333	2.03E2
Level-2	2.27E2	2.22E2	2.380E2	2.33E2
Level-3	2.78E2	2.62E2	3.625E2	2.55E2
Difference	0.93E2	0.19E2	2.71E2	0.52E2

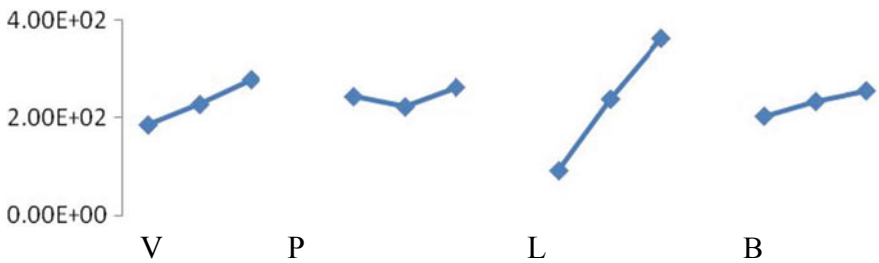


Fig. 3 Response graphs of NO_x

$$CO_2 = 1.045 + 0.15L + 0.001B - 0.002 * LL + 0.0001VP + 0.001VB + 0.001LV \tag{3}$$

(R² = 0.971).

From Eq. (3), it can be observed that load and blend are most significant on carbon dioxide shown in Table 6. Though the individual effect of compression ratio and pressure is not identified as significant, their presence as interaction terms is also identified shown in Fig. 4.

From Fig. 5, it can be observed that the factor load is highly significant on carbon dioxide, followed by the factor blend. In addition to the individual effect of load, its interaction with blend and its square term entering into the model is shown in Table 7. Though the individual effect of injection pressure and compression ratio is not identified as significant, their interactions, i.e., *VP*, *VB*, and *PB* entering into the model are shown in Fig. 6.

$$HC = 118.219 - 9.713 * V - 2.910 * L + 0.526 * B + 0.255 * VV$$

Table 6 Parameter estimates for carbon dioxide

Model	Unstandardized coefficients		Standardized coefficients	T	Significance
Constant	1.045	0.378	–	4.784	0.000
<i>L</i>	0.150	0.021	0.997	8.410	0.000
<i>B</i>	+0.001	0.034	–0.849	–2.726	0.008
<i>LL</i>	–0.002	0.001	–0.183	–1.705	0.092
<i>VP</i>	0.0001	0.001	–0.163	–3.073	0.003
<i>VB</i>	0.001	0.002	0.403	2.422	0.018
<i>PB</i>	0.000	0.002	0.478	2.743	0.008
<i>LV</i>	0.001	0.001	0.205	3.124	0.003
Model	Sum of squares	<i>df</i>	Mean square	<i>F</i>	Significance
<i>ANOVA</i>					
Regression	61.743	7	8.820	335.348	0.000 g
Residual	1.920	73	0.026	–	–
Total	63.663	80	–	–	–

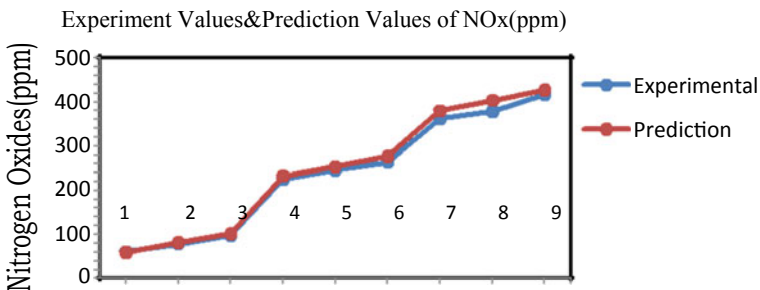


Fig. 4 Experimental and prediction values of NO_x

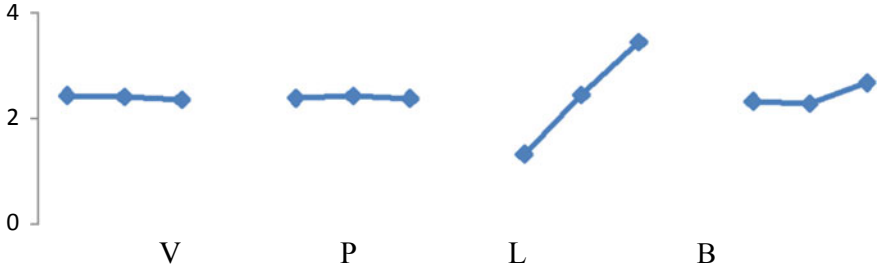


Fig. 5 Response graphs of CO2

Table 7 Level means for carbon dioxide

	V	P	L	B
Level-1	2.44	2.39	1.33	2.33
Level-2	2.41	2.43	2.45	2.28
Level-3	2.36	2.38	3.45	2.68
Difference	0.08	0.01	2.12	0.35

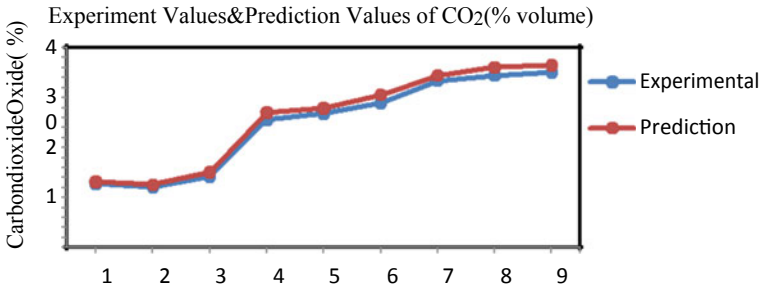


Fig. 6 Experimental and prediction values of CO2

$$+ 0.095 * LL + 0.093 * VL - 0.003 * PB + 0.014 * LB \tag{4}$$

From Eq. (4), it can be observed that load, compression ratio, and blend are most significant on hydrocarbons. Though the individual effect of pressure is not identified as significant, their presence as interaction terms is also identified shown in Table 8.

3 Discussions

From Fig. 7, it can be observed that the factor load is highly significant on hydrocarbons, followed by the factor compression ratio and pressure as shown in Fig. 8.

Table 8 Parameter estimates for hydrocarbons

Model	Unstandardized coefficients		Standardized coefficients	T	Significance
Constant	118.219	38.660	—	2.851	0.006
V	-9.713	4.486	-3.544	-2.009	0.048
L	-2.910	0.661	-3.186	-4.407	0.000
B	0.526	0.177	0.959	2.975	0.004
VV	0.255	0.151	2.975	1.690	0.095
LL	0.095	0.017	1.899	5.653	0.000
VL	0.093	0.036	1.658	2.607	0.011
PB	-0.003	0.001	-1.281	-4.262	0.000
LB	0.014	0.007	0.413	2.020	0.047

Model	Sum of squares	df	Mean square	F	Significance
<i>ANOVA</i>					
Regression	1151.898	8	143.987	32.617	0.000f
Residual	470.867	72	6.540	—	—
Total	1622.765	80	—	—	—

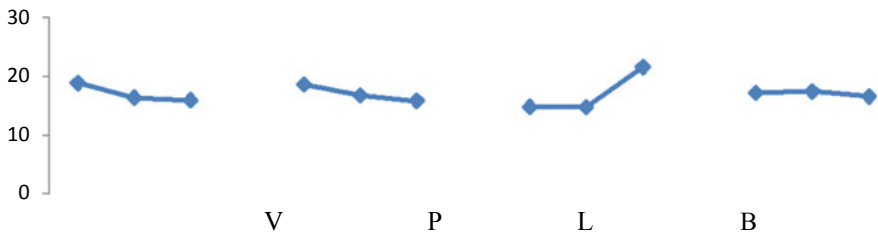


Fig. 7 Response graphs of HC

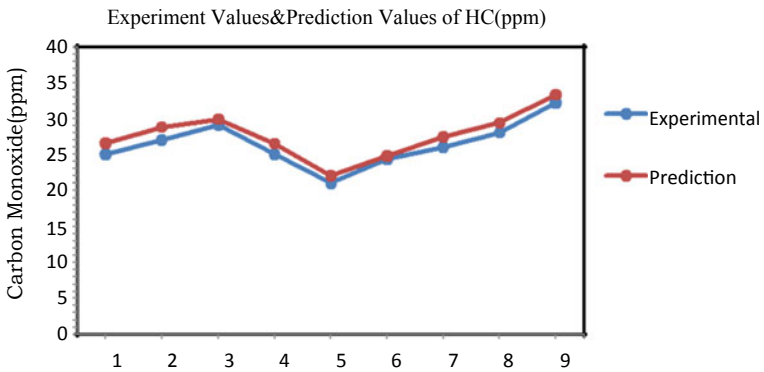


Fig. 8 Experimental and prediction values of HC

Table 9 Level means for hydrocarbons

	<i>V</i>	<i>P</i>	<i>L</i>	<i>B</i>
Level-1	18.9259	18.6667	14.8889	17.2593
Level-2	16.4444	16.8148	14.8519	17.4815
Level-3	16.0000	15.8889	21.6296	16.6296
Difference	2.9259	2.7778	6.7777	0.8519

In addition to the individual effect of load and compression ratio, interaction with pressure and blend and its square term entering into the model are shown in Table 9. Though the individual effect of blend is not identified as significant, their interactions, i.e., *VV*, *LL*, *VL*, *PB*, and *LB* are entering into the model.

4 Conclusions

- Biodiesel blends B20 provided the maximum brake thermal efficiency of all compression ratios.
- Exhaust emissions of carbon dioxide were reduced for biodiesel blends when compared with diesel values for all compression ratios and lower compression ratios have the advantage of further reduction in those emissions.
- The better nitrogen oxides emissions were observed with biodiesel blends compared to that of diesel fuel for all compression ratios.
- From the design of experiments, the optimum value of brake thermal efficiency was found at a higher value of load and blend and for any level of compression ratio and pressure.
- The optimum value of nitrogen oxides was found at lower values of compression ratio, load, blend, and for any level of pressure.
- Hydrocarbon emissions were increased at higher compression ratio because of rich pockets of fuel accumulation in the combustion chamber.
- From the model equations, the presence of interactions and second-order terms also identified, which can give further insight into the process.
- Model equations are also helpful to predict the required performance characteristic for a given set of input conditions.

References

1. A.W. Schwab, M.J. Daugherty, E.H. Pryde, A.J. Heakin, Fuel properties of eleven vegetable oils. Trans. ASAE **25**, 1472 (1982)

2. B.S. Nagarajaiah, K. Giriprakash, G. Acharya, Experimental investigation using alcohols and vegetable oils as fuels for CI engines, in *Proceedings of VII, National Conference on IC Engines and Combustion*. KREC, Srinivasnagar (D.K), India (1982)
3. C. Balaji, A. Ramesh, A nonlinear regression based multi-objective optimization of parameters based on experimental data from an IC engine fueled with biodiesel blends. *Biomass Bioenergy* **35**(2), 2171–2183 (2011)
4. S. Jindal, B.P. Nandwana, N.S. Rathore, Vashistha, Experimental investigation of the effect of compression ratio and injection pressure in a DI diesel engine running on jatropha methyl ester. *Appl. Ther. Eng.* **30**(5), 442–448 (2010)
5. N.G. Jo-Han, N.G. Hoon Kiat, G. Suyin, Advances in biodiesel fuel for application in compression ignition engines. *Clean. Technol. Environ. Policy* **12**(5), 459–493 (2010)
6. M. Karnwal, N. Hasan, A. Kumar, N. Siddiquee, Z.A. Khan, Multiresponse optimization of diesel engine performance parameters using Thumba biodiesel—diesel blends by applying the Taguchi method and grey relational analysis. *Int. J. Autom. Technol.* **12**(4), 599–610 (2011)
7. G. Pischinger, R.W. Siekmaam, A.M. Falcon. F.P. Fernandes, Results of engine and vehicle tests with methyl esters of plant oils as alternative diesel fuels, in *Proceedings of Fifth International Conference on “Alcohol fuel Technology”* Auckland, New Zealand (1982)

Simulation of Performance of Boiler System for a Bagasse Unit Using LabVIEW



Mahesh G. Emmi, Aravindrao M. Yadwad, Vinay V. Kuppast, B. S. Talikoti, and M. Sampanna

Abstract Cogeneration plants are one of the major power generation sources in this era of industrialization and automation. Bagasse is a by-product generated by the sugar industries on a large scale in India. The cogeneration plants use the bagasse produced by the sugar industries to generate power. Boiler system forms one of the primary components of the cogeneration plant. Designing a virtual model of the boiler system will help to model optimal systems. Simulation of the performance of the boiler system will aid in predictive maintenance as well. In this paper, a virtual model of a boiler system for a bagasse unit is designed in the LabVIEW software package. Such kind of performance analysis aids in better designs of actual models and predictive maintenance, which in turn saves time and reduces unwanted expenditures due to failures.

Keywords Boiler system · Bagasse unit · Simulation · LabVIEW

M. G. Emmi

The National Institute of Engineering, Mysore, Karnataka State, India

A. M. Yadwad

Department of Mechanical Engineering, The National Institute of Engineering, Mysore, Karnataka State, India

V. V. Kuppast

Department of Mechanical Engineering, Basaveshwar Engineering College, Bagalkot, Karnataka, India

B. S. Talikoti (✉)

Department of Mechanical Engineering, Pillai College of Engineering, New Panvel, Maharashtra 410206, India

e-mail: btalikoti21@gmail.com

M. Sampanna

Indian Cane Power Limited, Davangare, Karnataka, India

© Springer Nature Singapore Pte Ltd. 2021

G. S. V. L. Narasimham et al. (eds.), *Recent Trends in Mechanical Engineering*,

Lecture Notes in Mechanical Engineering,

https://doi.org/10.1007/978-981-15-7557-0_7

1 Introduction

Generation of power from sources which do not exploit our natural reserves and resources is a matter of concern in this era of industrialization. Cogeneration plants mainly have a boiler and a turbine system, which generates power in MW when supplied with proper fuel [1–4]. In this paper, a boiler system has been modelled in the LabVIEW software package. This virtual model of boiler system helps to analyse the performance of the system so that different output parameters and entities, which can improve the performance of the system can be determined. The distinct blocks which make a boiler system have been designed using formulae from standard references. The deigned virtual system has been validated by simulating it for known input parameters from an actual boiler system. The simulated signals and the actual signals are compared to verify whether the virtual model behaves the same way as that of the actual system when simulated for a known set of input and output parameters. [5–7].

2 Methodology

The methodology of the system is shown in Fig. 1. The boiler system has been designed in LabVIEW. The different system parameters include boiler firing rate, combustibility of the system, enthalpy of the fuel, enthalpy of water, enthalpy of coal, steam flow, transfer function, fuel gain and power to the turbine [8–10]. After modelling the system parameters by using their formulae, they are interconnected together depending upon their relationship with different entities.

After the virtual boiler system has been modelled, it is validated for a known set of parameters. Data from an actual cogeneration plant is considered and the behaviour

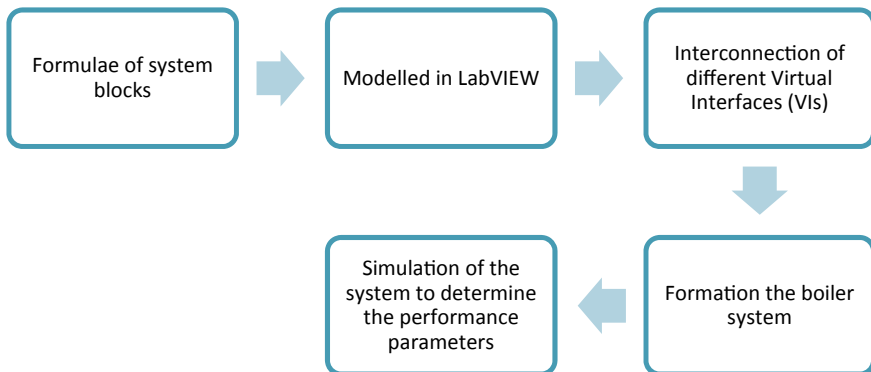


Fig. 1 Methodology

of the simulated system is analysed. If the same set of output parameters are observed with closely matching values, then the virtual model is said to behave as desired.

3 Boiler System

Figures 2 and 3 show the block diagram of the boiler system designed in LabVIEW and the Virtual Interface (VI), where the signatures of the simulated signals can be observed and analysed.

The boiler firing rate determines the energy transfer and decides the opening of the valves. The steam flow is the energy output from the boiler. The different enthalpies considered are for the energy stored in the system.

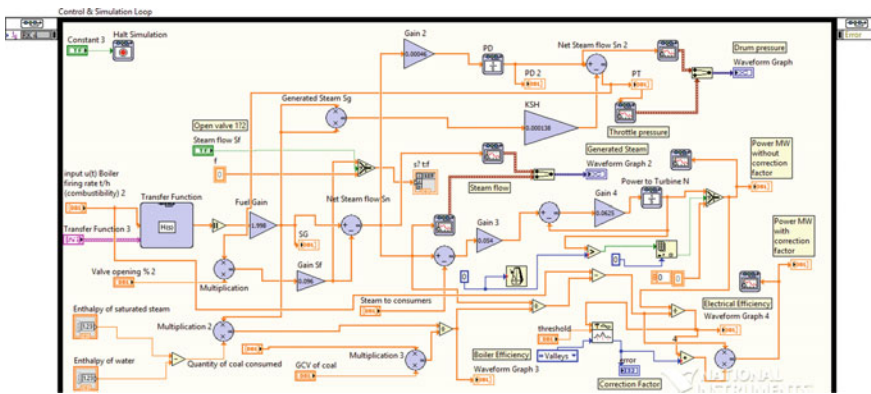


Fig. 2 Boiler system in LabVIEW

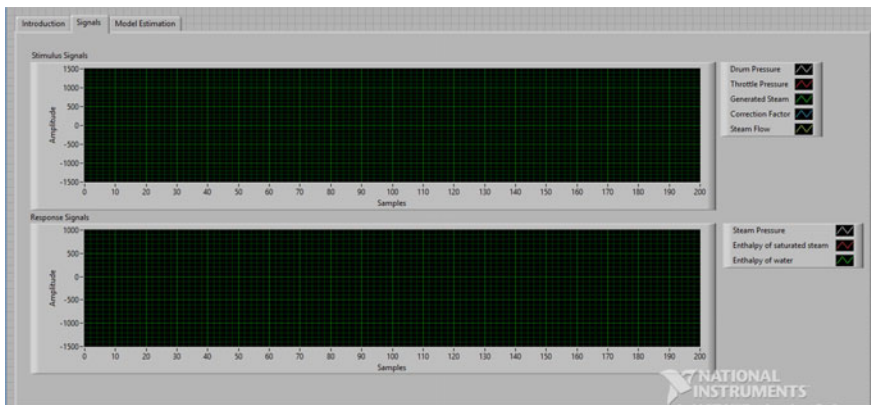


Fig. 3 Virtual interface to display various simulated signals

4 Results

The results showing the simulated signals are as shown in the figures below.

Figure 4 shows the signatures of the simulated signals. Figures 5 and 6 show the power generated by the system in MW. A separate entity of correction factor is considered to normalize the effect on the power generated during off-season days, when the quantity of bagasse and coal used as fuels differ. In Figs. 5 and 6, the signature in red indicates the simulated signal and the signature in white indicates

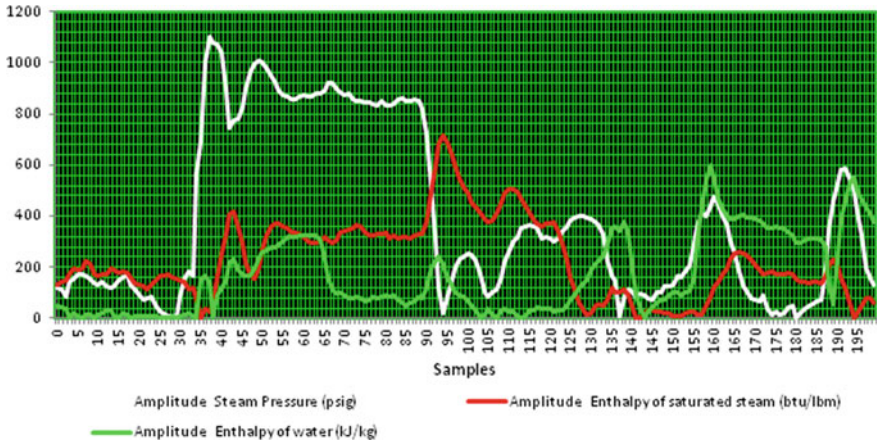


Fig. 4 Simulated signals of boiler output

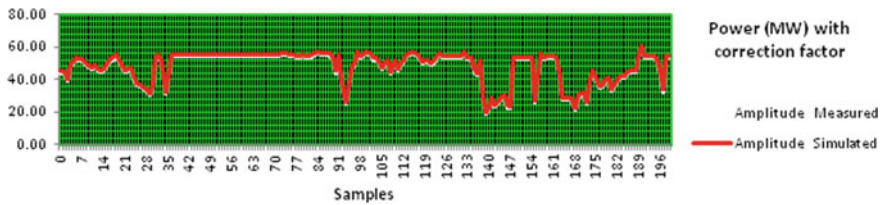


Fig. 5 Power (MW) with correction factor

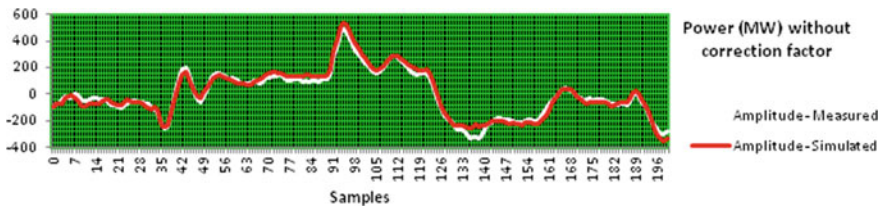


Fig. 6 Power (MW) without correction factor

the measured signals. As both the signatures are seen to closely match each other, it indicates that the designed boiler system is correctly validated.

5 Conclusion

The boiler system described in this paper provides high accuracy with automation by providing the parameters required for predictive maintenance. The system developed makes performance analysis less time consuming and is less expensive as compared to experimental methods.

References

1. Indian Cane Power Limited, Uttur Village, Tal.: Mudhol, Dist: Bagalkot, Pin: 587313 State: Karnataka (Data Analysis)
2. S. Gupta, P.C. Tewari, A.K. Sharma, Reliability and availability analysis of ash handling unit of a steam thermal power plant. *South Afr. J. Ind. Eng.* **20**(1), 147–158 (2009)
3. S. Hosseini, N. Safaei, M. Asgharpour, Reprioritization of failures in a system failure mode and effects analysis by decision making trial and evaluation laboratory technique. *Reliab. Eng. Syst. Saf.* **20**(1), 147–158 (2006)
4. S. Kumar, D. Kumar, N.P. Mehta N.P. Behavioral analysis of gasification and carbon recovery process in a urea fertilizer plant. *Microelectr. Reliab.* **36**(5), 671–673 (1995)
5. S. Kumar, G. Chattopadhyay, U. Kumar, Reliability improvement through alternative design. *Reliab. Eng. Syst. Saf.* **92**, 983–991 (2007)
6. Ankur Scientific Technologies Pvt. Ltd
7. Best practice manual for cogeneration prepared for Bureau of Energy Efficiency (under Ministry of Power, Government of India) Hall no. 4, 2nd Floor, NBCC Tower, Bhikaji Cama Place, New Delhi – 110066. Indian Renewable Energy Development Agency, Core 4A, East Court, 1st Floor, India Habitat Centre, Lodhi Road, New Delhi – 110003 By Devki Energy Consultancy Pvt. Ltd., 405, Ivory Terrace, R.C. Dutt Road, Vadodara – 390007, India (2006)
8. Energy performance assessment of boilers by Bureau of Energy Efficiency
9. L.S. To^{a,b,*}, V. Seebaluck, M. Leachd, Future energy transitions for bagasse cogeneration: Lessons from multi-level and policy innovations in Mauritius. *Energy Res. Soc. Sci.* **68–77** (2018) (Elsevier)
10. B. Mtunzi, N. Mampwheli, E. Meyer, Bagasse-based co-generation at Hippo Valley Estates sugar factory in Zimbabwe. *J. Energy S. Afr.* **23**(1) (2012)

Experimental Investigation of Performance, Emission and Combustion Characteristics of a Di-diesel Engine Fuelled with Aqueous Cerium Oxide and Aqueous Aluminium Oxide Nanoparticle Additives



P. Ravichandra Ganesh, K. Hemachandra Reddy, J. M. Babu, and M. Sarath Chandra

Abstract Experiments were conducted to determine the engine performance and emission characteristics of Direct Injection (DI)—diesel engine using aqueous cerium oxide nanoparticles (ACONP) and aqueous aluminium oxide nanoparticles (AAONP) as an additive in diesel, ethanol and surfactant blended fuel and were compared with diesel fuel. Blends were prepared by in proportions of Diesel 83%, Ethanol 15% and Surfactant 2% (Span 80) with 50 and 75 ppm aqueous cerium oxide and aqueous aluminium oxide nanoparticles as an additive, denoted as ACONP50, ACONP75, AAONP50 and AAONP75, respectively. The blends are prepared by uniform mixing of nanoparticles with the help of an ultrasonicator. Nanoparticles were acted as an oxygen-donating catalyst which improves the combustion process and results in complete combustion. This will also reduce the hydrocarbons (HC) and carbon monoxide (CO) emissions. It was observed that there is a significant enhancement of performances and decrease of exhaust emissions HC, CO, smoke,

P. Ravichandra Ganesh (✉)

Department of Mechanical Engineering, Dr. M. G. R. Educational and Research Institute, University, Chennai, Tamil Nadu 600095, India
e-mail: prcganesh@gmail.com

K. Hemachandra Reddy

Andhra Pradesh State Council of Higher Education, Mangalagiri, Andrapradesh, India
e-mail: konireddy@gmail.com

J. M. Babu

Department of Mechanical Engineering, Vel Tech Rangarajan Dr. Sagunthala R&D Institute of Science and Technology, Avadi, Chennai, Tamil Nadu 600062, India
e-mail: jmbabu@veltech.edu.in

M. Sarath Chandra

Department of Mechanical Engineering, Guru Nanak Institutions Technical Campus, Ibrahimpatnam, Hyderabad, Telangana, India

© Springer Nature Singapore Pte Ltd. 2021

G. S. V. L. Narasimham et al. (eds.), *Recent Trends in Mechanical Engineering*, Lecture Notes in Mechanical Engineering,
https://doi.org/10.1007/978-981-15-7557-0_8

slight increase in nitrogen oxides (NO_x) as compared to diesel fuel. The combustion parameters like cylinder pressure and heat release rates are increased for both nanoparticles as an additive which has been compared with pure diesel.

Keywords Di-diesel engine · Aqueous aluminium oxide nanoparticles (AAONP) · Aqueous cerium oxide nanoparticles (ACONP) · Surfactant · Performance · Emission

1 Introduction

Usage of diesel fuel and diesel engines is increasing day by day due to the increase of world population and for transportation as well as for other purposes. To reach the stringent emission norms, it is a necessity to investigate the new and renewable fuels like ethanol, methanol, and biodiesel. All over the world, it is easy to produce and store the ethanol when compared with other fuels. Using suitable emulsifier to diesel, ethanol blends can make a heterogeneous mixture up to one microparticle, liquid phase, emulsifier reduces the interfacial tension and increase the suspension stability. Addition of ethanol to diesel fuel blends affects the properties such as lubricity, viscosity, energy content, and certain number also reducing the ignition delay. Bioethanol is having high oxygen content in the fuel and is the main cause of the increase in CO emissions, but it can be compensated by the addition of nanoparticles. There is another cause that most of the countries were using ethanol as diesel fuel blends because of its low toxic emissions, lower risk of harm to the environment and a cleaner fuel. The main drawback of ethanol was corrosion effect of various diesel engine parts, but this can also overcome by using a transesterification process to produce the ethanol fuel. The main reason for selecting nanoparticles as additives in the fuel blends is very small in size and properties are different with compared to large micro-sized particles. Nanoparticles possessed desirable combustion characteristics of high heat and high-energy-releasing during combustion is the main cause to attract the most researchers to use the nanoparticles as additives in diesel fuel blends. The main objective of this study is to reduce the emissions, promotion of complete combustion, and enhanced performance using nanoparticles as additive with ethanol emulsified diesel fuel blends.

2 Literature Review

Ethanol is a good fuel to use in diesel engines with nanoparticles because of its lower energy density than the other liquids. Microexplosion occurred even before the droplet was ignited for the ethanol/nano-Al suspension this is due to aluminium particles were burned completely during the classical combustion stage [1]. The researchers used emulsifier surfactant (Tween 80) with ethanol and diesel fuel blends

and shown performance enhancement and reduced smoke emissions of the diesel engine as compared to diesel fuel [2]. The addition of cerium likely to increase the number of catalytic sites and oxidation rate. Also, the authors suggested that doping of cerium 25–100 ppm to the diesel fuel is beneficial to increase the efficiency, but adding more than 100 ppm is not advisable [3]. The combustion enhancement and reduction of HC emission 7.2% and smoke 47.6% are observed by the addition of Sarah and CNT each 50 ppm in E20 blended fuel [4]. If ethanol is used as emulsifying fuel in a diesel engine, which enhances the performance, combustion, and reduces the emissions except for NO_x it is because of the higher oxygen content of ethanol [5]. Using ethanol 10–15% in diesel engine results showed that reduced smoke emissions [6]. In general, the addition of cerium oxide nanoparticles enhances the engine performance, because its stable thermal characteristics promotes oxidation and acts as an effective catalyst to reduce the CO emission [7]. Investigation showed cerium oxide nanoparticles on compression ignition engine, which influences the increase of the BTE, reduces the emissions HC, CO, NO_x, and smoke opacity [8]. In our previous study, we used aqueous cerium oxide nanofluid in diesel, ethanol blends results proved reduced emission like HC, CO, smoke and slight increase in NO_x emission [9]. Addition of aluminium oxide nanoparticles on diesel, soybean biodiesel and ethanol blends enhances the combustion because of its better mixing property, and reduces the CO, unburned hydrocarbon and there is a slight increase of NO_x emission at full load condition [10]. The researchers used cerium oxide nanoparticles, which promotes complete combustion which is the main cause to reduce the exhaust emissions like HC, CO, and due to an enhanced combustion increase of oxygen content which increases the NO_x emission, the authors suggested that combination of both cerium oxide and ferro fluids may give better performance and reduced emissions [11]. The previous study used cerium oxide for diesel fuel as additives, which give better results as compared to zinc oxide nanoparticles by enhancement of performance and reduction of exhaust emissions [12]. The previous chapter, it is clear that there is 5% increase in BTE and reduction in emissions by the addition of cerium oxide nanoparticles to diesel fuel [13]. The investigation is focused on the effect of *n*-Al₂O₃ on diesel engine with diesel fuel in increasing the catalytic behaviour, reduce the ignition delay period and reduce the emissions like CO, smoke and NO_x [14]. This investigation proved that the addition of aluminium oxide nanoparticles improved the performance and reduction of NO_x and CO emissions but at peak load conditions HC emission was slightly higher than the diesel fuel [15]. The researchers used the aluminium oxide and iron oxide nanoparticles in mahua methyl ester (biodiesel), nanoparticles were acts as an oxygen-donating catalyst and gives oxygen for oxidation of unburned hydrocarbon and carbon monoxide at exhaust, and reduces the exhaust emissions [16]. In this papers authors used nano-aluminium and nano-aluminium oxide particles with ethanol and it is observed that the nano-aluminium oxide particles were actively participated in combustion and influences the combustion [17]. Using aqueous aluminium oxide nanoparticles as additives in diesel ethanol blends it is proved that exhaust emissions like CO, HC and smoke reduced and brake thermal efficiency increased [18]. The research were carried out the investigation on cottonseed oil and its blended fuel with nanoadditives

(cerium oxide) and results showed that lower fuel consumption, improved performance and reduced emissions like CO, HC but higher in NO_x emissions as compared to neat diesel fuel [19]. Researchers were focused on ZnO nanoparticles as an additive in diesel fuel and shown that nanoparticles addition is a new innovative idea for the future to reduce the engine exhaust emissions and enhancement of performance characteristics [20]. The researchers used cerium oxide nanoparticles in a diesel engine, which acts as an oxygen buffer and promote longer and complete combustion. Also observed that increasing the BTE with increasing of the dosing level of the nanoparticles [21]. This reviewed paper showed that using aqueous aluminium and cerium oxide nanoparticles fuel gets complete combustion, because of its improved combustion quality and reduces the fuel consumption, increased BTE and reduced exhaust emissions as compared to diesel fuel [22]. The researchers were used Ziziphus jujube oil with aluminium oxide nanoparticles and proved that SFC decreased by increasing the dosage of aluminium oxide nanoparticles and also observed that reduction in CO and smoke emissions [23].

3 Experimental Setup and Procedure

The performance and emission characteristics of a diesel engine with diesel, ethanol and surfactant fuel blends with the addition of aqueous aluminium oxide, aqueous cerium oxide nanoparticles (AAONP50, AAONP75, ACONP50 and ACONP75) were carried out on a single-cylinder, four strokes direct injection, naturally aspirated, air-cooled diesel engine. The fuel tank is connected to a graduated burette to measure the quantity of fuel consumed in unit time. The engine was coupled to an eddy current dynamometer to control engine speed and load. The performance characteristics of brake-specific fuel consumption (BSFC) and brake thermal efficiency (BTE) were calculated. The exhaust emissions CO, HC and NO_x were measured by using AVL-444 Digas analyzer. Smoke opacity is measured by using a Bosch smoke metre. All the tests are conducted by starting and warming up the engine with neat diesel and then switching to blended mixtures. At the end of the test, the engine is made to run with the neat diesel to flush out the blended fuels from the fuel line and the injection system. The performance and emission characteristics are drawn and compared with diesel fuel. The schematic layout of the experimental setup is shown in Fig. 1. The details of engine specifications are shown in Table 1.

3.1 Experimental Fuels

The commercial diesel fuel was used for the preparation of fuel blend procure from the local diesel outlet. AAONP fluid and ACONP are purchased from Reinste Nano Ventures Pvt. Ltd. New Delhi. Ethanol (99.9% purity) and Span 80 were purchased at the local market in Chennai.

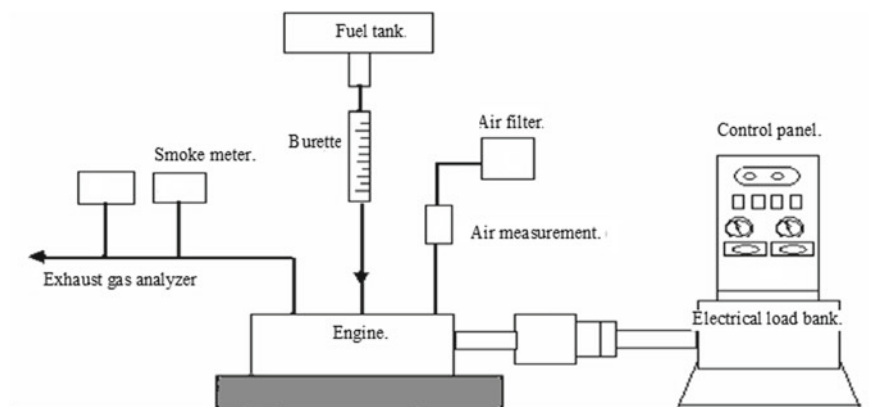


Fig. 1 Schematic diagram of experimental setup

Table 1 Engine specifications

Brake power	4.4 kW
Speed	1500 rpm
Compression ratio	17.5:1
Bore	87.5 mm
Stroke	110 mm
Type of ignition	Compression Ignition
Type of engine cooling	Air cooling
Loading system	Eddy current dynamometer

3.2 Preparation of Fuel Blend

The dosing level of the nanoparticles in the fuel blend varied from 50 to 75 ppm, The phase separation of diesel and ethanol fuel is prevented by using a surfactant (Span 80). The mixture was prepared by using ultrasonicator, which is subjected to high-speed blending in an ultrasonic bath to improve the stability of the blended mixture. Ultrasonicator was used to apply constant agitation time of 30 min to form a uniform mixture without segregation of nanoparticles. The exhaust emissions CO, HC and NO_x were measured by using AVL-444 Digas analyzer. Smoke opacity is measured by using a Bosch smoke metre. All the tests are conducted by starting and warming up the engine with neat diesel and then switching to blended mixtures. At the end of the test, the engine is made to run with the neat diesel to flush out the blended fuels from the fuel line and the injection system.

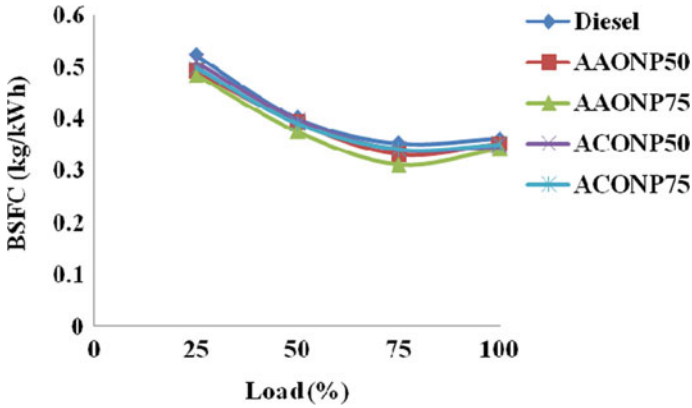


Fig. 2 BSFC with load

4 Results and Discussion

4.1 BSFC Variation with Load

From the graph Fig. 2, it is observed that there is very less fuel consumed with the addition of AAONP75 fuel blend as compared to other nanoparticle blends and diesel fuel, it is because of uniform mixing and complete combustion of nanoparticles in the fuel blend.

4.2 BTE Variation with Load

By the addition of nanoparticles, it is observed that there is an increase of BTE as compared to diesel fuel for various loads on the engine is shown in Fig. 3. Nanoparticles are producing high heat during their combustion which is the main reason to increase the BTE, there is a 7% increase of BTE for AAONP75 as compared with that of diesel fuel at 75% load.

4.3 HC Variation with Load

The variation of HC emission with load is shown in Fig. 4, it is observed that addition of AAONP to the fuel blends reduces the HC emission as compared to diesel fuel and other fuel blends. It is also observed that using AAONP 75 blend, HC emissions decreased by 17% compared with that of diesel fuel at peak load. It is because of the complete combustion of fuel by the addition of metal oxide nanoparticles.

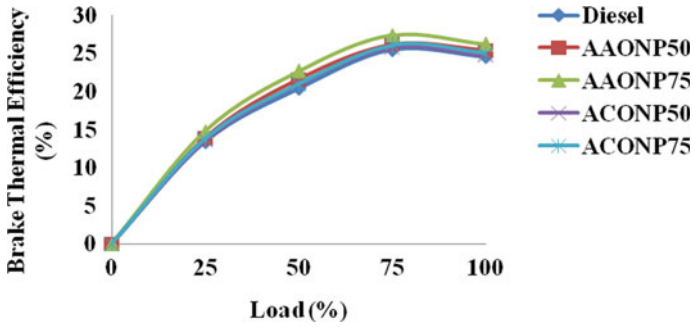


Fig. 3 BTE variation with load

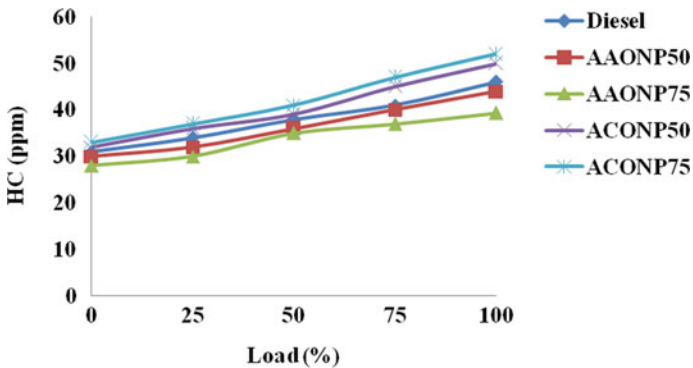


Fig. 4 HC emission with load

4.4 CO Emission Variation with Load

The variation of CO emission with varying load conditions of the engine are shown in Fig. 5. It is very clear that by the addition of nanoparticles in diesel fuel blends there is a reduction of CO emissions for all engine loads. The maximum CO emissions at maximum load for diesel, AAONP75, ACONP75 are 0.16%, 0.135%, and 0.139%, respectively. Increasing the dosing level of AAONP, CO emissions are decreased. It is because of the enrichment of oxygen by the addition of ethanol in the fuel blend, which causes complete combustion of fuel to convert the CO into CO₂.

4.5 NO_x Emission Variation with Load

Figure 6 shows the variation of NO_x with load. From the graph, it is observed that metal oxide nanoparticle addition increases the NO_x emission. It might be

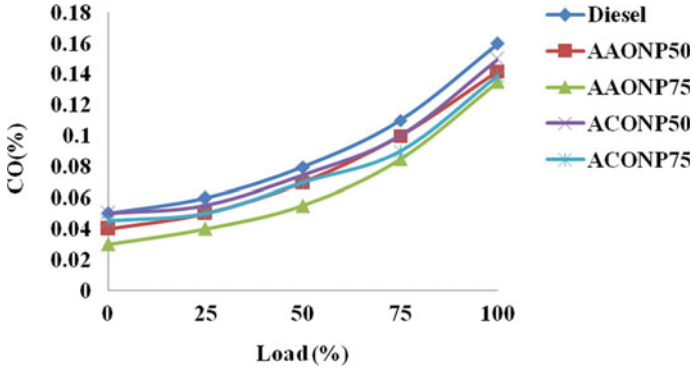


Fig. 5 CO emission variation with load

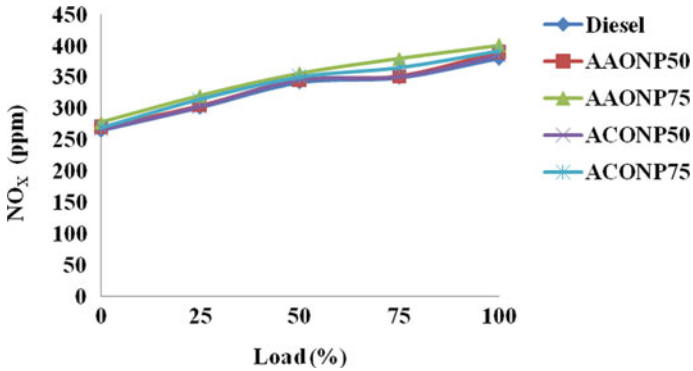


Fig. 6 NO_x emission with load

because of nanoparticles addition which increases the combustion heat and exhaust gas temperature.

4.6 Smoke Opacity Variation with Load

From Fig. 7, it is observed that for diesel fuel the smoke opacity is higher as compared with that of AAONP and ACONP additive blends, at a maximum load smoke opacity of diesel, AAONP75 and ACONP75 are 56.4%, 39.7% and 42.9%, respectively. AAONP 75 blends have less smoke opacity as compared with diesel.

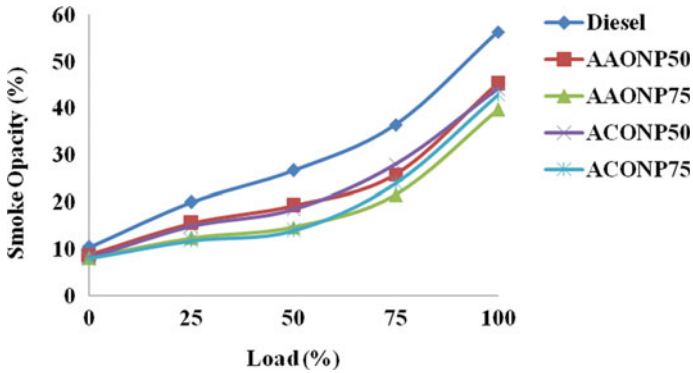


Fig. 7 Smoke emission with load

4.7 Cylinder Pressure Variation with Crank Angle

The cylinder pressure in diesel engine varies with the fraction of fuel burnt in the premixed combustion phase. The peak pressure in the cylinder describes the ability of fuel mixing with air and burning in the combustion chamber. Variation of cylinder pressure with the crank angle for diesel, AAONP50, ACONP50, AAONP75 and ACONP75 fuel blends at 75% load is shown in Fig. 8. From the graph, it is observed that ACONP75 fuel blend shows higher peak pressure 65.046 bar compared with diesel fuel 61.87 bar. This increase in pressure might be due to an increase in ignition delay and rapid combustion of fuel. Similar trends are observed by Arul Mozhi Selvan et al. [4].

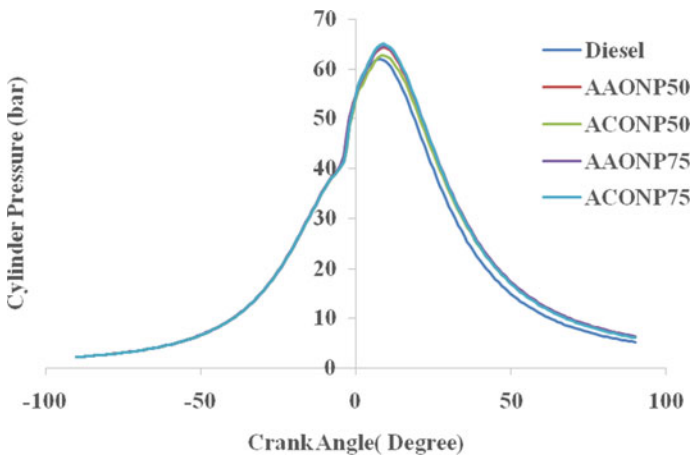


Fig. 8 Cylinder pressure with crank angle

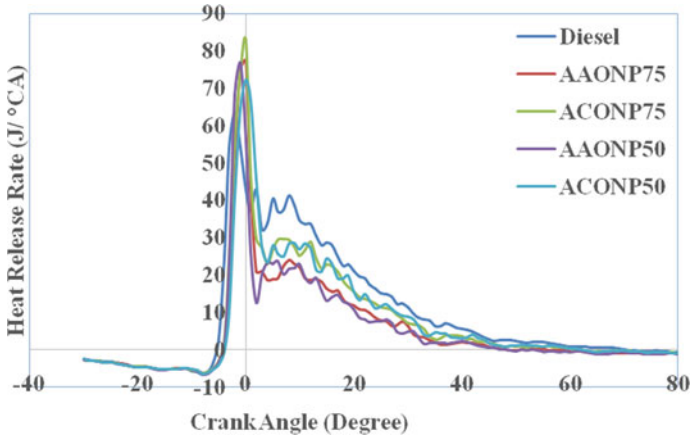


Fig. 9 Heat release rate with crank angle

4.8 Heat Release Rate Variation with Crank Angle

The variation of heat release rate with crank angle at 75% load for diesel, AAONP50, ACONP50, AAONP75, and ACONP75 fuel blends are shown in Fig. 9. The longer delay period by the addition of cerium oxide nanoparticle additives in the fuel blend might be the reason for the rate of pressure rise and high heat release rate in the combustion chamber. The heat release rate of ACONP75 fuel blend is higher than other fuel blends. Heat release rate of ACONP75 and diesel fuel are 82.75 J/°CA and 63.61 J/°CA, respectively. The results are comparable with Arul Mozhi Selvan et al. [4] and used cerium oxide nanomaterials and carbon nanotube (CNT) with diesterol fuel blend.

5 Conclusion

Performance, emission and combustion characteristics of nanoparticles additives (AAONP ACONP) with ethanol and surfactant blended fuel were discussed in this paper. By using additives, there is a change of physicochemical properties, combustion characteristics of hydrocarbon fuels, and improved surface area to volume ratio. Through the addition of nanoparticles, there is an enhancement of BTE and reduction of the BSFC. It is observed that nanoparticles are thermally stable and promote the oxidation which reduces the emissions like CO and HC. The main reason for the production of smoke in diesel engines by incomplete combustion and non-uniform mixture, adding nanoparticles less than micro-sized particles are uniformly mixed with the blends and causing complete combustion of fuel blends that reduced the smoke emissions. The combustion parameters like cylinder pressure and heat release

rates are increased for both nanoparticle additives in different proportions. An experimental investigation work is still in progress on the nanoparticles size, dosing levels and mixing of both nanoparticles at a particular quantity may reduce the NO_x emissions by also producing the ethanol on a large scale at low down cost can replace the diesel fuel by ethanol.

References

1. Y. Gan, L. Qiao, Combustion characteristics of fuel with the addition of nano and micron-sized aluminium particles. *Combust. Flame* **158**, 354–368 (2011)
2. R. Parthasarathi, S. Gowri, C.G. Sarvanan, Experimental investigation of performance, emission and combustion characteristics of kirloskar TVI di diesel engine using diesel-ethanol—surfactant as fuel. *ARPN J. Eng. Appl. Sci.* **7**(11) (2012). ISSN 1819-6608
3. H. Jung, D.B. Kittelson, M.R. Zachariah, The influence of a cerium additive on ultrafine diesel particle emissions and kinetics of oxidation. *Combust Flame* **142**, 276–288 (2005)
4. V. Arul Mozhi Selvan, R.B. Anand, M. Udayakumar, Effect of cerium oxide nanoparticles and carbon nanotubes as fuel-born additives in dieseltrol blends on the performance, combustion and emission characteristics of a variable compression ratio engine. *Fuel* **130**, 160–167 (2014)
5. B.K. Debnath, U.K. Saha, N. Sahoo, A comprehensive review on the application of emulsions as an alternative fuel for diesel engine. *Renew. Sustain. Energy Rev.* **42**, 196–211 (2015)
6. N. M. Ribeiro, A.C. Pinto, C.M. Quintella, G.O. da Rocha, The role of additives for diesel and diesel blended (ethanol or biodiesel) fuels: a review. *Energy Fuels* **21**(4), 2433–2445 (2007)
7. K. Srinivasa Rao, B.L.V.S. Gupta, K. Mallikarjuna Rao, G. Sambasiva Rao, Effects of cerium oxide Nanoparticles addition in diesel and bio diesel on the performance and emission analysis of CI engine. *Int. J. Eng. Trends Technol.* **19**, 39–43 (2015). ISSN 2231-5381
8. S.P. Venkatesan, P.N. Kadires, Influence of an aqueous cerium oxide nanofluid fuel additive on performance and emission characteristics of a compression ignition engine. *Int. J. Ambient Energy*. <http://doi.org/10.1080/101430750.2014.882863>
9. P. Ravichandra Ganesh, K. Hemachandra Reddy, Experimental investigation on the performance and the emission characteristics of DI Diesel Engine using diesel-ethnol blends with aqueous cerium oxide nanofluid as additive. *Appl. Mech. Mater.* **787**, 741–745 (2015)
10. T. Shaafi, R. Velraj, Influence of alumina nanoparticles, ethanol and isopropanol blend as additive with diesel-soybean biodiesel blend fuel: combustion, engine performance and emissions. *Renewable Energy* **80**, 655–663 (2015)
11. A.A. Ranaware, S.T. Satpute, Correlation effects of cerium oxide nanoparticles and ferrofluid on the performance and emission characteristics of a C.I. engine. *IOSR J. Mech. Civil Eng.* **55**–59. ISSN 2278-1684
12. S.Ch. Rao, M. Srinivasa Rao, Performance analysis of di diesel engine fuelled with diesel along with nano additives. *Int. J. Eng. Trends Technol.* **24**, 107–110 (2015)
13. C. Ajin, Sajeevan, V. Sajith, Diesel engine emission reduction using catalytic nanoparticles: an experimental investigation. **2013**, I.D 589382, 1–9 (2013)
14. S.P. Venkatesan, Influence of aluminium oxide nanoparticle additive on performance and exhaust emissions of diesel engine. *Am.-Euras. J. Sci. Res.* **10**(2), 88–92 (2015)
15. N. Sasi Kumar, M. Senthil Kumar, Investigation on the performance and emission characteristics of a diesel engine using water-diesel—nano fluid emulsion as fuel. *J. Chem. Pharm. Sci.* (2015). ISSN 0974-2115
16. C. Syed Alam, C.G. Sarvanan, Performance enhancement of common-rail diesel engine using Al₂O₃ and Fe₃O₄ nanoparticles blended biodiesel. *Int. Res. J. Eng. Technol.* **02**, 1400–1410 (2015)

17. M. Jones, C.H Li, Abdollah, G.P. Peterson, Experimental study of combustion characteristics of nano-scale metal and metal oxide additives in biofuel(ethanol). *Nanoscale Res. Lett.* **6**(1), 246, 6–11 (2011)
18. P. Ravichandraganesh, K. Hemachandra Reddy, experimental investigation on the performance, emission and combustion characteristics of di-diesel engine using diesel—ethanol blends and aqueous aluminum oxide nanofluids as additive. *Int. J. Pollut. Res.* **35**(4), 785–790 (2016)
19. S.P. Kattela, R.K.R. Vysyaraju, S.R. Surapaneni et al., *Environ. Sci. Pollut. Res.* **26**, 1661 (2019). <https://doi.org/10.1007/s11356-018-3704-5>
20. A. Selvaganapathy, A. Sundar, B. Kumaragurubaran, P. Gopal, An experimental investigation to study the effect of various nanoparticles with diesel on DI diesel engine. *ARPJ. Sci. Technol.* **3**(1). ISSN 2225-7217 (2013)
21. P. Akashkumar, C. Nagesh, J.M. Babu, J. Aatmesh, K.C. Vora, Production and engine performance and emission evaluation of Karanja and Jatropha-based biodiesel. In: (SAE-China) S. (eds) *Proceedings of the 19th Asia Pacific Automotive Engineering Conference & SAE-China Congress 2017: Selected Papers. SAE-China 2017. Lecture Notes in Electrical Engineering*, vol 486. Springer, Singapore (2019)
22. J.M. Babu, K.S. Prasad, P.R. Ganji, C. Ravikiran, R. Velu, Analysis on the effect of pilot injection strategies on combustion and emission characteristics of palm-munja biodiesel/diesel blend on CRDI diesel engine. *Int. J. Ambient Energy* (2019)
23. B. Ashok, K. Nanthagopal, D. Arumuga Perumal, J.M. Babu, A. Tiwari, A. Sharma, An investigation on CRDi engine characteristic using renewable orange-peel oil. *Energy Convers. Manage.* **180**(15), 1026–1038 (2019)

Emission Characteristics of CSOME in CRDI Diesel Engine with Multiple Injection Strategy



Ramesh Babu Nallamothe, Anantha Kamal Nallamothe,
and Seshu Kishan Nallamothe

Abstract Diesel engines are successful in commercial applications both on-road and off-road due to their higher thermal efficiency and fuel economy. CO and HC emissions are less from diesel engines compared to its counterpart gasoline engine. But NO and PM (smoke) emissions are higher due to heterogeneous combustion. Simultaneous reduction of NO_x and smoke became a tough task faced by researchers to comply with the stringent emission regulations imposed upon. On the other hand, biodiesel as a replacement of petro-diesel in diesel engine applications is found to be a good means of solving the problems like depletion of fossil fuel and environmental degradation. The high temperature in the combustion chamber causes the formation of NO_x and heterogeneous mixing that causes smoke formation. In this work, an attempt is made to study the influence of splitting injection on NO_x and smoke in CRDI diesel engine operated with cottonseed oil biodiesel blend (B20). The injection was split into three pulses, namely pre, main, and post. The dwell between pre and main was varied, and dwell between main and post was fixed at 3° CAD. A fixed quantity of 0.5 mg/cycle fuel was injected in the post, whereas the fuel injection in pre is 10% of the main injection. At different main injection timings, the dwell between main and pilot varied. The post-injection is maintained with a dwell of 3 CAD, which is very closely coupled with the main injection. From the recommended injection timing of 23° bTDC, the main injection timing along with post and pilot was retarded in steps of 3°. Baseline data was obtained with a petro-diesel single injection and B20 single injection at recommended 23° bTDC. For smoke reduction, the dwell of 10 CAD observed to be the best at all main injection timings. For NO_x reduction 20 CAD is better. For trade-off between NO_x and Smoke, in overall Dwell

R. B. Nallamothe (✉)

Mechanical Systems and Vehicle Engineering Department, School of Mechanical Chemical and Materials Engineering, Adama Science and Technology University, Adama, Ethiopia
e-mail: ramesh.babu@astu.edu.et

A. K. Nallamothe · S. K. Nallamothe

School of Industrial and Information Engineering, Politecnico Di Milano, Milan, Italy
e-mail: ananthakamal@gmail.com

S. K. Nallamothe

e-mail: seshukishan1997@gmail.com

© Springer Nature Singapore Pte Ltd. 2021

G. S. V. L. Narasimham et al. (eds.), *Recent Trends in Mechanical Engineering*,
Lecture Notes in Mechanical Engineering,
https://doi.org/10.1007/978-981-15-7557-0_9

10 CAD is observed to be better. It is found that splitting injection is very much helpful in simultaneous reduction of harmful emissions like NO_x and smoke from diesel engines.

Keywords Biodiesel · Dwell · Pilot injection · Post-injection · Retardation

1 Introduction

Depletion of fossil fuels is the prime concern of the world these days, which is caused due to the usage of petroleum fuels at higher rates to meet ever-growing energy demand world over. Another issue haunting the world now is the harmful emissions from the burning of fossil fuels and their negative impact on the environment. With the growth of the population, the usage of diesel is increasing in transportation and industrial applications to meet the energy requirements causing the release of tons and tons of dangerous pollutants adding to the atmospheric air. Serious human health problems are caused by these emissions in addition to other negative consequences like global warming and acid rains. The emissions from the burning of petroleum fuels are subjected to stringent environmental regulations imposed by various countries world over, to minimize the damage caused to the environment. For researchers, automobile manufacturers, and industries, it became a big challenge to comply with environmental regulations. For reducing environmental degradation, dependence on petroleum fuels and conserve sources of conventional fuels, different ways and means are being tried with these days.

Resorting to the usage of bio-based fuels like bioethanol, biomethanol, and biodiesel which are homegrown, eco-friendly, and renewable is one way of mitigation of the fuel-related problems being faced. The problems like over-dependence on the oil importation, depletion of conventional fuel resources, environmental damage, etc. can be solved by bio-based fuels. Another way which is tried with the improvement of the combustion process, by improving the design of combustion chamber, modifying the fuel injection system, etc. which improves the fuel economy, efficiency of combustion process, reduces the greenhouse gases, and other harmful emissions.

Straight vegetable oils, which are biodegradable, renewable, are another promising alternative to conventional diesel fuel. But due to their higher viscosity, straight vegetable oils cannot be directly used in unmodified diesel engines. The engine gets damaged if SVO is directly used in the engine due to deposits in the combustion chamber. For bringing down the higher viscosity of the straight vegetable oils, well-established procedure called transesterification process can be used. Diesel equivalent called biodiesel can be produced by reacting triglycerides present in vegetable oil with alcohol. KOH or NaOH is normally used as a catalyst during this reaction. Valuable by-product glycerin comes out [1].

Therefore, the usage of biodiesel which can be used in unmodified diesel engines as a replacement to conventional diesel has multiple environmental benefits. Biodiesel is non-exclusive, biodegradable, non-flammable, renewable, non-toxic,

environment friendly, and like diesel fuel [2]. The main advantages of biodiesel include the following: it can be blended with diesel fuel at any proportion; it can be used in a CI engine with no modification; it does not contain any harmful substances, and it produces less harmful emissions to the environment than diesel fuel. Triglycerides present in the SVO can be conveniently converted to biodiesel using transesterification process. During transesterification process, triglycerides react with light alcohols in the presence of a catalyst to mono alkyl esters. It is the most accepted industrial route to produce biodiesel [3].

NO_x emission is a serious environmental problem, which plays a key role in causing global warming and atmospheric ozone destruction [4]. Photochemical smog forms due to the presence of NO_x . Smog has a very bad effect on plants, materials, visibility eyes, throat and also causes the asthmatic effect. Human beings and plants are also get affected by the acid rains caused by NO_x mixing with water vapor. Well known after gas treatment technique with higher potential of NO_x reduction, which uses urea solution as reducing agent is Selective Catalytic Reduction (SCR) system [5]. Usage of urea solution for the reduction of NO_x in diesel engines is two decades old technique. Since then, many applications have been developed, some of which have reached commercialization [6]. But, it is still a challenge for researchers. With the implementation of multiple injection strategy, in newly developed engines with common rail direct injection system, it is possible to reduce the formation of NO_x further during combustion process [7, 8].

Ignition delay of the initial pulse can be reduced by splitting the injection into two or more events. With this combustion extends to expansion stroke reducing the fraction of fuel burned in pre-mixed stage. Formation of NO_x depends on the fraction of fuel burned in the pre-mixed stage. As the fraction of fuel burned in the pre-mixed stage, the net amount of NO_x gets reduced in split injection [9]. Emission of particulate matter is another big issue in diesel engines. At high loads, multiple injections method is more effective in reducing particulate emissions. At light and intermediate loads, a combination of EGR and multiple injection strategy can be used for reducing overall emissions. But a higher rate of EGR leads to increase in particulate emission which may cause degradation of lubricant leading to increased engine wear. Also, with increased EGR Brake Specific Fuel Consumption (BSFC) increases, which is another major concern. In this work, experiments were conducted with a combination of EGR and 5 pulse injection [10]. Proper dwell between injections was significant as small dwell led to the situation of single injection while long reduced the effect of pre-mix combustion. Dwell of around 10 CAD for pilot injection reduces emission efficiently. Around 21 CAD bTDC injection timing of the first injection was observed to be optimum for simultaneous reduction of NO_x and soot [11]. The petroleum resources are depleting at an accelerated rate. The prices of petroleum fuels subjected to fluctuations causing a negative economic impact in many countries. There is a need for every country to look more intensively for alternative fuels. Biofuels, the major alternative fuels attracting the growing attention of various countries world over [12]. The level of harmful emissions is alarmingly high. If it is left untreated and appropriate measures not taken at the right time, the level of emission grows further and further. The levels of harmful tailpipe emissions from

city-bound vehicles found to be exceeding NEMA ambient air quality data [13]. Also not complying with the World Bank ambient air quality guidelines. Daily exposure to these high levels of tailpipe emissions causes various health problems to human beings. The health complications increase overtime with increasing concentration levels of harmful emissions. Several mitigation methods can be applied to reduce the emission level such as reduce consumption of fossil fuels and increase efficiency in transport usage of energy [14–16].

2 Methodology

The main objective of this work is to study the effect of multiple injection strategy on the reduction of NO_x and smoke with retardation of injection and varying the dwell between pre and main. In this work, a new scheme of experiments with multiple injection strategy was employed to understand the influence of various parameters on the emissions from the engine. The multiple injection scheme used in this work consists of three injection pulses, pilot (pre)-main-post. The fuel quantity in the pilot injection pulse is fixed as 10% of the main fuel injection pulse. Fixed fuel quantity of 0.5 mg/cycle is used in post-injection. The retardation was done from 23° to 11° in 3° interval. The dwell is varied from 10 CAD to 20 CAD in three steps. Long term consumption of cottonseed oil is very much dangerous to human health in many aspects. Cottonseed oil which is non-edible is used for the preparation of biodiesel. Biodiesel is prepared using transesterification process.

The steps followed in this work are as given below

- Extraction of oil from cottonseeds using a mechanical press.
- Preparation of biodiesel using transesterification process.
- Characterization of biodiesel.
- Preparation of B20 blend.
- Testing the performance of CRDI diesel engine with diesel and B20 in single injection for base data and B20 with multiple injection strategy varying injection timing.
- Comparing the emissions from a single injection and multiple injection.

2.1 Engine Setup

The engine used in this research is a single cylinder, four stroke, CRDI Variable Compression Ratio (VCR) engine. The specifications of engine are given in Table 1. The engine is connected to eddy current dynamometer for the purpose of varying load. Various instruments and sensors for measurement engine operating parameters and combustion-related parameters like pressure, crank angle, fuel flow, airflow, load, temperature, etc. are provided. High-speed data acquisition system is used to interface the signals to the computer. The errors involved in the measurements are negligible.

The setup consists of a stand-alone panel box. The panel box is consisting of the twin fuel tank and airbox. Other measuring instruments like fuel flow measuring unit, manometer, airflow and fuel flow measuring transmitters, process indicator, piezo powering unit, etc. are fixed on panel box (Fig. 1).

For the purpose of measuring flow rate of engine cooling water, rotameters are provided. Open ECU which is programmable is used in CRDI VCR engine. Diesel injection is controlled by ECU. The system consists of ECU, wiring harness, injector, fuel common rail with rail pressure sensor and pressure regulating valve, fuel pump, crank position sensor, etc. With this setup, it is possible to study the engine performance with varying EGR ratios and compression ratios. It is possible to measure almost all engine performance parameters in addition to combustion analysis and heat balance measurements.

The scheme of experiments employed in this work is brand new, no research work was reported so far on such experimentation. The work is all about understanding the influence of various engine operating parameters on levels of emissions from the engine while multiple injection strategy is employed.

Fig. 1 Experimental setup



Table 1 CRDI Engine Specifications

Engine	Kirloskar, Single cylinder, Four stroke water cooled, VCR
Stroke	110 mm
Bore	87.5 mm
Capacity	661 cc
Power	3.5 kW
Speed	1500 RPM
Compression ratio	12–18
Injection system	CRDI with open ECU
Injection pressure	300 bar
Dynamometer	Eddy current dynamometer
Dynamometer arm length	185 mm

Table 2 Properties of biodiesel (Eta laboratories)

Properties	B100
Density @15 °C (gm/cm ³)	0.8865
Kinematics viscosity @40 °C	4.85
Flash point (°C)	149
Fire point (°C)	160
Cloud point (°C)	+1
Gross calorific value (kJ/kg)	40,695
Cetane number	50.8
Copper strip corrosion @50 °C for 3 h	Not worse than no 1
Acid value as mg of KOH/gm	0.063
Carbon residue	0.041%
Sulfur	0.0043%

The multiple injection used is consisting of three fuel pulses, pilot (pre)-main-post. Many trial experiments were conducted, to find the optimum pilot fuel quantity and post fuel quantity. It is found that 10% of the main injection fuel is best for pilot injection and a fixed fuel quantity of 0.5 mg/cycle in post-injection is better. Crank angle degrees of 10 is used as a dwell between the pilot and main injections. Post-injection is very closely coupled with the main injection with a dwell period of 3 degrees after the main injection. Main injection timing is retarded from the recommended injection timing of 23°–11° bTDC. The influence of this retardation on NO_x emission and smoke is measured. B20P10M20P3 stands for biodiesel blend 20, pilot injection with a dwell of 10°, main injection at 20°, and post-injection with a dwell of 3°.

3 Results and Discussions

3.1 Biodiesel Characteristics

The properties of prepared CSO biodiesel is given in Table 2.

3.2 NO_x Emission

It is observed from the above figures that with multiple injection the NO_x emission reduced considerably. From Fig. 2, it is noted that at M11 the NO_x emission is reducing as the dwell between the pilot and main increasing from 10 CAD to 20

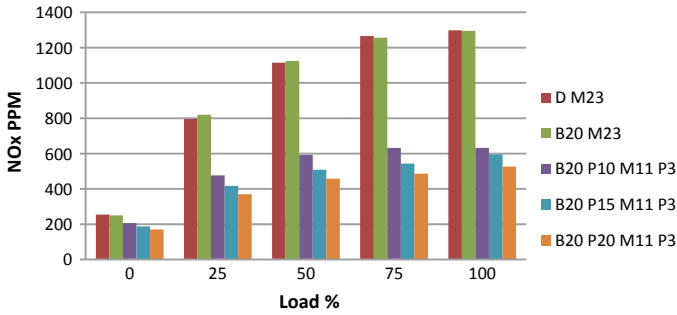


Fig. 2 NO_x emission at M11

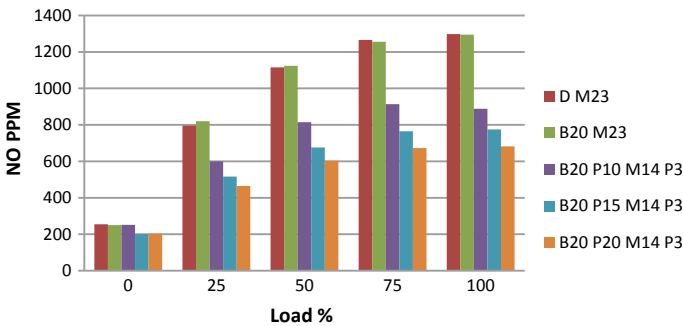


Fig. 3 NO_x emission at M14

CAD. There is a maximum reduction of 56.91% with a dwell of 20 CAD is compared to single injection M23.

At M14 also similar trend of reducing NO_x emission with an increase in the dwell period. Maximum reduction of 49.75% is noted with a dwell of 20CAD compared to single injection with a load of 6 kg (Fig. 3).

At M17, Fig. 4, dwell 10 CAD found to be better than others. The maximum reduction in NO_x emission is 33.58% with a load of kg. It is observed that the effect is more influential at a load of kgs. As the main injection timing is retarded the NO_x emission observed to be reducing due to a reduction in the peak temperatures developed in the combustion chamber. Multiple injection strategy is observed to be more effective in reducing NO_x at part load condition. There is an increment in NO_x with P10 M23 P3. In overall, the dwell of 20 CAD is observed to be better for NO_x reduction at M17.

It is observed that the rate of rise in NO_x is reducing with increasing the load. At M20 with the dwell of 15 and 20 CAD, the engine didn't work smoothly. The dwell of 10 CAD is better (Fig. 5).

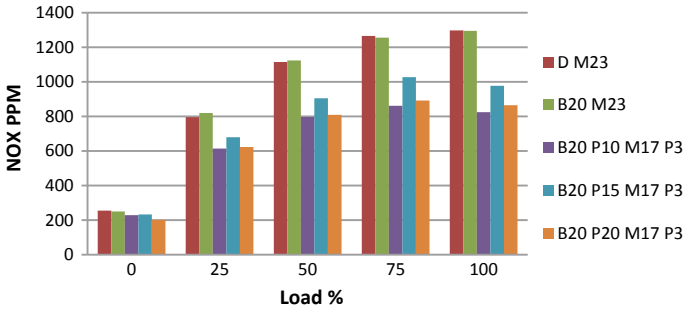


Fig. 4 NO_x emission at M17

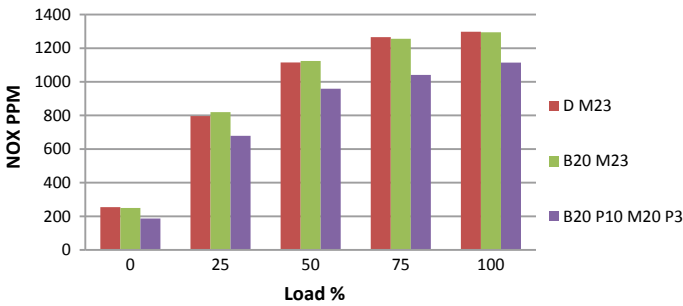


Fig. 5 NO_x emission at M20

3.3 Opacity

From the above figures, it is observed that splitting the fuel injection has a considerable effect on smoke emission. Maximum reduction of smoke is noted at M14 with a dwell of 10 CAD with 6 kg load. In this condition, the reduction in smoke is 58.93%. The reduction of smoke at M11 with a dwell of 10 CAD 55.32% with a load of 6 kg (Figs. 6, 7, 8, 9 and 10).

It is observed that the engine is hesitating at higher load with higher dwells of 15 and 20 CAD at M23 and M20. The dwell period of 10 CAD observed to be the best at all main injection timings.

The retardation of multiple injection with main injection retardation from 23° bTDC to 11° bTDC, smoke emission is considerably affected. Smoke opacity reduced gradually up to the main injection 14° and then starts increasing with further retardation. The reduction is 69.1%, 62.23%, 58.93%, 48.68%, 18.29% with load of 0%, 25%, 50%, 75%, 100%, respectively, at P10 M14 P3.

At retarded injection timing higher dwell caused more smoke at higher loads.

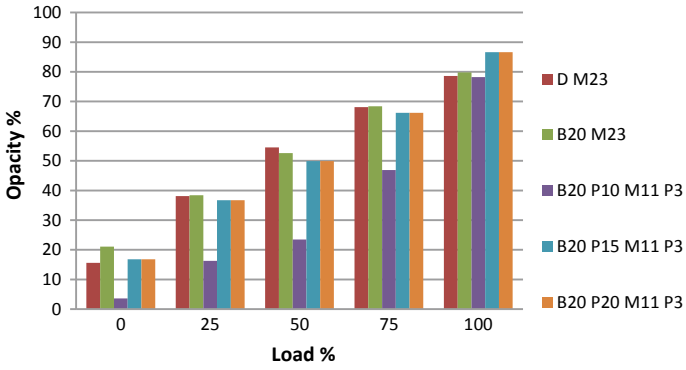


Fig. 6 Opacity at M11

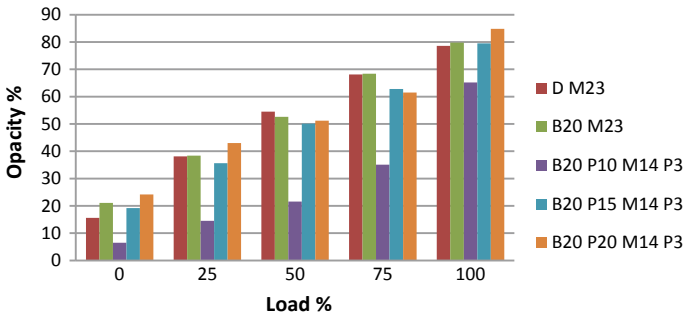


Fig. 7 Opacity at M14

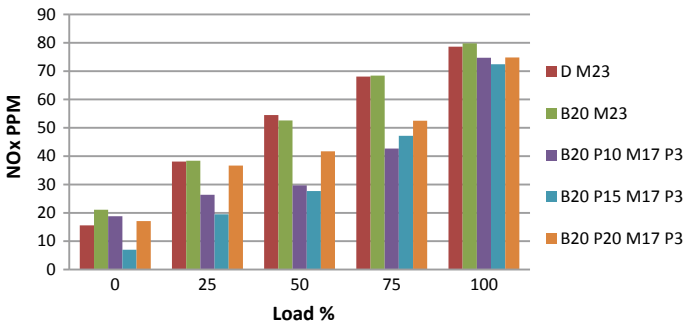


Fig. 8 Opacity at M17

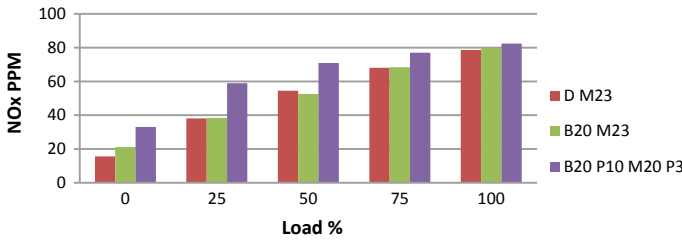


Fig. 9 Opacity at M20

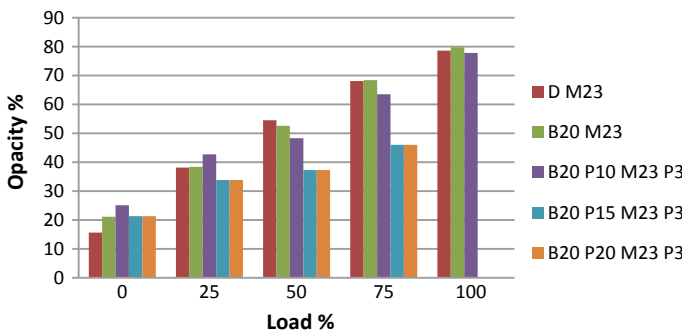


Fig. 10 Opacity at M23

4 Conclusions

- It is observed that multiple injection is a good means of having trade-off between smoke and NO_x emissions.
- Retardation of multiple injection up to M11 helped in reducing both NO_x and smoke. Further retardation caused a rise in smoke.
- P10 M11 P3 is better for smoke and NO_x tradeoff.
- The dwell period of 10 CAD observed to be the best at all main injection timings for smoke reduction, whereas for NO_x reduction 20 CAD is better. For better trade-off between NO_x and smoke, in overall dwell period of 10 CAD is better.
- Further combustion-related analysis is required to understand completely the influence of multiple injection.
- Multiple injection strategy seems to be more efficient than conventional in reducing emission due to their capability in controlling heat release rate and hence peak temperature. Multiple injection is better than single injection in optimizing the trade-off between NO_x and smoke due to their efficiency in reducing initial high temperatures and supporting combustion of late injection.
- Reduction in emissions was improved with multiple pre-main-post injection strategy, as pre-injection supports main injection combustion and reduced delay while post-combustion helps in oxidation of soot particles without impact on NO_x.

- Proper dwell between injections was significant as small dwell led to the situation of single injection while long reduced the effect of pre-mix combustion. For pilot injection dwell around 10 CAD reduces emission efficiently.
- Around 21 CAD bTDC injection timing of first injection was observed to be optimum for simultaneous reduction of NO_x and smoke.

Acknowledgments We are thankful to Marine engineering department, Andhra University, for giving this opportunity to work on biodiesel applications in diesel engines. We are also thankful to Sri Venkateswara research center, Kanchipuram for providing necessary research facilities.

References

1. P.S. Shelkea, N.M. Sakharea, S. Lahanea, Investigation of combustion characteristics of a cottonseed biodiesel fuelled diesel engine, in *Global Colloquium in Recent Advancement and Effectual Researches in Engineering, Science and Technology (RAEREST 2016)*. Procedia Technol. **25** (2016)
2. Y. Putrasar, A. Nur, A. Muharam, Performance and emission characteristic on a two cylinder DI diesel engine fuelled with ethanol-diesel blends, in *International Conference on Sustainable Energy Engineering and Application (ICSEEA)*. Energy Procedia **32** (2013)
3. A.S.A.E. Atabani, Non-ediblevegetable oils: a critical evaluation of oil extraction, fatty acid compositions, biodiesel production, characteristics, engine performance and emissions production. *Renew. Sustain. Energy Rev. J.* 211–245 (2013)
4. T. Pushparaj, S. Ramabalan, Green fuel design for diesel engine combustion, performance and emission analysis, in *International Conference on Design and Manufacturing IConDM*. Research Scholar, Tamil Nadu, India (2013)
5. G. Busca, L. Lietti, G. Ramis, F. Berti, Chemical and mechanistic aspects of the selective catalytic reduction of NO_x by ammonia over oxide catalysts: a review. *Appl. Catal. B: Environ.* **18**(1–2), 1–36 (1998)
6. H. Bosch, F.J.J.G. Janssen, Catalytic reduction of nitrogen oxides: a review on the fundamentals and technology. *Catal. Today*, **2**(369) (1988)
7. R.A. Perry, D.L. Siebers, Rapid reduction of nitrogen oxides in exhaust gas streams. *Nature* **324**, 657–658 (1986)
8. R. Imarisio et al., Multiple injection, a cost effective solution for emission reduction of common-rail DI Diesel Engines. *Aachener Kolloquium Fahrzeug-und Motorentechnik* **9**, 1047–1062 (2000)
9. M. Badami, et al., Influence of Multiple injection strategies on emissions, combustion noise and BSFC of a DI common rail diesel engine, in *SAE Technical Series*, No. 2002-01-0503 (2002)
10. Z. Gao, W. Schreiber, The effects of egr and split fuel injection on diesel engine emission. *Int. J. Autom. Technol.* **2**(4), 123–133 (2001)
11. R.B. Nallamothu, A.K. Nallamothu, S.K. Nallamothu, I.N. Niranjana Kumar, B.V. Appa Rao, Emission analysis of CRDI diesel engine fueled with cotton seed oil biodiesel with multiple injection strategy. *Int. J. Emerging Technol. Innov. Res.* **5**(9), 707–712 (2018). ISSN 2349-5162
12. R.B. Nallamothu, G. Fekadu, Prof B.V. Appa Rao, Comparative performance evaluation of gasoline and its blends with ethanol in gasoline engine. *GJBAHS* **2**(4), 100–106 (2013). ISSN 2319-5584
13. S. Neway, R.B. Nallamothu, S.K. Nallamothu, A.K. Nallamothu, Investigation on pollution caused by gasoline and diesel fuelled vehicles. *Int. J. Eng. Trends Technol. (IJETT)* **V36**(7), 376–381 (2016). ISSN 2231-5381

14. R.B. Nallamotheu, K.N. Anantha, K.N. Seshu, I.N. Niranjana Kumar, B.V. Appa Rao, Effect of multiple injection strategy on combustion of cotton seed oil bio-diesel in CRDI diesel engine, in *Recent Trends in Mechanical Engineering*, Lecture Notes in Mechanical Engineering, ed. by G. Narasimham, A. Babu, S. Reddy, R. Dhanasekaran (Springer, Singapore, 2020)
15. R.B. Nallamotheu G. Birbira, I.N. Niranjana Kumar, B.V. Appa Rao, N. Seshu Kishan, A review on performance of biodiesel in engines with and without addition of nanoparticles. *Int. J. Manage. Technol. Eng. IJMTE/1592 IX(I)* (2019)
16. R.B. Nallamotheu M. Lemma, I.N. Niranjana Kumar, B.V. Appa Rao, N. Anantha Kamal, N. Seshu Kishan Performance of cotton seed biodiesel with nano additives in diesel engines: a review. *J Appl. Sci. Comput. VI(II)*, 142–147 (2019)

Impact of Process Parameters on Peak Temperature Inside the Workpiece During Friction Stir Welding of AA5083 Aluminum Alloys



M. Shiva Chander, M. Ramakrishna, and B. Durgaprasad

Abstract An experimental work was completed of weldability of 5 mm-thick Aluminum alloy 5083 metal plates. This work was done with the help of FSW process. The map of experiments was finished on universal milling. The process parameters are probe revolving velocity of 710, 900, and 1200 rpm, the cross speed of at 20, 30, and 40 mm/min were used. The pin geometry of tool was taper threaded profile. The samples were prepared for microstructure analyses, Rockwell hardness measurements, SEM analysis, and tensile testing. The K-Type thermocouples of 8 were arranged to find the temperatures at different places on the plates. It was ascertained that the properties acquired were mechanically very sound. And these properties were achieved at optimum tool rotational speed. The agreement was good from the analysis between mechanical properties and microstructure.

Keywords Friction stir welding · 5083 aluminum alloy · Pin profile · Microstructure · Temperature distribution · Mechanical properties

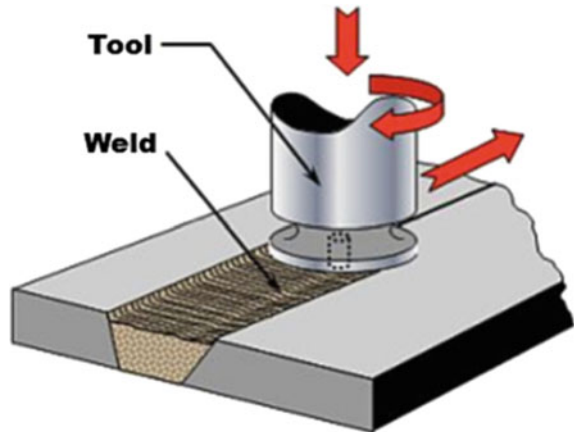
1 Introduction

The 5083 Al alloy displays enhanced deterioration resistance to salt water, superior in mechanical properties. Formability, machinability, and weldability are good for this process. This alloy is extensively benefited for welded parts for shipbuilding, railway vehicles. It has the pinnacle intensity of the non-heat-treatable amalgams. [1, 2] This compound isn't favored for use in temperatures in excess of 65 °C to

M. Shiva Chander (✉) · B. Durgaprasad
Department of Mechanical Engineering, JNTU Anantapur, Anantapuramu, A.P, India
e-mail: shiva.mothukuri11@gmail.com

M. Shiva Chander
Department of Mechanical Engineering, Center for Materials and Manufacturing, S R Engineering College, Warangal, Telangana, India

M. Ramakrishna
Department of Mechanical Engineering, NOVA College of Engineering & Technology, Vijayawada, A.P., India

Fig. 1 The FSW process

a destructive situation. [3] Plenty of literatures were prepared on the joint capacity of 5083 Al alloy. [4–6] Al composites are rubbing blend welded (FSW). At that point the properties of plastic are acquired, as an outcome of grain refinement [7]. FSW changes over a heterogeneous microstructure to a progressively homogeneous is shown in Fig. 1. And it also helps to refine the microstructure before not getting its melting temperature. The pieces of Al metal plates are joined by means of high amount of pressure.

2 Literature Review

Cho et al. [8] revealed the cause of method parameters on microstructure and mechanical properties. He also did investigation on optimization of process parameters.

Ilangovan et al. [9] in his examination of FSW process, an endeavor has been made to fasten together. He utilized three unlike tool pin probes like straight, taper, and threaded cylindrical. The analysis was done on elastic properties and microhardness for the welded joint. By this examination, the establishment was done that the utilization of threaded pin profile adds to recovered stream of resources linking two composites.

Emamian et al. [10], in his study he was identified that rising rotational speed the temperature increases and increasing welding speed, temperatures come down.

Satish Kumar [11] tested the cause of tool rotational speed on FSW 5083 Aluminum composite. It is observed that at revolution velocity of 710/40 traverse speed by threaded profile carried about great mechanical properties.

Mishra and Ma [12] explained the design of tool (pin geometries) that was able to produce adequate temperature and mixing the plasticized materials. He also

Table 1 Base metal properties

Substance	Density	UTS (Mpa)	Yield strength (MPa)
Al5083	2.67	2.66	134

explained that heat generation depends on process parameters such as rotational speed, traveling speed, and pin profiles.

3 Investigational Practice

3.1 Material

The metal pieces of 5 mm depth AA5083 Al alloy were sliced into size 150 mm × 60 mm × 5 mm. And these were machined with square butt joint pattern. The existing pattern was furnished by holding the metal pieces in butt location by using especially planned and fabricated fixture. FSW was conceded out using non-consumable tools prepared of high-speed steel. Base metal properties were shown in Table 1. Chemical composition of the AA5083 work material is shown in Table 2.

3.2 FSW

The welding was carried out with altering tool rotation speed on a universal milling machine. The tool, viz taper with threaded profile, was utilized to make the joints. The process parameters and tool proportions are as shown in Table 3.

The typical AA5083 Al alloy by chemical composition: 4.35% Mg, 0.52% Mn, 0.15% Si, 0.08% Cr, 0.26% Fe, 0.20% Zn, 0.014% Ti and the left one Al, with temper

Table 2 Chemical composition of Al 5083 alloy

Material	Mg	Mn	Si	Cr	Fe	Zn	Ti	Cu	Al
AA5083	4.5	0.7	0.4	0.15	0.4	0.25	0.15	0.1	Rest

Table 3 FSW Process parameters

Process parameter	Values/Types
Substance used	AA5083
Joint type	Butt joint
Substance thickness (mm)	5
Tool revolving speed (rpm)	710, 900, and 1120
Cross speed (mm/min)	20, 30, and 40
Length of weld (mm)	75

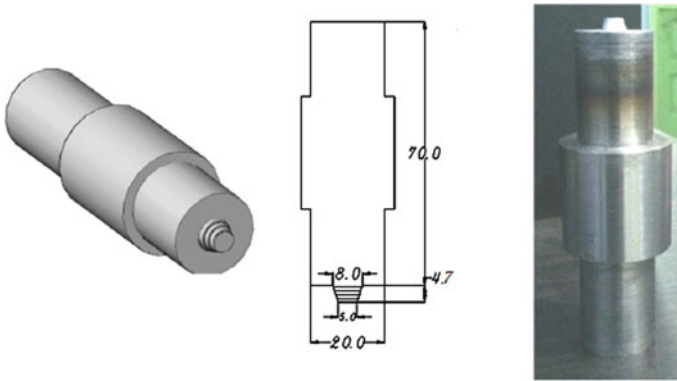


Fig. 2 Tool geometry (taper with threaded)

Fig. 3 FSW process on AA5083 plates



point O, was utilized for experiment. The workpiece sizes were 150 mm × 60 mm × 5 mm. The tool geometry and friction stir welding process with thermocouples shown in Figs. 2 and 3.

4 Results and Discussions

4.1 Tensile Test

Later FSW process, all the specimens were cut into ASTM standards as per the dimensions to test the mechanical properties. Nine specimens were tested, and their best joint values were considered. Specimens for tensile testing were sliced into ASTM standards. Bar charts show the results between ultimate tensile strength v/s rotational speeds. From the aftereffects of pliable test, it very well may be examined

that a definitive rigidity influenced by the apparatus profile of the welding instrument. [8, 10] The results are shown in Table 4. Tensile test specimens and top views of welds were shown in Figs. 4, 5 and 6.

From the above charts shown in Fig. 5, it is to be evident that a definitive elasticity (UTS) is supplementary to a tool revolving speed of 900 rpm. The reason here is because the heat contribution is satisfactory at that circumstance. From the graph, the % Elongation is added for 900 rpm and less at 710 and 1120 rpm.

Table 4 Mechanical properties by using taper threaded tool profile

Tool revolution speed (rpm)	Welding speed (mm/min)	Tensile stress (N/mm ²)	Impact strength (J)	%Elongation	Hardness (Hv)	Yield stress
710	20	203.810	40	6.40	70	166.251
710	30	210.105	38	5.6	76	175.634
710	40	254.559	52	10.56	87	190.808
900	20	187.519	20	9.00	61	149.913
900	30	225.590	20	6.92	76	159.109
900	40	282.231	54	14.40	73	207.748
1120	20	213.666	32	5.04	74	184.754
1120	30	257.241	50	14.28	74	191.493
1120	40	235.792	20	5.16	73	184.011

Fig. 4 Tensile test specimens



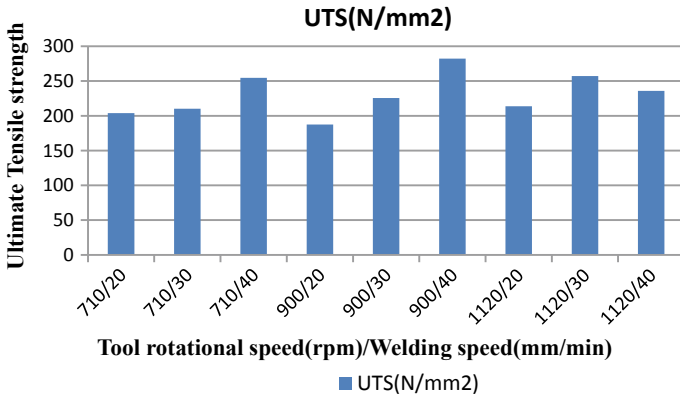


Fig. 5 Bar graphs for different mechanical properties

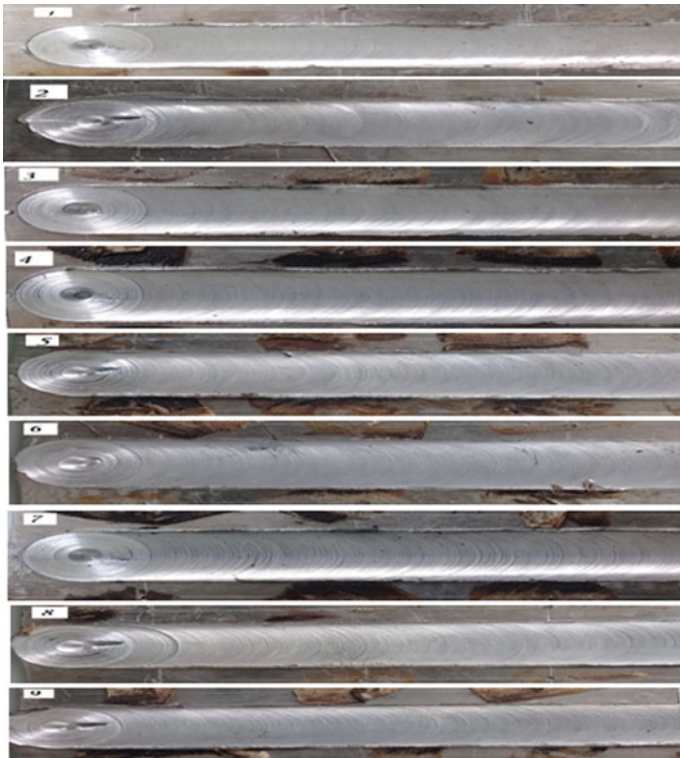


Fig. 6 Top views of 5083 plates after FSW

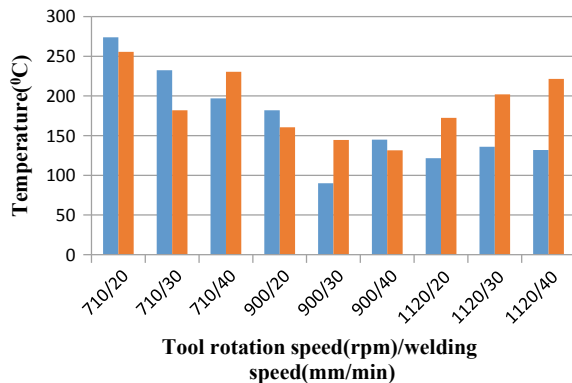
The elasticity is acquired at moderate warmth supply. Also, by expanding the instrument pivot speed past 900 rpm the rigidity diminishes, because of the explanation that the precious stones are reallocated and there is a coarse grain structure acquired. The rate change in the rigidity is relied upon to be 6.1% by utilizing Tapered strung barrel-shaped shoulder apparatus as the welding velocity ascends from 710 to 1120 rpm [13–15]. Among 9 joints in FSW process, the best joint acquired is at 900 rpm and welding speed 40 mm/min. The temperature distribution in both advancing and retreating side at various parameters are shown in Table 5. And the relationship between the temperature distribution and tool rotational speed were shown in Fig. 7.

From the graph, it is shown that temperature increases from rising tool rotational speed starting at 710–900 rpm. But the temperature decreases from 900 to 1120 rpm. At 900 rpm, the heat formation is sufficient to weld the joints [11]. The graph plotted between temperature and welding speeds were shown in Fig. 8.

Table 5 Temperatures at dissimilar rotational speeds and welding speeds

Sample no	Pin profile	Revolution velocity (rpm)	Welding velocity (mm/min)	Heat creation (°C)	
				Advancing side	Retreating side
1	Cylindrical taper with threaded	710	20	274	255.5
2		710	30	232.5	182
3		710	40	197	230.5
4		900	20	182	160.5
5		900	30	90	144.5
6		900	40	145	131.5
7		1120	20	121.5	172.5
8		1120	30	136	202
9		1120	40	132	221.5

Fig. 7 Graph between Temperature Vs tool rotational speed



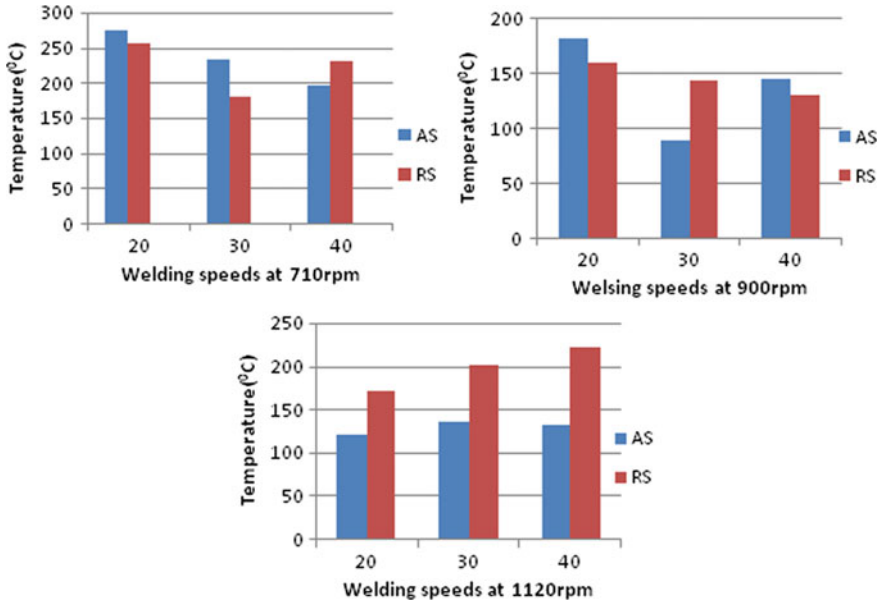


Fig. 8 Graph between temperature versus welding speeds

4.2 Impact Strength

Charpy Impact test was done to check the unexpected burden quality of the welded sector at various tool revolution speeds. The impact strength is more at 900 rpm and cross speed of 40 mm/min [14]. And it is correlated with ultimate tensile strength achieved at that condition. And the impact test specimen was shown in Fig. 9.

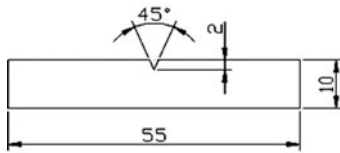


Fig. 9 Charpy impact test specimens

4.3 Microstructure Observations

The apparatus spinning velocity is imperative factor which controls the microstructure grain size. The accompanying perceptions were examined.

Microstructure Results—Effect of FSW on AA5083 Assessment of structural properties at unlike zones of the weldments was done was shown in Fig. 10. These were performed by using optical microscope. Figure 10e indicates that the microstructure is having fine grains, and the structure reveals that the grains are recrystallized. Grain size was acquired half of the base material. The fine strength properties % Elongation and impact strength. Consistent grain growth can be seen at 1120 rpm. The grain size is small at the top of the weld, which was in the region of the tool shoulder. From the microstructure study, the figure (f) indicates a extremely high fine and smooth grain structure, i.e., the grain size approximately equal to the half the grain range of base metal for the joint condition at 900 rpm and welding speed 40 mm/min.

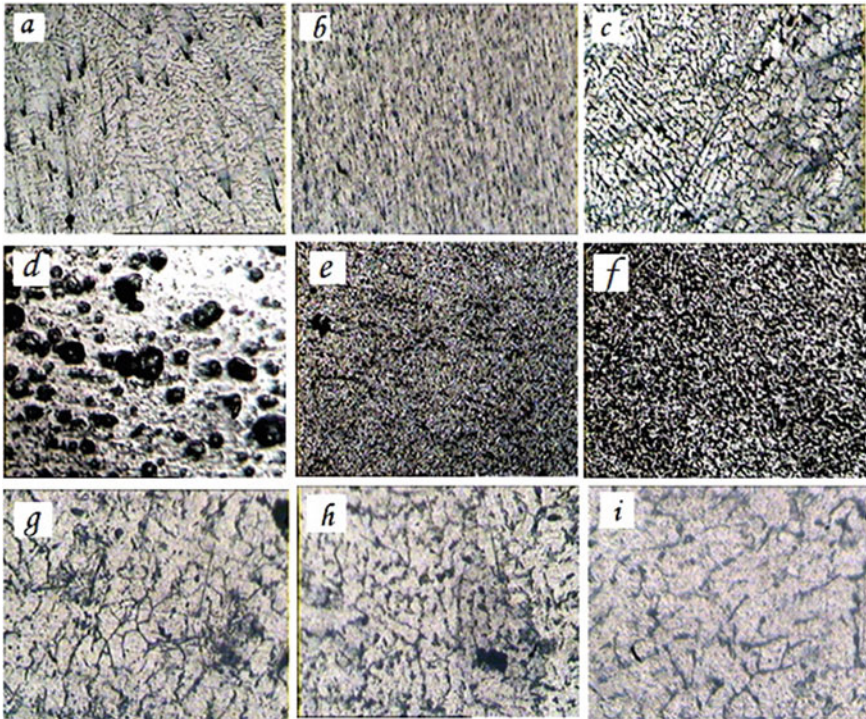


Fig. 10 a–i are microstructure photographs by using conical taper tool at 710 rpm, 900 rpm, and 1120 rpm at welding speeds of 20, 30, and 40 mm/min, respectively

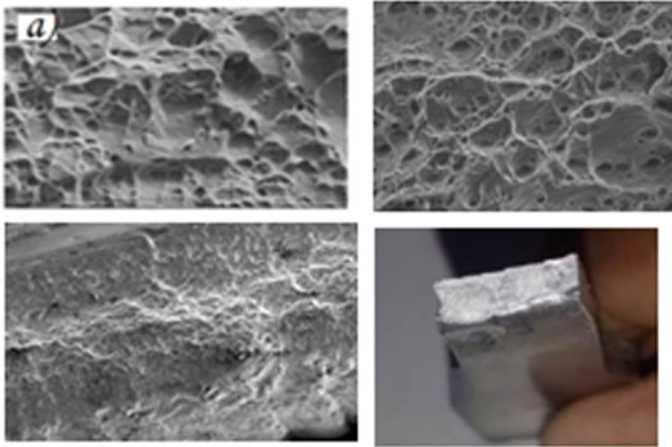


Fig. 11 SEM photographs at 900 and 1120 rpm

4.4 SEM Analysis

The fractured FSW tensile specimens showed obvious necking/plastic deformation for the specimen at 900 rpm shown in Fig. 11. The fractographs of the FSW examples uncover dimple break designs with teared edges brimming with micropores. And the specimen at 900 rpm and welding speed at 40 mm/min exhibited much better mechanical properties, because there were no deeper dimples, micropores, and teared edges present [9].

5 Conclusions

From the examination, the accompanying ends have been drawn

- For Al5083, at 900 rpm and at cross speed at 40 mm/min, by utilizing Tapered with strung profile device the mechanical properties gained were generally positive.
- It has likewise been recognized that the progressions in elasticity happen for various instrument rotational rates. The rigidity brings into being to be more noteworthy at 900 rpm and 40 mm/min and a lesser sum at 900 rpm and 20 mm/min, because of more warmth created at 40 mm/min when contrasted with 20 mm/min [8].
- Evaluation of basic properties at various places of the weldments utilizing optical magnifying instrument was done. Microstructure of the joint is best at 900 rpm with fine grain structure. Hence the flaw-free joint occurred at 900 rpm with enhanced mechanical properties.
- With the increase in rotational speed the ultimate tensile strength increases [12].

- Uniform grain refinement obtained 900 and 1120 rpm. The scanning electron microscope exhibits no dimples in the fracture zone at 900 rpm and obtained as a strong joint.
- Hence the optimum condition for welding of AA5083 joints at various welding speeds is 900 rpm and 40 mm/min.

Acknowledgments A special thanks to HOD, Principal and Management, S R Engineering College Warangal for providing the research facilities in the center for Materials and Manufacturing to carry out research work. Their support and encouragement are highly appreciable and acknowledged.

References

1. W.M. Thomas, E.D. Nicholas, J.C. Needham, M.G. Murch, P. Temple Smith, C.J. Dawes, Friction stir welding, International patent application No. PCT/GB92102203 and Great Britain patent application No. 9125978.8 (1991)
2. R.S. Mishra, friction stir welding and processing. *Mat. Sci. Eng. R* **50** (2005). *Int. Schol. Sci. Res. Innov.* **10**(1) (2016) 13 scholar.waset.org/1999.2/10003197 *World Acad. Sci. Eng. Technol. Int. J. Chem. Mol. Nucl. Mater. Metall. Eng.* **10**(1), 1–78 (2016)
3. M. Koilraj, V. Sundareswaran, S. Vijayan, S.R. Koteswara Rao, Friction stir welding of dissimilar aluminum alloys AA2219 to AA5083—Optimization of process parameters using Taguchi technique. *Mater. Des.* **42**, 1–7 (2012)
4. N.T. Kumbhar, G.K. Dey, K. Bhanumurthy, Friction stir welding of aluminium alloys. *Barc Newsl.* **321**, 11–17 (2011)
5. T. DebRoy, H. Bhadeshia, Friction stir welding of dissimilar alloys—A perspective. *Sci. Technol. Weld. Joining* **15**(4), 266–270 (2010)
6. M. Peel, A. Steuwer, M. Preuss, P.J. Withers, Micro-structure, mechanical properties and residual stresses as a function of welding speed in aluminium AA5083 friction stir welds. *Acta Mater.* **51**, 4791–4801 (2003)
7. S. Sattari, H. Bisadi, M. Sajed, Mechanical properties and temperature distributions of thin friction stir welded sheets of AA5083. *Int. J. Mech. Appl.* **2**(1), 1–6 (2012)
8. J.-H. Cho, S.H. Han, C.G. Lee, *Mater. Lett.* **180**, 157 (2016)
9. M. Ilangovan, S. Rajendra Boopathy, V. Balasubramanian, Effect of tool pin profile on microstructure and tensile properties of friction stir welded dissimilar AA 6061–AA 5086 aluminium alloy joints. *Defence Technol.* **11**(2), 174–184 (2015)
10. S. Emamian, M. Awang, F. Yusof, P. Hussain, The effect of pin profiles and process parameters on temperature and tensile strength in friction stir welding of AL 6061 Alloy, in *The Advances in Joining Technology* (Springer, 2019)
11. P. Satish Kumar, Influence of tool revolving on mechanical properties of friction stir welded 5083 Aluminum alloy, in *Materials today Proceedings, ICMPC-2016*, pp. 2214–7853
12. R.S. Mishra, Z.Y. Ma, Friction stir welding and processing. *Mater. Sci. Eng. R.: Rep.* **50**(1–2), 1–78 (2005)
13. K. Santhosh, A. Devaraju, Practices in FSW welding and investigate effect of tool turning speed on tensile properties and microhardness of dissimilar aluminium alloys 2024 & 6061. *Int. J. Mech. Eng. Technol.* **8**(11), 165–172 (2017)
14. D. Raghavendra, Optimizing the process parameters of friction stir welded AA 6061-T6 alloy using Taguchi orthogonal technique. *Int. J. Curr. Eng. Sci. Res. (IJCESR)* **1**(4), 48–55 (2014)
15. P.S. Kumar, M.S. Chander, Effect of tool pin geometry on friction stir welded dissimilar aluminium alloys—(AA5083 & AA6061). *Int. J. Mech. Eng. Technol.* **9**(647–653), 647–653 (2018)

Optimization of Friction Welding Process Parameters for Weldment of Aluminium–Copper Electrical Connector



Balkeshwar Singh, Worku Mamuye, and Moera Gutu Jiru

Abstract Friction welding of aluminium and copper has been widely used in electrical transmission in production of bimetallic (lug) or connectors. The use of dissimilar metal connector is to prevent high electrical losses due to contact resistance and mechanical contact between aluminium and copper which is not permanent in their application for the fact of environmental degradation. Galvanic corrosion between the two metals in mechanical contact is savour and it is technically distractive; hence friction welding of the two metals solved the problem by introducing technically acceptable joint between the two metals. Mechanical strength of the connectors has been very important to withstand stress caused by heat and mechanical force. Electrical resistance behaviour has also been highly important. The aim of this research has to optimize process parameters that gave the best electrical and mechanical properties of the weldment. The selected materials and method are different and unique from any other studies. Optimization of welding parameter that gave two characteristics of their performances such as strength and electrical resistance when optimized successfully. Grey relational analysis, ANOVA and Taguchi method have been used for the optimization process. Vertical drilling machine was used for the friction welding process and the machine was 1.7 KW power with the rotational speed of 3060 RPM. The optimization of the process parameters of the friction welding, i.e. RPM, friction pressure and friction time was conducted. The obtained optimum setting for two performance output characteristics such as strength and electrical resistance was friction time at 20 seconds, friction pressure 117 (MPa) and 1050 (RPM). Furthermore, based on two performance studies, friction pressure has a basic parameter that determined the desired response.

B. Singh (✉) · M. G. Jiru

Department of Mechanical Design & Manufacturing Engineering, Adama Science and Technology University, Adama, Ethiopia
e-mail: deanacademic12@gmail.com

M. G. Jiru

e-mail: jirata2010moti@gmail.com

W. Mamuye

Department of Mechanical Engineering, Hawassa University, Hawassa City, Ethiopia
e-mail: workumab@gmail.com

© Springer Nature Singapore Pte Ltd. 2021

G. S. V. L. Narasimham et al. (eds.), *Recent Trends in Mechanical Engineering*,
Lecture Notes in Mechanical Engineering,
https://doi.org/10.1007/978-981-15-7557-0_11

Keywords Friction welding · Dissimilar metal connector · Grey relational analysis · Electrical resistance · Mechanical strength

1 Introduction

Friction welding is a solid-state welding process for joining two similar or dissimilar materials. It is used widely throughout various manufacturing processes where high production rates are required [1]. Friction welding conditions are generally selected based on experience or study reports. However, the establishment of a method to decide the conditions in response to the phenomena which occurred during friction welding is needed. This is because the optimum welding conditions varied for each welding machine [2].

Effective simulation software was given in the simulation of the friction welding process for specific geometries [3]. The simulation process was specific for single geometry and one material. This showed that friction welding process variables should be optimized for a specific application when it is needed. There is no general rule of friction welding parameter setting that worked for every application. This clearly showed the process is dependent on many conditions such as machine, material, application requirement and so on. It is necessary to produce a design of experiment and optimization for each machine [4]. Selection of best process parameter for each machine individually needed time and capital. The technique to satisfy this problem is using design of experiment tools to optimize process parameters.

When joining dissimilar metals such as copper and aluminium, problems such as brittle inter-metallic compounds are created in the joint. As such, the friction welding parameters and their settings must be carefully selected to achieve strong welds and minimize rejections. Operating at non-optimum process condition might result in undesirable output such as [5]

1. Partial destruction and involvement of inter-metallic layer;
2. Non-uniform heating of the cross-section of the welded specimens;
3. Increase in the overheating of the metal.

Optimum parameter selection can minimize the effect of these problems. Therefore, this study optimized process parameters such as strength and resistance for its application in the electrical connector.

The problems with the selection of other welding processes of these metals are first, there is a case to generate an inter-metallic compound and involvement of the other metal flake in the interface of the materials. Second, in the case of metals with very different melting points or flow stresses, it is difficult to be welded, because only the metal with lower melting point softened and the material with the higher melting point could not decrease the flow stress [6].

Certain physical properties of copper and aluminium, like the high electric and thermal conductivity, enable their common application in electric power, and other areas, in the form of bimetals [7]. The necessity for joining copper and aluminium is important for electric conductors or cable endings. Joining elements, used for

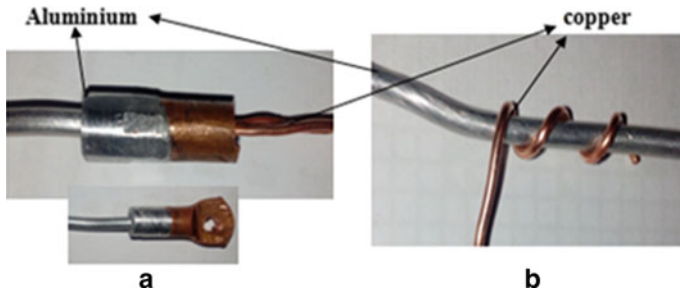


Fig. 1 a The use of electrical connector. b Without using connector indicated the usual connection problem

connecting copper and aluminium cables was mostly made by creating a mechanical contact between the two metals, that is by folding them or bolting of the two metals as shown in Fig. 1. Poor joining method in Al/Cu joints is unreliable for a long time. The reasons for this are the followings

1. The weakening of the joint during its use at higher temperatures which is caused due to different linear Al and Cu thermal expansion coefficients;
2. A large transient electrical resistance at the interface, which is one of the problems of a joint based on the mechanical type of connection;
3. The occurrence of galvanic action due to the mechanical contact between copper and aluminium which is a serious problem in the electric transmission failure.

Thus, bond with better performance between Al and Cu is achieved with an inter-diffusion of the solid-state atoms. The procedure, with which such a connection is formed, is called friction welding. When aluminium and copper are in contact in air, the aluminium can be expected to be attacked severely by galvanic corrosion. Therefore, it is advisable to use a friction welded bimetallic lug to prevent galvanic corrosion in electrical connections between aluminium–copper terminals [8].

The main objective of this research is to optimize the process parameters of friction welding for two performances characteristic. The two performance measures are better electrical and mechanical properties (less resistance and good strength, respectively). The result from this study is used to eliminate rejection from the welding process. The result has high application in the production process of bimetallic electrical connectors with the same process parameters and machine specifications.

2 Materials and Methodology

2.1 Material Selection

The aluminium and copper metal were cut into pieces of rod. The workpiece length was dependent on the machine and the fixture dimensions. Buckling of the workpiece was the main problem that needs a solution. The buckling problem was solved by minimizing the length of the workpiece. The other problems were the off centering of the workpiece from the axis of rotation. The main reason for centring problem was the machine rigidity or vibration of the machine during operation at maximum rpm and maximum pressure.

The diameter of the workpiece was 8 and 9.5 mm for copper and aluminium, respectively. The workpiece image has shown in Fig. 2. To enhance the welding process, the diameter of copper was smaller than aluminium. In addition to that the workpiece surface is made very flat and smooth to enhance the friction heat.

The workpiece is kept straight to eliminate the vibration of the workpiece on its axis of rotation. Due to thermal expansion properties of aluminium, it expanded near the weld area and large axial shortening caused the decrease in the length. To compromise loss of material and axial shortening proper length was taken for aluminium.

2.1.1 Material Property

Chemical analysis, mechanical properties, electrical properties of copper and aluminium has been given in Tables 1 and 2. These properties are unique properties obtained for the materials. The data has been given in detail in tabular form, and all properties that are especially needed for this research are given in detail format. Copper and aluminium metals rod has been received from BELAYAB cable factory. The copper and aluminium metals have been used in this factory to produce electrical transmission copper wires and aluminium wires [9–11].



Fig. 2 The work piece

Table 1 Copper material data

Size (mm)		8	
Standard Specification		ASTM B49/ISBN 1977	
S. No.	Parameter	Specification	
		DUCAB	ASTM B49
1	Oxygen (PPM) 200–400	–	100–165
2	Surface oxide (Angstrom)	Max. 500 A	Max. 750
3	Diameter variance (mm)	±0.38	±0.38
4	Conductivity %IACS	>100 IACS	Min. 100
5	Elongation %	>40	Min. 30
6	Tensile strength (N/mm ²)	>200–400	–
7	Surface	Smooth	Smooth
<i>Chemical analysis</i>			
Element		ASTM B49	BSEN 1977
Selenium		2 ppm	2
Tellurium		2 ppm	2
Bismuth		1 ppm	2
Group total(Se + Be + Ti)		3 ppm	3
Antimony		4 ppm	4
Arsenic		5 ppm	5
Tin		5 ppm	–
Lid		5 ppm	5
Iron		10 ppm	10
Nickel		10 ppm	–
Sulphur		15 ppm	15
Silver		25 ppm	25
Total impurities (Max. in ppm)		65 ppm	65
Copper%		99.98%	–
Co + Fe + Si + Sn + Zn + Ni maximum—20 ppm			

2.2 Optimization Method

Grey relational analysis, Taguchi and ANOVA methods were used to optimize multiple output performance. Optimization of multiple performance characteristics such as resistance and mechanical strength was conducted.

For the multiple performances characteristic optimizations the following process of calculation was performed

1. The normalization of the process output data;
2. Grey relational coefficient calculation from the normalized data;

Table 2 Aluminium material data

Standard specification		ASTM H14/1350		
Size (mm)		9.5		
Tensile strength (MPa)		103–138		
Elongation %min (250 mm gauge length)		15		
Resistivity Ω mm ² /m max		0.02808		
Equivalent volume of conductivity %ISCS Min.		61.4		
Element%	DAC specification		ASTM B233	
	Min.	Max.	Min.	Max.
Aluminium	99.7	–	99.5	–
Silicon		0.1		0.1
Iron		0.2		0.4
Zinc		0.02		0.05
Gallium		0.02		0.03
Vanadium + Titanium		0.02		0.02
Copper		0.05		0.05
Manganese		0.01		0.01
Chromium		0.01		0.01
Boron		0.05		0.05
Arsenic		0.009		–
Heavy element (Cd + Hg + Pb)		0.0095		–
Other elements each		0.03		0.03
Other elements total		0.1		0.1

3. Grey relational grade calculation from grey relational coefficients and obtaining the optimized parameter setting from grey relational grades;
4. Analysis of variance (ANOVA) of the final simplified single output from the grey relational analysis grade;
5. Confirmation test.

3 Process Parameter Selection

RPM, friction pressure and friction time were the three parameters chosen for the friction welding process. Based on statistical analysis, simplified L9 design of experiment was used. Output parameters were electrical resistance and strength of the element. The parameter selection was a difficult task and it entirely depended on the machine conditions. Table 3 shows the selection of the friction welding process parameters.

Table 4 shows the parameter assigned for the friction welding process at level 1, level 2 and level 3.

Table 3 Input parameter selection for the friction welding process

Symbol	Parameter	Level 1	Level 2	Level 3
C	RPM	1050	1550	3060
B	Friction pressure (MPa)	78	97	117
A	Friction time (s)	5	15	20

Table 4 Parameter assignment

Parameter	Level	Level	Level
RPM	Low (-1)	Medium (0)	High (+1)
Pressure level	Low (-1)	Medium (0)	High (+1)
Time of welding	Low (-1)	Medium (0)	High (+1)

4 Experimental Setup for Friction Welding

In this particular study, vertical drilling machine was used for the friction welding process. The machine specification was 3060 RPM, 1.7 KW power. Detail machine setup is presented in Fig. 3. Workpiece holding and hydraulic pressure gauge have shown clearly in the figure. The hydraulic oil added cylinder and piston was placed as shown by the arrow. The upward force was applied from the downward table, and it was directly transferred to the workpiece area. The force was also transferred from the workpiece to the pressure gauge. The pressure gauge senses the force/pressure applied to the hydraulic oil inside the piston-cylinder arrangement. The pressure gauge reads the pressure exerted on the workpiece from 78 to 117 MPa for each experiment. This pressure was converted by relating the force applied to the workpiece area.

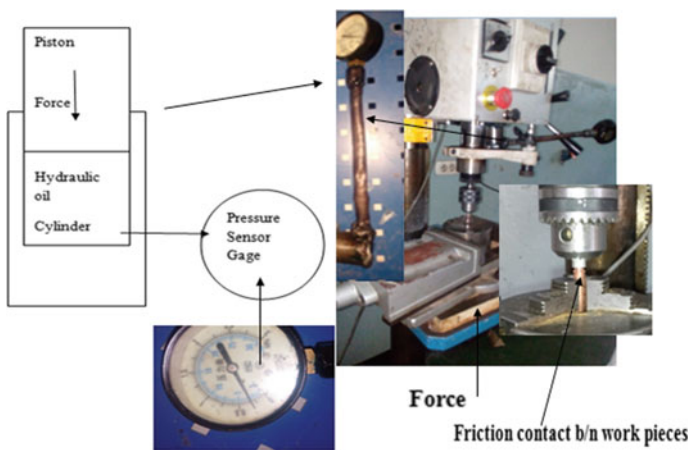


Fig. 3 Friction welding setup

First, the drilling machine was rotated to some speed. Then, the workpieces were frictionally contacted to each other with the application of gradual pressure from the table of the drilling machine. The pressure was indicated in the gauge setup as shown in Fig. 3. The workpieces were allowed to friction for a specified time when the pressure was applied. The machine spindle stopped when the material was plasticized and the constant pressure was applied until removal of the sample. The speed, the pressure and the time were recorded for each experiment.

4.1 Experimental Result of Welding Process

Results of nine samples of friction welding of aluminium and copper on drilling machine have shown in Fig. 4. The experiment was performed in series by recording the friction time, the RPM and the friction pressure. Each weldment was performed in the specified parameter value.

Each specimen has a length of 10 cm, and diameter of copper and aluminium were 8 and 9.5 mm, respectively. To measure the tensile strength of the friction welds, a universal testing machine of 10 KN was used. After the tensile load was known from the test machine the strength was calculated by dividing the load by the workpiece area. For example, experiment no 8 the tensile force was 5.07 KN, and the workpiece area was 50.24 mm^2 . Therefore, tensile strength was 100.915 MPa.

5 Electrical Resistance Measurement of Weldment

Totally nine samples of weldments were produced for an electrical test has shown in Fig. 5. The weldment was reduced from the original size to 5 mm in diameter. All



Fig. 4 Nine samples weldment of aluminium and copper



Fig. 5 Samples for electrical resistance measurement

the samples were equal in diameter because the resistance electrical property varies when the size is different.

The circuit was designed based on the voltage drop principle and Kelvin four-wire test method. The test was performed by adjusting the current amount in three levels. This was done because of the voltage drop is minimum and to get a significant voltage drop, the current level was adjusted for three stages to getting the final reading. The increase in the current was 100, 2000 and 10,000 m-amp. The voltage was resolved from the voltmeter at 2000 m-amp and based on this current level, the resistance was calculated from the Eq. (1).

$$V = I R \quad (1)$$

where V = voltage drop; I = current inside the test specimen; R = resistance measured from current and voltage drop.

6 Results of Tensile Strength and Electrical Resistance Measurement

Based on the MINITAB software, L9 design of experiment was selected. Three factors RPM, friction pressure and friction time are used, and the values of the parameter are presented in Table 5. The tensile test machine recorded the tensile force and dividing this force by the area of workpiece, the tensile strength was calculated. Resistance in ohm was obtained from the current and voltage values on ammeter and multimeter. The voltage was the value of the potential drop across the test specimen (welding interface). On the other hand, the current value was the constant current supplied by the system to the test specimen and flowing through it constantly. Finally, the tensile strength and resistance measurement results are shown in Table 5. The result presented in Table 5 showed that tensile strength was varying throughout the experiment. This clearly showed that the tensile strength of the weldment was largely influenced by the process parameter.

From the above discussion, the maximum tensile strength was at experiment no. 8, which indicated that the process parameter selection was very important for obtaining overall good quality weldment. In this analysis, the electrical resistance

Table 5 Tensile strength and resistance measurement results

Run	Friction time (s)	Friction pressure (MPa)	RPM	Tensile strength (MPa)	Load at breakage (KN)	Resistance (Ω)	Average temperature ($^{\circ}\text{C}$)
1	5	78	1050	1.393	0.07	2.5×10^{-5}	40.39
2	5	97	1550	32.444	1.63	1.5×10^{-5}	39.18
3	5	117	3060	87.978	4.42	1.5×10^{-5}	110.13
4	15	78	1550	43.789	2.2	1.5×10^{-5}	67.48
5	15	97	3060	72.651	3.65	2×10^{-5}	65.42
6	15	117	1050	86.783	4.36	1.5×10^{-5}	65.84
7	20	78	3060	47.373	2.38	1.5×10^{-5}	95.62
8	20	97	1050	100.915	5.07	1.5×10^{-5}	52.34
9	20	117	1550	4.378	0.22	1×10^{-5}	120.7

and the tensile strength were simultaneously combined to obtain the best parameter for improvement of both output responses.

7 Grey Analysis of Multi-performance Optimization

In the grey relational analysis, experimental results (tensile strength and resistance) were first normalized in the range between 0 and 1, which was also called the grey relational generation. The grey relational coefficient was calculated from the normalized experimental data to express the relationship between the desired and actual experimental data. Then, the grey relational grade was computed by averaging the grey relational coefficient corresponding to each process response. The overall evaluation of the multiple process responses was based on the grey relational grade.

In the study, a linear data preprocessing method [12] for the tensile strength was the higher the better and was expressed as

$$x_i(k) = \left[\frac{y_i(k) - \min.y_i(k)}{\max.y_i(k) - \min.y_i(k)} \right] \quad (2)$$

The resistance which was the lower the better can be expressed as

$$x_i(k) = \left[\frac{\max.y_i(k) - y_i(k)}{\max.y_i(k) - \min.y_i(k)} \right] \quad (3)$$

where $x_i(k)$ = the value after gray relational generation, $\min.y_i(k)$ = the smallest value of $y_i(k)$ for the k th response and $\max.y_i(k)$ is the largest value of $y_i(k)$ for the k th response.

Table 6 Normalization of the response

Experimental No.	Tensile strength after data processing (Normalizing)	Resistance after data processing (Normalizing)
Reference sequence	1.0000	1.0000
1	0.0000	0.0000
2	0.312	0.6666
3	0.87	0.6666
4	0.426	0.6666
5	0.716	0.3333
6	0.858	0.6666
7	0.462	0.6666
8	1.0000	0.6666
9	0.03	1.0000

Table 6 showed the sequences after the grey relational generation. An ideal sequence was $x_0(k)$ ($k = 1, 2, \dots, 9$) for two responses. The definition of the grey relational grade in the grey relational analysis was to show the relational degree between the nine sequences [$x_0(k)$ and $x_i(k)$ $i = 1, 2, \dots, 9; k = 1, 2, \dots, 9$]. The grey relational coefficient $\xi_i(k)$ can be calculated as

$$\xi_i(K) = \left[\frac{\Delta_{\min} - \zeta \Delta_{\max}}{\Delta_{0i}(K) - \zeta \Delta_{\max}} \right] \tag{4}$$

where $\Delta_{0i} = x_0(k) - x_i(k)$ was the difference of absolute value between $x_0(k)$ and $x_i(k)$; $\xi =$ distinguishing coefficient (0–1); $\Delta_{\min} =$ smallest value of Δ_{0i} and $\Delta_{\max} =$ largest value of Δ_{0i} .

The grey relational coefficient results for the experimental layout are shown in Table 7. Table 7 shows that the resistance variation is very negligible from one experiment to another. On variable measurement, the result of resistance indicates the electrical resistance is not the variable responsible for the process. As can be seen from the measurement result the variation of the resistance is very small when the process is varying from one to the other input parameter thus another additional response is needed for optimization. In application point of view, if resistance is the only important response needed for final output, then any combination of process parameter yields good weldments of negligible resistance. In this study, resistance and tensile strength of the weldment is equally important and the two performance optimization of process parameter is essential and needed to obtain the best process parameter.

After averaging the grey relational coefficients, the grey relational grade γ_i can be obtained as

Table 7 Deviation sequence

Experimental No.	Tensile strength after data processing (Normalizing)	Resistance after data processing (Normalizing)
Deviation sequence	$\Delta_{oi} (1)$	$\Delta_{oi} (2)$
1	1.0000	1.0000
2	0.688	0.3334
3	0.13	0.3334
4	0.574	0.3334
5	0.284	0.6667
6	0.142	0.3334
7	0.538	0.3334
8	0	0.3334
9	0.97	0.0000

$$\gamma_i = \frac{1}{n} \sum_{k=1}^n \xi_i(k) \tag{5}$$

where n = number of process responses.

Table 8 shows that larger the grey relational grade represents higher the relational between the variables and lower the grey relational grade represents lesser relational between the variables. From Table 8, experiment no. 8 is the most powerful relation between the output parameters. In this analysis multi-objective optimization is converted to single grey relational analysis as shown in Table 8. From the grey relational analysis, it can optimize the multi-performance of two output parameters such as resistance and strength. The grey relational grade was analyzed based on main effect plot to get the optimum parameter settings for multi-performance as shown in Fig. 6. The higher grey relational grade will be close to the optimal condition. Using the grey relational grade value, the mean of the grey relational grade for each level

Table 8 Grey relational coefficient ξ_i and grey relational grade γ_i

Experimental No.	$\xi_i(1)$	$\xi_i(2)$	γ_i	Rank
1	0.3333	0.3333	0.3333	9
2	0.4208	0.5999	0.51035	8
3	0.7936	0.5999	0.6967	2
4	0.4655	0.5999	0.5327	7
5	0.6377	0.4285	0.5331	6
6	0.7788	0.5999	0.68935	3
7	0.4816	0.5999	0.54075	5
8	1	0.5999	0.7999	1
9	0.3401	1	0.67005	4

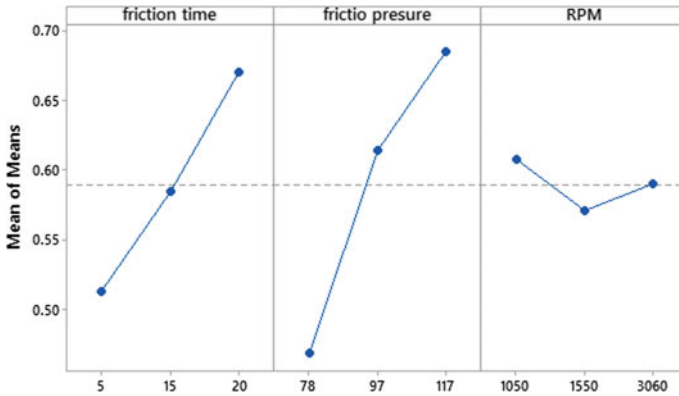


Fig. 6 Taguchi/ANOVA analysis main effect plot of grey relational grade

Table 9 Response table for grey relational grade value

Level	Friction time	Friction pressure	RPM
1	0.5134	0.4689	0.6075
2	0.5850	0.6144	0.5710
3	0.6702	0.6853	0.5902
Delta	0.1568	0.2164	0.0365
Rank	2	1	3

of different factors and the total mean of the grey relational grade is summarized in Table 9.

7.1 Main Effect Plot of Grey Relational Grade

Based on the main effect plot as shown in Fig. 6, the optimal level of the process parameters such as friction time is 20 s, friction pressure is 117 (MPa) and 1050 (RPM). Rotational speed at a high level (1450 RPM), friction pressure at a low level (39.2 MPa) and friction time at a low level (4 seconds) was given optimum result for mechanical strength [5]. The result of this analysis is very deferent from the literature result. The difference in the result may be for two reasons. In the present case, the optimization is for two performance strength and electrical resistance simultaneously. But from the literature the response is for strength. Table 9 shows that the friction pressure is the most important parameter and friction time is the second important parameter. RPM is the least important parameter for two response performance (strength and electrical resistance).

Total mean of the grey relational grade which is 0.5896.

8 ANOVA Analysis

The main purpose of the ANOVA was to investigate which factors significantly affected the performance characteristic. This is accomplished by separating the total variability of the grey relational grades, which is measured by the sum of the squared deviations from the total mean of the grey relational grade, into contributions by each process parameter and error [13]. The total sum of the squared deviations SS_T from the total mean of the grey relational grade was calculated as

$$SS_T = \left[\sum_{j=1}^p (y_i - y_m)^2 \right] \tag{6}$$

where p = number of experiments in the orthogonal array and y_j = mean of the grey relational grade for the j th experiment.

The percentage contribution by each factor to the total sum of the squared deviations SS_T was used to evaluate the importance of the process parameter change on the performance characteristic. In addition, the F -test was also used to determine which factor has a significant effect on the performance characteristic. Usually, the change of a determined factor has a significant effect on the performance characteristic when the F -value was large [14].

Result of ANOVA Table 10 indicated that friction pressure is the most significant factor for affecting the multiple performance characteristics. Based on the previous discussion, the optimal factors are RPM at level 1, friction pressure at level 1 and friction time at level 1.

Table 11 indicated that the higher percentage contribution for the process was friction pressure which happened to be 48% and the next contribution was from the

Table 10 Analysis of variance (ANOVA) for grey relational grade

Source	DF	Adj. SS	Adj. MS	F -value	P -value
Friction time	2	0.036965	0.018478	0.90	0.525
Friction pressure	2	0.073050	0.036525	1.79	0.359
RPM	2	0.002000	0.001000	0.05	0.953
Error	2	0.040894	0.020447		
Total	8	0.152900			

Table 11 Percentage contribution

Parameter	Percentage contribution (%)
Friction time	24
Friction pressure	48
RPM	1.33

friction time which is 24% and RPM has a very small contribution for the process which happened to be 1.333%.

9 Confidence Interval and Confidence Level

The confidence interval is the interval of upper and lower bonds which shows the grey relational grade of the confirmation test between the confidence interval with 95% confidence. The confidence interval for the predicted mean of the grey relational grade on the confirmation experiment was calculated by Eq. (7).

$$CI = \left[\hat{\phi} \pm \left\{ F_{\alpha;1;f_c} \times V_c \left(\frac{1}{n_{eff}} + \frac{1}{r} \right) \right\}^{1/2} \right] \tag{7}$$

The calculated value of the confidence interval was $CI = 0.7659 \pm 0.17578$ with upper limit = 0.94169 and lower limit = 0.59012. In the confirmation test, the grey relational grade must be between the intervals in order to justify the result.

The grey relational grade of the confirmation experiment is between the CI which proved the result obtained in. Based on the CI result, the mean of the grey relational grade for confirmation experiment was 95% chance to be between the CI (0.94169–0.59012).

From 95% confidence test, it could be possible to predict the output result of the process for mass production of weldments. The forecast in mass production was performed in two deferent ways. One if the chance of the mean of the output grey relational grade was around the 95% confidence interval, then it could predict the quality of the weldment based on the 95% confidence level. On the other hand, if it could predict the quality of the weldment with 95% confidence, then it could estimate the defect in mass production. On achieving the above significant then the next was to minimize the defective weldments out of a large number of mass production which indeed was the area of importance in this study for application point of view when mass productions of weldments were performed.

10 Confirmation Test

The estimated grey relational grade \hat{y} using the optimal level of process parameters can be calculated as

$$\hat{y} = \left[y_m + \sum_{i=1}^q (y_i - y_m) \right] \tag{8}$$

Table 12 Summary of optimization result

Condition description	Optimal machining parameters		
	Parameters in 8th trial experiment	Grey theory prediction	Verification experiment
Level	A20B97C1050	A20B117C105	A20B117C1050
Load (KN)	5.07		5.502
Resistance 4 (Ω)	1.5×10^{-5}		1×10^{-5}
Grey relational grade	0.7129	0.73439	0.7659
Improvement in grey relational grade = 0.053			

where \hat{y} = Estimated grey relational grade, γ_m = Total mean of the grey relational grade, \bar{y}_i = Mean of the grey relational grade at the optimal level, q = Number of process parameters that significantly affect the multiple performance characteristics [15].

Based on the Eq. (8), the estimated grey relational grade using the optimum process parameter could be obtained. Table 12 shows the results of the confirmation experiment using optimal process parameters.

CI = Confidence interval = Upper limit = 0.94169, lower grey relational grade of confirmation test is 0.7659 which is between the confidence interval. As shown in Table 12, when the load increased from 5.07 to 5.502 KN then Resistance (Ω) is greatly reduced from 1.5×10^{-5} to 1×10^{-5} . Through this study, it is clearly seen that multiple performance characteristics in the welding process are greatly improved.

Based on the above discussion, the results obtained are very important in the decision-making for process performance and selection of process parameters. This is important for two reasons the first is it reduces the defect in mass production and the other is to minimize the effect of process parameter variation on the quality of the weldments or the products when it is used in other applications such as electrical connectors, circuit connectors, etc.

11 Conclusion

In this research study, the experimental task was carried out in detail including friction welding process setup on drilling machine. Experimental setup for resistance test, process parameter selection and measurement systems for process parameters were performed in detail. Friction weldments of aluminium and copper were friction welded on the designed setup and test of process parameters were also performed.

Based on the optimization analyses the process has improved. The load and resistance have improved by 8.76% and 33.333%, respectively. The multi-performance optimized parameter setting has obtained and its friction time is 20 seconds, friction pressure is 117 (MPa) and 1050 (RPM). A verification experiment was

also performed based on the optimized setting. Pressure has significant for the multi-performance output such as resistance and strength.

In order to test the predicted results, confirmation experiment was performed at optimum conditions. The mean of the relational grade for the confirmation experiment is 0.7659 which is in the range of 95% confidence interval. Hence, the model has justified based on the confirmatory test.

From the multi-objective optimization it was concluded that

1. From the ANOVA and Grey relational analysis, the tensile strength and the resistance are optimized.
2. The pressure is significantly important for multi-performance characteristic with 48% importance for the process.
3. Multi-performance optimized parameter setting has obtained and it is presented as friction time is 20 seconds, friction pressure is 117 (MPa) and 1050 (RPM).
4. The 95% confidence level proved that the grey relational grade for confirmation test is between the CI which indicates the optimization has justified.

Compliance with Ethical Standards **Conflict of Interest** The authors declare that they have no conflict of interest.

References

1. W.B. Lee, S.B. Jung, Effects of intermetallic compound on the electrical and mechanical properties of friction welded Cu/Al bimetallic joints during annealing. *J. Alloys Compounds* **390**(1–2), 212–219 (2005)
2. M. Kimura, Effect of friction welding condition on joining phenomena and mechanical properties of friction welded joint between 6063 aluminium alloy and AISI 304 stainless steel. *J. Manuf. Process.* **26**, 178–187 (2017)
3. M. Sahin, Joining of aluminium and copper materials with friction welding. *Int. J. Adv. Manuf. Technol.* **49**(5–8), 527–534 (2010)
4. A.Z. Sahin, Analysis of the friction welding process in relation to the welding of copper and steel bars. *J. Mater. Process. Technol.* **82**(1–3), 127–136 (1998)
5. N.R. Rosli, Improving process quality in friction welding for bimetal lugs. *Jurnal Mekanikal* **38**(1), 38–50 (2015)
6. R.A. Tsujino, Development of Al/Cu dissimilar joint by new friction welding method. *J. Jpn. Soc. Des. Eng.* **51**(3), 181–196 (2016)
7. M. Maalekian, Friction welding—critical assessment of literature. *Sci. Technol. Weld. Joining* **12**(8), 738–759 (2007)
8. I.M. Bhamji, *Development of the Linear Friction Welding Process* (University of Manchester, Material Science, The University of Manchester, Manchester, UK, 2012)
9. S.S. Bharathi, Mechanical properties and microstructural characteristics of friction welded dissimilar joints of aluminium alloys. *Trans. Ind. Inst. Met.* **71**(1), 91–97 (2018)
10. Ducab, Retrieved from www.ducab.com (2018)
11. W. Li, Interface microstructure evolution and mechanical properties of Al/Cu bimetallic tubes fabricated by a novel friction-based welding technology. *Mater. Des.* **134**, 383–393 (2017)
12. Z. Wang, L. Zhu, J.H. Wu, Grey relational analysis of correlation of errors in measurement. *J. Grey Syst.* **8**(1), 73–78 (1996)

13. S. Balasubramanian, S. Ganapathy, Grey relational analysis to determine optimum process parameters for wire electro discharge machining. *Int. J. Eng. Sci. Technol.* **3**(1), 95–101 (2011)
14. H. Hasani, A.T. Somayeh, A. Ghafour, Grey relational analysis to determine the optimum process parameters for open-end spinning yarns. *J. Eng. Fibers Fabr.* **7**(2), 81–86 (2012)
15. C.L. Lin, Use of the Taguchi method and grey relational analysis to optimize turning operations with multiple performance characteristics. *Mater. Manuf. Process.* **19**(2), 209–220 (2004)

A Study on Effect of Cutting Fluids on Surface Roughness of EN 8 Steel Turning Using Taguchi Method



V. Kumar, P. Surendernath, and K. Amarnath

Abstract Surface completion is one of the essential worries during machining of different materials in the machining tasks. In this way, it is extremely fundamental for controlling the required surface quality to have the decision of streamlined cutting parameters. The present trial study is worried about the improvement of cutting parameters (profundity of cut, feed rate, axle speed, and cutting liquids). In the present work, turning activities were done on EN 8 steel via carbide cutting instrument in wet condition, and the mix of the ideal degrees of the parameters was acquired. The Analysis of Variance (ANOVA) was utilized to think about the presentation surface roughness and cutting forces qualities in turning operation. The results of the analysis show that none of the factors were found to be significant.

Keywords EN 8 steel · Cutting parameters · Analysis of variance (ANOVA) · Surface roughness

1 Introduction

Turning

Turning is the expulsion of metal from the external measurement of a pivoting round and hollow workpiece. Turning is utilized to lessen the breadth of the workpiece generally to a predetermined measurement.

V. Kumar · P. Surendernath · K. Amarnath (✉)
Kamala Institute of Technology and Science, Huzarabad, Karimnagar, Telangana, India
e-mail: amarnath.kandagatla@gmail.com

V. Kumar
e-mail: yadavk062@gmail.com

© Springer Nature Singapore Pte Ltd. 2021
G. S. V. L. Narasimham et al. (eds.), *Recent Trends in Mechanical Engineering*,
Lecture Notes in Mechanical Engineering,
https://doi.org/10.1007/978-981-15-7557-0_12

1.1 Cutting Parameters

In turning the speed and movement of the slicing apparatus is indicated through a few parameters. These parameters are chosen for every task dependent on the workpiece material apparatus material device size and that's only the tip of the iceberg.

- Cutting feed—The separation that the cutting instrument or workpiece progresses during one uncut of the axle estimated in Inches Per Revolution (IPR). In certain activities the apparatus advances into the workpiece and in others the workpiece advances into the instrument. For a multi-point device the slicing feed is likewise equivalent to the feed per tooth estimated in Inches Per Tooth (IPT) and increased by the number of teeth on the cutting instrument.
- Cutting speed—The speed of the workpiece surface with respect to the edge of the cutting instrument during a cut estimated in Surface Feet every Minute (SFM).
- Spindle speed—The rotational speed of the axle and the workpiece in cycles every minute (RPM). The shaft speed is equivalent to the cutting rate partitioned by the perimeter of the workpiece where the cut is being made.
- Feed rate—The speed of the slicing device's development with respect to the workpiece as the device makes a cut. The feed rate is estimated in inches every minute (IPM) and is the result of the cutting feed (IPR) and the shaft speed (RPM) Fundamental introduction on CNC.

A CNC machine enables you to do complex machining with less experience on the grounds that the PC controls the machine so as to make convoluted cuts. On the off chance that you need to deal with your manual machine aptitudes there's nothing ceasing you yet meanwhile utilizing a CNC machine you wouldn't be constrained to what you can do physically.

CNC machines additionally help when outrageous precision is required. While high exactness is conceivable on a manual machine with cautious estimating and cutting the procedure takes quite a while and a great deal of consideration. A CNC machine makes the procedure a lot simpler cutting exceptionally precise pieces quicker than a manual administrator can [1, 2].

A CNC machine may cost in excess of a manual machine which is a distinct thought. Notwithstanding the machine itself you likewise need a reasonable PC to run the product which is an extra expense. On the off chance that you spend more cash in advance however you may effortlessly have the option to recover those expenses—perhaps more—by sparing time on generation runs. This is particularly valid on the off chance that you have to make an enormous number of parts or in the event that you make profoundly complex parts. Rather than being attached to the machine for quite a long time you can structure the parts you need and let the PC handle the controls saving your time for other work [3, 4].

2 Materials and Methods

Introduction to EN 8 Steel

Instrument steel alludes to an assortment of carbon and composite steels that are especially appropriate to be made into devices. Their reasonableness originates from their unmistakable hardness, protection from scraped spot, their capacity to hold a forefront, as well as their protection from misshapening at raised temperatures (red-hardness).

Apparatus steel is commonly utilized in a warmth treated state. With a carbon content somewhere in the range of 0.7–1.5%, device steels are made under deliberately controlled conditions to create the required quality. The manganese substance is frequently kept low to limit the likelihood of splitting during water extinguishing [5, 6]. In any case, appropriate warmth treating of these steels is significant for sufficient execution, and there are numerous providers who give tooling spaces planned to oil extinguishing [7, 8].

Device steels are made to various evaluations for various applications.

Apparatus steels are additionally utilized for exceptional applications like infusion shaping on the grounds that the protection from scraped spot is a significant rule for a form that will be utilized to deliver a huge number of parts.

CUTTING TOOL MATERIAL - CEMENTED CARBIDE

Physical Properties	Metric
Density	14.95 g/cc
Mechanical Properties	Metric
Hardness, Rockwell A	91.9
Hardness, Vickers	1575
Rupture Strength	2200 MPa
Compressive Strength	6200 MPa
Component Elements Properties	Metric
Cobalt, Co	6.0 %
WC	94 %

Table 1 Input parameters for machining

Factors	Process parameters	Level 1	Level 2	Level 3
A	Cutting speed (rpm)	600	1200	1800
C	Cutting fluids	Servo oil	sunflower	Palm kernel

Table 2 L9 orthogonal array

Sl. No.	Speed	Cutting fluids
1.	1800	Servo oil
2.	1800	Palm Kernel
3.	1800	Sun lower
		Servo oil
4.	1200	
5.	1200	Palm Kernel
6.	1200	Sunflower
7.	600	Servo oil
8.	600	Palm Kernel
9.	600	Sunflower

Input Parameters

See Table 1.

Design of Experiments (DOE)

See Table 2.

3 Results and Conclusion

Cutting Force Calculations

$$K_s = (N_e \times 60 \times 10^3 \times \text{Coefficient of Efficiency}) / (\text{Depth} \times \text{Feed} \times \text{Cutting Speed})$$

$$\text{Coefficient of Efficiency} = 0.8$$

$$K_s = (4.65 \times 60 \times 10^3 \times 0.8) / (0.4 \times 200 \times 1200)$$

$$K_s = 550N$$

SPEED – 1800rpm

Feed = 200mm/min, Depth of cut – 0.4mm

Cutting Force

$$N_e = (\text{Depth} \times \text{Feed} \times \text{Cutting Speed} \times K_s) / (60 \times 10^3 \times \text{Coefficient of Efficiency})$$

$$N_e = 4.65\text{KW}$$

$$K_s = (N_e \times 60 \times 10^3 \times \text{Coefficient of Efficiency}) / (\text{Depth of cut} \times \text{Feed} \times \text{Cutting Speed})$$

$$\text{Coefficient of Efficiency} = 0.8$$

$$K_s = (4.65 \times 60 \times 10^3 \times 0.8) / (0.4 \times 200 \times 1800)$$

$$K_s = 1150\text{N}$$

2. SPEED – 1200rpm

Feed = 200mm/min, Depth of Cut – 0.4mm

Cutting Force

$$N_e = (\text{Depth} \times \text{Feed} \times \text{Cutting Speed} \times K_s) / (60 \times 10^3 \times \text{Coefficient of Efficiency})$$

$$N_e = 4.65\text{KW}$$

Cutting Forces Table SURFACE ROUGHNESS VALUES

3. SPEED – 600rpm

Feed = 200mm/min, Depth of cut – 0.4mm

$$K_s = (4.65 \times 60 \times 10^3 \times 0.8) / (0.4 \times 200 \times 600)$$

$$K_s = 465.2\text{N}$$

FACTORS WORKSHEETS

4	C1	C2.T	C3
	SPEED	CUTTING FLUIDS	SURFACE ROUGHNESS
1	1800	SERVOOIL	3.45
2	1800	PALMKERNOL	4.12
3	1800	SUNFLOWER	3.15
4	1200	SERVOOIL	4.72
5	1200	PALMKERNOL	3.91
6	1200	SUNFLOWER	4.01
7	600	SERVOOIL	4.95
8	600	PALMKERNOL	4.15
9	600	SUNFLOWER	4.21

Taguchi Design - Factors

Assign Factors

To columns of the array as specified below

To allow estimation of selected interactions

Fact	Name	Level Values	Column	Level
A	SPEED	1800 1200 600	1	3
B	CUTTING FLUIDS	SERVOIL PALMKERNOL SUNFLOWER	2	3

Help OK Cancel

EXPERIMENTALPHOTOS:

Raw material: EN 8 STEEL

Dimensions: Diameter =30 mmLength =220 mm



Workpiece positioning



CNC Machine

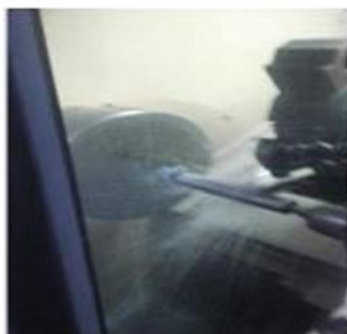
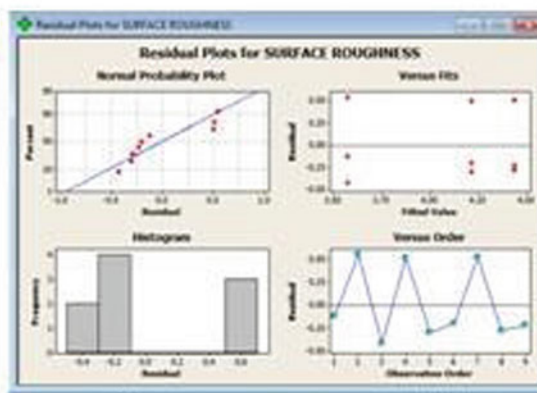
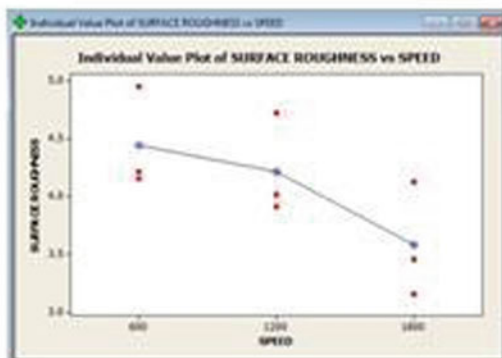


Fig.:CNC process




PLOTS



Surface Roughness measuring

Test Report



Hyderabad Engineering Labs
NABL Accredited Lab, An ISO 9001 and ISO 45001 Certified Lab
Phone: +91-72 07 077870, Telefax: 040-23075650, M: +91-08 85 599600
E-mail: sbh@hyderabadenglabs.com, hyderabadenglabs@gmail.com
Website: www.hyderabadenglabs.net

MATERIAL TESTING SERVICES
METALLURGICAL, NDT & BUILDING (CIVIL) MATERIALS

5-B-16/10, Praashanthi Nagar, Indl. Estate, Kukatpally, Hyderabad - 500 072, India.

SURFACE ROUGHNESS TEST REPORT

01. Customer : M/s. KAMALA INSTITUTE OF TECHNOLOGY AND SCIENCE,
Huzurabad, Karimnagar.

02. Work Order No & Date : HHEL/19/11360 Dt: 06.07.2019.

03. GP.No. & Date : Request Form Dt: 06.07.2019.
Sample Received Date Dt: 06.07.2019.
Tested Date Dt: 06.07.2019.

04. T.C.No. & Date : M-1716-B Dt: 06.07.2019.


05. Sample Description : CNC Turning

06. Specification : Steel Alloy

Equipment Used: SurfTest, Model: SE-210, Make: Mitutoyo, S.No: 3073031609,
Calibration Due Date: 03.10.2019.

S.No.	Sample Identification	Surface Roughness (Ra)
		in microns (μm)
		Average
01	STEP.01	3.45
02	STEP.02	4.12
03	STEP.03	3.15
04	STEP.04	4.72
05	STEP.05	3.91
06	STEP.06	4.01
07	STEP.07	4.95
08	STEP.08	4.15
09	STEP.09	4.21

Lab Test No: M-11360
Note: 1) This result pertains to the samples received at Lab Premises.
2) This T.C. cannot be reproduced except in full without our written permission.
3) Ref: Name plate at 0'

For HYDERABAD ENGINEERING LABS
Authorized Signature


4 Conclusion

In this paper an attempt to make use of ANOVA technique to optimize cutting parameters during high speed turning of EN 8 tool steel using cemented carbide cutting tool.

The cutting parameters are speed, feed rates for turning of workpiece EN 8 device steel. In this work, the ideal parameters of cutting rate are 600, 1200, and 1800 rpm,

and feed rate is 200 mm/min. Trial work is directed by thinking about the above parameters. Cutting powers, surface harshness esteems are approved tentatively.

The experiment conducted with above parameters and different cutting fluids such as servo oil, sunflower refined oil, and palm kernel oil provided the following results discussed below.

By observing the experimental results and by ANOVA, the following conclusions can be made. To minimize the cutting forces, the optimal parameters are spindle speed—600 rpm, feed rate—200 mm/min, and depth of cut—0.4 mm. To get better surface finish, the optimal parameters are spindle speed—1800 rpm, feed rate—200 mm/min, and sunflower refined oil.

References

1. Using the Response Surface Method to Optimize the Turning Process of AISI 12L14 Steel
2. M.A. El Baradie, Cutting liquids part 1. *J. Charact. Mater. Handl. Innov.* 786–787 (1996)
3. A. Radoslav Raki, B. Zlata Raki, The influence of the metal working liquids on machine apparatus disappointments **252**(5–6), 438–444 (2002)
4. K. Amarnath, P. Surendernath, V. Kumar, Experimental investigation to optimize process parameters in drilling operation for composite materials. *Lect. Notes Mech. Eng.* ISBN 978-981-15-1123-3 (2019)
5. M.H. Greeley, R.E. Devor, S.G. Kapoor, N. Rajagopalan, The impact of liquid administration approach and operational changes on metal working liquid usefulness. *Diary Assemb. Sci. Design.* **126** (2004)
6. N. Bashir Andrei, Proceedings on the institution of mechanical architects, part J. *J. Design. Tribol.* (2004)
7. OSHA, Metal Working Liquids: Safety and Wellbeing Best Practices Manual. Salt Lake City, US dept. of Labor, OSHA (1999)
8. R.B. Aronson, Machine Tool 101: Section 6, Machine Servers Assembling Designing, pp. 47–52 (1994)

Study on Mechanical Behavior of Friction Stir Welded Nylon-6 Sheets



Santosh K. Sahu, Kamal Pal, Susmita Das, and Avisek Tripathy

Abstract The use of thermoplastics is vastly popular in advanced industrial and aerospace sectors due to unique mechanical properties. The solid-state friction stir welding is seen as one of a kind of the significant joining strategies to overcome heat incited fusion welding deficiencies. This friction stirred solid-state welding method can be effectively used to join poor thermal conductive materials. This work presents the practicability of friction stir butt-welded nylon-6 sheet using cylindrical profile tool pin. Tool rotational speed and tool traverse speed are the key factors which affect the weld strength and micro-hardness variation along the weld centerline. At 1800 rpm, tool rotational speed and 20 mm/min tool traverse speed the highest joint efficiency was found to be 41%. The weld joint strength was discovered poor at low tool rotational speed and high traverse speed; however, both the process variables were significant over joint quality. The maximum number of failures during tensile test was found advancing side of the weld zone. The stress-elongation outline specified a brittle failure in the heat-affected weld interface welds. The joint efficiency has, however, been found to be reduced significantly due to predominant material gather up from advancing to retreating side along with significant hardness variation from stirred weld zone to heat-affected zone as per hardness deviation graph.

Keywords Friction stir welding · Joint strength · Micro-hardness · Nylon-6

S. K. Sahu (✉) · K. Pal · S. Das
Department of Production Engineering, Veer Surendra Sai University of Technology, Burla,
Sambalpur, Odisha 768018, India
e-mail: santosh.lenovo@gmail.com

K. Pal
e-mail: kpal5676@gmail.com

S. Das
e-mail: susmitadas103@gmail.com

A. Tripathy
Department of Mechanical Engineering, Guru Nanak Institutions Technical Campus,
Ibrahimpattam, Ranga Reddy District, Telangana 501506, India
e-mail: avisek89@gmail.com

1 Introduction

Nowadays, thermoplastics have high consideration in the leading manufacturing sectors. Their lightweight material which increases the overall efficiency is one of the most important reason for their popularity and other benefits such as high specific strength, flexibility in design, low production value, lightweight, etc. essentially shaped a base for its wide applicability [1, 2]. Adhesive bonding and mechanical fastening have been employed for years to joint thermoplastic materials. The adhesive bonding cannot place any quality test. Thus, it is difficult to predict joint failure. The bonding method also desires surface preparation which decreases process efficiency. Mechanical fastening using nuts, bolts, rivets etc. produces additional weight. The traditional fusion welding methods cannot be employed to weld thermoplastics material because of their low-melting point. One of the resolves to this problem can be friction stir welding (FSW), because in this method solid-state welding easily joins the material without melting the base material.

In December 1991 'The Welding Institute (TWI), UK' created and patented friction stir welding [3]. This new technique was employed in the preliminary phase to join aluminum alloys using conventional welding techniques. The friction stir weld feature has mostly achieved by tool rotational speed, welding speed at various tool plunging rates [4]. Afterward, this method has also proposed to different similar to dissimilar thermoplastic welding. In this method, the tools are commonly designed having two parts, i.e., shoulder and pin which is rotated and plunged into the workpiece with traverse along with the joint line. The FSW is found to be an effective joining method for some cases with satisfactory joint strength.

It has been detected that the thermoplastic materials become distorted as the tool plunges into the workpiece. Hence, the FSW tool was altered with a new design comprised of the stationary rectangular shoe with a heating coil positioned inside the shoe for necessary heat to the weld [5]. The pin profile of the tool is considered very significant to improve the quality of the joint. The cylindrical grooved tool was superior in polyethylene welding in which the tool plunging rate has no major effect on weld quality [6]. However, the joint efficiency of ABS sheets considerably develops using the conical pin rather than cylindrical pin profile [7]. On the other hand, the left hand threaded pin profile was inspected with clockwise and anticlockwise rotation on the nylon-6 welding [8]. It was determined that the threaded pin helps to the movement through the grooves of the thread in case of anticlockwise tool rotation that resulted in superior joint strength.

In the last twenty years, thermoplastics material has been found to be tremendously popular in several engineering applications. However, it was a challenging work to achieve appropriate joint efficiency for this kind of low thermal conductive nylon-6 sheet. There are several works of parametric study on welded joint strength by friction stir welding on polymeric materials. Tool selection is the main reason because material mixing is important. The joint efficiency will increase by using appropriate tool design with capability to blend the softened thermoplastic material at various different range of parameters. There is hardly any work on the mechanical behavior

of the FSW joint using stress–strain diagram along with micro-hardness deviation in nylon-6 weld. Hence, the present work addresses the improvement of friction stir weld joint quality using cylindrical pin profiles and stress–strain diagram with micro-hardness along the weld bead centreline in detail.

2 Experimental Procedure

The base material selected for the experiment is a nylon-6 sheet of 100 mm × 100 mm × 6 mm. Nylon-6 is a lightweight engineering thermoplastic which has an extensive range of properties and applications. It is a good balance of properties including high strength, good elongation, high energy to break, and stiffness, hence used as structural materials. Table 1 lists the thermal and mechanical properties of the base material. By using a 2 ton, 3-axes Computer Numeric Controlled Friction Stir Welding machine (ETA technology PVT. LTD., Bangalore), the nylon-6 sheets were butt welded. The two samples have been properly fixed on the fixture with zero root gaps. The experimental setup with a fixture arrangement is displayed in Fig. 1.

The FSW tool used for the investigation has been machined from H13 tool steel having an 18 mm shoulder diameter, 6 mm pin diameter, and 5.6 mm pin length as shown in Fig. 2. To determine the range of both rotational speed and traverse speed various trial experiments were conducted. The tool was traversed above the joint line and the pin face. The constant tool tilt angle of 1° and plunging depth of the

Table 1 Thermal and mechanical properties of Nylon 6

Density (g/cc)	Ultimate tensile strength (MPa)	Co-efficient of linear expansion (per °C) × 10 ⁻⁶	Melting temperature (°C)	Conductivity (W/mk)
0.91	46.7	85	220	0.21

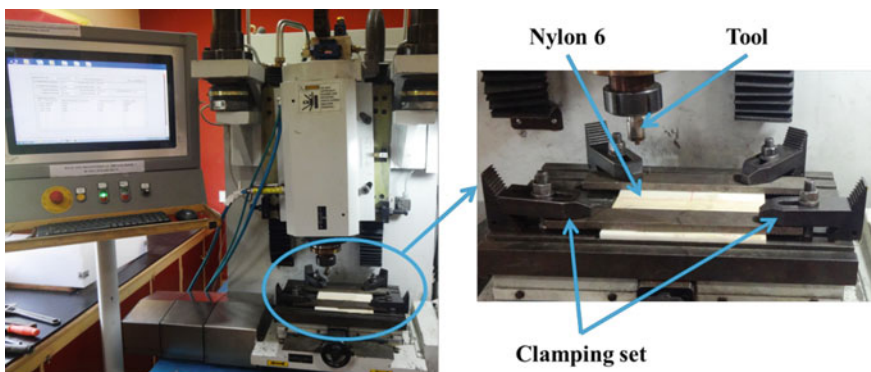


Fig. 1 Experimental setup with fixture arrangement

Fig. 2 FSW tool with cylindrical pin

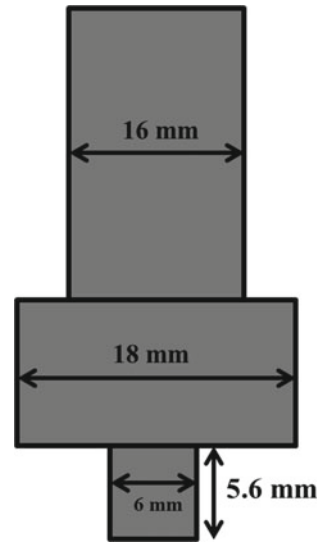


Table 2 FSW process parameter and their respective levels

Process parameter	Level 1	Level 2	Level 3
Rotational speed (rpm)	1000	1800	2600
Traverse speed (mm/min)	10	20	30

tool 0.1 mm were provided to the tool during the experiments. The three levels of each process parameters were considered for final experiments as shown in Table 2. There were 9 experiments that have been carried out in this investigation. After the weld, the tensile test sample was prepared in the perpendicular direction of welding using Universal Testing Machine (Instron 1344) at 0.1 mm/min strain rate. The weld specimens for tensile test were arranged according to ASTM D638 standard [9]. All the welded samples were cut 20 mm length along the weld cross-section for hardness testing. The micro-hardness along the weld centerline on each polished weld bead sample has been measured using ‘Shore D hardness tester’.

3 Results and Discussion

The present work successfully welded the nylon-6 sheet using cylindrical pin profile. Several welded joint quality characteristics such as weld zone hardness (H_w), heat-affected zone hardness along both advancing side ($H_{\text{haz,AS}}$), and retreating side ($H_{\text{haz,RS}}$) of the welded sample and ultimate tensile strength (joint efficiency) with respective welding experiment are presented in Table 3. The welded sample appearance is shown in Fig. 3. With a considerable increase in tool traverse speed at different

Table 3 Experimental parametric settings with corresponding weld quality features

Exp. No.	RS (rpm)	TTS (mm/min)	Shore D hardness				UTS (MPa)	Efficiency (%)	Failure zone	
			H_w	$H_{\text{HAZ},AS}$	$H_{\text{HAZ},RS}$	$H_{\mu\text{HAZ}}$				ΔH
1.	1000	10	62	60	54	57	5	9.3	19.91	HAZ(RS)
2.	1000	20	71	67	58	62.5	8.5	14.87	31.84	HAZ(AS)
3.	1000	30	64	52	42	47	17	7.57	16.21	HAZ(AS)
4.	1800	10	68	62	59	60.5	7.5	13.85	29.66	HAZ(AS)
5.	1800	20	68	66	60	63	5	19.14	40.99	HAZ(AS)
6.	1800	30	68	67	60	63.5	4.5	10.62	22.74	HAZ(AS)
7.	2600	10	64	61	55	58	6	10.62	22.74	HAZ(AS)
8.	2600	20	71	62	61	61.5	9.5	16.32	34.95	HAZ(AS)
9.	2600	30	69	67	66	66.5	2.5	9.58	20.51	HAZ(AS)

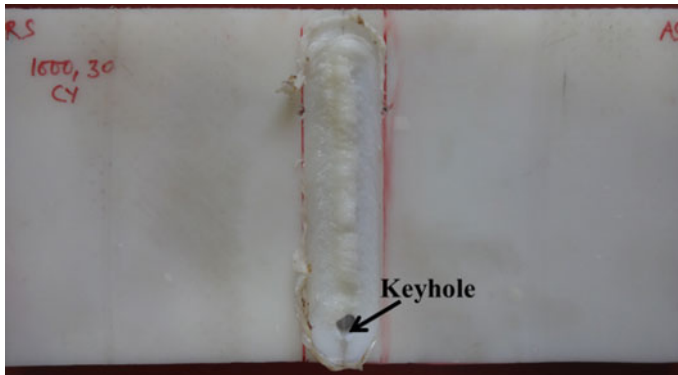


Fig. 3 Welded sample

tool rotational speeds using cylindrical pin profile as presented in the paper, there was an expressive improvement in the weld reinforcement height. There were minor circular ring-shaped ripples as tool impressions have been noticed at higher tool rotation speed. However, the keyhole defect was found at the end of each weld bead profile.

3.1 Effect of Process Parameter on Joint Strength

The butt weld performance during tensile testing had been inspected with the help of the stress-elongation graph. The output response of ultimate joint strength with corresponding percentage elongation of the solidified welds is indicated in Figs. 4 and 5. Tensile strength of base nylon-6 sheet was found to be 46.7 MPa. The maximum ultimate tensile strength of 19.14 is achieved at intermediate tool rotational speed (1800 rpm) and tool traverse speed (20 mm/min) as shown. The joint efficiency extensively stretched with the variation in tool traverse speed and tool rotational speed as shown in Fig. 4. The highest weld joint efficiency was 40.99% of the strength of the base material, with a drastic reduction in elongation percentage (less than 10%) than base nylon-6 (49%). Thus, the ultimate joint strength, as well as percentage elongation, were both improved with an increase of welding speed and consequently reduced with further increase considering different tool rotational speeds. The stress-elongation performance of the joint is illustrated in Fig. 5. The type of joint failure during tensile testing had been inspected as per the developed stress-elongation diagram with micro-hardness variation through weld centreline [10–13].

The ultimate joint strength with corresponding elongation (%) of the weld base material nylon-6 was 19.14 MPa and 49%, respectively, as shown in Fig. 5. The stress was dropped quickly after getting the ultimate point representing brittle fracture even in base nylon-6 feasibly due to strain hardening influence. On the other hand, the

Fig. 4 Effect of tool rotational speed on tensile strength

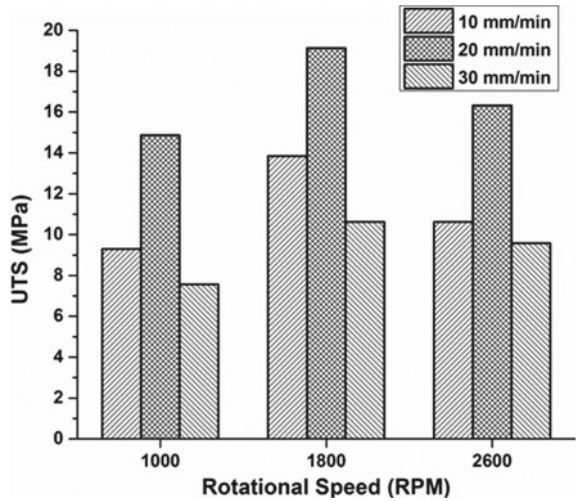
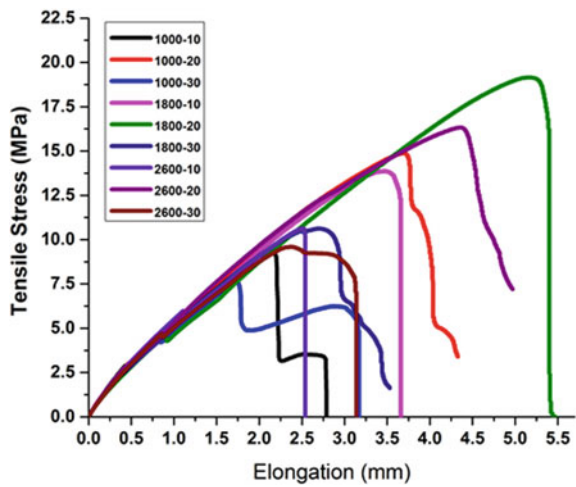
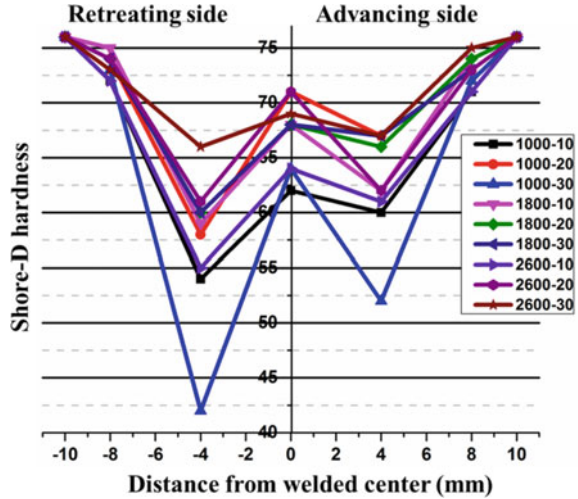


Fig. 5 Stress-elongation diagram of welded joints



weakest joint efficiency was 16.57% at low tool rotation speed (1000 rpm) with high welding speed (30 mm/min). There has been a major enhancement in both joint efficiency and elongation capability at center point experimental situation, i.e., medium tool traverse speed 20 mm/min or intermediate tool rotational speed 1800 rpm or both.

Fig. 6 Variation of shore *D* hardness with process variable



3.2 Effect of Process Parameter on Weld Micro-hardness

The results of micro-hardness test of all the samples are shown in Table 3. The Shore *D* hardness of base material was found to be 76. The Shore *D* hardness was found to be reduced at weld joint interface, i.e., weld stirred zone to thermomechanical-affected zone or heat-affected base material as found earlier in dissimilar thermo-plastic welding [14, 15]. This non-uniform micro-hardness for individual weld joints is shown as per Shore *D* hardness measurement at 4 mm weld centerline to both advancing side and retreating side, respectively. Hardness decreases because of slow cooling rate due to low thermal conductive material. The drop in hardness along the retreating side was more predominant than advancing side of the tool rotation as shown. However, the advancing side weld interface was found to be weakest in most of the cases as shown in Fig. 6. It can, therefore, be concluded that material gathers up from advancing to retreating side or insufficient stirring of material was more significant rather than hardness drop on joint strength. Thus, the hardness drop was inversely proportional to joint efficiency.

4 Concluding Remarks

The friction stir butt welding was found to be highly feasible to join nylon-6 sheets with satisfactory joint efficiency by applicable selection of welding parameter settings. The mechanical behavior of the weld joint due to tensile load along with micro-hardness deviation through the weld centreline has been examined. The conclusions may be summarized as follows:

- The joint efficiency can be significantly improved up to 40.99% at the intermediate tool rotational and tool traverse speed (i.e., RS 1800-TS 20).
- The joint strength reductions are mostly due to material gather up from tool advancing side to retreating side along with significant hardness deviation from weld to heat-affected zone.
- At low tool rotational speed with high welding speed, the weld feature was found very poor because of insufficient weld heat input.

Acknowledgments The welding experiments and post-weld measurement works have been carried out with the assistance and facilities at Friction Stir Welding Laboratory and Metrology Laboratory, IIT-Kharagpur.

References

1. J.F. Amancio-Filho, S.T. Dos Santosh, Joining of polymers and polymer-metal hybrid structures: recent developments and trends. *Polym. Eng. Sci.* **47**, 21–25 (2009)
2. P. Kah, R. Suoranta, J. Martikainen, C. Magnus, Techniques for joining dissimilar materials metals and polymers. *Rev. Adv. Mater. Sci.* **36**(3), 152–164 (2014)
3. D.C. Thomas WM, E.D. Nicholas, J.C. Needham, M.G. Church, P. Templesmith, *Friction Stir Butt Welding*. UK Patent G.B. Patent (1991)
4. R.M. Leal, C. Leitão, A. Loureiro, D.M. Rodrigues, P. Vilaça, Material flow in heterogeneous friction stir welding of thin aluminium sheets: effect of shoulder geometry. *Mater. Sci. Eng. A* **498**, 384–391 (2008)
5. A. Bagheri, T. Azdast, A. Doniavi, An experimental study on mechanical properties of friction stir welded ABS sheets. *Mater. Des.* **43**, 402–409 (2013)
6. V. Jaiganesh, D. Jaya, E. Gopinath, Effect of spindle speed, feed rate and axial load on friction stir welding of polyethylene plates, in *International Conference on Advances in Design and Manufacturing (ICAD&M 14)*, pp. 238–242 (December, 2014)
7. N. Sadeghian, M.K. Besharati Givi, Experimental optimization of the mechanical properties of friction stir welded acrylonitrile butadiene styrene sheets. *Mater. Des.* **67**, 145–153 (2015)
8. K. Panneerselvam, K. Lenin, Joining of Nylon 6 plate by friction stir welding process using threaded pin profile. *Mater. Des.* **53**, 302–307 (2014)
9. ASTM D638 Standard Test Method for Tensile Testing of Plastics. *Annual Book of ASTM Standards*
10. M.K. Bilici, A.I. Yukler, Effects of welding parameters on friction stir spot welding of high density polyethylene sheets. *Mater. Des.* **33**(1), 545–550 (2012)
11. N. Mendes, A. Loureiro, C. Martins, P. Neto, J.N. Pires, Effect of friction stir welding parameters on morphology and strength of acrylonitrile butadiene styrene plate welds. *Mater. Des.* **58**, 457–464 (2014)
12. P.N. Banjare, P. Sahlot, A. Arora, An assisted heating tool design for FSW of thermoplastics. *J. Mater. Process. Technol.* **239**, 83–91 (2017)
13. B. Du, X. Yang, K. Liu, Z. Sun, D. Wang, Effects of supporting plate hole and welding force on weld formation and mechanical property of friction plug joints for AA2219-T87 friction stir welds. *Weld. World* **63**(4), 989–1000 (2019)
14. M. Rezaee Hajideh, M. Farahani, N. Molla Ramezani, Reinforced dissimilar friction stir weld of polypropylene to acrylonitrile butadiene styrene with copper nanopowder. *J. Manuf. Process.* **32**, 445–454 (2018)

15. M. Moreno-Moreno, Y. Macea Romero, H. Rodríguez Zambrano, N.C. Restrepo-Zapata, C.R.M. Afonso, J. Unfried-Silgado, Mechanical and thermal properties of friction-stir welded joints of high density polyethylene using a non-rotational shoulder tool. *Int. J. Adv. Manuf. Technol.* **97**(5–8), 2489–2499 (2018)

Optimization and Characterization Study on Deposition of Aluminium 6063 Over IS 2062 Low Carbon Steel by Friction Surfacing



Dillip Kumar Sahoo, Bhulok Sundar Mohanty, A. Jaswanth,
and D. Abhinay Varma

Abstract The present work exhibits the correlation between process variables and coating geometry on friction surfaced deposition of aluminium 6063 over IS 2062 low carbon steel. A 3^3 factorial design technique and RSM were carried out through Taguchi method using Minitab software. Furthermore the existence model was validated by corresponding collateral experiments. Impact of discrepancy in Axial force (4, 5, 6 kN), Rotational speed (1500, 2000, 2500 rpm) and Transverse speed (75, 150, 300 mm/min) on coating width, thickness, interface temperature and bond strength was investigated. Results showed that at optimum condition of rotational speed 2500 rpm, axial force 5 kN and transverse speed 75 mm/min, the observed coating width = 20.24 mm, thickness = 2.42 mm, interface temperature = 408 °C and bond strength = 92.2 Mpa, respectively. Mechanical strength of the coating was analyzed by push-off test and hardness test which shown a higher hardness value at substrate coating interface than mechtrode material.

Keywords Friction surfacing · Coating variables · Factorial design · RSM · Microhardness

D. K. Sahoo (✉) · B. S. Mohanty · A. Jaswanth · D. Abhinay Varma
School of Mechanical Engineering, Sathyabama Institute of Science & Technology, Chennai, TN,
India

e-mail: dillipkumarsahoo@gmail.com

B. S. Mohanty

e-mail: bhulokmohanty16@gmail.com

A. Jaswanth

e-mail: aduadduri@gmail.com

D. Abhinay Varma

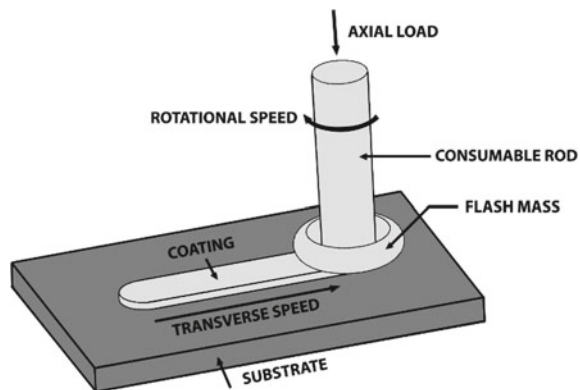
e-mail: abhinay97@gmail.com

1 Introduction

Recent days the Friction Surfacing (FS) cladding process has become a very important field of research since its ability to join similar/dissimilar materials allowing to create Functionally Graded Materials (FGM) and, therefore, friction surfacing technologies enable advanced microstructural design, enhancing the properties of the substrate material. The friction surfacing process involves a rotating consumable rod (mechtrode) experiencing with downward axial force on the base material (substrate), resulted frictional heat at the interface of mechtrode and substrate plate which causes the viscoplastic deformation at the mechtrode material. After providing certain dwell period and during transverse movement of the consumable rod the deposition occurs on the substrate plate. The principle and operation of the friction surfacing process are displayed in Fig. 1. During coating, the applied layer reaches the temperature just below the melting temperature of mechtrode and undergoes the plastic deformation. Generally, the bonding strength depends on the self-cleaning at the interface region and the amount of heat and pressure generated for the enhancement of diffusion across the interface region. Consumable materials known for better thermal conductivity are most appropriate for this process of coating. Homogeneous, high mechanical strength, good adherence, less dilution and limited heat affecting zone at the interface were some of the major advantages of FS process.

The concept of FS was first developed by Klopstock and Neelands in 1941 during their patent work for joining dissimilar metals by frictional heat [1]. From there on, many researchers have investigated different combinations of substrates and coating materials which includes soft metal over hard metal and hard metal over soft metal, etc. In their work, Rafi et al. [2] studied the microstructural features on coating AISI H13 tool steel over low carbon steel by FS and observed a sound metallurgical bonding with martensitic microstructural fine grain size at the substrate coating interface. Kumar et al. [3] confirmed a relationship between the process parameters of FS and physical geometry of the coating during deposition of AA6063 aluminium alloy over IS2062 mild steel and also observed the influence of process parameters

Fig. 1 Principle of friction surfacing



FS on mechanical strength of the coating. During their experimental study, Prasad Rao et al. [4] examined the formation of thermal profiles for different combinations of mechtrode/substrates including both ferrous and nonferrous materials and found a good metallurgically bonded coating occurred, when the flow stress of the plasticized mechtrode material is nearly equal with the localized stress developed by axial load. Puli and Ram [5] evaluated the microstructural features of FS coatings of martensitic AISI 440C over low carbon steel and revealing well-bonded coatings with excellent interlocking at the centre of the coating interface while at the edges of the deposition, poor quality bonding was observed. In their presentation, Chandrasekaran and Batchelor [6] observed on the coating specimen obtained from various consumable rods like tool steel, inconel, and aluminium and titanium rods onto mild steel substrates by FS and found a dense strong coating between tool steel and Inconel compared to the deposition of aluminium over mild steel at high pressure. For achieving a strong deposit of stainless steel over aluminium, Stegmuller et al. [7] designed an experimental setup and correlated the fundamental process parametric relation by using standard and inductive heating approach of FS. In their experimental work, Khalid Rafi et al. [8] studied the consequence of transverse speed on deposition of stainless steel over low carbon steel substrate by FS and found an increase in hardness value of the coating during the apply of lower transverse speed condition compared to higher range of transverse speed. During their feasibility study, Jujare et al. [9] studied the influence of process parameters during the copper coating over mild steel using the FS method by taking constant axial load of 2 kN. Vitanov and Voutchkov [10] referred to the significance of intelligent support systems used for optimizing the process parameters of FS and its effectiveness during the experimental work. Puli and Janaki Ram [11] has done the experimental work on the deposition of AISI 316L over the mild steel substrate by FS. A large amount of stacking faults energy with high dislocation density was found in the coatings at higher temperature which in turn resulted in substantial plastic deformation during FS process. Development of low temperature at substrate coating interface suppresses the δ -ferrite formation which improved the anticorrosion properties of the coating obtained from FS process. Vitanov et al. [12] identified the correlation between the input variables with the process response and developed predictive models for new friction surfacing applications. The Response Surface Methodology (RSM) was used to optimize the yield parameters of FS between Stellite 6 and AISI316 stainless steel which showed the velocity ratio between the feed rate of the mechtrode and the traverse rate of the substrate was the most governing factors compared to other process responses. Govardhan et al. [13] have studied the corrosion performance analysis on deposition of austenitic stainless steel over mild steel by FS and suggested the uses of FS coating on manufacture of pumps for chemical industry and pressure vessel for petrochemical industry.

The experimental study demonstrates the single-track friction surfacing process using Aluminium 6063 on IS2062 low carbon steel. Experimental design techniques and Response Surface Methodology (RSM) were used for optimizing the process response on coating specially coating width, thickness, interface temperature and bond strength. An attentive review of literature relevant to the FS backs up the claim

of the lack of this type of optimization study on the coating between these specific material combinations.

2 Materials and Experimental Methods

2.1 Materials

The experimental work was done on deposition of nonferrous materials (AA 6063 Aluminium alloy) over ferrous materials (IS 2062 low carbon steel) by friction surfacing process. IS 2062 low carbon steel was taken as the substrate plate with the dimensions of 150 mm × 100 mm × 6 mm and aluminium 6063 alloy is used as mechtrode material with 18 mm diameter and 100 mm length. The chemical composition of both substrate and mechtrode material was displayed in Tables 1 and 2, respectively. Some of the major mechanical properties of both materials are shown in Table 3.

2.2 Experimental Setup

The experimental work was carried out in a conventional friction surfacing machine with a single pass deposition with a length of about 100 mm. At the beginning of the friction surfacing process, both the mechtrode rod and substrate plate were cleaned

Table 1 Chemical composition of low carbon steel

Materials	C	Mn	P	S	Si	Cr	Ni	Mo	N	Fe
Composition	0.17	0.65	0.026	0.01	0.20	0.01	0.01	–	–	Balance

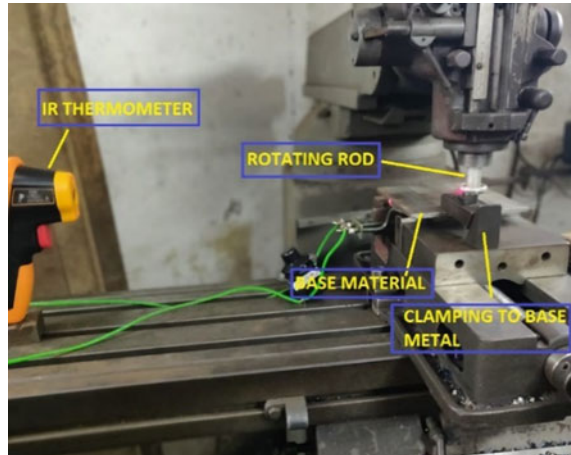
Table 2 Chemical composition of Aluminium AA6063 alloy

Material	Si	Fe	Cu	Mg	Mn	Cr	Zn	Al
Composition	0.044	0.16	0.0041	0.2832	0.0132	0.0024	0.0001	Balance

Table 3 Mechanical properties of low carbon steel and aluminium alloy

Material	Yield stress (Mpa)	Ultimate strength (Mpa)	Hardness (HV)
Low carbon steel (IS 2062)	250	410	266
Aluminium 6063	170	241	83

Fig. 2 Friction surfacing
Experimental setup



with acetone solution to abolish the impurities. With the help of milling machine, the substrate plate maintained a roughness at a range from 5.9 to 6.5 μ in order to intensify the friction during coating. The mechtrode was mounted on the spindle of the FS machine and the substrate material clamped rigidly on both sides. The experiments were conducted under ambient condition and maintaining a dwell period of 12–15 s. The deposition process initiated when the temperature of substrate-mechtrode contact area reached nearly 440 °C (called viscoplastic condition). A plastic overflow of hot mechtrode materials over the substrate plate was visualised as a result a thick layer (1–3 mm) was deposited over substrate plate. The experimental setup of the FS process is shown in Fig. 2.

2.3 IR Thermometer

During FS process, the temperature measurement at the substrate coating interface was done by using a NC-IR thermometer IRX-68 HTC, which was calibrated to measure the temperature at a range between –50 and 1850 °C. It was operated with optical resolution of 50:1 with adjustable emissivity from 0.1 to 1. The emissivity value for low carbon steel and aluminium was taken as 0.24 and 0.56, respectively. The IR thermometer was positioned at an appropriate distance of nearly 1 m from the surfacing zone.

2.4 Push-off Test

The push-off test was performed to understand the interfacial bonding strength between the substrate and coating materials. The test specimen should be made into a circular area from the substrate that creates an inner circle in the absence of coating material and the outer circular area to appear as an circular space consisting of both substrate and coating. A part of the inner circular area in the annular space must be exposed to axial loading and the test was conducted in a 100 KN INSTRON UTM testing machine by applying a continuous compressive load until the bond fails.

2.5 Design of Experiments

The design of experiments was based on using the 3^3 factorial method with three levels of each input parameter. The selection of lower and higher level of the input process parameters was based on the reported literature work and also considering the constraints of experimental setup. (see Table 4). Based on totally randomized experimental design, a sum of 9 experimental runs were produced by using the MINITAB 17 software and were displayed in Table 5.

Table 4 Level of process parameters

Symbol	Process parameter	Level			Unit
		1	2	3	
AF	Axial force	4	5	6	kN
RS	Rotational speed	1500	2000	2500	rpm
TS	Transverse speed	75	150	300	mm/min

Table 5 Design matrix for experiment

Experiment No.	Axial force (kN)	Rotational speed (rpm)	Transverse speed(mm/min)
E1	4	1500	75
E2	4	2000	150
E3	4	2500	300
E4	5	1500	150
E5	5	2000	300
E6	5	2500	75
E7	6	1500	300
E8	6	2000	75
E9	6	2500	150

3 Results and Discussion

3.1 Optimization of Parameters for the Response Variables

Coating of aluminium over low carbon steel for the mentioned combinations (see Table 5) was successfully done and the output parameters, i.e. coating width, coating thickness, temperature and bond strength were displayed in Table 6. Using a linear scale (% of error) the coating width and coating thickness were measured. Three values of mean and standard deviation are taken for each output parameters and mentioned in the observation (refer Table 6).

The acceptability of the developed model was tested through ANOVA analysis. In the present study, multiple regression analysis was carried out between four dependent variables (i.e. coating width, thickness, interface temperature, bond strength) with three independent variables (axial load, rotational speed and transverse speed). Pearson correlation analysis was used to correlate among both the dependent and the independent variables which suggested that the model is said to be significant within the confidence limit only if the calculated P-value is less than 0.01 at the desired level of confidence (95%). The developed mathematical model for all combinations of dependent and independent variables was found to be significant at 95% confidence level (shown in Tables 7, 8, 9 and 10).

Regression equation. The selected model was expressed in a second-degree response as follows:

$$\begin{aligned} \text{Coating Width} = & 0.86 + 4.975 F + 0.014640 RS - 0.1564 TS \\ & - 0.003247 F * RS + 0.01826 F * TS + 0.000028 RS * TS \end{aligned} \tag{1}$$

$$\begin{aligned} \text{Coating Thickness} = & -1.555 + 1.1635 F + 0.002732 RS - 0.01817 TS \\ & - 0.000683 F * RS + 0.001624 F * TS + 0.000004 RS * TS \end{aligned} \tag{2}$$

Table 6 Observed output parameters

Experiment No.	Mean coating width (mm)	Mean coating thickness (mm)	Mean interface temp (°C)	Mean bonding strength (Mpa)
E1	18.84 ± 0.26	2.28 ± 0.32	416 ± 14	58.6 ± 2.3
E2	19.72 ± 0.17	2.21 ± 0.20	428 ± 27	71.2 ± 1.5
E3	19.1 ± 0.32	1.96 ± 0.15	452 ± 16	66.7 ± 1.2
E4	18.28 ± 0.36	1.86 ± 0.21	446 ± 16	62.8 ± 1.7
E5	19.42 ± 0.85	2.10 ± 0.12	435 ± 09	77.6 ± 2.1
E6	20.24 ± 0.42	2.42 ± 0.18	408 ± 21	92.2 ± 1.4
E7	17.92 ± 1.24	1.96 ± 0.24	421 ± 11	64.4 ± 1.7
E8	18.62 ± 0.25	2.24 ± 0.32	439 ± 18	74.2 ± 1.1
E9	19.32 ± 0.15	1.72 ± 0.15	458 ± 10	84.6 ± 1.5

Table 7 ANOVA table for coating width

Source	DF	Adj. SS	Adj. MS	F-value	P-value
Regression	6	8.33482	1.38914	113.52	0.009
F (kN)	1	2.11493	2.11493	172.83	0.006
RS (rpm)	1	2.72740	2.72740	222.88	0.004
TS (mm/min)	1	1.88545	1.88545	154.08	0.006
F * RS	1	2.32201	2.32201	189.75	0.005
F * TS	1	2.09691	2.09691	171.36	0.006
RS * TS	1	1.26849	1.26849	103.66	0.010
Error	2	0.02447	0.01224		
Total	8	8.35929			

Model summary

S	R-sq.	R-sq. (adj.)	R-sq. (pred.)
0.110621	99.71%	98.83%	89.58%

Table 8 ANOVA table for coating thickness

Source	DF	Adj. SS	Adj. MS	F-value	P-value
Regression	6	0.185409	0.030901	149.45	0.007
F (kN)	1	0.115696	0.115696	559.55	0.002
RS (rpm)	1	0.094973	0.094973	459.33	0.002
TS (mm/min)	1	0.025450	0.025450	123.08	0.008
F * RS	1	0.102649	0.102649	496.45	0.002
F * TS	1	0.016581	0.016581	80.19	0.012
RS * TS	1	0.031064	0.031064	150.24	0.007
Error	2	0.000414	0.000207		
Total	8	0.185822			

Model summary

S	R-sq.	R-sq. (adj.)	R-sq. (pred.)
0.0143793	99.78%	99.11%	82.48%

$$\begin{aligned} \text{Interface Temperature} = & 148.27 + 25.564 F + 0.01478 RS - 0.2500 TS \\ & - 0.002130 F * RS + 0.01394 F * TS + 0.000082 RS * TS \end{aligned} \quad (3)$$

$$\begin{aligned} \text{Bond Strength} = & 47.88 - 2.280 F - 0.01787 RS + 0.3197 TS + 0.004855 F * RS \\ & - 0.04334 F * TS - 0.000049 RS * TS \end{aligned} \quad (4)$$

The coating width and thickness of the produced specimen decreases as rotational speed and transverse speed of the mechtrode increases. The interface temperature increases towards higher rotational speed with lower transverse speed. The bond strength is strongly influenced by rotational speed and axial force. (refer Figs. 3, 4,

Table 9 ANOVA table for interface temperature

Source	DF	Adj. SS	Adj. MS	F-value	P-value
Regression	6	3147.10	524.517	1270.30	0.000
F (kN)	1	55.86	55.856	1306.66	0.001
RS (rpm)	1	2.78	2.779	65.02	0.015
TS (mm/min)	1	4.82	4.817	112.69	0.009
F * RS	1	1.00	0.999	23.37	0.040
F * TS	1	1.22	1.223	28.60	0.033
RS* TS	1	10.57	10.565	247.15	0.004
Error	2	0.09	0.043		
Total	8	3147.19			

Model summary

S	R-sq.	R-sq. (adj.)	R-sq. (pred.)
0.206753	100.00%	99.99%	99.72%

Table 10 ANOVA table for Bond strength

Source	DF	Adj. SS	Adj. MS	F-value	P-value
Regression	6	47.3994	7.8999	374.73	0.003
F (kN)	1	0.4442	0.4442	21.07	0.044
RS (rpm)	1	4.0631	4.0631	192.73	0.005
TS (mm/min)	1	7.8757	7.8757	373.58	0.003
F * RS	1	5.1904	5.1904	246.20	0.004
F * TS	1	11.8133	11.8133	560.36	0.002
RS * TS	1	3.8367	3.8367	181.99	0.005
Error	2	0.0422	0.0211		
Total	8	47.4416			

Model summary

S	R-sq.	R-sq. (adj.)	R-sq. (pred.)
0.145196	99.91%	99.64%	90.60%

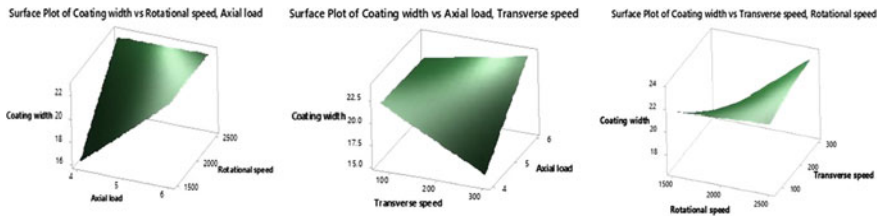


Fig. 3 Surface plots of coating width versus **a** axial load and rotational speed, **b** axial load and transverse speeds, **c** rotational speed and transverse speed

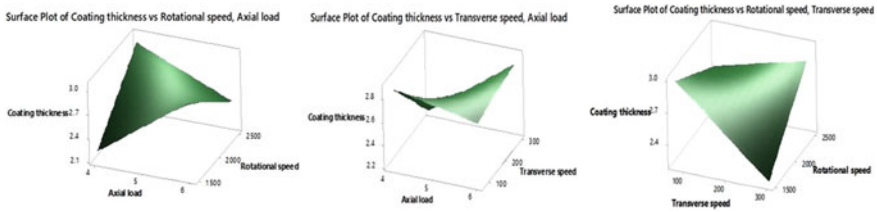


Fig. 4 Surface plots of coating thickness versus **a** axial load and rotational speed, **b** axial load and transverse speeds, **c** rotational speed and transverse speed

5 and 6). Coating width and thickness of the samples were strongly influenced by transverse speed which determines the rate of material deposition on the substrate. Higher transverse speed produced thinner deposits due to shorter heat exposure time periods between substrate and mechtrode, which causes lesser grain growth and finer bainitic microstructures formation at coating interface [14]. High combination of rotational speed and axial force with lower transverse speed produces flatter and more uniform deposits. The implementation of friction surfacing process is best suited for requiring thin deposits, strongly bonded with minimum dilution. It can be expected that by applying higher rotational speed will increase the friction force at the interface, which will enhance the heat generation and affect bonding efficiency positively [15].

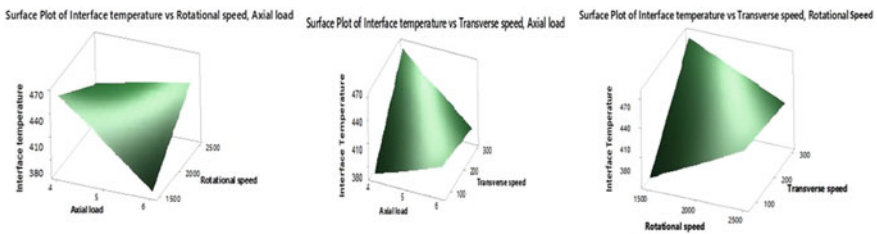


Fig. 5 Surface plots of interface temperature versus **a** axial load and rotational speed, **b** axial load and transverse speeds, **c** rotational speed and transverse speed

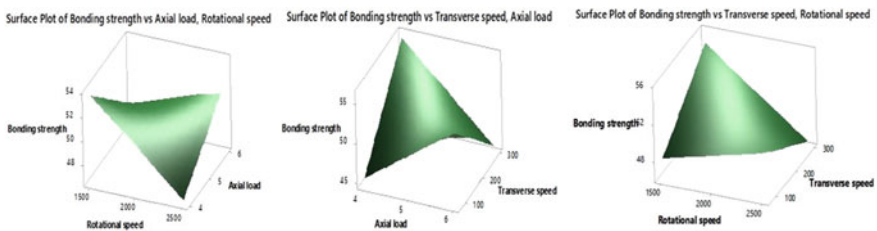


Fig. 6 Surface plots of bond strength versus **a** axial load and rotational speed, **b** axial load and transverse speeds, **c** rotational speed and transverse speed

To verify the predicted model the collateral experiments were conducted. The model was used to predict the value of coating width, thickness, interface temperature and bond strength within the experimental range, without performing the actual surfacing. It can be seen that the observed experimental results very much adhere to the predicted values from the model (see Figs. 7, 8, 9 and 10).

The aim of this experimental work is to produce the coating that should have maximum coating width, maximum coating thickness, minimum interface temperature and maximum bond strength of the coating. Equal weight of 1 was assigned to all response variables so that more focus to be given on finding the solution for the response variables within the specified limit during the optimization process. The

Fig. 7 Comparison between experimental and predicted results for coating width

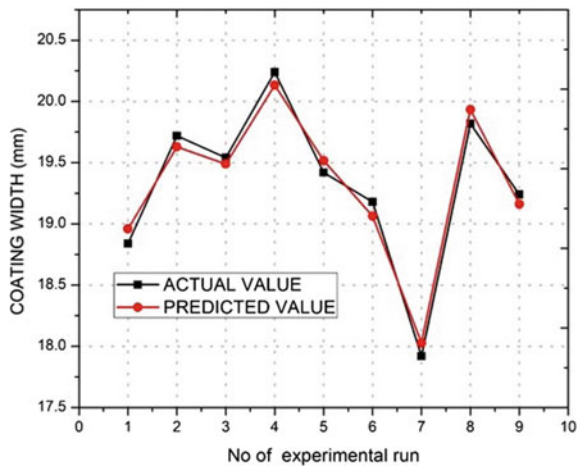


Fig. 8 Comparison between experimental and predicted results for coating thickness

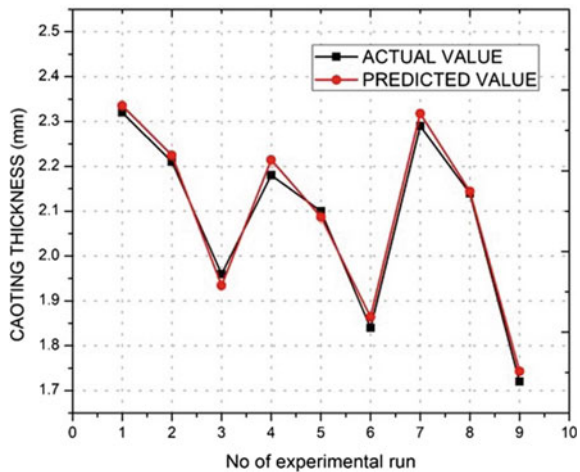


Fig. 9 Comparison between experimental and predicted results for interface temperature

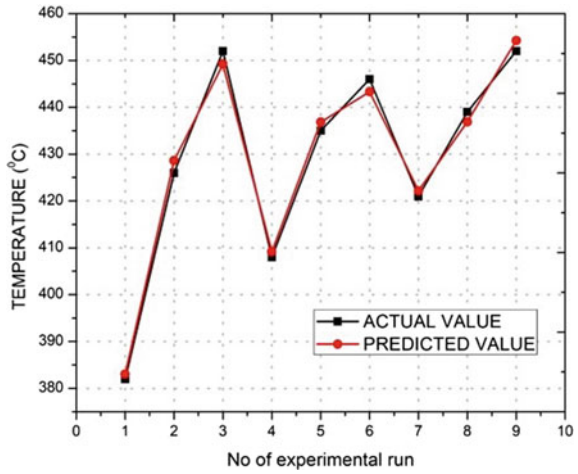
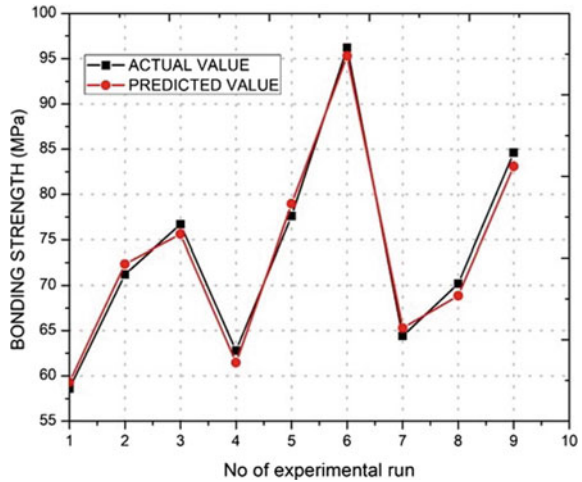


Fig. 10 Comparison between experimental and predicted results for bond strength



optimum values of the response variables with respect to each input parameters were displayed in Table 11.

Table 11 Optimization of the parameters for the response variables

Parameter	Goal	Minimum	Maximum	Target	Weight
Coating width (mm)	Max.	17.92	20.24	20.24	1
Coating thickness (mm)	Max.	1.72	2.42	2.42	1
Interface temp (°C)	Min.	408	458	408	1
Bond strength (MPa)	Max.	58.6	92.2	92.2	1

During the optimization process the value of weight was considered as 1, as all the response variables (coating width, thickness, interface temperature and bond strength) were directly influenced by all the input parameters like rotational speed, axial force and transverse speed applied on substrate. The results showed that at optimum condition of rotational speed 2500 rpm, axial force 5 kN and transverse speed 75 mm/min, the following experimental values were obtained. Optimized coating width = 20.24 mm, optimized thickness = 2.42 mm, optimized interface temperature = 408 °C and optimized bond strength = 92.2 MPa.

4 Mechanical Testing

4.1 Vickers Microhardness Test

The Micro Vickers hardness test uses a Vickers indenter applied into a surface through a pre-determined force and suitable for all kinds of surface treatment process. Normally, the force on the indenter held for nearly 10 s for the optical measurement of the diagonal lengths of indenter to determine the size of the impression. Microhardness test was conducted as per ASTM E384—2017 Standards with load of 1 kgf and the experimental setup is shown in Fig. 11a. For all the obtained samples, the hardness readings were taken at the coating interface in the longitudinal direction at 5 different points with 10 mm apart namely (a), (b), (c), (d) and (e) which is

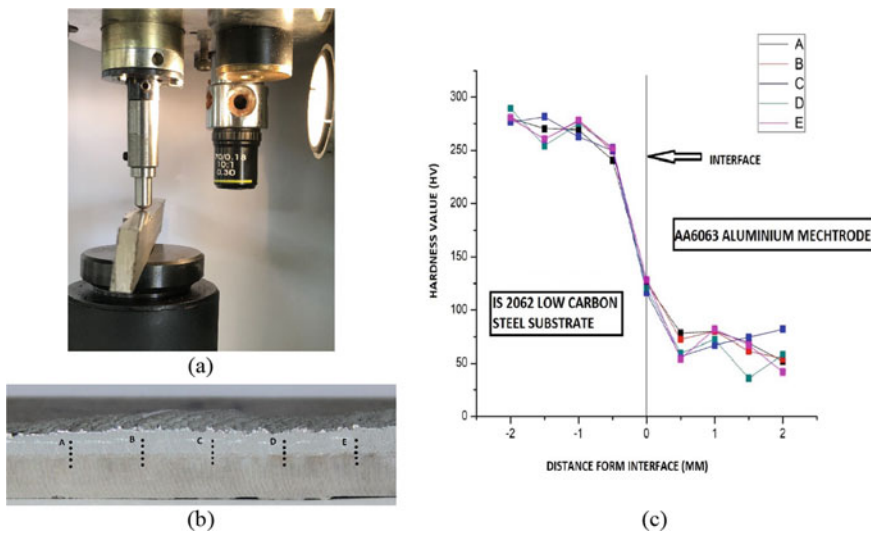


Fig. 11 Microhardness **a** experimental setup, **b** longitudinal direction of coating, **c** hardness profile. Process parameter axial force 5 kN, rotational speed 2500 rpm and transverse speed = 75 mm/min

shown in Fig. 11b. The result indicates a higher value of hardness at the substrate coating interface (range of 124–142 HV) compared to the hardness value of rotating aluminium rod as shown in Fig. 11c. Higher hardness at the coating interface is due to the development of microstructures during plastic deformation phase of the coating followed by rapid cooling of both substrate and mechtrode materials after the process. The axial force and rotational speed of the mechtrode have a significant role on increasing the hardness of the coating and barely affected by the transverse speed of the rod.

5 Conclusion

From the presented experimental work, the following conclusion can be drawn.

1. Based on the 3³ factorial design method, it was noticed that the mechtrode rotational speed and transverse speed played a significant role in the formation of coating width and thickness. Increase in value of rotational speed and transverse speed decreases the width and thickness of the coating.
2. Axial force and mechtrode rotational speed contribution are more for development of interfacial temperature and bond strength. Higher axial force and rotational speed result higher interface temperature.
3. The optimum values of process parameters are optimum width = 20.24 mm, thickness = 2.42 mm, interface temperature = 408 °C and bond strength = 92.2 Mpa at a input parameter of axial force 5 kN, rotational speed 2500 rpm and transverse speed 75 mm/min.
4. An appreciable increase in hardness value was observed at the substrate coating interface for all the obtained samples. The hardness value at a range of 124–142 HV was seen coating interface which is higher than the hardness value consumable aluminium rod (75 HV).

References

1. H. Klopstock, A.R. Neelands, U.K. Patent 572789 (1994)
2. H.K. Rafi, G.D.J. Ram, G. Phanikumar, K.P. Rao, Microstructural evolution during friction surfacing of tool steel H13. *Mater. Des.* **32**, 82–87 (2011). <https://doi.org/10.1016/j.matdes.2010.06.031>
3. B.V. Kumar, G.M. Reddy, T. Mohandas, Influence of process parameters on physical dimensions of AA 6063 aluminium alloy coating on mild steel in friction surfacing. *Defence Technol.* **11**, 275–281 (2015). <https://doi.org/10.1016/j.dt.2015.04.001>
4. K. Prasad Rao, P.A.V. Sreenu, H.K. Rafi, M.N. Libin, K. Balasubramanian, Tool steel and copper coating by friction surfacing—A thermography study. *J. Mater. Process. Technol.* **212**, 402–407 (2012). <https://doi.org/10.1016/j.jmatprotec.2011.09.023>

5. R. Puli, G.D. Janaki Ram, Microstructures and properties of friction surfaced Coatings in AISI 440C martensitic stainless steel. *Surf. Coat. Technol.* **207**, 310–318 (2012). <https://doi.org/10.1016/j.surfcoat.2012.07.001>
6. M. Chandrasekaran, A.W. Batchelor, Friction surfacing of metal coatings on steel and aluminium substrate. *J. Mater. Process. Technol.* **72**, 446–452 (1997). [https://doi.org/10.1016/S0924-0136\(97\)00209-4](https://doi.org/10.1016/S0924-0136(97)00209-4)
7. M.J.R. Stegmuller, P. Schindele, R.J. Grant, Inductive heating effects on friction surfacing of stainless steel onto an aluminium substrate. *J. Mater. Process. Technol.* **216**, 430–439 (2015). <https://doi.org/10.1016/j.jmatprotec.2014.10.013>
8. H. Khalid Rafi, G.D. Janaki Ram, G. Phanikumar, K. Prasad Rao, Friction surfacing of austenitic stainless steel on low carbon steel: studies on the effect of traverse speed, in *Proceedings of the World Congress on Engineering 2010* vol. II (WCE, London, June 30–July 2 2010)
9. T. Jujare, A. Kumar, S.V. Kailas, K.U. Bhat, Friction surfacing of mild steel by copper: a feasibility study. *Procedia Mater. Sci.* **5**, 1300–1307 (2014). <https://doi.org/10.1016/j.mspro.2014.07.445>
10. V.I. Vitanov, I. Voutchkov, Process parameters selection for friction surfacing applications using intelligent decision support. *J. Mater. Process. Technol.* **159**, 27–32 (2005). <https://doi.org/10.1016/j.jmatprotec.2003.11.006>
11. R. Puli, G.D. Janaki Ram, Corrosion performance of AISI 316L friction surfaced coatings. *Corros. Sci.* **62**, 95–103 (2012). <https://doi.org/10.1016/j.corsci.2012.04.050>
12. V.I. Vitanov, N. Javaid, D.J. Stephenson, Application of response surface methodology for the optimisation of micro-friction surfacing process. *Surf. Coat. Technol.* **204**, 3501–3508 (2010). <https://doi.org/10.1016/j.surfcoat.2010.04.011>
13. D. Govardhan, A.C.S. Kumar, K.G.K. Murti, G.M. Reddy, Characterization of austenitic stainless steel friction surfaced deposit over low carbon steel. *Mater. Des.* **36**, 206–214 (2012). <https://doi.org/10.1016/j.matdes.2011.07.040>
14. J. Gandra, R. Miranda, P. Vilaça, Performance analysis of friction surfacing. *J. Mater. Process. Technol.* **212**, 1676–1686 (2012). <https://doi.org/10.1016/j.jmatprotec.2012.03.013>
15. R. Puli, G.J. Ram, Dynamic recrystallization in friction surfaced austenitic Stainless steel coatings. *Mater. Charact.* **74**, 49–54 (2012). <https://doi.org/10.1016/j.matchar.2012.09.001>

Determination of Bending Force and Bend Angle of Sheet Metal Welds



R. Uday Kumar

Abstract Bending is one of the important sheet metal forming process. At present, the trend for light weight vehicles along with attractive and complicated geometric shapes is growing in a rapid way. The reduction in weight of the vehicle is to get a reduction in fuel consumption and its emissions. So that various sheet metal blanks are used in almost all aircraft, the automotive, ship, and navy applications to create complex geometric shaped components and to meet the present trends as well. So that sheet metal blank should be formed into the desired shaped component. This can be achieved by various sheet metal forming operations. In this study, various sheet metallic blanks with and without welded are considered and are tested on bending experimental setup. The bending test is conducted for sheet metals and in this process the bending angle and corresponding bending forces are found for various sheet metal with and without welds.

Keywords Sheet metal blank · Bending test · Bending force and bend angle

1 Introduction

Sheet metal is simply a metal which is formed into thin and flat pieces. It is one of the fundamental forms used in metal-working processes, and it can be cut and bent into a wide variety of shapes. Everyday countless objects are fabricated from sheet metal [1–3]. Compared to those materials made of casting or forging, sheet metal parts offer the advantages of lightweight and versatile shape which is the main advantage in Automobile and Aircraft domains. Sheet metals include a very wide range of consumer and industrial products such as applications in the manufacture of cars bodies, trains, aeroplane wings, farm equipment, office equipment, furniture, house appliances, computers, machine components and beverage cans, and many other things [4, 5].

R. Uday Kumar (✉)

Department of Mechanical Engineering, Mahatma Gandhi Institute of Technology, Gandipet, Hyderabad, India

e-mail: udaykumar403@gmail.com

© Springer Nature Singapore Pte Ltd. 2021

G. S. V. L. Narasimham et al. (eds.), *Recent Trends in Mechanical Engineering*,

Lecture Notes in Mechanical Engineering,

https://doi.org/10.1007/978-981-15-7557-0_16

Bending of sheets and plates is widely used in forming parts such as corrugations and flanges. Bending is a forming operation in which a sheet metal is subjected to bending stress thereby a flat straight sheet is made into a curved sheet [6, 7]. The sheet gets plastically deformed without change in thickness. Die and punch are used for bending. If a v-shaped die and punch are used, then the bending is called v-bending [8].

During bending of a sheet metallic strip, the material toward the outward of the neutral axis is subjected to tensile stress and the material toward the inside is subjected to compressive stress. Bend radius (R) is the radius of curvature of the bent sheet inside the bending which is considered from the center of arc [9]. The neutral axis remains at the center of the thickness of the sheet for elastic bending, whereas for plastic bending the neutral axis shifts toward the inside of the bend. The rate of elongation of outer fibers is generally greater than the rate of contraction of inner fibers [10, 11]. Therefore, there is a thickness reduction at the bend section. Though we have many bending techniques in this research we considered three-point bending test.

2 Experimental Methodology

In this research paper, the four steel sheet metal specimens are considered. The four sheet metals are cold rolled and hot rolled steel sheet metals. In that two specimens are individually plane specimens and other two specimens are prepared through TIG and Gas welded butt joints. The test specimens are shown as Hot Rolled Steel Sheet in Fig. 1, Cold Rolled Steel Sheet in Fig. 2, TIG Welded Sheet (Hot and Cold Rolled together) in Fig. 3, and Gas Welded Sheet (Hot and Cold Rolled together) in Fig. 4. The bending test is performed on UTM to evaluate bending characteristics.

The dimensions of each metallic sheet specimens are as follows:

Length of the sheet metal	–	210 mm
Width of the sheet metal	–	65 mm
Thickness of the sheet metal	–	2 mm

Fig. 1 Hot rolled steel sheet

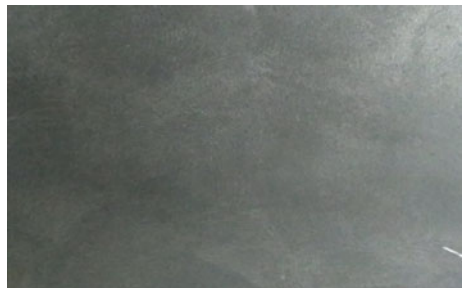


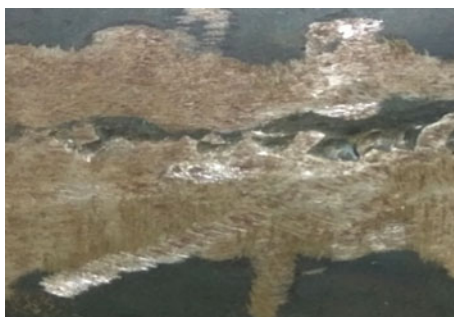
Fig. 2 Cold rolled steel sheet



Fig. 3 TIG welded sheet (hot and cold rolled)



Fig. 4 Gas welded sheet (hot and cold rolled)



For conducting the bending test, bending fixture is supported on the platform of hydraulic cylinder of the Universal Testing Machine as shown in Fig. 5. The loading is held in the middle crosshead. When the load is applied on the sheet metal the angle of bend is measured and the corresponding bending load is noted down. This experiment is performed on Universal Testing Machine (UTM) of model: UTM 40 Ton.

Fig. 5 UTM with special attachment of bending fixture of model: UTM 40 ton



3 Results and Discussion

The bending test experiment is performed on various sheet metal blanks individually and the blanks are made by TIG (both hot rolled and cold rolled) and Gas welding (both hot rolled and cold rolled). The deformed shapes of the four specimens of Hot Rolled Sheet is shown in Fig. 6, Cold Rolled Sheet is shown in Fig. 7, TIG welded both hot and cold rolled sheet is shown in Fig. 8, and Gas welded both cold and hot rolled sheet is shown in Fig. 9.

Table 1 shows that the bending angles (after deformation) are obtained during the complete bending test of each test specimen steel sheet.

Table 2 shows that the bending force or loads (after deformation) are obtained during the complete bending test of each sheet.

Fig. 6 Deformed hot rolled steel sheet



Fig. 7 Deformed cold rolled steel sheet



Fig. 8 Deformed TIG welded sheet (hot and cold rolled)



Fig. 9 Deformed gas welded sheet (hot and cold rolled)

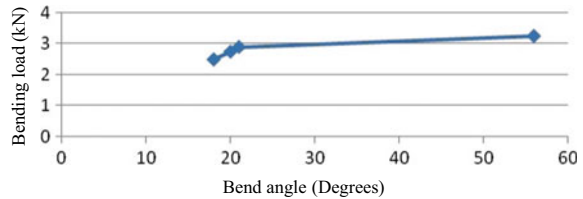


Table 1 Bending angle of test specimens

S. No.	Type of sheet metal	Bend angle (°)
1	Hot rolled steel sheet	18
2	Cold rolled steel sheet	20
3	TIG welded sheet (hot and cold rolled together)	21
4	Gas welded sheet (hot and cold rolled together)	56

Table 2 Bending force or load of test specimen

S. No.	Type of sheet metal	Bending force or load (kN)
1	Hot rolled steel sheet	2.50
2	Cold rolled steel sheet	2.75
3	TIG welded sheet (Hot and cold rolled together)	2.90
4	Gas welded sheet (Hot and cold rolled together)	3.25

Fig. 10 Bending angle varies with bending load

For the same thickness of 2 mm Hot Rolled and Cold Rolled steel sheets, the bend angle and bending load were found out to be high for the Cold Rolled steel sheet than that of a Hot Rolled steel sheet.

Figure 10 Shows the graph between bending angle versus corresponding bending loads.

From Fig. 10, it can be said that for the same thickness of 2 mm TIG welded sheet (Hot Rolled and Cold Rolled) and Gas welded sheet (Hot Rolled and Cold Rolled) the bending angle and bending load were found out to be good for the TIG welded sheet (Hot Rolled and Cold Rolled) than that of a Gas welded sheet (Hot Rolled and Cold Rolled).

From the results, it is confirmed that bend angle and bending load increases gradually from Hot Rolled steel sheet to Cold Rolled steel sheet and followed by TIG welded sheet (Hot Rolled and Cold Rolled) to a large extend of Gas welded sheet (Hot Rolled and Cold Rolled) which indicates that behind that angle of bend there will be no more load that will be acting as in case of HR steel, CR steel, and in TIG welded sheets or fracture will may occur as in case of Gas welded sheet.

4 Conclusions

Following conclusions are drawn from the present research work:

- Bending load is higher in cold rolled steel sheet
- Bending angle is obtained highest in cold rolled steel sheet
- Gas welded sheet (Hot and Cold Rolled together) is represented with highest bend angle and bending load among the rolled steel sheets with and without welded sheets.

- Better bendability in Hot Rolled steel sheet when compared to Cold Rolled steel sheet.
- Better bendability in TIG welded sheet when compared to Gas welded sheet.
- Finally, better bendability in Hot Rolled steel sheet when compared to other three samples and, therefore, more amount of bending can be achieved and in case of Gas welded Sheet it holds good amount of load up to just before the fracture point than any other three samples.
- Bending maintains a major role in forming of sheet metal operations. The bending characteristics depend on grain directions.

While choosing a material for a job, it is important to know the difference between the different types of raw material available with required factors, how it is used and the advantages included by it in the industry or construction of the project.

References

1. S.P. Keeler, *Understanding Sheet Metal Formability*, vol. 2
2. K. Narsimhan, V.M. Nandedkar, Formability testing of sheet metals. *Trans. Ind. Inst. Metals* **49**(5), 34–40 1996
3. M.E.M. Abid et al., Bending of sheet metal (st37) using 90° to estimate blank dimensions. *Int. J. Emerg. Technol.* **2**(1), 54–60 (2015)
4. K.M. Zhao, B.K. Chun, J.K. Lee, Finite element analysis of tailor-welded blanks. *Int. J. Mech. Eng.* **37**(9), 117–120 (2001)
5. M.R. Stoudt, L.E. Levine, Li Ma, Designing a uniaxial tension/compression test for springback analysis in high-strength steel sheets. *Exp. Mech.* **57**(1), 155–163 (2017)
6. G. Tasew, A. Jaswal, Development of single hydraulic cylinder operated sheet metal bending machine. *Development* **5**(01) (2018)
7. M. Raupach, et al., Mesh refinement study and experimental validation for stretch bending of sheet metals. *J. Phys.: Conf. Ser.* **896**(1) (2017) (IOP Publishing)
8. J. Timosh. Rupture instability in bending and deep drawing process. *Int. J. Mech. Sci.* **9**(6), 27–35 (1997)
9. A.A. Zadpoor et al., Mechanics of tailor welded blanks. *Key Eng. Mater.* **344**, 373–382 (2007)
10. N.P. Padghan, et al., Force analysis of metal sheet in bending operation on sheet bending machine. *Int. J. Eng. Res.* **4**(5), 11–16 (2015)
11. A. Kulkarni, Sheet metal bending machine. *Int. J. Eng. Res. Technol.* **2**(3), 45–52 (2013)

A Novel Approach for Reducing Delamination During Drilling of CFRP by Response Surface Methodology (RSM) Integrated with the Taguchi Method



Tarakeswar Barik , Sourav Kumar Jena, Avisek Tripathy, Kamal Pal, and Suchismita Parida

Abstract Carbon fiber reinforced polymers (CFRPs) laminates are one of the lightweight materials that have been around for a while in the manufacturing sector for its superior properties. However, the aviation industries are considered as the prime shopper of these fibrous composites in building structural parts of airplanes. Despite having some delectable properties like high strength, high fatigue resistant, high stiffness, high resistant to a corrosive environment, etc. it has been kept in the difficult-to-cut category. The machining of the CFRPs is quite tricky due to the anisotropic, heterogeneous, and abrasive nature. Drilling is considered as the final machining operation in the assembly line in most of the cases as holes are the absolute need in assembling purpose. However, the wedge-shaped drill, while cutting high strength fibers, produces various types of damages like delamination, surface roughness, fiber pullout, matrix breakage, etc. Among these, delamination is considered as the most vital and can influence the joint quality for which it needs a more significant concern. In this particular experiment, the drilling experiments have been designed by using Taguchi's L_{18} orthogonal array. The drilled persuaded damage like delamination factor and two sensory output parameters such as thrust force and

T. Barik (✉) · S. K. Jena · K. Pal
Department of Production Engineering, Veer Surendra Sai University of Technology, Burla,
Sambalpur, Odisha 768018, India
e-mail: tarakes18@gmail.com

S. K. Jena
e-mail: ae65402@gmail.com

K. Pal
e-mail: kpals5676@gmail.com

A. Tripathy
Department of Mechanical Engineering, Guru Nanak Institutions Technical Campus, Hyderabad,
India
e-mail: avisek89@gmail.com

S. Parida
Department of Mechanical Engineering, Mayurbhanj School of Engineering, Baripada 757107,
India
e-mail: suchi77parida@gmail.com

torque has been acquired using data acquisition system and further analyzed and effort has been made to relate with the hole quality. Finally, a multi-objective optimization of the responses was made by utilizing the response surface methodology (RSM) approach. The delamination damages found to be less with a parameteric setting in case of lower feed rate (0.025 mm/rev), small point angle tool (108°), and at a higher spindle speed (3125 rpm).

Keywords CFRP · Thrust force · Torque · Delamination · Radar diagram · RSM

1 Introduction

Composite materials like carbon fiber reinforced polymers (CFRPs) possess superior mechanical and physical properties such as high strength-to-weight ratio, high stiffness, corrosion resistance, fatigue resistance make it as the first choice for structure making industries [1, 2]. However, regardless of its properties, it has been kept in the hard-to-machine category contrary to metal machining. In structure making industries like aerospace, automobile, and sports goods manufacturing units, these composite materials are used in an extensive manner. However, in structure making industries the parts are produced separately and necessitate a secondary machining process for the final assembly. In addition to this, metallic plates are also used with the composite laminate in stack form for providing additional strength to the final product in making various parts of airplane structure to provide extra rigidity [3, 4]. However, in joining several parts in an assembling line by employing riveted or bolted joints that necessitates a hole-making process [1, 5]. The traditional drilling process is considered as the most economical and primary process in making holes [6]. Due to the inhomogeneous and abrasive nature of CFRP, the drilling of these laminates is quite different as compared to the traditional metal machining [7]. Therefore, during drilling these materials drill induced defects like delamination, matrix cracking, fiber pullout that usually occurs [6]. Delamination is the foremost among the flaws occurred during drilling as it directly influences the quality and life of the joints, simultaneously the acceptability of the total product [4, 8, 9]. However, by selecting optimal input parameters and modifying the drill geometry the delamination defects can be minimized rather than completely irradiated [1, 10–13]. Delamination factor defined as the inter-laminar failure due to the separation of the layers while drilling on the upper surface of the composite laminate [14]. The selection of machining input variables, such as feed rate and speed, influence its occurrence that needs attention. However, among the input variables the feed rate is mostly responsible for the occurrence of delamination damages as it directly encompasses in rising the thrust force [10, 12, 15]. The another machining variable, spindle speed also has an effect on the amount of thrust force generated during drilling where higher thrust force causes less amount of delamination defects [6]. Similarly, the geometry of the drill tool also has its consideration in reducing drill hole-related damages like delamination factor. In this regard, a lower point angle tool is preferred as compared to

higher one as it produces lesser thrust force [1]. Therefore, the delamination defect-free hole can be accomplished with a parametric variables setting of lower feed rate and a higher speed along with a low point angle tool while drilling fibrous composite laminates like CFRP. However, for an optimal parametric setting the output response characteristics should be optimized by using a suitable optimization technique.

In recent years, for saving the machining time and to protect against losses, so as to improve the product quality various optimization techniques has been used [8, 16–32]. The response surface methodology (RSM) has been used to analyze the response parameters by which the total improvement of a system has been achieved for getting maximum benefits with minimum effort [17]. This methodology can be applied with a set of input parameters that effects the outputs and can optimize the variables one after another for the best possible outcomes [18].

In this study, Taguchi's L_{18} orthogonal array (total number of 18 experiments) has been used for preparing the experimental design using Min-Tab software. The drilling experiments were performed on a CNC milling center which has been attached with a data acquisition system. The data acquisition system comprises a dynamometer (KISTLER 9257b), an amplifier (KISTLER 5070) along with a personal computer for the storage of the acquired data. The thrust and torque data has been acquired with the help of this data acquisition system at a sampling rate of 1000 Hz. However, the drilling experiments were done on the woven CFRP laminate of 10 mm thickness. The delamination factor has been calculated using optical photographs of the holes, which was taken with help of microscope, was further analyzed using an Image-J software. Finally, the output responses were optimized using the response surface methodology (RSM) optimization technique and the deviation to the experimental output with predicted one has been presented through a radar diagram.

2 Experimental Procedures

2.1 Workpiece and Tool Configuration

The CFRP has various noble properties that suit in designing structural components as enlightened by numerous researchers. Nevertheless, as it has been placed in the category of hard-to-machine material. Therefore, this particular work considered drilling of CFRP laminates as a challenging task regarding and to accomplish some conclusive presumptions regarding drilling of this material. The material used is in the form of a laminate plate of 10 mm thickness which has been made up of by hand lay-up technique. The carbon prepregs having a high tensile strength of 6000 Mpa used in this laminate is of 0.5 mm thickness and alternative stack with epoxy. The reinforcement carbon prepregs have been placed with an orientation of $[0^\circ/-45^\circ/90^\circ/45^\circ]$ [4, 8, 26]. The matrix used in laminate making process is epoxy (type—Araldite LY-556) with hardener (Aliphatic amine HY-95) and the curing of the material was done at ambient temperature. The composite laminate has been cut

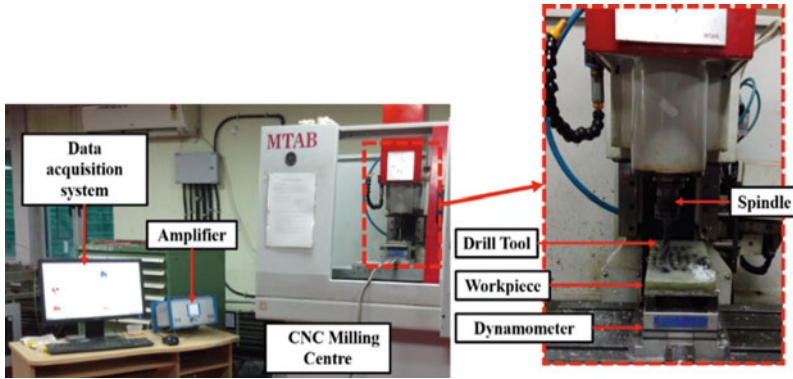


Fig. 1 Experimental setup with the workpiece placed on the dynamometer setting

in the size of 200 mm \times 100 mm \times 10 mm so that it can be clamped on the fixture designed and placed on the dynamometer, as shown in Fig. 1.

In this experiment, tungsten carbide twist drill bit has been used in drilling with two different point angles (θ) (108° and 118°), keeping other geometrical features constant. However, for reducing man-machine error the drilling experiments were carried out thrice for each parameter setting and the average value was taken for further analysis.

2.2 Machine

The drilling experiments were carried out on a 3-axis milling center (M-Tab) having a maximum speed of 5000 rpm with a vertical feed of 3000 mm/min. however, the machining center has been attached with Dynamometer (Type—KISTLER 9257b) along with an amplifier (Type—KISTLER 5070) with pre-installed Dynoware software. The real time thrust force and torque data has been stored in a data acquisition system for further analysis. However, for acquiring noise-free data, a sampling rate of 1000 Hz has been chosen.

2.3 Drilling Condition and Input Parameter Setting

The input variables and the levels were selected after performing adequate numbers of trail experiments. The drilling condition has been kept as dry drilling, as the CFRP chips were in the form of powder, and by mixing with the coolant, it may deteriorate the drilled hole surface. However, the drilling of CFRPs with higher feed rates may lead to excessive fiber pullout. Therefore, a moderated range of feed has been selected.

Table 1 Drilling parameters and levels

Level	θ (°)	N (rpm)	f (mm/rev.)
1	108	1125	0.025
2	118	2125	0.05
3	–	3125	0.075

Similarly, high speed suits the drilling quality but extreme spindle speed may lead to fiber-matrix cracking; therefore, a suitable range has been chosen. Likewise, separate drill bits with different point angles have been selected. The experimental design has been prepared with a 2-level of point angle (θ), 3-level of spindle speed (N), and 3-level of feed rate (f) as shown in Table 1. Similarly, for performing the experiment in a well-organized manner the design of the experiment was prepared with a Taguchi’s L_{18} orthogonal array prepared using Min-Tab software.

In this study, one-dimensional delamination factor (F_d) only in the entry side has been calculated by the following formula [6]:

$$F_d = D_{\max}/D_{\min} \tag{1}$$

where

D_{\max} the maximum delaminated area diameter

D_{\min} the nominal area diameter.

However, in order to reduce the man–machine error for each input variable setting drilling experiments has been performed three times, and the average of the results was taken for further analysis. The delamination factor for each drilled holes has been calculated using the Image-J software of the photographed images using an optical microscope.

2.4 Response Surface Methodology (RSM)

Optimization is a process by which the total improvement of a system has been made for getting maximum benefits with minimum effort [30]. However, the intention behind the optimization process is to find out the condition of a procedure when applied to a system that gives the best likely response. In the early eternities, traditional one variable method was used for optimization, where one variable used to be optimized once. Where the interaction between the variables is found to be missing, on the other hand, it required more time and considered an expensive process [30]. These problems were overcome by adopting a newer multivariate technique called response surface methodology (RSM). RSM methodology is a multi-response variable interactive technique, which utilizes inbuilt mathematics and statistical methods to deal with the experimental responses within a frame of a polynomial equation [17, 18, 30]. This methodology can be applied with a set of input parameters that affects

the outputs and can optimize the variables one after another for the best possible outcomes.

However, before optimizing the process variables, the design of an experiment with all process variables is prepared by adopting a suitable matrix design [30]. Various responses matrix-like full factorial design, central composite design, Box–Behnken design, etc. are executed for quadratic responses. In this particular experiment, a full factorial experimental design matrix has been used for arranging the tests to be performed.

3 Result and Discussions

In this section, the parametric influence of process variable on the output response characteristics such as drilled induced thrust force, torque with process output delamination has been studied in details. The experimental results in the form of sensory data and actual output responses delamination factor have been tabulated in Table 2. However, the real-time signal of thrust and torque acquired during drilling was studied in details and tried to co-relate it with the drilled quality as well as drilled induced defects like delamination factor.

Table 2 Drilling parameters sequence and respective process outputs

Expt. No.	θ	N	f	F_d	F_z	M_z
1	108	1125	0.025	1.568	32.710	0.590
2	108	1125	0.05	1.731	38.775	0.850
3	108	1125	0.075	1.986	51.356	1.107
4	108	2125	0.025	1.302	28.984	0.510
5	108	2125	0.05	1.336	39.417	0.866
6	108	2125	0.075	1.528	47.813	1.087
7	108	3125	0.025	1.223	28.665	0.669
8	108	3125	0.05	1.426	38.553	0.670
9	108	3125	0.075	1.686	50.545	1.087
10	118	1125	0.025	1.458	29.003	0.582
11	118	1125	0.05	1.752	42.015	0.511
12	118	1125	0.075	1.992	56.562	0.707
13	118	2125	0.025	1.456	32.212	0.796
14	118	2125	0.05	1.758	45.921	0.806
15	118	2125	0.075	1.881	58.580	0.861
16	118	3125	0.025	1.339	29.365	0.698
17	118	3125	0.05	1.659	41.750	0.754
18	118	3125	0.075	1.778	55.289	0.901

3.1 Analysis of Drilled Thrust Force and Torque Acquired During Drilling

A typical thrust force and corresponding drilled persuaded torque signal have been shown in Fig. 2 (Expt. #4). The thrust force in its initial phase starts very smoothly but, as soon as the drill touches (around 4.5 s) the upper surface of the laminates, it rises very stiffly that can be seen from the figure. The corresponding torque also shows the same phenomenon; it also increased very sharply as the drill touches the laminate. The thrust force goes on increasing as long as the drill wedge tip ultimately gets into the laminate, and drilling operation becomes smoother (around 14 s.). Similarly, the torque also goes on rising until it reaches the peak and drops simultaneously as soon as the drilling becomes steady. Hereafter, the drilling becomes steady and it can be noticed from figure until the tip or the chisel edge comes out of the laminate and makes the drilling a bit unsteady. At every moment, a stiff decline in thrust force can be seen. However, there is an increase as the flutes of the drill tries to come out of the laminate.

In this study, regression equation of the second-order polynomial of thrust force and torque has been developed using the response surface methodology (RSM) optimization technique as given by Eqs. 2 and 3. Besides developing modeled equations, the analysis of variance (ANOVA) technique has also been used to check the adequacy of the models at a 95% confidence level. The *R*-sq. value, *p*-value, and *F*-value (model competence factors) for all the sensory parameters are shown in Table 3, where the *R*-sq. values found to be more than 85% for all the responses. Similarly, the *p*-value of all the outputs was found to be less than the standard value of 0.005, which makes all the models acceptable with a higher degree of fitness.

Fig. 2 A typical thrust force and torque signal variation with time

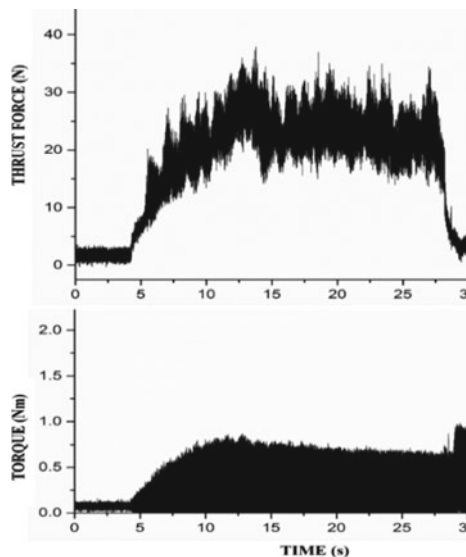


Table 3 Model competency factors of respective process outputs

Output responses	R-sq.	R-sq. (adjacent)	F-value	p-value
F_z	98.16%	96.52%	60.02	0.000
M_z	89.38%	79.93%	9.46	0.001

$$F_z = 68.7 - 0.437\theta - 0.0045N - 1206f - 0.000001N * N + 1096f * f + 0.000065\theta * N + 13.66\phi * f + 0.0080N * f \quad (2)$$

$$M_z = -0.28 + 0.0057\theta - 0.000986N + 81.8f - 0.000000N * N + 90.8f * f + 0.000011\theta * N - 0.746\theta * f - 0.00010N * f \quad (3)$$

The response surface plot for the drilled induced thrust force and corresponding torque has been shown in Figs. 3 and 4, distinctly. It can be seen from the optimized surface plot of thrust force (Fig. 3), the feed rate has the substantial impact, followed by the drill spindle speed and the drill tool point angle. The thrust force tends to increase as the feed rate increases and vice versa. Similarly, the point angle also affects the thrust force, as with a higher point angle tool produces greater thrust, as



Fig. 3 Response surface plot for thrust force (F_z)

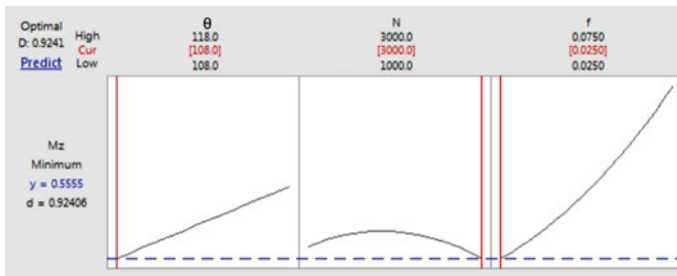


Fig. 4 Response surface plot for torque (M_z)

Table 4 Model competency factors of delamination factor

Output responses	R-sq.	R-sq. (adjacent)	F-value	p-value
F_d	89.34%	79.86%	9.42	0.001

can be seen from the figure. Nevertheless, the thrust force is seen to be abridged with an increase in drill spindle speed (N).

The variation of torque w.r.t feed, speed, and point angle have been shown in Fig. 4. It can be seen that the feed rate has a maximum impact on the variation of torque, followed by point angle and spindle speed. The optimal parametric setting for minimum thrust force is $\theta = 108^\circ$, $N = 3000$ rpm, $f = 0.025$ mm/rev, and the optimal output for the thrust force is 28.6231 N, which is 0.14% less than that of experimental 28.665 N. Similarly, in the case of torque, the optimal parametric setting for the least torque is 0.5555 Nm, which is 20.33% lower than that of the experimental 0.69 Nm.

3.2 Influences of the Parametric Variables on the Delamination (F_d)

In this particular study, the response surface methodology (RSM) optimization technique was used in developing the regression equation of the second order for the delamination factor (Eq. 4.). The model competence factors like R-sq. value, p-value, and F-value can be seen from Table 4, where the R-sq. values found to be more than 85% for all the responses. Similarly, the p-value of all the outputs was found to be less than the standard value of 0.005, which makes all the models acceptable with a higher degree of fitness.

$$\begin{aligned}
 F_d = & 3.11 - 0.0129\theta - 0.001448N - 11.4f \\
 & + 0.000000N * N - 16.9f * f \\
 & + 0.000009\theta * N + 0.194\theta * f - 0.00025N * f \qquad (4)
 \end{aligned}$$

The variation of delamination factor w.r.t feed, speed, and point angle has been shown in Fig. 5. It can be seen that feed rate has the maximum impact on the delamination defect followed by drill spindle speed and drill tool point angle. The optimal parametric setting for minimum delamination factor has been found at a parametric setting of $\theta = 108^\circ$, $N = 2838.38$ rpm, $f = 0.025$ mm/rev, and the optimal output for the delamination factor is 1.2195, which is 8.2% less than that of experimental 1.223.

In Fig. 6, the interaction effect of delamination defect with various input variables has been plotted in the form of interaction plot. The delamination factor was seen to increase with an increase in point angle significantly. Whereas, the rise in spindle speed reduces the delamination factor as the thrust produced is less. However, if the feed rate has been increased, the delamination defect tends to increase at a constant

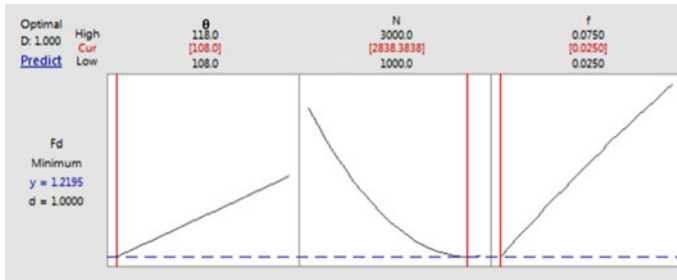


Fig. 5 Response surface plot for delamination factor (F_d)

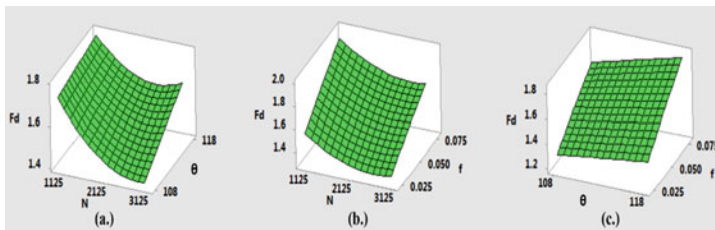
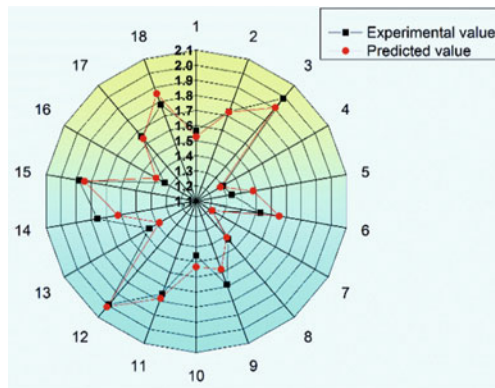


Fig. 6 Surface response plot of the F_d with f , N , and θ

speed and point angle tool and vice versa. Similarly, the point angle also plays a very crucial role in minimizing the delamination factor, as the higher point angle tool encourages the defects.

The radar diagram has been plotted by taking the experimental data and predicted the value of the respected experiments (Fig. 7). In the figure, the deviation between the two values is seen to be very minimum, proving the accuracy of the model with the experimented value during the drilling process.

Fig. 7 Radar diagram showing the experimental and predicted value for all experiments



4 Conclusions

In this study, an empirical investigation of drilling in woven CFRP laminates was carried out with various parametric settings and variation in drill tool geometry. The thrust force, as well as torque, were analyzed concerning the hole quality and the following conclusions were made.

- The drilling experiments were conducted with various parametric setting of input variables and the hole surface quality as well as the thrust force and torque can be controlled by a suitable process variable setting.
- It was found that the drilled induced thrust force increases with an increase in feed rate and vice versa, whereas the drill spindle speed increase has an adverse effect on it which also suits the reduction in the delamination factor.
- The selection of the drill tool geometry also has an effect on the hole integrity. It was found that with a lower point angle drill (108°) less drilled induced thrust force was produced in comparison to a higher point angle drill (118°).
- The torque also affects the drill hole quality as it directly influences the stability of the drill.
- In the initial stage of the drilling process due to the presence of the chisel edge in the twist drill produces a higher amount of thrust, which gradually got stable as the drilling progress deep into the laminate.
- The initial stiff rise in thrust force resulted in entry-level delamination damages on the upper piles of the laminate at the initial stage when the drill tries to get into it.
- Delamination factor is the major among all of the defects that occurred in the drilling of fibrous laminates, which directly varies with the thrust force. The higher feed rate produces a higher thrust force, to higher delamination factor.
- Delamination factor found higher in case of higher feed rate (0.075 mm/rev.), higher point angle drill tool (118°) and lower spindle speed (1125 rpm).
- The lowest value of delamination (1.223) was found with the parameter setting of $\theta = 108^\circ$, $N = 3125$ rpm, and $f = 0.025$ mm/rev.
- The response surface analysis optimization integrated with ANOVA has been carried out, the optimal parameter setting for minimum delamination factor has been found at a parametric setting of $\theta = 108^\circ$, $N = 2838.38$ rpm, $f = 0.025$ mm/rev, with an optimal output of 1.2195, which is 8.2% less than that of experimental.
- Thus, it concluded that the optimization process improves the selection of the parametric setting for enhancing the overall drilled hole quality.

Acknowledgments The authors admirably acknowledge the support of the Department of Production Engineering, VSSUT, Burla for the assistance throughout the experiments and measuring the drilled hole quality features.

References

1. D.F. Liu, Y.J. Tang, W.L. Cong, A review of mechanical drilling for composite laminates. *Compos. Struct.* **94**(4), 1265–1279 (2012). <https://doi.org/10.1016/j.compstruct.2011.11.024>
2. C. Soutis, Carbon fibre reinforced plastics in aircraft construction. *Mater. Sci. Eng. A* **412**, 171–176 (2005). <https://doi.org/10.1016/j.msea.2005.08.064>
3. E.C. Botelho, R.A. Silva, L.C. Pardini, M.C. Rezende, A review on the development and properties of continuous fiber/epoxy/aluminum hybrid composites for aircraft structures. *Mater. Res.* **9**(3), 247–256 (2006). <https://doi.org/10.1590/S1516-14392006000300002>
4. T. Barik, S. Sarangi, Assessment on hole quality during drilling of Al/CFRP stack, in *Advances in Unconventional Machining and Composites* (2020), pp. 757–770. https://doi.org/10.1007/978-981-32-9471-4_64
5. A. Hrechuk, V. Bushlya, J.E. Ståhl, Hole-quality evaluation in drilling fiber-reinforced composites. *Compos. Struct.* **204**, 378–387 (2018). <https://doi.org/10.1016/j.compstruct.2018.07.105>
6. T. Barik, K. Pal, S. Parimita, P. Sahoo, K. Patra, Monitoring of hole surface integrity in drilling of bi-directional woven carbon fiber reinforced plastic composites, in *Proc. Inst. Mech. Eng. Part C J. Mech. Eng. Sci.* (2020). <https://doi.org/10.1177/0954406220906292>
7. S.C. Lee, S.T. Jeong, J.N. Park, S.J. Kim, G.J. Cho, Study on drilling characteristics and mechanical properties of CFRP composites. *Acta Mech. Solida Sin.* **21**(4), 364–368 (2008). <https://doi.org/10.1007/s10338-008-0844-z>
8. T. Barik, S. Biswal, K. Pal, Parametric optimization in drilling of fiber reinforced composites for reduced delamination, in *Proceedings of 6th International 27th All India Manufacturing Technology, Design and Research Conference* (2016), pp. 0–4
9. T. Barik, S. Parimita, K. Pal, Parametric study and process monitoring on drilling of CFRP composites, in *Proceedings of 10th International Conference on Precision, Meso, Micro and Nano Engineering (COPEN 10)*, pp. 953–957 (2017)
10. J. Xu, C. Li, M. Chen, M. El Mansori, F. Ren, An investigation of drilling high-strength CFRP composites using specialized drills. *Int. J. Adv. Manuf. Technol.* **103**(9–12), 3425–3442 (2019). <https://doi.org/10.1007/s00170-019-03753-8>
11. Y. Karpat, O. Bahtiyar, B. Değer, B. Kaftanoğlu, A mechanistic approach to investigate drilling of UD-CFRP laminates with PCD drills. *CIRP Ann. Manuf. Technol.* **63**(1), 81–84 (2014). <https://doi.org/10.1016/j.cirp.2014.03.077>
12. W. Chen, Some experimental investigations in the drilling of CFRP composite laminates. *Int. J. Mach. Tools Manuf.* **37**(8), 1097–1108 (1997). [https://doi.org/10.1016/S0890-6955\(96\)00095-8](https://doi.org/10.1016/S0890-6955(96)00095-8)
13. M. Fernandes, C. Cook, Drilling of carbon composites using a one shot drill bit. Part I: Five stage representation of drilling and factors affecting maximum force and torque. *Int. J. Mach. Tools Manuf.* **46**(1), 70–75 (2006). <https://doi.org/10.1016/j.ijmactools.2005.03.015>
14. U.A. Khashaba, Delamination in drilling GFR-thermoset composites. *Compos. Struct.* **63**(3–4), 313–327 (2004). [https://doi.org/10.1016/S0263-8223\(03\)00180-6](https://doi.org/10.1016/S0263-8223(03)00180-6)
15. S.R. Karnik, V.N. Gaitonde, J.C. Rubio, A.E. Correia, A.M. Abrão, J.P. Davim, Delamination analysis in high speed drilling of carbon fiber reinforced plastics (CFRP) using artificial neural network model. *Mater. Des.* **29**(9), 1768–1776 (2008). <https://doi.org/10.1016/j.matdes.2008.03.014>
16. P. Suresh, K. Marimuthu, S. Ranganathan, T. Rajmohan, Optimization of machining parameters in turning of Al–SiC–Gr hybrid metal matrix composites using grey-fuzzy algorithm. *Trans. Nonferrous Met. Soc. China (English Ed.)* **24**(9), 2805–2814 (2014). [https://doi.org/10.1016/s1003-6326\(14\)63412-9](https://doi.org/10.1016/s1003-6326(14)63412-9)
17. R.H. Myers, D.C. Montgomery, Response surface methodology. *IIE Trans.* **28**(12), 1031–1032 (1996). <https://doi.org/10.1080/15458830.1996.11770760>
18. J. Suthar, S.N. Teli, S. Lad, Application of response surface methodology in drilling of carbon fiber application of response surface methodology in drilling of carbon fiber reinforced polymer composite (CFRP). *Int. J. Sci. Eng. Res.* **9**(January), 347–350 (2018)

19. S. Datta, A. Bandyopadhyay, P.K. Pal, Grey-based Taguchi method for optimization of bead geometry in submerged arc bead-on-plate welding. *Int. J. Adv. Manuf. Technol.* **39**(11–12), 1136–1143 (2008). <https://doi.org/10.1007/s00170-007-1283-6>
20. Y.C. Lin, H.S. Lee, Optimization of machining parameters using magnetic-force-assisted EDM based on gray relational analysis. *Int. J. Adv. Manuf. Technol.* **42**(11–12), 1052–1064 (2009). <https://doi.org/10.1007/s00170-008-1662-7>
21. C.L. Lin, J.L. Lin, T.C. Ko, Optimisation of the EDM process based on the orthogonal array with fuzzy logic and grey relational analysis method. *Int. J. Adv. Manuf. Technol.* **19**(4), 271–277 (2002). <https://doi.org/10.1007/s001700200034>
22. T. Rajmohan, K. Palanikumar, M. Kathirvel, Optimization of machining parameters in drilling hybrid aluminium metal matrix composites. *Trans. Nonferrous Met. Soc. China (English Ed.)* **22**(6), 1286–1297 (2012). [https://doi.org/10.1016/s1003-6326\(11\)61317-4](https://doi.org/10.1016/s1003-6326(11)61317-4)
23. E. Kilickap, Optimization of cutting parameters on delamination based on Taguchi method during drilling of GFRP composite. *Expert Syst. Appl. J.* **37**, 6116–6122 (2010). <https://doi.org/10.1016/j.eswa.2010.02.023>
24. A. Aggarwal, H. Singh, Optimization of machining techniques—A retrospective and literature review. *Sadhana* **30**(6), 699–711 (2005)
25. R. Stone, K. Krishnamurthy, A neural network thrust force controller to minimize delamination during drilling of graphite-epoxy laminates. *Int. J. Mach. Tools Manuf.* (1996). [https://doi.org/10.1016/0890-6955\(96\)00013-2](https://doi.org/10.1016/0890-6955(96)00013-2)
26. K. Palanikumar, L. Karunamoorthy, R. Karthikeyan, Multiple performance optimization of machining parameters on the machining of GFRP composites using carbide (K10) tool. *Mater. Manuf. Process.* **21**(8), 846–852 (2006). <https://doi.org/10.1080/03602550600728166>
27. A. Krishnamoorthy, S. Rajendra Boopathy, K. Palanikumar, J. Paulo Davim, Application of grey fuzzy logic for the optimization of drilling parameters for CFRP composites with multiple performance characteristics. *Meas. J. Int. Meas. Confed.* **45**(5), 1286–1296 (2012). <https://doi.org/10.1016/j.measurement.2012.01.008>
28. S. Pal, S.K. Malviya, S.K. Pal, A.K. Samantaray, Optimization of quality characteristics parameters in a pulsed metal inert gas welding process using grey-based Taguchi method. *Int. J. Adv. Manuf. Technol.* **44**(11–12), 1250–1260 (2009). <https://doi.org/10.1007/s00170-009-1931-0>
29. N. Tosun, H. Pihtili, Gray relational analysis of performance characteristics in MQL milling of 7075 Al alloy. *Int. J. Adv. Manuf. Technol.* **46**(5–8), 509–515 (2010). <https://doi.org/10.1007/s00170-009-2118-4>
30. M.A. Bezerra, R.E. Santelli, E.P. Oliveira, L.S. Villar, L.A. Escalera, Response surface methodology (RSM) as a tool for optimization in analytical chemistry. *Talanta* **76**(5), 965–977 (2008). <https://doi.org/10.1016/j.talanta.2008.05.019>
31. T. Rajmohan, K. Palanikumar, S. Prakash, Grey-fuzzy algorithm to optimise machining parameters in drilling of hybrid metal matrix composites. *Compos. Part B Eng.* **50**, 297–308 (2013). <https://doi.org/10.1016/j.compositesb.2013.02.030>
32. R.S.K. Krishnamurthy, Neural network thrust force controller to minimize delamination during drilling of graphite—Epoxy laminates. *Int. J. Mach. Tools Manufact.* **36**, 985–1003 (1996)

Application of MCDM Methods for Process Parameter Optimization in Turning Process—A Review



Ch. Divya, L. Suvarna Raju, and B. Singaravel

Abstract Optimization of process parameters in machining process leads to enhancement in process outcomes. Turning process is one of the primary operations in manufacturing industries. Multi-Criteria Decision Making (MCDM) concepts are used by researchers to optimize the process parameters in turning process. These MCDM methods are used to rank and find out the best combination of process parameters from given number of alternatives. In this study, a detailed literature survey is carried out in the area of application of different MCDM methods which are used for optimization of turning process parameters. There are different MCDM methods are available, but in this work only focused application related to manufacturing domain and methods are reviewed namely Technique for Order Preference by Similarity to Ideal Solution (TOPSIS), VlseKriterijumska Optimizacija I Kompromisno Resenje in Serbian (VIKOR), Multi-Objective Optimization on the basis of Ratio Analysis (MOORA) method, and Analytic Hierarchy Process (AHP) method. The result of review work indicates that the above-mentioned MCDM methods are capable of solving multiple criteria problems for turning process parameter optimization.

Keywords Turning process · Machining parameter optimization · MCDM · TOPSIS · VIKOR · MOORA · AHP

Ch. Divya (✉) · L. S. Raju
Department of Mechanical Engineering, Vignan's Foundation for Science, Technology & Research, Vadlamudi, Andhra Pradesh, India
e-mail: divyareddy.chinthala@gmail.com

L. S. Raju
e-mail: drlsrajuvu@gmail.com

B. Singaravel
Department of Mechanical Engineering, Vignan Institute of Technology and Science, Deshmukhi, Hyderabad, Telangana State, India
e-mail: singnitt@gmail.com

1 Introduction

In turning process, an important work is to predict appropriate process parameters for achieving high machining performance. Generally, standard handbook and previous experience data are used for appropriate process parameters. But, in most of the situation, this is not an accurate one. Hence, proper optimization procedure is required to obtain optimal combination of parameters for machining. The optimum process parameters lead to better performance in terms of output parameters such as good surface quality, minimum cutting forces, low power consumption and good functional life [1, 2]. Optimization can be defined as the procedure of determination of optimum solution from all possible solution. This optimum solution is used to maximize or minimize a particular objective function. Optimization process can be categorized into single response based and multi-response based. Multi-response optimization problem involves optimizing two or more than two objective parameters simultaneously [3]. MCDM methods are statically approached which are widely used to select the best alternative among given numbers of alternatives. MCDM methods can be used to rank and find out optimum machining condition [4, 5]. There are various types of MCDM methods available and few methods are successfully applied for process parameters optimization. The objective of this article is to review on TOPSIS, VIKOR, MOORA, AHP methods for process parameter optimization in turning process.

2 Background

2.1 *Technique for Order Preference by Similarity to Ideal Solution (TOPSIS) Method*

TOPSIS is one of the MCDM methods that is used to rank the best alternative from given number of alternatives. TOPSIS can be used to solve multi-criteria problems effectively. The basic idea of TOPSIS method is that the optimum solution has the shortest distance from positive ideal solution and farthest from negative solution. The main advantage of this method is to solve multiple criteria problem and find out the best possible solution in systematic way by determination of tangible and intangible factors. The various steps involved in TOPSIS method for determination of the best combination of process parameters are explained as follows [6].

- Problem explanation and objectives description.
- Formation of decision matrix.
- Normalization of input data.
- Determination of weighted normalized decision matrix.
- Determination of positive ideal solution and negative ideal solution.
- Determination of separation measure.

- Determination of relative closeness to positive ideal solution.
- Rank the preference order.

2.2 VlseKriterijumska Optimizacija I Kompromisno Resenje in Serbian (VIKOR)

VIKOR method is a type of MCDM methods which is also known as compromise ranking procedure. VIKOR involves ranking and selection of best alternatives by involving multi-criteria ranking index. VIKOR method involves MOO to solve multiple criteria industrial problem. VIKOR procedure finds a compromise solution by considering high group utility as maximum and opponent individual regret as minimum. The following steps involved in VIKOR procedure are as follows [7].

- Problem definition and objective formulation.
- Construction of decision matrix.
- Normalized decision matrix estimation.
- Determination of positive and negative ideal solutions.
- Estimation of utility measure and regret measure.
- VIKOR index calculation.
- Rank the order of preference.

2.3 Multi-objective Optimization on the Basis of Ratio Analysis (MOORA) Method

MOORA approach is a type of MCDM method, and it has capability to solve multi-criteria objective problems. MOORA approach is considered maximization (beneficial) and minimization (non-beneficial) alternatives for prediction of optimum alternatives and also eliminates unsuitable alternatives. The following procedures are used for MOORA method [8].

- Problem statement description and objective function establishment.
- Construction of decision matrix.
- Normalization of input data.
- Normalized assessment determination.
- Normalized assessment determination by considering weight criteria assumption.
- Rank the normalized assessment.

2.4 Analytic Hierarchy Process (AHP)

AHP is a type of MCDM methods employed for prediction of optimum alternatives from the set of alternatives. It has logical procedure for representing the element of

any problem, hierarchically. It is also used to calculate the weight criteria of each objective by Eigenvectors method and global priorities of various attributes. The various steps involved in AHP method are discussed below [9].

- Problem description and establishment of its objectives.
- Construction of decision matrix.
- Normalization of input data.
- Calculation of weight criteria using pair-wise comparison matrix.
- Calculation of the composite performance scores.
- Rank the composite performance scores.

3 Literature Survey

The literature is collected and highlighted in different perspectives, namely turning process parameters optimization using TOPSIS method, VIKOR method, MOORA method, and AHP method.

TOPSIS method is very simple approach to solve multiple objectives simultaneously. Palanisamy and Senthil [10] applied Taguchi-Grey Relational Analysis (GRA) method for optimization of turning process parameters. TOPSIS was used to prove the similarity of results obtained. Similarly, Ramesh et al. [11], Balaji et al. [12], Palanisamy and Selvaraj [13], Narayanan et al. [14], and Nipanikar et al. [15] applied TOPSIS method for optimization in turning process parameters. The results were compared with Taguchi-GRA method. Khan and Maity [16] used TOPSIS method to optimize process parameters in turning process. The result indicated that the proposed TOPSIS was used by decision-makers and researchers for prediction of optimum parameters. Bhardwaj et al. [17] optimized process parameters to obtain optimum Material Removal Rate (MRR), Surface Roughness (SR), and Machining Time (MT) in tuning process using TOPSIS method. Majumdera and Sahab [18] used MOORA and TOPSIS methods as optimization tool in turning process. The proposed methods were used plays a vital role in optimization. Arif Gok [19] used TOPSIS coupled with fuzzy environment for optimization of turning process parameters. The results were compared with Taguchi-GRA method. Koyee et al. [20, 21] Khan and Maity [22] used TOPSIS with fuzzy environment. Rao [6] evaluated machinability factors using combined TOPSIS and AHP method in turning of titanium alloys. Two case studies were presented to explain the applicability of the combined TOPSIS and AHP method. The method used for optimization of machining parameters simultaneously for multiple numbers of objectives. AHP method was used to estimate the weight criteria of each output parameter. Similarly, Singaravel and Selvaraj [23], Abhang and Hameedullah [24] used combined TOPSIS and AHP method for optimization of turning process parameter optimization. Parida and Routara [25] used TOPSIS method combined with Taguchi method to optimize process parameters in turning process. The result revealed that TOPSIS is a simple procedure to execute and eliminates complex modeling and simulations. Similarly, Lan [26], Singh et al. [27], and Balasubramanian and Selvaraj [28] used Hybrid TOPSIS and Taguchi method.

Thirumalai and Senthilkumar [4] used NSGA II for relative closeness value obtained from TOPSIS method in turning process parameter optimization. Also, Asokan and Senthilkumar [29] used NSGA II-based TOPSIS method. The proposed method provided appropriate procedure to select optimum process parameters. Singaravel et al. [30] used MOORA coupled with entropy concept for the selection of optimum process parameters. The result indicated that the proposed method was used to solve multi-objective problem effectively.

Khan et al. [31] used MOORA method with fuzzy environment for optimization of process parameters in turning process. The result revealed that the proposed method was capable to predict optimum parameters with specified cutting conditions. Maity and Pradhan [32] used MOORA method coupled with Taguchi method for process parameter optimization. The optimum results were predicted using MOORA and Taguchi method. Khan and Maity [33] used VIKOR method for process parameter optimization in turning process. Kumar et al. [34] used VIKOR method combined with AHP method for process parameter optimization in turning process. Singaravel and Selvaraj [35] used AHP method for prediction of optimum process parameters in turning process. The result revealed that AHP method was capable to solve multi-objective optimization problem effectively (Table 1).

4 Discussions and Conclusions

This study reported various MCDM methods used for process parameter optimization in turning process. Numbers of works have been reported on different MCDM methods for turning process parameters optimization. In this study, TOPSIS, VIKOR, MOORA, and AHP methods are focused. TOPSIS method determines the optimum solution from given number of alternatives. It determines optimum solution by the shortest distance from the ideal solution and largest distance from the negative ideal solution. It has simple calculation method, does not require any assumption regarding coefficient and complicated software. MOORA method determines the optimal solution by considering beneficial (maximization) and non-beneficial (minimization) objectives. It has simple mathematical problems and not requires any complicated software to perform. VIKOR method estimates the optimum solution from the given number of alternative and provides compromise solution by high group utility for the majority and low individual regret for the opponent. The AHP method is used to select the best alternatives among the given set of alternatives. It has a logical procedure for representing the element of any problem, hierarchically. This method is used to calculate the relative importance of each criterion by Eigenvector method with pairwise comparison matrix and overall priorities of various attributes. From literature, it is clear that MCDM methods can be used as MOO tool. These techniques are used to optimize multiple numbers of process parameters and are applicable to all types of manufacturing processes simultaneously. Other MCDM methods not focused in this work like WASPAS, ELECTRE, and ARAS methods also can be used for MOO. From the literature, it is noticed that among all MCDM methods, TOPSIS influences

Table 1 Turning process parameters optimization using different MCDM methods

S. No.	Authors	Methodology used	Parameters used
1	Palanisamy and Senthil [10]	TOPSIS	FC and SR
2	Ramesh et al. [11]	TOPSIS	SR and TW
3	Balaji et al. [12]	TOPSIS	FC and SR
4	Palanisamy and Selvaraj [13]	TOPSIS	SE, MRR, and Microhardness (MH)
5	Narayanan et al. [14]	TOPSIS	MRR and SR
6	Nipanikar et al. [15]	TOPSIS	SR and TW
7	Khan and Maity [16]	TOPSIS	SR, FC, TW, and temperature (T)
8	Bhardwaj et al. [17]	TOPSIS	SR, MRR, MT
9	Majumdera and Sahab [18]	TOPSIS	SR, PC, and tool vibration
10	Gok [19]	Fuzzy TOPSIS	SR and FC
11	Koyee et al. [20]	TOPSIS	SR and cutting force (FC)
12	Koyee et al. [21]	Fuzzy TOPSIS	FC, PC, TW, chip volume ratio
13	Khan and Maity [22]	Fuzzy TOPSIS	SR, FC, and TW
14	Rao [6]	Combined TOPSIS and AHP	TW, PC, and SR
15	Singaravel and Selvaraj [23]	Combined TOPSIS and AHP	MH, SR, and MRR
16	Abhang and Hameedullah [24]	Combined TOPSIS and AHP	SR and MRR
17	Parida and Routara [25]	Hybrid Taguchi and MCDM	MRR and SR
18	Lan [26]	Hybrid Taguchi and MCDM	SR, TW, and MRR
19	Singh et al. [27]	TOPSIS in the Taguchi method	SR and MRR
20	Balasubramaniyan and Selvaraj [28]	Hybrid Taguchi and TOPSIS	Circularity and cylindricity error
21	Thirumalai and Senthilkumaar [4]	NSGA II and TOPSIS	SR, Tool life (TL) FC, MRR, and PC
22	Asokan and Senthilkumaar [29]	NSGA II and TOPSIS	SR, TL, FC, MRR
23	Singaravel et al. [30]	MOORA and entropy method	SR, MH and MRR
24	Khan et al. [31]	Fuzzy MOORA	FC, SR, and TW

(continued)

Table 1 (continued)

S. No.	Authors	Methodology used	Parameters used
25	Maity and Pradhan [32]	MOORA coupled with Taguchi method	TW, SR, and chip reduction coefficient
26	Khan and Maity [33]	VIKOR method	FC, SR, and MRR
27	Kumar et al. [34]	Combined AHP and VIKOR	MRR, SR, and MT
28	Singaravel and Selvaraj [35]	AHP	SR, MH, and MRR

more than 60% than other methods for optimization of process parameters in turning process. This is may be due to TOPSIS approach is easy to understand and execute. The result of review work revealed that MCDM methods are easy to execute, systematic, and effective. MCDM methods require almost half of the computational time and less software usage with other methods such as Taguchi method and metaheuristic approaches. It could be alternative to other optimization techniques. Many studies are involved with optimization of process parameters with surface roughness, material removal, and tool wear. Other parameters like microhardness, residual stresses, and white layer thickness to be focused. MCDM methods (Ex.AHP) are also possible to estimate relative importance of output parameters. It can be used to enhance the optimization precisely.

Acknowledgements This review work is used to support DST-SERB funded project of ECR/201/001097.

References

1. M. Nalbant, H. Gökkaya, G. Sur, Application of Taguchi method in the optimization of cutting parameters for surface roughness in turning. *Mater. Des.* **8**, 1379–1385 (2007)
2. D.G. Thakur, B. Ramamoorthy, L. Vijayaraghavan, Study on the machinability characteristics of superalloy Inconel 718 during high speed turning. *Mater. Des.* **30**, 1718–1725 (2009)
3. E. Aliakbari, H. Baseri, Optimization of machining parameters in rotary EDM process by using the Taguchi method. *Int. J. Adv. Manuf. Tech.* **62**, 1041–1053 (2012)
4. R. Thirumalai, J.S. Senthilkumar, Multi-criteria decision making in the selection of machining parameters for Inconel 718. *J. Mech. Sci. Tech.* **27**, 1109–1116 (2013)
5. L.I. Tong, C.C. Chen, C.H. Wang, Optimization of multi-response processes using the VIKOR method. *Int. J. Adv. Manuf. Tech.* **31**, 1049–1057 (2007)
6. R.V. Rao, Machinability evaluation of work materials using a combined multiple attribute decision-making method. *Int. J. Adv. Manuf. Tech.* **28**, 221–227 (2006)
7. S.K. Gauri, S. Chakraborty, A study on the performance of some multi-response optimization methods for WEDM processes. *Int. J. Adv. Manuf. Tech.* **49**, 155–166 (2010)
8. A. Ray, Green cutting fluid selection using multi-attribute decision making approach. *J. Inst. Engi. (India): Ser, C* **96**, 35–39 (2014)

9. F.A. AlKaabneh, M. Barghash, I. Mishael, A combined analytical hierarchical process (AHP) and Taguchi experimental design (TED) for plastic injection molding process settings. *Int. J. Adv. Manuf. Tech.* **66**, 679–694 (2013)
10. D. Palanisamy, P. Senthil, Optimization on turning parameters of 15-5PH stainless steel using Taguchi based grey approach and TOPSIS. *Arch. Mech. Eng.* **63**, 397–412 (2016)
11. S. Ramesh, R. Viswanathan, S. Ambika, Measurement and optimization of surface roughness and tool wear via grey relational analysis, TOPSIS and RSA techniques. *Measurement* **78**, 63–72 (2016)
12. V. Balaji, S. Ravi, P.N. Chandran, Optimization on cryogenic CO₂ machining parameters of AISI D2 steel using Taguchi based grey relational approach and TOPSIS (2018)
13. A. Palanisamy, T. Selvaraj, Optimization of turning parameters for surface integrity properties on incoloy 800H superalloy using cryogenically treated multi-layer CVD coated tool. *Surf. Rev. Lett.* **26**(02), 1850139 (2019)
14. N.S. Narayanan, N. Baskar, M. Ganesan, M.P. Jenarathanan, S. Praveen, Evaluation and optimization of surface roughness and metal removal rate through RSM, GRA, and TOPSIS techniques in turning PTFE polymers, in *Advances in Manufacturing Technology* (Springer, Singapore, 2019), pp. 595–605
15. S. Nipanikar, V. Sargade, R. Guttedar, Optimization of process parameters through GRA, TOPSIS and RSA models. *Int. J. Ind. Eng. Comput.* **9**, 137–154 (2018)
16. A. Khan, K. Maity, Application of MCDM-based TOPSIS method for the selection of optimal process parameter in turning of pure titanium. *Benchmark.: Int. J.* **24**, 2009–2021 (2017)
17. V. Bhardwaj, M.K. Gaur, V. Chaturvedi, S. Agrawal, optimization of machining parameters for nylon 6 composite in CNC lathe using PCA-based TOPSIS. *Int. J. Manuf. Mater. Process.* **4**, 36–47 (2018)
18. H. Majumder, A. Saha, Application of MCDM based hybrid optimization tool during turning of ASTM A588. *Decis. Sci. Lett.* **7**, 143–156 (2018)
19. A. Gok, A new approach to minimization of the surface roughness and cutting force via fuzzy TOPSIS, multi-objective grey design and RSA. *Measurement* **70**, 100–109 (2012)
20. R.D. Koyee, R. Eisseler, S. Schmauder, Application of Taguchi coupled fuzzy multi attribute decision making (FMADM) for optimizing surface quality in turning austenitic and duplex stainless steels. *Measurement* **58**, 375–386 (2014)
21. R.D. Koyee, U. Heisel, R. Eisseler, S. Schmauder, Modeling and optimization of turning duplex stainless steels. *J. Manuf. Process.* **16**, 451–467 (2014)
22. A. Khan, K. Maity, Application potential of combined fuzzy-TOPSIS approach in minimization of surface roughness, cutting force and tool wear during machining of CP-Ti grade II. *Soft. Comput.* **23**, 6667–6678 (2019)
23. B. Singaravel, T. Selvaraj, Optimization of machining parameters in turning operation using combined TOPSIS and AHP method. *Tehnicki Vjesnik* **22**, 1475–1480 (2015)
24. L.B. Abhang, M. Hameedullah, Selection of lubricant using combined multiple attribute decision making method. *Adv. Prod. Manage.* **7**, 39–50 (2012)
25. A.K. Parida, B.C. Routara, Multiresponse optimization of process parameters in turning of GFRP using TOPSIS method. *Int. Scholar. Res. Not.* 1–10 (2014)
26. T.S. Lan, Taguchi optimization of multi-objective CNC machining using TOPSIS. *Inf. Technol. J.* **8**, 917–922 (2012)
27. A. Singh, S. Datta, S.S. Mahapatra, Application of TOPSIS in the Taguchi method for optimal machining parameter selection. *J. Manuf. Sci. Prod.* **11**, 49–60 (2011)
28. S. Balasubramanian, T. Selvaraj, Application of integrated Taguchi and TOPSIS method for optimization of process parameters for dimensional accuracy in turning of EN25 steel. *J. Chin. Inst. Eng.* **40**, 267–274 (2017)
29. P. Asokan, J.S. Senthilkumar, Intelligent selection of machining parameters in turning of Inconel-718 using multi objective optimization coupled with MADM. *Int. J. Mach. Mach. Mater.* **8**, 209–225 (2010)
30. B. Singaravel, T. Selvaraj, S. Vinodh, Multi-objective optimization of turning parameters using the combined MOORA and entropy method. *Trans. Can. Soc. Mech. Eng.* **40**, 101–111 (2016)

31. A. Khan, K. Maity, D. Jhodkar, An integrated fuzzy-MOORA method for the selection of optimal parametric combination in turning of commercially pure titanium, in *Optimization of Manufacturing Processes* (Springer, Cham, 2020), pp. 163–184
32. K. Maity, S. Pradhan, December. Optimization of titanium grade 5 alloy using dry machining by MOORA coupled with Taguchi method, in *Proceedings of 6th International & 27th All India Manufacturing Technology, Design and Research Conference (AIMTDR-2016)* (College of Engineering, Pune, Maharashtra, India)
33. A. Khan, K. Maity, A novel MCDM approach for simultaneous optimization of some correlated machining parameters in turning of CP-titanium grade 2. *Int. J. Eng. Res. Afr.* **22**, 94–111 (2016)
34. R. Kumar, R. Kumar, S. Gaurav, C. Saurabh, Optimization of process parameters during CNC turning by using AHP & VIKOR method. *Int. J. Eng. Res. Technol.* **2**, 3478–3480 (2013)
35. B. Singaravel, T. Selvaraj, Multi criteria optimisation using analytic hierarchy process in turning operation. *IJMMM* **19**, 218–229 (2017)

Effect of Hybridization, Influence of Surface Modification on the Properties and Optimization of bio fiber Composites



G. Venkatesha Prasanna, M. Nikhil, and A. Sai Kiran

Abstract The target of the researcher and the work was to examine the tensile, flexural, and compressive properties of biofiber strengthened composites. The legitimacy and advantage of utilizing regular filaments was their effective accessibility, simple and safe dealing with, and biodegradable nature. While biofibers reveal commendable physical and mechanical properties, it shifts with the plant source, species, and geography. In the present work, bagasse–henequen filaments were utilized at the following fixations: 5, 10, 15, 20, 25, and 30 wt%. Untreated and soluble base-treated bagasse–henequen filaments were fortified in the epoxy/vinyl ester mix and composites have been created by hand lay-up strategy. The bagasse–henequen strands were salt-treated for 12 and 24 h in 10% NaOH. Composites were assessed as far as their microstructure and mechanical properties. 25% wt. filaments 24 h NaOH (soluble base)-treated composites have demonstrated prevalent and optimum values than untreated and 12-h-treated composites.

Keywords Bagasse–henequen fibers · Chemical treatment and mechanical tests · Morphology

1 Introduction

In a large portion of the cases, the fortification would be more grounded, stiffer, and harder than the resin. In the present situation, there is an expanding requirement for eco-accommodating materials with moderately high solidarity to weight proportion. Fake strands in particular Kevlar, carbon, glass, and aramid have been broadly

G. Venkatesha Prasanna (✉) · M. Nikhil · A. Sai Kiran
Department of Mechanical Engineering, CVR College of Engineering, Hyderabad 501510, India
e-mail: gvpvcvrmech@gmail.com

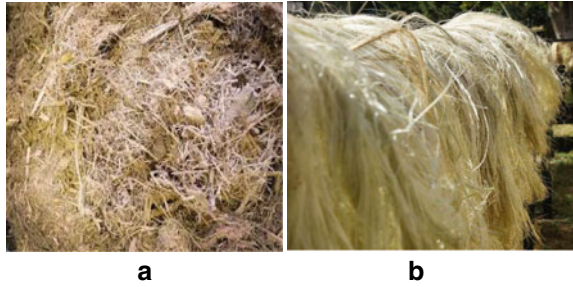
M. Nikhil
e-mail: prasannavg22@gmail.com

A. Sai Kiran
e-mail: gvpsagar4@gmail.com

utilized in polymer-based composites in view of their high quality and firmness properties. The poor biodegradability, introductory handling costs, recyclability, vitality utilization, machine scraped area, and well-being risks of engineered FRPs were a genuine and significant issue, starting today. Biostrands strengthened composites can fathom both the presentation and air issues. Anyway, the antagonistic effects by engineered strands prompted change of enthusiasm from manufactured filaments to regular/sustainable strands [1–3]. Normal filaments have been utilized as an elective asset to engineered strands just as fortification for polymer composite materials. Regular strands contain cellulose, hemicelluloses, gelatin, lignin, and waxes [4–6]. The dampness retention property of normal strands constrains the use of numerous common filaments as reasonable support in the creation of composites. Polymer grid is hydrophobic in nature. This outcomes fiber and lattice contrary and results in poor cement holding between the fiber and the network. The reason for this surface alteration was to diminish their water ingestion property and furthermore to improve the similarity with gum. Polymer lattice composites are regularly coetaneous with cutting edge materials for very good quality applications in the fields, for example, building and development, military, transportation, airplane industry, marine, and others. A ton of specialists have manufactured composites containing various filaments, and these strands were named as half breed composites. The crossbreed composites demonstrated preferred mechanical properties over mono-fiber composites. In the creation of composites, the estimation of mechanical properties assumes a significant job in quality control. Due to the progression in composite framework innovation, the composite testing techniques and test hardware have gotten advanced. The polymer mix has numerous favorable circumstances in terms of the items for explicit end-use applications and upgrading sap's successful usage, execution, and properties [7–9].

Thermoplastics have just a little level of the propelled composite market, yet the thermoset plastics add to chief share of more than 70% in the composites manufacture. As a result of their inbuilt capture structure, these resins turned into the most huge polymers with regard to superior. Epoxy sap is a multipurpose and by and largely used system material for diverse purposes, for instance, impelled composites, hardware parts, electrical circuit board materials, and rocket supplies, considering its unmatched properties like incredible holding limit, warm, mechanical and dielectric properties. Epoxy polymers have been broadly used as coatings, pastes, molding blends, and polymer composite materials in light of their better thermomechanical properties and marvelous processability. Nonetheless, the consumption of thermoset materials is frequently constrained in view of low durability property. At that point, mixing strategy can be utilized productively to beat the second rate properties of both the parts. Polymer mixes possessing miscibility produce a enhanced than ever material from less unrivaled separate segments. In this manner, when the mass measures of epoxies are utilized, generally it will mix with toughening specialists. Vinyl ester a toughening material can be utilized alongside epoxy materials. Vinyl ester is the extra result of an epoxy pitch with unsaturated carboxylic corrosive, for example, acrylic or methacrylic acid. In view of the adaptability present in the structure of epoxy, it is utilized as one of the mixed materials right now. To improve the exhibition attributes in cutting edge designing applications, toughening of epoxy material is important

Fig. 1 **a** Bagasse fiber.
b Henequen fiber



to improve its malleable property and hardness. The hardness of the epoxy polymer was impressively expanded by mixing it with adaptable polymers and elastomers [4, 10, 11]. Thus a reasonable polymeric material was required to improve the effect of opposition, stress–strain properties by holding firmness, glass change temperature, and warm security of the epoxy pitch. For accomplishing this, the advancement of a between cross-connected polymer system of thermoset-thermoset mixes was considered in view of their expanded mechanical properties. Vinyl ester will be the for the most part utilized thermosetting material in view of their less expense and great mix of properties like synthetic opposition, mechanical and warm properties. The hydroxyl bunches upgrade the extremity of Vinyl ester and encourage bond and color wetting properties, which drove the wetting of the strands in fiber fortified plastics (FRP). For this reason, a mix of epoxy/vinyl ester (90/10% w/w) polymers were readied. Composite examples with the 5, 10, 15, 20, 25, and 30 wt%. substance of untreated, soluble base-treated bagasse–henequen strands with mix of epoxy/vinyl ester were fabricated.

2 Experimental

2.1 Materials

The two resins namely: 1. epoxy Araldite LY 556 as resin, hardener HY 951 2. Vinyl ester

The two fibers namely: 1. Henequen fiber 2. Bagasse fiber were used to fabricate the composites

2.2 Surface Modification of Natural Fibers

Due to the nearness of hydrophilic hydroxyl bunches in the regular filaments, little issues happen along the interface during the support of characteristic fibril into the

matrix. This hydrophilic nature ruins the powerful and effective holding of strands with grid. Aside from this, gelatin, oil, and waxy substances spread the receptive utilitarian gatherings of the fiber and go about as an obstruction to interlock with the framework. For improving the adequacy of interfacial union, fibril face should be altered utilizing (NaOH) soluble base/concoction medicines.

2.3 Chemical (Alkali) Treatment

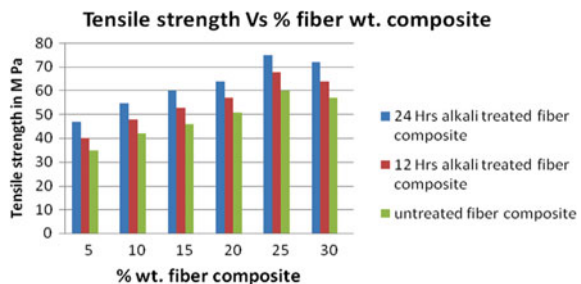
So as to improve the viability of interfacial attachment/holding, fibril surface should be altered with various substances, responsive added substances, and coupling specialists. Substance activities produce progressively impulsive groups on the outside of the fiber and this encourages capable association with the framework. Surface alteration of filaments by soluble base treatment with convergence of NaOH: 10 wt% was done for 12 and 24 h right now. After the soluble base treatment, the filaments were inundated in refined water for 24 h to expel the remaining NaOH. Further washing was done with refined water containing a modest quantity of acidic corrosive. Filaments were then dried out in a boiler at 70 C for 3 h.

3 Results and Discussion

3.1 Tensile Properties

Composites for the tensile test, with 150 mm × 15 × 3 mm, were tested as per ASTM standards. Tensile strength of the composites was examined by using Universal testing machine with a cross-head speed of 50 mm/min. The impact of fiber stacking and strands surface change by the soluble substance treatment on the malleable property of biofibril composites is shown in Fig. 2. Typically, synthetically treated biofibrils strengthened composites forces of higher elasticity than the untreated fiber fortified composites. If there should be an occurrence of natural biocomposites, the

Fig. 2 Tensile strength of untreated and alkali-treated composites

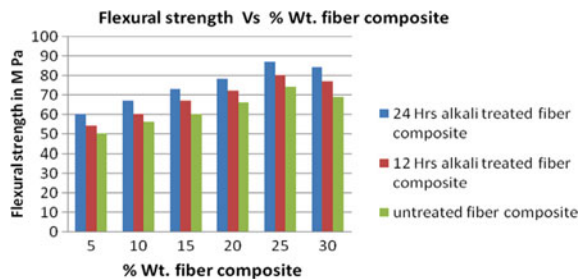


repellency and poor similarity between hydrophobic lattice and hydrophilic characteristic strands which would unfavorably influence the interfacial holding between fiber surface and network and which brings about diminishing of the support limit of the fiber because of the deficient and ill-advised pressure move from the grid to fibers [5, 9, 12]. The rigid qualities of untreated, soluble base-treated bagasse–Henequen filaments fortified composites found to increment up to 25% Wt., 24-h-treated fiber composite than 5,10, 15, 20, and 30% untreated, 12-h-treated composite and afterward it diminished with expanding fiber load, i.e., at (30% fiber load) [11]. The most elevated rigid qualities saw at around 25% Wt. 24-h-treated fiber composite stacking was a direct result of better fiber circulation in framework material and less fiber cracks [9, 13, 14, 11]. Subsequently, the interfacial glue holding among fiber and framework imparts whether the fiber will improve the rigidity of composites by moving an applied burden. The pressure move among framework and filaments in a composite was not just controlled by the characteristic properties of the fiber and lattice, yet additionally influenced by the geometric parameters and fiber plan inside the network, for example, fiber circulation [7, 12, 15, 16, 17].

3.2 Flexural Strength

The specimens with dimensions 150 mm × 15 mm × 3 mm were fabricated and tested for flexural properties as per ASTM D 5943-96 specifications. The changes in the values of flexural strength as a function of fiber load with and without alkali treatment were indicated in Fig. 3. As of the test it was seen that the flexural property of the bagasse–henequen strands fortified epoxy/vinyl ester mixed composite which demonstrated higher and ideal estimation of the flexural property was seen at 25% fiber stacking and 24 h soluble base treat treated biofibril composites [18]. This is credited to the decrease of the hydrophilic idea of bagasse–henequen strands because of the coupling of the hydroxyl gathering of fiber with 24 h soluble base treatment. The 24 h antacid treatment occupied the void spaces by diminishing the repellency of fiber and adjusts lopsided fiber than 12-h-treated and untreated composites. Furthermore, it decreases fiber breadth and in this manner expands the perspective proportion [8, 19]. Consequently builds the successful fiber surface zone for good bond with the

Fig. 3 Flexural strength of untreated and alkali-treated composites



grid. The treatment of fibrils additionally expanded interfacial attachment between the bagasse–henequen strands/fibrils and the polymer framework material [16, 20].

3.3 Compressive Strength

The specimens of composites were fabricated and tested for compressive strength properties as per ASTM D specifications. The change in the values of compressive strength property with respect to fiber quantity with and without surface modification is shown in Fig. 4. It was likewise seen that 25% wt. fiber load 24 h soluble base treated biostrand composites showed better and ideal condition for compressive property than the other 24 h alkali treated, 12 h antacid treated, and untreated biocomposites [14, 19, 21, 17]. The ideal condition was a direct result of idyllic fiber stacking, and compound treatment, which advanced the better interfacial holding between strands polymers mix brought about sufficient stress move and execution [9, 12, 20, 11]. Past works uncover that fiber surface alteration by compound treatment of 24 h lessens the fiber’s distance across and builds surface harshness in a powerful manner [16, 22, 17]. The surface treatment by methods for NaOH, gives the path for the expulsion of undesirable materials like waxes, oils, pollutions, hemicellulose, and lignin from the regular strands, yields the higher level of (alpha) cellulose in characteristic filaments and furthermore cleans the fiber surface [8, 11, 17]. Soluble base treatment advances increasingly in successful region of the fiber’s surface required for damping by the polymer so as to have great holding [12, 15, 23] and results in improved mechanical properties.

Contrasting the estimations of untreated and salt-treated bagasse–henequen strands uncovers that 24 h antacid treated composite in the filaments framed a superior unpleasant surface and collaboration on the fiber surface, which is credited to the further decrease of the hydrophilic idea of bagasse–henequen filaments because of the coupling of the hydroxyl gathering of fiber with 24 h soluble base treated composite. The recuperating of fiber additionally extended the interfacial bond between the bagasse–henequen fibrils and the polymer lattice material [16, 24, 11]. Subsequently, the most raised compressive quality was seen at 25% wt. fiber stacking. Furthermore,

Fig. 4 Compressive strength of untreated and alkali-treated composites

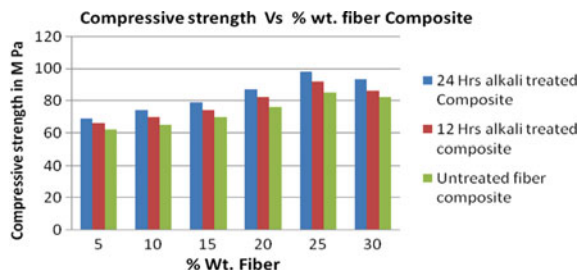
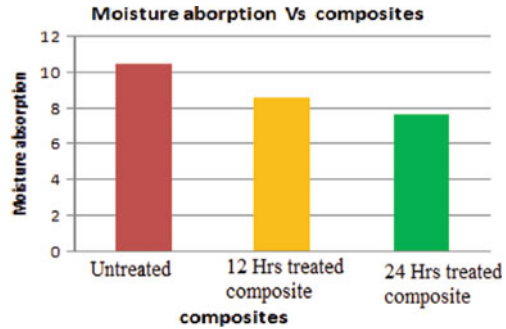


Fig. 5 Represents the absorption of moisture content by untreated and treated bagasse–henequen fiber composites



24 h of substance treatment mostly consumed the vacant spaces of fiber and alters lopsided strand, which gave the required outside surface [18, 25–32].

3.4 Moisture Content Test

Figure 4 shows the rate retention of dampness amount by natural fiber composite, soluble base-treated composites. The biostrands composite begins from the hydrophilic idea of the fiber display hydrophilic properties [7, 9]. Be that as it may, the antacid delicate hydroxyl bunches present among the atoms are separated, which at that point respond with water particles (H-OH) and move out from the fibril arrangement. Because of this, hydrophilic hydroxyl bunches are diminished and expand the strands dampness opposition property. [8, 14]. The rate assimilation of dampness amount by natural fiber composite is more when contrasted with the soluble base-treated composites [13, 33, 11] (Fig. 5).

3.5 Morphology

Figure 6 presents the images of the bagasse–henequen filaments, when compound treatment. Treated strands gang lower lignin content, due to the fractional expulsion of wax substances and oil particles spread the materials and distension of crystalline cellulose request [12, 34]. It is seen that the substance treatment has expelled the surface flotsam and jetsam from the fiber, the vast majority of the lignin and halfway expulsion of wax, oil and brings about unsympathetic surface and increment in the successful zone [9, 33]. This harsh surface encourages both mechanical interlocking and the better improvement in holding response because of the introduction of the hydroxyl gatherings to the network, along these lines expanding the fiber–framework bond [9, 19, 17].

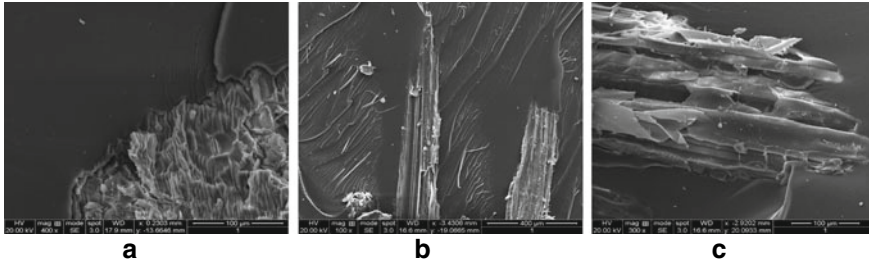


Fig. 6 a Untreated composite. b 12 h alkali treated. c 24 h alkali-treated composite

4 Conclusion

The work completed shows that the surface change of strands by synthetic treatment extensively improves the fiber quality, fiber–polymer blend interfacial bond, and subsequently the exhibition of the characteristic fiber composites. The tractable, compressive, and flexural property was seen to have improved for both 12 and 24 h soluble base-treated composites. The outcomes show that the malleable, compressive, and flexural quality of the composites expanded with increment in fiber stacking up to 25% and past 25% indicated an abatement in mechanical properties. Moderately abundance measure of fiber rests onto each other instead of being blended in with lattice at 30% fiber loads and generally less measure of fiber and fiber crack is seen at 20% fiber loads which additionally prompts diminish pressure move capacity. The rate retention of dampness amount by natural fiber composite is more when contrasted with salt-treated composites. Yet, with the concoction treatment or surface change of filaments, it was seen as conceivable to upgrade the properties of the composites with the expulsion and halfway lessening of polluting influences, hemicellulose, oils, waxes, and lignin from the surfaces of the strands, and yields harsh surface geology. Synthetic treatment improves the perspective proportion of filaments and builds the fortifying productivity of the fiber with the improvement of stress move from the lattice to stack bearing fibers which demonstrated structure SEM.

References

1. A.C. Karmarker, G. Hinrichen, Processing and characterization of jute fiber reinforced thermoplastics polymers. *Polym. Plast. Technol. Eng.* **30**(5–6), 609–618 (1991)
2. G.Venkatesha Prasanna, J.N. Kumar, K.A. Kumar, *Optimisation & Mechanical Testing of Hybrid Bio Composites Author links open overlay panel*
3. R.T. Morrison, R.N. Boyd, *Organic Chemistry* (Prentice-Hall, London, 1989)
4. A.M. Edeerozey, H.M. Akil, A.B. Azhar, M.Z. Ariffin, Chemical modification of kenaf fibres. *Mater. Lett.* **61**, 2023–2025 (2007)
5. H.U. Zaman, M.A. Khan, R.A. Khan, M.A. Rahman, L.R. Das, A. Mamun, Role of potassium permanganate and urea on the improvement of the mechanical properties of jute polypropylene composites. *Fibers Polym.* **11**(3), 455–463 (2010)

6. G. Venkatesha Prasanna, Modification and optimisation of mechanical properties bio fibers blended composites, *Internation. J. Engg. Technol.* **7**(2.33), 799–801
7. G. Venkatesha Prasanna, in *Influence of Fiber length and Chemical Treatment on the Mechanical Properties of Blended Composites*. (Springer, 2020)
8. M.S. Sreekal, S. Thomas, Effect of fibre surface modification on water-sorption characteristics of oil palm fibres. *Composites Science and Technology* **63**, 861–869 (2003)
9. G. Venkatesha Prasanna, G. Tirunagari Jayadeep, N. Poornabhodha, Chemical treatment, influence of fiber content and optimization of hybrid natural fibers reinforced composites. *Spring. Smart Innovation Syst. Technol. (SIST)*, 2190–3018. ISSN: 2019
10. G.Venkatesha Prasanna, *Impact of Fiber length & Chemical alteration on the Mechanical Properties of Blended Composites*. (Springer, 2020)
11. M.M.K. Rao, M. Rao, Extraction and of natural properties, Extraction and tensile fibers, Vakka, date, bamboo, composite structure. **7**, 288–295 (2007)
12. G.Venkatesha Prasanna, N.J. Kumar, C. Harish, Chemical treatment and analysis of mechanical properties of hybrid biocomposites. *Int. J. Mech. Prod. Eng. Res. Dev.* ISSN (P): 2249–6890; ISSN (E):, 2249–8001, Special Issue: 189–193 (2018)
13. K. John, S.V. Naidu, Effect of fiber content and fiber treatment on flexural properties of sisal fiber/glass fiber hybrid composites. *J. Reinf. Plast. Compos.* **23**, 1601–1605 (2004)
14. X. Colom, F. Carrasco, P. Pagès, J. Cañavate, Effects of different treatments on the interface of HDPE/lignocellulosic fiber composites. *Compos. Sci. Technol.* **63**, 161–169 (2003)
15. G. Venkatesha Prasanna, K. Venkata Subbaiah, A. Varada Rajulu, Chemical Resistance, impact, flexural, compressive properties and optimization of fibers of natural fibers reinforced blend composites. *Sch. J. Eng. Res.* **1**(6), 85–89 (2012)
16. H. Harani, S. Fellahi, M. Bakar, Toughening of epoxy resin using hydroxyl- terminated polyester. *J. Appl. Polym. Sci.* **71**, 29–38 (1999)
17. G. Venkatesha Prasanna, K. Kethamukkala, K.A. Kumar Surface modification, characterization & optimization of hybrid bio composites. *Springer. The smart innovation, syst. Technol.* ISSN 2190–3018 (2019)
18. D.N. Saheb, J.P. Jog, Natural fiber polymer composites: a review. *Adv. Polym. Technol.* **18**, 351–363 (1999)
19. J. Chakrabarty, M.M. Hassan, M. Khan, Effect of surface treatment on betel nut (areca catechu) fiber in polypropylene composite. *J. Polym. Environ.* **20**, 501–506 (2012)
20. A.K. Saha, S. Das, D. Bhatta, B.C. Mitra, Study of jute fiber reinforced polyester composites by dynamic mechanical analysis. *J. Appl. Polym. Sci.* **71**, 1505–1513 (1999)
21. R.M.N. Arib, S.M. Sapuan, M.M.H.M. Ahmad, M.T. Paridah, H.M.D. Zaman, Mechanical properties of pineapple leaf fiber reinforced polypropylene composites. *Mater. Des.* **27**(6), 391–396 (2006)
22. X. Zhiwei, H. Yudong, S. Yuanjun, Z. Chunhua, L. Li, “ Surface characteristics of rare earth treated CFs and interfacial properties of composites. *J. Rare Earths* **25**, 462–468 (2007)
23. D.E. Akin, G.R. Gamble, W.H. Morrison, L. Rigsby, Chemical and structure analysis of fibre and core tissues from flax. *J. Sci. Food Agric.* **72**, 155–165 (1996)
24. J. Seena, P. Koshy, S. Thomas, The role of interfacial interactions on the mechanical properties of banana fibre reinforced phenol formaldehyde composites. *Compos. Interfaces* **12**, 581–600 (2005)
25. M. Anguilar-Vega, C.A. Cruz-Ramos, Properties of henequen cellulosic fibers. *J. Appl. Polym. Sci.* **56**(10), 1245–1252 (1995)
26. X.R. Zhang, P. Zhao, X.Q. Pei, Q.H. Wang, Q. Jia, Flexural strength and tribological properties of rare earth treated short CFs/polyimide composites. *Ex. Poly. Lett.* **1**(10), 667–672 (2007)
27. G. Venkatesha Prasanna, K. Venkata Subbaiah, Modification, flexural, impact, compressive properties and chemical resistance of natural fibers reinforced blend composites. *Malays. Polym. J.* **8**(1), 38–44 2013
28. M.K. Alamgi, M.H. Monimul, R.M. Islam, A.K. Bledzki, *BioResources* **5**, 1618–1625 (2010)
29. R. Punyamurthy, D. Sampathkumar, R.P. Ranganagowda, B. Bennehalli, P. Badyankal, S.C. Venkateshappa, Surface modification of abaca fiber by benzene diazonium chloride treatment

- and its influence on tensile properties of abaca fiber reinforced polypropylene composites. *Ciencia Tecnologia dos Materials* **26**(2), 142–149 (2014)
30. M. Baiardo, E. Zini, M. Scandola, Flax fiber polyester composites. *Compos. A Appl. Sci. Manuf.* **35**(6), 703–710 (2004)
 31. G. Venkatesha Prasanna, in *Surface Modification, Characterization and Optimization of Hybrid Bio Composites* (Springer, 2020)
 32. M.M.K. Rao, R.A.V. Prasad, R. M.N.V. Babu, A.V.S.S.K.S. Gupta, Tensile properties elephant grass fiber reinforced Polyester composite. *Mater. Sci.* **42**, 2666–2672 (2007)
 33. S. Qianqian, C. Xianhua, Effect of rare earths surface treatment on tribological properties of CFs reinforced PTFE composite under oil lubricated condition. *J. Rare Earths* **26**(4), 584–592 (2008)
 34. K.L. Pickering, Y. Li, R.L. Farrell, M. Lay, Interfacial modification of hemp fiber reinforced composites using fungal and alkali treatment”. *J. Biobased Mater. Bioenergy* **1**, 109–117 (2007)
 35. D. Ray, B.K. Sarkar, A.K. Rana, N.R. Bose, The mechanical properties of vinyl ester resin matrix composite. *Compos. A. Appl. Sci. Manuf.* **32**, 119–127 (2001)
 36. G. Venkatesha Prasanna, T. Jayadeep, K.M. Reddy, Influence of fiber length & surface treatment on the mechanical properties of hybrid composites, Springer. *The smart innovation, syst. Technol.* ISSN 2190–3018 (2019)

Review on Processing and Characterization of Duplex Stainless Steels



Rayappa Shrinivas Mahale, V. Shamanth, and P. C. Sharath

Abstract Duplex stainless steels are a grade of stainless steels which consists of ferrite and austenitic phases in balanced proportions, hence they have excellent corrosion and mechanical properties. Duplex stainless steels find their major applications in oil and gas industries, chemical process plants, pulp and paper industry, and desalination plants. The widely used duplex stainless steel grades are 2205, 2304, and 2507. In this review, the preparation of DSS Nanopowders by planetary ball milling procedure, consolidation of metal powder by Selective Laser Sintering technique, and microstructural characterization techniques like Scanning electron microscopy, X-ray diffraction is elaborated.

Keywords Duplex stainless steels · Powder metallurgy · Scanning electron microscopy · Production of duplex stainless steels

1 Metallurgy of Duplex Stainless Steels

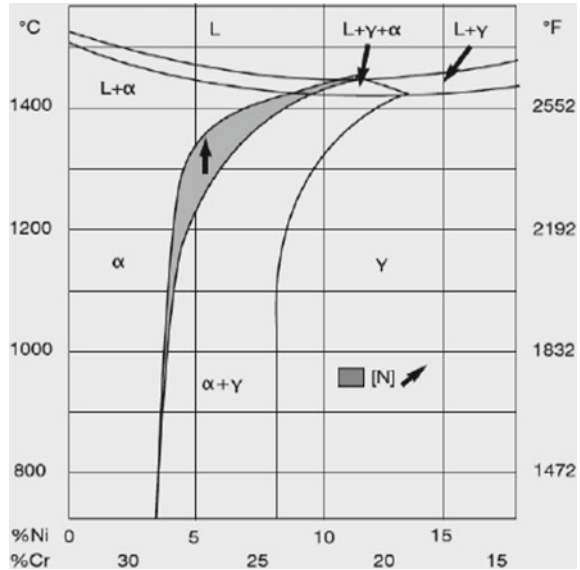
The characteristic feature of duplex stainless steel is its high chromium content (Approximately 20–25.4%) but low content of Nickel (1.4–7%) when compared to austenitic grades. For balancing the microstructure Molybdenum (0.3–4%) and Nitrogen additions are essential [1]. Nitrogen is strong austenitic enhancer and also it increases the strength. Manganese can also be added as a replacement to Nickel and it increases the solubility of nitrogen in the material.

R. S. Mahale (✉) · V. Shamanth
School of Mechanical Engineering, REVA University, Bengaluru, India
e-mail: rayappamahale@gmail.com

V. Shamanth
e-mail: shamanth.v@reva.edu.in

P. C. Sharath
School of Engineering and Technology, Jain Deemed to be University, Bengaluru, India
e-mail: pcsharath1988@gmail.com

Fig. 1 Fe–Cr–Ni ternary phase diagram with 68% iron. *Source* IMOA [8], p. 10



The metallurgical behavior of DSS can be studied in detail with the help of Fe–Cr–Ni ternary phase diagram plotted for 68% iron content (Fig. 1). From the above diagram, it is clear that Fe–Cr–Ni alloys solidify as ferrite (α) and some of the alloys transform into austenite (γ) when the temperature reaches 1000 °C. The ferrite–austenite phase balance in the microstructure can be studied with the help of multi-variable linear regressions [2].

$$\begin{aligned} Cr_{eq} &= \%Cr + 1.73\% Si + 0.88\% Mo \\ Ni_{eq} &= \%Ni + 24.55\% C + 21.75\% N + 0.4\% Cu \\ \%Ferrite &= -20.93 + 4.01 Cr_{eq} - 5.6 Ni_{eq} + 0.016T \end{aligned}$$

where T = Annealing temperature ranging from 1050 to 1150 °C.

Nitrogen addition can rapidly increase the rate of transformation of ferrite to austenite by increasing the temperature.

2 Processing of Duplex Stainless Steels

2.1 Continuous Casting Process

Continuous casting is widely used method to solidify 750 million tons of steel produced every year in the world. This method offers high level of productivity and improved quality compared to the conventional ingot casting method.

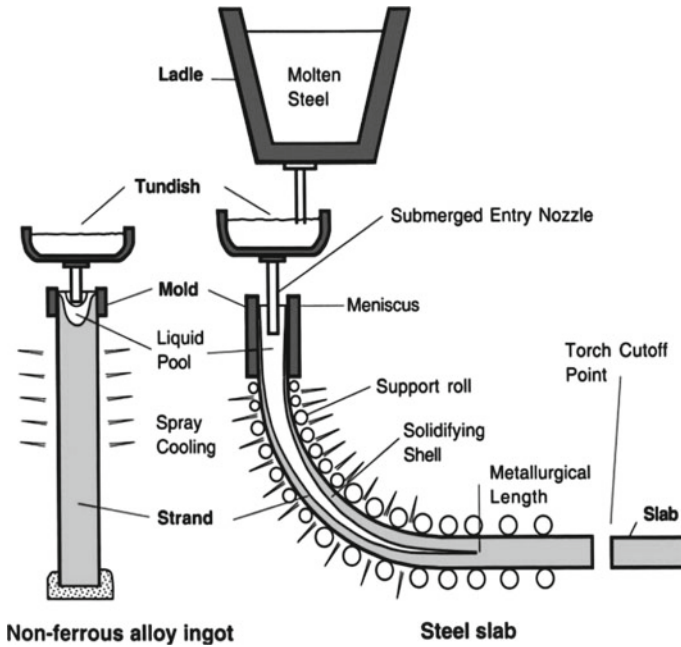


Fig. 2 Continuous casting process. *Source* Groover [9], p. 132

As mentioned in Fig. 2, the molten metal is poured with the help of temporary container (Tundish) which in turn dispense the molten metal to continuous casting molds. Steel begins to solidify at the outer regions when it travels through the water-cooled mold. Water sprayers are used to accelerate the cooling process. After cooling the metal is bent from vertical to horizontal orientation and finally cut into sections and fed continuously to the rolling mills.

Argon Oxygen Decarburization (AOD) is a refining process used in production of steels with low carbon and low silicon levels. The steel produced by this metal has more corrosion resistant, heat resistant, and malleable. AOD can be performed in three steps:

- (i) Decarburization
- (ii) Reduction
- (iii) Desulfurization.

In decarburization, oxygen gas is blown from the top of the furnace and oxygen with inert gas like Argon or Nitrogen is fed from the bottom surface. This process removes carbon by generating CO gas, 97% Cr is retained by the end of this process.

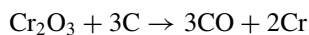
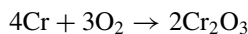
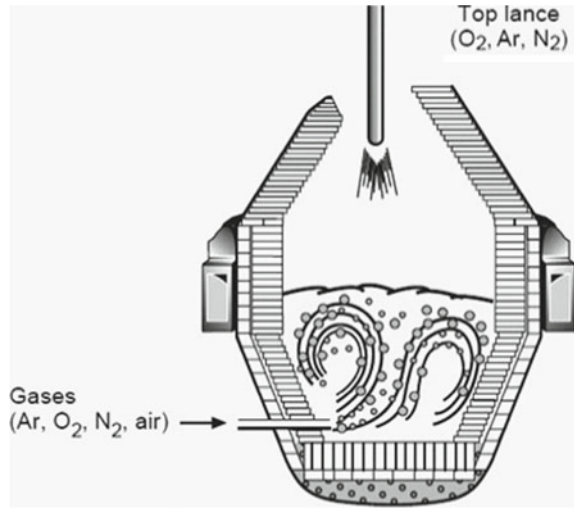
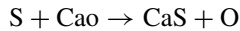


Fig. 3 Argon oxygen decarburization process.
 Source Raja [10]



Reduction will recover chromium from the slag. Reduction mix includes silicon alloy or Aluminum which are added to remove metallic oxides from the slag.

Desulfurization is achieved by adding high concentrations of lime to the slag. Oxygen is removed by adding sufficient quantities of Aluminum or silicon.



Vacuum Oxygen Decarburization (VOD) process is used particularly to obtain stainless steels with less carbon, hydrogen, and nitrogen levels. In this process, ladle is kept in the vacuum chamber with oxygen lancing facility. Oxidation of carbon over chromium leads to minimum chromium losses. Silicon is oxidized by carbon. Decarburization rate is controlled by controlling flow rate of oxygen. Aluminum and lime are added in sufficient proportions to desulphurize the melt.

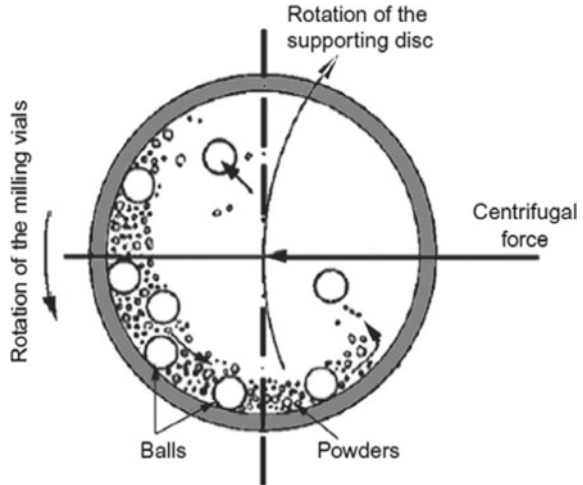
3 Production of Nanopowders by Ball Milling Technique

Ball milling is a dry and high energy technique which comes basically under Mechanical Alloying. This technique deforms the powder particles by the impact of milling balls which in turn plastically deforms the powder particles thereby creating the new surfaces and enables the particles to weld together [3].

The milling techniques are categorized as

1. Tumbler ball mill
2. Planetary ball mill
3. Vibratory ball mill

Fig. 4 Planetary ball mill.
 Source EL-Eskandarany [4]



4. Attrition ball mill
5. High energy mill.

The present study uses high energy dual planetary ball mill to consolidate metal powders [4]. The planetary ball mill consists of jar made of hard material such as tungsten carbide or stainless steel and sometimes nitrides and oxides are also used. The bowl cap is made of same material and it is used for the purpose of locking. Hard metal balls are kept in the jar and these are also made from tungsten carbide or stainless steel. The bowl is mounted on the disc which rotates in clockwise direction and the bowl will rotate in counterclockwise direction. During the rotation, the centrifugal force reaches up to 20 times gravitational acceleration [4]. Since the directions of rotation of disc and bowl are opposite, the centrifugal forces are also opposite. The milling stock and powder will alternately roll on the inner wall of the bowl and are randomly spread across the bowl at high speed.

4 Selective Laser Sintering

The process uses laser energy to convert metal powders into useful components; a loose polymer-coated metal powder is fused by laser energy, and then it is converted to required shape. A CAD model of the part is transformed numerically into thin slices, 75–250 μm [5].

Steps involved in SLS Process:

- Step 1. thin layer of heat fusible powder is deposited on top of the build cylinder.
- Step 2. layer of powder is fused by laser source as it traces the computer-generated slice.

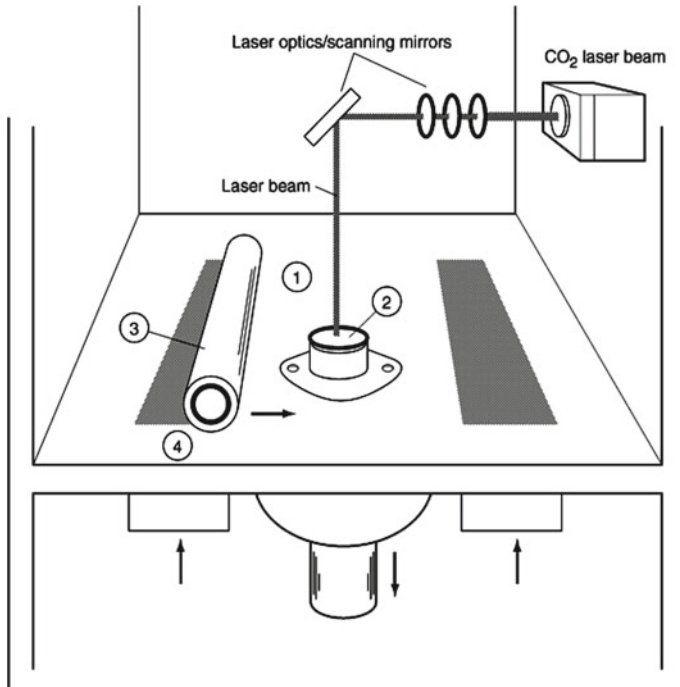


Fig. 5 Selective Laser Sintering Process. *Source* ASM Handbook [5]

- Step 3. the layer formed is held firmly by fused plastic coating on the $55\ \mu\text{m}$ particles. The fused layer is lowered by workstations and is reduced from 75 to $250\ \mu\text{m}$ and a new layer of powder is rolled on the top of fused layer.
- Step 4. laser fusing in turn bonds the particles together and support platform moves the part downward a layer and the process repeats until the part is completed fully, i.e., layer by layer.

The final product has a green strength of $2.7\ \text{Mpa}$ and is to be handled carefully. The unfused powder falls from fused part and that can be recycled further. The fused part is impregnated with acrylic resin and then dried at $50\ ^\circ\text{C}$. The dried part along with blocks of copper is heated in a graphite crucible by considering $70\% \text{N}_2$ and $30\% \text{H}_2$ up to $1120\ ^\circ\text{C}$.

At $300\ ^\circ\text{C}$ polymer burns out and the cross-linked polymer still remains to strengthen the part. At $700\ ^\circ\text{C}$ the iron particles are to be sintered and bonded [5]. At $1083\ ^\circ\text{C}$ copper melts and start to occupy the pores by capillary action. Finally, the part is removed when furnace turns to the room temperature. Selective Laser Sintering (SLS) and Selective Laser Reactive Sintering (SLRS) are the best examples of Solid Free-from Fabrication (SFF) technologies.

5 Microstructural Characterization

5.1 X-Ray Diffraction (XRD)

XRD is a most useful nondestructive technique to identify phases present in specimens, and this technique helps to study physical state of the sample such as texture, grain size, and crystal perfection [6]. XRD techniques are classified as single crystal and polycrystalline techniques. The information obtained can be categorized based upon position, intensity, and the shape of diffraction peaks.

X-Rays are a part of electromagnetic spectrum having wavelengths from 1 to 100 Å. Diffraction patterns may be analyzed by considering (i) diffraction angles that correspond to the obtained peak and (ii) relative intensities of peaks with a diffraction standard.

Angular distributions of the peak intensities obtained in the spectrum are determined using Bragg's equation:

$$n\lambda = 2d \sin \theta$$

where 'n' is an integer, 'λ' is the wavelength of radiation, 'd' is the spacing of lattice planes obtained for diffracted beam, and 'θ' is the angle of diffraction.

X-Rays are generated using diffractometer by accelerating electron beam on to the metal target contained in vacuum tube. The high energy electrons eject ground state electrons from metal target and thereby creating holes, and refilling of ground states will be possible by the emission of X-Rays.

$$eV = h\gamma,$$

where 'h' is Planck's constant. The X-Ray wavelength 'λ' is proportional to the reciprocal of this frequency and is given by

$$\lambda = c/v,$$

Fig. 6 X-Ray diffraction spectrum of 1040 steel having 0.4% C. *Source* Brandon and Kaplan [7]

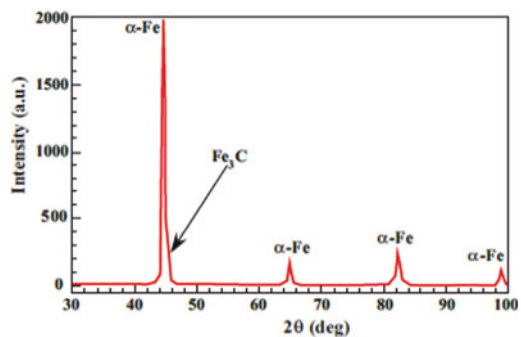
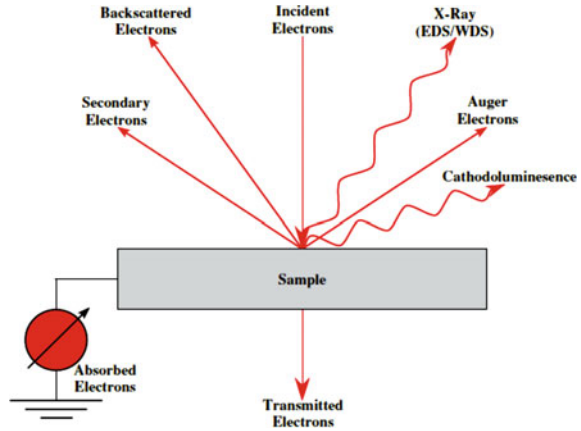


Fig. 7 Electron beam incident on a solid sample generating various signals. *Source* Brandon and Kaplan [7], p. 263



where ‘c’ is the light velocity in the medium through which the X-Rays propagate. The minimum wavelength on the accelerating voltage of X-Ray tube is given by

$$\lambda_{\min} = 1.243/V,$$

where ‘λ’ is measured in nanometers and ‘V’ is in kilovolts [7].

5.2 Scanning Transmission Electron Microscopy (STEM)

In SEM, the test surface of the specimen is bombarded with an electron beam to provide information for producing an image [6]. SEM reveals information regarding grain boundaries, mechanical deformations, inclusion and phase distributions, fracture surfaces and corrosion.

In SEM, microscope column is kept under vacuum. Some SEMs use separate vacuum pumping and degassing system if a Field Emission Gun (FEG) is used to generate the electrons [7]. SEM Signal detection system includes high energy backscattered electrons, low energy secondary electrons, characteristic X-Rays. The characteristic X-Rays may be detected either by Energy Dispersive Spectroscopy (EDS) or by Wavelength Dispersive Spectroscopy (WDS). In EDS, the exited photons are collected and the spectrum of energy-dependent photon intensity is analyzed to determine the chemical composition of the sample.

Figure 8 shows the different detectors used in STEM imaging. Bright Field detector counts the number of electrons per unit time as a function of the position of the electron beam focused on the sample. Electrons scattered to larger angles can be detected using High-Angle Annular Dark Field (HAADF) detector.

Fig. 8 STEM mode imaging using High-Angle Annular Dark Field (HAADF), Annular Dark Field (ADF), and Bright Field (BF) detectors. *Source* Brandon and Kaplan [7], p. 235

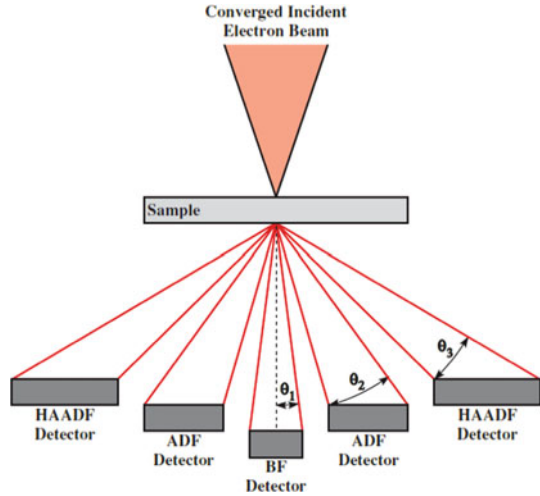
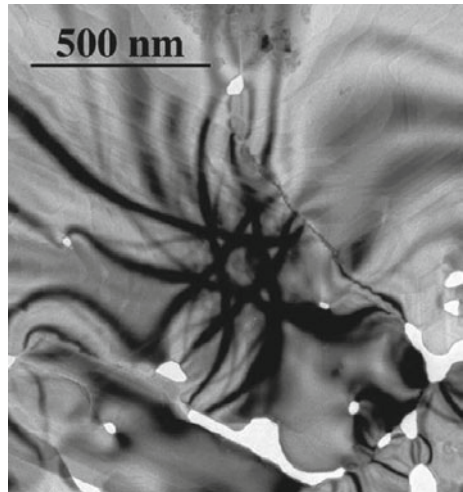


Fig. 9 Bright field micrograph. *Source* Brandon and Kaplan [7], p. 228



6 Conclusion

AOD and VOD processes eliminate the disadvantages of ladle metallurgy process. Vacuum converter technology is moreover useful in production of duplex grades with high nitrogen content.

Powder metallurgy technique can be adopted to manufacture products with complicated shape and geometry which can be incorporated mainly for mass production.

Fig. 10 HAADF STEM micrograph. *Source* Brandon and Kaplan [7], p. 236

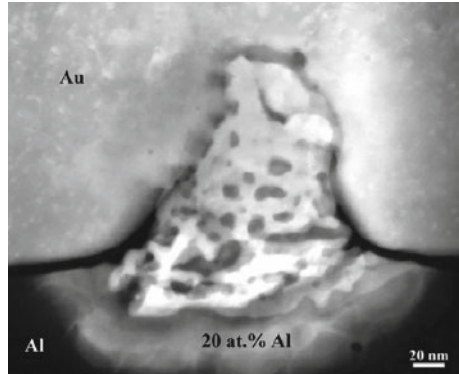
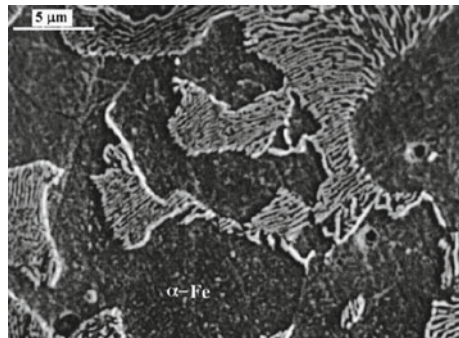


Fig. 11 SEM Micrograph of etched 1040 steel. *Source* Brandon and Kaplan [7], p. 228



Ball milling is used over the past five decades for particle size reduction and powder blending. It is the most powerful nanotechnology tool for preparing a wide range of crystalline materials used for characterization.

Sintering approach can be considered as one of the powerful technique in powder consolidation. Selective laser sintering uses laser energy to transform metal powders into useful parts. Near net shape components can be produced by prealloyed matrix powders. XRD and PXR techniques are widely used to study the diffraction patterns of polycrystalline samples. SEM provides three dimensional depth information of the specimen by recording two different images and the process is called as stereoscopic imaging.

References

1. V. Shamanth, K.S. Ravishankar, K. Hemanth, Duplex Stainless Steels: Effect of Reversion Heat Treatment. *Stainless Steels Alloy* (2019). <https://doi.org/10.5772/intechopen.80007>
2. Practical Guidelines for The Fabrication of Duplex Stainless Steels, 2nd edn. (International molybdenum association, London, 2009)

3. S. Seetharaman, in *Fundamentals of Metallurgy*. (Woodhead publishing Ltd, Cambridge Ltd., 2005)
4. M.S. EL-Eskandarany, in *Mechanical Alloying, Nanotechnology, Material Science And Powder Metallurgy* (Elsevier Inc., Amsterdam, 2015)
5. ASM Handbook, in *Powder Metal Technologies and Applications*, vol. 7. (ASM International, 1998)
6. ASM Handbook, in *Material Characterization*, vol. 10. (ASM International, 1992)
7. D. Brandon, W.D. Kaplan, in *Microstructural Characterization of Materials*, 2nd edn. (John Wiley & Sons, London, March 2008). ISBN: 978-0-470-02785-1
8. IMO, in *Practical Guidelines for the Fabrication of Duplex Stainless Steel* (1999)
9. M.P. Groover, in *Fundamentals of Modern Manufacturing: Materials, Processes, and Systems*, 5th edn. (John Wiley & Sons, London, October 2012). ISBN: 9781118393673
10. B.V.R. Raja, in *An Overview on Refining Technologies for Stainless Steels* (Steel world, 2008)

Prediction of Wear Characteristics of Polymer Composites by ANN Modified by GA



V. L. Raja, K. Muralidharan, and R. Dhanasekaran

Abstract Wear characteristics of any material are highly improved by reinforcing it with particulates. Wear resistance enhanced materials are very much essential in industries today. To reduce the cost of the composites, naturally available materials are preferred as reinforcements. Industrial waste in the powder form is reinforced with Nylon in various concentrations and wear tests were conducted at different parameters. The specific wear rate was found by experiments. Artificial Neural Network which is equivalent to biological network is usually used to predict the characteristics of the materials. An artificial neural network was developed to predict the wear rate of these composites. To get precise results, various techniques are being followed by researchers in developing the architecture of the neural network. The architecture of the developed network was optimized by applying genetic algorithm to obtain high accuracy in the predicted values. The neural network developed was able to predict the wear rates with more than 98% accuracy.

Keywords Nylon · Particulate reinforcement · Wear · ANN · GA

1 Introduction

Nylon 66 is found to be suitable for various industrial applications where wear and tear of the components is involved. Various studies have been made on the Nylon 66 composites reinforced with fibers.

V. L. Raja (✉)

Department of Mechanical Engineering, Muthayammal Engineering College, Rasipuram Tamil Nadu, 637408, India

e-mail: vlraja73@gmail.com

K. Muralidharan

Department of Mechanical Engineering, Sona College of Technology, Salem 636005, India

R. Dhanasekaran

Department of Mechanical Engineering, Gurunanak Institute of Technology, Hyderabad, India

© Springer Nature Singapore Pte Ltd. 2021

G. S. V. L. Narasimham et al. (eds.), *Recent Trends in Mechanical Engineering*,

Lecture Notes in Mechanical Engineering,

https://doi.org/10.1007/978-981-15-7557-0_21

Fly ash is a by-product of any combustion process and is a land pollutant. The production of fly ash could not be avoided, and hence the researchers have found a way to reduce the problem by using it as an reinforcement. Fly ash was reinforced along with graphite by VenkatPrasat et al. [1], in aluminum matrix and the composites showed enhanced wear resistance. Fly ash improved the mechanical and heat-resistant properties of Nylon 6, and the increase was found to be more when large-sized particles were used by Bose and Mahanwar [2].

Artificial neural network (ANN) is a computational simulation technique that could be considered as equivalent to biological network. It is used to predict various properties of different materials. Wang et al. [3] used it to predict the results of abrasion and mechanical properties of rubber composites. The predicted results were found to be in good agreement with the experiment results. Çay et al. [4] predicted the performance of an engine run on alternative fuel, which was in close agreement with the experimental results. Velten et al. [5] used ANN to predict the wear volume of polymeric material-based bearings using ANN and found that though the prediction quality was good there was still scope of improvement. The application of this technique in polymer composites is well reviewed by Zhang and Friedrich [6]. ANN was applied by Zhu et al. [7] to predict tribological properties of carbon fiber and TiO₂ particle-reinforced polytetrafluoroethylene composites. They found that the predicted results were generally in good agreement with experimental data but friction coefficient held a closer correlation with the input parameters than wear volume loss and suggested that improved results could be obtained from a further optimization of the network and an increasing availability of measurement data. Of late, various modifications such as genetic algorithm (GA) was introduced in the development of the network to get more precise results with less data sets. Mohebbi et al. [8] used GA to optimize the number of neurons, the learning rate, and the momentum rate in their developed network to predict the liquid densities of refrigerant mixtures and found that the predicted results were good. Panda et al. [9] used shuffled frog-leaping algorithm as the training algorithm and applied it to channel equalization, which yielded better results than the contemporary equalizers. Reihanian et al. [10] used GA and ANN to predict the stress and optimum sintering temperature of compacted iron powder. Esmaeili and Dashtbayazi [11] used GA-modified ANN to predict the characteristics of Al/SiC nanocomposites where GA was applied to find out the optimized input values. Essa e tal. [12] used ANN with Harris Hawk optimizer to predict the productivity of solar still. Pazhamanni [13] employed ANN to predict the tensile strength of 3D printed models and found the error between the predicted and experimental results was 5%.

From the literature review, it is evident that studies on the development of an ANN that is capable of predicting the wear characteristics of the fly ash-filled Nylon 66 are scarce. Also in general, the training algorithm, learning rate, etc. are fixed in the early studies which do not have the ability to find the optimized results accurately and are also time consuming. In this study, a novel attempt has been made to develop a GA-modified ANN to predict the wear properties accurately and time efficiently for Nylon 66 reinforced with fly ash particles

2 Experimental Procedures

2.1 Experimental Procedures

Though the materials used and the experimental procedures were followed according to the previous study [14, 15], the testing parameters were different on two counts namely sliding velocity and applied normal load. The tests were performed at three sliding velocities of 1, 3, and 6 m/s and at three normal loads of 10, 20, and 30 N.

2.2 Methodology of ANN and GA

Basically, ANN has three types of layers connected by neurons: input, hidden, and output layers. Inputs are given in the input layer, and the output is obtained from the output layer. The hidden layer is the one where the computation takes place and depending on the number of layers and number of neurons, the prediction quality will be better. Not all the networks could have the same architecture. It varies from material to material, property to property, and when applied to composites, from composition to composition. So, it is necessary to develop a network that will predict closer to the accurate value, for every individual material or composite.

The neural network developed is trained by an algorithm using experimental data. Then it is used to predict the output for new input values. The predicted values are checked with experimental values which have not been used for training. While training the network, optimum learning rate and optimum strength of the interconnected neurons are calculated and given to get quality prediction. There are different algorithms by default to train the network. These algorithms have definite network structure that will not be suitable for all materials or composites. So proper modification is required in the architecture of the network and algorithm selected, and at the same time, the other factors such as learning rate should be optimized.

GA, in general, works as follows. In the first step, an initial random solution or population is created. The fitness values for these solutions are determined. The chromosomes are selected for crossover based on the fitness values. Then, crossover of the chromosomes is made and then mutation takes place in a random manner. Then, again the fitness values for the new population are determined. These steps continue until the desired objective such as the best solution or better fitness values are reached.

In this study, 80% data were used to train the developed network. Using these data, the network was trained by six different algorithms which are used in different cases. The details of the various algorithms used and other data are given in Table 1. The remaining 20% of data were used for validation. By giving these 20% data as input, the output was predicted by the trained network. The error which is fitness value, was calculated for the results from all the algorithms, and the algorithm that had least error was selected as the best algorithm.

Table 1 Details of the variables used in GA

Number of neurons	1–50
Number of hidden layers	1–10
Training algorithms	Trainlm, trainbfg, trainrp, trainscg, traincgf, traincgp
Chromosome length	2
Population size	10
New children	5
Mutation rate	0.2
Mutated chromosomes	2

Then, the architecture of that best algorithm was optimized using GA. First, for the initial random population the number of layers was considered to be from 1 to 10 and number of neurons to be from 1 to 50. The network architecture initially was taken as one hidden layer and one neuron. The network was trained with the training data and then the values were predicted. The fitness solutions for these values are given as follows:

$$\text{Fitness}(\text{HL}, N) = \text{EV} - \text{PV} \quad (1)$$

where HL is the number of hidden layers, N the number of neurons, PV the predicted value, and EV the experimental value. As far as the PV and EV are closer, the fitness value is high. Then, the iteration of the GA begins with three factors, selection, crossover, and mutation. After calculating the fitness value based on the initial population, the best five sets of chromosome those have the high fitness value are selected for crossover. The gene of the first chromosome was crossed over to second chromosome and its gene to third chromosome and so on. The gene of the fifth chromosome was crossed over to the first chromosome. The mutation rate was selected as 0.2 as per the previous study and the present problem. So, the number of mutations in a generation was $0.2 \times 5 \times 2 = 2$. These mutations happen in a random manner in which both genes, that is, the number of layers and the number of neurons, have the chances of being muted. The number of neurons was changed between 1 and 50 and the number of layers was changed from 1 to 10. At the end of this step, new generation of population of 10 chromosomes comprising five muted chromosomes and five selected best chromosomes, which were later muted, was generated.

Initially, the error value, which is the fitness value of GA, was given as 2. The target error value was fixed as 5×10^{-6} , which means the predicted value and the actual value were very close. When the fitness value reached 5×10^{-6} , the iteration was stopped and the number of neurons and the number of hidden layers found at that step were taken as optimized set. Using this architecture, the neural network computed the value for the given input values. A unique code was written to execute this logic in Matlab.

3 Results and Discussion

The total number of experimental data set was 54, which was randomly divided into 43 (80%) training data and 11 (20%) validating data sets. Table 2 gives the average error of the network trained by eight benchmark algorithms.

From Table 2, traincgp algorithm, which is with least mean error among eight algorithms, is found to be the best algorithm. The architecture of the network trained by this algorithm is modified using GA. The architecture of the modified network is given in Table 3.

The developed code is run and the wear rates are evaluated using Matlab which is shown in Fig. 1. The relationship between the predicted and the experimental results is shown in Fig. 2. The validity of the model has also been checked from Table 4 where a comparison is made between the predicted and measured wear rates of the composites and the percentage of error is calculated. A very good agreement can be noted between the experimental and the proposed network responses. These results

Table 2 Fitness values of different algorithms

Trainlm	Trainbfg	Trainrp	Trainscg	Traincgf	Traincgp
0.000036	0.000033	0.000026	0.000039	0.000024	0.000018

Table 3 Results of the genetic algorithm

No. of iterations	No. of layers	No. of neurons
5	2	2

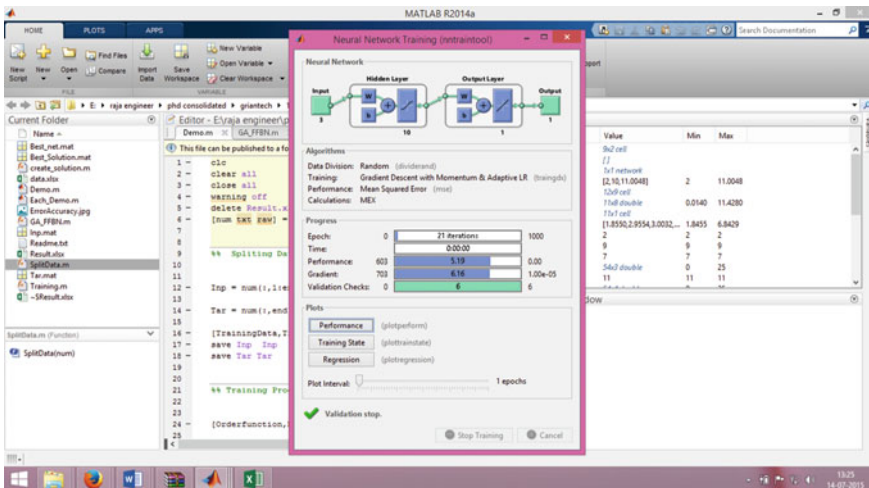


Fig. 1 Code run in matlab to predict the wear rates

Fig. 2 Relation between the predicted and experimental wear rates

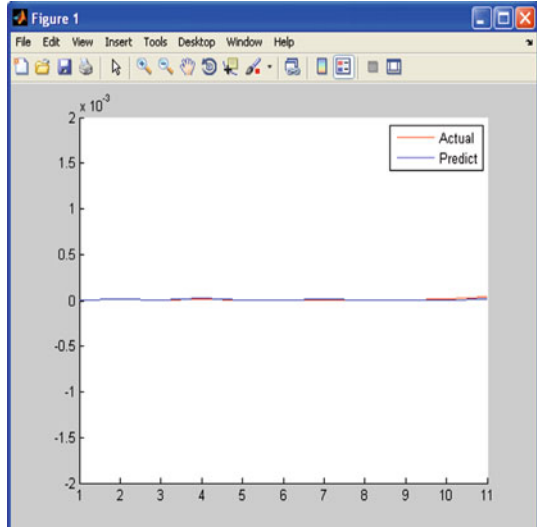


Table 4 Comparison between predicted and experimental wear rates

Data no	Experimental value	Predicted value	Error % (absolute)
1	0.00000518	0.00000518316	0.0610039
2	0.0000194	0.00001939934	0.003402062
3	0.00001965	0.000019652	0.0101781
4	0.00002834	0.00002725923	1.696436133
5	0.00000658	0.00000658013	0.001975684
6	0.00001204	0.00001204467	0.038787375
7	0.00001635	0.00001634970	0.001834862
8	0.00001524	0.00001524008	0.000524934
9	0.00003825	0.00003825142	0.003712418
10	0.0000014	0.0000139324	0.482857143
11	0.00006245	0.0000625247	0.119615693

indicate the high capability of the ANN in predicting the wear rates of the developed network.

4 Conclusions

Nylon 66 was reinforced with fly ash in different weight fractions from 5 to 25% in steps of 5%. The wear tests were conducted at three velocities and three normal loads keeping the sliding distance constant. A GA-modified ANN was developed and

trained to predict the wear rate of the composites. The predictions made with GA-modified ANN completely agree with the experimental results with the maximum error being 1.7%.

References

1. S. VenkatPrasat, N. Radhika, B. Anandavel, L. Arun, N. Praveen, Influence of parameters on the dry sliding wear behaviour of aluminium/fly ash/graphite hybrid metal matrix composites. *Eur. J. Sci. Res.* **53**, 280–290 (2011)
2. S. Bose, P.A. Mahanwar, Effect of flyash on the mechanical, thermal, dielectric, rheological and morphological properties of filled nylon 6. *J. Miner. Mater. Charact. Eng.* **3**, 65–89 (2004)
3. B. Wang, J.H. Ma, U.P. Wu, Application of artificial neural network in prediction of abrasion of rubber composites. *Mater. Des.* **49**, 802–807 (2013)
4. Y. Çay, A. Çiçek, F. Kara, S. Sağiroğlu, Prediction of engine performance for an alternative fuel using artificial neural network. *Appl. Therm. Eng.* **37**, 217–225 (2012)
5. K. Velten, R. Reinicke, K. Friedrich, Wear volume prediction with artificial neural networks. *Tribol. Int.* **33**, 731–736 (2000)
6. Z. Zhang, K. Friedrich, Artificial neural networks applied to polymer composites: a review. *Compos. Sci. Technol.* **63**, 2029–2044 (2003)
7. J. Zhu, Y. Shi, X. Feng, H. Wang, X. Lu, Prediction on tribological properties of carbon fiber and TiO₂ synergistic reinforced polytetrafluoroethylene composites with artificial neural networks. *Mater. Des.* **30**, 1042–1049 (2009)
8. A. Mohebbi, M. Taheri, A. Soltani, A neural network for predicting saturated liquid density using genetic algorithm for pure and mixed refrigerants. *Int. J. Refrig* **31**, 1317–1327 (2008)
9. S. Panda, A. Sarangi, S.P. Panigrahi, New training strategy for neural network using shuffledfrog-leaping algorithm and application to channel equalization. *Int. J. Electron. Commun.* **68**, 1031–1036 (2014)
10. M. Reihanian, S.R. Asadollahpour, S. Hajarpour, K.H. Gheisari, Application of neural network and genetic algorithm to powder metallurgy of pure iron. *Mater. Des.* **32**, 3183–3188 (2011)
11. R. Esmaceli, M.R. Dashtbayazi, Modeling and optimization for microstructural properties of Al/SiCnanocomposite by artificial neural network and genetic algorithm. *Expert Syst. Appl.* **41**, 5817–5831 (2014)
12. F.A. Essa, M. Abd Elaziz, A.H. Elsheikh, An enhanced productivity prediction model of active solar still using artificial neural network and Harris Hawks optimizer. *Appl. Therm. Engg.* **170**, 115020 (2020)
13. R.V. Pazhamannil, P. Govindan, P. Sooraj, *Prediction of the tensile strength of polylactic acid fused deposition models using artificial neural network technique* (Mater, Today, 2020)
14. V.L. Raja, A. Kumaravel, Studies on physical and mechanical properties of silica fume filled polymer composites for mechanical components. *Polym. Polym. Comp.* **23**(6), 427–434 (2015)
15. V.L. Raja, A. Kumaravel, Comparative study on the wear properties of fly ash and silica fume filled nylon composites. *App. Mech. Mat.* **592–594**, 1277–1284 (2014)

Experimental Investigation of Mohair Fibrous Composite Material on Mechanical Properties



K. Amarnath, R. Venumadhav, and E. Sreedhar

Abstract Due to the scarcity of regular materials, Global R&D are mainly focusing on an alternative to regular materials and composite materials had found the place as alternative materials, due to its high specific strength, high resistance to fatigue and corrosion, integration in function, low manufacturing and maintenance costs, and mainly due to its greenhouse nature. In this paper, an experimental study was conducted on newly developed natural fiber using mohair epoxy composite biodegradable material by investigating its mechanical properties. Natural fiber Mohair is taken in different compositions with commercial epoxy LY556 and HY951 hardener in different weight percentages for making composite materials to find the properties of it.

Keywords Mohair · Mechanical properties of natural fiber · Goat hair · Natural composite materials

1 Introduction

In a rapid pace of global development, many of the conventional materials are exhausting which cannot be replaced by the other materials, but composite materials can fulfill the needs by providing the desired product properties with a good surface finish at lesser cost and weight with eco-friendly nature in all the fields of manufacturing units [1, 2]. These composite materials are high in resistance to fatigue, stiffness to weight ratio, and corrosion degradation. These materials have directional tailoring capabilities in the manufacturing process which will save time and manufacturing operation cost. Many research scholars showing interest in fibers as it has more aspect ratio of length to a diameter which is less in discontinuous fibers. Fibre-reinforced matrix will have high specific strength and modulus which can be known by fiber properties like shape, orientation, composition, and properties

K. Amarnath (✉) · R. Venumadhav · E. Sreedhar

Department of Mechanical Engineering, Kamala Institute of Technology and Science, Huzurabad, Karimnagar, Telangana, India

e-mail: amarnath.kandagatla@gmail.com

© Springer Nature Singapore Pte Ltd. 2021

G. S. V. L. Narasimham et al. (eds.), *Recent Trends in Mechanical Engineering*,

Lecture Notes in Mechanical Engineering,

https://doi.org/10.1007/978-981-15-7557-0_22

of resin. So, appropriate adhesive property of the resin system will give the higher microcracking strains in laminates so that resin will deform with the same extent as fiber [3–5]. This leads to the invention of polymers in twentieth century which have poor biodegradability that increases the demand for new composite materials based on biodegradable resources such as natural fibers like Hemp, Sisal, Coconut coir, Animal hair, etc. Several literatures are published on natural biodegradable resources based on plant fibers; however, animal fiber materials have been rarely reported [6, 7]. Animal hair is very strong due to Cortex Keratin property which comprises of iron (20–220 ppm), copper (10–20 ppm), zinc (190 ppm), iodine, and several essential elements [8–10]. In this paper, experimental investigation of natural fiber from animal hair (mohair) composite material is done (Figs. 1 and 2).

Fig. 1 Influence of fiber and resin properties

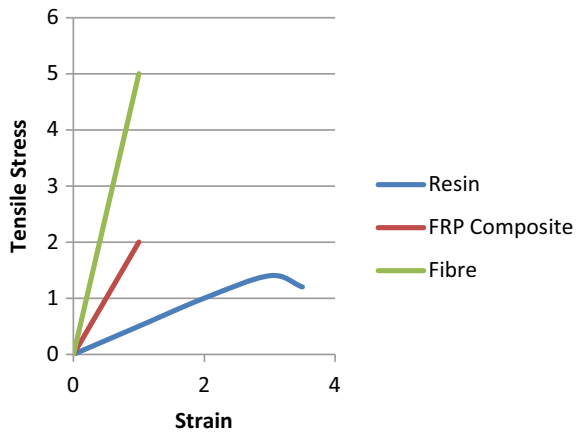


Fig. 2 Stress—strain graph of PMC composites in PMC composites

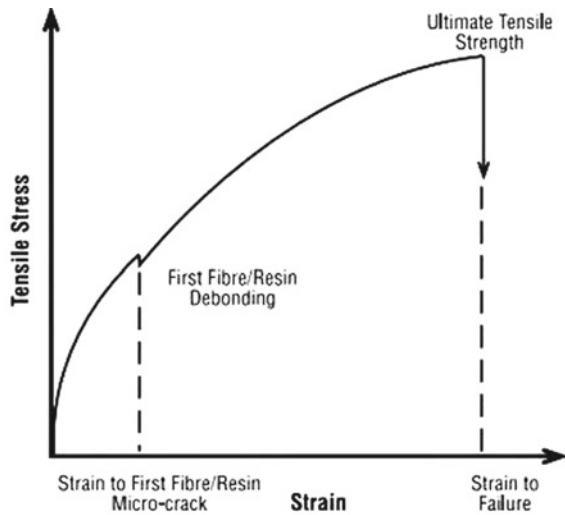


Table 1 wt% of different specimens of goat hair

Specimen	Goat hair wt%	Weight	Epoxy %	Epoxy weight
Composite-1	20	53	80	212
Composite-2	30	80	70	187
Composite-3	37.5	100	62.5	166
Composite-4	40	107	60	160
Composite-5	50	133	50	133
Composite-6	60	166	40	110

2 Experimental

2.1 Material and Method

In this paper, as per the ASTM standards, specimens are prepared by using goat hair which are natural fibers. Fiber length varies from 25 to 135 mm, bulk 1.18–1.31 gm/cc, diameter lies from 75 to 115 microns, tensile strength 85–110 MPa, moisture absorption around 7%, and elongation at shear between 30 and 60%, and all the composite plate of materials are prepared based on wt% of fiber mixed with epoxy and hardener in 10:1 ratio. In this investigation, six specimens of natural composite materials are prepared mainly consisting of goat hair.

2.1.1 Composite Preparation

Six composite specimens are prepared as per the ASTM standards by using goat hair with five layers, each specimen with a different wt%, formulated below in the table under compression molding method which will uniformly distribute compactness and dimensional accuracy overall to the specimen (Table 1).

3 Investigation of Mechanical Properties

Hair structure, anisotropic, hair size, etc., will enhance the tensile strength, flexural modulus, and stiffness properties of the composites. In this paper, different mechanical properties of goat hair fibrous composites are investigated and tabulated.

Table 2 Tensile strength bar chart

Composites	Ultimate strength (MPa)	Young’s modulus (MPa)
Composite-1	27	421
Composite-2	29	452
Composite-3	33	515
Composite-4	32	49
Composite-5	28	436
Composite-6	27	429

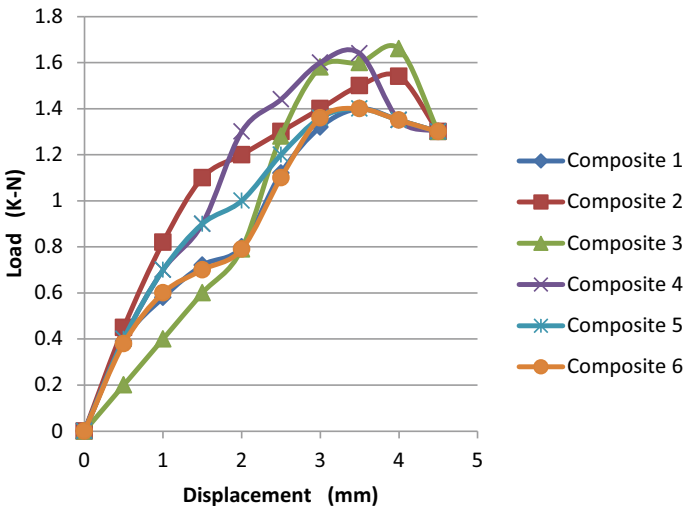


Fig. 3 Load versus displacement graph

3.1 Tensile Strength

Tensile testing specimens are prepared as per the ASTM D638-03 standards. Investigation is conducted on six different wt% specimens and the results are tabulated below. It is observed from the table that specimen with 37.5 wt% of goat hair has the maximum ultimate strength and Young’s modulus value (Table 2; Figs. 3 and 4).

3.2 Flexural Strength

Test specimens are prepared as per the ASTM D790 standards in which specimens are subjected to three points bending for every 0.7-mm increment in displacement

Fig. 4 Stress versus strain graph

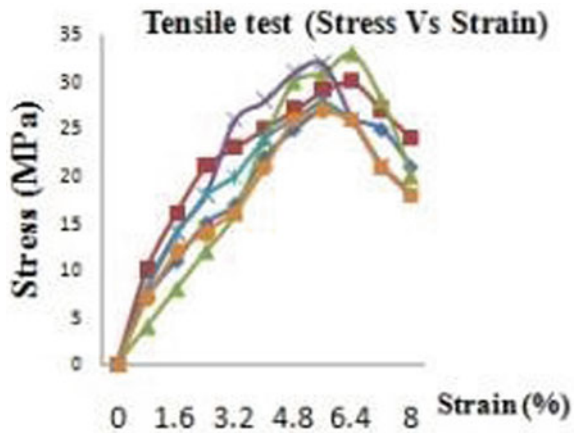


Table 3 Flexural strength

Composites	Flexural strength (MPa)
Composite-1	1.8
Composite-2	2
Composite-3	2.3
Composite-4	2.2
Composite-5	1.9
Composite-6	1.85

and values obtained are tabulated below. It is observed from the table that specimen with 37.5 wt% of goat hair has the maximum value (Table 3; Fig. 5).

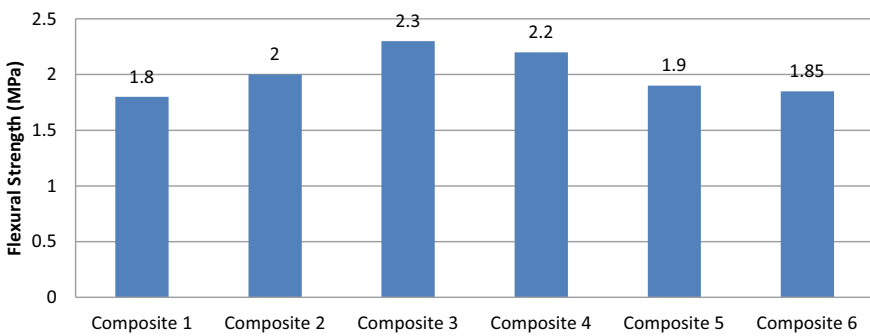
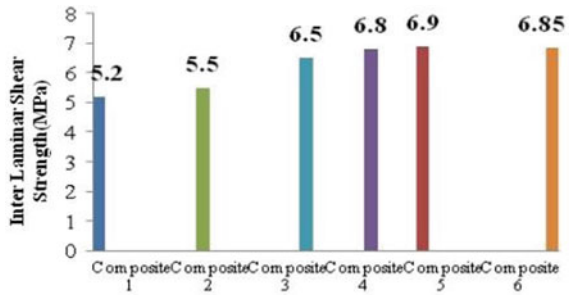


Fig. 5 Flexural strength bar graph

Table 4 Inter-laminar shear strength test values

Composites	ILSS (MPa)
Composite-1	5.2
Composite-2	5.5
Composite-3	6.5
Composite-4	6.8
Composite-5	6.9
Composite-6	6.85

Fig. 6 Inter-laminar shear strength test bar graph



3.3 Inter-laminar Shear Strength (ILSS) Test

ILSS test of goat hair specimens are prepared as per the dimensions of ASTM D2344 Standards and every 0.2-mm increment in displacement values are tabulated as shown below. It can be observed that specimen 5 with 50% of goat hair has given the maximum value in the test (Table 4; Fig. 6).

4 Result and Discussion

Test specimens are prepared as per ASTM D256 standards, in which all the specimens are subjected to IZOD tests and impact energy of each specimen is calculated as shown below in the table. It can be observed that specimen 5 with 50% goat hair has high impact value (Table 5; Fig. 7).

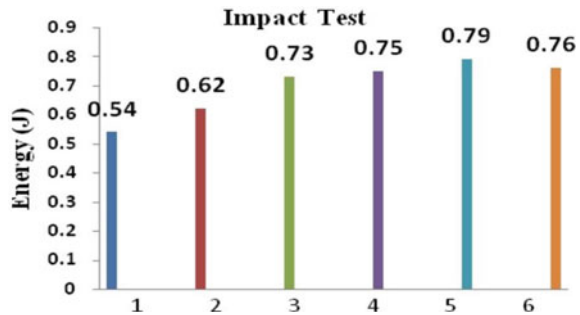
5 Conclusion

As per the standards, experimental investigation of mechanical properties was carried out on composite material prepared from goat hair which is a natural fiber as consolidated results are tabulated below. From the results, it can be observed that

Table 5 Impact test values

Composite 1	Specimen 1.1	Specimen 1.2	Specimen 1.3	Specimen 1.4	Specimen 1.5	Mean (Joules)
	0.51	0.51	0.55	0.56	0.57	
Composite 2	Specimen 2.1	Specimen 2.2	Specimen 2.3	Specimen 2.4	Specimen 2.5	
	0.58	0.6	0.62	0.64	0.66	
Composite 3	Specimen 3.1	Specimen 3.2	Specimen 3.3	Specimen 3.4	Specimen 3.5	
	0.7	0.71	0.73	0.76	0.75	
Composite 4	Specimen 4.1	Specimen 4.2	Specimen 4.3	Specimen 4.4	Specimen 4.5	
	0.71	0.72	0.74	0.78	0.8	
Composite 5	Specimen 5.1	Specimen 5.2	Specimen 5.3	Specimen 5.4	Specimen 5.5	
	0.75	0.77	0.79	0.81	0.83	
Composite 6	Specimen 6.1	Specimen 6.2	Specimen 6.3	Specimen 6.4	Specimen 6.5	
	0.71	0.73	0.75	0.8	0.81	

Fig. 7 Impact test bar graph



composite 1 with wt% fiber 20% got the least mechanical properties values compared to the remaining specimens. It can also be observed that composite 3 with wt% fiber 37.5% got maximum values for all the mechanical properties on average compared to other specimens prepared using the same fiber with different wt% compositions. Since the specimen prepared with wt% of 37.5% goat hair, natural fiber can be selected for future experiments.

Specimen	Tensile strength (MPa)	Young's modulus (MPa)	Flexural strength (MPa)	ILSS	Impact strength (Joules)
Composite-1	27	523	1.8	5.2	0.54
Composite-2	29	547	2	5.5	0.62

(continued)

(continued)

Specimen	Tensile strength (MPa)	Young's modulus (MPa)	Flexural strength (MPa)	ILSS	Impact strength (Joules)
Composite-3	33	598	2.3	6.5	0.73
Composite-4	32	569	2.2	6.8	0.75
Composite-5	28	598	1.9	6.9	0.79
Composite-6	27	569	1.85	6.8	0.76

References

1. K.N. Bharath, M. Pasha, B.A. Nizamuddin, Characterization of natural fiber-matrix composites at different operating conditions. *J. Indus. Text.* 1–22 (2014)
2. C. Helepciuc, A natural material used in civil engineering. *ScienceDirect* 63(67) (2017)
3. N. Štirmer, B. Milovanović, J.M. Sokol, Cement composites reinforced with sheep's wool, in *ScienceDirect (Department of Materials, University of Zagreb, Croatia)*
4. C. Sanjeevmurthy, G. Rangasrinivas, Tensile properties of natural fiber-hybrid composites. *Int. J. Mod. Eng. Res.* 2(2) (2012)
5. B. Stalin, Mechanical performance of goat hair fiber with modified composites. *Int. Conf. Eng. Solutions* (2016)
6. Y. Ou, Y. Yao, G. Li. B. Mobasher, Mechanical characterization of the tensile properties of glass fiber and its reinforced polymer (GFRP). *MDPI J.* (2016)
7. K. Krishan, in *Composite Materials Science and Engineering*. (Springer) ISBN 0-387-98409-7
8. R. Kumar, Mechanical properties of natural fiber composite. *Sci. Park Res. J.* 3(4) (2013)
9. A. Kumar, *A study on mechanical behaviour of hair fiber reinforced epoxy composites*. B.Tech thesis (NIT Rourkela, 2014)
10. K. Amarnath, P. Surendernath, V. Kumar, Experimental investigation to optimize process parameters in drilling operation for composite materials, lecture notes in mechanical engineering ISBN 978-981-15-1123-3 (2019)

FE Analysis of Superplastic Forming Complex Shapes in Aluminum-Coated Magnesium Alloys



J. Kandasamy

Abstract Magnesium alloys known for its lightweight and high stiffness serve the aerospace and automotive industries. The flammable property of magnesium alloy restricts its applications under certain circumstances. To overcome this limitation and to reduce the intensity of flammability, aluminum is coated on AZ31B magnesium alloys. Near net shape forming of industrial products with intricacies in geometry are simulated in MSC.MARC/MENTAT on aluminum-coated magnesium alloys. Investigations on the forming time and final thickness distribution on the product for different D/H ratios are conducted. The gas pressure profile for optimum time is obtained for improved thickness distribution. The thickness distribution conserves the material for a given target strain rate and uniformity in thickness of the product is observed.

Keywords SPF simulation · Al-coated mg alloys · Complex shapes

1 Introduction

Gas forming is an advanced method of complex thin-walled part production adopted in the aerospace and automotive industry. To increase the hot forming ability and improve the mechanical properties of the final products, the utilization of superplasticity effect is desired. Most industrial superplastic thermoforming consists of forming superplastic sheet into a variety of hollow products of complex and styled shapes (thin-walled vessels, covers, and panels) into dies of appropriate shapes. The thickness distribution in the product and the forming time are of the utmost industrial importance. Superplasticity is the ability of fine-grained polycrystalline materials to exhibit neck-free elongations prior to fracture while deforming at elevated temperatures. It is characterized by a high sensitivity of stress to strain rate with a generally

J. Kandasamy (✉)

Department of Mechanical Engineering, Maturi Venkata Subba Rao Engineering College,
Nadergul, Telangana 501510, India

e-mail: professorkandan@gmail.com

© Springer Nature Singapore Pte Ltd. 2021

G. S. V. L. Narasimham et al. (eds.), *Recent Trends in Mechanical Engineering*,

Lecture Notes in Mechanical Engineering,

https://doi.org/10.1007/978-981-15-7557-0_23

low value of flow stress within the deforming material, usually depicted by a logarithmic relationship. It is a viable technique to form complex-shaped structures, has exceptional formability and significantly superior dimensional tolerance. Fine-grain size to the order of 10 microns, a maximum value of strain rate sensitivity index m , a homologous temperature range of 0.4–0.5 T_m (Homologous Temperature) and fine dispersion of thermally stable particles are basic requirements of superplasticity. Superplasticity could be achieved by different ways viz., through grain boundary sliding of fine grains, internally developed tensile plastic deformation through intergranular slip or dislocation, and through diffusion creep phenomena. The sheet to be formed is placed within a closed die cavity and then heated while gas is evenly applied with pressure to plastically deform the metal at very high strains into a complex-shaped, single-piece component. During superplastic deformation, the metal becomes uniformly thinner over the entire part. The necking phenomena are avoided in the superplastic range, thereby tensile failure because the material does not develop internal cavities. Superplastic forming is used by the aerospace industry to fabricate complex components to the near net shape as a single piece. It serves as an economical process by reducing the number of individual parts and the assembly cost often associated with making complicated components. For instance, a single sheet can be formed into a complex arrangement of ribs, stiffeners, and skin as a single-piece part. Superplastic forming is credited with weight and cost savings on virtually every modern aircraft. However, superplastic forming is not always the most economical process. Superplastic forming usually offers an economic alternative when a small to medium number of complex parts, which are normally manufactured with expensive materials having low formability, are required.

2 Literature Review

Bengough is one among the first researchers to report superplasticity in a metallic material [1]. He described how “a certain special brass ... pulled out to a fine point, just like glass would do, having an enormous elongation.” An $\alpha + \beta$ brass was used and a maximum elongation of 163% was achieved at a temperature of 700 °C [1]. Pearson took a Bi–Sn eutectic wire, conducted hot extrusion tests, and reported a 2000% elongation [2]. Jovane carried out an approximate analysis on a circular diaphragm (of constant thickness) clamped at the circumference and subjected to hydrostatic pressure on one side of the sheet. A stepwise loading path was derived with a proposed method, which enabled the strain rate to be maintained within a predetermined optimal superplastic range throughout the process [3]. Enikeev and Kruglov developed an engineering model to predict the thickness distribution of the hemispherical dome at different depths of forming. They considered non-uniform thickness distribution during superplastic forming (unlike the Jovane [1] model), and a pressure–time cycle was calculated based on the proposed model. The thickness distribution does not take into account the strain rate sensitivity (m) and is, therefore, material-independent [4]. Auora et al. observed that variation of m and K with strain

rate has a significant influence on bulge time and thickness distribution. The authors noted that better predictions can be made if the effect of strain rate is accounted [5]. Cornfield and Johnson predicted thinning factor as a function of the fractional height (above the base of the dome) for m varying from 0.3 to 1. They noted that irrespective of m value, the average thickness was approximately equal to the actual thickness at a fractional height of ~ 0.43 . They also concluded that to form bulge domes greater than hemispherical, only materials with higher values of ' m ' will avoid catastrophic failures [6]. Holt predicted bulge profile and sheet thickness distribution as a function of the variables of pressure, geometry, time, K , and m . He conducted bulging of a flat circular sheet into a female die and also bulging of another rectangular sheet into 90° V grooves considering non-uniformity of thickness distribution. Agreement is better for $m = 0.5$ than for $m = 0.2$. He concluded that the bulge profile is more circular and the strain distribution more uniform when m is larger [7]. Yang et al. carried out constant-pressure blowing and constant strain rate (variable-pressure blowing). Also, a step-change pressure forming process to shorten the forming time spans was proposed and examined. They characterized the forming behaviors of 7475 Al alloy and compared the forming efficiencies of variable-pressure forming processes to those of constant-pressure forming ones. They suggested that through the application of the easy-to-operate step-change pressure forming processes, a significant improvement of forming efficiency can be attained [8]. Ragab presented approximate theoretical solutions for the equations relating to thermoforming of superplastic materials by free bulging of a circular sheet into a cylindrical die, which can be used to predict thickness distributions and forming times for the thermoformed parts (assumed complete sticking with die walls). He compared experimental results for Zn–22Al eutectic alloy and Sn–38Pb sheets formed at 250 °C, with the proposed theoretical solutions and concluded the results as satisfactory [9]. Jarrar designed optimum gas pressure profiles for Aluminum AA5083 to achieve shorter cycle times in production. Similar to Yang et al. [8], he compared step-change pressure forming with constant strain rate forming. Results suggest that, for free bulge forming of AA5083 at 500 °C, single-, two- and three-step isobaric forming produces the same part thickness uniformity within shorter forming times compared to forming at a constant maximum strain rate [10]. Ramesh et al. performed superplastic forming on AA5086 aluminum alloy and determined the approximate time for the sheet metal to attain the set temperature and also the most favorable temperature and pressure necessary for achieving the deformation of the workpiece based on equal thickness as per a steady-state equation derived. They concluded that cavitation density increases with an increase in the strain rate and that forming temperature for the material to exhibit superplastic behavior is 450 °C [11]. Jarrar et al. investigated the feasibility to fabricate triangular channels at the bottom of a shallow cup by altering the aspect ratios of both the cup and the triangular channel. Thickness distribution and pressure profile from Abaqus simulations were validated with experimental results to assess the effect of altering the geometries (aspect ratios). Increment in the depth of primary feature (cup) was found to affect maximum thinning in the formed part. Minimum thickness was observed at the channel entry radius for cases of sharper radii, shallow cup depths, and acute channel angles [12]. Jarrar et al. enlisted the

challenges and future prospects of superplastic formation. More research to come up with materials having high strain rate and low-temperature formability, constitutive material modeling, and advanced heating methods are needed for the widespread use of SPF in the industry. Techniques to optimize the process (or a combination of techniques such as Hybrid SPF) are required, in order to reduce the forming time without compromising the quality of components [13]. The effect of die entry radius and friction coefficient on optimum pressure profile, thickness distribution, and forming time was studied; there is a swift change in the optimum pressure required when the rate of radius change is greater than the change in thickness, thickness distribution was found to vary with an increase in die entry radius, increase in friction coefficient decreases the optimum pressure needed for forming, and more thinning was observed at the bottom corner of the rectangular die [14]. Kumaresan et al. studied the effect of a thermomechanical treatment (TMT) process, aimed at refining the grain size of AA7075 to reduce the forming time and improve the integrity of the formed component. By varying parameters such as forming pressure and sheet thickness, the effect on cavitation, microstructure and thickness distribution was observed. They found that for a given sheet thickness, there is a certain pressure which gives a higher thinning factor and lesser cavity volume fraction for AA7075 [15]. Lee et al. carried out rapid forming tests on superplastic AA5083 in an attempt to decrease the significantly higher forming time required in SPF. A circular cup with a depth to diameter ratio of 1:2 was formed in 70 s with a thickness decrement of two thirds with a stretching of the circular sheet area by an order of 3. A higher strain rate was maintained, especially after the sheet–die contact, hence reducing the overall forming time. High strain rate for shorter spans does not give any negative effects, hence leading to an interesting finding that forming speeds can be suitably increased to reduce the overall forming time. Cavitation was observed at locations where the plastic strain was concentrated and it was concluded that lower temperatures could increase the cavitation effect [16]. Luckey et al. demonstrated a two-stage superplastic forming method using a preformed cavity developed with FEA design iterations. To overcome the thickness distribution difficulties and wrinkles with the conventional single-stage SPF, the sheet was firstly pre-stretched to take the shape of a preformed cavity placed up the die and then the pressure was reversed so that the sheet moves down to finally take the shape of the primary bottom die. Critical 2D preform cross-sectional analysis in ABAQUS (Implicit) and the final 3D analysis were done on LS-DYNA (Explicit). The advantage of iterative design with FEA was fully realized as the shape of the preform cavity was highly non-intuitive and would definitely have required significant experimental trials to achieve the optimum thickness profile and a wrinkle-free component [17]. Bing et al. simulated the fabrication of 3D titanium hollow fan blades with key steps in fabrication as twisting, hot forming, and SPF. Combination of SPF/DB (Diffusion bonding) was employed using core and face sheets. The pressure cycle was only slightly influenced by the thickness ratio between the core and face sheets. It was observed that forming force was found to increase, when the twisting rate, descending velocity, strain rate, and sheet thickness ratio was increased, whereas the friction coefficient had negligible influence [18]. Samekto et al. modeled superplastic behavior of AA5083 by performing implicit and explicit analysis in ABAQUS and

LS-DYNA, respectively, with a pressure control algorithm subroutine. The pressure–time cycle generated by the static and dynamic analysis was compared and it was noticed that static gave better results as it solves the global equilibrium equation with a physical approach unlike dynamic, but the dynamic procedure was found to be more time-efficient. Effect of strain rate sensitivity ‘ m ’ was modeled efficiently by LS-DYNA, and it was concluded that change in ‘ m ’ affected thickness distribution significantly, whereas friction coefficient change had a minute impact on ‘ m ’ [19]. Jarrar et al. compared five different constitutive material models to determine the material model that accurately predicts the deformation behavior of AA5083. It was confirmed that if the evolution of dome pole thickness during forming is to be predicted, the cavitation effect has to be accounted for in the model. Although it was observed that at higher strains there was much deviation between simulation and experimental results in all models, a material model with the inclusion of cavitation effect gives more reliable results consistent with experimental outcomes (than other models). They also pointed out the shortcomings of other material models in which the dome pole thickness evolution was shown to be independent of applied pressure [20]. Aksenov et al. proposed a pressure-control technique to maintain the equivalent stress at a specified level in the sheet during forming of commercial aluminum alloy ALNOVI-U. The dome height data obtained during the experiment are used to obtain the continuously changing values of stress, strain, and strain rate at the dome pole. A distinguished feature presented is that it includes stress–strain curves obtained from biaxial testing conditions which give data near to the prevailing conditions in the sheet during free bulging, hence better simulation predictions [21]. Majidi et al. investigated the high-speed blow forming of an automotive component and sought to optimize the process parameters involved in the hybrid SPF presented in the paper. Reversed hydraulic pressure is applied to the near formed component (after free bulging), to conform it to the complex shape of the die. They also discussed the effect of varying element size and friction coefficient on the thinning characteristics of the sheet. Another interesting observation was that a variable m value (VmV) model was found to give better predictions about the thinning characteristics of complex industrial components [22]. Majidi et al. presented a new framework for efficiently characterizing the deformation behavior and assess the formability of the deforming sheet under Hybrid SPF (SPF/QPF). The inclusion of Young’s modulus and its observed variation during forming was shown to draw better predictions. Also, it was pointed out that temperature change affects yield stress but it does not have an effect on the isotropic hardening behavior of the deforming sheet. The forming limit curve (FLC) was characterized for three strain paths (uniaxial tension, plane strain, and biaxial tension) and it was concluded that biaxial case has the least formability when compared with the other two paths [23]. Kappes et al. carried out pneumatic bulge tests on a developing grade of aluminum alloy AA5456 along with the usage of laser-inscribed grids for in-situ strain measurements to identify the crucial material and process parameters, hence ultimately correlating the experimental findings with the finite element simulations (after plugging the obtained material parameters from bulge tests as input for simulations). Isobar superplastic forming limit curve (SFLC) was extracted from the bulging experiment to assess the strain distributions

and manufacturability of the formed component from simulations. Also, a bracket usually made from AA5083 was formed with the aforementioned AA5456 alloy and it was observed that the bracket failed (fractured) to achieve the usual final shape with the chosen process parameters, otherwise feasible with AA5083 [24–26]. The pressure-forming time sets generated from the above code will be combined with the results of the next code (total forming time), to plot the combined final P–T curve for the respective forming depths (20, 40, 60, and 80 mm).

3 Finite Element Simulation and Boundary Conditions

Boundary conditions are to be set such that there is a fixed displacement of the nodes at the sheet's circumference to ensure that the proper gripping condition is maintained in the analysis. Adaptive stepping option in software takes up inputs such as initial fraction of loadcase time, minimum and maximum fractions of loadcase time, and the maximum number of steps allowed in addition to the desired recycle to be performed per increment and automatically calculates the time step required at different instants during the analysis. Superplasticity control parameters are given under "Loadcase" section along with the finishing criterion for the analysis (percentage of nodes in contact). The two methods of strain rate sampling in the software are maximum strain rate and target strain rate. The process pressure is automatically calculated during the analysis. The pressure magnitude is adjusted such that the equivalent strain rate in the part is at or close to the user-specified target strain rate. The equivalent strain rate in the part is an average value calculated by sampling a suitable subset of elements. The recommended scheme is one in which elements with a strain rate greater than a cut-off factor times the maximum element strain rate are sampled. This maximum strain rate is based on a smoothing algorithm described below. The cut-off factor can vary between 0 (all elements below the maximum are sampled) and 1 (only the elements with maximum strain rate are sampled). The recommended value for the cut-off factor is 0.7–0.9 (default value is 0.8). To reduce undesirable oscillations in the pressure–time history, a pressure smoothing algorithm is incorporated. The type of element used in the analysis is Element 18, a four-noded, iso-parametric, arbitrary quadrilateral element for membrane applications

4 Selection of Material and Material Properties

Material constant, $K = 254 \text{ MPa}$

Strain rate sensitivity, $m = 0.5$

Target strain rate, $\dot{\epsilon} = 0.001 \text{ s}^{-1}$

Superplastic temperature, $T = 450 \text{ }^\circ\text{C}$

Minimum Pressure, $P_{\min} = 7 \times 10^{-6}$ MPa

Maximum Pressure, $P_{\max} = 200$ MPa (Figs. 1, 2, 3, 4 and 5; Tables 1, 2, 3 and 4).

Frictional Trials: 0.3, 0.4, 0.5, and 0

Four frictional trials are simulated with friction coefficients as 0.3, 0.4, 0.5, and 0 for case-1 (both single-stage and two-stage). Arc Length Versus Element Thickness plots are extracted to assess the effect of friction on the thickness distribution of the SPF component (Fig. 6).

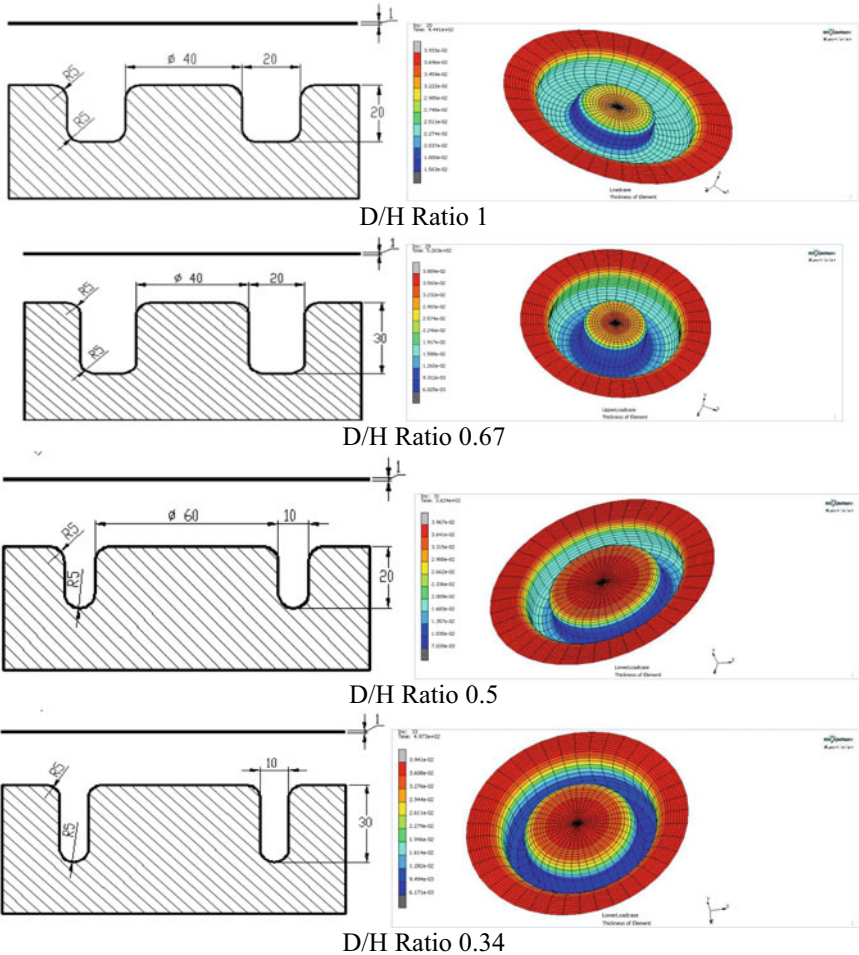


Fig. 1 Cross-sectional views of dies with different *D/H* ratios (diameter of form/height of form) and their simulation in MSC.MARC/MENTAT

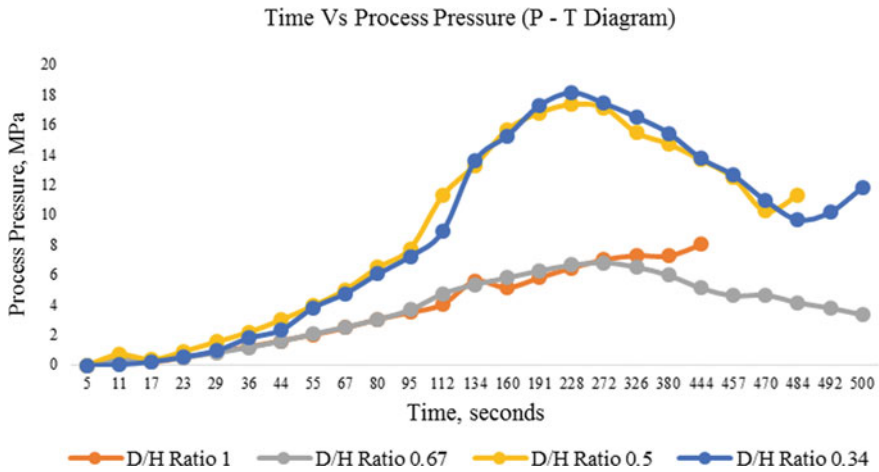


Fig. 2 Variation of time versus process pressure (P-T diagram)

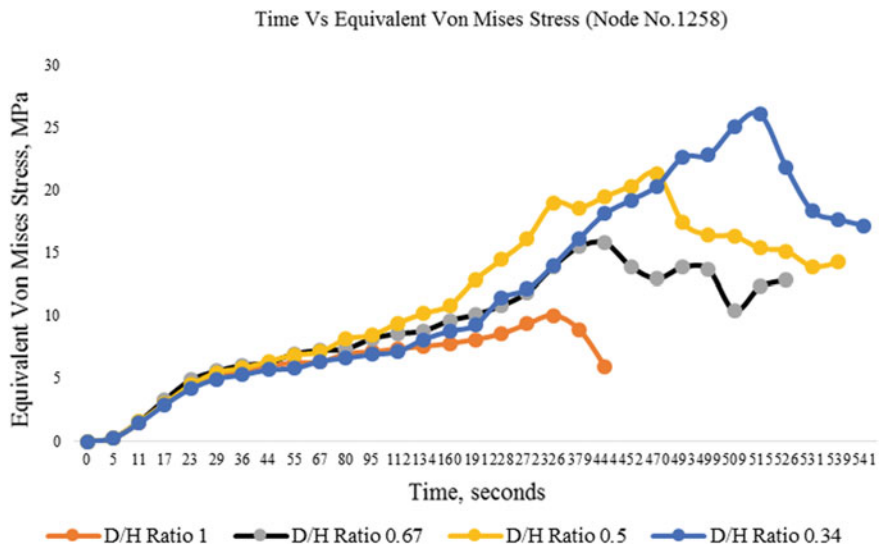


Fig. 3 Variation of time versus equivalent von-mises stress for node No. 1258

5 Results and Discussions

The model predicts thickness variation without taking into account the material characteristics, extracting thickness distributions from the model will not aid while comparing them with numerical simulations for the same *D/H* ratios. P-T curves obtained are similar in profile, but the pressure required is predicted to be quite low

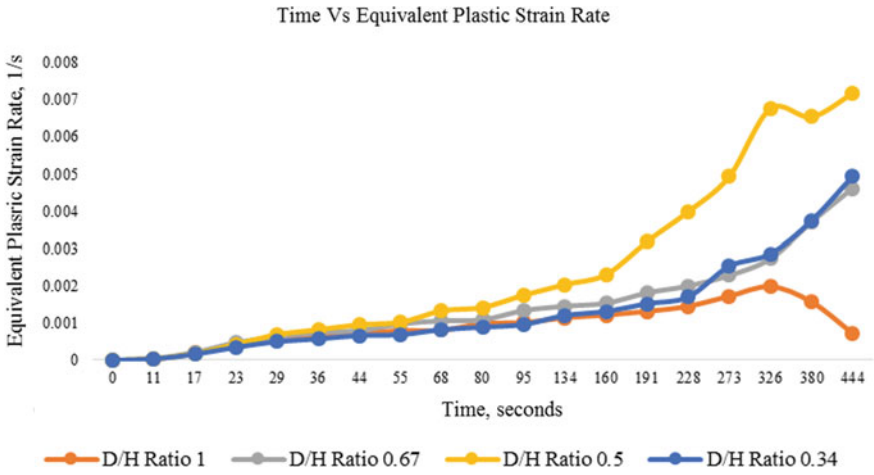


Fig. 4 Variation of time versus equivalent plastic strain rate

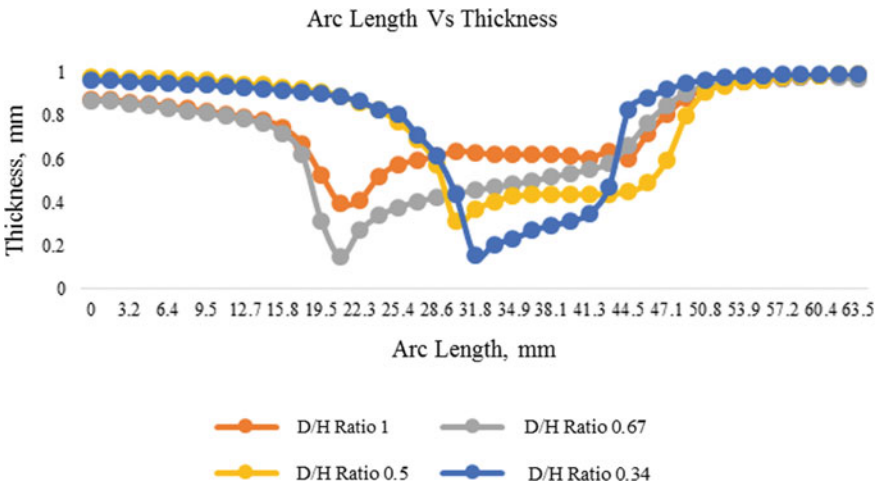


Fig. 5 Variation of arc length versus thickness

Table 1 Chemical composition of AZ31B

Element	Al	Zn	Mn	Si	Cu	Ni	Ca	Mg
Comp. by % wt	2.9	1.1	0.49	0.1	0.05	0.03	0.04	Balance

as the model does not take into account the frictional characteristics during deformation. Also because the thickness behavior is averaged in the model for simplification,

Table 2 Mechanical properties of AZ31B

Ultimate tensile strength (MPa)	Yield strength (MPa)	Modulus of elasticity (GPa)	Poisson's ratio	Density (kg/m ³)	Melting point (°C)
290	220	45	0.35	1770	630

Table 3 Chemical composition of die steel

Element	C	Mn	S	Cr	Mo	Va
Composition by % wt	0.4	0.3	1.0	4.8	1.5	1.0

Table 4 Mechanical properties of die steel

Ultimate tensile strength (MPa)	Yield strength (MPa)	Modulus of elasticity (GPa)	Poisson's ratio	Density (kg/m ³)	Melting point (°C)
1500	1350	215	0.3	7800	1427

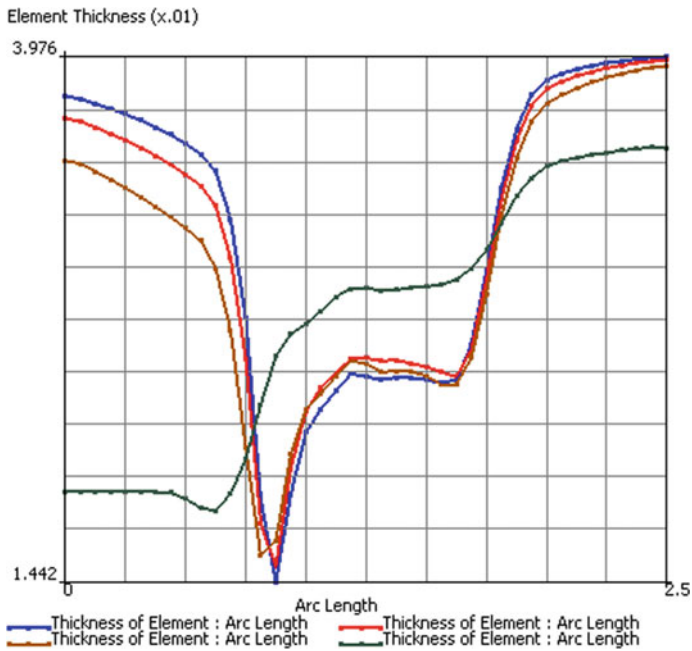


Fig. 6 Comparison of thickness distribution for *D/H* ratios for 1, 0.67, 0.5, and 0.34 with friction

the pressure values with time are not seen to be matching with the numerical simulations for the respective forming depths. The pressure required for SPF forming in adaptive meshing is predicted to be high in all since the refined mesh captures the behavior effectively while deformation. With adaptive meshing, there is better prediction of thickness at the top fillet of the cylindrical component, because of fine mesh refinement kept near the two fillets (top and bottom for all D/H ratios. Least thickness is observed at the inside fillet for all the four cases because of the annular fillet at the center. As the friction coefficient increases, the thickness of the sheet is preserved at the top flat portion where the sheet also experiences normal force because of the gas pressure. This is observed by a shift in the Arc Length Vs Thickness curves in single-stage superplastic forming. On the other hand, when the friction coefficient is made zero in the simulation, the same top portion discussed before experiences a drastic reduction in thickness because of the decreased frictional force. The same thickness preservation is seen at the periphery of the component but with a minimum shift in the frictional curves. As a result, the middle recess which experiences the most deformation gets thinned as the frictional coefficient value is increased from 0.3 to 0.5, in order to accommodate the sheet thinning phenomenon from the sheet portion which does not touch the die.

6 Conclusions

The explicit code MSC.MARC/MENTAT with power-law material constitutive equation can be used to accurately model the thinning behavior of aluminum-coated magnesium alloys for single-stage SPF, and to reduce the number of experiments the finite element based software can be utilized for parameters optimization. Material thinning was reduced with the least thickness percentage difference ranging from 61 to 23% is observed. Critical areas for all the cases under single-stage superplastic forming were observed to have been increased in thickness. FEA can be used to guide the design a single-stage SPF die such that the thickness profile is improved without wrinkles. The necking that can develop in SPF when forming over tight radii and/or into high aspect ratio cavities can be eliminated by first preforming the sheet to redistribute metal thickness and alter the manner in which the sheet fills the cavity.

Acknowledgments The authors would like to thank the sponsors of the project, University Grants Commission, South Eastern Regional Office (UGC/SERO), Hyderabad, for financial assistance vide Reference No. F. MRP-6742/16 (SERO/UGC) under the Minor Research Project Scheme. Due thanks to DMRL, Hyderabad, for the help rendered in using MSC.MARC/MENTAT.

References

1. G.D. Bengough, A study of the properties of alloys at high temperatures. *J. Inst. Metals* **7**, 123–174 (1912)
2. C.E. Pearson, The viscous properties of extruded eutectic alloys of lead-tin and bismuth-tin. *J. Inst. Metals* **54**, 111–123 (1934)
3. F. Jovane, An approximate analysis of the superplastic forming of a thin circular diaphragm: theory and experiments. *Int. J. Mech. Sci.* **10**, 403–427 (1968)
4. F.U. Enikeev, A.A. Kruglov, An analysis of the super plastic forming of a thin circular diaphragm. *Int. J. Mech. Sci.* **37**(5), 473–483 (1995)
5. Y. Aoura, D. Ollivier, A. Ambari, P. Dal Santo, Determination of material parameters for 7475 Al alloy from bulge forming tests at constant stress. *J. Mater. Process. Technol.* **145**, 352–359 (2004)
6. G.G. Cornfield, R.H. Johnson, The forming of super plastic sheet materials. *Int. J. Mech. Sci.* **12**, 479 (1970)
7. D.L. Holt, An analysis of the bulging of a super plastic sheet by lateral pressure. *Int. J. Mech. Sci.* **12**, 491–497 (1970)
8. C.F. Yang, L.H. Chiu, S.C. Lee, Super plastic forming of 7475 Al alloy by variable-pressure blowing. *Scripta Mater.* **34**(10), 1555–1560 (1995)
9. A.R. Ragab, Thermoforming of super plastic sheet in shaped dies. *Met. Technol.* **10**, 340–348 (1983)
10. Firas Jarrar, Designing gas pressure profiles for AA5083 super plastic forming. *Procedia Eng.* **81**, 1084–1089 (2014)
11. S. Ramesh Babu, S. Deivanayagam, M. Aravind, Determination of material parameters during super plastic forming of AA 5086 alloy. *Procedia Eng.* **97**, 1379–1386 (2014)
12. F. Jarrar, M. Liewald, P. Schmid, A. Fortanier, Superplastic Forming of triangular channels with sharp radii. *J. Mater. Eng. Perform.* **23**(4), 1313–1320 (2014)
13. F. Jarrar, D. Sorgente, S. Aksenov, F. Enikeev, On the Challenges and prospects of the super plastic forming process. *Mater. Sci. Forum* **941**, 2343–2348 (2018)
14. M. Balasubramanian, K. Ramanathan, V.S. Senthil Kumar, Mathematical modeling and finite element analysis of super plastic forming of Ti–6Al–4V alloy in a stepped rectangular die. *Procedia Eng.* **64**, 1209–1218 (2013)
15. G. Kumaresan, K. Kalaichelvan, Experimental studies of a rectangular cup formation of Al 7075 alloy in SPF. *Procedia Mater. Sci.* **6**, 892–896 (2014)
16. S. Lee, Yu Y.-H., Wu H.-Y., Wang J.-Y., C.-P. Chang, Rapid forming of super plastic aluminium alloy 5083. *Mater. Sci. Technol.* **17**(11), 1413–1416 (2001)
17. G. Luckey, Jr., P. Friedman, K. Weinmann, Two-stage design and experimental validation of 2-stage super plastic forming die. *J. Mater. Process. Technol.* **209**, 2152–2160 (2009)
18. Z. Bing, L. Zhiqiang, H. Hongliang, L. Jinhua, B. Bingzhe, Three dimensional FEM simulation of titanium hollow blade forming process. *Rare Metal Mater. Eng.* **39**(6), 963–968 (2010)
19. H. Samekto, K. Roll, Finite element analysis of super plastic forming process using LS-DYNA, in *4th European LS-DYNA Users Conference* (Ulm, 2003)
20. F. Jarrar, R. Jafar, O. Tulupova, F. Enikeev, N. Al-Huniti, Constitutive modeling for the simulation of the superplastic forming of AA5083. *Mater. Sci. Forum* **838–839**, 512–517 (2016)
21. S.A. Aksenov, D. Sorgente, Investigation of stress-strain behavior of a sheet material using free bulging test. *Procedia Eng.* **207**, 1892–1897 (2017)
22. O. Majidi, M. Jahazi, N. Bombardier, Finite element simulation of high-speed blow forming of an automotive component. *Metals* **8**, 901 (2018)
23. O. Majidi, M. Jahazi, N. Bombardier, Characterization of mechanical properties and formability of a super plastic Al–Mg alloy. *J. Phys.: Conf. Ser.* **1063**, 012165 (2018)
24. J. Kappes, M. Liewald, S. Jupp, C. Pirchl, R. Herstelle, Designing super plastic forming process of a developmental AA5456 using pneumatic bulge test experiments and FE-simulation. *Prod. Eng. Res. Dev.* **6**, 219–228 (2012)

25. D.A. Pereira, M.H.F. Batalha, A.F. Carunchio, H.B. Resende, Analysis of super plastic forming process applied to aerospace industry: case study of Al 5083 alloy, in *Aerospace Technology Congress*, October 2016
26. F.K. Abu-Farha, M.K. Khraisheh, Mechanical characteristics of superplastic deformation of AZ31 magnesium alloy. *J. Mater. Eng. Perform.* **16**, 192–199 (2007)

Failure Analysis of GFRP Composite Reinforced with Semimetals for Marine Applications



Pala Srinivasa Reddy, Inkulu Anil Kumar, Satuluri Srikiran,
and Dannana Suresh

Abstract The main aim of the project is to design and fabricate the material required to prepare surfboard. GFRP composites are used for preparing the laminates, either unidirectional or bidirectional. Experimental analysis is performed using Compression test, Impact test, and Drop Weight Impact Test on the material after the specimen is immersed in normal water and seawater for a period of 720 h (30 days), moisture absorption test is further carried out. Both analytical and experimental analyses are compared on the specimen and further results have been observed. In addition to these results, design and analysis of surfer board is done to meet the requirements. GFRP composites are prepared using American Society for Testing Materials (ASTM) and Indian Standard Organization (ISO) standards. Fiber-reinforced composite materials are demanded by the industry, especially for the applications where weight reduction is critical because of their high specific strength, ability to resist corrosion. The present work aims at the evaluation of various mechanical properties of glass fiber-reinforced polymer composites (GFRP) with the inclusion of multi-walled carbon nanotubes (MWCNTs) in different weight fractions. The specimens are compared with the inclusion of MWCNTs to the neat composite.

Keywords Glass fiber-reinforced polymer · Moisture absorption · Compression after impact (CAI) · Solid works · Resultant displacement · Equivalent strain

P. Srinivasa Reddy (✉) · I. Anil Kumar (✉) · D. Suresh
Assistant Professor, Department of Mechanical Engineering, Lendi Institute of Engineering & Technology, Jonnada, Andhra Pradesh, India
e-mail: palasrinivasreddy@gmail.com

I. Anil Kumar
e-mail: anil.mec14@gmail.com

S. Srikiran
Professor and Head of the Department, Department of Mechanical Engineering, Lendi Institute of Engineering & Technology, Jonnada, Andhra Pradesh, India
e-mail: ssrikiran@gmail.com

1 Introduction

A composite material made from two or more constituent materials with significantly different physical or chemical properties that, when combined, produce material with characteristics different from the individual components. The individual components remain separate and distinct within the finished structure, differentiating composites from mixtures and solid solutions [1]. A greater understanding of the role of variation in tensile properties with the orientation of fibers in the laminate was acquired through the experiments [2]. Shivamurthy et al. [3], found that mechanical properties of glass/epoxy composite, namely Young's modulus, tensile strength, flexural strength, impact strength, and wear resistance, show improvement with the addition of carbon nanotube flakes. The reinforcements impart their special mechanical and physical properties to enhance the matrix properties. A synergism produces material properties unavailable from the individual constituent materials, while the wide variety of matrix and strengthening materials allows the designer of the product or structure to choose an optimum combination. Such composites are highly suitable for manufacturing of bearing liners, gears, seals, cams, wheels, brakes, rollers, clutches, bushings, and so forth. Studies on electrical properties of graphite filled composites by Goyal and Kadam [4] and Bhattacharya et al. [5] revealed that these composites are also suitable to shield electromagnetic interference in electronic devices. Huttunen-Saarivirta et al. [6] studied the effect of particle shape on AWJ erosion process using silica sand abrasive. It was observed that spherical-shaped or blunted-edged abrasives tend to create ductile fracture with low MRR and angular shaped abrasive with sharp edges resulting in brittle fracture contributing to higher MRR. The effect of particle size on the erosion of titanium workpiece was studied by Yerramareddy and Bahadur [7] and El Tobgy et al. [8], using experimental and finite element analysis, respectively. Alberdi et al. [9] studied the suitability of machinability model developed for metals to use it in composite materials. The machinability index was found to vary with thickness and compositions of the composite. These are a subgroup of composite materials as well as a subgroup of ceramics. They consist of ceramic fibers embedded in a ceramic matrix. The matrix and fibers can consist of any ceramic material, whereby carbon and carbon fibers can also be considered a ceramic material. Investigations on the effect of process parameters by Azmir and Ahsan [10] on glass fiber-reinforced epoxy composites infer that hardness, operating pressure, were significant control factors, which affect surface roughness (R_a) and a mathematical model, was developed by authors to predict R_a . Further analysis of machined surface by Azmir and Ahsan [11] shows that at a jet angle of 90° glass fibers were found to be perfectly chopped. Glass fiber is lightweight, strong and less brittle. The best part of fiberglass is its ability to get molded into various complex shapes. A review on traditional machining of composites by Teti and Abrao et al. highlights the problems such as exposure of fibers to environmental attack, material degradation due to localized heating, poor dimensional accuracy, shorter tool life, delamination, and fiber pull out due to anisotropic, non-homogeneous, and abrasive nature of such composite materials. Khan and Haque [12] investigated the machining performance

of various abrasives on glass workpiece. Studies on the effect of jet pressure on cotton FRP composite by Wang and Guo [13] reported that the delamination occurs due to incapability of jet penetration into composite at lower operating pressures. Study of kerf taper angle produced on glass and graphite-reinforced epoxy composite was made by Shanmugam et al. [14] and also developed a model to predict delamination length. Authors observed that, at higher operating pressures, considerable surface taper and delamination are found on the cut surface due to higher feed rates, flow turbulence, and brittle nature of composite material. Gokendiz Naser [15] investigated that polymer-based composites offer several advantages for naval architects and boat builders to archive effective and reliable structures. Perillo and Jorgensen [16] stated that damage development due to impact needs to be understood to evaluate the consequences of the impact on composite structures, failure analysis was performed using 3D solid works so as to identify the interlaminar deformation.

2 Experimental Details

Fiberglass is a lightweight, extremely strong, and robust material. Its bulk strength and weight properties are also very favorable when compared to metals, and it can be easily formed using molding processes. The glass fiber composites strength/weight ratios are higher than those of most other materials and their impact resistance is phenomenal. Further, they possess good electrical properties, resistance to moisture and outdoor weathering and resistance to heat and chemicals. Hand lay-up is an open molding method suitable for making a wide variety of composites products from very small to very large. Production volume per mold is low; however, it is feasible to produce substantial production quantities using multiple molds. Hand lay-up is the simplest composites molding method, offering low-cost tooling, simple processing, and a wide range of part sizes. Design changes are readily made. There is a minimum investment in equipment. With skilled operators, good production rates and consistent quality are obtainable. Hand lay-up technique is the simplest method of composite processing. The infrastructural requirement for this method is also minimal (Figs. 1, 2, 3, 4, 5 and 6).

Fig. 1 Hand lay up technique

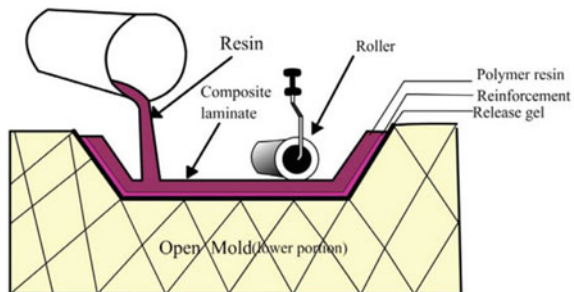




Fig. 2 Preparation of specimen



Fig. 3 Magnetic stirrer mixing semi metal



Fig. 4 Neat composite specimens



Fig. 5 MWCNT inclusion specimens for compression and impact test

Fig. 6 Specimens (compression and impact) after weighing



First of all, a release gel is sprayed on the mold surface to avoid the sticking of polymer to the surface and to remove dust particles wherever found. Thin plastic sheets are used at the top and bottom of the mold plate to get a good surface finish of the product. Reinforcement in the form of woven mats is cut as per the mold size and placed at the surface of mold. Then thermosetting polymer in liquid form is mixed thoroughly in suitable proportion with a prescribed hardener (curing agent) and poured onto the surface of mat already placed in the mold. The Epoxy Resin and hardener are taken in the ratio of 2:1 and also MWCNT in the powdered form is taken in different weight proportions. The polymer is uniformly spread with the help of brush. Second layer of mat is then placed on the polymer surface and a roller is moved with a mild pressure on the mat–polymer layer to remove any air trapped as well as the excess polymer present. The process is repeated for each layer of polymer and mat, till the required layers are stacked. The time of curing depends on type of polymer used for composite processing. For epoxy based system, normal curing time at room temperature is 24–48 h (Figs. 7, 8 and 9).

Fig. 7 Universal testing machine and compression testing machine



Fig. 8 Specimen with and without the inclusion of MWCNT subjected to compression

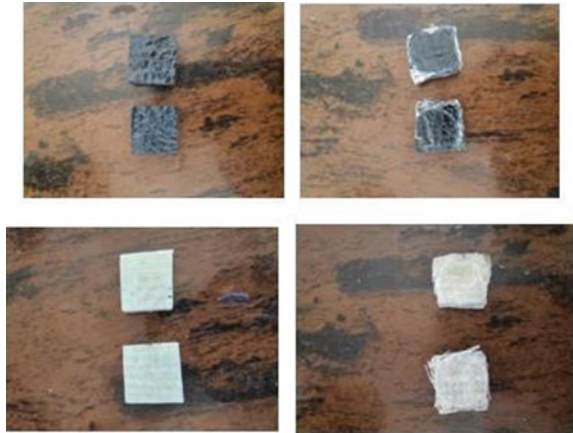


Fig. 9 Specimen subjected to Impact test with and without the inclusion of MWCNT



A Universal Testing Machine is used to test the tensile stress and compressive strength of materials. It is named after the fact that it can perform many standard tests like tensile, compression, bend, puncture, and flexural tests on materials, components, and structures. UTM or Urchin Tracking Module is a simple code that can be attached to any URL to generate Google Analytics data for digital campaigns.

In this test, specimens are weighed in dry condition and let them immersed in freshwater for 24 h. The specimens are immersed in both seawater and normal water. After 24 h of immersion, those are taken out from water and wipe out with a cloth. Then, specimens are weighed in wet condition. The difference between weights is the water absorbed by specimen Again the test is performed by immersing the specimens for the next 24 h. Continue this experiment for 480 h.

The percentage of water absorption is then calculated. The less water absorbed by specimen the greater its quality. The good quality specimen does not absorb more than 20% water of its own weight. Water absorption is used to determine the amount of water absorbed under specified conditions. Factors affecting water absorption include type of plastic, additives used, temperature and length of exposure. The data sheds light on the performance of the materials in water or humid environments.

The effect of water absorption on the mechanical properties of flax-reinforced bio-epoxy composites has been studied by the immersion of the samples in water at room temperature. It shows that water absorption increases with an increase in fiber weight fraction due to a higher cellulose content (Figs. 10 and 11; Table 1).

Fig. 10 Specimens Immersed in Normal water and Seawater for testing (impact and compression)



Fig. 11 Weight of specimen to undergo compression and impact before dipping in normal and seawater



Table 1 The weight of epoxy resin and hardener and MWCNT required to prepare a specimen

S. No.	% Comp	Resin (g)	Hardener (g)	% Weight
Specimen 1	0.00	53.33	26.66	0
Specimen 2	0.010	56	28	0.8
Specimen 3	0.015	56.53	28.26	1.2
Specimen 4	0.020	57.6	28.80	1.6
Specimen 5	0.025	58.67	29.33	2.0

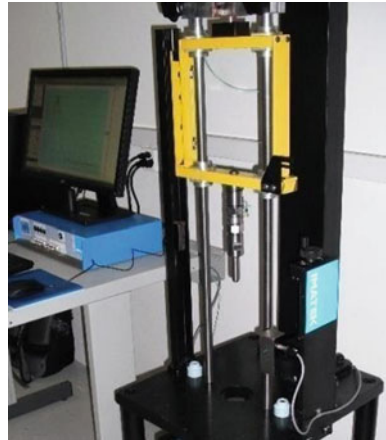
Drop Weight Impact Test method was to drop a weight in a vertical direction, with a tube or rails to guide it during the “free fall.” Once again, with the height and weight known, impact energy can be calculated. Since the falling weight either stopped dead on the test specimen or destroyed it in passing through, the only results that could be obtained were of a pass/fail nature (Fig. 12).

3 Plan of Experiments

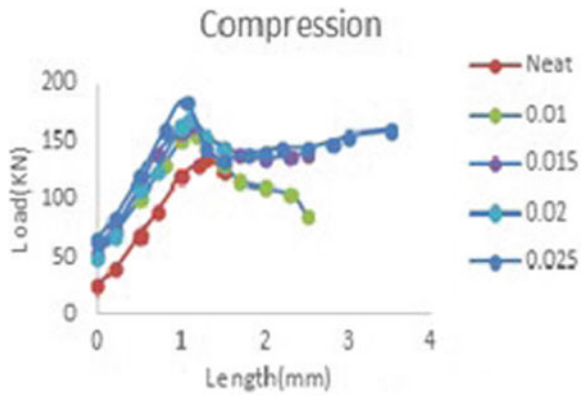
3.1 *Moisture Test for Compression and Impact of the Specimen with and Without Inclusion of MWCNT*

See Graphs 1, 2 and Tables 2, 3, 4, 5, 6 and 7.

Fig. 12 Drop weight impact test machine



Graph 1 Compression test on normal water



Graph 2 Compression test on seawater

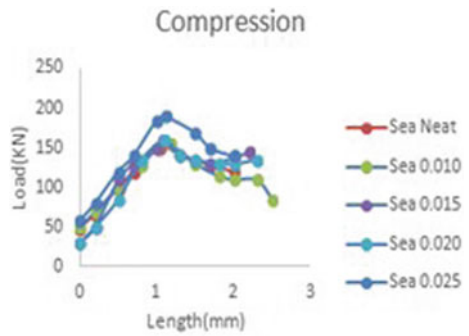


Table 2 Moisture absorption test for specimen that undergo compression in seawater

Time (h)	Moisture gain (%)				
Time	0% CNT	0.010% CNT	0.015% CNT	0.020% CNT	0.025% CNT
0	2.027	2.427	2.493	2.025	2.403
92	4.054	4.854	4.987	4.050	4.807
184	8.108	9.708	9.974	8.10	9.614
368	16.216	19.416	19.948	16.20	19.228
736	32.432	38.832	39.896	32.40	38.456

Table 3 Moisture absorption test for specimen that undergo compression in normal water

Time (h)	Moisture gain (%)				
Time	0% CNT	0.010% CNT	0.015% CNT	0.020% CNT	0.025% CNT
0	2.925	2.210	3.342	2.793	3.274
92	5.851	4.421	6.684	5.586	6.549
184	11.702	8.842	13.368	11.172	13.098
368	23.404	17.684	26.736	22.344	26.196
736	46.808	35.368	53.472	44.688	52.392

Table 4 Moisture absorption test for specimen that undergo impact in seawater

Time (h)	Moisture gain (%)				
Time	0% CNT	0.010% CNT	0.015% CNT	0.020% CNT	0.025% CNT
0	4.237	3.614	3.953	3.826	4.535
92	8.474	7.228	7.906	7.653	9.070
184	16.948	14.456	15.812	15.306	18.140
368	67.792	28.912	31.624	30.612	36.280
736	46.808	57.824	63.248	61.224	72.560

Table 5 Moisture absorption test for specimen that undergo Impact in normal water

Time (h)	Moisture gain (%)				
Time	0% CNT	Time	0% CNT	Time	0% CNT
0	4.854	4.756	4.952	4.239	4.819
92	9.708	9.513	9.905	8.478	9.638
184	19.416	19.026	19.810	16.956	19.276
368	38.832	38.052	39.620	33.912	38.552
736	77.664	76.104	79.240	67.824	77.104

Table 6 Drop weight test for specimen in seawater

% Composition of MWCNT	Specimen thickness(mm)	Energy absorbtion (J)	Duration time (s)	Impact strength (J/mm ²)
0.00	10	32	2.12	0.0581
0.010	10	44	2.14	0.080
0.015	10	46	2.11	0.0836
0.020	10	48	2.0	0.0872
0.025	10	50	2.125	0.090

Table 7 Drop weight test for specimen in normal

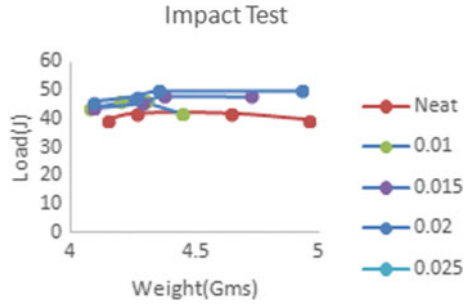
% Composition of MWCNT	Specimen thickness(mm)	Energy absorbtion (J)	Duration time (s)	Impact strength (J/mm ²)
0.00	10	34	2.18	0.0618
0.010	10	46	2.135	0.836
0.015	10	44	2.152	0.080
0.020	10	46	2.021	0.0836
0.025	10	48	2.126	0.0872

4 Drop Weight Impact Test

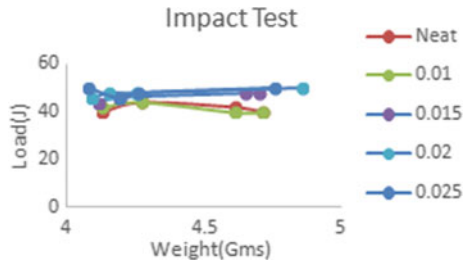
4.1 Water Compression Test for Normal Water Versus Seawater

Given above is a plot for Load (KN) versus Length (in mm) for immersion of glass fiber-reinforced composite material specimens in Normal Water versus Seawater. Glass fiber-reinforced composites with different weight fractions 0, 0.010, 0.015, 0.020, 0.025% are considered for testing the compressive strength inside the specimen. When the specimen is subjected to sudden impact or shock loads, it may undergo delamination, which can be considered as a failure in other terms. Inclusions of different weight fractions of multi-wall carbon nanotubes (MWCNTs) in glass fiber-reinforced composites show improvement in withstanding the load when compared to a neat composite. The graph with 0.025% inclusion of MWCNTs in glass fiber-reinforced composites exhibits the resistance when compared to other inclusions 0, 0.010, 0.015, and 0.020%. 0.025% inclusion of MWCNTs gives peak values even after the elongation in the specimen is identified (Graphs 3 and 4).

Graph 3 Impact test on normal water



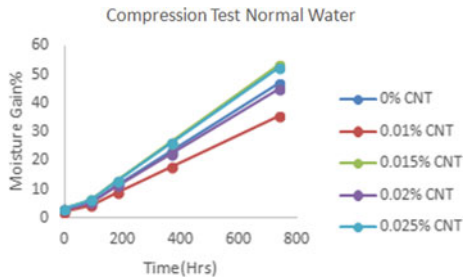
Graph 4 Impact test on seawater



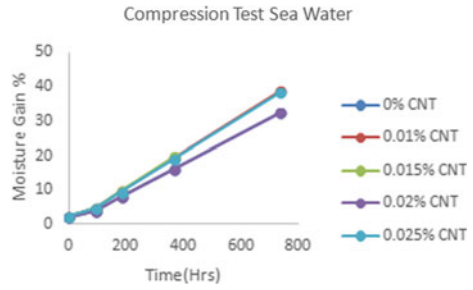
4.2 Impact Test for Normal Water Versus Seawater

The above is a plot for Load (J) versus Weight (in Gms) for immersion of glass fiber-reinforced composite material specimens in Normal Water versus Seawater. Glass fiber-reinforced composites with different weight fractions 0, 0.010, 0.015, 0.020, 0.025 are considered for testing the impact strength inside the specimen. When the specimen is subjected to sudden impact or shock loads, it may undergo delaminating, which can be considered as a failure in other terms. The graph with 0.025% inclusion of MWCNTs in glass fiber-reinforced composites exhibits the resistance when compared to other inclusions 0, 0.010, 0.015, and 0.020% (Graphs 5, 6).

Graph 5 Moisture absorption test for specimen subjected to compression under normal water



Graph 6 Moisture absorption test for specimen subjected to compression under Seawater

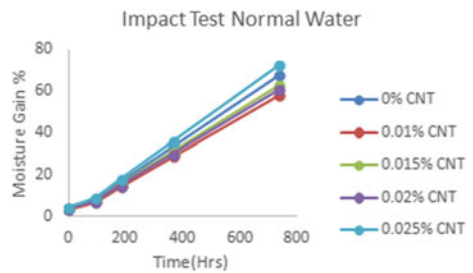


4.3 Moisture Absorption Test for Normal Water Versus Seawater

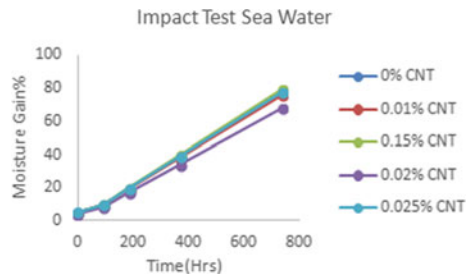
The above is a plot for Moisture Gain (%) versus Time (h) for the specimen immersed in normal water and seawater simultaneously. Glass fiber-reinforced composites with different weight fractions 0, 0.010, 0.015, 0.020, 0.025% are considered for testing the moisture content inside the specimen. When the specimen is subjected to sudden impact or shock loads, it may undergo delaminations, which can be considered as a failure in other terms (Graphs 7, 8).

The above is a plot for Moisture Gain (%) versus Time (h) for the specimen immersed in normal water and seawater simultaneously. Glass fiber-reinforced composites with different weight fractions 0, 0.010, 0.015, 0.020, 0.025% are considered for testing the moisture content inside the specimen. When the specimen is

Graph 7 Moisture absorption test for specimen subjected to Impact under normal water



Graph 8 Moisture absorption test for specimen subjected to Impact under Seawater



subjected to sudden impact or shock loads, it may undergo delamination, which can be considered as a failure in other terms.

Inclusions of different weight fractions of MWCNTs in glass fiber-reinforced composites show improvement in withstanding the load when compared to a neat composite. The graph with 0.025% inclusion of MWCNTs in glass fiber-reinforced composites exhibits the resistance when compared to other inclusions 0, 0.010, 0.015, 0.020, and 0.025% inclusion of MWCNTs. As the moisture content is high near to the sea, so the amount of water absorption will be greater when compared to normal water.

5 Results and Discussions

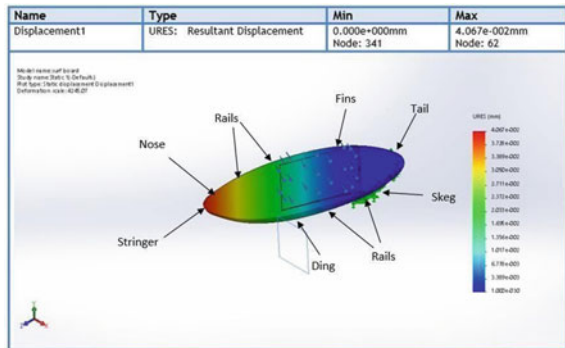
5.1 Surfboard

A surfboard is majorly used as a surface water sport in which the wave rider rides on the forward or deep face of a moving wave which usually carries the surface toward the shore. Sometimes strong currents and water action at those depths can also slant the surfboard creating an impact which can result in severe injuries to the surfer. Two major forces are at the plane gravity which pulls the surfer and the board down. The buoyant force which actually pushes the floating surfboard up in the opposite direction. It is clear that during this case, the surfboard might be subjected to compressive force depending upon the amount of load that is applied on the load.

Figure 13 represents a 3D solid model of the surfboard, it indicates the resultant displacement that is acted upon the surfboard when a certain quantity of mass is distributed on the surface o the board.

Figure 14 indicates the stringer is subjected to direct contact with the seawater creating stress concentration from the nose to stringer will be high when compared to stress concentration on rails, skeg, and fins and on the tail. The above figure represents resultant displacement and equivalent strain applied to the surfboard. As the front

Fig. 13 Parts of surfboard



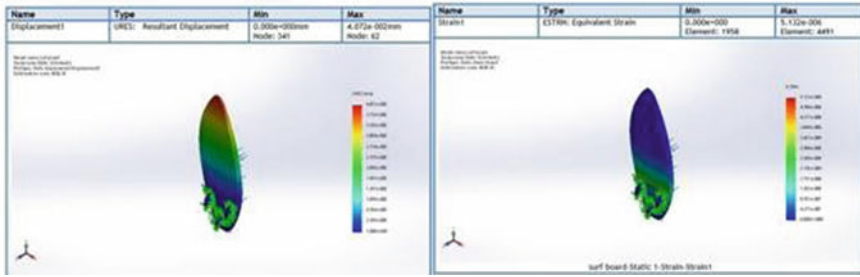


Fig. 14 Stringer’s resultant displacement and equivalent strain

Table 8 Surfboard stringer specifications

Design specification	With inclusion of CNT	Without inclusion of CNT
Min. displacement (mm)	0.00e+000	0.00e+000
Max. displacement (mm)	4.072e-002	4.432e-002
Min. strain (mm)	0.00e+000	0.00e+000
Max. strain (mm)	4.777e-006	5.132e-006
Load on body (N)	1960	2145

part on the surfboard which consists of stringer, nose, ding is in direct contact with the waves on the sea further direct load is acted upon the above said part due to which the part of the surfboard is in direct contact with the water creates more impact which results in very minimal elongation on certain parts of the surfboard (Table 8).

Figure 15 indicates resultant displacement and equivalent strain for rails of a surfboard. Rails are where the deck and the bottom meet. Like the other parts of the surfboard, rails have their part to play in shaping the overall performance of a surfboard. The shape of rails determines how water flows over them when the board is planning or turning. Rails will set into the wave to a depth relative to the rider’s

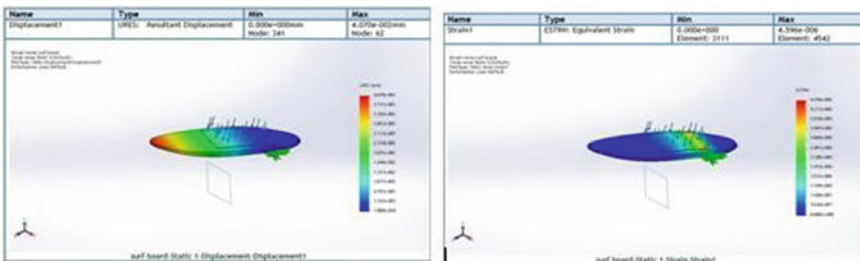


Fig. 15 Rail’s resultant displacement and equivalent strain

weight; heavier surfers need more volume so it can either be put into thickness which increases the rail size or length or width.

Figure 16 indicates the stringer is subjected to direct contact with the seawater creating stress concentration from the nose to stringer will be high when compared to stress concentration on rails, skeg, and fins and on the tail. The above figure represents resultant displacement and equivalent strain applied to the surfboard. As the front part on the surfboard which consists of stringer, nose, ding is in direct contact with the waves on the sea further direct load is acted upon the above said part due to which the part of the surfboard is in direct contact with the water creates more impact which results in very minimal elongation on certain parts of the surfboard (Table 9).

Figure 17 indicates surfboard fin or skeg, which is hydrofoil, mounted at the tail of the surfboard. A Skeg is a key component in a surfer board, which improves the directional stability and has the ability to accelerate the structure. Single fins are very widely used for surfing purpose. Mostly a Skeg is a structure that is subjected

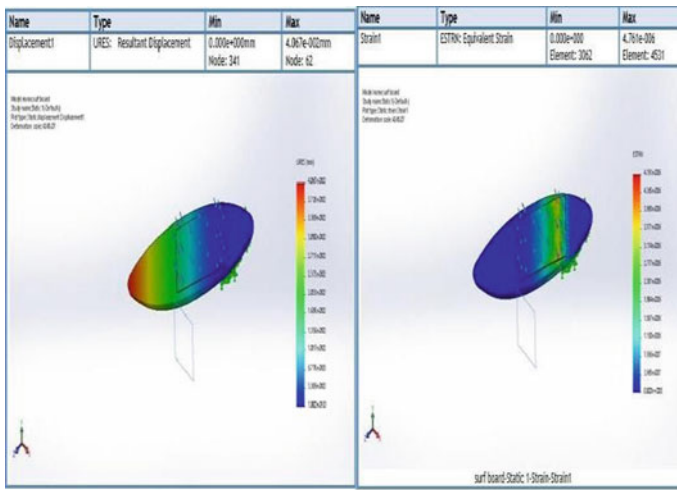


Fig. 16 Skeg’s resultant displacement and equivalent strain

Table 9 Surfboard rails specifications

Design specification	With inclusion of CNT	Without inclusion of CNT
Min. displacement (mm)	0.00e+000	0.00e+000
Max. displacement (mm)	4.067e-002	4.433e-002
Min. strain (mm)	0.00e+000	0.00e+000
Max. strain (mm)	4.761e-006	5.519e-006
Load on body (N)	1960	2145

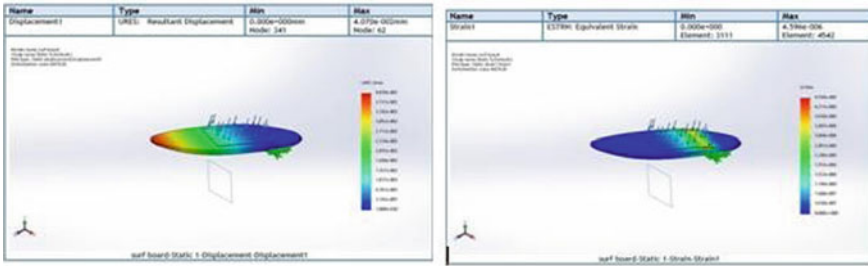


Fig. 17 Skeg’s resultant displacement and equivalent strain

to shock and impact loads. The above figure represents the resultant displacement and equivalent strain on skeg or fin of a surfboard.

6 Comparison of Surfboard Results with and Without Inclusion of CNT

6.1 Stringer of Surfboard

Figure 18 indicates the stringer is subjected to direct contact with the seawater creating stress concentration from the nose to stringer, which will be high in without inclusion of CNT when compared to inclusion of CNT.

Figure 19 represents equivalent strain applied on the surfboard. The stringer is subjected to direct contact with the waves on the sea further direct load is acted upon the above said part due to which the part of the surfboard is in direct contact with the water creating more impact that results in minimal elongation on certain parts of the surfboard.

Fig. 18 Stringer of surfboard representing resultant displacement

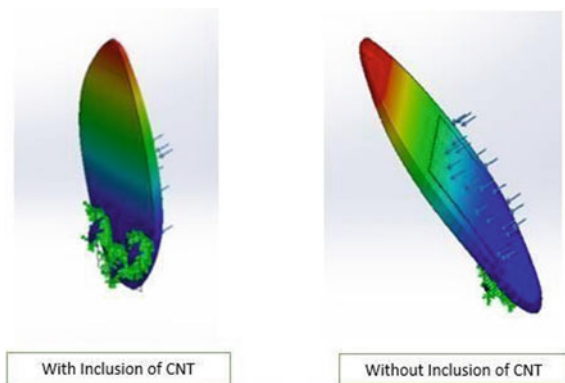
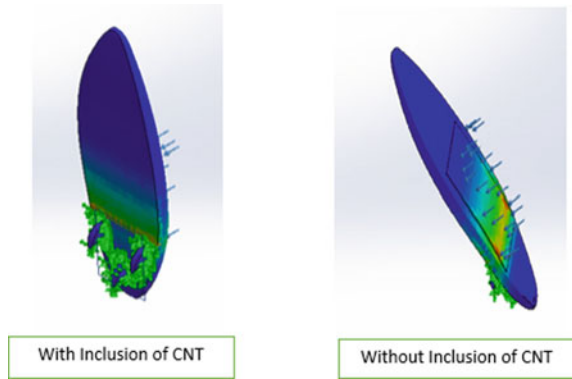


Fig. 19 Stringer of surfboard representing equivalent strain



6.2 Rails of Surfboard

Figure 20 indicates the rails are subjected to direct contact with the seawater creating stress concentration, which is less from the nose to the stringer and will be high when compared to stress concentration on stringer and Skeg.

Figure 21 represents equivalent strain applied on the surfboard. The rails are subjected to direct contact with the waves on the sea further direct load is acted upon the above said part due to which the part of the surfboard is in direct contact with the water creates more impact which results in very minimal elongation on certain parts of the surfboard (Fig. 22; Table 10).

Fig. 20 Rails of surfboard representing resultant displacement

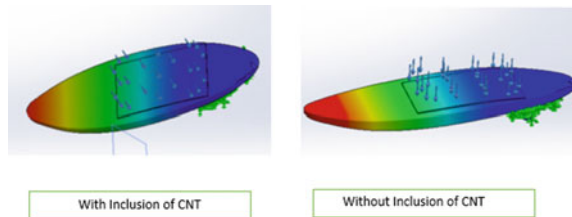


Fig. 21 Rails of Surfboard representing Equivalent Strain

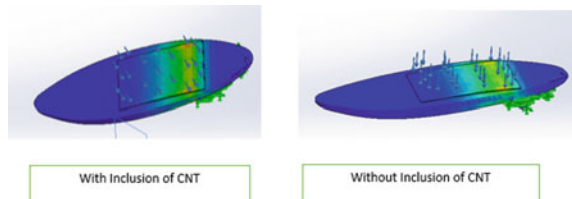


Fig. 22 Skog on surfboard representing resultant displacement

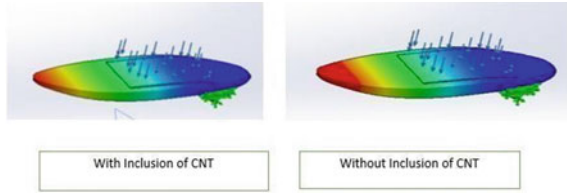


Table 10 Surfboard skog specifications

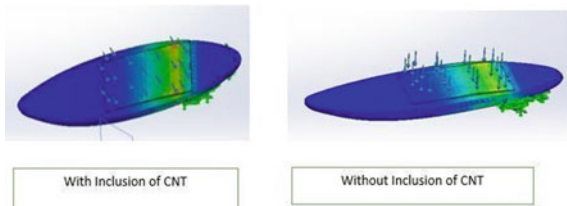
Design specification	With inclusion of CNT	Without inclusion of CNT
Min. displacement (mm)	0.00e+000	0.00e+000
Max. displacement (mm)	4.070e-002	4.432e-002
Min. strain (mm)	0.00e+000	0.00e+000
Max. strain (mm)	4.596e-006	5.5004e-006
Load on body (N)	1960	2145

6.3 Skog of Surfboard

The above figure indicates the rails are subjected to direct contact with the seawater creating stress concentration from the nose to stringer will be high when compared to stress concentration on stringer and skog (Fig. 23).

The above figure represents equivalent strain applied on the surfboard. The skog is subjected to direct contact with the waves on the sea further direct load is acted upon the above said part due to which the part of the surfboard is in direct contact with the water creates more impact which results in very minimal elongation on certain parts of the surfboard.

Fig. 23 Skog of surfboard representing equivalent strain



7 Conclusion and Future Scope

In the current study, epoxy glass fiber-reinforced polymer composite laminate with MWCNT as filler material in different weight fractions have been studied for moisture absorption test in normal water and seawater simultaneously for a certain period. The results are compared with material immersion in normal water and seawater, various mechanical properties are carried out on the material, for compression test the specimen which is of 0.025% inclusion of CNT exhibited better results when immersed in normal water and seawater, whereas during impact testing, the specimen which is of 0.020% exhibited better results when compared. Composite materials have a great potentiality of application in structures subjected primarily to compressive loads. Composite materials have attractive aspects like the relatively high compressive strength, good adaptability in fabricating thick composite shells, low weight, low density, and corrosion resistance.

References

1. S. Pichi Reddy, P.V. Chandra Sekhar Rao, A. Chennakesava Reddy, G. Parmeswari, *Tensile and Flexural Strength of Glass Fiber Epoxy Composites* (Department of Mechanical Engineering, L.B. Reddy College of Engineering, Mylavaram, Andhra Pradesh)
2. B.C. Ray, D. Rathore, *Environmental Damage and Degradation of FRP Composites* (Department of Metallurgical and Materials Engineering, National Institute of Technology, Rourkela)
3. B. Shivamurthy, K. Udaya Bhat, S. Anandhan, Mechanical and sliding wear properties of multi-layered laminates from glass fabric/graphite/epoxy composites. *Mater. Des.* **44**, 136–143 (2013)
4. R.K. Goyal, A. Kadam, Polyphenylene sulphide/graphite composites for emi shielding applications. *Adv. Mater. Lett.* **1**(2), 143–147 (2010)
5. S. Bhattacharya, R.P. Tandon, V.K. Sachdev, Electrical conduction of graphite filled high density polyethylene composites: experiment and theory. *J. Mater. Sci.* **44**(9), 2430–2433 (2009)
6. E. Huttunen-Saarivirta, F.H. Stott, V. Rohr, M. Sch utze, Particle angularity effects on the elevated- temperature erosion-oxidation behaviour of aluminium diffusion coatings on 9% Cr steel. *Wear*, **261**(7–8), 746–759 (2006)
7. S. Yerramareddy, S. Bahadur, Effect of operational variables, microstructure and mechanical properties on the erosion of Ti–6Al–4V. *Wear* **142**(2), 253–263 (1991)
8. M.S. ElTobgy, E. Ng, M.A. Elbestawi, Finite element modeling of erosive wear. *Int. J. Mach. Tools Manuf* **45**(11), 1337–1346 (2005)
9. A. Alberdi, A. Suárez, T. Artaza, G.A. Escobar-Palafox, and K. Ridgway, Composite cutting with abrasive water jet. *Procedia Eng.* **63**, 421–429 (2013)
10. M.A. Azmir, A.K. Ahsan, A study of machining process on glass/epoxy composite laminate. *J. Mater. Process. Technol.* **209**(20), 6168–6173 (2009)
11. M.A. Azmir, A.K. Ahsan, Investigation on glass/epoxy composite surfaces machined by machining. *J. Mater. Process. Technol.* **198**(1–3), 122–128 (2008)
12. A.A. Khan, M.M. Haque, Performance of different abrasive materials during abrasive water jet machining of glass. *J. Mater. Process. Technol.* **191**(1–3), 404–407 (2007)
13. J. Wang D.M. Guo, A predictive depth of penetration model for abrasive water jet cutting of polymer matrix composites. *J. Mat. Process. Technol* **121**(2–3), 390–394 (2002)
14. D.K. Shanmugam, T. Nguyen, J. Wang, A study of delamination on carbon nano tubes/epoxy composites in abrasive waterjet machining. *Compos. A* **39**(6), 923–929 (2008)

15. G. Nesar, Polymer based composites in marine use: history and future trends. *Procedia Eng.* **194**, 19–24 (2017)
16. G. Perillo, J.K. Jorgensen, Numerical/Experimental study of the impact and compression after impact on GFRP composites for wind/marine applications. *Procedia Eng.* **167**, 129–137 (2016)
17. W.M. Andreas, R. Kovacevic, *Principles of Abrasive Water Jet Machining* (Spinger, London, UK, 1998)
18. M. Junkar, B. Jurisevic, M. Fajdiga, M. Grah, Finite element analysis of single-particle impact in abrasive water jet machining. *Int. J. Impact Eng* **32**(7), 1095–1112 (2006)
19. M.A. Azmir, A.K. Ahsan, A study of abrasive water jet machining process on glass/epoxy composite laminate. *J. Mater. Process. Technol.* **209**(20), 6168–6173 (2009)
20. D.K. Shanmugam, S.H. Masood, An investigation on kerf characteristics in abrasive waterjet cutting of layered composites. *J. Mater. Process. Technol.* **209**(8):3887–3893

Mechanical Behavior in Tungsten Carbide-Reinforced Aluminum Composites



Yamuzala Sai Ratnakar  and Allu Venkata Pradeep

Abstract In rubbing components, the wear property of the material is found to be a significant consideration. To enhance the wear property of Aluminum (Al), which is most widely used for its better strength to weight ratio, Tungsten Carbide (WC), which is highly abrasive in nature, is reinforced in different weight fractions of aluminum (2.5, 5, 7.5, and 10%) to form a metal matrix composite (MMC) by fabricating through powder metallurgy and stir casting techniques. The specimens surface topologies were studied for the dispersion of WC in Al by performing Scanning Electron Microscopy (SEM) analysis, the tests for wear and hardness were performed and the results were compared for both the fabrication techniques by checking the variation of results, if any, which is mainly dependent on the dispersion of tungsten carbide in aluminum. Eventually, it was investigated that the wear property of the specimens fabricated through stir casting technique was increased up to 7.5% and declined after that, whereas the wear property got increased up to 10% when fabricated through powder metallurgy technique. This is quite evident that the WC dispersion in Al is the prime factor enhancing the properties, where powder metallurgy proved to have better dispersion over stir casting technique.

Keywords Metal matrix composite · Powder metallurgy · Wear rate · Hardness test · Scanning electron microscopy analysis

Y. S. Ratnakar (✉)

Department of Mechanical Engineering, Lendi Institute of Engineering & Technology, Jonnada, AP, India

e-mail: ratnakarmtech@gmail.com

A. V. Pradeep

Department of Mechanical Engineering, Vignan's Institute of Engineering for Women, Visakhapatnam, AP, India

e-mail: venkatpradeepallu@gmail.com

© Springer Nature Singapore Pte Ltd. 2021

G. S. V. L. Narasimham et al. (eds.), *Recent Trends in Mechanical Engineering*,

Lecture Notes in Mechanical Engineering,

https://doi.org/10.1007/978-981-15-7557-0_25

1 Introduction

A composite material consists of reinforcement placed in a matrix. A metal matrix composite is a combination of two different metals to obtain a new material. Metal matrix composites have enhanced the whole mechanical properties of the matrix than the pure metal. Aluminum (Al), due to its lightweight and corrosion resistance, replaced the ferrous element in recent years. It is the third most abundant material available in nature. Al has a large coefficient of linear expansion and its tensile strength lies in the range of 70–700 MPa. There is a growth in using Tungsten Carbide (WC) as reinforcement for Al matrix since the former is known for its wear-resistant properties. WC wears up to 100 times longer than steel in conditions including abrasion and erosion. Since the Al–WC composites have a very small grain size of particles, they have good ductility and interference strength [1, 2]. TengkeYe investigated the effects of Silicon Carbide (SiC) particle size on the mechanical properties and the failure mechanisms of Al/SiC composites under compression with strain rates ranging from 0.001 to 5200 s⁻¹ were investigated. Al/SiC composites consisting of 65 wt% SiC particles with an average size of 10 and 50 μm were studied [3].

T. Jaya Kumar investigated the mechanical behaviour of aluminum alloy and reinforced with nanoparticle composites such as magnesium oxide and SiC via liquid metallurgy technique. Aluminum alloy and composites are characterized by Scanning Electron Microscopy coupled with Energy Dispersion X-ray spectroscopy (SEM-EDX). The tensile properties of Al alloy and composites are examined under room temperature (30 °C) and at elevated temperatures (200, 350 °C). The microstructure results reveal that the SiC and MgO particles are uniformly distributed within the matrix and exhibited better interface bonding [1].

The WC is used as reinforcement in Al metal matrix composite with different weight percentages. The fabrication can be done in many methods like stir casting, liquid metallurgy, powder metallurgy, etc. Fabrication of composites is usually done by the stir casting process among different processes available since it is inexpensive, Refs. [2, 4]. Powder metallurgy consists of three main steps viz. powder mixing, die preparation and sintering. Powder metallurgy (PM) is a widely used method for producing metal matrix composites. Pressing into the desired shape of form (compacting), and then heating the compressed material under a controlled atmosphere to bond the material (sintering) is a powder metallurgy process to blend fine powdered materials. As processing takes place in solid state, it minimizes the reaction between the constituents of the composite. Compacting and sintering are often combined in one step during hot pressing [1].

Anand et al. [2] studied the fabrication of aluminum–silicon carbide with mica in stir casting method to obtain a hybrid MMC by varying mica in three different compositions. Along with WC, sometimes fly ash can also be used as reinforcement in aluminum composites [5]. Selvam [6] prepared the WC particulate of 2.5, 5, 7.5, and 10% on mass fraction basis through powder metallurgy technique and found that an increase in WC particulate increases the density of performs. Some experiments

Table 1 Composition of aluminum and tungsten carbide through stir casting

Specimens name	MMC (Al) (g)	Reinforced material (WC in wt%)	WC (g)
A	30	2.5	0.75
B	30	5	1.5
C	30	7.5	2.25
D	30	10	3

have been conducted by varying weight fraction of SiC [7, 8]. It was found that the hardness and impact strength increased with increase in weight percentage of SiC [9, 10]. Abdizadeh [11] introduced MgO nanoparticles to aluminum matrix which caused increasing of hardness values.

Wear of the materials under nonabrasive conditions is found out using a pin on disk apparatus, by conducting a test for selected sliding distance and for selected values of load and speed. When the pin starts wearing out, then the maximum value of equivalent stresses are increased [4]. Wear resistance increases with increase in reinforcement like WC, fly ash, or SiC [4, 6, 9, 10, 12]. Wear resistance of WC is better than that of tool steels, Ref. [1, 13].

2 Fabrication

2.1 Stir Casting

Stir casting is a basic procedure for producing metal matrix composite materials, in which the reinforcement material is integrated into the molten metal by stirring. Aluminum is poured into the pit furnace and melted above 800 °C. At this temperature, tungsten carbide of 2.5 wt% of aluminum is added to the molten aluminum. Then it is stirred thoroughly at a constant speed of 300 rpm with a stirrer. After the completion of stirring process, the molten solution is poured into a crucible to obtain the specimens of required dimensions. After a few seconds, water quenching is done to relieve the stresses induced in the specimens and the same procedure is repeated for tungsten carbide of remaining weight % of aluminum, i.e., 5, 7.5, and 10% (Table 1).

2.2 Powder Metallurgy

Powder metallurgy can be defined as a technique in which materials or components can be made from metal powders. The major advantage of this technique is that the need for metal removal processes can be reduced to a great extent. Powder metallurgy

Table 2 Composition of aluminum and tungsten carbide through powder metallurgy

Specimens name	MMC (Al) (g)	Reinforced material (WC in wt%)	WC (g)
A	180	2.5	4.5
B	180	5	9
C	180	7.5	13.5
D	180	10	18

consists of three main procedural steps viz., powder compaction, die pressing, and sintering. In powder compaction, the metal powder is closely packed by applying high pressure in a die. The powder is compacted to the required shape and then ejected from the die. The pressure ranges from 150 to 700 MPa. In sintering process, the metal is taken in the form of a powder and placed into a mold. After compaction in the mold, the material is heated for a long period of time. Generally, the sintering temperatures are taken in the range of 70–90% of the melting point of the metal. In our case, i.e., for Al, the temperatures for sintering will lie in the range of 580–600 °C. The sintering time, i.e., the heating time will be around 3 h (Table 2).

3 Experimental Details

3.1 Wear Test

The wear test is conducted according to ASTM G99-17 STANDARD Test Method for Wear Testing with a Pin-on-Disc apparatus. A pin on disc apparatus consists of a motor drive, revolution counter, pin specimens holder, a lever arm, and a wear measuring system. The specifications of the pin on disk used are:

3.2 Specifications

- Pin size: 12 mm
- Wear disc diameter: 165 mm
- Wear disc thickness: 8 mm
- Wear track diameter: 60 mm
- Length of the specimens: 30 mm
- Max disc rotation: 2000 rpm
- Max load: 200 N
- Max frictional force: 200 N
- Temperature: 40 °C
- Length: 400 mm

- Wear range: -2 mm to $+2$ mm.

3.3 Hardness Test

Hardness is defined as the property of a material to resist plastic deformation. The hardness test is carried out according to ASTM E10–18—Standard Test Method for Brinell Hardness of Metallic Materials on Brinell hardness test apparatus. In this test, the test material is indented with an 8-mm-diameter hardened stainless steel ball which is subjected to a load of 10 kg for 10–15 s. The test material is left with an indentation whose diameter is measured with a low powered microscope. Brinell Hardness Number is found by using the formula

$$\text{BHN} = \frac{2P}{\pi D \left(D - \sqrt{D^2 - d^2} \right)} \quad (1)$$

where

- P applied force (kgf)
- D diameter of indenter (mm)
- d diameter of indentation (mm).

4 Results and Discussion

4.1 For Stir Casting

Wear Results

From the above comparison, the wear rate for specimens A, B, and C gradually decreased, and for the specimens D the wear rate increased. The optimum wear rate is observed in specimen C (7.5% WC of base Al). The below graphs depict the wear rate values for 350 s (Figs. 1, 2, 3, 4 and 5; Table 3).

Hardness Results

After calculation of BHN values for Stir Casting specimens,

For specimens A, BHN = 37.91

For specimens B, BHN = 41.911

For specimens C, BHN = 46.838

For specimens D, BHN = 72.46 (Fig. 6; Table 4).

Fig. 1 Graphs for wear rate at 2.5% WC in stir casting process

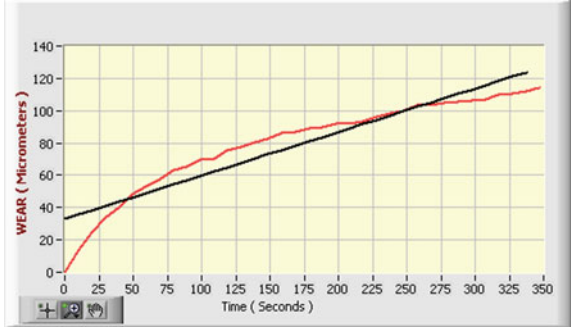


Fig. 2 Graphs for wear rate at 5.0% WC in stir casting process

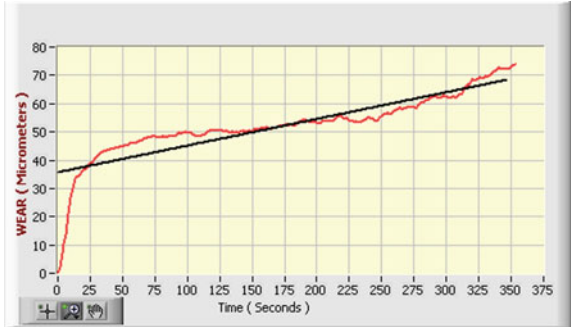
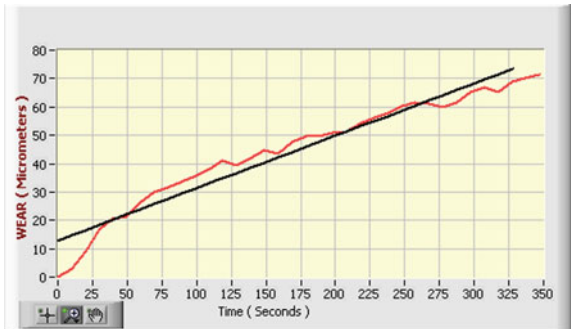


Fig. 3 Graphs for wear rate at 7.5% WC in stir casting process



4.2 For Powder Metallurgy

Wear Results

From the Table 5, the wear rate for all specimens got gradually decreased with the increase in WC into Al. The below graphs depict the wear rate values for 350 s (Figs. 7, 8, 9 and 10).

Fig. 4 Graphs for wear rate at 10% WC in stir casting process

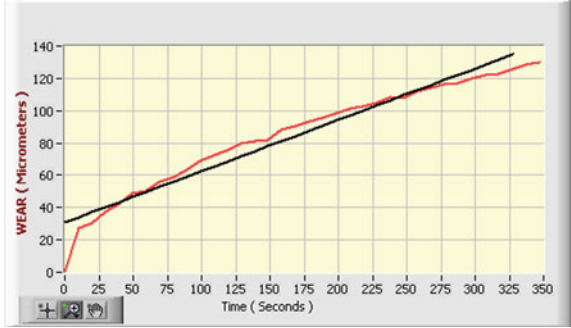


Fig. 5 Bar chart for wear rates of stir casting specimens with error bar

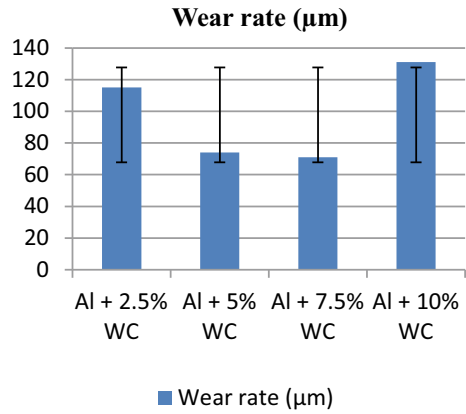


Table 3 Wear rate values for stir casting specimens

Specimens name	Load (N)	Wear rate (in micrometer)
A	10	115
B	10	74
C	10	71
D	10	132

Fig. 6 Graph showing the hardness values for stir casting specimens with error bar

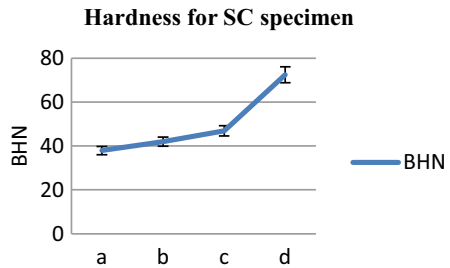


Table 4 BHN values for stir casting specimens

Specimens	Diameter of indenter (mm)	Diameter of indentation (mm)	BHN value
A	8	1.8	37.91
B	8	1.72	41.91
C	8	1.62	46.83
D	8	1.3	72.46

Table 5 Wear rate values for powder metallurgy specimens

Specimens name	Load (N)	Wear Rate (micrometer)
A	10	103
B	10	68
C	10	63
D	10	58

Fig. 7 Graphs for wear rate of powder metallurgy specimen at 2.5% of WC



Fig. 8 Graphs for wear rate of powder metallurgy specimen at 5.0% of WC



Fig. 9 Graphs for wear rate of powder metallurgy specimen at 7.5% of WC



Fig. 10 Graphs for wear rate of powder metallurgy specimen at 10% of WC



Wear Rate Analysis

See Fig. 11.

Hardness Results

After calculation of BHN values for powder metallurgy specimens,

Fig. 11 Bar chart for wear rates of powder metallurgy specimens with error bar

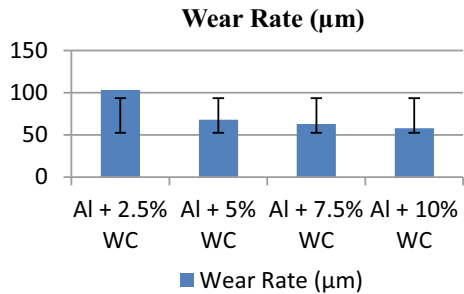


Fig. 12 Graph showing the hardness values for powder metallurgy specimens with error bar

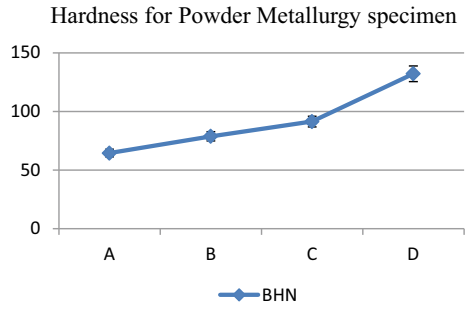


Table 6 BHN values for powder metallurgy specimens

Specimens	Diameter of indenter (mm)	Diameter of indentation (mm)	BHN value
A	8	1.4	64.49
B	8	1.27	78.74
C	8	1.13	91.4
D	8	0.98	132.1

For specimen A, BHN = 64.49

For specimen B, BHN = 78.74

For specimen C, BHN = 91.40

For specimen D, BHN = 132.1 (Fig. 12; Table 6).

4.3 Scanning Electron Microscope (SEM) Analysis

Stir Casting Specimens

See Figs. 13, 14, 15 and 16.

Fig. 13 SEM image of stir casting specimen with 2.5% of WC

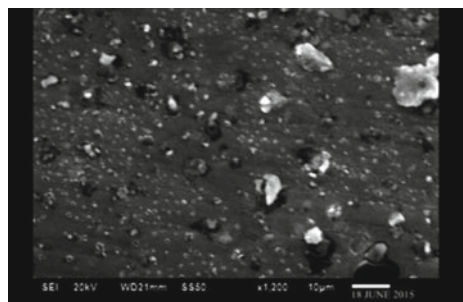


Fig. 14 SEM image of stir casting specimen with 5.0% of WC

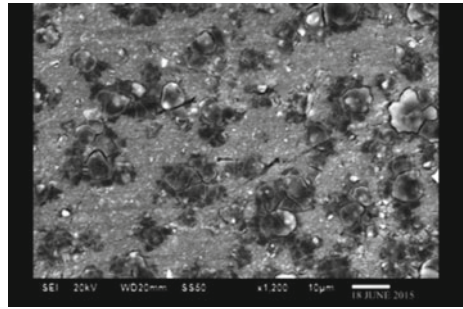


Fig. 15 SEM image of stir casting specimen with 7.5% of WC

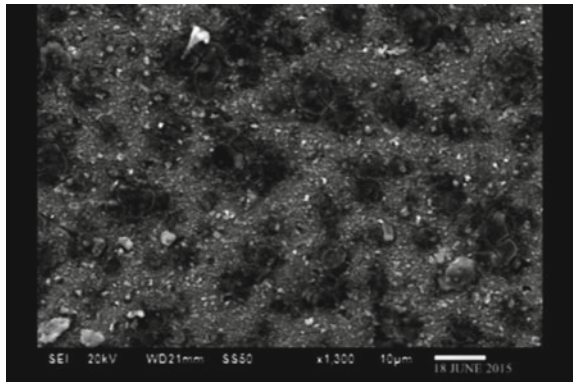
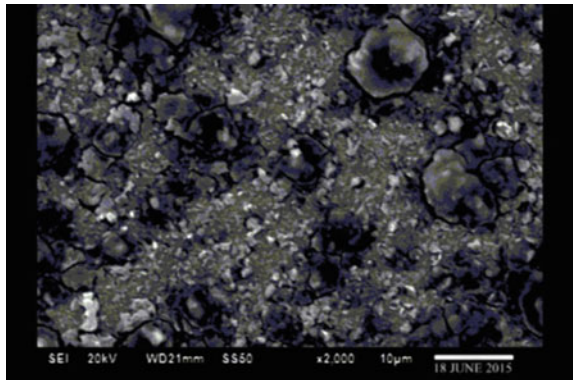


Fig. 16 SEM image of stir casting specimen with 10% of WC



Powder Metallurgy Specimens

See Figs. 17, 18, 19 and 20.

Fig. 17 SEM image of powder metallurgy specimen at 2.5% of WC

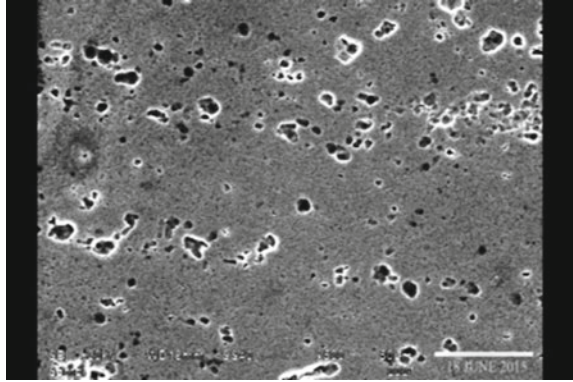


Fig. 18 SEM image of powder metallurgy specimen at 5.0% of WC

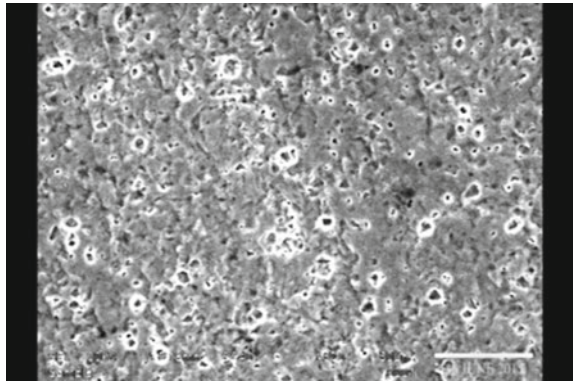


Fig. 19 SEM image of powder metallurgy specimen at 7.5% of WC

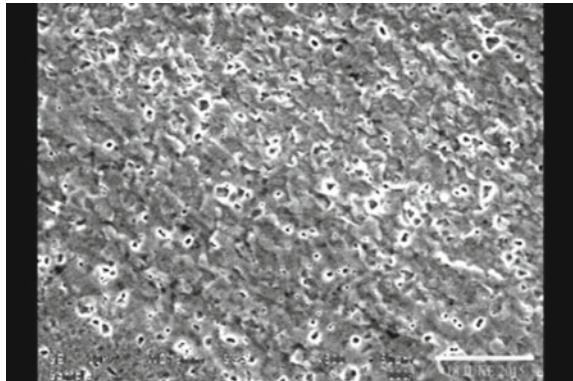
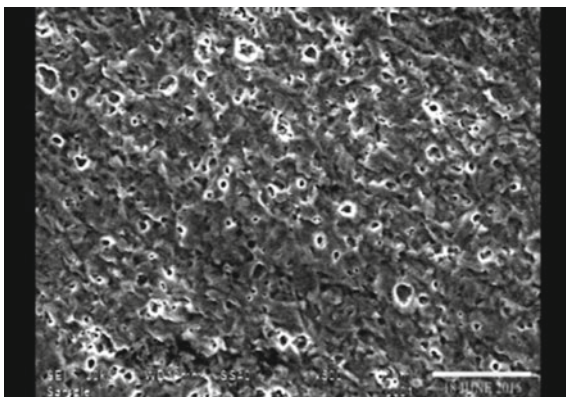


Fig. 20 SEM image of powder metallurgy specimen at 10% of WC



5 Conclusion

The metal matrix specimens were fabricated through the techniques of powder metallurgy and stir casting for different weight fractions of WC (2.5, 5, 7.5, and 10%) reinforced with Al. Tests for wear and hardness were conducted on all the specimens and it was observed that the wear resistance for Al got increased with the inclusion of WC in it, this tendency was followed up to the specimens of 7.5% fabricated through stir casting, whereas the same was increased till the last specimens of 10% WC fabricated through PM. Also, this trend of increasing hardness was found in the specimens of both the techniques but the hardness was found to be more at any given specimen fabricated by PM than the specimens of stir casting. The surface topology of all the specimens was analyzed for particle dispersion using Scanning Electron Microscopy (SEM) and was found that the dispersion of WC in Al is finer and free from agglomerations in specimens of PM compared to the specimens of stir casting. From this, it is quite evident that the dispersion of reinforcement in metal matrix composite is very important in enhancing the properties and eventually it can be concluded that the components produced by the PM technique possess better properties than the components produced by the stir casting technique.

References

1. A. Sadooghi, et al., Investigating the influence of ZnO, CuO, Al₂O₃ reinforcing nanoparticles on strength and wearing properties of aluminum matrix nanocomposites produced by powder metallurgy process. (IOP Science, August 2019)
2. H.P.R. Pydi, Microstructure exploration of the aluminum-tungsten carbide composite with different manufacturing circumstances. *Int. J. Soft Comput. Eng. (IJSCE)* **2**(6) (2013). ISSN 2231-2307
3. T. Ye, Y. Xu, Effects of SiC particle size on mechanical properties of SiC particle reinforced aluminum metal matrix composite. *Mat. Sci. Eng. A* **753**(10), 146–155 (2019)

4. M. Giridharadhayalan, Studies on wear behaviour of shot peened EN 47 steel using finite element method. *IJREAT Int. J. Res. Eng. Adv. Technol.* **3**(1) (2015)
5. G. Amarnath, Microstructure and tribological behaviour of aluminium reinforced with tungsten carbide particulate and flyash metal matrix composites. *Int. J. Res. Eng. Technol.* eISSN 2319-1163, pISSN 2321-7308
6. B. Selvam, Densification behavior of aluminium reinforced with tungsten carbide particulate metal matrix composite processed by p/m. *IOSR J. Mech. Civil Eng. (IOSR-JMCE)* 24–29 e-ISSN 2278-1684, p-ISSN 2320-334X
7. T. Jaya Kumar, et al., Investigation of hot tensile behavior of silicon carbide and magnesium oxide reinforced aluminum matrix composites (Springer, 8th August 2019)
8. T. Anand, Investigation of mechanical properties in aluminum silicon carbide mica hybrid metal matrix composite. *Int. J. Eng. Sci. Adv. Technol.* **5**(2), 112–117
9. M. Singla, Development of aluminium based silicon carbide particulate metal matrix composite. *J. Miner. Mater. Character. Eng.* **8**(6), 455–467 (2009)
10. Vikas Chawla, Study of wear properties of Al–SiC composites. *J. Miner. Mater. Character. Eng.* **8**(10), 813–819 (2009)
11. H. Abdizadeh, Investigation of microstructure properties of nano MgO reinforced Al composites manufactured by stir casting and powder metallurgy methods: a comparative study. *Compos.: Part B* **56**, 217–221 (2014)
12. M.R. Anoop, Wear rate analysis of nano-coated cutting tool. *Int. J. Adv. Res. Sci. Eng.* **4**(11) (2015)
13. M. Kandeva, Wear-resistance of aluminum matrix microcomposite materials. *Tribol. Ind.* **33**(2) (2011)

Simulation of Bridge Deck Made-Up of Fibre Reinforced Polymer Composites Reinforced with ZrO_2



I. Anil Kumar, P. Srinivasa Reddy, M. Balajee, and R. Jagadeesh Kumar

Abstract Composite material of glass fibre base is a very promising material for future structures. It is possible to create a bridge span consists of steel main beams and GFRP deck. For identifying the kind of glass fibre and type of polymer matrix or type of adhesive with steel or concrete, there are very interesting directions of searching line. The project presented with results of compression, tensile and impact analysis of GFRP composite. It will be described with the examples of bridges where GFRP deck have been constructed with main steel beams. Deterioration of concrete bridge decks has become a serious problem in recent years due to corrosion of steel reinforcement. There is also a need to replace existing bridge decks to accommodate the demand to increase the traffic load. The concept of using rapid deck replacement introduces an attractive approach, which minimizes traffic interruption and consequently reduces replacement costs. This project proposes an innovative glass fibre-reinforced polymer (GFRP) bridge deck as an excellent solution for the infrastructure of highway bridges. The proposed composite deck, patented by War drop Engineering Incl. Faroex Ltd., consists of a series of equilateral triangular section tubes produced by the filament winding process. Glass fibres are wound at varying angles, including fibres in the longitudinal direction, to achieve the target transverse and longitudinal strengths. The bridge deck consists of modules that are formed when several of the uncured, wound, triangular elements are placed between two pultruded plates and are subsequently cured into a single module of bridge decking. These modules delivered to the site and within hours they are installed. By virtue of the very materials and processes used, glass fibre-reinforced polymer (GFRP) bridge decks offer high strength, lightweight and easy handling for installation. Most importantly, the absence of steel in the deck

I. Anil Kumar (✉) · P. Srinivasa Reddy (✉) · M. Balajee · R. Jagadeesh Kumar
Department of Mechanical Engineering, Lendi Institute of Engineering & Technology, Jonnada,
Andhra Pradesh, India

e-mail: anil.mec14@gmail.com

P. Srinivasa Reddy

e-mail: palasrinivasreddy@gmail.com

M. Balajee

e-mail: balajimugada@gmail.com

© Springer Nature Singapore Pte Ltd. 2021

G. S. V. L. Narasimham et al. (eds.), *Recent Trends in Mechanical Engineering*,

Lecture Notes in Mechanical Engineering,

https://doi.org/10.1007/978-981-15-7557-0_26

ensures that corrosion will never occur. This project provides a description of the deck, fabrication process and test results of a portion of the deck.

Keywords GFRP composite · Filament winding · Mechanical properties · Simulation · Damage · Behaviour · Corrosion

1 Introduction

Fibre reinforced polymer (FRP) materials have emerged as an alternative material for producing reinforcing bars for concrete structures. FRP composites are alternative to steel reinforcement, especially in aggressive environments, mainly due to their high corrosion resistance. The advantages of FRP fibres are high strength and lightweight, corrosion resistance, dimensional stability, low thermal conductivity, no conductivity, electromagnetic transparency, impact resistance and low lifecycle costs. The disadvantages of the FRP composites are high initial costs, their susceptibility to mechanical damage and fire, inability to bend in the field, longer load transfer lengths, poor shear strength and low strain to failure [1]. Due to other differences in the physical and mechanical behaviour of the FRP materials versus steel, unique guidance on the construction of concrete structures reinforced with FRP bars is needed. FRP composites are the combination of polymeric resins, acting as matrices or binders, with strong and stiff fibre assemblies, which act as the reinforcing phase.

Good exploration of new materials, like composite GFRP, creates the possibility to improve this technology and makes comparison analysis with traditional standard of materials. Composite materials are the future of building structures. The durability of structures is always a very important parameter [2]. The past applications of CFRP in bridge structures like improving tapes, lines (wants) of cable-stayed bridges have given open gate for composite materials. GFRP polymer with glass fibre is a good alternative for traditional material. The properties of GFRP are anisotropy (depending on the type of reinforcement), low density, physical and mechanical properties of composite depending on its components and their respective proportions, high resistance to corrosion and oxidation, relatively high mechanical properties and ability to form complex shapes. Relatively low cost compared to other kinds of fibres makes E-glass fibres the most commonly used fibres available in the construction industry [3]. The disadvantages of glass fibres are a relatively low Young's modulus, the low humidity and alkaline resistance as well as low long-term strength due to stress rupture. GFRP composite material is suitable for decks of bridge structures and footbridges applications [4].

Bridges are very important components of infrastructure development of a nation and are composed of several components such as decking slabs, girders, trusses, bearings, abutments and piers. The bridge deck is a structural component that distributes and transmits been provided on the sustainability of GFRP bridge deck panels. The main scope of the present investigation is to study the experimental behaviour of hand lay-up multicellular GFRP composite the live loads to the girders and then to the

substructure of a bridge. The bridge decks require maximum maintenance because of corrosion and deterioration [5]. Conventional materials and technologies, although suitable for bridge deck applications, lack of durability and fatigue for demanding applications, and in some cases are susceptible to rapid deterioration. Life cycle analysis estimates indirect costs to the user due to traffic delays and lost productivity at more than 10 times the direct cost of repair. In recent years, high-performance fibre-reinforced polymer (FRP) composite materials have been identified as an excellent candidate for rehabilitating deteriorated bridges. One of the most promising applications for this high-performance material is bridge decking. FRP plate elements are used in bridge construction predominantly as deck slabs mainly because of their low self-weight, high corrosion and fatigue resistance, and very little installation time, resulting in minimal traffic interruption [6]. Potential applications for FRP decks are a new design, replacement of under-strength decks in existing bridges and the provision of temporary running surfaces. Due to the low elastic modulus of GFRP materials, GFRP reinforced sections exhibit higher deformability when compared to equivalent reinforced steel sections [7]. Hence, the deflection criterion governs the design of intermediate and long-spanning sections reinforced with GFRP bars. Investigations on FRP bridge decks were conducted through laboratory tests on FRP deck components and field tests on FRP bridges. Alagusundaramoorthy and Veera-Sudarsana Reddy investigated the load–deflection behaviour of GFRP composite deck panels under static loading [8]. Vovesny and Rottera carried out analysis and design of a new bridge deck panel made of GFRP. Zhu and Lopez presented results obtained from an experimental and analytical study of a newly developed lightweight composite bridge deck system composed of pultruded trapezoidal GFRP tubes and outer wrap [9]. From the analytical model, it was found that shear deformation must be considered for the accurate prediction of GFRP panels. Mara et al. examined the efficiency of GFRP system with the traditional system and found that FRP decks contribute to potential cost savings over the life cycle of bridges and a reduced environmental impact. Ascione et al. presented experimental results on the mechanical performance of composite beams obtained by bonding GFRP rectangular pultruded panels by means of an epoxy structural adhesive [10]. No significant loss of performance in terms of failure load is observed, but an increase of pre-failure stiffness was observed. Further, it is observed that the research investigations carried out on hand lay-up FRP composite bridge decks under static and fatigue behaviour of prototype decks are scanty. A brief description has bridge deck panels under static and fatigue loading.

1.1 Hand Lay-Up Technique

Hand lay-up technique is the simplest method of composite processing. It is a fabrication process in which fibre reinforcements are placed by hand and then wet with resin. The infrastructural requirement for this method is also minimal. The processing

Fig. 1 Hand Lay-up technique for fabrication



Fig. 2 Mould for fabricating a GFRP specimen



steps are quite simple. The manual nature of this process allows for almost any reinforcing material to be considered, chopped strand or mat. Similarly, the resin and catalyst blend can be manipulated to allow for ideal processing conditions. Hand lay-up method finds application in many areas like aircraft components, automotive parts, boat hulls, deck, etc. Generally, the materials used to develop composites through the hand lay-up method (Fig. 1).

In the final steps of spray-up process, workers compact the laminate by hand with rollers. Wood, foam or other core material may then be added, and a second spray-up layer embeds the core between the laminate skins. The part is then cured, cooled and removed from the reusable mould (Fig. 2).

2 Procedure for Manufacturing of Composite Material

2.1 Making of Standard Specimen

Firstly, we took the materials in the required quantity. Added epoxy and hardener in the ratio 10:1 (i.e., 10 parts of resin mixed with 1 part of hardener underweight proportion). GFRP sheet was cut into the required dimension (100 * 100 mm). The mixture of resin and hardener was taken and made to stir for a certain amount of time for the uniformity of the mixture. GFRP of the required dimension was taken and placed on the frame. The mixture was applied on the GFRP sheet and uniformly and the pressure was applied for the distribution of mixture throughout the layer. Then

Fig. 3 Preparing a specimen as per standards



the next layer of GFRP was placed on the mixture and the mixture was applied. This process was repeated until it attains ASTM standard dimensions. It was allowed to dry and harden the workpiece (Fig. 3).

Firstly, we took the materials in the required quantity. Add epoxy and hardener in the ratio 10:1 (i.e. 10 parts of resin mixed with 1 part of hardener underweight proportion). Then Zirconium dioxide (ZrO_2) of 0.1, 0.2, and 0.3% of the weight of mixture was added to the mixture and was mixed well. GFRP sheet was cut into the required dimension. GFRP of standard dimension was taken. The mixture was applied on GFRP sheet uniformly and the pressure was applied on the mixture and sheet for uniform distribution of mixture. Then the next layer of GFRP was placed on the mixture and the mixture was applied. This process was repeated until the dimensions reach the standard specimen dimension. Pressure was applied on the specimen and made to dry and harden off the specimen. Later the supports and the pressure is removed from the workpiece (Fig. 4).

3 Compression Test

Compression test is a very common testing method that is used to establish the compressive force or crush resistance of a material and the ability of the material to recover after a specified compressive force is applied and even held over a defined period of time. In other words, it is the test used to know the strength of the material or resistance of the material under compressive loading.

A compression test is any test in which a material experiences opposing forces that push inward upon the specimen from opposite sides or is otherwise compressed, “squashed”, crushed, or flattened. The test sample is generally placed in between two plates that distribute the applied load across the entire surface area of two opposite faces of the test sample and then the plates are pushed together by a universal test machine causing the sample to flatten. A compressed sample is usually shortened in the direction of the applied forces and expands in the direction perpendicular to the force. A compression test is essentially the opposite of the more common tension test (Figs. 5, 6, 7 and 8).



Fig. 4 Fabricating the specimen using hand lay-up technique



Fig. 5 Compression Testing for given GFRP sample

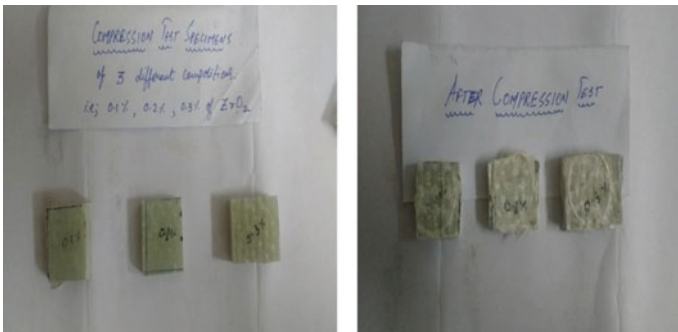


Fig. 6 Specimen before and after compressive test



Fig. 7 Specimen before and after impact test



Fig. 8 Specimen before and after tensile test

4 Simulation in Catia

CATIA software is a multi-platform software suite for computer-aided design (CAD), computer-aided manufacturing (CAM), computer-aided engineering (CAE), PLM and 3D, developed by the French company Dassault Systems. It is a platform to create simulation models and perform analyses for events such as the movement of trains on bridge decks and to find out the stresses that are developed in the bridge deck when it is subjected to external load (Figs. 9, 10 and 11).

Figure 12 shows the variation in total deformation, von Mises and von Mises strain on a bridge deck, the surface of the deck is slightly affected by the applied load.

Figure 13 shows the variation in total deformation, von Mises and von Mises strain on a bridge deck, the surface of the deck is slightly affected by the applied load.

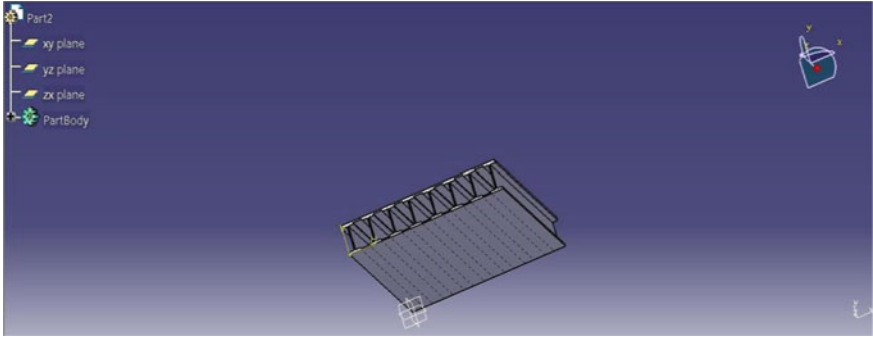


Fig. 9 Design of bridge deck

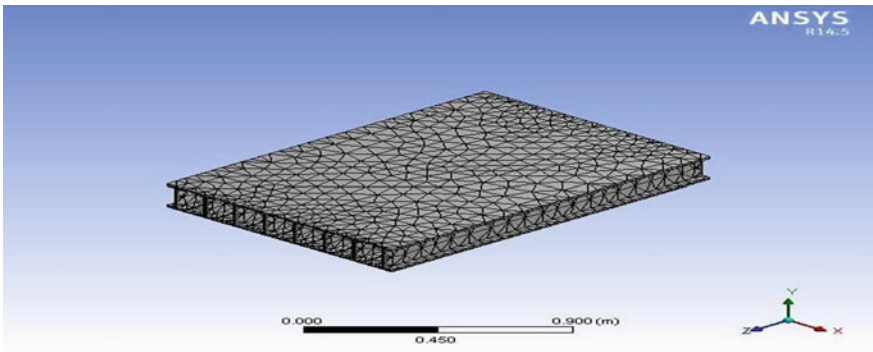


Fig. 10 Tetrahedron meshing of bridge deck

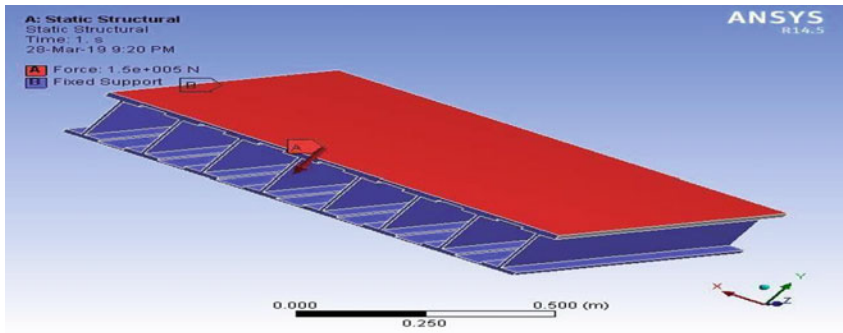


Fig. 11 Applying boundary conditions to the bridge deck

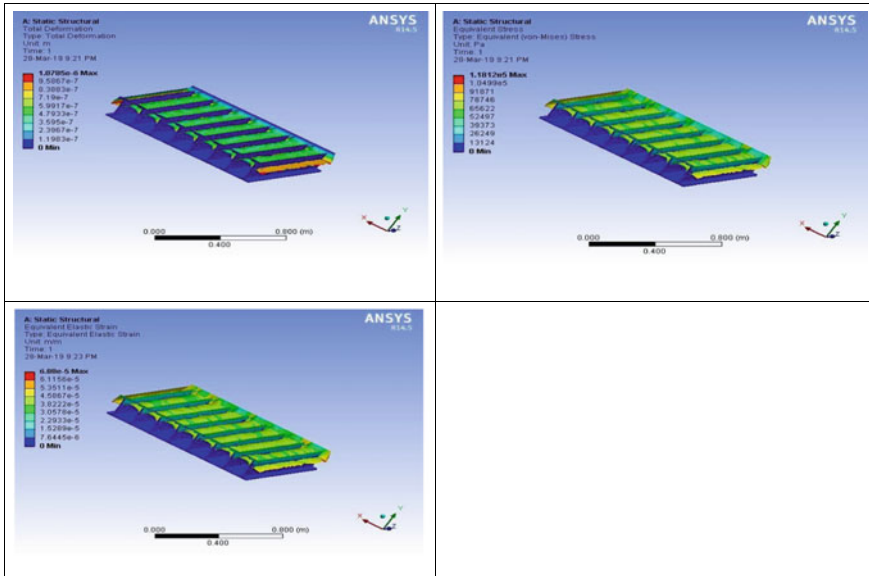


Fig. 12 Total deformation, Von Mises stresses, Von Mises strain on the bridge deck for 0% of ZrO₂

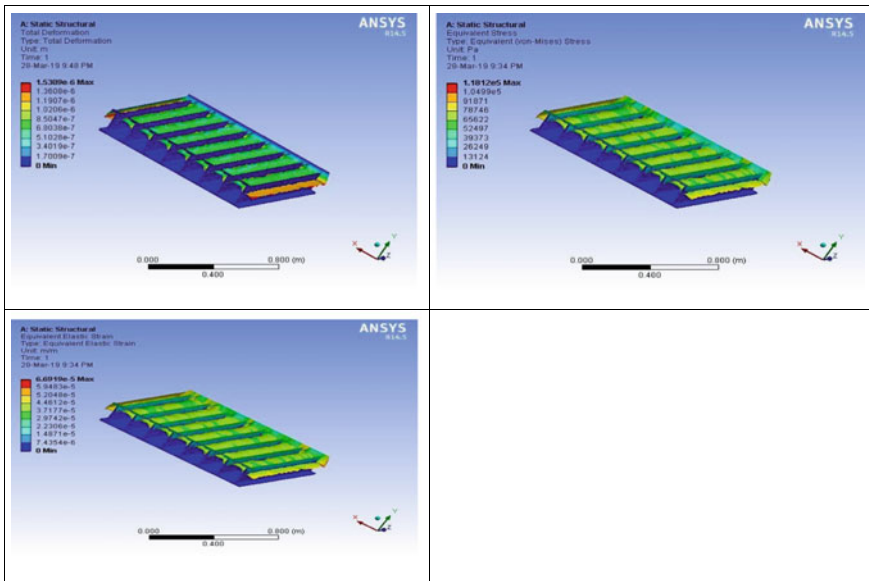


Fig. 13 Total deformation, Von Mises stresses, Von Mises strain on the bridge deck for 0.1% of ZrO₂

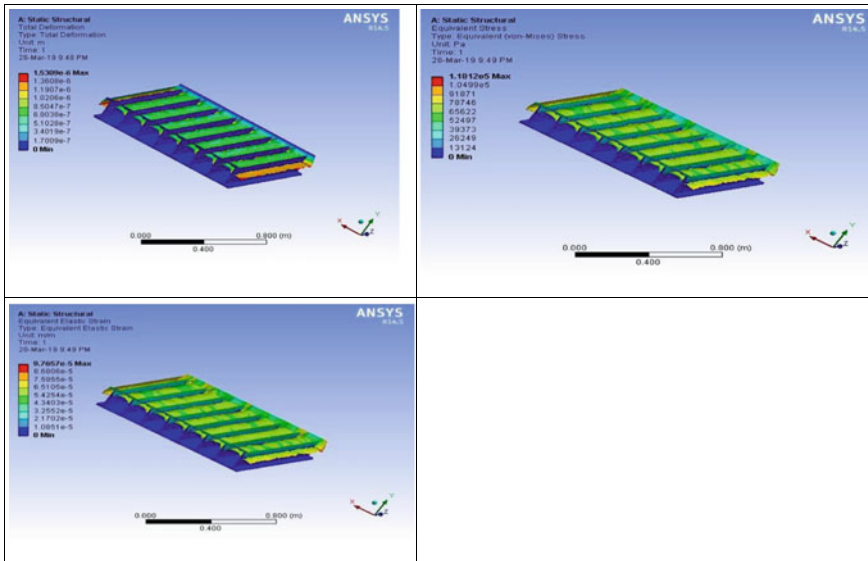


Fig. 14 Total Deformation, Von Mises stresses, Von Mises strain on the bridge deck for % of ZrO₂

Figure 14 shows the variation in total deformation, von Mises and von Mises strain on a bridge deck, the surface of the deck is slightly affected by the applied load.

Figure 15 shows the variation in total deformation, von Mises and von Mises strain on a bridge deck, the surface of the deck is slightly affected by the applied load.

Out of all the applied loads on different weight fractions of ZrO on glass fibre-reinforced polymer composites 0.3% inclusion of particulate exhibited less deformation, while and 0% or neat composite have been subjected to more deformation. Similarly, 0.3% inclusion of ZrO in glass fibre-reinforced composite exhibited less stress and strain on the structure which has the highest inclusion of ZrO (Table 1).

5 Results and Discussions

Graph 1 is for Stress Versus Strain for compression Test of GFRP composite. Here, 0% weight fraction of ZrO₂ exhibits less strength when it is subjected to an external load, 0.2% inclusion of ZrO₂ have good strength to weight ratio over a point of time and 0.3% inclusion of ZrO₂ have exhibited better results when the material is subjected to load (Tables 2, 3, 4, 5 and 6).

Graph 2 is for Stress Versus Strain for Tensile Test of GFRP composite. Here, 0% weight fraction of ZrO₂ exhibit less strength when it is subjected to an external load, 0.2% inclusion of ZrO₂ have good strength specimen is subjected to tensile

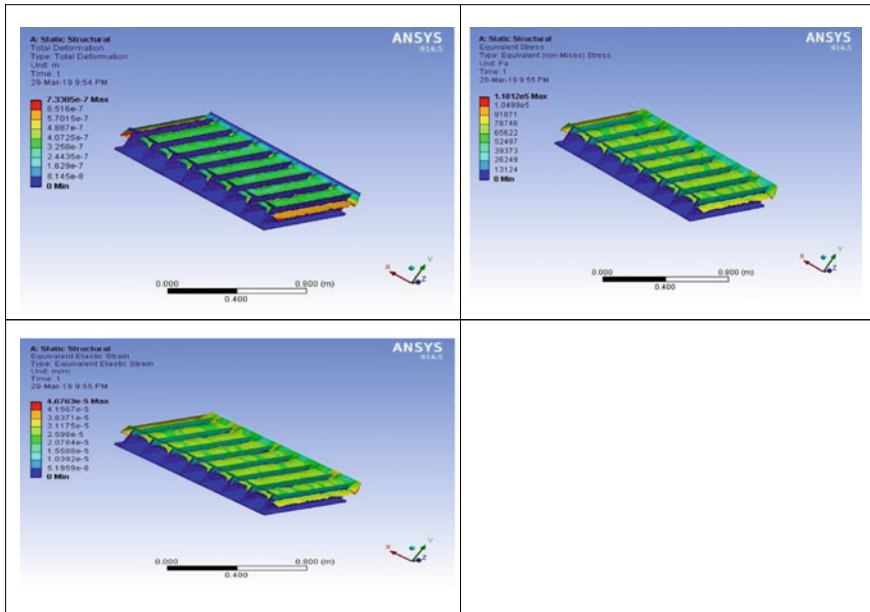
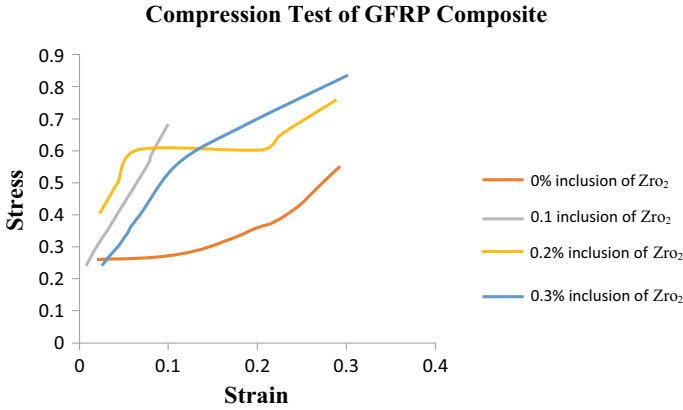


Fig. 15 Total Deformation, Von Mises stresses, Von Mises strain on the bridge deck for % of ZrO₂

Table 1 Properties of GFRP with 0, 0.1, 0.2 and 0.3% of ZrO₂

%	Density (Kg/m ³)	Young's modulus (MPa)	Poisson's ratio	Bulk modulus (Pa)	Tensile yield strength (MPa)	Compressive yield strength (MPa)	Tensile ultimate strength (MPa)	Compressive ultimate strength (MPa)
0	2850.6	1655.7	0.21	1.02 × 10 ⁷	110.24	101.22	111	657.8
0.1	2851.2	1786.2	0.21	1.02 × 10 ⁹	113.33	113.33	142	733.4
0.2	2852.4	1224	0.21	7.03 × 10 ⁸	156.5	156.5	195.83	753.8
0.3	2853.6	2556	0.21	1.46 × 10 ⁹	165.56	165.56	207.04	817.76

load. 0.1% inclusion of weight fraction of ZrO₂ in GFRP composite exhibit more flexibility and strength when a load is acted upon it (Table 7).



Graph 1 Stress versus strain for compression test of GFRP composite

Table 2 Total deformation for 0, 0.1, 0.2 and 0.3% of ZrO₂

% of ZrO ₂ in specimen (%)	Total deformation (in meter)
0	$1.07 \times 10^{(-6)}$
0.1	$1.049 \times 10^{(-6)}$
0.2	$1.053 \times 10^{(-6)}$
0.3	$7.33 \times 10^{(-7)}$

Table 3 Von misses stress for 0, 0.1, 0.2 and 0.3% of ZrO₂

% of ZrO ₂ in specimen (%)	Von misses stress (in pascal)
0	1.18×10^5
0.1	1.18×10^5
0.2	1.18×10^5
0.3	1.18×10^5

Table 4 Von misses strain for 0, 0.1, 0.2 and 0.3% of ZrO₂

% of ZrO ₂ in specimen (%)	Von misses strain
0	$6.88 \times 10^{(-5)}$
0.1	$6.69 \times 10^{(-5)}$
0.2	$6.76 \times 10^{(-5)}$
0.3	$6.67 \times 10^{(-5)}$

6 Future Work

Composite materials will be widely used in aerospace, marine, civil, automobile, sports, chemical industries, nanocomposite, natural fibre composite, consumer and

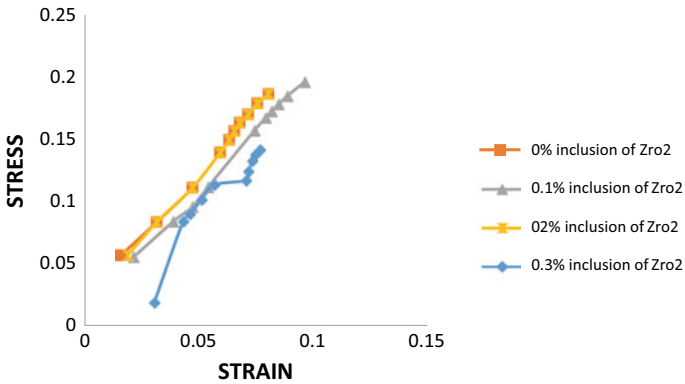
Table 5 Compression test for different weight fractions of Zro on GFRP composite

S. No.	Property	Neat laminate	0.1% Composition of ZrO ₂	0.2% Composition of ZrO ₂	0.3% Composition of ZrO ₂
1.	Compression strength	562.28	733.4	753.8	817.76
2.	Load at peak	140.27	183.35	188.45	204.44
3.	Elongation at peak	1.04	1.16	1.08	1401.08

Table 6 Tensile test for different weight fractions of ZrO₂ on GFRP composite

S. No.	Property	Neat laminate	0.1% Composition of ZrO ₂	0.2% Composition of ZrO ₂	0.3% Composition of ZrO ₂
1.	Tensile strength	99.475	141.145	194.24	416.43
2.	Load at yield	37.09	21.105	26.245	28.03
3.	Elongation at yield	9.100	8.950	7.378	8.428

Tensile Test for Zro₂ included GFRP Composite



Graph 2 Stress versus Strain for tensile test of GFRP composite

Table 7 Impact test for different weight fractions of ZrO₂ on GFRP composite

S. No.	Property	Neat laminate	0.1% Composition of ZrO ₂	0.2% Composition of ZrO ₂	0.3% Composition of ZrO ₂
1.	Impact strength	40.5	43.75	46.25	49

sports good, etc., because of best construction capability and also resist the vibration and absorb the shock.

We thus observed from the results obtained from our experimentation that the strengths of the laminates go on increasing with an increase in the percentage of zirconium dioxide. The experimentation was done with the composition namely 0.1% of ZrO_2 , 0.2% of ZrO_2 , 0.3 of ZrO_2 along with neat specimen laminate. We found that the compression, tensile impact strengths are growing with the increase of composition of Zro. So in future, experimentation can be done by increasing the composition of ZrO_2 more than 0.3% that is 0.4, 0.5, 0.6%, etc., so that the results obtained can prove us that the strengths are still increasing or decreasing after a level of extent.

7 Conclusion

Compression strength and the tensile strength of different compositions of the laminates vary accordingly with the change in percentage of the composition of ZrO_2 . Moreover, the strengths are high for all the compositions compared with the neat laminate. This composite material is used broadly in bridge decks which give the support to withstand the load. This material can be replaced by the existing ones. It is of low cost and easy to manufacture. In future applications, it plays a crucial role in the fabrication of bridge deck. It can withstand high loads compared to the ones which are used now. We hope that it will be used to a vast extent in the future for the manufacturing of the bridge deck and in various fields.

Simulation of CATIA and ANSYS carried out on total deformation, von Mises stress and von Mises strain on designed deck proved that this type of deck panel has sufficient strength to be used for the construction of temporary bridges. The modal analysis of vibration is very important and interesting in bridge designing process. Thus, it clearly experiments that GFRP composite with the mixture of ZrO_2 can be considered for the construction of the bridge deck with good strength to weight ratio to increase the lifetime.

References

1. T. Keller, M. Schollmayer, Plate bending behavior of a pultruded GFRP bridge deck system. *Compos. Struct.* **64**, 285–295 (2004)
2. W. Sebastian, T. Keller, Influences of polymer concrete surfacing and localized load distribution on behavior up to failure of an orthotropic FRP bridge deck. *Compos. B Eng.* **45**, 1234–1250 (2013). <https://doi.org/10.1016/j.compositesb.2012.07.050>
3. M., Vovesny, T. Rotter, GFRP bridge deck panel, in *23rd Czech and Slovak International Conference Steel Structures and Bridges 2012*, Podbanské, 26–28 Sept 2012 (2012)

4. B. Stankiewicz, Composite GFRP deck for bridge structures, in *23rd Czech and Slovak International Conference Steel Structures and Bridges 2012*, Podbanské, 26–28 Sept 2012 (2012)
5. B. Stankiewicz, Composite material GFRP and ductal in decks of bridge structures. *J. Mat. Sci. Eng. A* **4**, 282–289 (2014)
6. ASTM D 3039, *Standard Test Method for Tensile Properties of Polymer Matrix Composite Materials* (American Society for Testing and Materials 2002)
7. P.K. Majumdar, Strength and life prediction of FRP composite bridge deck. Dissertation submitted to the Faculty of the Virginia Polytechnic Institute, Blacksburg, Virginia, April, 2008
8. P. Alagusundaramoorthy, R. Veera Sudarsana Reddy, Testing and evaluation of GFRP composite deck panels. *Ocean Eng.* **35**(3–4), 287–293 (2008)
9. M. Vovesny'a, T. Rottera, GFRP bridge deck panel. *Proc. Eng.* **40**, 492–497 (2012)
10. F. Ascione, G. Mancusi, S. Spadea, M. Lamberti, F. Lebon, A. Maurel-Pantel, On the flexural behaviour of GFRP beams obtained by bonding simple panels: an experimental investigation. *Compos. Struct.* **131**: 55–65 (2015)

Friction and Wear Characteristics of Austenitic Stainless Steel Against Ceramic Disc



V. Sumalatha, P. Ravinder Reddy, A. Krishnaiah, and G. S. Reddy

Abstract This paper focuses on investigating wear behavior of Austenitic stainless steel-304 using pin-on-disc wear testing tribometer in as-received condition. Wear behavior is of particular concern as the frictional force and coefficients of friction are known to influence the wear significantly. In this study, we have taken austenitic stainless steel (304) as a pin which makes point contact against the mating surface of alumina ceramic disc. Sliding distance and speed are maintained constant during the P-o-D experiments. Experimental runs carried out with load on the pin at three different weights. The scientific data so obtained, viz wear, frictional force, and coefficient of friction are plotted employing *Origin Graphs*. The microstructure of worn-down surface is characterized using a Scanning Electron Microscope. Results obtained found with a good agreement of wear behavior of austenitic stainless steels. Frictional force and coefficient friction fluctuated severely when the load is applied. The SEM investigations indicate that moderate loading on stainless steel will preserve anti-galling characteristics while offering resistance to wear. However, the 3 kg loading on the pin exhibited a microscopic scale transfer, adhesion and spalling of the material of the pin during sliding. SEM studies revealed that moderate loading preserved anti-galling characteristics of the material of the pin. Results of these investigations will have an impact on applications leading to orthopedic stainless

V. Sumalatha · G. S. Reddy (✉)

Department of Mechanical Engineering, Sreenidhi Institute of Science and Technology, Hyderabad, Telangana, India
e-mail: gsreddy@sreenidhi.edu.in

V. Sumalatha

e-mail: suma3484@gmail.com

P. Ravinder Reddy

Department of Mechanical Engineering, Chaitanya Bharathi Institute of Technology, Hyderabad, Telangana, India

e-mail: reddy.prr@gmail.com

A. Krishnaiah

Department of Mechanical Engineering, Osmania University College of Engineering, Hyderabad, Telangana, India

e-mail: arakanti@gmail.com

© Springer Nature Singapore Pte Ltd. 2021

G. S. V. L. Narasimham et al. (eds.), *Recent Trends in Mechanical Engineering*,

Lecture Notes in Mechanical Engineering,

https://doi.org/10.1007/978-981-15-7557-0_27

steel implants used against broken bones which are analogous to ceramic. The wear tests have bearing on the products used in ceramic brake pads, ceramic disc brakes of automobiles and railway trucks.

Keywords Pin-on-disc · Wear testing tribometer · Austenitic-304 · SEM

1 Introduction

Wear can be defined as the phenomenon of removing material from surfaces due to mutual interaction with a corresponding mating surface [1]. It is known that many machines lose their durability and reliability due to wear [2]. Wear rates often change drastically depending upon the selection of the materials, components, and methods used [3]. The wear may be either good for certain applications or it could be detrimental in other applications. Wear is undesirable in almost all machine applications such as in gears, cams, bearings, bushes, brake pads, human bones, and so on. In a well-designed tribological system, the removal of material is a very slow process but it is very steady and continuous. Many of us think that wear is a property of a material but the fact is that not only the material but also its response to other materials cause in a given tribological system. Hence, it is necessary to evolve with various materials and components which are frequently used, less expensive, and readily available in the market [4]. The research study should aim at improving resistance to wear leading to longer lives of components used in large-scale manufacturing processes. Four different types of stainless steel, namely ferritic, austenitic, martensitic, and precipitation-hardened 17–4 pH are frequently used in various applications ranging from geysers, nozzles, orthopedic implants, surgical tools, cutlery, and gas turbine nozzles. Among the four different types only austenitic stainless steel is nonmagnetic therefore widely used as orthopedic implants besides its other industrial uses such as cryogenic tanks, containers for corrosive fluids, and cutlery because of their high strength, corrosion resistance, and excellent formability [5]. Tribological conditions prevail when used as orthopedic implants. We have chosen this alloy to investigate pin-on-disc wear characteristics under different loadings while maintaining a constant speed of rotation against alumina ceramic disc. A ceramic disc somewhat closely represents bone in the human body in which the pin is in continuous contact with the rotating ceramic disc [6]. The data acquisition system of the Winducom records the frictional force, wear a function of time or number of revolutions, although it is often coefficient of friction (COF) also calculated with the frictional force values on the same axes as the function of time [7, 8].

2 Experimental Details

Experiments were conducted using a pin-on-disc tribometer model WINDUCOM 2010, given in Fig. 1. The data acquisition system is shown in Fig. 2. Austenitic stainless steel AISI 304 cylindrical bar of 6 mm diameter has been cut into three samples of each size 6 mm diameter and 30 mm long using a band saw machine. Edges of the cut pieces were deburred to remove the flash. Initial hardness was measured using the Rockwell ‘C’ scale. An alumina ceramic disc of 90 mm diameter with 10 mm thickness was used.

Three experiments were conducted at different loads for 1, 2, and 3 kg. A speed of 500 RPM maintained constantly throughout for all three samples. Duration of experiments was computed from the relationship, $SD = \frac{\pi \cdot d \cdot n \cdot t}{60000} = 1000 \text{ m}$. In all three experiments, SD of 1000 m is maintained constant, where d = wear track diameter, n = speed in RPM, and t = time in seconds. Wear and frictional force readings were recorded up to the point of time that the sliding distance has reached 1000 m. Using *Origin Pro2019*, graphs were drawn for analysis of the data.

Fig. 1 Pin-on-disc tribometer WINDUCOM 2010

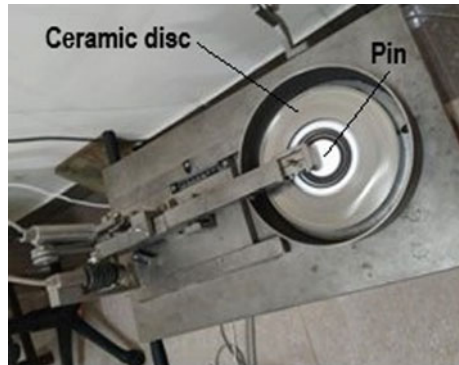


Fig. 2 Data acquisition system



Chemical composition in weight % of the austenitic stainless steel as determined by using ICP-OES and ASTM E1019 methods is as follows: Fe–18.74%Cr–8.39%Ni–1.50%Mn–0.14%Si–0.03%C–0.016%P–0.003%S. Weight of the samples was determined by weighing in a precision balance prior to and after the pin-on-disc tests.

3 Methodology

Chemical composition: The as purchased stainless steel has been tested for chemical analysis using ICP-OES and ASTM E1019 method at Lucid Laboratories [6], Hyderabad, India. **Specimens:** The austenitic stainless steel round bar was cut into four specimens of each size 6 mm diameter and 30 mm long using a horizontal band saw machine. **Pin-On-Disc:** The samples were tested for wear and frictional force using a Pin-On-Disc Tribometer. The data acquisition system has recorded the wear and frictional force. Coefficient of friction was computed. **Scanning Electron Microscopy (SEM):** Following the wear test, the surface of the worn-out specimen was examined under VEGA3 **TESCAN** make SEM investigate in-depth characteristics of wear at various magnifications. SEM images at four different magnifications, namely 100x, 500x, 1000x, and 2,000x, were taken. **Energy-Dispersive X-ray Spectroscopy (EDS) or Energy-Dispersive spectroscopy (EDS)** analysis has been made to investigate the chemical characterization of the worn-down surfaces.

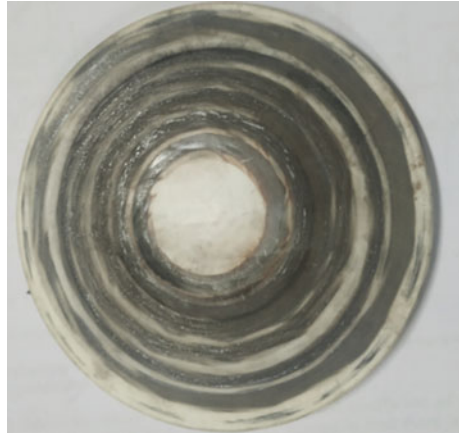
4 Results and Discussion

The Pin-on-Disc experiments using AISI 304 austenitic stainless steel as pin and alumina ceramic as disk have been carried out at 500 RPM up to a sliding distance of 1000 m at three different loads of 1, 2, and 3 kg. Figure 3 displays pin specimens after the wear test. The ceramic disc after wear tests is shown in Fig. 4. The data as obtained has been plotted: (i) wear *versus* time and (ii) frictional force *versus* time.

Fig. 3 304-Austenitic stainless steel pin specimens after wear test



Fig. 4 Ceramic disc after wear out



4.1 Effect of Load on Wear

Wear in microns *versus* time in seconds plot is shown in Fig. 5. Wear of the pin with 2 kg load increased from about 10–50 μm compared to 1 kg wear test. A dramatic increase in wear from 10 to 950 μm is found to be increased for the 3 kg load test.

Three-kg load test has accelerated the wear; as a result, debris up to great depth is seen. Figure 5 shows the variation in wear with respect to time at varying loads of 1, 2, and 3 kg, while the speed maintained constant. It is observed that increasing the load led to wear that is visible when observed at magnifications greater than 1000X. This is due to the fact that the duration of abrasion is the same for varying the load, while the length of rubbing is more in case of higher load.

Fig. 5 Wear versus time curves under different loadings of 1, 2, and 3 kg

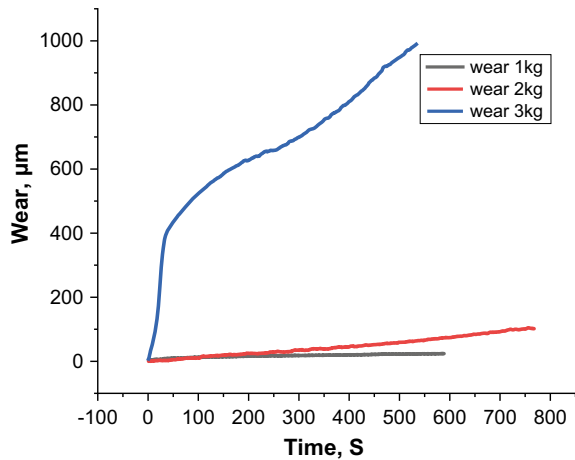
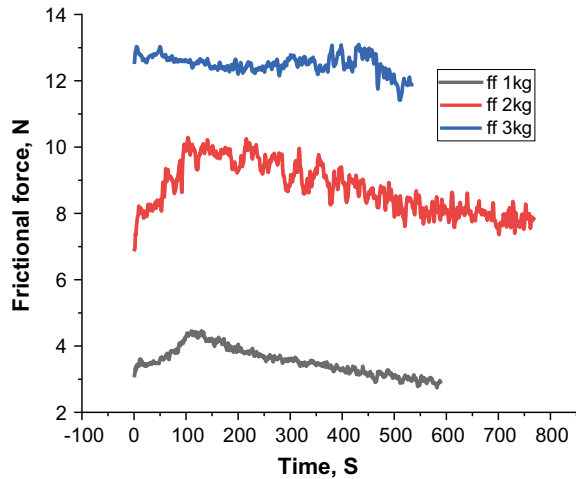


Fig. 6 Frictional force versus time under different loadings of 1, 2, and 3 kg



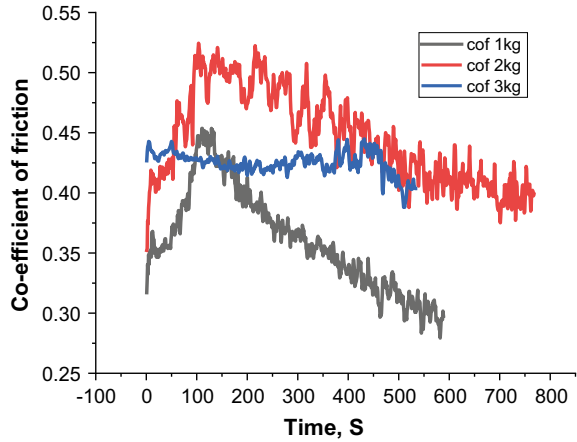
4.2 Effect of Load on Frictional Force

With increasing load, the frictional force has increased as shown in Fig. 6. Up to 100 s, the frictional force has increased followed by gradual decreasing. However, in the case of a 3 kg load experiment has revealed more or less constant frictional force for up to 450 s, followed by a gradual decrease. Figure 6 shows the variation in the frictional force with respect to time at varying loads of 1, 2, and 3 kg, while at a constant speed. It is observed that increasing the load has led to an increase in frictional force.

4.3 Effect of Load on the Coefficient of Friction

The effect of load is investigated on coefficient of friction as a function of time, while the speed of rotation is maintained constant. Increased surface roughening followed by adhesion of debris to the pin appears to be the cause for the variation of coefficient of friction with the increasing load. This is due to the fact as the normal load increases, frictional heat generates at the contact surface and hence strength of the material decreases as shown in Fig. 7.

Fig. 7 Coefficient of friction versus time under different loadings of 1, 2, and 3 kg



4.4 Effect of Load on Scanning Electron Microstructure of the Worn-Down Surfaces

Worn surfaces of the AISI 304 austenitic stainless steel pins were characterized for microstructures by TESCAN scanning electron microscope. The worn-out surface was etched with isopropyl alcohol to remove dust particles. The scanning electron micrographs of wear surfaces shown in Figs. 8, 9, and 10 are, respectively, for 1 kg, 2 kg, and 3 kg loads. The 1 kg load wear test has exhibited brittle crack (Fig. 8). Worn-out surface of the 2 kg load wear test has displayed wear grooves and delamination of debris arising from layers can be seen in Fig. 9. Worn surface of the 3 kg load wear test has clearly exhibited large chunks of wear debris up to a great depth are seen.

The wear behavior of pin is found to be quite similar for all load conditions and higher wear track width is also formed. Some regions of the wear track are shown in the highlighted areas with high magnification. The worn pins have more areas,

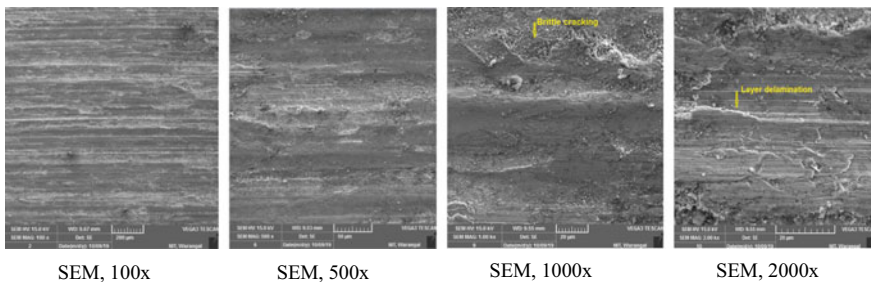


Fig. 8 Scanning electron micrographs of worn-down surface after the wear test under 1 kg load

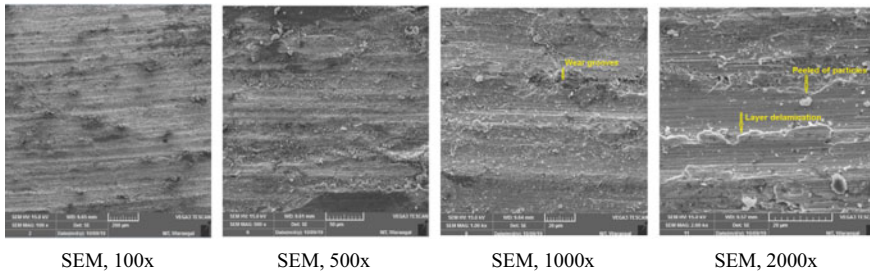


Fig. 9 Scanning electron micrographs of worn-down surface after the wear test under 2 kg load

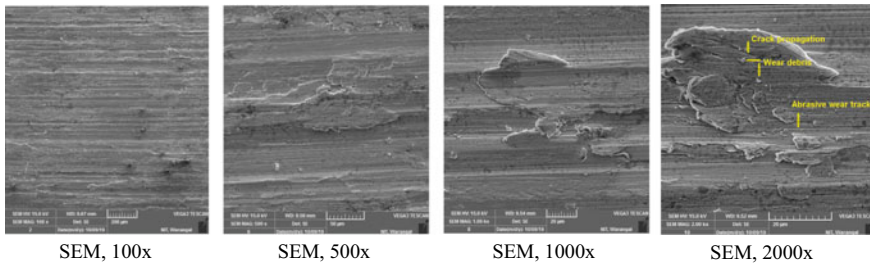


Fig. 10 Scanning electron micrographs of worn-down surface after the wear test under 3 kg load

where the material is removed from surface in the form of large craters, delamination, scratches, grooves, micro-cuts, and debris. However, the pins are not severely damaged. It shows that wear effect of 304-austenitic steel as observed for 2 kg loading, the wear rate increases rapidly when compared with that of 1 kg. Figure 8 shows wear effect of AISI 304 austenitic steel at 3 kg loading. Wear rate increased rapidly as observed at 2000x magnification.

Smaller lumps of the material of the pin stainless steel are formed. The lumps undergo work hardening, abrade disc surface, delaminate, and end up into the groove. Oxide particles combine with debris undergo further hardening causing galling. An increase in friction force in forming operations is usually indicative of galling [7, 8]. The reason is that the adhered hard patches and local cold-welding between them will obstruct the relative sliding.

Figures 8, 9, and 10 show the microstructure of rough (dark) and fine (gray) chromium carbides with varying chromium content. The chromium content is higher in rough carbides than in the fine carbides.

EDS analysis on worn-down surfaces is carried out to detect probable material of specific composition which may have occurred while wearing out. In Figs. 11 and 12, the EDS analysis reveals the existence of oxide layer on the surface. Both spectrums 1 and 2 have shown the presence of oxide. Moderate increase in oxide thickness does not improve the friction and galling properties [9]. Small radius has

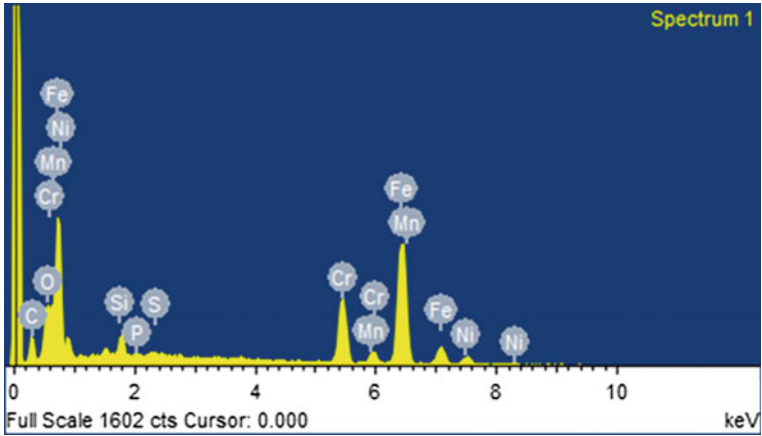


Fig. 11 EDS analysis of the worn surface of specimen spectrum 1

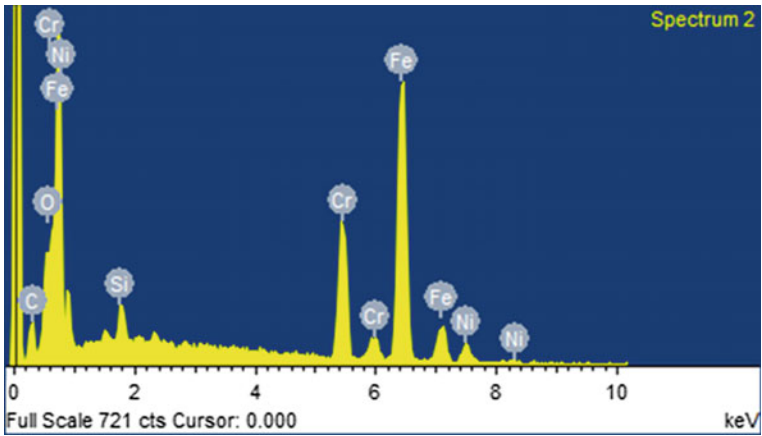


Fig. 12 EDS analysis of the worn-down surface of specimen spectrum 2

impacted on stress concentration and thereby affecting the galling behavior of the specimen [10].

Stainless steels are usually exposed to service temperatures of the order of 816 °C because of their resistance to corrosion, good high-temperature strength and oxidation resistance, as lubrication is not practical at high temperatures a good resistance to wear and galling is an important requirement. Stainless steel is selected for such an application because of its desirable anti-galling characteristics. The SEM investigations indicate that moderate loading on stainless steel will preserve anti-galling properties while offering resistance to wear.

5 Conclusion

The purpose of this research is to investigate the effect of load on wear, frictional force, and coefficient of friction of 304-austenitic stainless steel pins against alumina ceramic disc by employing a pin-on-disc apparatus. Based on the experimental results obtained from pin-on-disc and microstructural analysis of wear surfaces by SEM have led to new findings:

1. It is observed that severe damage due to wear occurred with 3 kg applied load in the dry condition when compared to tests carried out at 1 and 2 kg loads.
2. We conclude that the wear behavior and frictional force are found to be less for low loads when compared to tests carried out at higher loads resulting in higher wear and higher frictional force.
3. Wear increased with increasing applied load, sliding distance and time, while the coefficient of friction fluctuated.
4. At 2 kg load, the coefficient of friction is higher than the test of 3 kg applied load. However, it did not exhibit significant differences when compared with that of 1 kg test.
5. Adhesion, plastic deformation, and delaminated oxide layer wear mechanism are observed on worn surfaces of 304-austenitic stainless steel.
6. The SEM investigations indicate that moderate loading on stainless steel will preserve anti-galling properties while offering resistance to wear.

References

1. V. Raghavan, *Material Science and Engineering* (PHI Learning, New Delhi, 2016)
2. J. Salguero, *Application of Pin-on-disc Techniques for the Study of Tribological Interferences in the Dry Machining of A92024-T3(Al-Cu) Alloys* (July, 2018)
3. S. Sharma, A. Sharma, Investigation of wear characteristics of aluminum disc with pin-on-disc tribometer. *Int. J. Sci. Eng. Res.* **6**(1) (January, 2015) ISSN 2229–5518 (1932)
4. W. Grzesik, *Investigation of Friction and Wear Mechanisms of Tin Coated Carbide Against Ti-6Al-4 V Titanium Alloy Using Pin-on-disc Tribometer* (2009)
5. R.P. Nair, *The Use of the Pin-on-disc Tribology Test Method to Study Three Unique Industrial Applications*
6. M.X. Wei, *Wear and Friction Characteristics of a Selected Stainless Steel* (2011)
7. J.H. Magee, Wear of stainless steel, ASM handbook, friction, lubrication and wear technology, *ASM Int.* **18**, 710–724 (1992)
8. American Iron and Steel Institute, *High Temperature Characteristics of Stainless Steels. A Designers Hand book series*, No. 9004. Nickel Development Institute, Washington, DC (1979)
9. S.R. Hummel, Development of a galling resistance test method with a uniform stress distribution. *Tribol. Int.* **41**(3), 175–180 (2008)
10. A.P. Harsha, P.K. Limaye, R. Tyagi, A. Gupta, J. Mater. Eng. Perform. **25**, 4980–4987 (2016)

Fiber Surface Treatment and Quantity, Impact on the Performance of Biocomposites



Gowdagiri Venkatesha Prasanna, A. Nikhil Nihar, G. Lokesh, and N. Naga Sai

Abstract The principle intention of this compound treatment was to diminish the water ingestion property of regular strands and furthermore to improve the similarity with a grid. At present, biocomposites are created by mixing 90% unsaturated polyester–vinyl ester grid and fortifying the normal strands into the framework mix. The mechanical presentation of the composites was likewise impacted by fiber amount and concoction treatment of the strands. Surface of the filaments was changed by soluble base treatment prompting higher crystallinity of strands. The examination of malleable, compressive, and flexural properties of Banana–Luffa strands strengthened biocomposites was done for 10, 20, 30, and 40% and half amount of surface adjusted composites and other untreated biocomposites. The 40% fiber amount benzene diazonium chloride-treated composite showed higher and ideal condition for the previously mentioned mechanical properties than 5% NaOH-treated, 10% NaOH-treated, and 10, 20, 30, and 50% fiber amount chemical-treated and -untreated biocomposites.

Keywords Banana–luffa fibers · Surface treatment · Mechanical tests

1 Introduction

By and large counterfeit strands like carbon, Kevlar, glass, and aramid have been broadly utilized in polymer-based composites due to their, low weight, high quality, and solidness properties. Aside from the favorable circumstances utilizing manufactured filaments in different applications, these counterfeit strands have genuine restrictions regarding their biodegradability, introductory handling costs, recyclability, vitality utilization, machine scraped area, wear and well-being risks, and so on. To conquer this emergency, the need for characteristic/inexhaustible filaments-based composites is requesting to make the world ‘green’ fibers [1]. Common strands have been utilized as an elective material to engineered filaments just as support for

G. V. Prasanna (✉) · A. Nikhil Nihar · G. Lokesh · N. Naga Sai
Department of Mechanical Engineering, CVR College of Engineering, Hyderabad 501510, India
e-mail: 22gowdagiri@gmail.com; prasannavg22@gmail.com

© Springer Nature Singapore Pte Ltd. 2021
G. S. V. L. Narasimham et al. (eds.), *Recent Trends in Mechanical Engineering*,
Lecture Notes in Mechanical Engineering,
https://doi.org/10.1007/978-981-15-7557-0_28

polymer composite materials. Regular strands, for the most part, comprise of cellulose, hemicelluloses, gelatin, lignin, and waxes [2]. The water retention property controlled by the normal filaments restricts the utilization of these strands as potential support in the manufacture of composites. Polymer network is hydrophobic in nature. This may cause fiber and lattice contrary and results in powerless interfacial holding between the fiber and the network. The primary intension of this synthetic treatment is to diminish the water retention property of the common strands and furthermore to improve the similarity with the polymer framework. The polymer mix has numerous points of interest in terms of the items for explicit end-use applications and upgrading sap's powerful usage, execution, and properties [3].

Unsaturated polyester is a flexible and broadly utilized network material for different applications, for example, propelled composites, equipment parts, electrical circuit board materials, and rocket supplies, due to its great holding capacity, warm, mechanical, and dielectric properties. Epoxy tars have broadly utilized in light of their unrivaled thermomechanical properties and fantastic processability. Be that as it may, the utilization of thermoset materials is regularly constrained in view of low durability property. Further mixing system can be utilized productively to beat the sub-par properties of both the segments. Miscible polymer mixes produce recently improved material from less predominant individual segments [4]. In this way, when the mass measures of epoxies are utilized, for the most part, it will mix with toughening operators [4]. Vinyl ester is a toughening material which can be utilized alongside epoxy materials. Vinyl ester is the extra result of an epoxy pitch with unsaturated carboxylic corrosive, for example, acrylic or methacrylic corrosive. Because of the adaptability present in the structure of epoxy, it is utilized as one of the mix materials in the present work. The hardness of the epoxy pitch is expanded by mixing it with adaptable polymers and elastomers [4, 5]. Subsequently, a reasonable polymeric material was expected to improve the effective opposition, stress-strain properties by holding firmness, glass progress temperature, and warm solidness of the epoxy pitch. To accomplish this, advancement of a between cross-connected polymer system of thermoset-thermoset mixes were examined in view of their expanded mechanical properties [6, 7]. Vinyl ester is the generally utilized thermosetting material on account of their less expense and great blend of properties like convection obstruction, mechanical, and warm properties. The hydroxyl bunches improve the extremity of vinyl ester and encourage bond and color wetting properties, which drove the wetting of the strands in grid [4, 8, 9]. For this reason, a mix of epoxy/vinyl ester (90/10% w/w) polymers was readied. Composite examples with the 10, 20, 30, 40% and half wt. the substance of untreated, soluble base, and benzene diazonium chloride-treated Banana-Luffa strands with a mix of epoxy/vinyl ester were created.

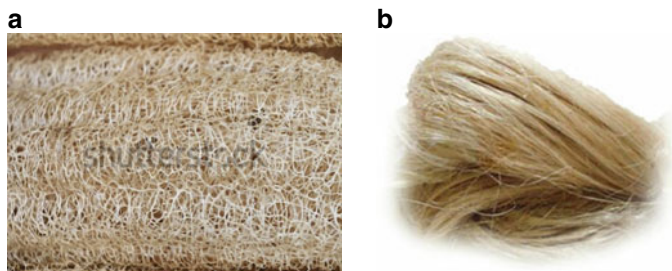


Fig. 1 a Luffa fiber, b Banana fiber

2 Experimental

2.1 Materials

The two resins, namely 1. Unsaturated polyester and 2. Vinyl ester.

The two Fibers, namely 1. Luffa fiber and 2. Banana fiber were used to fabricate the composites.

2.2 Surface Modification of Natural Fibers

Because of the nearness of hydrophilic hydroxyl bunches in the common strands, not many issues happen along with the interface during the support of normal fiber into the framework. The hydrophilic idea of regular filaments frustrates the powerful holding of strands with the network. Aside from this, gelatin, oil, and waxy substances spread the responsive useful gatherings of the fiber and go about as a hindrance to interlock with the lattice. To improve the adequacy of interfacial glue holding, the surface of fiber should be changed with various substance medications.

2.3 Chemical (Alkali) Treatment

So as to improve the adequacy of interfacial grip/holding, fiber surface should be changed with various concoction medications, receptive added substances, and coupling specialists. Compound medications produce increasingly receptive gatherings on the outside of the fiber and this encourages proficient coupling with the network. Surface change of strands by antacid treatment with various centralizations of NaOH: 5 wt% and 10 wt% was completed right now. Fibrils after the salt activity were inundated in refined water for 24 h to expel the lingering sodium hydroxide.

Extra cleaning was finished utilizing refined water having a limited quantity of acidic corrosive. Fibrils a short time later dried out by keeping in an oven at 70 °C for 3 h.

2.4 Preparation of Benzene Diazonium Chloride

Hydrochloric corrosive of concentration 8 cm³ was added to a bubbling cylinder containing 3 cm³ of phenylamine (aniline) and 10 cm³ of water; the blend was shaken until amine gets disintegrated, and afterward, the arrangement was cooled to 5 °C by using an ice shower. After that, the concentration of sodium nitrite (3 g in 8 cm³ of water), pre-cooled to 5 °C, was included. The temperature of the blend was kept up underneath 10 °C during the expansion of sodium nitrite [4, 8].

2.5 Benzene Diazonium Treatment of Banana–Luffa Fibers

Banana–Luffa filaments were slashed to a length of 10 mm, washed with refined water, and then dried out in a stove at 70 °C for 24 h. The dried strands were submerged in a 6% NaOH arrangement taken in a 2.0 L glass measuring glass for 10 min at around 5 °C. A late arranged diazo arrangement was then emptied gradually into the above blend with consistent mixing. Filaments were then taken out, washed with cleanser arrangement followed by refined water, and lastly, dried outside for 48 h [5, 10].

2.6 Fabrication of Blended Hybrid Biocomposites

The mould cavity was coated with a thin layer of hard wax for the easy release and withdrawal of fabricated composite specimens. Then after the wax was cured, a thin layer of aqueous solution of polyvinyl alcohol (PVA) was applied. Biofiber hybrid composites were fabricated using the hand lay-up technique. Then the hybrid biofibers of the untreated and treated Banana–Luffa fibers were reinforced to the matrix blend to get the required biocomposite specimens for the investigation of performance and mechanical properties. Then air bubbles were removed carefully by using the roller with gentle rolling. For the purpose of a complete cure, composite samples were post-cured at a temperature of 80 °C for 2 h by keeping the specimens in a hot oven. After the complete curing, untreated and treated samples of biocomposite specimens were tested [4, 11].

3 Results and Discussion

3.1 Tensile Strength Properties

Composite specimens for the tensile strength test, prepared with 150 mm × 15 mm × 3 mm, were evaluated as per the ASTM standards. Due to the hydrophilic nature of biofibers, i.e., water absorption, incongruity was observed among the biofibrils and matrix which then leads to an improper and inadequate dampability, which results in substandard properties of composites. To overcome this, alkali treatment of fibrils was carried out and which decreases its hydrophilic tendency and thus progress compatibility with the matrix. The influence of fibrils exterior modification by the substance treatment, % alkali treatment, and fiber quantity on the tensile property of biocomposites was indicated in Fig. 2 [4, 5, 12]. In case of untreated biofiber composites, the repellency among hydrophobic matrix and hydrophilic biofibers would unfavorably affect the interfacial bonding among fibrils surface and matrix and result in a decrease in the fortification capability of the fiber due to the inferior stress transfer from the matrix to fibers [13–15]. Among the various surface modifications performed, it was also observed that 40% fiber quantity benzene diazonium chloride-treated composite shows the higher and optimum condition for the tensile property than the 5% NaOH-treated, 10% NaOH-treated, and 10, 20, 30 and 50% fiber quantity chemically treated and untreated biocomposites [4–8]. The uppermost tensile strength was observed for 40% fiber loading due to the better fiber sharing in a matrix material which improved the morphological properties. In benzene diazonium chloride treatment, the surface of the fibrils turns out to be progressively uniform because of the disposal of small-scale voids and thus the stress transfer capacity between the definitive cells improves [5, 6, 8, 12]. Though appreciable higher tensile strength was notified in alkali-treated Banana–Luffa fibers composites, however, noteworthy enhance was noticed in the tensile strengths of benzene diazonium chloride-treated

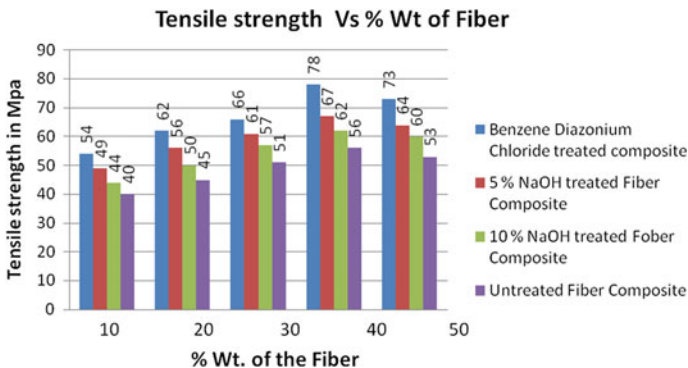


Fig. 2 Tensile strength of untreated, alkali-treated and benzene diazonium chloride-treated composites

Banana–Luffa fiber composites. Benzene diazonium chloride treatment deprives the hydrophilic nature of Banana–Luffa fibers compared to alkali treatment due to the coupling of the hydroxyl group of fiber with benzene diazonium chloride [8, 16, 17]. Chemical treatment diminishes fiber diameter and thereby enhances the aspect ratio and increases surface roughness [2, 5, 8]. Along these, lines improve the compelling fiber surface territory for a good bond with the grid which prompts increment in the interfacial grip between the Banana–Luffa filaments and the polymer lattice material [11, 16, 17]. The examination unmistakably recommends that the synthetic response framed a solid interface with fiber cell dividers and coupling response happens between benzene diazonium chloride and cellulose of fiber bringing about the development of a diazocellulose compound, which represents the watched huge increment in ductile properties of composites [5, 17–19]. The ideal condition was a result of ideal fiber amount and concoction (benzene diazonium chloride) treatment, which advanced the better interfacial cement holding between filaments framework mix brought about sufficient pressure move and execution [1, 8, 11, 20]. Be that as it may, whereas at higher fiber amount, i.e., 50% fiber amount even benzene diazonium chloride-treated composite, 5% NaOH-treated, 10% NaOH-treated and -untreated biofiber composite showed mediocre values [5, 8, 21, 22]. The surface treatment by methods for both benzene diazonium chloride, NaOH, gives the route for the evacuation of undesirable materials like waxes, oils, polluting influences, hemicellulose, and lignin from the common strands notwithstanding diminishing of dampness retention, yields the higher level of (alpha) cellulose in normal filaments and furthermore cleans the fiber surface [4, 8, 23]. Benzene diazonium chloride treatment advances increasingly powerful zone of the fiber's surface required for wetting by the polymer contrasted with antacid treatment to have great holding [5, 11, 16–24] and results in upgraded mechanical properties.

3.2 *Flexural Properties*

The specimens with dimensions 150 mm × 15 mm × 3 mm were fabricated and tested for flexural properties as per ASTM D 5943-96 specifications. The variety in the estimations of flexural quality as an element of fiber amount, with and without synthetic treatment appeared in Fig. 3. From the test, it was seen that the flexural property of the 40% fiber amount, benzene diazonium chloride-treated biostrands composite demonstrated higher, and predominant incentive than the 40% fiber amount, 5% NaOH-treated, 10% NaOH-treated, 10, 20, 30 and 50% fiber amount untreated and treated composites [1, 8, 11, 20, 26]. Because of more antacid focus at 10% NaOH than the 5% NaOH, overabundance delignification of the fiber happens, which brought about debilitating or harming of the fibril surface and diminished flexural quality, demonstrated by Fig. 3 [4, 9, 16–27]. High fiber–grid similarity, great fiber–framework communication and holding was watched for 5% NaOH-treated biofibrils composite than 10% NaOH-treated biocomposites [5, 8, 24, 27]. Better

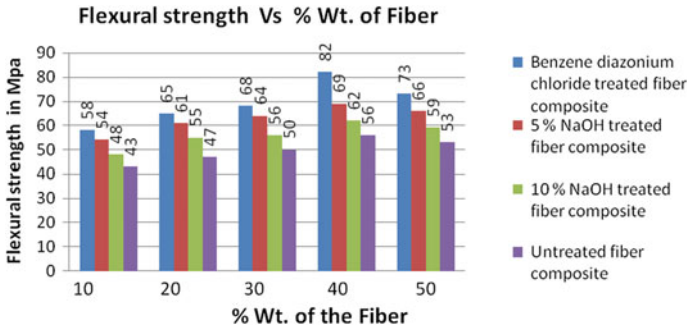


Fig. 3 Indicates the change of flexural property of unprocessed and chemically treated composites with the variation percentage of fibers content

and significant improvement of fiber appropriation in a lattice, perspective proportion and stress move limit was seen in benzene diazonium chloride-treated biofibrils composites than in salt-treated and -untreated biofibrils composites [6, 8, 11, 16, 28].

3.3 Compressive Strength

The specimens were fabricated and tested for Compressive strength properties as per ASTM D specifications. The change in the values of compressive strength property with respect to fiber quantity with and without surface modification is shown in Fig. 4. It was also observed that benzene diazonium chloride-treated biocomposites exhibited higher and optimum condition for compressive property than the alkali-treated and -untreated biocomposites [1, 7, 11]. The optimal condition was because of optimum fiber loading, and chemical treatment, which promoted the better interfacial bonding between fibers–matrix blend resulted in adequate stress transfer and

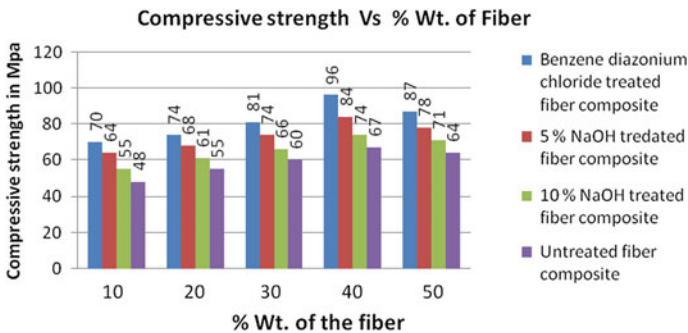


Fig. 4 Compressive strength of untreated, alkali-treated and benzene diazonium chloride-treated composites

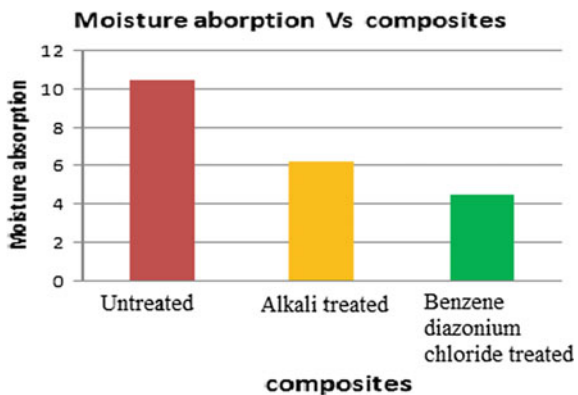
performance [5, 8, 21]. Previous works reveal that fiber surface modification by chemical treatment reduces the fiber's diameter and increases surface roughness [4, 5, 29]. However, the decrease in compressive property of the composite was noticed at 50% fiber quantity. For 50% fiber content untreated and treated composites (high fiber load), a decrease in the compressive property indicates poor fiber–matrix interfacial bonding and microcrack formation at the interface leads to insufficient stress transfer [5, 11, 16, 17]. Hence, highest compressive strength was observed at 40% fiber loading. Furthermore, benzene diazonium treatment fills the voids spaces of fiber and aligns uneven fiber, more as compared alkali-treated composite [5, 8, 12, 16].

3.4 Moisture Content Test

Figure 5 shows the rate ingestion of dampness amount by natural fiber composite, antacid-treated and Benzene diazonium chloride-treated composites. The biofilaments composite start from the hydrophilic idea of the fiber display hydrophilic properties [4, 5]. Be that as it may, the soluble base delicate hydroxyl bunches present among the atoms are separated, which at that point respond with water particles (H–OH) and move out from the fibril structure [4–6, 12]. Because of this, hydrophilic hydroxyl bunches are diminished and expands the filaments dampness obstruction property [1, 21]. The rate assimilation of dampness amount by biofibril composite is more when contrasted with soluble base-treated and Benzene diazonium chloride-treated composites [4–6, 11, 29].

$$\% \text{ water absorption} = 100 \times (W_f - W_i) / W_i.$$

Fig. 5 Moisture content absorption of untreated, alkali-treated and benzene diazonium chloride-treated composites



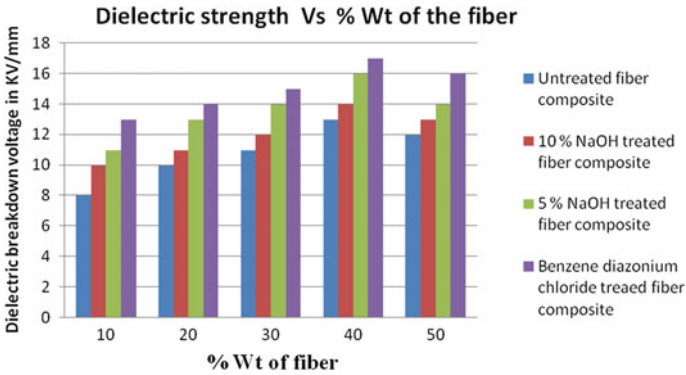


Fig. 6 Reveals the dielectric strength of untreated and chemical treated composites

3.5 Dielectric Strength

To examine the dielectric quality of untreated, soluble base-treated, and benzene diazonium chloride-treated composites, the composite examples were made according to the ASTM D-149 principles. The composites having measurements of 120 mm × 120 mm × 3 mm were fortified with strands a single way along 120 mm length. The dielectric separate voltage was found at five focuses on every example, and the normal worth was considered for investigation. The test was done at 50 Hz recurrence and room temperature. Computerized micrometer of 0.001 mm least tally was utilized to discover the thickness of the composites at a separate point. It was likewise apparent to see that the dielectric quality of half breed fiber composites increments with increment in the amount of fiber from 10 to 40% weight of fiber yet diminishes at half fiber amount composite [4, 5, 11]. At half fiber amount composite, the decline in dielectric quality was because of poor interfacial holding between the filaments and network mix [5, 8, 11, 16, 22].

4 Conclusion

The work shows that the compound treatment significantly improves the fiber quality, fiber-grid attachment and thus the presentation of the normal fiber composites. The elastic, compressive, and flexural properties was seen to have improved for both salt and benzene diazonium chloride treatment of fiber composites. The outcomes show that the ductile, compressive, and flexural qualities of the composites expanded with increment in fiber stacking up to 40% and past 40% it demonstrated a diminishing in pliable, compressive and flexural quality. Moderately overabundance measure of fiber rests onto each other as opposed to being blended in with network at half fiber loads, which additionally prompts diminished pressure move capacity. The rate

retention of dampness amount by natural fiber composite was more when contrasted with soluble base-treated and benzene diazonium chloride-treated composites. Yet, after the substance treatment or surface change of strands, it was discovered that upgrade in the properties of the composites with the evacuation of debasements like hemicellulose, oils, waxes, dampness, and lignin from the surfaces of the filaments and yields harsh surface geology, which improves the perspective proportion of strands and builds the fortifying effectiveness of the fiber with the improvement of stress move from the lattice to stack bearing strands.

References

1. A.M. Edeerozey, H.M. Akil, A.B. Azhar, M.Z. Ariffin: Chemical modification of Kenaf fibres. *Mate. Lett.* **61**, 2023–2025 (2007)
2. A.C. Karmarker, G. Hinrichen, Processing and characterization of jute fiber reinforced thermoplastics polymers. *Polym. Plast. Technol. Eng.* **30**(5–6), 609–618 (1991)
3. G. Venkatesha Prasanna, K. Venkata Subbaiah, A. Varada Rajulu, Chemical resistance, impact, flexural, compressive properties and optimization of fibers of natural fibers reinforced blend composites. *Scholarly J. Eng. Res.* **1**(6), 85–89 (2012)
4. G. Venkatesha Prasanna, *Surface Modification, Characterization and Optimization of Hybrid Biocomposites*. Springer (2020)
5. G. Venkatesha Prasanna, *Influence of Fiber length and Chemical Treatment on the Mechanical Properties of Blended Composites*. Springer (2020)
6. R. Punyamurth, D. Sampathkumar, B. Bennehalli, P. Badyankal, S.C. Vekateshappa, Surface modification of abaca fiber by benzene diazonium chloride treatment and its influence on tensile properties of abaca fiber reinforced polypropylene composites. *Ciencia Tecnologia dos mater.* **26**(2), 142–149 (2014)
7. K.L. Pickering, Y. Li, R.L. Farrell, M. Lay, Interfacial modification of hemp fiber reinforced composites using fungal and alkali treatment. *J. Biobased Mater. Bioenergy* **1**, 109–117 (2007)
8. G. Venkatesha Prasanna, *Fiber Surface Treatment and Quantity, Impact on the Performance of Biocomposites*. Springer (2020)
9. S. Qianqian, C. Xianhua, Effect of rare earths surface treatment on tribological properties of CFs reinforced PTFE composite under oil lubricated condition. *J. Rare Earths* **26**(4), 584–592 (2008)
10. H. Harani, S. Fellahi, M. Bakar, Toughening of epoxy resin using hydroxyl-terminated polyester. *J. Appl. Polym. Sci.* **71**, 29–38 (1999)
11. G. Venkatesha Prasanna, N.K. Jha, C. Harish, Chemical treatment and analysis of mechanical properties of hybrid biocomposites. *Int. J. Mech. Prod. Eng. Res. Dev.* ISSN(P): 2249–6890; ISSN (E): 2249–8001, Special Issue: 189–193 (2018)
12. G. Venkatesha Prasanna, N.K. Jha, *Optimisation and Mechanical Testing of Hybrid Biocomposites*. Elsevier, *Materials Today*, pp. 1395–1404 (2019)
13. R.M.N. Arib, S.M. Sapuan, M.M.H.M. Ahmad, M.T. Paridah, H.M.D. Zaman, Mechanical properties of pineapple leaf fiber reinforced polypropylene composites. *Mater. Des.* **27**(6), 391–396 (2006)
14. M.K. Alamgi, M.H. Monimul, R.M. Islam, A.K. Bledzki, *Bioresources* **5**, 1618–1625 (2010)
15. R.T. Morrison, R.N. Boyd, *Organic Chemistry* (Prentice-Hall, London, 1989)
16. G. Venkatesha Prasanna, G. Tirunagari Jayadeep Nikhitha Poornabhodha, *Chemical Treatment, Influence of Fiber Content and Optimization of Hybrid Natural Fibers Reinforced Composites*. Springer, *The Smart Innovation, Systems and Technologies (SIST)*. ISSN: 2190–3018 (2019)

17. G. Venkatesha Prasanna, K. Venkata Subbaiah, Modification, flexural, impact, compressive properties and chemical resistance of natural fibers reinforced blend composites. *Malaysian Poly. J.* **8**(1), 38–44 (2013)
18. M. Sampath Kumar, R. Dhanasekaran, S. Ahmed, B. Praveen Kumar, Experimental investigation of tensile and flexural properties of *Luffacylindrica*, banana, sisal and glass reinforced epoxy composites. *Int. J. Recent Sci. Res.* **8**(2), 15634–15639 (2017)
19. D.E. Akin, G.R. Gamble, W.H. Morrison, L. Rigsby, Chemical and structure analysis of fibre and core tissues from flax. *J. Sci. Food Agric.* **72**, 155–165 (1996)
20. X. Colom, F. Carrasco, P. Pagès, J. Cañavate, Effects of different treatments on the interface of HDPE/lignocellulosic fiber composites. *Compos. Sci. Technol.* **63**, 161–169 (2003)
21. H.U. Zaman, M.A. Khan, R.A. Khan, M.A. Rahman, L.R. Das, A. Mamun, Role of potassium permanganate and urea on the improvement of the mechanical properties of jute polypropylene composites. *Fibers Polym.* **11**(3), 455–463 (2010)
22. M. Baiardo, E. Zini, M. Scandola, Flax fiber polyester composites. *Compos. A Appl. Sci. Manuf.* **35**(6), 703–710 (2004)
23. D.N. Saheb, J.P. Jog, Natural fiber polymer composites: a review. *Adv. Polym. Technol.* **18**, 351–363 (1999)
24. K. John, S.V. Naidu, Effect of fiber content and fiber treatment on flexural properties of sisal fiber/glass fiber hybrid composites. *J. Reinf. Plast. Compos.* **23**, 1601–1605 (2004)
25. J. Chakrabarty, M.M. Hassan, M. Khan, Effect of surface treatment on betel nut (areca catechu) fiber in polypropylene composite. *J. Polym. Environ.* **20**, 501–506 (2012)
26. A.K. Saha, S. Das, D. Bhatta, B.C. Mitra, Study of jute fiber reinforced polyester composites by dynamic mechanical analysis. *J. Appl. Polym. Sci.* **71**, 1505–1513 (1999)
27. X.R. Zhang, P. Zhao, X.Q. Pei, Q.H. Wang, Q. Jia, Flexural strength and tribological properties of rare earth treated short CFs/polyimide composites. *Ex. Poly. Lett.* **1**(10), 667–672 (2007)
28. M. Anguilar-Vega, C.A. Cruz-Ramos, Properties of henequen cellulosic fibers. *J. Appl. Polym. Sci.* **56**(10), 1245–1252 (1995)
29. M.S. Sreekal, S. Thomas, Effect of fibre surface modification on water-sorption characteristics of oil palm fibres. *Comp. Sci. Technol.* **63**, 861–869 (2003)
30. J. Seena, P. Koshy, S. Thomas, The role of interfacial interactions on the mechanical properties of banana fibre reinforced phenol formaldehyde composites. *Compos. Interfaces* **12**, 581–600 (2005)

Compressive and Impact Behavior of Nanoscale Hybrid Composite Materials



Mohd. Minhajuddin Saif, Dasari V. Ravi Shankar,
and Mohd. Manzoor Husain

Abstract The use of polymer matrix composites has been increased exponentially for the past. Marine, aeronautical, automobile, and space structures are the areas where fiber-reinforced composites are very widely used for their specific properties like high tensile strength, high strength to weight, inert to the environment, etc. These conventional fiber-reinforced polymers (FRP) fall short of both compressive strength and impact strength. To overcome these challenges, an attempt is being made to develop the properties of FRP composites (glass/epoxy) by adding nanofiller. Three different types of nanoparticles are used: (i) multi-wall carbon nanotube (MWCNT), (ii) Nanosilica (NS), (iii) Nano-Iron oxide (NI) with four different weight percentages 0.1, 0.2, 0.5, and 1.0%. The experiments reveal a significant enhancement in the compression and impact behavior for Glass/Epoxy FRP when modified with nanofillers.

Keywords GFRP · MWCNT · Compressive strength

1 Introduction

The fiber-reinforced polymer materials are very considerably used in automobile, aeronautic, marine, civil sector, and defense industries for replacing the conventional metals like steel, aluminum, and their alloys [1]. This replacement of metals and their alloys with composites is because of high specific stiffness and strength

Mohd. Minhajuddin Saif (✉)
Department of Mechanical Engineering, JNTUH, Hyderabad 500085, India
e-mail: Minhajuddin.saif@mjclege.ac.in

D. V. Ravi Shankar
TKRCET, Ranga Reddy District, India
e-mail: shankardasari@rediffmail.com

Mohd. Manzoor Husain
JNTUH, Hyderabad 500085, India
e-mail: manzoorjntu@gmail.com

which leads to the overall improvement in material properties. Composite materials face critical issues like high brittleness, low compressive strength, high cost, manufacturing repeatability, etc. Subsequently, there is a need to overcome these issues for mainstream acceptance of composite materials in conventional engineering applications.

Various methods such as modifying fiber/matrix interface, matrix modification, and fiber hybridization are reported to increase the resistance to impact and providing a great amount of tolerance to damage in FRP [2–4]. Though the fiber hybridization is a cost-effective method to improve the impact properties of the FRP components [5, 6], matrix modification by use of nanofillers could be an alternate. And this would be more optimal methodology which would enhance the resistance toward impact and improved tolerance toward damage. By improving the polymer matrix properties, composite materials properties can be improved and the above-mentioned issues can be resolved. One way of enhancing the properties of the polymer matrix is by modifying it by nanofiller. If the reinforcement additives of composite materials have one or more dimensions in nanoscale, these are referred to as nanoscale composites [7, 8]. Carbon nanotubes (CNTs) were used by most of the researchers for fabricating nanoscale composite materials, as this material has a high potential with combined benefits of high hardness and higher absorption capabilities. Other than that, it also exhibits a high strength and stiffness, improved hardness, and low density with high length to diameter ratio. These high aspect ratios of CNTs leads to high surface area and a suitable interface, for transfer of stress in composites, is obtained through high surface areas of CNT. It is found that multi-wall carbon nanotubes [MWCNTs] are more capable in the transfer of stress from the polymer to CNTs than single-wall carbon nanotube [9]. Gojny et al. contradicted that high surface area leads to high surface energy and undesirable attractive force that would lead to excessive agglomeration [10]. To overcome this specific problem of agglomeration, various methods such as regression shear stirring and sonication were reported [11–13].

Santos et al. [14] used two different fillers; (a) cork powder and (b) nanoclay investigated the resistance toward impact and the tolerance toward damage of Kevlar/epoxy composite. An increase in impact load-bearing capacity was observed and was also reported that the quantity of increment would be influenced by the type of filler. The damaged area of laminate with nanoclay as filler was increased by 29%. Athanasios et al. [15] examined the resistance toward the impact of carbon fiber-reinforced polymer (CFRP) with MWCNT as fillers under different weight percentages. Maximum improvement was observed for 0.5 wt% CNT-doped specimens.

Waas and Lee [16] conducted a study on the micro mechanism of composite failure of FRP laminate in compression loading, where it was observed for a laminate with a low volume fraction of fiber a splitting failure mode, whereas with a high volume fraction of fiber, a splitting/kink banding failure mode was observed. Harris and Piggott [17] conducted studies under compression loading on composites structures made with three reinforcements: (i) glass, (ii) carbon, and (iii) aromatic polyamide fibres. Later, it was reported that the 'Rule of Mixtures' in an FRP composite (glass–polyester) with an apparent fibre strength existence in a range of 1.3–1.6 GPa, the

tensile, and compression moduli were equal with respect to two different limiting fiber volume fractions (V_f), 0.31 and 0.46. Matrix yield strength and composite strength are directly proportional to each other at a higher fraction of volume, whereas a composite with epoxy resin matrix was having more strength than polyester-based composites at the same matrix yield strength. When volume fraction is maintained at 0.30, they observe a slight decrease in the stiffness of carbon fiber and also they appear to be weaker in compression than they are found to be when in tension.

In the present study, three different nanoparticles, MWCNT, NS, and NI with four different weight percentages (a) 0.1%, (b) 0.2%, (c) 0.5%, and (d) 1.0% wts, are used as fillers in glass/epoxy composite (GFRE). The suspension of nanoparticles in the matrix system is done with the help of mechanical stirring followed by bath sonication. Two types of tests were performed one compression and other impacts.

2 Materials and Methods

The nanofilled polymer composite was prepared by using a mat comprising of 66% unidirectional glass fiber and 34% chopped stand making a total 600 GSM mat. A commercial-grade epoxy with a trade name of Lapox L12 was used as a matrix with appropriate hardener. The fillers (i) MWCNT, (ii) NS, and (iii) NI were used in present works were supplied by Intelligent Materials Pvt. Ltd, India.

The quality of the nanofiller was determined using SEM and TEM and the following were found. For MWCNT, the outer diameter was 30–50 nm, inner wall was 15–20 nm, and length was 10–15 μm with an apparent density being 0.21 g/cm^3 and the specific area of 110 m^2/g with a purity of 99.8%. A 50 nm spherical nanosilica was used which has a specific external available area of 110–120 m^2/g , the apparent density of 2.4 g/cm^3 , and a purity of 99.9%. A similar size specification was found for the iron oxide with a purity of 99.9%; however, the specific surface was of 30 m^2/g and the bulk density was 5.242 g/cm^3 .

A Hand Layup method was used for the fabrication of required samples in a mold of 325 mm \times 300 mm. Initially, the two halves of the mold are coated with wax on the inner sides which would play as a releasing agent. Later, E-glassfiber (four plies) as per the required dimensions are stacked in the mold after applying the modified resin. The modification in the resin was done by adding the required weight percentage of a particular nanoparticle in the resin. To produce a sound laminate, good dispersion of nanoparticles in resin is needed. This was done with the help of mechanical stirring followed by sonication (bath sonicator). The time duration for mechanical stirring was maintained for half an hour followed by one hour for sonication for all the weight percentage of nanoparticles. The required samples as per the standards were cut from a single laminate of a particular weight percentage and type of nanoparticles.

3 Methodology

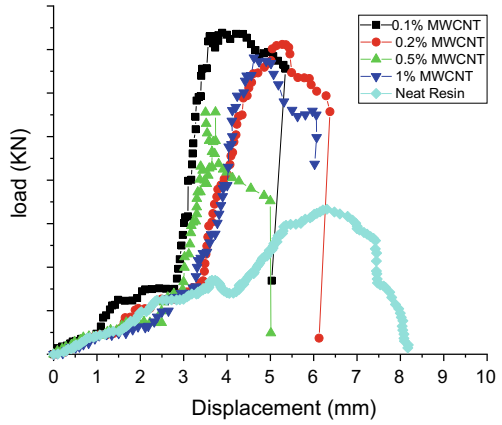
The compressing test was carried out as per ASTM D695, where the specimen is of the size of 25 mm × 25 mm. Such small size specimen is used to avoid buckling and premature failure of sharp corners. The small cross section of the specimen will also reduce friction. The speed of the movable jaw was maintained at 2 mm/min. The resistance offered by the specimen gives the force induced by the hydraulic systems into the specimen. The movement of the jaw gives the displacement specimen.

The impact testing was carried out as per ASTM D3763. A V notch is first prepared in sample of size 12.6 cm × 1.27 cm × 0.3 cm. The V notch was made at the centre of the specimen, which was placed between the fixtures such that the pendulum strikes the cracked side. Energy absorbed per meter was given as scale reading by sample thickness.

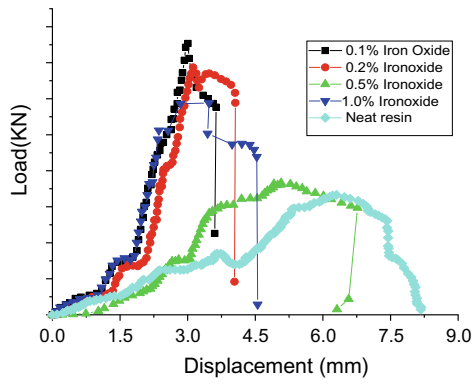
4 Results and Discussion

The compression test was performed as discussed in Sect. 3 and Fig. 1a–c represents the deviation of compressive load with a displacement of various set of nanoscale composites. For MWCNT set nanoscale composites, an increased ultimate compressive strength with an increased weight percentage of MWCNT is observed. It is increased to a percentage of 84% for 0.2% MWCNT from 74% for 0.1% of MWCNT. For 0.5% MWCNT sample, percentage increase is 65% when compared with neat composite. From 1.0%, the increase in strength is almost the same as 0.5%. The increase of ultimate compressive strength for the first two samples that is 0.1 and 0.2% is due to an increase in properties of the matrix due to the addition of MWCNT. As the quantity of MWCNT added is very less in these samples, even distribution of nanoparticles is very much possible. But for the samples of 0.5 and 1.0%, the quantity is high and this may lead to the increase in the van der Waals forces between nanoparticles resulting in a decrease in the dispersion of nanoparticles in the resin system. From Fig. 1b, an 89% increase in ultimate compressive strength is observed for 0.5% weight percentage. The minimum ultimate compressive strength is observed for 1.0% weight of nano-iron oxide sample which is 68% more than conventional composite. The difference in the behavior of the sample is due to the high density of nano-iron oxide when compared to MWCNT. This high density leads to a low quantity of nano-iron oxide particles when compared to that of MWCNT for same weight. So, a shift from 0.2 to 0.5% is absorbed for maximum strength in nano-iron oxide samples when compared to MWCNT samples. Figure 1c is for silica type of nanoparticles. In this, the ultimate compressive strength is going on increasing with the addition of nanoparticles. An increase of 140% is observed in 1.0% weight of nanosilica sample when compared to conventional composite. For 0.1% weight sample, the increase in ultimate compressive strength is increase by 81%. This variation of behavior when compared to other nanoparticles is due to the same molecular

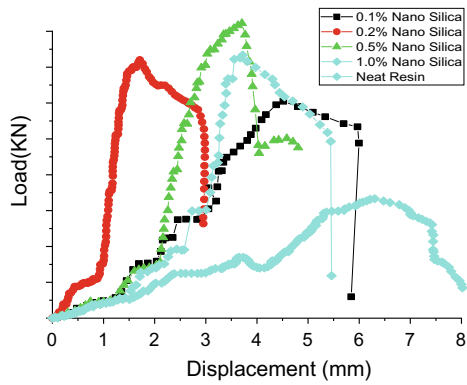
Fig. 1 Load vs displacement under compression for composite modified with **a** MWCNT **b** NI **c** NS



(a)



(b)



(c)

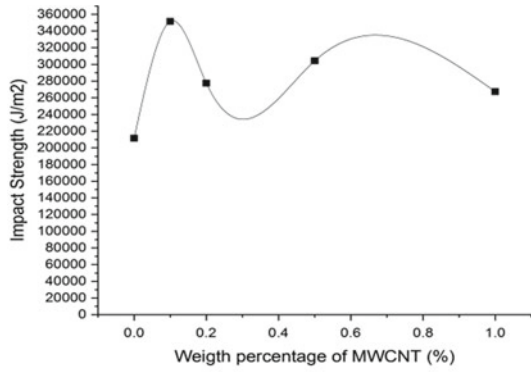
formula of nanosilica and glass fiber. This nanosilica acts as supporting reinforcement along with the glass fibers. Even agglomeration that takes place at high weight percentage will not act stress concentration point but are used to transfer the load.

The compression test was performed as discussed in Sect. 3 and Fig. 2a–c shows the impact strength with the variation of nanoparticles for MWCNT, NI, and NS set of nanoscale composites. For the MWCNT set of sample, the maximum impact strength is observed at 0.1% weight sample. The percentage increase in impact strength is 66% and the minimum increase is of 26% for 1.0%. In the case of nano-iron oxide set, it is observed to be an increase in impact strength by 127%. In the case of a set of silica nanoparticles, the maximum strength is 89% more when compared to conventional composite for 0.1% weight percentage silica set sample. The minimum increased in strength is 54% for 1.0% set of sample. Owing to the change of the morphological in resin during crystallization, this increase in impact strength is observed. For MWCNT and NS sets of samples, the impact strength reduces for 0.2 wt%, and thereafter, it remains constant. This decrease in impact strength is due the high quantity of MWCNT and NS compared to NI and this leads to the agglomeration of nanoparticles in a resin base.

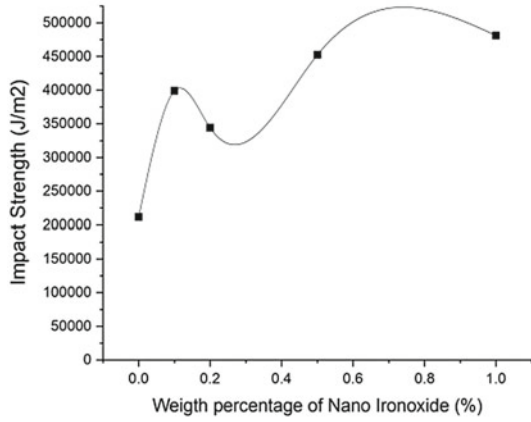
5 Conclusion

In this study, compressive strength and impact strength of nanoscale hybrid composite under different weight percentages and different nanoparticles were observed. The maximum increase in compressive strength by 89% for a sample modified with a nano-iron oxide-modified resin at a weight percentage of 0.5% is observed. The breaking point in the entire sample is much early when compared to neat resin; this is due to the brittle nature of nanoscale composite when compared to conventional composite. The impact strength has also been improved due to the addition of nanoparticles with a maximum increase of 127% for a GFRE sample modified with nano-iron oxide.

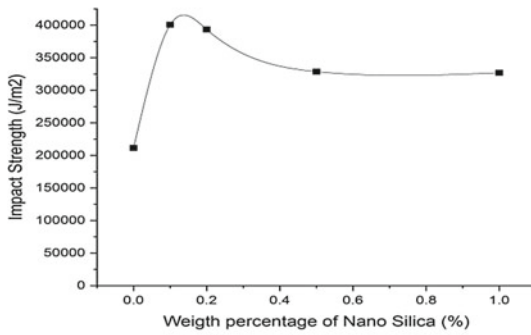
Fig. 2 Variation of impact strength for composite modified with **a** MWCNT **b** NI **c** NS



(a)



(b)



(c)

References

1. R.C. Santiago, R.L. Azevedo, A.F. Avila, M.A. Alves, Mechanical characterization of glass/epoxy composite material with nanoclay. *Proc. COBEM* (2007)
2. J. Gustin, A. Joneson, M. MahinFalah, J. Stone, Low velocity impact of combination kevlar/carbon fiber sandwich composites. *Comp. Struct.* **69**, 396–406 (2005)
3. G.L. Dai, S.L. Tae, S.C. Seong, Impact energy absorption characteristics of glass fiber hybrid composites. *Comp. Struct.* **46**, 267–278 (1999)
4. Y. Peter, J.B. Lawrence, The effect of glass/resin interface strengthen impact strength of fiber reinforced plastics. *Polym. Eng. Sci.* **18**, 062–072 (1978)
5. R. Ramasimha, N.K. Naik, H. Arya, N. ShamaRao, S. Prabhu, Impact response & damage tolerance characteristics of glass–carbon/epoxy hybrid composite plates. *Composites B* **032**, 565–574 (2001)
6. S. Jeelani, M. Hosur, M. Adbullah, Studies on the low-velocity impact response of woven hybrid composites. *Comps. Struc.* **067**, 253–262 (2005)
7. J.B. Donnet, Nano and Micro composites of polymers elastomers and their reinforcement. *Comps. Sci. Tech.* **063**, 1085–1088 (2003)
8. T.J. Pinavia, G.W. Beal, *Polymer-clay Nano-composites* (Wiley, New York, 2000)
9. P.M. Ajayan, L.S. Schadler, S.C. Giannaris, Load transfer in carbon nanotube epoxy composites. *Appl. Phys. Lett.* **73**, 3842–3844 (1998)
10. K. Schulte, F.H. Gojny, B. Fiedler, M. Wichmann, Influence of different carbon nanotubes on the mechanical properties of epoxy matrix composites—a comparative study. *Comp. Sci. Tech.* **65**, 2300–2313 (2005)
11. W. Ben, L. Yu-Hsuan, O.M. Tondin, L. Zhiyong, Z. Chuck, B. Wang, Investigation of the dispersion process of SWNTs/SC-15 epoxy resin nanocomposites. *Mater. Sci. Eng. A* **385**, 175–181 (2004)
12. M.M. Rahman, S. Zainuddin, M.V. Hosur, J.E. Malone, M.B.A. Salam, A. Kumar, S. Jeelani, Improvements in mechanical and thermo-mechanical properties of e-glass/epoxy composites using amino functionalized MWCNTs. *Comp. Struc.* **94**(8), 2397–2406 (2012)
13. S.S. Young, R.Y. Jae, Influence of dispersion states of carbon nanotubes on physical properties of epoxy nanocomposites. *Carbon* **43**(7), 1378–1385 (2005)
14. J.B. Santos, P.N.B. Reis, P. Santos, J.A.M. Ferreira, M.O.W. Richardson, Impact response of Kevlar composites with filled epoxy matrix. *Comp. Struc.* **94**, 3520–3528 (2012)
15. B. Athanasios, V. Kostopoulos, P. Karapappas, I.V. Antonios, P. Alkis, Impact and after-impact properties of carbon fibre reinforced composites enhanced with MWCNTs. *Comp. Sci. Tech.* **70**, 553–563 (2010)
16. M.A. Waas, S.H. Lee, Compressive response and failure of fiber reinforced unidirectional composites. *Int. J. Fract.* **100**, 275–306 (1999)
17. B. Harris, M.R. Piggott, Compression strength of carbon, glass and Kevlar-49 fibre reinforced polyester. *J. Mater. Sci.* **15**, 2523–2538

Study of Mechanical Properties of Coconut Coir Fiber-Reinforced Polymer Composites



Gondi Konda Reddy and H. Madhusudhana Reddy

Abstract In the present day situation, the usage of conventional material for building and manufacturing sectors is growing enormously. This leads to, at some point of time, the depletion of the conventional material due to heavy demand. Now, there is a necessity to think of other materials for different purposes for the development of new products. The other source is that which does not cause any pollution to the environment and, at the same time, gives the scope for replacing the existing materials. Generally, everybody knows that for construction, materials like steel and wood take the major part. But once there is a shortage of these materials, the other materials which provide the same purpose would get major importance in this particular research. The unconventional materials like natural fibers play a major role here. A lot of research is going on this field. But generally, the research is limited to a particular fiber that is available in plenty. The fibers like coconut, kenaf, and sisal are abundantly available in countries like ours. Here and there, some research is going on but it is only of limited scope to understand. Even countries like India produce a lot of agricultural waste every year. If this is used for the purpose of making usable products, there may be a demand for that, and there is employment potential for those companies or organizations. The authors are highly motivated to develop such products which can use and replace conventional materials.

Keywords Composite materials · Coconut fiber · Mechanical properties

G. K. Reddy (✉) · H. Madhusudhana Reddy
Department of Mechanical Engineering, Sreenidhi Institute of Science and Technology,
Hyderabad, Telangana, India
e-mail: kondareddy@sreenidhi.edu.in

H. Madhusudhana Reddy
e-mail: madhusudhanareddy@sreenidhi.edu.in

© Springer Nature Singapore Pte Ltd. 2021
G. S. V. L. Narasimham et al. (eds.), *Recent Trends in Mechanical Engineering*,
Lecture Notes in Mechanical Engineering,
https://doi.org/10.1007/978-981-15-7557-0_30

1 Introduction

The present day demand for the materials made of reusable and other natural fibers is constantly growing because of a lot of awareness in every individual on what is to be used to safeguard the environment from pollution, which is very important for future generations on the earth. The role of present researchers is to develop various composite materials by using the agricultural or industrial wastes. This in one way or the other way better for the industry and agri farmers; they sell and get some money out of it. As the expenditure on the other hand for agriculturists is increasing day by day, it is somewhat flexible to get benefited by selling their agricultural wastes. About the industrial by-products which are getting they can reuse it to generate some money out of it. Out of many fibers that are available in nature, cotton seems to of more tensile strength as compared to kenaf fiber. Sisal fiber is also to be tested for further results. Many experimental tests are carried out, more probably mechanical tests. The cellulose material which is present in the natural fibers gives strength to particular fibers. The quantity of cellulose and the bonding between the other fibers or a particular fiber is changing abruptly.

The aim of the research is fabricating the various composites with different proportions and testing them for their properties. One can find many materials that come with different fibers which really is a great achievement of the scientists. But still it has to grow to such an extent that it becomes a major industry. It is also helping mankind to serve for better materials, for example, the helmet worn by a rider of a two wheeler. The helmet is made from fibers arranged in such a way that it is lesser in weight. It is quite possible because it is made from fibers. But here, the binding material is also important. The binder may be of polymer material which is intact with the other fibers. One important property of the composite material is that is a nonconductor of electricity. But it is somewhat fire resistant. Even nowadays, chairs and furniture are made in the houses using composite material. Once it is developed, many companies would come forward to produce more products.

Even composites can try their role in two-wheeler and four-wheeler manufacturing. The parts made of steel and aluminum can be replaced by the natural fibers.

The clear analysis of the mechanical properties of sisal fiber with rice husk is explained and discussed by Konda Reddy et al. [1]. Here, the rice husk is kept to reduce the weight. The effect of beam length in the tensile properties for various natural fibers is conducted, and this work is carried out by Biswas et al. [2]. The properties and performances of natural fiber composites and their properties are explained in the book by Rockwell [3] in his paper. Reinforced plastics were studied and presented clearly by Schneider et al. [4]. The composites of plant oil-based resin are also considered and studied by Schoesser and Knothe [5]. The mechanical properties of kenaf fibers and kenaf were studied, presented, and explained [6]. The optimization of industrial hemp fiber for composites was studied and clearly explained

[7]. Fabricating and testing was carried out, and the work was explained by Sathyanarayana et al. [8]. Here in this paper, the fabrication and evaluation of the mechanical properties were carried out for coconut fiber.

2 Manufacturing Processes of Composite Material

The manufacturing of a composite is the most important task. Otherwise, it is not going to serve its purpose. The provision of various fibers in particular order systematically and pouring correct quantities of polymer and hardener are very much essential. If any of the compositions changes, the properties of the composite also change.

1. Open mold process
 - (a) Hand lay-up process,
 - (b) Spray-up process,
 - (c) Vacuum bag autoclave process, and
 - (d) Filament winding process.
2. Closed mold process
 - (e) Compression molding,
 - (f) Injection molding,
 - (g) Sheet molding compound (SMC) process, and
 - (h) Continuous pultrusion process.

In the open mold process, the hand lay-up process is easy to fabricate. The person who is doing the activity should wear the goggles and has to proceed. The goggles give flexibility to change the orientation of the fibers and pour the polymer. Here, the mold is kept on the floor first, and it is important that the surface is cleaned properly. Then the fibers are kept in the order by checking their weights. The correct quantity of polymer has to be poured. After that, the hardener is poured which makes the composite hard. Here, any combination of the composite material will change the properties of the material.

In the spray-up process, a gel is sprayed on the inside portion of the mold, otherwise, that will stick to the mold. It will not come out during the removing process. Here, the composite has to remove slowly without damaging the composite.

The vacuum bag autoclave process is some kind of an automatic process to fabricate the composite. In the filament winding process, the fibers are arranged by knitting them around the object. If the fiber is not properly wound, it cannot be removed after composite is formed.

The second order of molding processes, compression molding of the polymer, is sent into the mold which is already kept. Here, the fibers are kept compressed.

Injection molding is similar to the process done on plastics. In that case, plastic is the material but here, the polymer is injected into the mold cavity. In the SMC

Fig. 1 Pouring the liquid into the mold



process, the fibers are arranged in the order like sheet metals and the polymer is poured. Then, it will kept atmospheric air which will settle down as shown in Fig. 1.

3 Materials

The details of processing of the composites and the experimental procedures as followed for their mechanical characterization. The raw materials used in this work are

1. Natural Fibers (coir),
2. Hardener (HY-951),
3. Araldite, and
4. Pattern.

Natural fibers such as coir fiber-reinforced polymer composites have played a dominant role for a long time in a variety of applications for their high specific strength and modulus. The manufacture, use, and removal of traditional fiber-reinforced plastic, usually made of glass, carbon or aramid fibers-reinforced thermoplastic, and thermoset resins, are considered critical because of environmental problems. By natural fiber composites, we mean a composite material that is reinforced with fibers, particles or platelets from natural or renewable resources, in contrast to, for example, carbon or aramid fibers that have to be synthesized. Their properties are given in Table 1.

Advantages of Natural Fibers:

Compared to conventional reinforcement fibers like glass, carbon and Kevlar, natural fibers have the following advantages:

Table 1 Overview of properties of natural fiber

Plant fibers	Density (Kg/m ³)	Tensile strength (MPa)	Young's modulus (GPa)
Coconut coir	1150–1250	106–175	6–8

- Environmentally friendly,
- Fully biodegradable,
- Nontoxic,
- Easy to handle,
- Nonabrasive during processing and use,
- Low density/light weight,
- Source of income for rural/agricultural community,
- Renewable, abundant, and continuous supply of raw materials,
- Low cost,
- Free from health hazard (cause no skin irritations),
- High toughness, and
- Good thermal properties.

Properties of Natural Fiber:

- Lightweight,
- Resists most alkalis and acids,
- Resists stress cracking,
- Retains stiffness and flexibility,
- Low moisture absorption,
- Nonstaining, and
- Easily fabricated.

Applications of Coir:

- Structural applications and
- Industrial tooling and composites.

Wax patterns are used in a casting process called investment casting. Plaster of Paris is usually used in making master dies and molds, as it gains hardness quickly, with a lot of flexibility during the setting stage.

Patterns are made of wood, metal, ceramic, or hard plastics and vary in complexity. A single piece pattern, or loose pattern, is the simplest. It is a replica of the desired casting—usually in a slightly larger size to offset the shrinkage of the intended metal. Gated patterns connect a number of loose patterns together with a series of runners that will be detached after shakeout. Segmented or multi-piece patterns create a casting in several pieces to be joined in post-processing. The pattern used for the experiment is shown in Fig. 2.

Match Plate Patterns:

Patterns with the top and bottom parts, also known as the cope and drag portions, are mounted on the opposite sides of a board. This adaptation allows patterns to be quickly pressed into the molding material. A similar technique called a cope and drag pattern is often used for large castings or huge production runs: in this variation, the two sides of the pattern are mounted on separate pattern plates that can be hooked up to horizontal or vertical machines and pressed into the molding material. When



Fig. 2 Pattern for sample preparation (composite of (250 mm × 25 mm × 10 mm))

the parting lines between the cope and drag are irregular, a follow board can be used to support irregularly shaped, loose patterns.

Sweep Patterns:

Sweep patterns are used for symmetric molds, which are contoured shapes rotated around a center axis or pole through the molding material. A sweep pattern is a form of skeleton pattern: any geometrical pattern that creates a mold by being moved through the molding material.

4 Methodology

Experimental Procedure

Overview of the Process:

Wax coat is first applied to the mold by hand for a high-quality surface. When the wax coat has cured sufficiently, roll stock fiber coir reinforcement is manually placed on the mold. The laminating mixture of Araldite and the hardener is applied by pouring, brushing, spraying, or using a paint roller. FRP rollers, paint rollers, or squeegees are used to consolidate the laminate, thoroughly wetting the reinforcement and removing entrapped air. Subsequent layers of coir/coir reinforcement are added to build laminate thickness.

Workstation Preparation:

An initial preparation of all the materials and tools that are going to be used is a fundamental standard procedure when working with composites. This is mainly because once the Araldite and the hardener are mixed, the working time (prior to the resin mix gelling) is limited by the speed of the hardener chemically reacting with the Araldite producing an exothermic reaction.

Here, Fig. 3 shows the applying of wax on the surface.

Fig. 3 Applying wax on the surface



Table 2 Sample composition

S. No.	Solution (%)	Coconut fiber (%)	Coconut coir weight (gms)	Hardener	Araldite
1.	97	3	2.47	8.2	72.83
2.	95	5	4.12	8.2	70.18
3.	93	7	5.77	8.2	68.53
4.	91	9	7.42	8.2	66.88
5.	89	11	9.07	8.2	62.53

Sample Preparation:

Composite laminates of (250 m × 25 mm × 10 mm) * 5 were fabricated. Density of unsaturated polyester resin (δ) = 1.2 g/cm³.

$$\text{Volume of the mold } (V) = 250 \text{ mm} \times 25 \text{ mm} \times 10 \text{ mm} = 62,500 \text{ mm}^3.$$

$$\text{Mass of resin } (m) = \text{Volume of mold} \times \text{Density of unsaturated polyester resin} = 62.5 \times 1.2 = 75 \text{ g.}$$

The samples with different proportions are given in Table 2.

Mold Preparation:

Before starting with the lay-up process, an adequate mold preparation must be done as shown in Fig. 4. Mainly, this preparation consists of cleaning the mold and applying a release agent on its surface to avoid the resin from sticking. In this

Fig. 4 weighing the coir according to the calculations



experiment, the mold preparation is simply taping the plastic sheeting to the tabletop. If this was an actual mold, the student would do the following:

- Clean the mold with a clean cloth;
- Apply and spread the release agent on the surface of the mold;
- Wait certain to set up the release agent;
- Buff with a clean cloth.

Lay-Up Process:

After all the materials are ready, the place for mold is to be identified. First of all, thoroughly mix the hardener. Generally, the suppliers give the details of the composition. The calculations of the different proportions are important in manufacturing the composite. The weight of all constituents and volume of the composite have to be calculated.

Many methods are there to measure the volume and weight. While preparing the composite, it is important that the proportions are followed exactly to get a better composite.

While pouring the hardener and polymer, it is to be noted that it is properly mixed. Otherwise, good quality composite cannot be obtained.

The first step is to mix the hardener and the resin. The proportions are usually given by the supplier and can be found on the containers of the hardener or resin. The portions can be either measured by weight or by volume but it is important to follow these proportions exactly as this is a complete chemical reaction, and all components must react completely for maximum strength of the matrix.

It is easiest to measure the proportions using the volume method and a screw in pump that inserts into the cans of resin and hardener. The hardener should be operated carefully because any contamination will initiate the chemical reaction and cause the resulting blend to harden.

Curing:

Curing is most important after preparing the composite, otherwise, it will break during removal from the mold and it may fail when the composite is used. So the prepared composite has to be cured properly under atmospheric temperature.

Cleaning:

After preparing the composite, it must be cleaned properly and removed from the mold. At least, it is better to keep it for one day after removed from the mold. Weighing the coir according to the calculations is shown in Fig. 4.

5 Results and Discussion

Natural fibers can improve strength but some of the fibers are not consistent, or are irregular in shape which influences the strength of the composite. In the study, coir fiber-reinforced composites have retained their tensile strength even after the addition

of compatibilizer and coir fiber, though there was a steady decrease in elongation values.

The preparation of test specimens depends on the purposes of the testing and on the governing test method or specification. A tensile specimen is usually a standardized sample cross-section. It has two shoulders and a gage (section) in between. The shoulders are large so they can be readily gripped, whereas the gage section has a smaller cross-section so the deformation and failure can occur in this area.

Based on coir percentage, the tensile properties of the component vary. A Universal Testing machine is used to test the component, and the values are tabulated below and the variation is plotted on the graph.

Tensile testing, also known as tension testing, is a fundamental materials science and engineering test in which a sample is subjected to a controlled tension until failure.

The result show that 7% (in the analysis, Table 3 and Fig. 5) of the coir fibers are finely distributed, and the interfacial bonding between the fiber and matrix is good, which contributed to higher tensile strength and tensile modulus.

Table 3 Tensile testing results

S. No.	% Wt of fiber	UTS in MPa	UTS in MPa	UTS in MPa	Average UTS in MPa
A	3	24.22	26.32	27.22	25.92
B	5	26.8	27.9	27.87	27.92
C	7	31.2	33.4	32.9	32.50
D	9	29.22	30.22	29.92	29.78
E	11	32.94	28.22	28.62	29.92

Fig. 5 Hardness testing machine (shore D hardness tester) model SHR-D-Di-Y2K hardness testing results



Table 4 Hardness testing machine (shore *D* hardness tester)

S. No.	Sample	Shore 'D' hardness
1.	A	81, 83, 83
2.	B	79, 80, 80
3.	C	76, 76, 75
4.	D	80, 81, 78
5.	E	80, 80, 80

As the fiber content increases, stiffness of the composite increases leading to decrease in elongation.

Shore hardness tester (Fig. 5) is used to determine the hardness of the fiber-reinforced polymer composite (Table 4).

According to the result obtained from the testing and characterization, the prepared biocomposite of 30 wt% of coir fiber-reinforced composite is suitable for making value-added products. The coir fibers can achieve better properties as fillers in biocomposites. The use of 5% NaOH coir fiber treated for 48 h, having reduced hydrophilic character, achieves better internal bonding with the hydrophobic polypropylene matrix. By applying the above experimental methods and successful formulation, ecofriendly sustainable coir fiber-reinforced green composite was prepared for commercial application.

6 Conclusion

Natural resources are a gift of nature to humans. It is important to sustain and procure them for the future. The usage of such renewable resources should be done economically and wisely to reduce or replace the petroleum-based sources. We should be aware of more fruitful ways to explore the maximum potential and utilization of natural fibers for the development of science and technology. According to experimental studies, the outcome of the project was as follows:

- The coir fiber biocomposite was successfully developed for testing for mechanical properties.
- The developed material can reduce the carbon footprint as it could incorporate renewable natural coir fiber.
- Density increases with increase in coir fiber content.
- The research based on coir fiber green composite was successfully completed, and the prepared coir green composite reduces the dependency on the conventional based polymers.

Scope and Objectives

In the present day, composites have many more advantages. They are environmental friendly. They do not cause any pollution to the environment. They can be used to

manufacture modern day cars and other automobiles. The present day furniture is also made with composites.

As fiber is grown in the fields by farmers, there is a huge potential to give better rates to the farmers who cultivate them. It is like an industry in the present era.

Research still has to be done on other fibers which are naturally available such as cotton.

Current work, chemically treated coir fiber, is used to reinforce polypropylene matrix to form a biocomposite material and fabricate value-added products by injection molding. The chemical treatment of coir fiber leads to minimizing the hydrophilic characteristics and diminishing the water absorption property of the composite.

To find the variations on the effect of coir fiber content on physical, mechanical, thermal, and morphological properties of composite.

Acknowledgments The authors are thankful to the management of Sreenidhi Institute of Science and Technology for their encouragement to complete this work.

References

1. G. Konda Reddy, H. Madhusudhan Reddy, C. Rathod, Typical analysis of sisal fibre and rice husk matrix with ECMALON 4413 resin. In: *National Conference on Technological Advances in Mechanical Engineering*. JNTUCEK, Kakinada (22–23 July, 2016)
2. S. Biswas, Q. Ahsan, I. Verpoest, M. Hasan, Effect of span length on the tensile properties of natural fibers. *Adv. Mater. Res.* **264–265**, 445–450 (2011)
3. R.M. Rowell, Natural fibers: types and properties. In: K. Pickering (ed.), *Properties and Performance of Natural-Fiber Composites*. Wood head Publishing Limited, Cambridge (2008)
4. J.P. Schneider, G.E. Myers, C.M. Clemons, B.W. English, *Eng. Plast.* **8**(3), 207 (1995). *Reinforced Plastics* **41**(11), 22 (1997)
5. T. Schloesser, J. Knothe, *Kunstst-Plast Europe* **87**(9), O'donnell, M.A. Dweib, R.P. Wool, Natural fiber composites with plant oil-based resin, *Comp. Sci. Technol.* **64**, 1135–1145 (1997)
6. Ochi, Mechanical properties of kenaf fibers and kenaf/PLA composites. *Mech. Mater.* **40**, 446–452 (2008)
7. K.L. Pickering, G.W. Beckermann, S.N. Alam, N.J. Foreman, Optimizing industrial hemp fiber for composites. *Composites Part A vol* **38**, 461–468 (2007)
8. G. Satyanarayana, K. Sukumarana, A.G. Kulkarnia, S.G. K. Pillai, P.K. Rohatgia, Fabrication and properties of natural fiber reinforced polyester composites. *Composites* **17**, 329–333 (1986). *Composites for infrastructure: a guide for Civil Engineers*. Wheat Ridge, CO: Ray Pub. Inc. (1998)

Processing and Characterization of 6061 Aluminium Alloy with Nickel (Ni) and Zirconium (Zr)



S. Arun Kumar and R. Raman Goud

Abstract In an aluminium alloy, there are many inventions and researches that are introduced since 1954, when there are only 75 compositions are present, and by now, there are 530+ composites of aluminium. This explains how much we can explore aluminium with combinations of different alloys out of which 6061 aluminium alloy used for making automobile bodies. This experiment is to find the tribological behaviour of nickel (Ni), zirconium (Zr) particles reinforced with 6061 aluminium alloy. Composites are manufactured by a liquid metallurgical process known as stir casting. The alloy combinations constitute of 1. nickel (Ni)—0.5% and zirconium (Zr)—0.5%, 2. nickel (Ni)—0.5% and zirconium (Zr)—1% and 3. nickel (Ni)—0.5% and zirconium (Zr)—1.5% with 6061 aluminium alloy as a base metal. Above mentioned are three sample materials that are prepared by stir casting followed by annealing or heat treatment to improve the grain growth [1].

Keywords Metal matrix composite · Stir casting · Heat treatment · Tensile testing · Brinell hardness test

1 Introduction

In the current scenario, metal matrix composites are used in various engineering fields such as automobile, aerospace and structural applications etc., because of their high strength to weight ratio prevents oxidation and high stiffness. Aim of this experiment is to find the optimum weight percentage of the zirconium (Zr) added to the nickel (Ni) using 6061 aluminium alloy as base. Zirconium is a transition metal that has good resistance to corrosion and high melting temperature, which is used to improve the high-temperature tensile strength and hardness of the material. Nickel (Ni) is also a transition metal that is ductile in nature, hard and prevents oxidation, having the crystal structure as face-centred cubic structure. When nickel (Ni) and zirconium

S. Arun Kumar (✉) · R. Raman Goud
Department of Mechanical Engineering, Gokaraju Rangaraju Institute of Engineering and
Technology, Hyderabad, Telangana, India
e-mail: arun4688@gmail.com

Table 1 Chemical composition (wt%) of the 6061 aluminium alloy used in the study

Chemical component	Cr	Cu	Mg	Si	Al
Weight (%)	0.16	0.2	1.05	0.43	98.16

(Zr) combined together with 6061 aluminium alloy results in an increase in tensile strength at 1% of zirconium (Zr) and 0.5% of nickel (Ni) and decreases on further more increase in 1.5% of zirconium (Zr). In the experiment, it is known the role of zirconium (Zr) in the aluminium alloy and weight percentage of zirconium effects in the behaviour of the casted material [2, 3]. Addition of the nickel and zirconium increases the hot tensile strength and hardness [4].

1.1 Material

6061 Aluminium Alloy:

6061 aluminium alloy is a precipitate and hardened alloy containing magnesium and silicon as its major alloying elements. It is one of the most versatile of the heat-treatable alloys and popular for its range of strength application and requirements, it possesses good toughness and excellent prevent oxidation.

Typical applications of 6061 aluminium alloy are transportation components, aircraft and marine fittings, machine processing equipment, recreation products as shown in Table 1.

2 Experimental Method

2.1 Stir Casting

Stir casting is an economic process for the production of aluminium matrix compounds. The process consists of a small crucible placed in a furnace [5, 6, 7]. Before the addition of the material into the furnace, the raw materials have to be weighed and calculated according to the composition of 6061 aluminium alloy with the following compositions 1. nickel (Ni)—0.5% and zirconium (Zr)—0.5%, 2. nickel (Ni)—0.5% and zirconium (Zr)—1% and 3. nickel (Ni)—0.5% and zirconium (Zr)—1.5%. The optimum amount of raw 6061 aluminium alloy is heated up to the melting point of 800 °C [8, 9, 10]. When the furnace reached up to the melting temperature, the motor-powered stirrer rotates resulting in better mixture of alloy. The stirring process has to continue for 5 min. After mixing, the composite in a molten state is poured into a fixed die, followed by a cooling process. The resultant composite will be in a form of flat plate (Fig. 1).

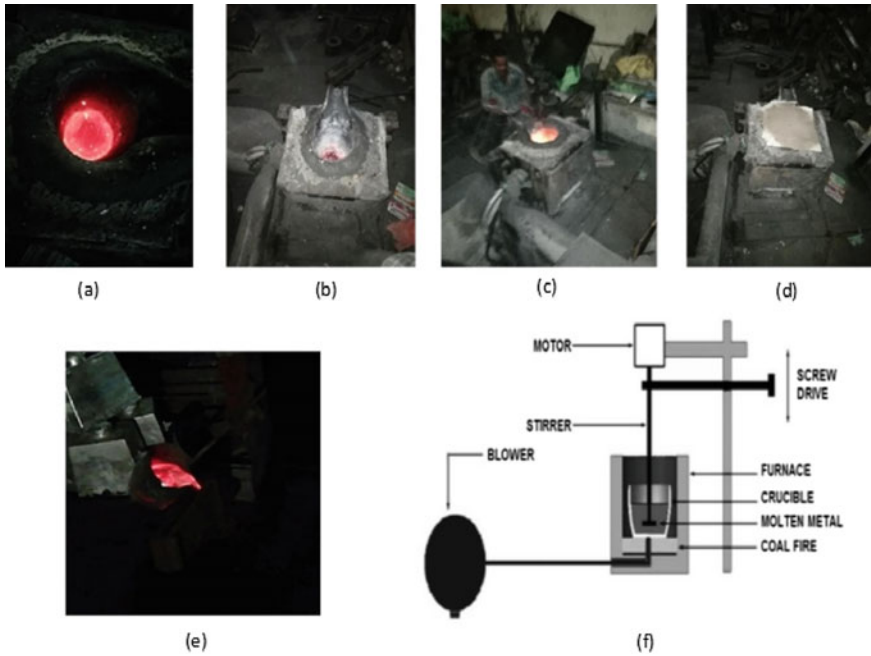


Fig. 1 a, b, c Melting of aluminium alloy, d adding nickel and zirconium, e pouring molten metal into fixed die, f Stir casting process

2.2 Annealing Process

Annealing or heat treatment is employed to improve the mechanical properties, grain size of the resultant composite. 475 °C is the optimum temperature for aluminium alloy for grain growth, better mechanical properties and zirconium dispersoids in resultant composite [11]. The casted specimens were subjected to 475 °C in furnace for 15 h and quenched, so that the nickel and zirconium fill the voids within the resultant composite and followed by heat treatment at 475 °C for 2 h again, so that the resultant composite improves mechanical properties.

3 Experimental Procedure

3.1 Tensile Testing

Tensile strength of a material is an important characteristic of a material it is useful to define elastic–plastic behaviour of a material by applying the tensile load on the material, specimens are made from the casted material 3 sample pieces from

each casted plates and machined to standard specimen of ASTM E8 tensile test samples are made in types of plates [12] and the sample pieces are tested to know the characteristics of the aluminium alloy by Universal Tensile Testing Machine (UTM) (Fig. 2).

The sample specimens are prepared for tensile test as per ASME E8 [13, 14] tensile test by milling operation as shown in Figs. 3 and 4.

The specimens are subjected to tensile load on UTM for obtaining the stress and strain diagram and yield strength of the composition prepared by stir casting and heat treatment process.

Fig. 2 Universal testing machine (UTM)



Fig. 3 Test sample before tensile test



Fig. 4 Test sample after tensile test



Fig. 5 Brinell hardness testing machine



3.2 Hardness Test

Hardness is an important property of the material, it defines the ability to resist the indentation or scratch over the surface of the material, it can be obtained from hardness testing methods such as Brinell hardness test, Vickers hardness test and Rockwell hardness test, to find the hardness of the material, a fixed force is applied to a given ball in case of Brinell hardness test and diamond in case of Vickers hardness test. When the indentation is small, then the material hardness is more, when the indentation is large, then the material hardness is less [15] (Fig. 5).

The hardness of aluminium alloy material 6061 aluminium alloy with nickel and zirconium alloy material is measured using Brinell hardness Testing (BHT) equipment. The load was applied for finding the hardness at 5 points and these will give the average hardness of the Al Ni and Zr compositions.

4 Results and Discussion

Stir Casting:

In stir casting, aluminium alloy is molten and stirred at 800 °C and then it is poured into the die to solidify, the pouring temperature is 780 °C, zirconium (Zr), nickel (Ni) are added to 6061 aluminium alloy at 800 °C and stirred for 20 min. The molten 6061 aluminium alloy, nickel 0.5% and zirconium 0.5, 1 and 1.5% alloy are poured in fixed dies to make a shape of material into plates. The material is made in the shape of plate and chemical test is made for the alloys containing aluminium nickel and zirconium composition. The following Table 2 shows the combination of different materials in the alloys prepared.

Tensile test:

Tensile test is conducted to characterize the elastic and plastic behaviours of prepared material by applying uniaxial tensile load. The test is performed on the test samples made as per the ASTM E8 standard. The tensile test provides the results of the following parameters: yield strength, tensile strength, elastic modulus, Poisson's ratio and elongation. 6061 aluminium alloy, nickel and zirconium fabricated using stir casting are cut into standard dimensions as per the ASTM E-8 standard by machining. The tensile test samples were mounted onto the universal testing machine and hold steadily using grippers. Force was applied using a hydraulic system to stretch the tensile component until it fails. The localized strain variations in the tensile samples were measured using extensometer in terms of load versus displacement curve. Engineering stress–strain relation was calculated for each specimen. The results are presented in Table 3.

Hardness:

The material hardness is measured using Brinell hardness tester BHN (BV 250 Spl) at a load of 250 kg applied for a duration of 10 s at five different locations on all

Table 2 Chemical composition (wt%) of the Al alloy made by stir casting in experiment

Sample No.	Cr	Cu	Mg	Si	Ni	Zr	Al
1.	0.16	0.27	1.05	0.36	0.51	0.52	97.13
2.	0.16	0.20	1.07	0.41	0.53	1.06	96.57
3.	0.16	0.22	1.02	0.39	0.54	1.57	96.1

Table 3 Characterization of the prepared aluminium alloy sample specimen

Sl. No.	Sample	Tensile strength in MPa	Yield stress in MPa	Hardness in HBW	Elongation (%)
1.	Al, Ni-0.5%, Zr-0.5%	126.455	99.43	64.9	3.12
2.	Al, Ni-0.5%, Zr-1%	218.86	174.41	85	3.14
3.	Al, Ni-0.5%, Zr-1.5%	77.443	58.146	55.7	2.26

samples. The hardness of the material is increased at 1% of Zr in aluminium alloy, and hardens is decreased when further more increase in Zr in alloy, which is seen at 1.5% Zr alloy.

$$BHN = \frac{2F}{\pi D \left[D - \sqrt{D^2 - d^2} \right]}$$

where,

- BHN Brinell hardness number
- F* Force applied on the work
- D* Diameter of ball
- d* Diameter of indentation.

Below figures represent the variation in the tensile strength and hardness for the samples for the experiment readings (Fig. 6).

The above figure shows the increasing trend of the tensile strength of the alloy as Ni and Zr at 0.5% and 1%, respectively, and further more increase in Zr leads to a drastic decrease in tensile strength (Figs. 7 and 8).

Fig. 6 Tensile strength variation with samples

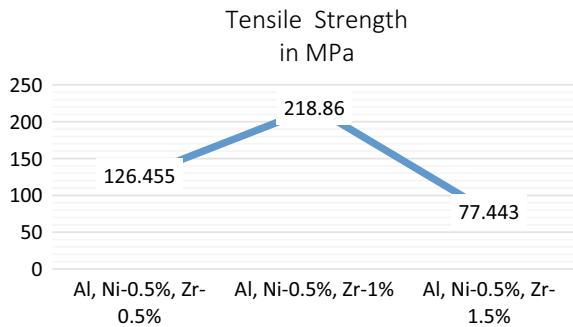


Fig. 7 Percentage of elongation of resultant components

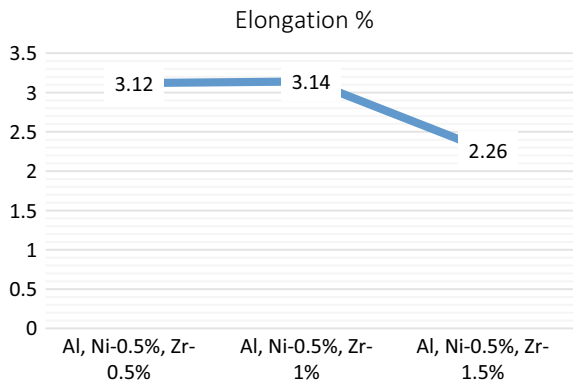
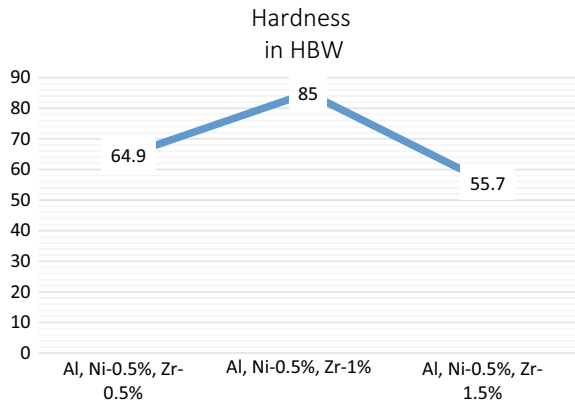


Fig. 8 Hardness of the resultant components



The above figure shows that the increasing trend of the hardness of the alloy as Ni and Zr at 0.5% and 1%, respectively, and further more increase in Zr leads to a drastic decrease in hardness.

5 Conclusion

The preparation and characterization of aluminium 6061 with nickel and zirconium were experimentally investigated. At the end of the work, the following conclusions are obtained:

1. Stir casting of the aluminium with nickel and zirconium alloy is prepared successfully at the temperature 800 °C.
2. Heat treatment or annealing process of the casting material for 15 h [11] improved the material mechanical properties and machining ability.
3. By increasing percentage of zirconium (Zr) in the 6061 aluminium and 0.5% nickel (Ni) alloy, there were changes observed in the material. The zirconium (Zr) per cent was added, 0.5, 1 and 1.5% were added to the material, the strength and hardness were improved at 0.5% zirconium (Zr) and 1% zirconium (Zr), and then further increase in zirconium to 1.5%, then tensile strength and hardness are showing decrease in trend.
4. Hardness is more at 1% of zirconium (Zr), 0.5% nickel (Ni) in 6061 aluminium alloy.
5. Tensile strength is maximum at 1% of zirconium (Zr), 0.5% nickel (Ni) in 6061 aluminium alloy.

References

1. G.-H. Majzoobi, J. Nemati, M.K. Pipelzadeh, S. Sulaiman, Characterization of mechanical properties of Aluminium alloy 6063 deformed ECAE
2. S.S. Owoeye, D.O. Folorunso, B. Oji, S.G. Borisade, Zinc-aluminum (ZA-27)-based metal matrix composites: a review article of synthesis, reinforcement, microstructural, mechanical, and corrosion characteristics
3. S.H. Zhou, F. Sommer, Calorimetric study of liquid and undercooled liquid $\text{Al} \pm \text{Ni} \pm \text{Zr}$ alloys
4. G.H. Garza-Elizondo, S.A. Alkahtani, A.M. Samuel, F.H. Samuel, Role of Ni and Zr in Preserving the strength of 354 aluminum alloy at high temperature
5. K. Ulhas, G.B. Annigeria, V. Kumar, Method of stir casting of aluminum metal matrix composites: a review
6. V. Mohanavel, K. Rajan, S.S. Kumar, A. Chockalingam, A. Royd, T. Adithiyaa, Mechanical and tribological characterization of the stir-cast Al-SiCp composites
7. V. Bharath, M. Nagara, V. Auradi, S.A. Koric, Preparation of a 6061 Al-Al₂O₃ MMC's by the stir casting and evaluation of mechanical and wear properties
8. K.N. Chethan, L.G. Keni, N.H. Padmaraj, D. Abhijit, R. Jain, Fabrication and mechanical characterization of aluminium alloy [6061] with conventionally prepared bamboocharcoal
9. N.V. Murthy, A. Prasad Reddy, N. Selvaraj, C.S.P. Rao, Dispersion of an alumina nano particles in Al 2219 alloy by ultrasonic assisted stir casting technique
10. C.Q. Chen, L.H. Huang, H.S. Liu, F. Zheng, Z.P. Jin, Isothermal sections of Al-Ni-Zr ternary system at 850 and 1050
11. W. Lefebvrea, F. Danoixa, H. Hallemb, B. Forbordc, A. Bostel, K. Marthinsend, Precipitation kinetic of Al₃(Sc, Zr) dispersoids in aluminium
12. P. Pandiyarajan, P. Marann, SMarimuthu, K.C. Ganesh, Mechanical and tribological behaviour of the metal matrix composite AA6061/ZrO₂/C
13. X.J. Wang, N.Z. Wang, L.Y. Wang, X.S. Hua, K. Wua, Y.Q. Wang, Y.D. Huang, Processing, microstructure and mechanical properties of micro-SiC particles reinforced magnesium matrix composites fabricated by stir casting assisted by ultrasonic treatment processing
14. A. Tony Thomas, R. Parameshwaran, A. Muthukrishnan, M. Aravind Kumaran, Development of feeding and stirring mechanisms for stir casting of aluminium matrix composites
15. N.M. Kumar, L.A. Kumaraswamidhas, Characterization and tribological analysis on Aluminium alloy 6061 reinforced with the AlN and ZrB₂ in situ composites

Static Structural Analysis of Hybrid Honeycomb Structures Using FEA



A. Chandrashekhar, Himam Saheb Shaik, S. Ranjan Mishra,
Tushar Srivastava, and M. L. Pavan Kishore

Abstract The following paper describes the behavior of hybrid honeycomb structures over solid-profiled structures. Sandwich panels being a major application of honeycomb structures exhibit very high stiffness-to-weight ratio, low mass–volume ratio, and high energy absorption capacity. The various hybrid hollow structures with finite boundaries (finite width and height), subjected to a uniaxial compressive load, are observed using the finite element method. The stress and deformation characteristics of these structures are calculated using ANSYS® 18.1. Subjected to cantilever conditions, the structures are processed in static structural simulations to obtain the corresponding data. In this paper, a comparison of various hybrid structures is conducted based on the obtained data to conclude their adaptability.

Keywords Hybrid honeycomb · Sandwich panels · Finite element method · Static-structural

1 Introduction

Material being a key factor for designing a product, the structure of the product plays a substantial role to determine the amount of material to be used. Structures used in the present-day scenario overcompensate for the load-bearing requisites of the products in question. Therefore, to obtain substantial results, many unconventional structures are adopted to optimize material consumption. Numerous applications of such utilize hollowed structures over solid-profiled structures in the purview of the required parameters. The selection of these hollowed structures is based on multiple factors such as stress distribution, deformation, manufacturability, etc. Over the years, honeycomb structures are opted due to their very high stiffness-to-weight ratio, low mass–volume ratio, and high energy absorption capacity.

A. Chandrashekhar · H. S. Shaik (✉) · S. Ranjan Mishra · T. Srivastava · M. L. Pavan Kishore
Department of Mechanical Engineering, Faculty of Science and Technology, ICFAI Foundation
for Higher Education, Hyderabad, India
e-mail: himam.mech@gmail.com

The aforementioned properties exhibited by the honeycomb structures are proven to be most desirable among most of the structures. The evolution of these structures has resulted in various hybrids that compensate for the requirements of the product sustaining more material during the production of such structures. The selection of these structures varies greatly with applications.

Along the years, many researchers have conducted various experiments to determine the usability of these hollowed structures in numerous applications. These structures are used as cores in sandwich panels extensively, which are thereby used in the aerospace, packaging industry, etc.

Mohammed et al. [1] described honeycomb sandwich structure under three conditions, namely, tension, compression, and bending, and studied its fracturing criteria in each of the given tests. The tests followed standard methods, the result of which was presented as post-test images. The paper physically describes the fractures formed due to the loading conditions.

Paik et al. [2] performed three types of experiments, namely, three-point bending tests, buckling/collapse tests under (in plane) axial compression and crushing tests under lateral pressure on an aluminum honeycomb sandwich panel specimen. The study also numerically described the behavior of the structure during these tests.

Tantikom et al. [3] investigated the intrinsic compressive stress–strain response of regularly cell structured materials. This intrinsic stress–strain response was characterized by the equivalent elastic stiffness and the collapsing deformation behavior.

Chen et al. [4] elaborated on the crushing behavior of honeycomb structures with finite width and height by considering the work-hardening of the constituent material [5]. Based on numerical results from FE analysis, it was found that stress–strain response for a finite honeycomb under uniaxial compression could be classified as Type I or Type II based on the deformation behavior. Type I was generated in the case of large relative thickness t/l or a large work-hardening coefficient, while Type II was observed for small relative thickness or a small work-hardening coefficient.

Farhadi et al. [6] studied the dynamic mechanical response of sandwich panels with square honeycomb core, which is carried out using ABAQUS software, made of an alloy of stainless steel austenitic. From the series of results obtained in this study [7], the advantage of using a sandwich structure with a cellular metal core had been demonstrated as a suitable candidate for deflection-limited designs capable of withstanding air blast loads.

Ashab et al. [8] studied the impact behavior of sandwich panels made of aluminum face sheets and aluminum corrugated core with different geometries, which is investigated using drop hammer apparatus. Pavan et al. [9] it was concluded from the absorbed energy that increasing panel height will cause an increase in absorbed energy.

Wang et al. [10, 11] studied five reinforced honeycomb structure that contributes to great improvement not only in the load-carrying capacity but also in energy absorption ability.

This paper focuses on simulating a few of the said reinforced honeycomb structures to better analyze their characteristics and usability. The finite element method

is adopted for the study of these models. The FEA software used in this paper is ANSYS® 18.1. The models used in this paper were self-developed with the aid of renowned CAD software like CATIA® V5R20 and SolidWorks® 2016. The results were further graphically compared to distinguish the uniqueness of each structure.

2 Hybrid Honeycomb Structures

A **honeycomb** is a cluster of hexagonal wax cells developed by honey bees in their nests to accommodate their honey, pollen, and brood. These wax structures are found to be light in weight and tenacious under the most drastic natural conditions. The manmade resemblance of these structures is known as **honeycomb structures**.

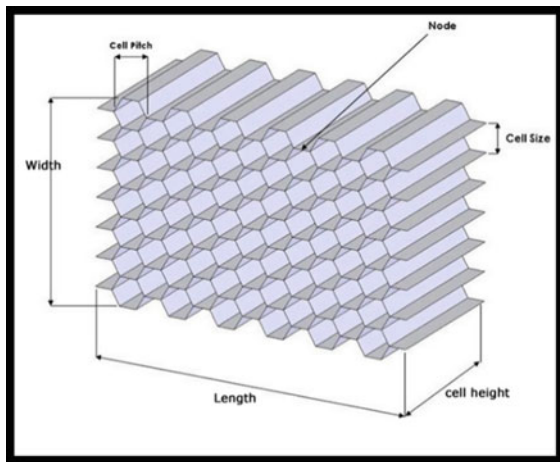
There are various parameters of a honeycomb structure, such as:

- Panel width
- Panel length
- Cell height
- Cell size
- Wall thickness
- Cell pitch.

A single unit of the honeycomb structure is called a **node**. The distance between two parallel faces of the node is called **cell size**. The distance between two vertices of a node is known as **cell pitch**. These parameters are illustrated in Fig. 1.

A honeycomb structure when reinforced with internal structures is termed as **hybrid honeycomb structures**. Various hybrid structures have been developed over the decade to further improve the adoption of these structures. In this paper, the

Fig. 1 Conventional honeycomb structure



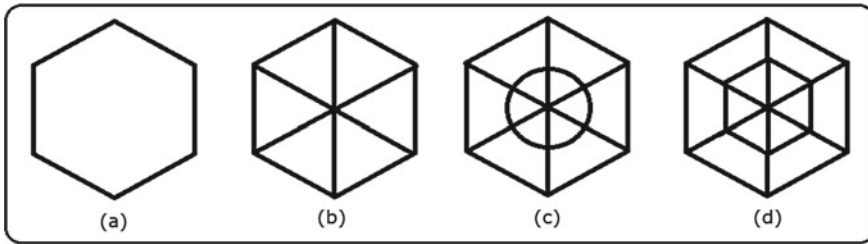


Fig. 2 Hybrid honeycomb profiles

analysis of conventional honeycomb structures in contrast to that of hybrid structures is carried out to determine the usability of such structures under desired preconditions.

The following are the profiles discussed in the current work (Fig. 2):

- (a) Honeycomb structure (Hex 1)
- (b) Cross-ribbed honeycomb structure (Hex 2)
- (c) Round-supported honeycomb structure (Hex 3)
- (d) Hexagonal supported honeycomb structure (Hex 4).

3 Methodology

3.1 Modeling

The geometry of the profile plays a major role in analyzing the structure's behavior toward the applied conditions. The dimensions of the profile are identical to the other, to ensure a uniform reference for the comparison of various structures in terms of their generated stress and deformation during simulation. The dimensions of each profile are as shown in Fig. 3 and the developed models are illustrated in Fig. 4.

The surface areas of each hybrid structure are analyzed using CAD-oriented tools present in SolidWorks®. These surface areas are compared graphically (Graph 1) pertaining to Table 1 as shown in Fig. 5.

3.2 Finite Element Analysis

The finite element method, being the most efficient method to simulate the behavior of structures to predetermined conditions, is adapted to study the characteristics of the said models. The method involves dividing a body into several uniform elements to observe the effects of the set boundary conditions on each element and aggregating the effect to justify the behavior of the said object as a whole. The accuracy of this method has been widely renowned and thus adopted throughout the world.

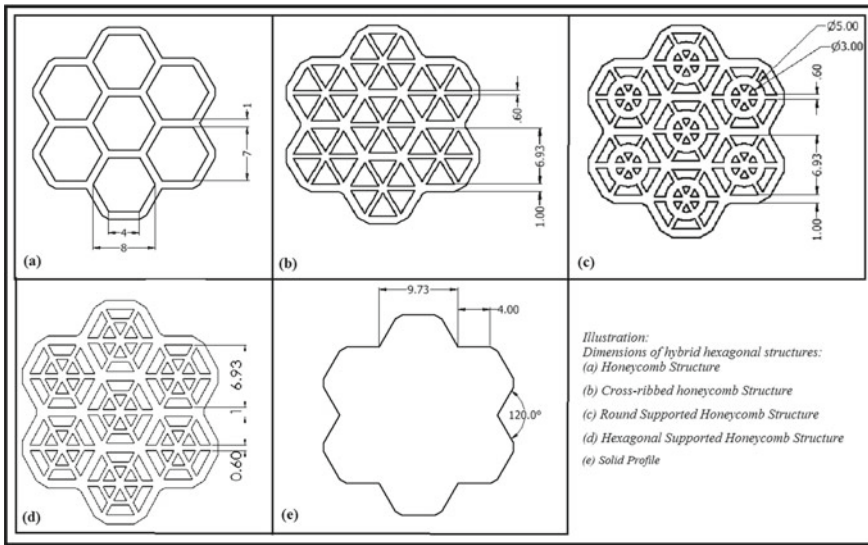


Fig. 3 Dimensions of hybrid honeycomb structures

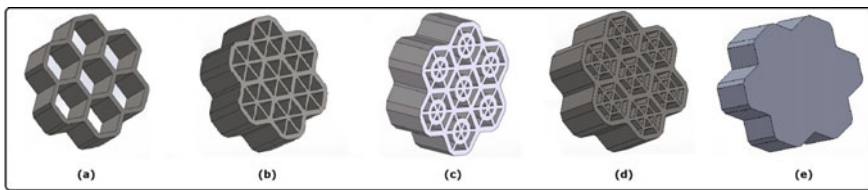
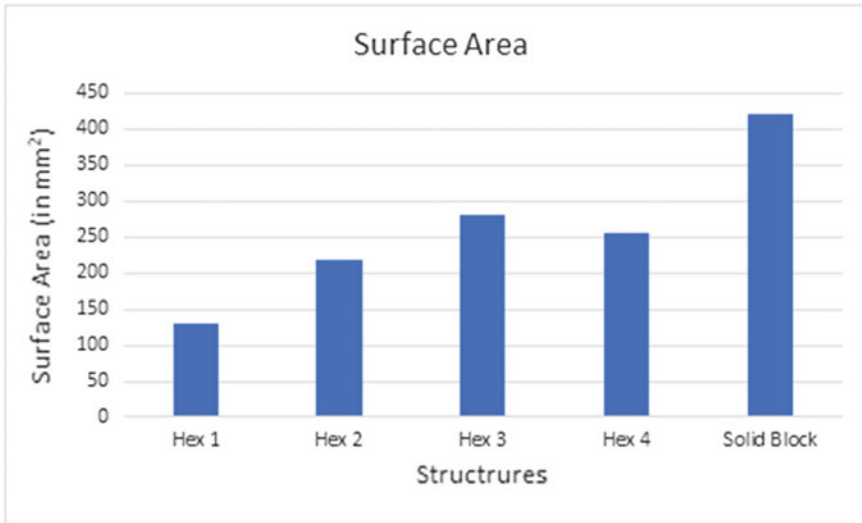


Fig. 4 Profiles of hybrid honeycomb structures

Table 1 Surface area comparison of hybrid honeycomb structures

Structure	Surface area (mm ²)
Hex 1	130.36
Hex 2	218.99
Hex 3	281
Hex 4	256.77
Solid block	421.35

The software environment used to study the said structures in this paper is ANSYS® 18.1, with the aid of that the structures are subjected to various boundary conditions under the static structural analysis. The material properties are imparted in the software environment, thereby making it more convenient to arrive at closer numerical results when considering the said material. Geometry of each structure is imported, meshed (divided into distinct uniform elements), and boundary conditions



Graph 1: Comparison of surface areas of hybrid honeycomb structures.

Fig. 5 Surface area of hybrid honeycomb structures

are applied. The desired results pertaining to appropriate boundary conditions are then obtained using the solver.

3.3 Preprocessing

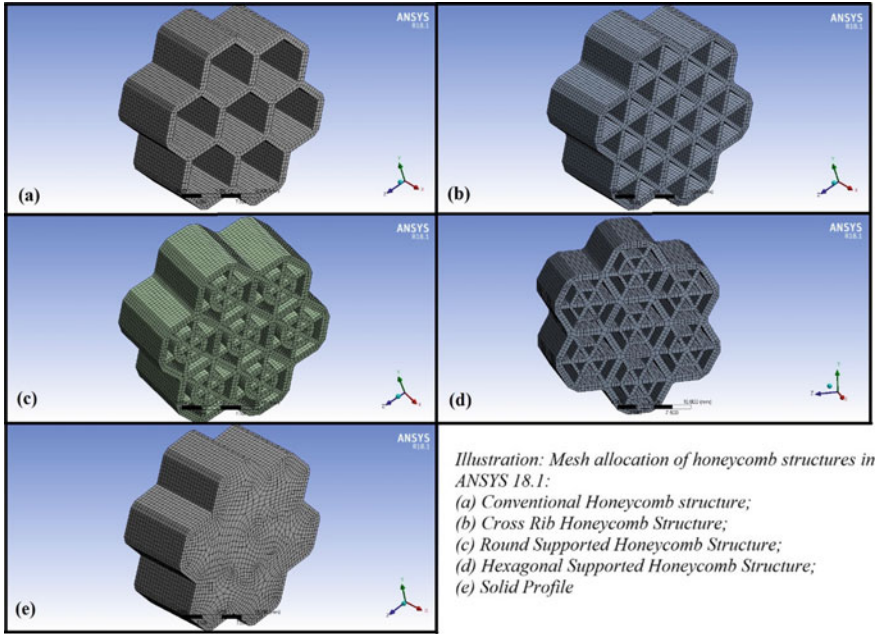
In this paper, each model is exported in the Step format (.stp), from SolidWorks® then imported into ANSYS® Workbench under static structural analysis. Structural steel is then imported using the material database into the analysis environment (Table 2). The model is then subjected to a fine mesh that is auto generated by the software.

Table 2 Adapted material properties

Material name	Structural steel
Density	7.85e-009 tonne/mm ³
Specific heat	4.34e + 008 mj/tonne/C
Young's modulus	2.00E + 05 MPa
Poisson's ratio	0.3
Bulk modulus	1.67E + 05 MPa
Shear modulus	76,923 MPa

Table 3 Mesh specifications of hybrid honeycomb structures

Structure	Solid	Hex 1	Hex 2	Hex 3	Hex 4
Number of nodes	123,421	59,202	110,755	140,251	135,272
Number of elements	28,520	10,560	19,160	26,040	23,660



*Illustration: Mesh allocation of honeycomb structures in ANSYS 18.1:
 (a) Conventional Honeycomb structure;
 (b) Cross Rib Honeycomb Structure;
 (c) Round Supported Honeycomb Structure;
 (d) Hexagonal Supported Honeycomb Structure;
 (e) Solid Profile*

Fig. 6 Meshed hybrid honeycomb structures in ANSYS® 18.1

The elements in the mesh largely consist of quad elements, the number of elements and nodes vary with each structure are listed in Table 3. The generated mesh is illustrated in Fig. 6.

3.4 Boundary Conditions

The model is subjected to cantilever conditions, i.e., one face of the linear structure is fixed and a uniform pressure is applied to the opposite face. A pressure of 10 MPa is applied to the present model to study the deformation and stress generated. The bounded dimensions of each structure are listed in Table 4.

Table 4 Bounded dimensions of each model

Bounding box	
Length X	10.000 mm
Length Y	24.784 mm
Length Z	23.463 mm

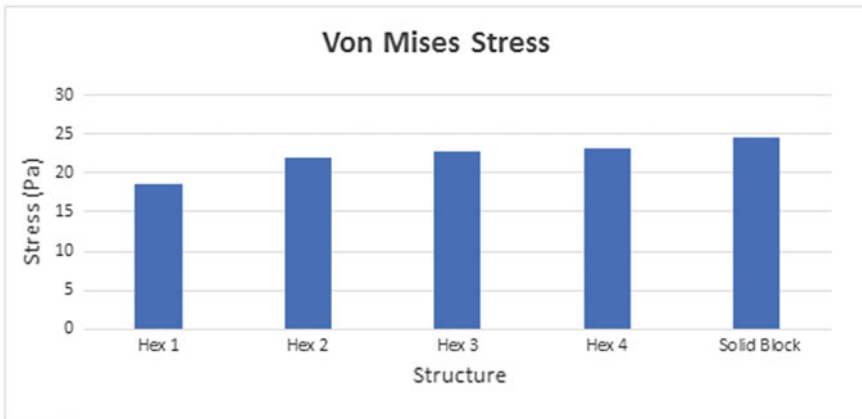
4 Results and Discussion

4.1 Von Mises Stress

The models when subjected to the aforementioned boundary conditions exhibit stress under uniaxial compressive load. The results thus obtained are compared graphically (Graph 2) pertaining to data tabulated in Table 5 as illustrated in Fig. 7. The stress distribution of the models is illustrated in Fig. 8.

Table 5 Von Mises stress generated in hybrid honeycomb structures

Structure	Von Mises stress (Pa)
Hex 1	18.641
Hex 2	22.002
Hex 3	22.886
Hex 4	23.222
Solid block	24.627



Graph 2: Von-Mises Stress comparison of hybrid honeycomb structures

Fig. 7 Von Mises analysis Result

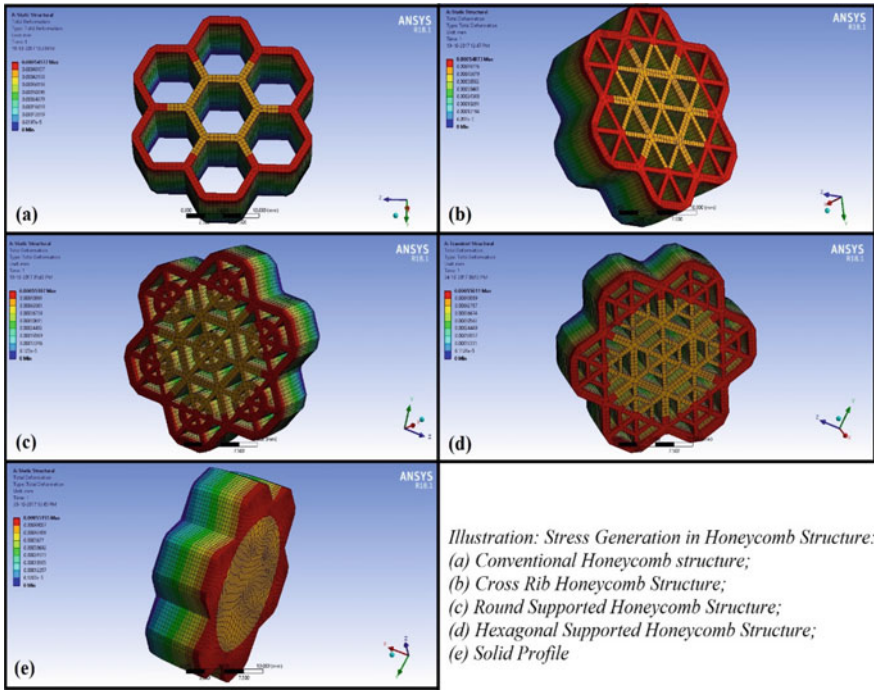


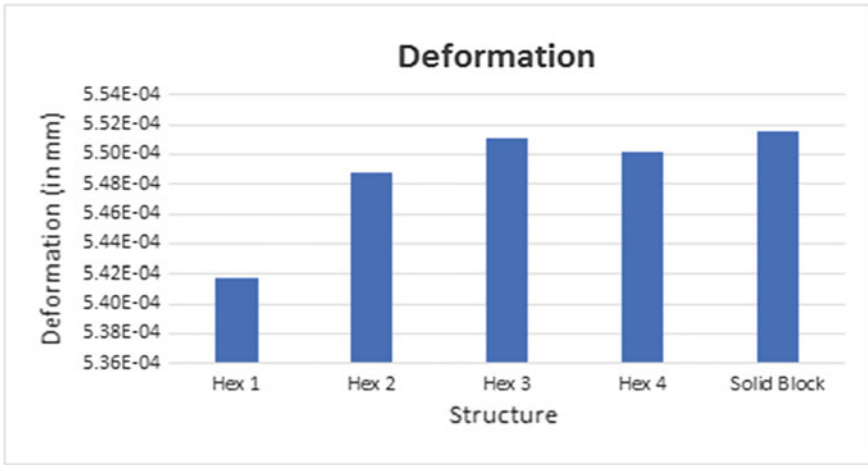
Fig. 8 Von Mises stress generated in hybrid honeycomb structures

4.2 Deformation

The deformation experienced by each model under the aforementioned conditions is described graphically (Graph 3) in accordance to the data mentioned in Table 6 (Shown in Fig. 9). The generated deformation is illustrated in Fig. 10.

Table 6 Deformation of hybrid honeycomb structures

Structure	Deformation
Hex 1	5.42E-04
Hex 2	5.49E-04
Hex 3	5.51E-04
Hex 4	5.50E-04
Solid block	5.52E-04



Graph 3: Deformation comparison of hybrid honeycomb structures

Fig. 9 Deformation analysis Result

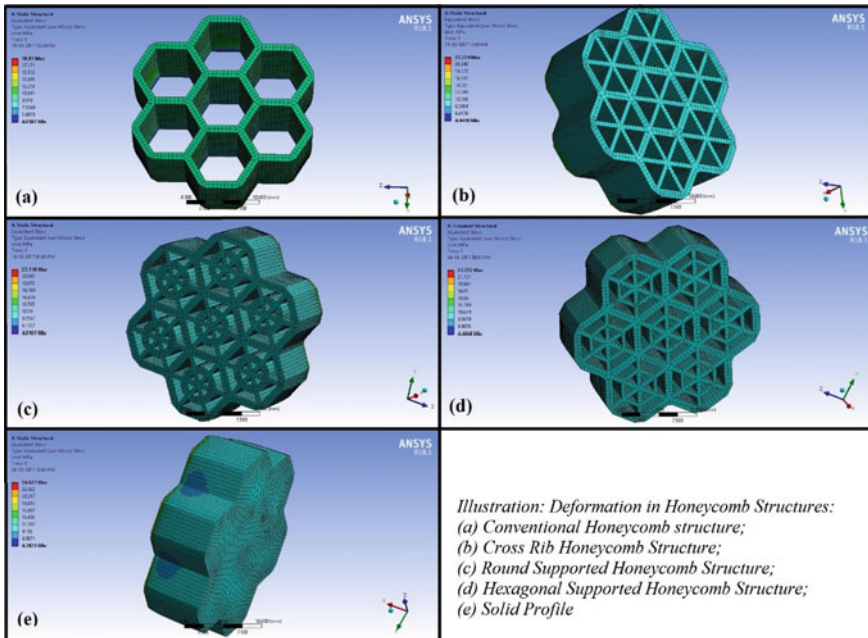
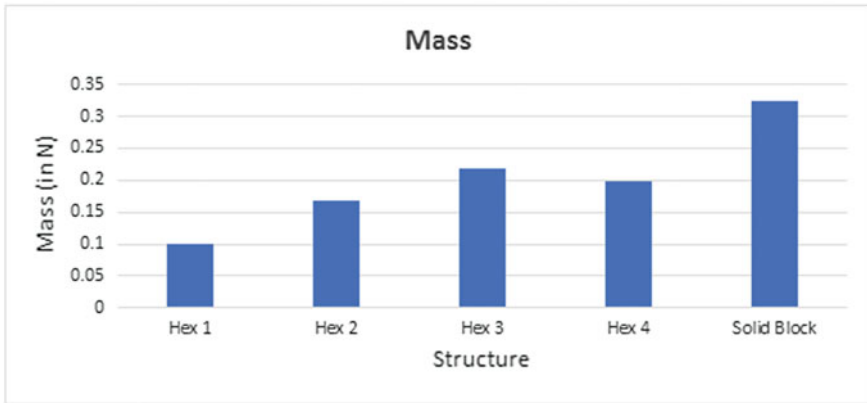


Fig. 10 Deformation of hybrid honeycomb structures

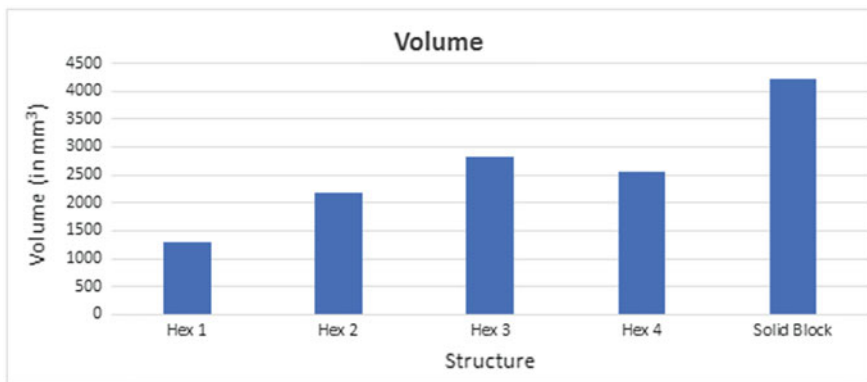
4.3 Mass and Volume

In order to compare the weight and volume of these structures, the data obtained from ANSYS® 18.1 simulation reports are compared graphically. The comparison of mass and volume of hybrid honeycomb structures is shown in Figs. 11 and 12, respectively. Since the dimensions of each model are identical, the masses and volumes are comparable in the purview of the structure’s application. The mass and volume of hybrid honeycomb structures are as shown in Tables 7 and 8.



Graph 4: Mass comparison of hybrid honeycomb structures

Fig. 11 Mass of hybrid honeycomb structures



Graph 5: Volume comparison of Hybrid honeycomb structures

Fig. 12 Volume of hybrid honeycomb structures

Table 7 Mass of hybrid honeycomb structures

Structure	Mass (N)
Hex 1	0.10036
Hex 2	0.16859
Hex 3	0.21708
Hex 4	0.19767
Solid block	0.32436

Table 8 Volume of hybrid honeycomb structures

Structure	Volume (mm ³)
Hex 1	1303.6
Hex 2	2189.9
Hex 3	2189.9
Hex 4	2567.7
Solid block	4213.5

5 Conclusion

With identical dimensions and boundary conditions, the comparison of various honeycomb structures suggests that, with a negligible difference in deformation, the stress generated in each honeycomb structure is drastically less as compared with a solid profiled structure. It is also observed that with the change in shape, the mechanical behavior of structures with similar dimension varies. The mass of these structures was also found to be around 40% less as compared with that of solid profile, thereby making it more conservative to adapt. With the hollow profile of these structures, they are bound to save a lot of material upon usage.

References

1. R. Mohammed et al., Damage behaviors of glass fabric honeycomb sandwich composite materials under static loading. *Int. J. Mech. Prod. Eng.* ISSN: 2320-2092
2. J.K. Paik et al., The strength characteristics of aluminium honeycomb sandwich panels. *Thin-Walled Struct.* **35**(3), 205–231 (1999)
3. K. Tantikom et al., In-plane compression response of regularly cell-structured materials. *Mater. Trans.* **45**(2), 509–515 (2004)
4. D.-H. Chen et al., in *Deformation of Honeycomb with Finite Boundary Subjected to Uniaxial Compression*. ISSN 2075-4701
5. Q. Chen et al., In-plane elastic buckling of hierarchical honeycomb structures. *Eur. J. Mech. A/Solid*
6. K. Farhadi et al., Numerical simulation of metallic honeycomb sandwich panel structures under dynamic loads
7. S. Heimbs et al., Honeycomb sandwich material modeling for dynamic simulation for aircraft interior, in *9th International LS—Dyna User Conference*

8. A.S.M. Ayman Ashab et al., Finite element analysis of aluminum honeycombs subjected to dynamic indentation and compression loads
9. P.K. Mamaduri, H.S. Shaik, A. Chandrashekhar, Comparative study for material effect on stress behavioural characteristics of rectangular plate. *Vibroengineering PROCEDIA* (2019). <https://doi.org/10.21595/vp.2019.21100>
10. Z. Wang et al., Comparison between five typical reinforced honeycomb structures. in *5th International Conference on Advanced Engineering Materials and Technology* (AEMT 2015)
11. S.P.S. Arora et al., Study the effect of core design on mechanical behaviour of honeycomb sandwich structures under three point bending. *Int. J. Innovative Res. Sci. Eng. Technol.* **5**(6) (2016) (An ISO 3297: 2007 Certified Organization)

Design and Random Vibrational Analysis of Horizontal Impact Hammer Crusher



S. Naveen, P. Praveen Kumar Reddy, and S. L. N. Reddy

Abstract During the crushing of a stone, sharpness of the blade decreases due to which deformations are observed on the blade, which reduce the efficiency of the blade. Hence it becomes necessary to check the blade structure for its crushing ability so that safety is achieved while crushing the stone. The FE model was developed to observe the stresses and deflections which are caused while crushing. Various iterations are performed and graphs are plotted and analyzed to see the deflections caused on the blade. This paper is presented to evaluate the frequencies and deflections caused on the blade and also to evaluate the stress caused on the rock, which gives better efficiency while crushing the rock. The model was created using CAD software, and Modal analysis was performed by using ANSYS Workbench 19.2.

Keywords Crush of stone · FE model · Frequencies · Deflections

1 Introduction

In industries, crushers [1] and machines which use tools to break or compress materials into small fractional chunks or denser masses are known as crushers. At the same time, mines and foundries are very small enterprises except for the few mines. Over the past few decades, foundries developed iron casting technologies and began to supplant other metals in many applications like cement industries and brick industries. This horizontal hammer crusher is more costly when compared to that of

S. Naveen (✉) · P. Praveen Kumar Reddy · S. L. N. Reddy
Department of Mechanical Engineering, Siddhartha Institute of Engineering and Technology,
Ibrahimpattam, India
e-mail: shanbaugn@gmail.com

P. Praveen Kumar Reddy
e-mail: praveen92reddy@gmail.com

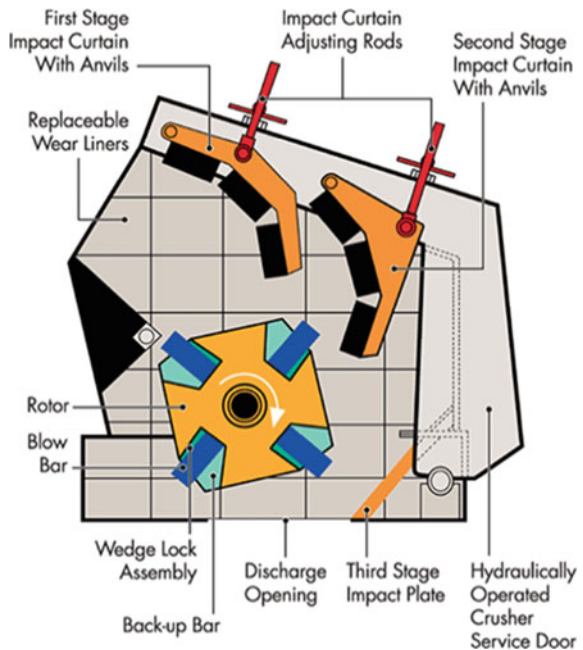
S. L. N. Reddy
e-mail: lnreddy_singa@yahoo.com

the vertical [2] hammer crushers. Hence the demand increased due to its crushing technology.

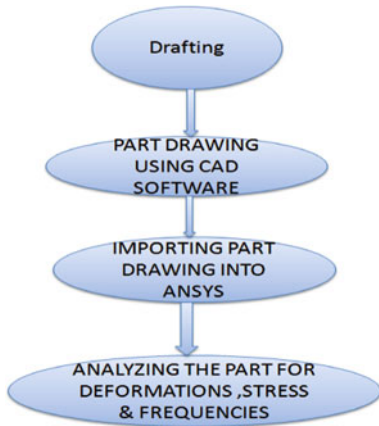
2 Literature Review

The crusher is a component [3] that is designed to reduce the large solid chunks of raw material into smaller rocks, gravel, or rock dust. Crushers may be used to reduce the size, or change the form, of waste materials so they can be more conveniently disposed of such that the pieces of different compositions can be differentiated. Crushing is the process of transferring a force amplified by mechanical advantage through a material made of molecules that bond together more strongly [4], and to resist deformation more than those in the material being crushed can do. Crushing devices [5] can hold material between two parallel or tangent solid surfaces, and apply sufficient force to bound the surfaces together to generate enough energy within the material used for crushing such that its molecules separate from fracturing. The earliest crushers were used by using hand stones, where the weight of the stone provided a boost to muscle power, used against a stone anvil (Fig. 1).

Fig. 1 Shows horizontal shaft impact crusher



3 Methodology

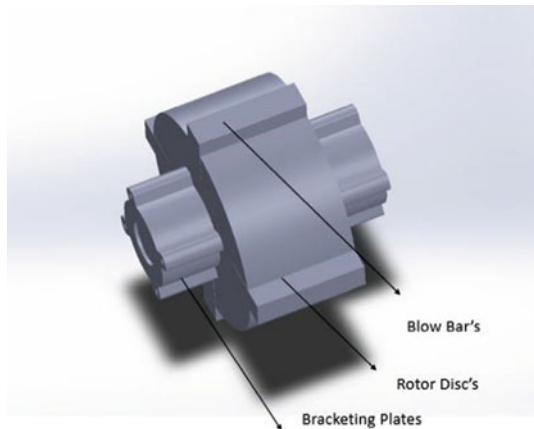


4 Results and Discussion

4.1 Design of Hammer Crusher Using CAD Software

- Step 1. Selecting the proper CAD software for designing the impact hammer crusher (Fig. 2);
- Step 2. Collecting the necessary information for designing the impact hammer crusher;
- Step 3. Designing the individual part by taking proper dimensions;
- Step 4. Assembling the individual parts by taking proper assembly constraints.

Fig. 2 Design of a hammer crusher using CAD software



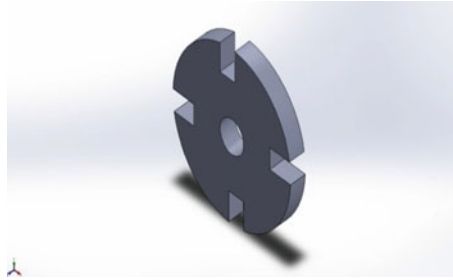


Fig. 3 Designing of a rotor disk

4.2 Designing of Rotor Disk

- Step 1. Open SOLIDWORKS software and select new option from the menu tab (Fig. 3).
- Step 2. Select the front plane from the tree diagram and sketch on that front plane.
- Step 3. Draw the outer circle of diameter 1500 mm, extrude the circle to create a 3D model.
- Step 4. Draw the inner circle of diameter of 30 mm on the extruded 3D sketch, by using Extrude cut create hole.
- Step 5. Create a groove for inserting blow bars with the help of 194 mm × 194 mm × 400 mm dimension; using pattern option, create the remaining four grooves (i.e. $n = 4$).

4.3 Designing of Blow Bars

- Step 1. Select the front plane and draw the rectangle of 194 mm × 194 mm × 400 mm.
- Step 2. Extrude the sketch of thickness 1500 mm to create the 3D model (Fig. 4).

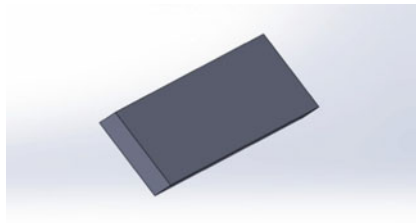


Fig. 4 Designing of blow bars

Fig. 5 Designing of rotor shaft

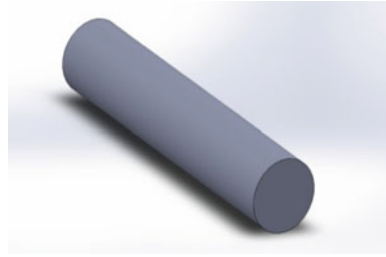


Fig. 6 Designing of bracketing plates



4.4 Designing of Rotor Shaft

- Step 1. Select the front plane and draw the circle of diameter 30 mm.
- Step 2. Extrude the sketch of thickness 1500 mm to create the 3D model (Fig. 5).

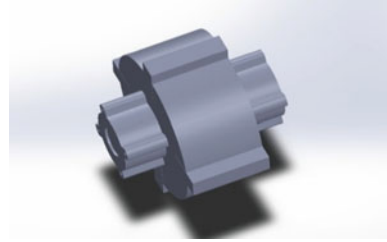
4.5 Designing of Bracketing Plates

- Step 1. Select the front plane and draw the circle of diameter 250 mm.
- Step 2. Extrude the sketch of thickness 250 mm to create the 3D model.
- Step 3. Create a hole of diameter 30 mm.
- Step 4. Create a hole 4 mm above the outer edge of the part (i.e. $n = 4$) (Fig. 6).

4.6 Assembly of Hammer Crusher

- Step 1. Open a new window, select the assembly option.
- Step 2. Insert all necessary components and assemble the hammer crusher by using assembly constraints.
- Step 3. Save the model and convert it into the IGES format (Fig. 7).

Fig. 7 Assembly of hammer crusher



5 Computer Aided Engineering

5.1 Modal Analysis

Modal analysis is the study of the dynamic properties of structures under vibrational excitation. Modal analysis, or the mode superposition method, is a linear dynamic-response procedure which evaluates and superimposes free-vibration mode shapes to characterize displacement patterns (Table 1).

5.2 Steps for Performing Modal Analysis

- Step 1. Open ANSYS Workbench.
- Step 2. Import parts using the IGES format using design modular.
- Step 3. Drag and drop modal analysis from the workbench tree.
- Step 4. Edit material properties by engineering data (Fig. 8).
- Step 5. Create the FEM modal by using the mesh option.
 - Number of total nodes = 20,543
 - Number of contact elements = 4676
 - Number of spring elements = 0
 - Number of bearing elements = 0
 - Number of solid elements = 3405
 - Number of total elements = 8081.
- Step 6. Assign material properties to the given modal.

Table 1 Material properties for analysis of hammer crusher

Material properties	E (Mpa)	V	Density (g/cm ³)
Manganese steel	187,000	0.29	7.7
Metric steel	210,000	0.27	6.5
Chrome steel	205,000	0.3	7.8

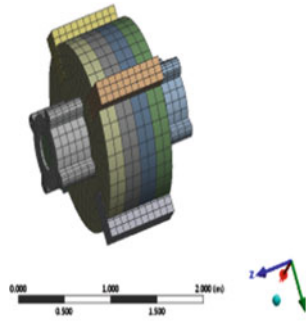


Fig. 8 Creating FEM modal using ANSYS workbench

Table 2 Stress and frequency values

S. No.	Material properties	Stress (Pa)	Frequency (Hz)	Deformation (M ²)
1.	Manganese steel	9.869e11	539.92	5.03475E-05
2.	Chrome steel	1.0967e12	618.39	5.97E-05
3.	Metric steel	1.2953e12	563.73	4.97E-05

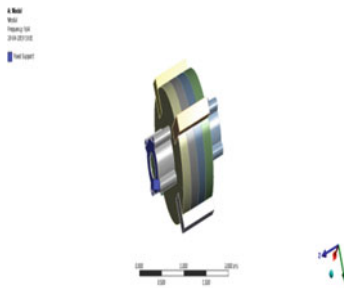


Fig. 9 Boundary conditions

Step 7. Give the boundary conditions for the given modal (Table 2; Figs. 9, 10, 11 and Graph 1).

6 Conclusion

In the comparison of the three types of materials for the design of an impact crusher for which the analysis is carried out, the stress and deformations are observed in the end of the bracketing plates. So this justifies the usage of bracketing plates. This is to ensure the prevention of failures due to vibrations caused on blow bars. All research works are done on the impact horizontal crusher through modeling

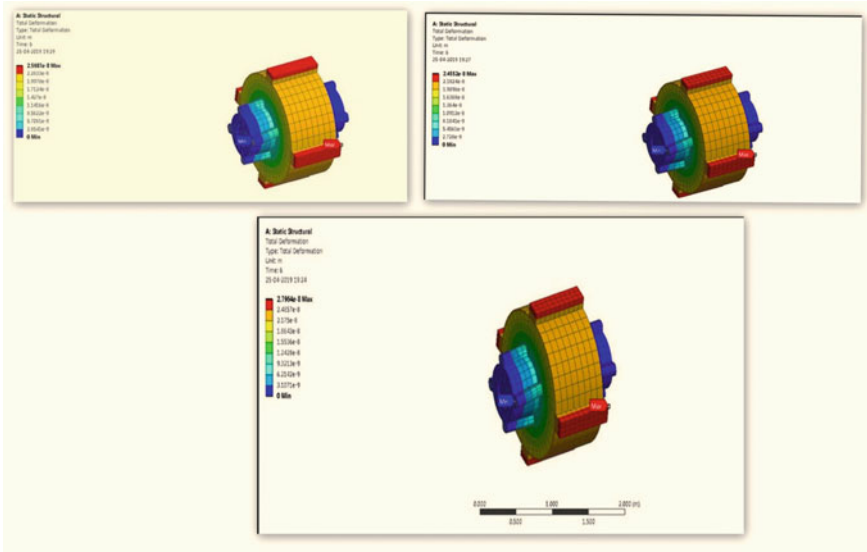


Fig. 10 Deformations of manganese steel, metric steel, and chrome steel

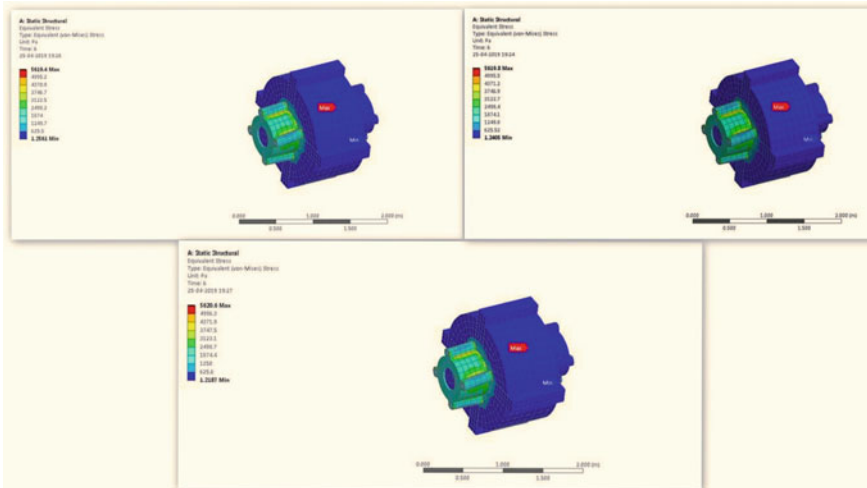
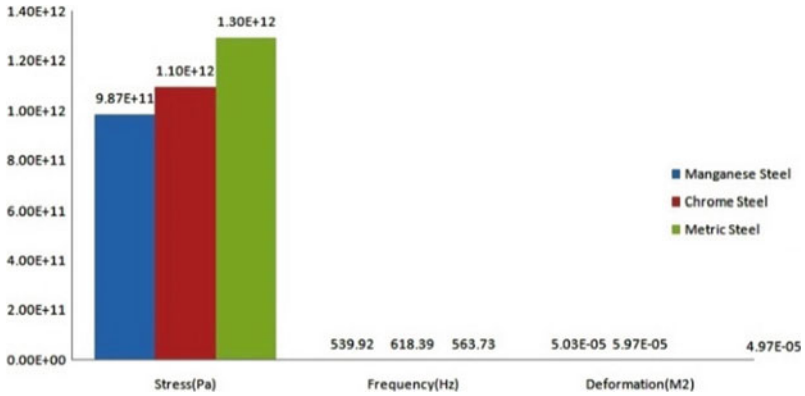


Fig. 11 Random vibrations of manganese steel, metric steel, and chrome steel

in SOLIDWORKS, and Random Vibrational analysis was performed using ANSYS 19.2 which showed the results for single design and various materials. But the present work is concentrated on the materials which withstand impact load of the rock. It is seen that Metric steel is much better when compared to Manganese steel and Chrome steel.



Graph 1 Shows the stress, frequencies, and deformation values of different material properties

References

1. S. Nikolov, Modeling and simulation of particle breakage in impact crusher. Int. J. Miner. Process 10 December 2004
2. N. Djordjevic, F.N. Shi, R.D. Morrison, Applying discrete element modeling to vertical and horizontal crushers and horizontal shaft impact crushers. Miner. Eng. **16**, 983–991 (2003)
3. R.S. Khurmi, J.K. Gupta, in *Text book of Machine Design*, pp. 788–790 (2005)
4. <http://en.wikipedia.org/wiki/Crusher>
5. <http://www.infominerals.com/impact-crusher.html>

Fault Diagnosis of Unbalanced Multirotor System



V. Hariharan, G. Rajeshkumar, and K. A. Ibrahim Sheriff

Abstract Rotating machines with center-hung dynamic balancing rotors are widely used in several industries. During operation, the rotor may gain or lose material due to the wear and deposition of foreign materials in the rotors. As a result of this, the rotor becomes unbalanced. Unbalanced rotor usually causes excessive machine vibration that generates large forces on the bearing. It also results in enormous power loss and leads to potential damage to the system. So, the vibrations caused by the rotor have to be continuously monitored to prevent the potential damage to the rotating machinery. In this project, experimental studies are performed on a dynamic rotor test apparatus to obtain the vibration response of the rolling element bearings in the rotating system under several masses with different running speed conditions. The shaft is attached with four rotors, each having different mass and rotating in different planes. The rotor shaft vibration responses on the bearings are obtained using piezoelectric accelerometer. Dual-channel vibration analyzer (ADASH) is used to analyze the obtained vibration data. The identification of system characteristics is to be carried out. The results thus obtained can be used for condition monitoring of the unbalanced rotor system.

Keywords Unbalanced rotor · Rotating machinery · Rolling element bearings

V. Hariharan (✉) · K. A. Ibrahim Sheriff
Department of Mechanical Engineering, Kongu Engineering College, Perundurai, Erode,
Tamil Nadu, India
e-mail: hariharanvag@gmail.com

K. A. Ibrahim Sheriff
e-mail: ibrahim@kongu.ac.in

G. Rajeshkumar
Department of Mechanical Engineering, PSG Institute of Technology and Applied Research,
Coimbatore, Tamil Nadu, India
e-mail: grajeshkumar.me@gmail.com

1 Introduction

Everything that rotates needs to be in a state of balance to ensure smooth running during operation. Unbalance is a very common source of vibration that is identified by excessive levels of vibration amplitudes. This occurs at a frequency that is synchronous with machine speed. Unbalance happens because of the density of materials which are uneven or shafts are not perfectly round shape or not mounted exactly in the center, etc. Mass unbalance in a rotating system often produces excessive synchronous forces that reduce the life span of various mechanical elements. Therefore, balancing is important in the manufacture and maintenance process of rotating machines.

The goal of the balancing a machine is to decrease the vibration with the rotational frequency by fixing the corrected masses in certain planes on the rotor. The centrifugal forces exerted by these masses can compensate the action of radial forces applied on the fixed parts of the machine. Moreover, in a multicondition machine, it is possible to decrease the vibration for one operating condition efficiently, but the change in the condition can increase the machine vibration significantly. An example of such a situation is the balancing of an electric machine when the geometrical rotor axis does not coincide with its rotation axis (dynamic eccentricity of the air gap). In such machines, it is possible to decrease the vibration of the operating condition, but the rotor vibration increases. The vibration of the machine and the rotor can increase when the operating conditions are changed. Some machines such as fans and blowers may develop unbalance as a result of erosion. In this chapter, balancing of one such unbalanced multirotor system is attempted using vibration signatures.

For many decades, it had been common to use solid couplings in turbomachinery. However, these couplings have a decisive influence on rotor dynamics. Sekhar and Prabhu [1] presented the effects of coupling misalignment on turbomachinery vibrations. It was shown that the location of the coupling with respect to the bending mode shape has a strong influence on the level of vibration. A theoretical model of a complete motor flexible coupling rotor was presented by Xu and Marangoni [2, 3]. They assumed that the flexible coupling behaves exactly as a universal joint to take the misalignment and unbalance effects into account. Prabhu [4] showed that an increase in misalignment had caused a change in the second harmonic of the vibration response. Simon [5] predicted the behavior of a large turbomachinery when subjected to unbalance and misalignment. Dewell and Mithchell [6] developed the expected vibration frequencies for a misaligned metallic disk-flexible coupling. The predicted dominant frequencies were 2X and 4X running speed components due to parallel misalignment.

Wattner [7] dealt with the design functions and case histories of gear couplings. He discussed the various types of misalignments, which may be encountered by the gear type of coupling. Palazzolo et al. [8] discussed forces and moments induced by gear coupling misalignment and unbalance. They reasoned that gear couplings can produce large static forces that can affect the vibration of turbomachinery. Bloch [9] showed how a change from conventional gear-type couplings to

more recent diaphragm coupling design could lower shaft stresses sufficiently to avoid shaft replacement during power up rates of centrifugal compressors. Gibson [10] derived the reaction forces generated by the different types of couplings. Mancuso [11] discussed the applications of flexible-type couplings for turbomachinery. Rosenberg [12] presented the critical speed behavior of rotating shafts driven by universal coupling. This paper presented the unbalance study of multirotor system and calculated the power consumption due to unbalance.

2 Experimental Setup of a MultiRotor System

Most of the literature revealed that a single-rotor or two-rotor systems are considered for balancing. In the present study, balancing of a multirotor system is considered. The main objectives of the study are:

- (i) to obtain the vibration response of the rolling element bearings in the existing rotating system under unbalanced conditions
- (ii) to measure the power consumption of the unbalanced system
- (iii) to balance the system using vibration signatures
- (iv) to measure the power consumption of the balanced system
- (v) to suggest a suitable method for condition monitoring of the system using vibration signatures.

The methodology of carrying out the above-said objectives is shown in Fig. 1. When several masses are revolved in different planes, they may be transferred to a common reference plane. This is the plane should pass through a point on the axis of rotation and perpendicular to it. The effect of transferring the revolving mass to the reference plane creates a force of magnitude equal to the centrifugal force of the revolving mass to act in the reference plane. The couple of magnitude is equal to the product of force and the distance between the planes of rotation to the reference plane. In order to have a complete balance of the several revolving masses in different planes, two conditions should be satisfied (i) the forces in the reference plane must be balanced, i.e., the resultant force must be zero and (ii) the couples about the reference plane must be balanced, i.e., the resultant couple must be zero.

2.1 Description of the Experimental Setup for Data Acquisition

The experimental facility used for the study is fabricated in the Research and Development Centre of Kongu Engineering College, Erode as shown in Fig. 2.

A system with four rotors is considered in the present study. These four rotors made of aluminum are rigidly fixed on the shaft at a fixed distance from the bearings by aligning nuts. Two deep groove ball bearings (SKF 6203) are used in the system.

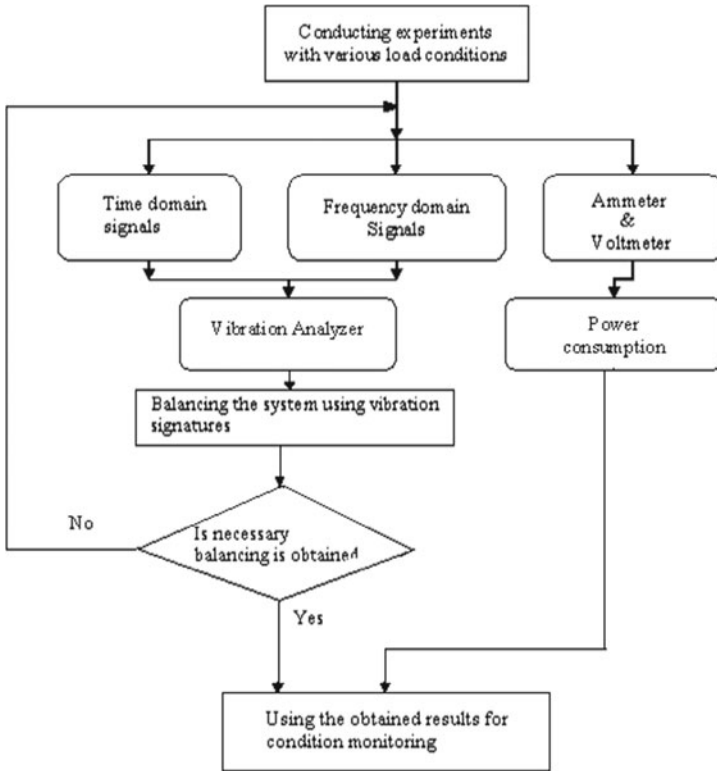


Fig. 1 Methodology of balancing a multirotor system vibration signatures

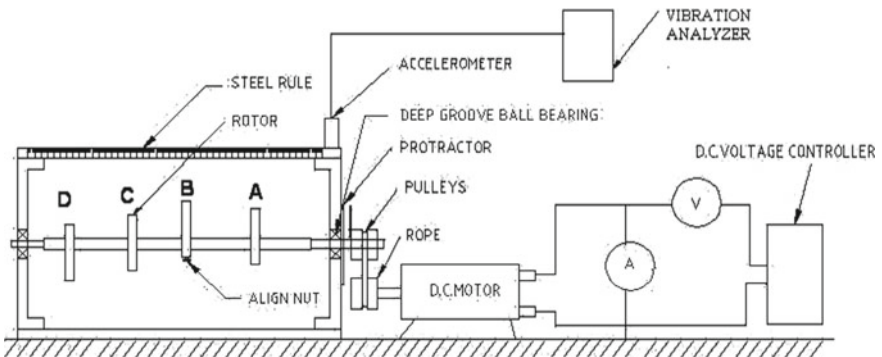


Fig. 2 Schematic of the experimental setup

The end bearings are rigidly supported on the steel frame. The two supports are connected by a steel rule at the top to measure and locate the rotor at a fixed distance from the bearings. The drive end of the support is fitted with a protractor with a pointer to measure and locate the angle of the rotor. The shaft is rotated by means of a belt drive through 0.56 kW D.C. motor. Further, the D.C. motor is connected with the D.C. voltage controller and the D.C. controller is used to adjust the power supply to get the different speeds of the system. A digital tachometer is used to measure the speed of the system. A calibrated piezoelectric accelerometer with a magnetic base and a high-resolution dual-channel vibration analyzer are used to measure the vibration spectrum at the balanced and the unbalanced conditions. Vibration signals are measured both at the vertical and horizontal directions at the drive end (DE) and the nondrive end (NDE). In this experiment, two numbers of SKF 6203, deep groove ball bearings of 17 mm bore diameter, 40 mm outside diameter, and 12 mm width are used to support the shaft ends. The multirotor system is connected with an ammeter and voltmeter to measure the power consumption during the balanced and unbalanced conditions.

3 Results and Discussion

3.1 Frequency Spectrum of Unbalanced Mass of 15 g

Frequency domain signals at ± 15 g unbalance is shown in Fig. 3 and it is observed that the peak vibration amplitude at 500 rpm under balanced condition is 1.513 mm/s at a frequency of 9 Hz, which is equal to the running frequency. For the same speed, peak vibration amplitudes are 1.792 mm/s and 1.666 mm/s with 15 g of unbalanced mass addition and mass subtraction, respectively. Peak amplitude at 9 Hz (1X) frequency indicates the unbalanced condition. Vibration amplitudes of unbalanced mass of +15 g addition and subtraction are 1.184 and 1.102 times larger than the amplitudes under balanced condition.

Similarly, vibration amplitudes of 4.081 mm/s and 1.756 mm/s are observed at 1000 rpm and 1500 rpm, respectively, under balanced condition. Table 1 shows the vibration amplitudes at 500, 1000, and 1500 rpm at both balanced and unbalanced conditions. From Table 1, it is observed that at 15 g of mass addition, the vibration amplitude is 1.293 times higher in the unbalanced system at 1000 rpm, while it is 5.689 times higher at 1500 rpm. Similarly, at 15 g of mass subtraction, vibration amplitudes of 1.112 and 1.925 times higher in the unbalanced condition at 1000 rpm and 1500 rpm are noticed.

From Table 1, larger vibration amplitudes are observed for the unbalanced mass addition than for the unbalanced mass subtraction at all speeds of DE and NDE. The large vibration amplitude observed during mass addition is due to large centrifugal force. When the mass of the balanced system is subtracted, the centrifugal effect is greatly reduced and results in smaller vibration amplitude.

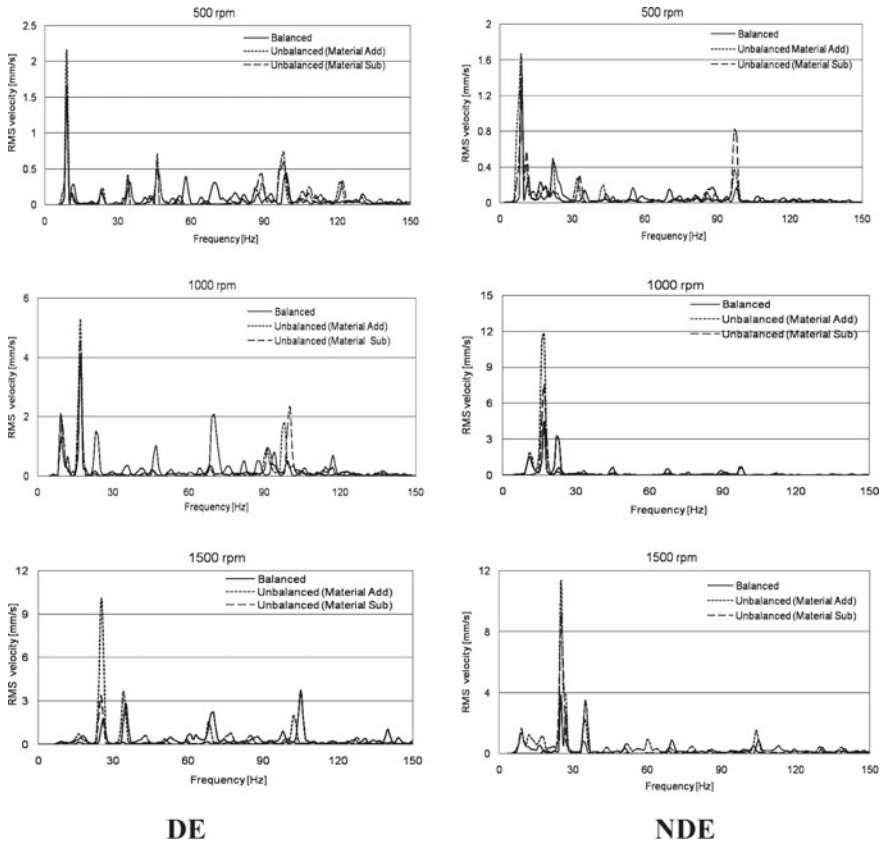


Fig. 3 Frequency spectrums of DE and NDE with 15 g mass unbalance

3.2 Frequency Spectrum of Unbalanced Mass of 30 g

Similarly, from the frequency spectrums of ± 30 g unbalance mass plots given in Fig. 4 at all speeds of drive end support bearing, peak vibration amplitude is observed at 9 Hz (1X). At 500 rpm, under balanced condition, vibration amplitude of 1.513 mm/s is seen at the frequency of 9 Hz, which is equal to the running frequency. For the same speed, peak vibration amplitudes are 2.325 mm/s and 1.788 mm/s at 30 g of mass addition and subtraction, respectively. Peak amplitude at 9 Hz (1X) frequency indicates the unbalanced condition. Vibration amplitudes with the unbalanced mass of +30 g addition and subtraction are 1.535 and 1.182 times higher than the amplitudes under balanced condition.

Similarly, vibration amplitudes of 4.832 mm/s and 1.756 mm/s are obtained at 1000 rpm and 1500 rpm, respectively, under balanced condition. From Fig. 5, it is observed that the vibration amplitudes at 1000 and 1500 rpm in unbalanced conditions are larger than that of the balanced condition. From Fig. 5, for an unbalanced mass

Table 1 Measured vibration amplitudes of balanced system and unbalanced system with 15 g mass addition/subtraction

Position	Speed (rpm)	Vibration amplitude (mm/s)			Deviation with mass addition	Deviation with mass subtraction
		Balanced condition	Unbalanced mass of + 15 g	Unbalanced mass of - 15 g		
E	500 (9 Hz)	1.513	1.792	1.666	1.184	1.102
	1000 (17 Hz)	4.081	5.275	4.538	1.293	1.112
	1500 (25 Hz)	1.756	9.989	3.382	5.689	1.925
NDE	500 (9 Hz)	1.402	1.637	1.549	1.167	1.105
	1000 (17 Hz)	4.475	11.784	7.487	2.633	1.673
	1500 (25 Hz)	3.833	11.373	9.027	2.967	2.355
			+30 g	-30 g		
DE	500 (9 Hz)	1.513	2.323	1.788	1.535	1.182
	1000(17 Hz)	4.832	6.052	5.404	1.252	1.118
	1500 (25 Hz)	1.756	11.230	6.966	6.395	3.967
NDE	500 (9 Hz)	1.402	2.461	1.749	1.756	1.248
	1000 (17 Hz)	4.475	14.911	9.463	3.332	2.115
	1500 (25 Hz)	6.515	14.484	6.307	2.223	0.968

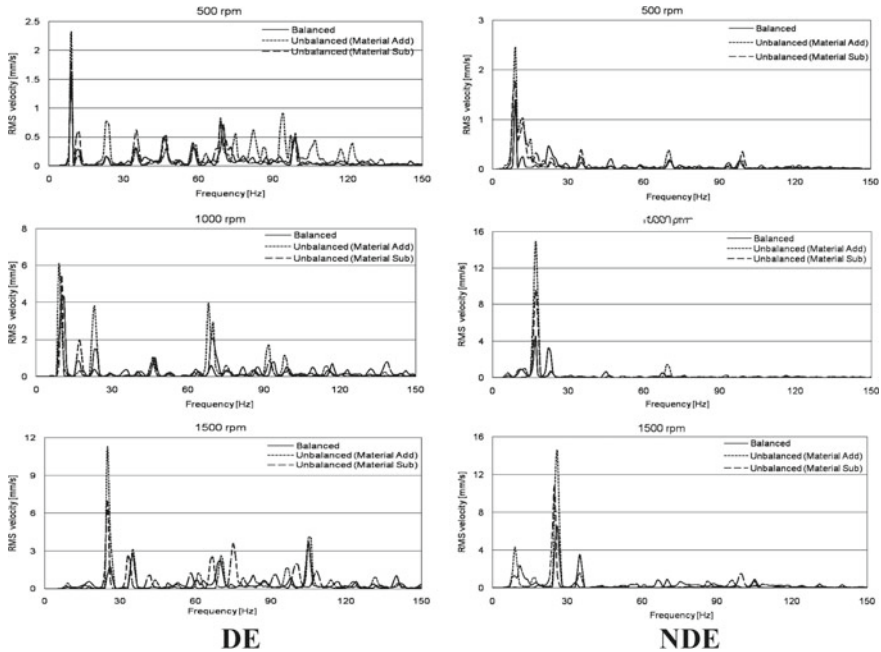
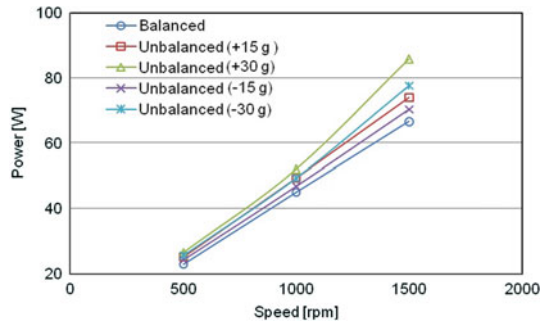


Fig. 4 Frequency spectrums with 30 g mass unbalance

Fig. 5 Variation of power consumption of multirotor system with unbalance



addition, it is observed that vibration amplitude is 1.252 and 6.395 times higher than the balanced condition at 1000 rpm and 1500 rpm, respectively. In the case of mass subtraction, vibration amplitude is 1.118 and 3.967 times more than the balanced mass at 1000 and 1500 rpm, respectively.

From Table 1, larger vibration amplitudes are observed for the unbalanced mass addition than that of the mass subtraction at all speeds of DE and NDE. Large vibration amplitudes are observed during mass addition due to the action of high centrifugal forces. When the mass of the balanced system is subtracted, the centrifugal effect gets reduced and results in relatively small vibration amplitudes.

3.3 Power consumption

The next objective of this study is to calculate the variation in power consumption due to the unbalance in the multirotor system. The multirotor system is connected with an ammeter and voltmeter to measure the power consumption during the balanced and unbalanced conditions. The powers consumed under both conditions are measured. Table 2 enlists the power consumption data for balanced and unbalanced conditions at 500, 1000, and 1500 rpm. From the recorded data, power consumption of balanced and unbalanced conditions is calculated. Figure 5 plots the power consumption of the balanced and unbalanced systems with mass addition and subtraction.

From Fig. 5, the observations are as follows:

- (i) If the speed of the shaft increases, the power consumption also increases for all the cases.
- (ii) At given speed, the power consumption is lower during the balanced condition.
- (iii) With the unbalance (either mass addition or mass subtraction), the power consumption increases at a given speed. Power consumption increases with the addition of mass and decreases with subtraction of mass.

Table 2 Power consumption

Speed N (rpm)	Balanced condition			Unbalanced condition											
				Material addition			Material subtraction								
				+15 g			-15 g								
	Voltage V (Volts)	Current I (amps)	Power P (watts)	Voltage V (Volts)	Current I (amps)	Power P (watts)	Voltage V (Volts)	Current I (amps)	Power P (watts)	Voltage V (Volts)	Current I (amps)	Power P (watts)			
500	27	0.85	22.9	28	0.90	25.2	28	0.98	26.6	27	0.90	24.3	27	0.95	25.7
1000	50	0.90	45.0	52	0.95	49.4	52	1.0	52.0	52	0.90	46.8	52	0.95	49.4
1500	74	0.90	66.6	74	1.00	74.0	78	1.1	85.8	74	0.95	70.3	74	1.05	77.7

4 Conclusion

The vibration signals can be effectively used to identify and balance the unbalance in the multirotor system with any number of rotors. In the present case, such an attempt has been made for a system with four rotors successfully. The concept of measuring power consumption can be used for condition monitoring of such systems. The power consumption obtained under perfect balancing condition can be kept as reference values. Any deviation will indicate the development of unbalance. Under these conditions, by additionally measuring vibration signatures, the unbalance can be correlated as demonstrated in this chapter.

References

1. A.S. Sekha, B.S. Prabhu, Effects of coupling misalignment on vibrations of rotating machinery. *J. Sound Vib.* **185**, 655–671 (1995)
2. M. Xu, R.D. Marangoni, Vibration analysis of a motor-flexible coupling-rotor system subject to misalignment and unbalance. Part I: experimental validation. *J. Sound Vib.* **1994**(176), 681–691 (1994)
3. M. Xu, R.D. Marangoni, Vibration analysis of a motor-flexible coupling-rotor system subject to misalignment and unbalance. Part I: Theoretical model analysis. *J. Sound Vib.* **176**, 663–679 (1994)
4. B.S. Prabhu, An experimental investigation on the misalignment effects in journal bearings. *STLE Tribol. Trans.* **40**, 235–242 (1997)
5. G. Simon, Prediction of vibration of large turbo-machinery on elastic foundation due to unbalance and coupling misalignment. *Proc. Inst. Mech. Eng.* **206**, 29–39 (1992)
6. D.L. Dewell, L.D. Mithchell, Detection of a misaligned disk coupling using spectrum analysis. *J. Vibr. Acoust. Stress Reliab. Des.* **06**, 9–16 (1984)
7. K.W. Wattner, High speed coupling failure analysis, in *Proceedings of the Fourth Turbomachinery Symposium* (Texas A&M, 2002), pp. 143–148
8. A.B. Palazzolo, S.R. Locke, M. Calistrat, R.W. Clark, A. Ayoub, D. Calistrat, P. Tang, Gear coupling misalignment induced forces and their effect on machinery vibration, in *Proceedings of the 21st Turbo machinery Symposium* (Texas A&M, 2008), pp. 83–96
9. H.P. Bloch, Less costly Turbo equipment uprates through optimized coupling selection, in *Proceedings of the 4th Turbomachinery Symposium*. (Texas A&M University, Gas Turbine Laboratories, 2002), pp. 149–152
10. C.B. Gibbson, Coupling misalignment forces, in *Proceedings of the 5th Turbo machinery Symposium, Gas Turbine Laboratories*, (Texas A & M University, College Station, TX, 1977), pp. 111–116
11. J. Mancuso, General purpose vs. special purpose couplings, in *Proceedings of the 5th Turbo machinery Symposium, Gas Turbine Laboratories* (Texas A & M University, College Station, TX, 1995), pp. 167–177
12. R.M. Rosenberg, On the dynamical behaviour of rotating shafts driven by universal (Hooke) coupling. *J. Appl. Mech.* **25**, 47–51 (1958)

Robust Design of Deterministically Synthesized Four-Bar Mechanism



Sanjay Matekar  and Ajay Fulambarkar

Abstract Robust design of mechanisms ensures that the intended task will be performed with minimum deviation from the target performance. In this paper, robust design of path-generating four-bar mechanism has been discussed. Deterministic synthesis has been performed to determine the mechanism parameter values for a vertical line path generation task. Five best deterministically synthesized mechanisms have been identified based on their objective function values. Optimum link tolerances and joint clearances have been designed for these mechanisms using Taguchi orthogonal arrays. Robustness of these mechanisms has been analyzed based on the normal distribution of responses. It has been observed that the fourth mechanism has been the best robust mechanism as it has the least mean and standard deviation. Thus, to design the robust mechanism, a set of deterministically synthesized mechanisms have to be analyzed for robustness after tolerance design.

Keywords Four-Bar mechanism synthesis · Robust design · Tolerance design · Taguchi orthogonal array

1 Introduction

Dr. Taguchi has defined the goal of robust design as to find a combination of parameter values along with the tolerances that give the smallest variation around the desired target [1]. The robustness for mechanisms is that the response of designed mechanism should deviate least from the specified task under the influence of uncertainties. In this paper, robust design of deterministically synthesized path generating four-bar mechanism has been discussed.

S. Matekar (✉)

Department of Mechanical Engineering, Sinhgad College of Engineering, Pune, India

e-mail: sanjay.matekar@pccoepune.org

A. Fulambarkar

Mechanical Engineering Department, Pimpri Chinchwad College of Engineering, Pune, India

© Springer Nature Singapore Pte Ltd. 2021

G. S. V. L. Narasimham et al. (eds.), *Recent Trends in Mechanical Engineering*,

Lecture Notes in Mechanical Engineering,

https://doi.org/10.1007/978-981-15-7557-0_35

The link length tolerances and joint clearances are the most influencing parameters for robustness of any mechanism [2–4]. The effect of link length tolerances and joint clearances on the slider displacement in a slider-crank mechanism have been simulated and experimentally validated by Matekar and Fulambarkar [2]. Deterministic synthesis has been performed to identify parameter values of mechanism. An objective function for path generation, as Root Mean Square (RMS) of error between the generated path points and the desired path points for the deterministic synthesis of four-bar mechanism has been used by Kunjur and Krishnamurty [5], Cabrera et al. [6], and Matekar and Gogate [3]. Taguchi method has been used for tolerance design of mechanism. The link length tolerances and joint clearances have been considered as control parameters for designing tolerances. While, deflection of links, operating temperature, and positioning angular error of input link have been considered as noises. Link length tolerances of four-bar mechanism for path generation considering manufacturing error as noise have been done by Kota and Chiou [4]. Tolerance design of control factors has been done using Taguchi method under the influence of noise for function generating four-bar mechanism by Chen and Huang [7]. Taguchi method with sensitivity mapping for tolerance design of function generating mechanism with joint clearance has been used to understand the effect of parameter variation on the performance of mechanism by Xianzhen and Zhang [8]. Tolerance design using Taguchi method of a function generating four-bar mechanism with only joint clearance as control parameter has been done by Huang et al. [9].

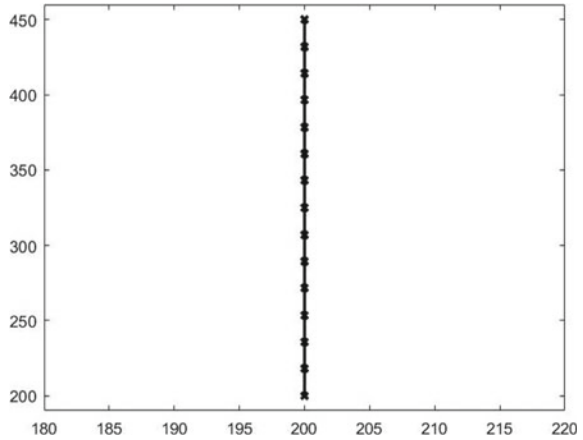
From the literature reviewed, it has been observed that for robust design of mechanism, the tolerance design of only the best deterministic mechanism has been done. In this paper, an attempt has been made to identify the best robust mechanism from the five best deterministically synthesized mechanisms by comparing their robustness after tolerance design.

The paper is organized as follows; deterministic synthesis of the path generating four-bar mechanism is discussed in Sect. 2. Section 3 discusses the tolerance design of the five best synthesized mechanisms. Conclusion is given in Sect. 5.

2 Synthesis of Path-Generating Four-Bar Mechanism

In this section, synthesis of four-bar mechanism for vertical line path generation task is discussed. The synthesis has been performed deterministically (i.e., at ideal conditions) using minimization of error between desired and generated path as objective function.

Fig. 1 Specified vertical line



2.1 Path Generation Task

Figure 1 shows the specified vertical line for the path generation task. The line is 250 mm length, from point (200, 200) to point (200, 450). 15 equispaced points on the line have been used for synthesis. A point on the coupler link of the four-bar mechanism traces the vertical line when the input link rotates by 360° .

2.2 Deterministic Synthesis of Path-Generating Four-Bar Mechanism

Figure 2 shows the parameters of a four-bar mechanism for path generation [3]. Where, ‘C’ is the coupler point that traces the specified path. θ_1 is the angle made by fixed link with horizontal axis. $r_1, r_2, r_3,$ and r_4 are the link lengths of the fixed, input, coupler, and output links, respectively. θ_2 is the angle made by input link with

Fig. 2 Parameters of four-bar mechanism for path generation

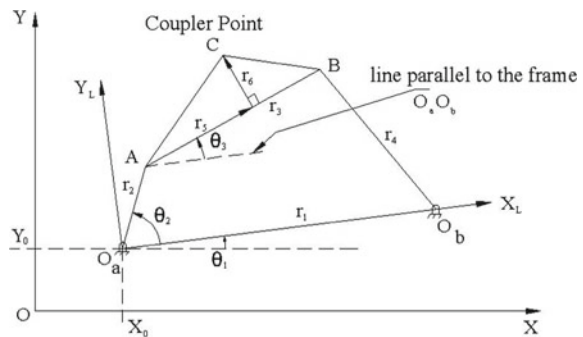


Table 1 Design parameters with limits

Design parameter	Lower limit	Upper limit
r_1 (mm)	50	800
r_2 (mm)	50	400
r_3 (mm)	50	400
r_4 (mm)	50	800
r_5 (mm)	30	400
r_6 (mm)	30	400
X_0 (mm)	-100	400
Y_0 (mm)	-100	400
θ_1 (rad)	0	6.28
θ_2^1 (rad)	0	6.28
$\Delta\theta_2$ (deg)	30	180

fixed link. r_5 and r_6 are the coordinates of the coupler point C in coupler link. X_0 and Y_0 are the coordinates of fixed pivot. Table 1 lists the lower and upper limits of design parameters for synthesis.

$$E_{\text{RMS}} = \sqrt{\frac{1}{n} \sum_{i=1}^n [(C_{xs}^i - C_{xg}^i)^2 + (C_{ys}^i - C_{yg}^i)^2]} \quad (1)$$

Equation (1) shows the objective function for mechanism synthesis as, minimization of Root Mean Square (RMS) of error between the desired path points and the generated path points. Where, $\{C_s^i\}$ are specified path points and $\{C_g^i\}$ are the generated path points.

A program has been written in MATLAB to determine the objective function value. Differential evolution has been used as the optimization algorithm. Mechanism synthesis has been performed to determine 500 mechanisms. Five best performing mechanisms have been identified for tolerance design by sorting the objective function values in ascending order. Table 2 lists the synthesized parameter values along with the objective function value of the identified five best mechanisms.

3 Tolerance Design of the Mechanisms

The deterministically synthesized mechanisms will deviate from the intended path due to manufacturing and assembly requirements. It is necessary to specify optimum link length tolerance for manufacturing and joint clearance for assembly under the influence of uncontrollable factors.

Table 2 Parameter values of best five mechanisms

Design variable	Mechanism number				
	1	2	3	4	5
r_1	775	760	706	736	666
r_2	233	227	229	244	237
r_3	353	358	388	388	380
r_4	665	694	639	610	536
r_5	35	72	56	126	52
r_6	400	396	400	400	392
X_0	366	374	373	370	356
Y_0	133	137	145	79	125
θ_1 (rad)	6.2451	6.2379	6.2768	0.1575	0.1146
Objective function value	0.5966	0.6185	0.6356	0.6612	0.6820

In this paper, link lengths $r_1 - r_6$ and joint clearances at both ends of coupler link, r_{c1} and r_{c2} of the four-bar mechanism have been considered as control factors. Tolerances have been designed for these control factors using Taguchi orthogonal arrays. Three uncontrollable parameters have been considered as noise factors, as, direction of the tolerance, deformation of link due to environmental conditions, and orientation of clearance link. L_{27} orthogonal array has been used for designing experiments of control and noise factors. Three levels of each control factor and noise factors have been considered for the tolerance design.

Following three levels of control factors have been considered:

1. Tolerance of each link $r_1 - r_6$ as, 1, 0.5, and 0.1% of deterministic length.
2. Joint clearance r_{c1} and r_{c2} as, 0.1, 0.5, and 1.0 mm.

Following three levels of noise factors have been considered:

1. The direction of the tolerance: on negative side (-1), no tolerance (0), on positive side (+1).
2. Deformation of link: 0.0005, 0.00, and -0.0005 mm/mm.
3. Orientation of clearance link: 0° , 72° , 144° , 216° , and 288° .

The experiments have been designed to understand the effect of noise factors on the control factor levels to identify the optimum control factor level. 27 experiments have been designed for eight control factors with three levels each which have been considered as inner array. 27 experiments have been designed for 14 noise factors with three levels each, which have been considered as outer array. The designed experiments have been analyzed using a program written in MATLAB. Each experiment in the inner orthogonal array has been analyzed for all the experiments in outer array and the mean result has been recorded. Figure 3 shows the first four-inner array experiments against the first outer array experiment each cell, stores the mean of outer array experiment.

Inner Array						Outer Array			
r1	r2	r3	r4	r5	r6	rc1	rc2	m_err_1	
0.01	0.01	0.01	0.01	0.01	0.01	0.1	0.1	1.71885	
0.01	0.01	0.01	0.01	0.005	0.005	0.5	0.5	3.313823	
0.01	0.01	0.01	0.01	0.001	0.001	1	1	6.250131	
0.01	0.005	0.005	0.005	0.01	0.01	0.1	0.5	3.481329	
									r1 -1
									r2 -1
									r3 -1
									r4 -1
									r5 -1
									r6 -1
									r1 0.0005
									r2 0.0005
									r3 0.0005
									r4 0.0005
									r5 0.0005
									r6 0.0005
									cl_ang_2 0
									cl_ang_1 0

Fig. 3 Experiments for tolerance design

The objective of mechanism synthesis has been to minimize the error, thus, smaller the better S/N ratio of the experiment results has been calculated using MINITAB. The S/N ratios for all the control factor levels have been plotted to identify optimum tolerance value. Figure 4 shows the S/N ratios plot for the first best mechanism. Where it can be observed that the overall mean for the completer analysis is -13.84 .

The optimum tolerance value for each control factor has been identified as the control factor level near zero. The optimum tolerances for the first best mechanism are obtained by observing Fig. 3. The optimum link length tolerances are $r_1 = 0.1\%$,

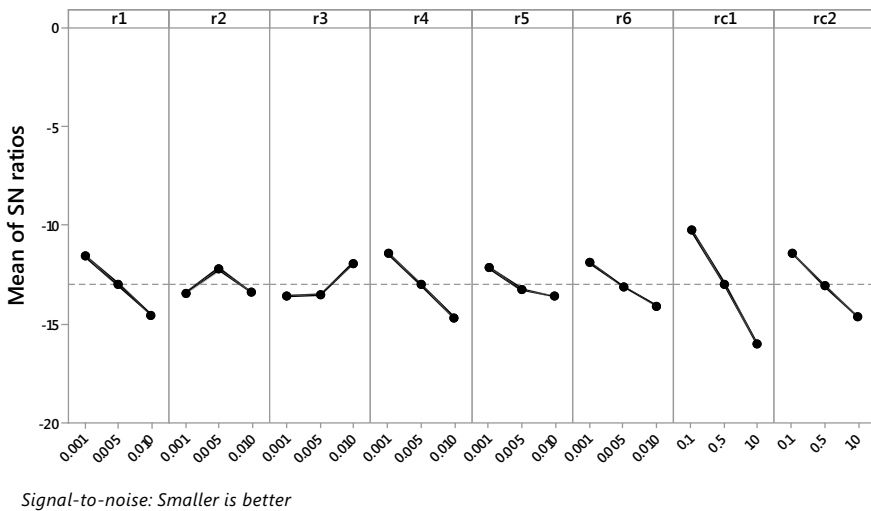


Fig. 4 S/N ratio plot for control factors

Table 3 Optimum tolerance allocation for five best mechanisms

Mechanism No.	Link length tolerance as % of link length						Joint clearance	
	r_1 (%)	r_2 (%)	r_3 (%)	r_4 (%)	r_5 (%)	r_6 (%)	CL_1	CL_2
1	0.1	0.5	1.0	0.1	0.1	0.1	0.1	0.1
2	0.1	0.5	0.5	0.1	1.0	0.1	0.1	0.1
3	0.1	0.5	1.0	0.1	0.5	0.1	0.1	0.1
4	0.1	0.5	1.0	0.1	0.1	0.1	0.1	0.1
5	0.1	0.5	1.0	0.1	0.5	0.1	0.1	0.1

$r_2 = 0.5\%$, $r_3 = 1\%$, $r_4 = 0.1\%$, $r_5 = 0.1\%$, $r_6 = 0.1\%$ of the link synthesized link length. The optimum joint clearances are $r_{c1} = 0.1$ mm and $r_{c2} = 0.1$ mm. The mechanism with these tolerances and joint clearances will perform robustly. Similar analysis has been performed for the remaining four mechanisms. Table 3 lists the optimum tolerances for all five mechanisms.

4 Result and Discussion

In the path-generating mechanism, the target is to have minimum error between generated and specified path. Thus the mechanism which will have its mean performance with smallest deviation will be the best robust mechanism. To identify the best robust mechanism from the five best deterministically synthesized mechanisms, mean and standard deviations of output of all five mechanisms with allotted tolerances have been calculated.

Figure 5 shows the normal distribution curves of all the five mechanism responses (RMS of error) with the allotted tolerances. It can be observed that the first, fourth, and fifth mechanisms mean performance have sifted by 0.7–0.9 RMS value, while second and third mechanisms have deviated by 10–36 RMS value. Thus, the second and third mechanisms with allocated tolerances will not perform robustly due to large deviation.

Figure 6 shows the normal distribution curve of first, fourth, and fifth mechanisms which are best performing. It can be observed that mean performance is in the range 1.368–1.596 and standard deviation is in the range 0.2839–0.2975, which are comparable. Fourth mechanism has the least mean value as 1.368 and with standard deviation of 0.2975 of all the three mechanisms. Thus, all three mechanisms will behave robustly, while the fourth mechanism will be the most robust as its mean performance is the least.

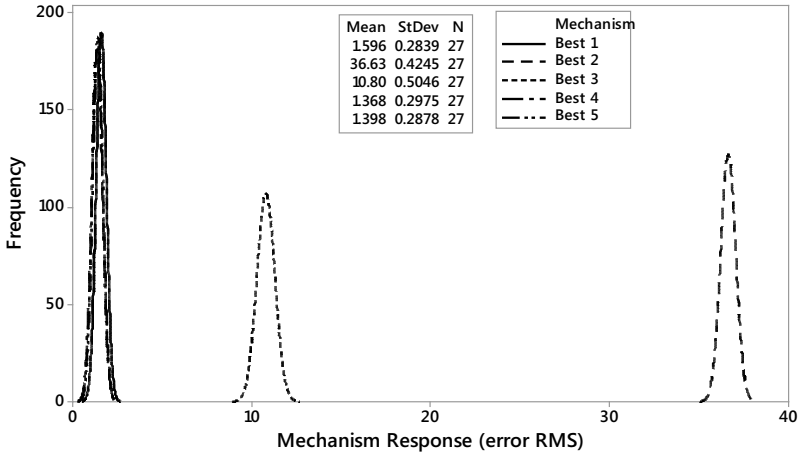


Fig. 5 Normal distribution of objective function values of all five mechanisms

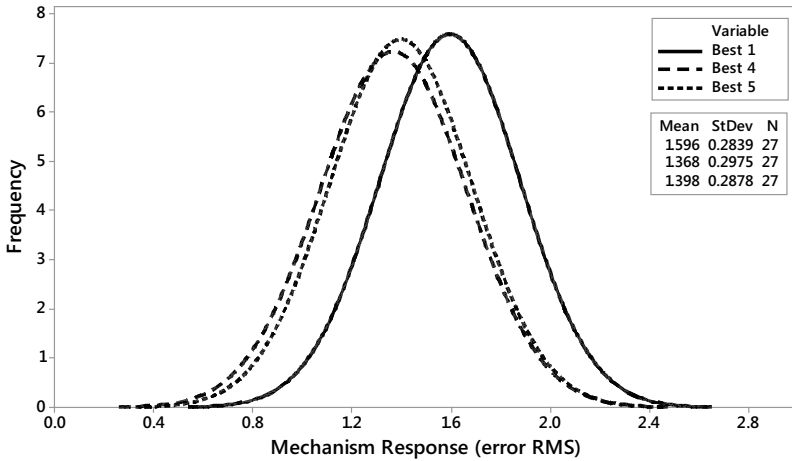


Fig. 6 Normal distribution of objective function values of all five mechanisms

5 Conclusion

It is necessary to specify link length tolerances and joint tolerances of the synthesized mechanism parameters such that it will perform robustly under the influence of uncertainties. In this paper, deterministic synthesis has been performed to identify five best mechanisms for vertical path generation task. Optimum tolerances have been allocated for these mechanisms using Taguchi orthogonal arrays as shown in Table 3.

It has been observed the mean performance of all the mechanisms has increased by 0.7–36 RMS value. The first, fourth, and fifth mechanisms have better robustness as their mean performance has been in the range 1.368–1.596 and standard deviation has been in the range 0.2839–0.2975. While, the second and third mechanisms mean has been deviated by 10–30 RMS value after tolerance allocation and will not perform robustly. The fourth mechanism has been the best robust mechanism with the least mean value as 1.368 which is better than 16% than the first best mechanism.

Thus, it can be concluded that the first best deterministic mechanism may not be the best robust mechanism. It can also be concluded that it is necessary to analyze a set of best deterministic mechanisms for robustness by allocating optimum tolerances before accepting the design. There is further scope to include this logic into the mathematical model for synthesis such that the optimum robust mechanism can be synthesized.

References

1. M. Phadke, in *Quality Engineering using Robust Design*, 2nd edn. (Pearson Education, 2012)
2. S. Matekar, A. Fulambarkar, Simulation and experimental validation of slider displacement in slider crank mechanism with connecting rod tolerance and joint clearance. *Int. Rev. Mech. Eng.* **12**(12), 965–974 (2018). <https://doi.org/10.15866/ireme.v12i12.15933>
3. S. Matekar, G. Gogate, Optimum synthesis of path generating four-bar mechanisms using differential evolution and a modified error function. *Mech. Mach. Theor.* **52**, 158–179 (2012). <https://doi.org/10.1016/j.mechmachtheory.2012.01.017>
4. S. Kota, S. Chiou, Use of orthogonal arrays in mechanism synthesis. *Mech. Mach. Theor.* **28**(6), 777–794 (1993). [https://doi.org/10.1016/0094-114X\(93\)90021](https://doi.org/10.1016/0094-114X(93)90021)
5. A. Kunjur, S. Krishnamurty, Genetic algorithms in mechanism synthesis. *J. Appl. Mech. Robot.* **4**(2), 18–24 (1997)
6. J. Cabrera, A. Simon, M. Prado, Optimal synthesis of mechanisms with genetic algorithm. *Mech. Mach. Theor.* **37**(10), 1165–1177 (2002). [https://doi.org/10.1016/s0094-114x\(02\)00051-4](https://doi.org/10.1016/s0094-114x(02)00051-4)
7. F. Chen, H. Huang, Application of Taguchi method on the tolerance design of a four bar function generating mechanism, in *ASME 2005 International Design Engineering Technical Conferences and Computers and Information in Engineering Conference*, vol. 7: *29th Mechanisms and Robotics Conference, Parts A and B*. (Long Beach, California, USA. 24–28 Sept 2005, pp. 727–733. <https://doi.org/10.1115/detc2005-84199>
8. H. Xianzhen, Y. Zhang, Robust tolerance design for function generation mechanisms with joint clearance. *Mech. Mach. Theor.* **45**(9), 1286–1297 (2010). <https://doi.org/10.1016/j.mechmachtheory.2010.04.003>
9. X. Huang, Y. Zhang, H. Lu, L. Tang, H. Li, Tolerance design for four bar function generating mechanisms with joint clearance using Taguchi method. *Adv. Mater. Res.* **118–120**, 517–521 (2010). <https://doi.org/10.4028/www.scientific.net/AMR.118-120.517>

Analysis of Various Cooling Mechanisms for Plastic Gears Using Decision Tree Algorithms



Sam Cherian, Abu Bakr Azam, and Lokavarapu Bhaskara Rao

Abstract Plastic gears are widely used by engineers in various engineering applications due to their reduced noise while working, low cost, lighter weight, chemical resistance, flexibility, and the ability to operate without lubrication. A disadvantage found in these drives is the thermal stresses induced during continuous operation. Incorporating cooling holes into the design of plastic spur gears can reduce the thermal stresses on the gears. These cooling holes promote increased stress and tooth deflection, thus exerting a negative effect. Various machine learning algorithms like the decision tree algorithms are used to correctly identify the gear specifications based on the amount of torque applied from factors like material, hole sizes, and maximum force that can be applied at certain temperatures pertinent to regular working conditions maintaining a factor of safety of 2. The decision trees were able to correlate various gear parameters and material properties with high accuracy to provide the means to select the gears based on three types of torques; from high torques of more than 10,000 N mm to low torques of less than 1000 N mm.

Keywords Cooling · Decision tree · FEM · Gears · Machine learning

1 Introduction

Gears are often required to operate at high torque and speed, while remaining competitively priced and highly reliable. Strength and service conditions are some of the factors that the gear material used for manufacturing depends on. The gears may be

S. Cherian (✉) · A. B. Azam · L. B. Rao
School of Mechanical and Building Sciences, Vellore Institute of Technology Chennai,
Vandalur-Kelambakkam Road, Chennai, Tamil Nadu 600127, India
e-mail: sc.samcherian@gmail.com

A. B. Azam
e-mail: abubakr.azam@live.com

L. B. Rao
e-mail: bhaskarbabu_20@yahoo.com

manufactured from metallic or non-metallic materials. In recent times, non-metallic gears have gained much popularity in various applications [1–4]. Some of these applications include small machines, household utensils like mixers, the food and textile industry, and also the automotive industry [2, 3]. Metal gears are now being replaced by non-metallic gears due to their economic advantages [2, 4] in addition to easy manufacturing [5], reduced noise, [6] and reduced rotational mass while working. Disadvantages include low structural and thermal properties due to an increase in tooth temperature [6, 7] while working and the ability to operate without lubrication [8]. The reduction of thermal stresses can be accomplished by incorporating cooling holes at different positions in the gear geometry to increase the heat lost due to convection to the environment [9, 10]. The point of meshing contact and the forces that act on the gear tooth need to be taken into consideration to decide the position of the cooling holes to be selected.

The general procedure for the design of spur gears based on the applications they are used in is done by extensive theoretical calculations [11] of static shear stress [8] and root stress [12] of the gear after which the optimum dimensions and tooth profile [13] of the gear are decided. The CAD model of this gear is then created and analyzed for failures using simulation software such as ANSYS [14]. For effective cooling to take place, optimum dimensions and position of the cooling holes must be determined by calculating the face temperature [8, 15] of the gear tooth. Surface temperature also plays a major role in tooth wear [2] that also eventually results in failure. The mechanical resistance of plastic gears is dependent on temperature [16, 17]. Therefore, calculation of the thermal stress acting on the gear tooth is also necessary to determine the size and location of the holes. This procedure is very extensive and tiresome accounting for the large amount of calculations necessary to determine the optimum configuration for a single application.

This paper focuses on using machine learning algorithms like the decision tree and classification algorithms to choose the dimensions of the gear as well as the position and diameter of the holes based on the torque being applied to the gear required in the application. This helps us to reduce the time spent on tiresome calculations, analysis and helps in obtaining the required gear with optimum cooling capabilities.

The two decision tree algorithms used in this study are the J48 algorithm, which is an open-source Java version of the C4.5 algorithm and the random tree algorithm. In the case of the J48 algorithm, there is only one root node for the entire training set; however, every partition in the decision tree is followed by a new node. For some number of samples in a partition S , some test attribute X is chosen. Additionally, the set is further partitioned to more sets, $S_1, S_2 \dots S_L$, which are added to the tree. Therefore, the decision tree's construction depends mainly on X , the test attribute. The entropy gain value is used for the selection criteria, which is essentially the measure of randomness in a variable; the highest gain is chosen to make the decisions [18, 19].

A larger size of the decision tree might lead to inaccuracies, hence a procedure named pruning is used to reduce the size of the tree by correcting poorly defined instances [20]. The random tree algorithm randomly constructs a tree, from the set of possible trees having some K features at each node, which are also random. This degree of randomness ensures equal chances of each tree getting sampled, resulting

in a uniform distribution. This algorithm is especially useful for generating efficient trees by the combination of large sets of random trees [18, 21].

A common method to assess the classification accuracy of both these algorithms, where the torque values are attributed to the various gear parameters, the confusion matrix can be used, which shows the number of correctly and incorrectly identified instances. Some other quantities like recall and precision can provide a deeper understanding of the matrix. Formulae (1), (2), (3), (4) explain these quantities in detail.

$$\text{Precision} = \frac{\text{True positives (TP)}}{\text{True positive (TP) + False positive(FP)}} \quad (1)$$

$$\text{Recall} = \frac{\text{True positives (TP)}}{\text{True positive (TP) + False negative(FN)}} \quad (2)$$

$$\begin{aligned} &\text{MCC(Matthews Corellation coefficient)} \\ &= \frac{\text{TP} \times \text{TN} - \text{FP} \times \text{FN}}{\sqrt{(\text{TP} + \text{FP})(\text{TP} + \text{FN})(\text{TN} + \text{FP})(\text{TN} + \text{FN})}} \quad (3) \end{aligned}$$

$$\begin{aligned} \text{F1 - measure} &= \text{Harmonic mean of recall and precision} \\ &= \frac{2\text{TP}}{2\text{TP} + \text{FP} + \text{FN}} \quad (4) \end{aligned}$$

True-positive and false-negative elements are classified correctly and false-negative elements are not classified correctly. Several similar quantities are used to assess the accuracy of the model since there is no particular quantity that can fully assess the credibility of any model. Two types of validation are used to enhance accuracy, k -fold cross-validation, which divides the data into k subsets and uses one of them for testing and the remaining for training. The other method is to split the dataset into two parts. The difference between a cross-validation check and the division of the dataset is when the validation is performed; cross-validation is done while constructing the tree, while the split dataset method is used only after the model is prepared.

2 Methodology

2.1 Gear Design

Using SolidWorks toolbox, gears of various parameters and applicable hole sizes were made. For faster convergence, small fillets based on the gear size were made on the junction of the tooth and the hub; absence of the fillets would increase stress

Table 1 Gear parameters

Face width (mm)	Module	Teeth	Hole radius (mm)
40	2	22	1, 1.3, 2
5	0.25	20	0, 0.17
10	1	20	0.75
15	1.375	20	1.15

concentration and yield unrealistic results. All the dimensions are mentioned in Table 1.

2.2 Analysis of Gears

ANSYS thermal and static structural analyses were conducted as shown in Figs. 1 and 2, respectively, to find out the maximum magnitude of force allowed for a factor of safety of 2.0. This factor of safety was the ratio of the ultimate stress of the material over the possible amount of stress. A fixed support was applied to the hub area. The tangential force in each case was applied on the top face of one tooth, using the assumption of the Lewis equation shown Eq. (5), where at a given time all the force is applied only on one tooth

$$F_t = P_c \sigma_b y b \tag{5}$$

The two thermal loads used in this study were the temperature on one face of the tooth and convection on the remaining surface area of the gear. The values of temperature were in the range of 50–80 °C, and the values of convection were based on free and forced convection of air which is 5 W/m² °C for free convection and 1000 W/m² °C for forced convection.

Fig. 1 Static thermal setup

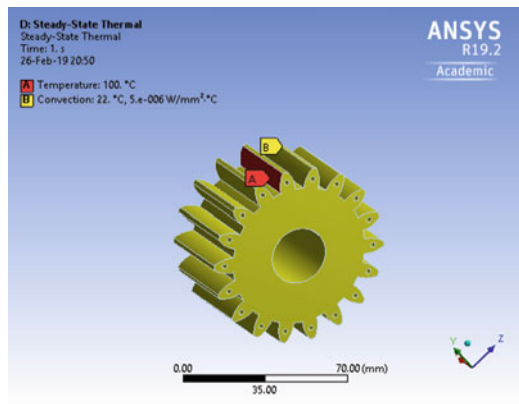


Fig. 2 Static structural setup

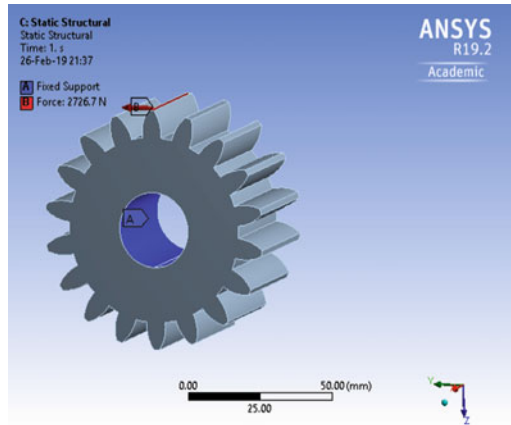


Table 2 Material properties

Material	Tensile ultimate strength (MPa)	Tensile yield strength (MPa)	Specific heat (J/kg °K)
Nylon 6/6	64	57	1700
Nylon 6/6 with 30% glass–fiber reinforcement	149	139	1520
Nylon 6	49.7	43.1	1700
Ultra-high molecular weight Polyethylene (UHMWPE)	43.2	24.3	1900
ABS plastic	44.3	41.4	1720
ABS + polycarbonate	45.2	35.1	1450
PEEK plastic	96.3	90.9	1443

The results obtained in the thermal analysis were merged with the static structural analysis, which ensured no difference in the mesh for both the analyses. To achieve better results, tetra mesh was applied to the geometry and the mesh size was reduced in the fillet areas, where the maximum stress was usually observed. The materials used for the analyses are commonly used to manufacture plastic gears, which are also used in this study are shown in Table 2.

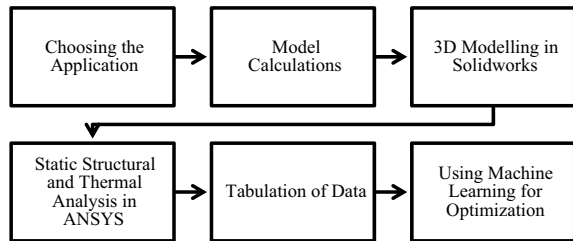
2.3 Machine Learning Setup

Data obtained from the analyses were combined in a Microsoft Excel worksheet. The format of the recorded data is shown in Table 3. Based on a simple formula, the

Table 3 Model dataset

Face width (mm)	Module	Teeth	Hole radius (mm)	Convection (W/m ² °C)	Temp (°C)	Material Ultimate Stress (N/mm ²)	Temperature coefficient (W/m °C)	Type
40	2	22	1.3	1000	50	140,000,000	1420	High torque
40	2	22	1.3	1000	50	43,200,000	1780	Medium torque

Fig. 3 Methodology flowchart



torque was calculated, which was used as a base to classify the given data into three categories; low, medium, and high torque.

A machine learning software named WEKA was used to process the dataset. From a multitude of algorithms, the decision tree algorithms were used as this algorithm finds the relations between the various parameters in the given dataset to produce a relation tree, which can be used as a catalog for selection. The number of teeth used was 22 to ensure that the resulting tree could be pertinent to the most commonly used gear teeth numbers and methodology flowchart as shown in Fig. 3.

The following decision tree algorithms were used:

1. Random tree algorithm
2. J48 algorithm.

The following types of testing were used:

3. Cross-validation (5, 10, 20)
4. Percentage split (30, 35, 40%).

3 Results and Discussion

An application used to prove the validity of the analyses is that of a wiper, with 50 W of power (Eq. 6) and 50 rpm of speed. The popular materials used are UHMWPE and Nylon 6 6. Theoretical calculations using the Lewis equation were performed,

which set limits on the materials and the tangential forces applied on the tooth, further justifying the use of such materials. Derivation of power proceeds from Eqs. (6)–(10).

Gear parameters: module: 2 mm number of teeth: 22 face width: 40 mm pressure angle (φ): 20°

Power transmitted:

$$P = 50 \text{ W} = \frac{2\pi NT}{60000} \tag{6}$$

$$T = 9549.3 \text{ Nmm} = \frac{F_t \times d}{2} = \frac{F_t \times Zm}{2} \tag{7}$$

$$\text{Lewis equation : } F_t = P_c \sigma_b y b \tag{8}$$

Lewis form factor for 200 full-depth involute teeth

$$y = \pi \left(0.154 - \frac{0.912}{Z} \right) \tag{9}$$

Velocity factor

$$C_v = \frac{1 + 0.25v_m}{1 + v_m} \tag{10}$$

The obtained value of stress was 5.5 MPa. Therefore, we can conclude that if the yield strength of the material is lesser than 5.5 MPa the gear will fail. Reusing the same equations to find the maximum amount of tangential force applied is shown in Table 4.

The force values used for the analyses are well below the maximum values, which are typical operating values hence the data obtained from the results are credible. The J48 decision tree was experimented with the number of cross-fold verifications and division of the training set. The best results were obtained, when the number of cross-fold verifications was 5; with a classification accuracy of 98.3%. The least number of nondiagonal elements in the confusion matrix in Table 5 and high value of the TP rate and the low value of the FP rate are seen in Table 6 among similar values show evidence of the model’s high accuracy, however, only the number of teeth and the material are linked in this model.

Table 4 Maximum force values

Material	Tangential force (N)
UHMWPE	1795.51
Nylon 6 6	3831.29
Nylon 6 6 (30% glass-fiber reinforcement)	5985.06

Table 5 Confusion matrix (J48)

Predicted condition			Actual condition
High Torque	Medium Torque	Low Torque	
20	0	0	High torque
0	12	1	Medium torque
0	0	26	Low torque

The random tree algorithm was able to provide a more comprehensive decision tree; everything except the number of teeth was taken into consideration with almost the same value of accuracy (97.72%) and with only 25% of the dataset used for training and decision tree (random tree) as shown in Figs. 4 and 5. Tables 7 and 8 show the confusion matrix and the detailed accuracy data, respectively.

4 Conclusions

Cooling holes in gears provide the necessary surface area for enhanced cooling but it affects the maximum load it can handle. The machine learning algorithms aid in preparing a catalog that suggests the best configurations possible for given loads. The random tree algorithm was able to provide a more comprehensive decision tree with high precision (0.97) and an accuracy of 97.2% based on the dataset which could help in avoiding many calculations, simulations, and experimental testing, hence reducing time and cost for manufacturers to manufacture spur gears with holes based only on the magnitude of torque provided from the customer. A machine learning model can have enhanced accuracy if the training set is large and diverse; however, increasing the number of parameters may or may not yield better results.

Table 6 Detailed Accuracy data (J48)

	TP rate	FP rate	Precision	Recall	F-measure	MCC	ROC area	PRC area	Class
	1.00	0.00	1.00	1.00	1.00	1.00	1.00	1.00	High torque
	0.92	0.00	1.00	0.92	0.96	0.95	0.95	0.94	Medium torque
	1.00	0.03	0.96	1.00	0.98	0.97	0.98	0.96	Low torque
Weighted average	0.98	0.01	0.98	0.98	0.98	0.97	0.98	0.96	

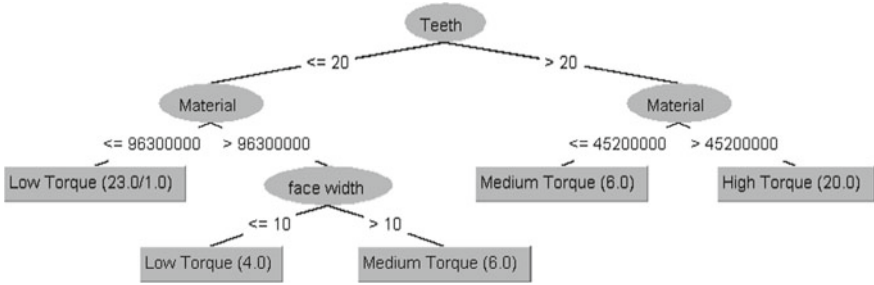


Fig. 4 Decision tree (J48)

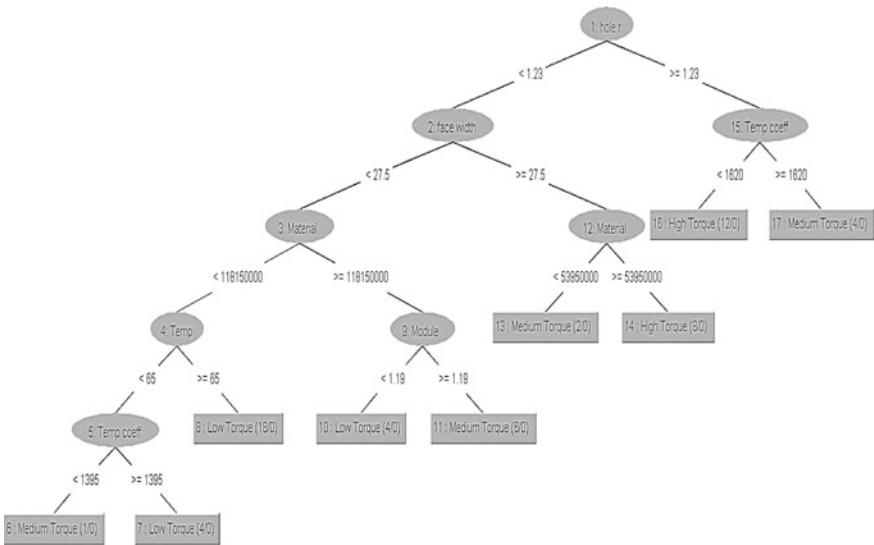


Fig. 5 Decision tree (random tree)

Table 7 Confusion matrix (random tree)

Predicted condition			Actual condition
High Torque	Medium Torque	Low Torque	
13	0	0	High torque
0	9	1	Medium torque
0	0	21	Low torque

Table 8 Detailed accuracy data (random tree)

	TP rate	FP rate	Precision	Recall	F-measure	MCC	ROC area	PRC area	Class
	1.00	0.00	1.00	1.00	1.00	1.00	1.00	1.00	High torque
	0.90	0.00	1.00	1.00	0.90	0.93	0.95	0.92	Medium torque
	1.00	0.04	0.96	0.97	1.00	0.95	0.97	0.95	Low torque
Weighted average	0.97	0.02	0.97	0.97	0.97	0.96	0.98	0.96	

References

1. T. Ramesh, K. Karthik, R. Ganesh, Design and analysis of plastics gear for heavy duty applications by FEA method. *Int. J. Mech. Eng. Technol.* **8**(7), 106–111 (2017)
2. K. Mao, W. Li, C. Hooke, D. Walton, Friction and wear behaviour of acetal and nylon gears. *Wear* **267**, 639–645 (2009)
3. N. Mehat, S. Kamaruddin, A. Othman, Modeling and analysis of injection moulding process parameters for plastic gear industry application. *ISRN Indus. Eng.* **2013**, 1–10 (2013)
4. A. Thirugnanam, J. Sathish, L. Rakesh, Contact analysis of spur gear using composite material (NYLO Cast). *Middle East. J. Sci. Res.* **20**(3), 362–363 (2014)
5. Y.K. Chen, S.N. Kukureka, C.J. Hooke, *J. Mater. Sci.* **35**, 1269–1281 (2000)
6. E. Passaglia, J.R. Knox, Viscoelastic behaviour and time-temperature relationships. *Eng. Des. Polymers*, 143–198 (1964)
7. V.M.G. Dominick, *Polymer Design Handbook* (Kluwer Academic Publications, Boston, 2000)
8. Z. Jiaying, K. Ilie, Static shear strength calculation of plastic helical gears mating with steel worm. *Int. J. Precis. Eng. Manuf.* **15**, 235–239 (2014)
9. H. Düzcükoğlu, R. Yakut, E. Uysal, The use of cooling holes to decrease the amount of thermal damage on a plastic gear tooth. *J. Fail. Anal. Prev.* **10**(6), 545–555 (2010)
10. D. Koffi, A. Bravo, L. Toubal, F. Erchiqui, Optimized use of cooling holes to decrease the amount of thermal damage on a plastic gear tooth. *Adv. Mech. Eng.* **8**(5), 1–13 (2016)
11. PSG College of Engineering, *Design Data Book* (Kalaikathir Achagam, Coimbatore, 2015)
12. H. Hasl, P.O. Liu, T. Tobie, K. Stahl and Forschungsstelle fuer Zahnraeder und Getriebebau (Gear Research Centre), Method for calculating the tooth root stress of plastic spur gears meshing with steel gears under consideration of deflection-induced load sharing. *Mech. Mach. Theor.* **111**, 152–163 (2017)
13. K. Biernacki, Selection of the optimum tooth profile for plastic cycloidal gears. *Proc IMechE Part C J Mech. Eng. Sci.* **228**(18), 3395–3404 (2014)
14. S. Rajeshkumar, S. Murugaiyan, A. Muruganandam, S. Sathishkumar, A. Kumar, Design and contact analysis of plastic spur gears using finite element analysis. *Int. J. Adv. Res. Trends Eng. Technol.* **3**, 370–375 (2016)
15. Doll, N.P., Modeling thermomechanical behavior of polymer gears. Thèse de doctorat (University of Wisconsin–Madison, Madison, WI, 2015)
16. R. Dhanasekaran, P. Senthil Kumar, S. Baskaran, Failure analysis of first stage planet gear. *Int. J. Emerg. Technol. Appl. Eng. Technol. Sci.* **3**, 476–478 (2010)
17. D. Walton, Y. Shi, A comparison of ratings for plastic gears. *Proc. Instit. Mech. Eng. Part C Mech. Eng. Sci.* **203**, 31–38 (1989)
18. S. Gupta, S. Abraham, V. Sugumaran, M. Amarnath, Fault diagnostics of a gearbox via acoustic signal using wavelet features, J48 decision tree and random tree classifier. *Indian J. Sci. Technol.* (2016)
19. G. Kaur, A. Chhabra, Improved J48 classification algorithm for the prediction of diabetes. *Int. J. Comput. Appl.* **98**, 13–17 (2014)
20. N. Bhargava, G. Sharma, R. Bhargava, M. Mathuria, Decision tree analysis on j48 algorithm for data mining. *Int. J. Adv. Res. Comput. Sci. Softw. Eng.* **3**(6), 1114–1119 (2013)
21. S.R. Kalmegh, Comparative analysis of WEKA data mining algorithm randomforest, randomtree and LADTree for classification of indigenous news data. *Int. J. Emerg. Technol. Adv. Eng.* **5**, 507–517 (2015)

Design and Analysis of Sedan Car *B*-Pillar Outer Panel Using Abirbara with S-Glass Fiber Hybrid Composites



Ramesh Babu Nallamothe and Melkamu Yigrem Yihunie

Abstract Automotive industries are struggling hard to optimize vehicle body through different ways; like shape for its aerodynamics and aesthetics, weight of materials to be used for fuel efficiency, material conservation, recyclability, and others. The century's competitive material in the industry is composite material especially natural composites are preferably based on different perspectives. As *B*-pillar is one of the critical structural support members of sedan cars, different considerations are taken to analyze and replace its outer panel with natural Nettle fiber composite. Mainly it should overcome two things; *B*-pillar must overcome the stress developed due to the system as it is a structural member and safeguard the occupant in the case of side crash. Considering these properties of the *B*-pillar, a natural fiber called Abirbara/Aleblabit/Ethiopian origin stinging nettle with S-glass hybrid composite was used to replace its outer panel with Ansys analysis. It is observed that Abirbara fiber, which can be extracted from the Abirbara plant is abundantly available in Ethiopia and is not yet used widely as composite materials. This work started with plant harvesting (collecting) and fiber extraction, which was performed through mechanical methods. The composites were prepared using chemically treated fiber with different orientations based on predetermined performance. Different mechanical properties were measured by using UTM machines and its tensile strength, compression strength, bending strength values are 153.166 MPa, 212.7 MPa, and 370 N peak load, respectively, whereas water absorption is 1.6% in 48 h. The model of the sedan car *B*-pillar panel was prepared by SpaceClaim software and analyzed for impact using Ansys software. Crush simulation of *B*-pillar panel with conventional material and composite material was computed. So the Ansys analysis shows that the energy absorption of EOSN fiber composite *B*-pillar panel is 2.61 and 0.15925 kJ for conventional materials. It is concluded that Abirbara composite can be used for *B*-pillar outer

R. B. Nallamothe (✉)

Mechanical Systems and Vehicle Engineering Department, School of Mechanical Chemical and Materials Engineering, Adama Science and Technology University, Adama, Ethiopia
e-mail: rbnallamothe@gmail.com

M. Y. Yihunie

Debre Tabor University, Debre Tabor, Ethiopia
e-mail: melkamu.yigrem@gmail.com

© Springer Nature Singapore Pte Ltd. 2021

G. S. V. L. Narasimham et al. (eds.), *Recent Trends in Mechanical Engineering*,
Lecture Notes in Mechanical Engineering,
https://doi.org/10.1007/978-981-15-7557-0_37

panel, which results in reduction of weight of the vehicle, fuel consumption, and an increase in energy absorption.

Keywords Abirbara/aleblabit plant · *B*-Pillar outer panel · Collision · Composite · EOSN fiber · EOSN–polyester composite

1 Introduction

Many automotive industries are using steel and related metals to manufacture vehicle body components due to its availability and easy of production, as the production and processing of steel are common for different applications.

The *B*-pillar of a car is the structure located between the front and rear doors of the cab. It does not only house electrical wiring and connection spots for the passenger seat belts but it also provides structural support for the cab in case of a side collision or rollover of the vehicle. Vibration generated from various sources should be considered in the design of a *B*-pillar. In this thesis work, the outer panel of the *B*-pillar was designed with low-weight composite material made up of biodegradable natural fiber and better energy absorption property.

Abirbara/Aleblabit/Ethiopian originated stinging nettle fiber is a plant from *Urtica Dioica* family, which is used as the source of fiber for domestic use (rope, whip) in rural parts of our country having comparable mechanical property (tensile strength, young's modulus, etc.) with jute and other leaf-based fibers. So far, this fiber was not common as reinforcement in the preparation of composite. In the case of domestic application, Abirbara fiber has a comparable property with jute. It is classified under the category of fibers extracted from the bast of the plant like hemp, jute, flax, etc.

The materials' weight in automotive manufacturing sector influences the fuel consumption that is directly related with the corresponding amount of emission to the atmosphere. As the weight increases, it takes even more amount of fuel, while the world fuel availability is running out beside continuous cost increment. Earth's environmental pollution is also the main issue in addition to fuel constraints. Even though there are different factors that can be mentioned as a reason for air pollution, vehicle exhaust takes maximum percentage. Out of that, weight of material used can be taken as one of the factors for high amount of emission released to the atmosphere from what it takes due to high amount of fuel consumption [1]. Natural fibers are an abundant and renewable resource, so their cost is relatively low compared with other synthetic fibers. They are eco-friendly and biodegradable and reduce the problem of solid waste production when used to replace nondegradable fillers. Natural fiber composites are a comparably strong, light-weighted materials can be used for the automobile body design and production in place of steels [2]. Natural fiber from Abirbara (Ethiopian Origin stinging nettle) that have high amount of cellulose chemical component responsible for better mechanical property is selected in this work. Stinging nettle is classified into shrub category with 30–45 species. It prefers fertile soil to grow 40 up to 120 cm in height. Stinging nettle as natural biomass,

the applications that have been developed are in livestock, medicine, cosmetics, and fibers. Nettle plants are covered with fine hairs like structures, especially in the leaves and stems. When it is touched, it releases chemicals that sting and trigger inflammation that causes redness, itching, bumps, and irritation to the skin [3].

The work focuses on the development of composite, modeling, and analysis of *B*-pillar outer panel from natural fiber composite material to replace the existing steel, literatures were reviewed related to sedan car body materials and its effect on human life, natural fibers, and its composite material property, and composites manufacturing techniques [4]. Studied that lighter materials are being developed to reduce automobile's weight for cost and emission reduction; out of those lighter materials, composite materials have been investigated for their probable use as impact energy-absorbing elements. Some of the composites that have been investigated for use in crashworthiness are alloy metallic-reinforced composites [5]. Investigated as weight is one of the basic fuel economy factors for automobile design, according to the test results, it is concluded that fuel economy improvement for weight decrement of 10% result shows in the range of 6–7% fuel economy increment [6]. Investigated as side impact of vehicles is the second most frequent types of accident, which has risk on passengers' life, composites have better crash energy absorption property than the existing material even though it is not familiar in the industry, whereas processing of the complex parts in one piece is much easier from composite. Also, by using composite materials for the *B*-pillar, reduction in weight can be achieved that leads to lesser fuel consumption.

Wild stinging nettle, binomial name, *Urtica Dioica*, is the most adaptable and abundant plant that is found in forests naturally. Nettle fiber productivity was observed that 19–21% of the stem out of which 70% are primary long fibers [7]. Ethiopian stinging nettle exhibits the following physical properties from textile production perspective such as a length of 5–75 cm, fineness 1.0–1.2 tex, diameter under $\times 400$ microscopic view 5–6 microns, a moisture content of 12.3%, and dry tenacity of 0.4–0.6 N/tex along with breaking extension of 2.0–2.5% [8]. The fiber separation methods prove the decreasing of noncellulosic ingredients in the order of mechanical, water, and chemical treatment methods [9]. Concluded that composites have significant economic potential when considering emerging advances in the polymer composite body-in-white design against the mild-grade steel body currently on the road. With the significant implications of a polymer composite body for vehicle light weighing and thereby improved fuel efficiency, these results come at a time when they are particularly validated.

Energy conservation and environmental pollution become a serious concern around the world; European and many developed countries are researching and developing electric vehicles to reduce fuel consumption and exhaust emissions. They study how to increase the battery capacity to increase vehicle mileage. However, electric vehicle has an outstanding problem in use that the car is very heavy because of the battery weight, charge capacity, and body structure, so that electric vehicle mileage decreases [10]. *B*-pillar of a car is the structure located between the front and rear doors of the cab. According to this work, the existing position of *B*-pillar in a vehicle's chassis, the upper and inner railings act as fixed members as they are fixed to roof

and bottom chassis of the vehicle. Thus, to carry out modal analysis on *B*-pillar, we choose to treat the upper and lower railings as fixed supports. The weight of the composite *B*-pillar is reduced drastically when compared with the existing mild steel *B*-pillar. The gross weight of the composite *B*-pillar is approximated to be around 2.255 kg, whereas the weight of the present *B*-pillar made of steel is 6.343 kg. The weight of the composite is 64.207% less when compared with the steel *B*-pillar [11]. The important modification done by alkaline treatment is the disruption of hydrogen bonding in the network structure, thereby increasing surface roughness. The treatment changes the orientation of the highly packed crystalline cellulose order, forming an amorphous region. It has been reported that alkaline treatment has two effects on the fiber [12]:

- It increases surface roughness resulting in better mechanical interlocking.
- It increases the amount of cellulose exposed on the fiber surface.

Chemical treatments reduce some portion of hemicelluloses, lignin, pectin, wax, and oil-covering materials. Thus fiber surface became more homogeneous due to the elimination of microvoids. Stress transfer capacity between alternate cells improved and increases effective fiber surface area for good adhesion with matrix. It decreases the hydrophilic nature of fiber by raising its cellulose content and stabilized the material. Natural fiber-reinforced polymer composites have beneficial properties such as low density, less expensive, and reduced solidity when compared with synthetic composite products, thus providing advantages for utilization in commercial applications (automotive industry, buildings, and constructions); companies are shifting to composites to design different components like Ford (Mondeo CD 162, Focus) use composite for floor plates, door inserts, door panels, *B*-pillar, and boot liner [13]. Natural fibers have the potential to reduce vehicle weight. The use of natural fibers can minimize harmful pollutants, and their eventual breakdown is environmentally benign. Natural fibers emit less CO₂ when they break down than is absorbed during plant growth. Fiber-producing crops are easy to grow [14]. Zinc borate shows excellent fire resistance performance and can be therefore widely used in polymer, rubber, fiber, paint, and ceramic industries [15, 16].

2 Materials and Methods

2.1 Materials

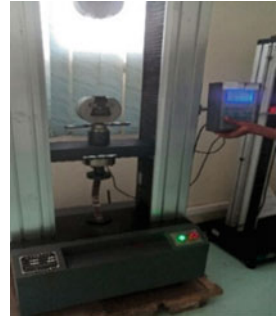
The materials used in this work starting from Ethiopian origin stinging nettle plant collecting up to final *B*-pillar analysis were discussed. In this composite materials' work, two main composite components were considered. Those are reinforcements and the matrix constituents. Abirbara plant/EOSN/and S-glass fibers (synthetic fibers), resin, wax, release agent, gel coat, and miscellaneous items are used. The equipment used are weighing machine, cloth (for swapping a wax applied

Fig. 1 Tensile test

plat), stirrers, metal plate, weighting materials, measuring cylinder, universal testing machine.

UTM test machines were used in this work to conduct different mechanical properties of prepared composite material are indicated in Figs. 1, 2, 3 and 4.

Fig. 2 Impact tester**Fig. 3** Bending test

Fig. 4 Compression test

2.2 Methods

Abirbara/Ethiopian origin stinging nettle was collected after drying on the field, which takes around 5–6 months after germination. Its height measures from 2 to 3 m depending on the soil fertility. Plant harvesting process can be accomplished using different equipment, in this work traditional farm machinery like Machid, small axe, etc., were used. Figure 5 shows the collected Ethiopian origin stinging nettle.

After collection, two approaches can be used to extract the fiber:

- The first one is soaking Abirbara stem with its bast into the water at least for 10–12 h; as the bast becomes easy to remove then separates the bast of Ethiopian origin stinging nettle from the stem and process it for better fiber quality. This process makes the fiber extraction easy and protects fiber from breakdown but some of the fibers are destroyed.
- The second method is first crush the stem and then collect the bast from weak internal structure of the hollow plant as shown in Fig. 6.

The time requirement to soak Abirbara fiber in NaOH depends on the concentration of base with a concentration ranges from 2% up to 10% in distilled water. So time varies from 2 to 8 h by observing the physical change takes place in the solution. As unwanted components of the fiber are removed, it was washed with distilled and freshwater again and again until the base/NaOH component is removed.

Fig. 5 Ethiopian origin stinging nettle

Fig. 6 Steam and fiber of the plant



Fig. 7 Different fiber arrangements



3 Result and Discussion

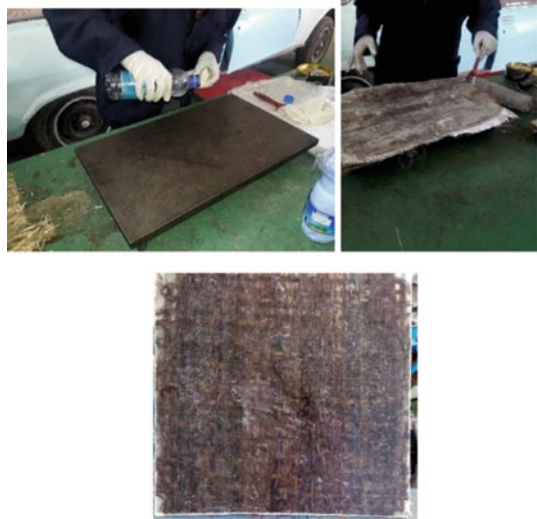
3.1 Composite Preparation

Fiber orientation determines the ability of fibers to withstand against effective loads, and with increasing the orientation angle; the fiber's load-carrying ability decreases as the angle between load and fiber direction increases, which leads to the occurrence of separation between polymeric matrix (general purpose resin) and reinforcement fibers (Abirbara fiber + S-glass fiber) as a result to detach bonding between matrix and fibers, where the forces stretched the matrix and causing the material to shear at the interface between matrix and fibers and this leads to failure. Different fiber arrangements are shown in Fig. 7.

3.2 Hand Layup Process

Out of different processes used to develop FRC, hand lay-up technique was used in this work by compromising its drawback as shown in Fig. 8. A steel mold of 410 mm length by 410 mm width metal plate from Adama Science and Technology University, power train lab was used for hand lay-up process.

To have the resin and fiber composition, it is possible by subtracting the summation of fibers' weight from the composites' weight. As the measurement shows that nettle fiber weights 215.5 g and a single layer of S-glass woven is 68.0 g in one plat production. While in this composite plat production with a frame of 400 mm by 300 mm, two layers of glass fiber one in the bottom and the other one in the top are used. So the total mass of fibers used for this sample becomes $215.5 \text{ g} + 2(68.0 \text{ g})$

Fig. 8 Hand lay-up process

= 351.5 g while the matrixes weight can be determined by subtracting from plate weight that measures 1217 g is 865.5 g. Finally, density can be calculated as follows $\rho = (1217 \text{ g} / ((40 \times 39.5 \times 0.545) \text{ cm}^3)) = 1.4133 \text{ g/cm}^3$.

Generally, the composite preparation was carried out through following steps.

1. The purified and dried EOSN fiber was arranged according to the required fiber orientation, in this work, three fiber orientations with better performance (0° , 90° , and $0^\circ/90^\circ$ woven) are used based on literatures.
2. S-glass fiber woven was prepared for the size of metal surface plate (mold).
3. Determine the weight of nettle fiber and S-glass fiber to be used.
4. Polyester resin is mixed with 1% of catalyst and steered for 15 min., which helps to minimize the composites' curing time.
5. Apply PVA and wax on the mold surface by using clean cloth, respectively.
6. The first single S-glass layer is placed on the mold then matrix is applied and it was dispersed well with the help of brushes and roller. After checking as the resin spreads well, prepared EOSN fiber orientation layer over the resin. Again apply the matrix and swab very well to avoid trapped air with natural fiber to prevent the formation of porosity, which initiates crack for failure. The third layer was added with similar fashion as previously.
7. Finally, load is applied to remove excess resin and attain the minimum thickness of the composite material.

3.3 Testing and Analysis

Test specimens were prepared as per the ASTM standards for using the band saw machine available in the country. The characterization of the mechanical properties

was as per ASTM standards, so for tensile test ASTM D3039, for compression test ASTM D695, and for flexural test ASTM D6272. Each test was verified with an average of three samples for each of three fiber orientations (0°, 90°, and 0°/90° woven).

The average value of tensile strength of three types of fiber orientation after applying correction factor is shown in Fig. 9. So the B-pillar can have a tensile strength of 153.166 MPa.

The comparison of peak load, deformation, and compression strength of those different types of fiber orientation (0°, 90°, and 0°/90° woven) taken from UTM machine display is shown in Fig. 10. Compression test results for different fiber orientations are shown in Fig. 11. Bending test comparison, impact test comparison, and water absorption rate are shown in Figs. 12, 13, and 14, respectively.

Total strain energy (toughness) U_{total} , that a B-pillar panel can absorb can be determined as in Eqs. (1) and (2) by multiplying maximum strain energy with its volume for composite material and steel, respectively.

For EOSN composite;

$$U_{total} = U_{max} \times B\text{-pillar volume}$$

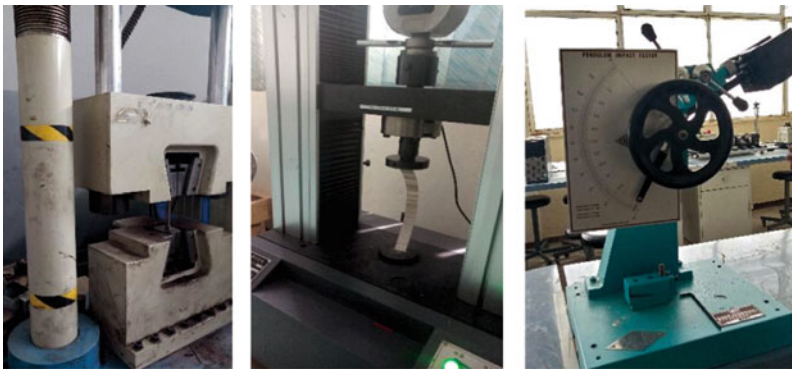
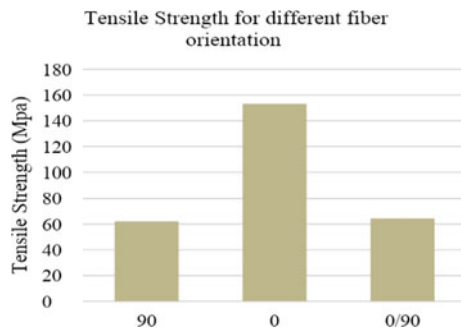


Fig. 9 Test machines

Fig. 10 Tensile strength of different fiber orientations



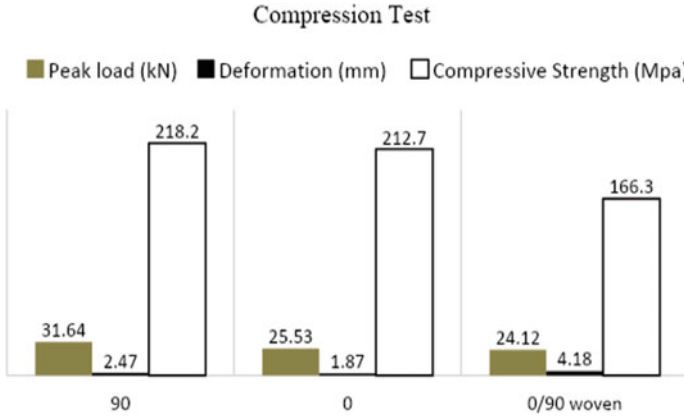


Fig. 11 Compression test results for different fiber orientations

Fig. 12 Bending test comparison

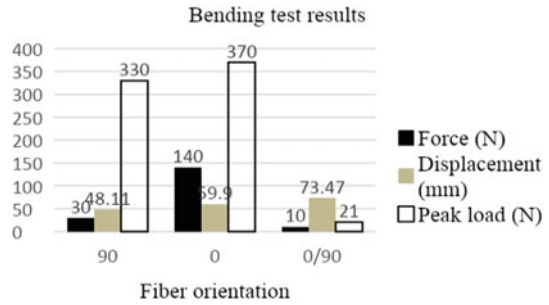


Fig. 13 Impact test comparison

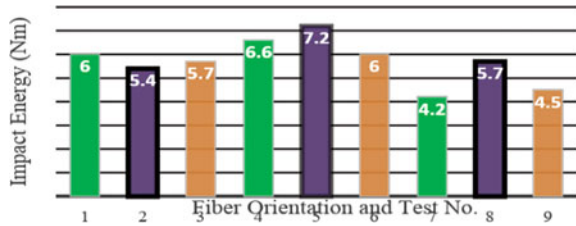
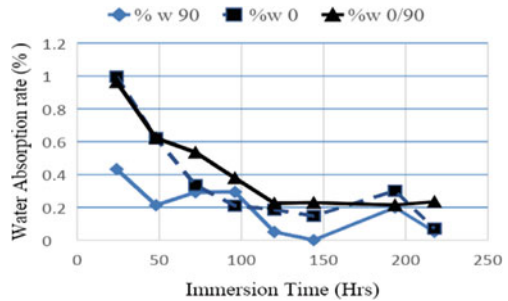


Fig. 14 Water absorption rate



$$\begin{aligned}
 &= (60556 \text{ MPa}) \times (0.000398 \text{ m}^2) \\
 U_{\text{total,EOSN}} &= 0.00261 \text{ MN m} = 2.61 \text{ KN m} \tag{1}
 \end{aligned}$$

For steel component;

$$\begin{aligned}
 U_{\text{total}} &= U_{\text{max}} \times B \text{ - pillar volume} \\
 &= (0.4 \text{ MPa}) \times (0.00039812 \text{ m}^2) \\
 U_{\text{total,steel}} &= 0.00015925 \text{ MN m} = 0.15925 \text{ KN m} \tag{2}
 \end{aligned}$$

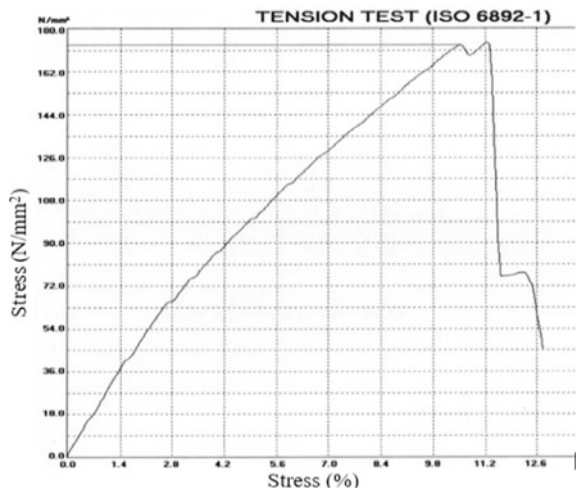
Generally, EOSN composite newly designed B-pillar outer panel can absorb 2.61 kJ of energy out of vehicles colliding energy of 111.1 kJ, whereas the existing outer panel absorbs 0.15925 kJ energy out of 111.4 kJ colliding energy due to its speed and mass. The model of the B-pillar and tensile test results are shown in Figs. 15 and 16, respectively.

In this work, it is tried to compare the energy absorption property, weight reduction, and others of Ethiopian origin stinging nettle fiber and S-glass fiber with

Fig. 15 Model of the B-pillar



Fig. 16 Tensile test result



polyester resin matrix composite with carbon steel (conventional material used to manufacture *B*-pillar shown in Fig. 17).

The energy summary graph (shown in Fig. 18) that the kinetic energy of the *B*-pillar decreases upon the collision, whereas its internal energy is going to increase up to rebounding.

Fig. 17 *B*-pillar analysis setup

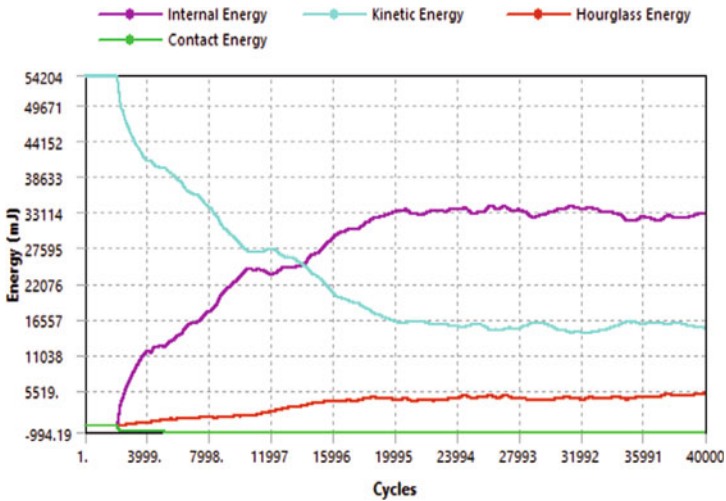
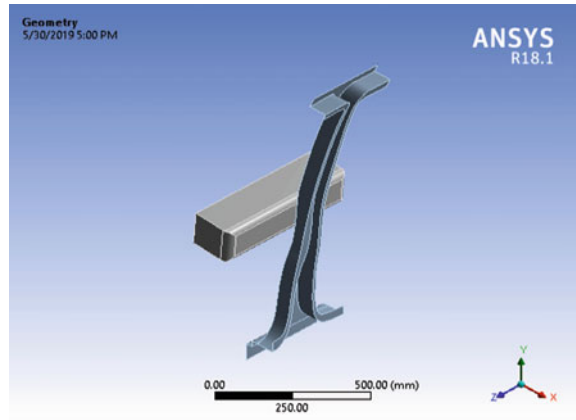


Fig. 18 EOSN composite energy summary graph

4 Conclusion

- B-pillar of sedan car is a structural member with three components; internal panel, reinforcement (main part), and outer panel. Outer panel of B-pillar was designed to replace with natural fiber composite material to enhance the vehicles' performance.
- Nettle is a plant that has more than 40 species in the world and did not study in detail yet. Ethiopian origin stinging nettle has a fiber.
- Three fiber orientations (0° , 90° , and $0^\circ/90^\circ$) nettle and S-glass layer with polyester resin composite are conducted in this thesis work.
- 0° fiber-oriented composite has a tensile strength of 153.166 MPa, whereas 90° fiber-oriented composite has 62.1 MPa and $0^\circ/90^\circ$ woven has 64.367 MPa.
- For compressive mechanical property, 0° and 90° fiber-oriented composites have better strength with 212.7 MPa and 218.2 MPa, respectively, whereas $0^\circ/90^\circ$ has a strength of 166.3 MPa. Bending test also conducted and 0° fiber-oriented composite deforms up to 59.9 mm at a peak load of 370 N.
- The weight difference within 217.5 h immersion in tap water gives a weight difference of 0.2244 g, 0.4801 g, and 0.5729 g for 90° , 0° , and $0^\circ/90^\circ$ woven, respectively.
- Abirbara composite of 0° was preferable with an average of 153.166 MPa tensile strength and 212.7 MPa compression strength to design the panel. The software analysis was done based on these values. The energy absorption of composite material B-pillar outer panel can absorb 2.61 kJ of energy out of vehicles' collision energy of 111.1 kJ, whereas the existing outer panel absorbs 0.15925 kJ energy out of 111.4 kJ collision energy due to its speed and mass.

Acknowledgments We are thankful to Adama Science and Technology University for giving us the opportunity to work on this title.

References

1. S.A. Valerievich, Advanced materials of automobile bodies in volume production. *European Transport/Trasporti Europei* **56**(10), 1–10 (2014). ISSN 1825–3997
2. M.R. Sanjay, G.R. Arpitha, L.L. Naik, K. Gopalakrishna, B. Yogesha, Applications of natural fibers and its comp sites: an overview. *Nat. Resour.* **7**(3), 108–114 (2016). <https://doi.org/10.4236/nr.2016.73011>
3. N.P.G. Suardana, I.A. Suryawan, I.S. Winaya, I.B. Suyasa, T.T. Nindhia, Study of stinging nettle (*urtica dioica* L.) fibers reinforced green composite materials, in *7th International Conference on Key Engineering Materials* (ICKEM, 2017): <https://doi.org/10.1088/1757-899x/201/1/012001>, 1–7
4. A.E. Ikpe, I.B. Owunna, P. Satope, Design optimization of a B-pillar for crashworthiness of vehicle side impact. *J. Mech. Eng. Sci.* **11**(2), 2693–2710 (2017). ISSN (Print): 2289-4659; e-ISSN: 2231-8380

5. Alma Hodzic, Robert Shanks, *Natural Fiber Composites Materials, Processes and Properties* (Woodhead Publishing Limited, Cambridge, 2014)
6. T. Ashokkumar, B. Hailu, A new accident proof material design for B-pillar of a car. *Int. J. ChemTech Res.* CODEN (USA): IJCRGG **11**(07), 01–11. ISSN: 0974-4290, ISSN (Online):2455-9555 (2018)
7. K. Rajasekar, Experimental testing of natural composite material. *IOSR J. Mech. Civil Eng.* (IOSR-JMCE) **11**(2) Ver. III, 1–9 (2014). e-ISSN: 2278-1684, p-ISSN: 2320-334X
8. G.A. Tadele, Separation and characterization of Ethiopian origin nettle fiber. *Int. J. Eng. Res. Technol.* (IJERT) **5**(03), 259–262 (2016). ISSN: 2278-0181
9. M. Kumaresan, S. Sathish, N. Karthi, Effect of fiber orientation on mechanical properties of sisal fiber reinforced epoxy composites. *J. Appl. Sci. Eng.* **18**(3), 289–294 (2015). <https://doi.org/10.6180/jase.2015.18.3.09>
10. M.N.M. Ansari, A review on natural fiber reinforced polymer composite and its applications. *Hindawi Publ. Corporation Int. J. Polym. Sci.* **2015**, 1–15 (2015). Article ID 243947
11. B.D. Patil, S. Joglekar, Vibration analysis of composite reinforced B-pillar used in automobiles. *Int. J. Innovative Res. Sci. Eng. Technol.* **6**(7), 2319–8753. ISSN(Online). <https://doi.org/10.15680/ijirset.2017.0607222>, 14242–14250
12. C.C. Ojukwu Martins chubuiket, Study on chemical treatments of jute fiber for application in natural fiber reinforced composites (NFRPC). *Int. J. Adv. Eng. Res. Sci.* (IJAERS) **21**–26 (2017)
13. K. Sardar, Characterization and investigation of tensile test on kenaf fiber reinforced polyester composite material. *Int. J. Recent Dev. Eng. Technol.* **2**(6)104–112 (2014). ISSN 2347-6435(Online)
14. L. Cioara, Nettle fiber (*Urtica Dioica*), Between Myth and Reality. *Buletinul AGIR nr. 3/2016 iulie-septembrie*, 19–25 (2016)
15. B.Z. Dholakiya, *Use of Non-Traditional Fillers to Reduce Flammability of Polyester Resin Composites* (Texas State University, San Marcos, Texas, USA, 2009)
16. D.W. Negera, Dr. J. Bhaskaran, I. Ilmi, Dr. R.B. Nallamotheu, Characteristics of hybrid composite made of false banana fiber and sisal fiber. *Int. J. Eng. Adv. Technol* (IJEAT) **9**(2) (2019). Scopus. ISSN: 8958

Design and Analysis of Shock Absorber



N. Ankitha and M. R. S. Rupa Sri

Abstract Shock absorber is a mechanical device designed to smooth out or damp shock impulse, and dissipate kinetic energy. In this work, suspension system is designed and a 3D model is created using CATIA V5R21. Structural analysis is done on the shock absorber by varying different spring materials. Spring materials are spring steel, phosphorus bronze, beryllium copper, and titanium alloy. To validate the strength of the model, the structural analysis on the helical spring is done. The analysis is done by considering loads, bike weight, and single, double riding. Finally, comparison is done for different materials to verify which material suits for spring in shock absorber.

Keywords Impulse · Shock absorber · Helical spring

1 Introduction

A shock absorber or damper is a mechanical device designed to smooth out or damp shock impulse and dissipate kinetic energy.

Pneumatic and hydraulic shock absorbers commonly take the form of a cylinder with a sliding piston inside. The cylinder is filled with a fluid (such as hydraulic fluid) or air. This fluid-filled piston/cylinder combination is a dashpot [1].

The shock absorbers' duty is to absorb or dissipate energy. Shock absorbers are an important part of automobile and motorcycle suspensions, aircraft landing gear, and the supports for many industrial machines. Large shock absorbers have also been used in structural engineering to reduce the susceptibility of structures to earthquake damage and resonance [2]. A transverse mounted shock absorber, called a yaw damper, helps keep railcars from swaying excessively from side to side and are

N. Ankitha (✉) · M. R. S. Rupa Sri
CVR College of Engineering, Hyderabad, India
e-mail: graceankitha@gmail.com

M. R. S. Rupa Sri
e-mail: rupamada4@gmail.com

important in passenger railroads, commuter rail, and rapid transit systems because they prevent railcars from damaging station platforms [3].

A shock absorber is designed to smooth out a sudden shock impulse and dissipate kinetic energy. Shock absorbers are an important part of a vehicle's suspension. In a vehicle, it will reduce the effect of traveling over any rough ground. If there were no shock absorbers, the vehicle would just have a very bouncy ride, as energy is stored in the springs and then released to the vehicle.

2 Experimental Details

A shock absorber contains five components/parts, they are

- Upper mount: It connects shock absorber to vehicle chassis, and it supports the vehicle weight.
- Lower mount: It connects shock absorber to axle, near the wheel.
- Spring: A suspension spring is an element which absorbs shocks from the road surface and later gets dampened with the help of shock absorber.
- Oil pad: It dissipates heat energy through fluid.
- Rod: It connects all the above parts.

2.1 Materials Used

Spring steel: Spring steel is a name given to a wide range of steels used in the manufacture of springs.

Copper alloy: Beryllium copper (BeCu) also known as copper beryllium (CuBe), beryllium bronze and spring copper, is a copper alloy with 0.5–3% beryllium and sometimes other elements.

Titanium alloy: Titanium alloys are metals that contain a mixture of titanium and other chemical elements. Such alloys have very high tensile strength and toughness (even at extreme temperatures) [3].

Phosphorus bronze: Phosphor bronze is an alloy of copper with 0.5–11% of tin and 0.01–0.35% phosphorus.

3 Methodology

The objective of this work is to design the components by considering different configurations in terms of different materials [1, 3, 4].

- Build the CATIA model of all the individual components of shock absorber by using CATIA V5 R21.

- Assemble the modeled components using CATIA V5 R21.
- Perform structural analysis of the model in ANSYS WORKBENCH 17.2 using spring steel, copper alloy, titanium alloy, and phosphorus bronze.

3.1 Design Calculations for Spring

Material: Steel (modulus of rigidity) (G) = 41,000 N/mm²

Mean diameter of a coil (D) = 62 mm

Diameter of wire (d) = 8 mm

Total no. of coils (n_1) = 18

Height (h) = 220 mm

Outer diameter of spring coil (D_0) = $D + d = 70$ mm

No. of active turns (n) = 14

Weight of bike (w) = 125 kgs

Net weight of one person = 75 Kgs

Weight of two persons = $75 \times 2 = 150$ Kgs

Weight of bike + persons = 275 Kgs

Rear suspension = 65%

65% of 275 = 165 Kgs

Considering dynamic loads, it will be double (W) = 330 Kgs = 3234 N

For single shock absorber weight = ($w/2$) = 1617 N = (W)

Spring index[Ⓞ] = $7.75 = 8$

Solid length (L_s) = $n_1 \times d = 18 \times 8 = 144$ mm

Free length of spring (L_f) = solid length + maximum compression + clearance
between adjustable coils (L_f) = $144 + 282.698 + 0.15 \times 282.698$

(L_f) = 469.102

Spring rate (K) = 5.719

Pitch of coil, Stresses in helical springs (P) = 26

Maximum shear stress induced in the wire (τ) = 499.519 N/mm²

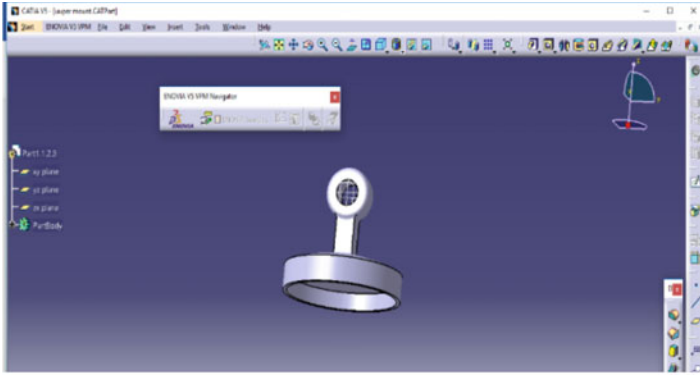
Values of buckling factor (KB) = 0.05 (for hinged and spring)

The buckling factor for the hinged end and built-in end springs

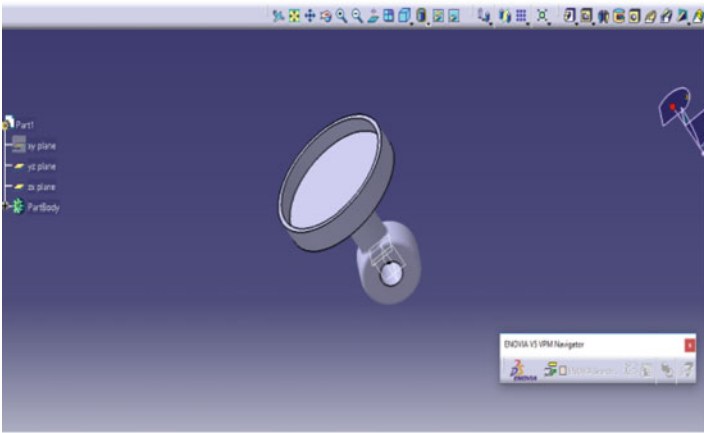
(W_{cr}) = $5.719 \times 0.05 \times 469.102 = 134.139$ N

3.2 Modeling of Shock Absorber Design in CATIA

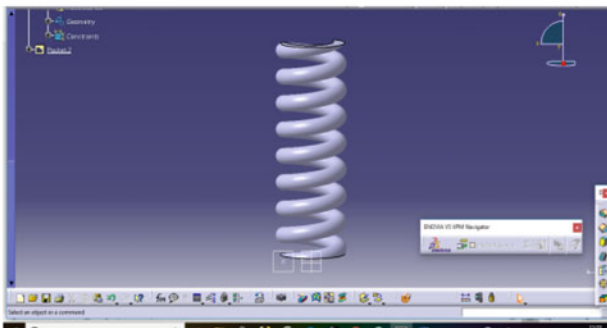
Figure 1a–f show the Modeling Of Shock Absorber Design in CATIA



(a) Upper Mount

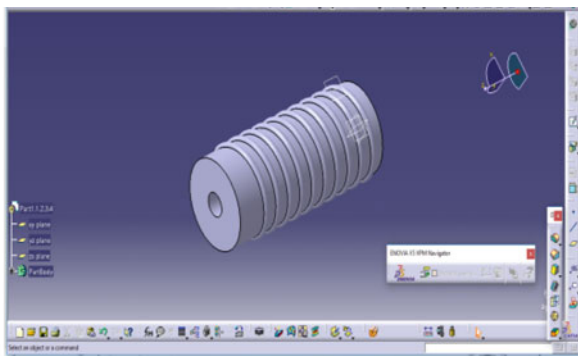


(b) Lower Mount

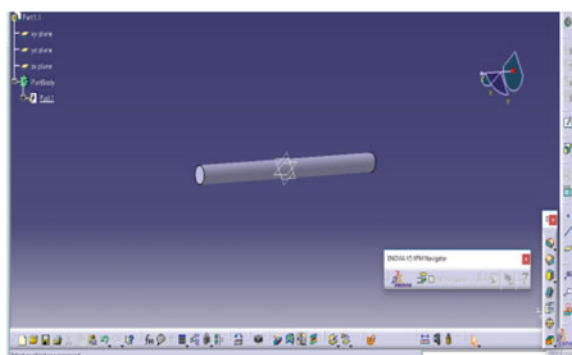


(c) Spring

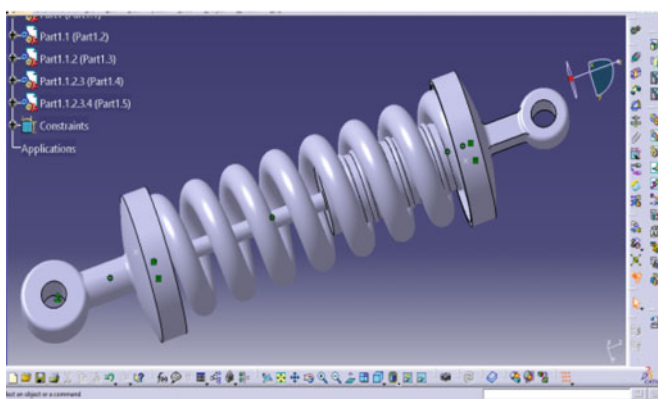
Fig. 1 a Upper mount. b Lower mount. c Spring. d Oil pad. e Rod. f Assembling all the parts



(d) Oilpad



(e) Rod



(f) Assembling all the parts

Fig. 1 (continued)

Table 1 Material properties

S. No.	Material	Young's modulus (N/m ²)	Density (Kg/m ³)	Poisson's ratio
1	Spring steel	202×10^9	7820×10^6	0.292
2	Copper alloy	130×10^9	8100×10^6	0.285
3	Titanium alloy	102×10^9	4850×10^6	0.3
4	Phosphorus bronze	103×10^9	8160×10^6	0.34

3.3 Analysis of Shock Absorber

Material used for the analysis of the structure [5]:

The shock absorber CATIA model is converted to “iges” format to import in the ANSYS workbench software; after importing the geometry, four different materials are assigned; they are Spring steel, Copper alloy, Titanium alloy, and Phosphorus bronze.

3.4 Material Properties

Material Properties are tabulated below (Table 1).

After assigning all the material properties such as Young's modulus and Poisson's ratio, the part undergoes model file where meshing is done. [1, 2]

The model is divided into finite pieces called nodes. Two nodes are connected by a line called Element. This network of elements together is called a Mesh. The boundary conditions are applied on the nodes and elements.

Generate the mesh of the imported component as shown in Fig. 2a, b.

3.5 Load Calculations

Weight of bike (w) = 125 Kgs

Let weight of one person = 75 Kgs

Weight of two persons = $75 \times 2 = 150$ Kgs

Weight of bike + persons = 275 Kgs

Rear suspension = 65%

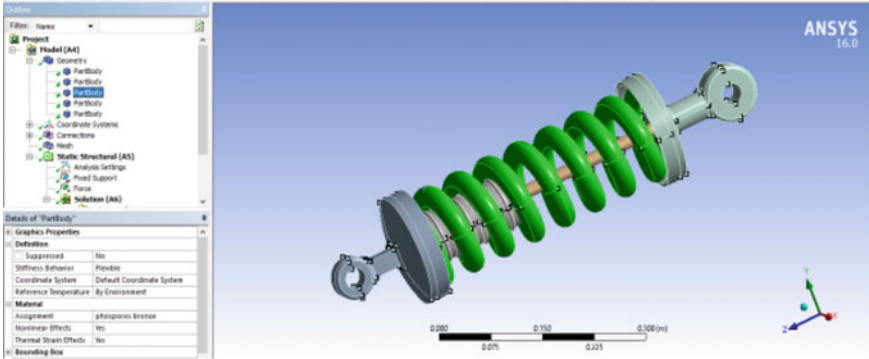
65% of 275 = 165 Kgs

Considering dynamic loads, it will be double (W) = 330 Kgs = 3234 N

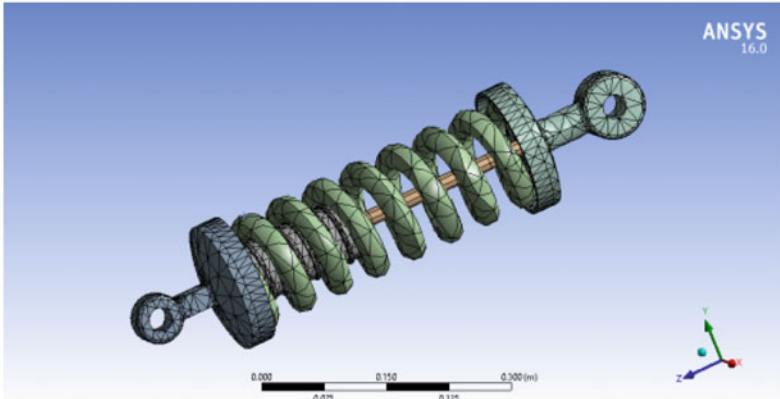
For single shock absorber weight = ($w/2$) = 1617 N = (W)

Insert the Fixed support at one end and force of 1617 N at another end as shown in Fig. 3a-l.

By applying the above load, the deformations and stress values are noted for different materials [4].



(a) Meshed part



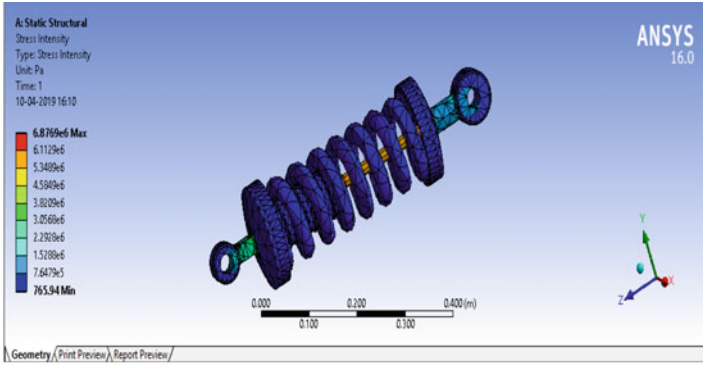
(b) Meshed part

Fig. 2 a Meshed part. b Meshed part

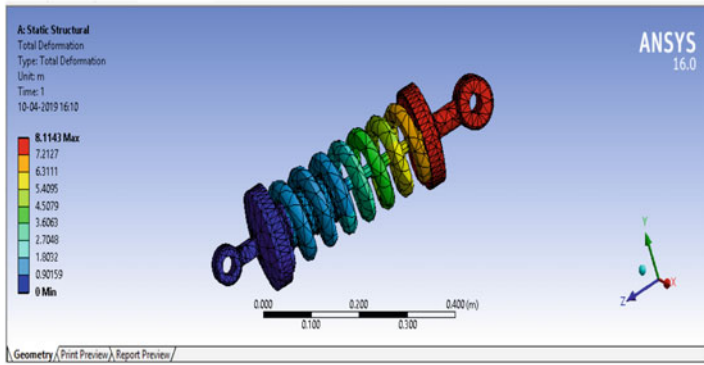
4 Results and Discussion

The structural analysis on the helical spring is done by varying different spring materials like spring steel, titanium alloy, copper alloy, and Phosphorus bronze.

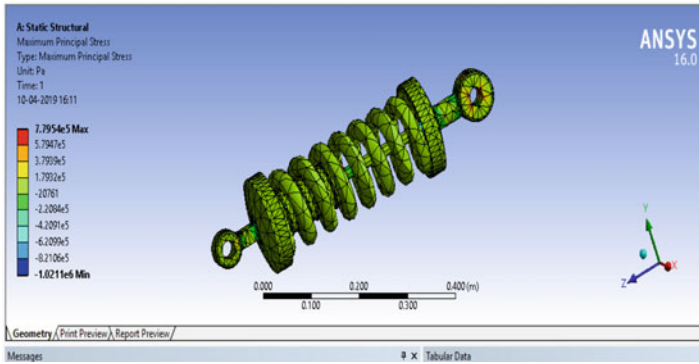
The stress intensity factor is used in fracture mechanics to predict the stress state near the tip of a crack caused by a remote load or residual stresses. For a material with high total deformation value will get a low stiffness value, so we considered stress intensity values. Based on stress intensity values, Phosphorus bronze is suitable among four materials as shown Table 2.



(a) Stress intensity of spring steel

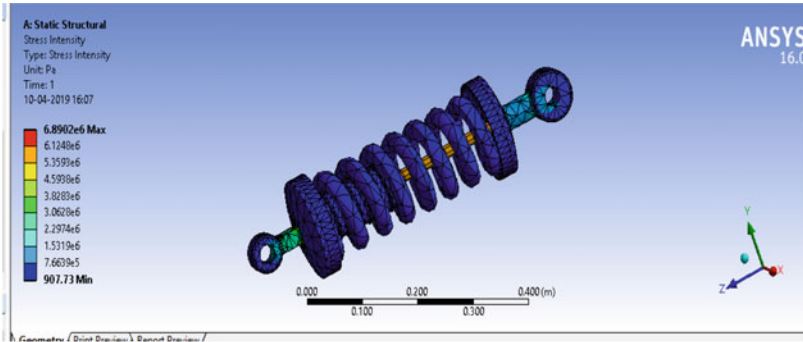


(b) Total deformation of spring steel:

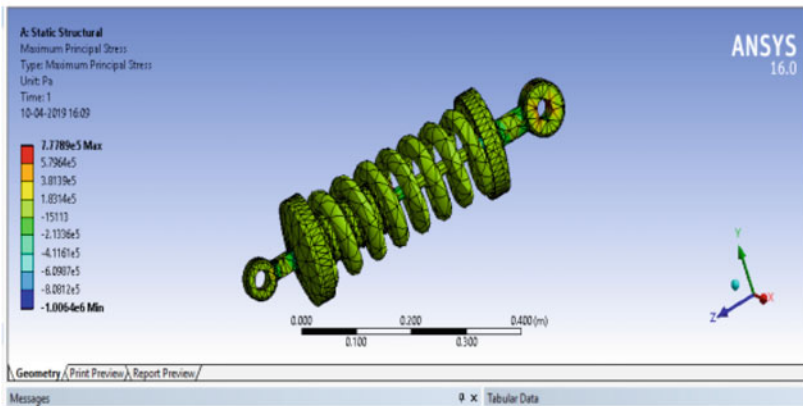


(c) Max principal stress of spring steel

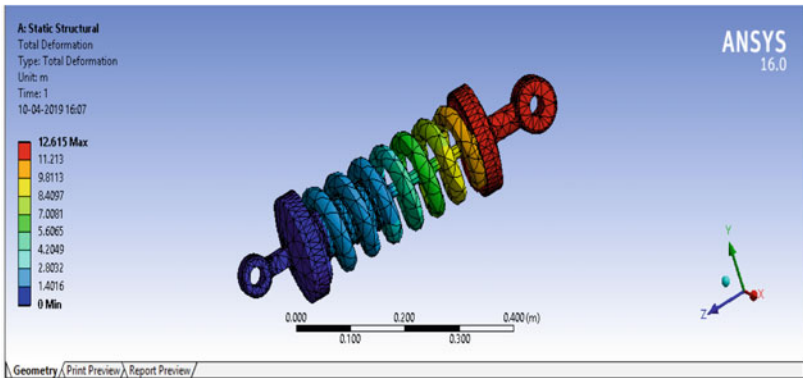
Fig. 3 a Stress intensity of spring steel. b Total deformation of spring steel. c Max principal stress of spring steel. d Stress intensity for copper alloy. e Max principal stress of copper alloy. f Total deformation of copper alloy. g Stress intensity of titanium alloy. h Max principal stress of titanium alloy. i Total deformation of titanium alloy. j Stress intensity of phosphorus bronze. k Max principal stress of phosphorus bronze. l Total deformation of phosphorus bronze



(d) Stress intensity for copper alloy

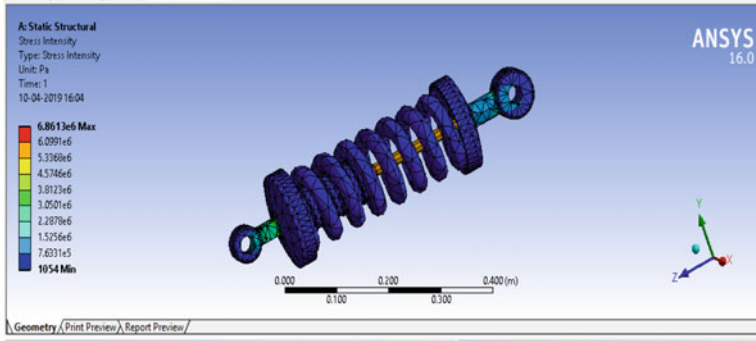


(e) Max principal stress of copper alloy

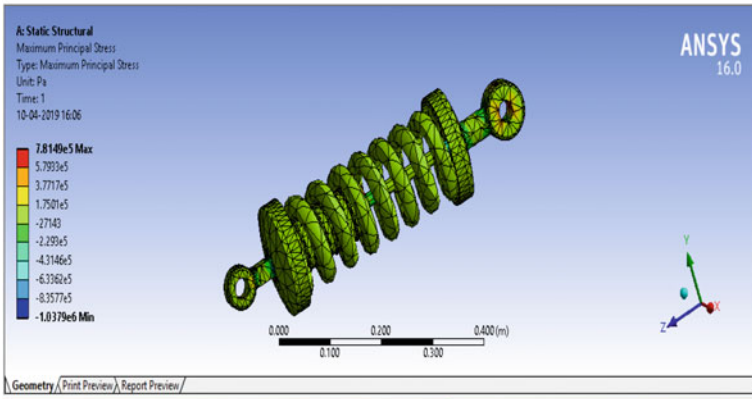


(f) Total deformation of copper alloy

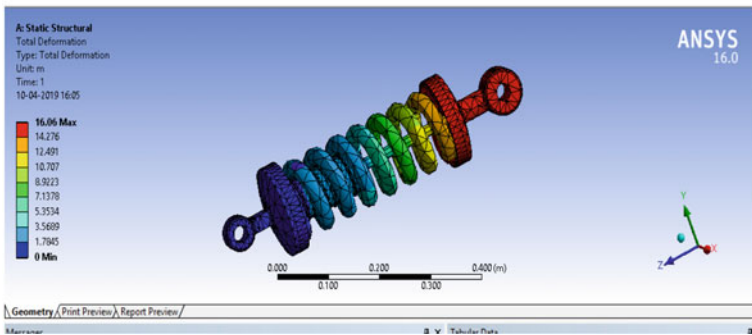
Fig. 3 (continued)



(g) Stress intensity of Titanium alloy

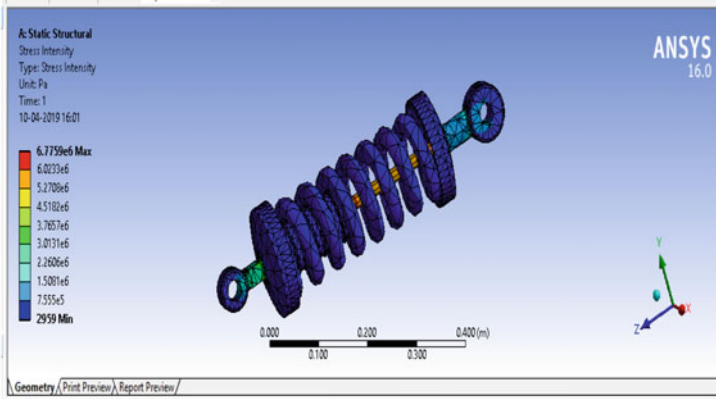


(h) Max principal stress of Titanium alloy

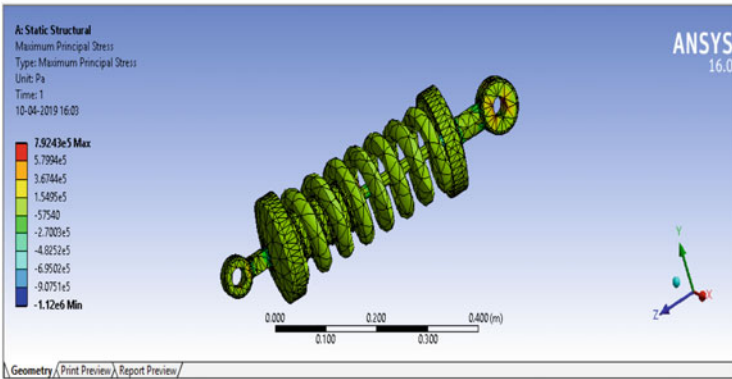


(i) Total deformation of Titanium alloy:

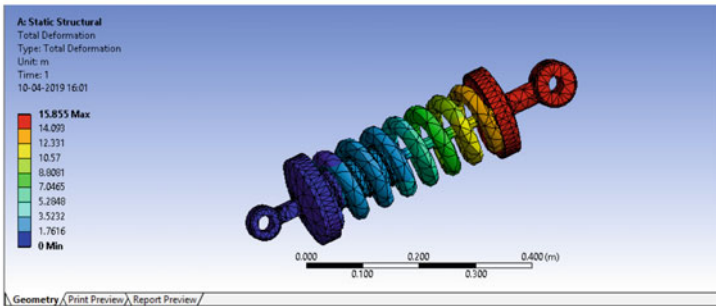
Fig. 3 (continued)



(j) Stress intensity of Phosphorus Bronze



(k) Max principal stress of Phosphorus Bronze



(l) Total deformation of Phosphorus Bronze:

Fig. 3 (continued)

Table 2 Comparison chart

S. No.	Parameters	Spring steel	Copper alloy	Titanium alloy
1	Stress intensity (N/mm ²)	6.876	6.890	6.86
2	Total deformation (m)	8.11	12.61	16.06
3	Max principal stress (N/mm ²)	0.779	0.777	0.78

5 Conclusion

In this project, shock absorber assembly is designed for a 125 kg bike.

- Modeling of shock absorber is done in CATIA V5 R21 software by using different commands and features.
- And analysis is carried out in ANSYS workbench 16.0 software by converting CATIA model file into “igs” file and importing it to ANSYS.
- Structural analysis is done on shock absorber.
- Four different materials such as Spring steel, Copper alloy, Titanium alloy, and Phosphorus bronze are applied for analysis.
- Maximum principal Stress, Total deformation, and Stress intensity of each individual material on given load condition are studied, noted, and tabulated.
- From the result table, we can conclude that Phosphorus bronze is showing least stress intensity against given load condition compared to other three materials.
- Therefore, when the availability of titanium alloy is more and cost of titanium material is affordable, then the scope of materials for springs with titanium alloy is preferable.
- Thus, Phosphorus bronze material is preferable for the future scope because of least stress intensity value and high max principal stress compared to other three materials.

References

1. K.G. Reybrouck, A non-linear parametric model of an automotive shock absorber. SAE Technical Paper Series 940869 (1994)
2. D. Kim, Analysis of hydraulic shock—absorber and implementation on the vehicle suspension systems, M.S. Thesis, Seoul National University, S. Korea (1993)
3. R. Mollica, Nonlinear dynamic model and simulation of a high pressure Monotube shock absorber using the bond graph method. M.S. Thesis, (Massachusetts Institute of Technology, Cambridge, MA, 1997)
4. S.W. Duym, R. Stiens, G.V. Baron, K.G. Reybrouck, Physical modeling of the hysteretic behaviour of automotive shock absorbers (No. 970101). SAE Technical Paper (1997)
5. R. Mollica, K. Youcef-Toumi, A nonlinear dynamic model of a Monotube shock absorber, in *Proceedings of the American Control Conference, Albuquerque* (NM, June 1997), pp. 704–708

Design and Optimization of a Two-Stage Gearbox Using GearTrax



Kalyan Sekhar, Pradyumna Dharmadhikari, Shreyash Panchal,
and Lokavarapu Bhaskara Rao

Abstract The ATV transmission system comprises a CVT gearbox along with the axles and hubs which in turn drives the vehicle. The gearbox coupled with CVT provides optimal torque and power at all times. This paper focuses on the design and optimization of a two-stage reduction gearbox for BAJA All-Terrain Vehicle. Based on the CVT's high- and low-end ratios and different road resistances, the required reduction ratio of the gearbox is calculated. Also, the gradeability factor and maximum acceleration required were the factors taken into account for determining the reduction ratio. Standard AGMA procedures were utilized to scrutinize the design of gears and shafts by using force equations.

Keywords Gearbox · GearTrax · HPSTC · AGMA · CVT · Shaft

1 Introduction

The conventional OEM gearboxes that are available globally do not succour to the further optimization of vehicle parameters. Available gearboxes have a higher weight to volume ratio [1]. Non-compatibility with required reduction ratio suitable for ATV in recent years evokes the need to design and optimize a custom gearbox conforming to desirable vehicle parameters.

K. Sekhar · P. Dharmadhikari · S. Panchal · L. B. Rao (✉)
School of Mechanical and Building Sciences, Vellore Institute of Technology Chennai,
Vandalur-Kelambakkam Road, Chennai, Tamil Nadu 600127, India
e-mail: bhaskarbabu_20@yahoo.com

K. Sekhar
e-mail: kalyansekhar101@gmail.com

P. Dharmadhikari
e-mail: pradyumna7598@gmail.com

S. Panchal
e-mail: panchalshreyash36@gmail.com

Centre of Gravity influences active performance variables like maximum acceleration and maximum tilting angle. The performance parameters that are taken into account consider only physical details of the vehicle, but dependency on engine power unit is non-existent [2]. Focus on the engagement of AGMA equations and design factors to foster gear model plays an indispensable role in the advancement for optimization of transmission components [3]. Recent developments in this field are assisted by the implementation of software like (KISSsoft) to handle innumerable iterations simultaneously avoiding human errors [4]. Gears are continuously progressive mechanical design. Disposition of mathematical models to upgrade gear and its constituent parameters produces relatively augmented design [5]. Non-Dominated Sorting Genetic Algorithm technique reduces the size of the gear efficaciously, giving out maximum power without conceding strength [6].

Inferences made from the above research paper shows that utmost priority has been given for moderation of gearbox in terms of volume. However, theoretical calculations have been done using AGMA 2001 D-04 standard equations [7]. Incorporating these calculated values in GearTrax™ (ed. 2017) generates highly optimized gear model. GearTrax™ facilitates in exploiting repetitive updated usage of data for the smallest possible progress of transmission elements, providing advantageous circumstances to calculate the stresses on the Highest Point of Single Tooth Contact (HPSTC). The load sharing properties show the maximum load during contact act on HPSTC and LPSTC [8, 9]. HPSTC is principal loading point in any gear, and bending stress present at root fillet of gear is calculated using forces acting on it. Using AGMA equation and FEM (Finite Element Method), the results for both gears were verified [9–11]. Designing of shafts involves combined equation for bending and torsional loads, known as DE-Goodman equation. Iterations of the shaft are converged until the infinitesimally small value of diameter differs.

2 Torque Requirement

The anticipated driving resistance is a pertinent variable to design vehicle transmission. The four most essential factors used while calculating overall resistances are air resistance, acceleration resistance, gradient resistance and wheel resistance.

2.1 Wheel Resistance

Wheel resistance is the opposing force acting on the rolling wheel, which mainly comprises three aspects: rolling, wheel and slip. Equation (1) is used to calculate wheel resistance [12].

$$F_r = f_r * m_f * g * \cos(\alpha_{st}) \quad (1)$$

Table 1 Road resistance coefficient

Road surface	Rolling resistance coefficient (f_r)
<i>Film road surface</i>	
Smooth tarmac road	0.010
Smooth concrete road	0.011
Rough, good concrete surface	0.014
Good stone paving	0.020
Bad, worn road surface	
<i>Unmade road surface</i>	
Very good earth tracks	0.045
Bad earth tracks	0.160
Loose sand	0.150–0.300

Source Rolling resistance coefficient f_R (Automotive Transmission Fundamentals, Selection, Design and Application by Gisbert Lechner. Harald Naunheimer)

where

- F_r Wheel resistance
- f_r Coefficient for rolling resistance
- m_f Vehicle mass
- α_{st} Gradient angle

To calculate wheel resistance, rolling resistance coefficient is required, which is selected from Table 1 [12].

2.2 Air Resistance

Air tries to resist the movement of the vehicle, a backward force, which comprises pressure drag, surface resistance and induced resistance [12]. The standard air resistance is calculated from Eq. (2).

$$F_l = \rho * c_w * A * v^2 \tag{2}$$

where

- F_l Air resistance
- ρ Air density (Kg/m³)
- c_w Coefficient of drag
- a Frontal surface area of vehicle
- v Vector addition of vehicle speed and air speed

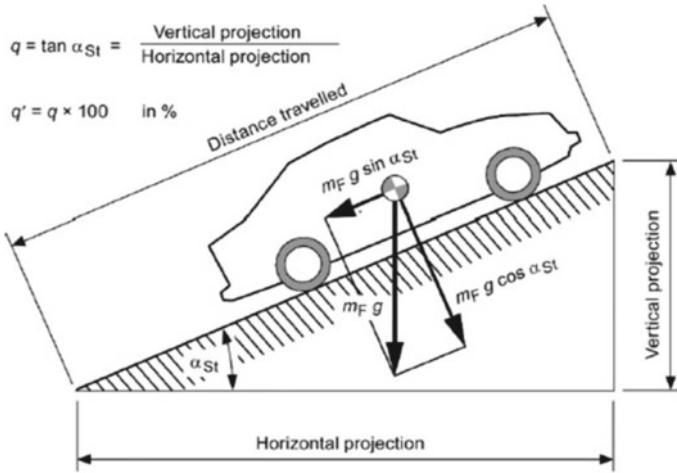


Fig. 1 Forces acting on the vehicle travelling uphill. *Source* Automotive Transmission Fundamentals, Selection, Design and Application by Gisbert Lechner. Harald Naunheimer

2.3 Gradient Resistance

Gradient resistance relates to the descending slope force and is evaluated with the mass acting on the centre of gravity. Figure 1 shows the various loads acting on vehicle [12].

As shown in Fig. 1, component of the weight of the vehicle is acted against forward motion which is gradient resistance and is calculated using Eq. (3).

$$F_{st} = m_f * g * \sin(\alpha_{st}) \tag{3}$$

where

- F_{st} Gradient resistance
- m_f Mass of the vehicle
- α_{st} Gradient angle

2.4 Acceleration Resistance

In addition to the opposing forces acting on the vehicle at constant speed, acceleration resistance acts when a vehicle accelerates. Acceleration resistance [12] is calculated using Eq. (4).

$$F_a = \lambda * m_f * a \tag{4}$$

Table 2 Parameters for/of ATV vehicle

Input parameters	Sign	Value
Coefficient of friction	f_r	0.16
Mass of vehicle (including driver)	m_f	225 kg
Gradeability angle	α_{st}	30°
Air density	ρ	1.99 kg/m ³
Coefficient of drag	c_w	0.5
Velocity of car	v	49 km/hr
Lambda	λ	1.1
Acceleration of car	a	2.83 m/s ²
Efficiency of CVT	E_1	0.88

where

- F_a Acceleration resistance
- m_f Mass of the vehicle
- a Acceleration of vehicle
- λ Rotational inertia coefficient

The parameters required to calculate the overall resistance are listed in Table 2.

Total driving resistance $F_{z,b}$ is calculated by adding Eqs. (1)–(4) represented by Eq. (5).

$$F_{z,b} = F_r + F_{st} + F_l + F_a \tag{5}$$

where

- $F_{z, b}$ Total driving resistance

Substituting the parameters, the calculated total force is 1334 N. After taking into consideration the wheel radius of 22 in. and engine torque, the optimal gear ratio is calculated to be 9. This gear ratio is divided into two-stage reduction [13].

3 Design of Gear Using AGMA Equation

Gear designing is done using standard AGMA equation, which consists of Bending and Contact stresses. Firstly, the theoretical bending stress acting on the gear teeth is calculated using AGMA. Equations (6) and (7) are utilized to calculate the theoretical bending stress [17].

$$\sigma = W^t K_o K_v K_s \frac{P_d}{F} \frac{K_m K_B}{J} \text{ (US Units)} \tag{6}$$

$$\sigma = W^t K_o K_v K_s \frac{1}{b m_t} \frac{K_H K_B}{Y_J} \text{ (SI Units)} \quad (7)$$

where

- W^t Tangential transmitted load (lbf)
- K_o Overload factor
- K_v Dynamic factor
- K_s Size factor
- P_d Transverse diametrical pitch
- F Face width of the narrower member (in mm)
- K_m Load distribution factor
- K_B Rim thickness factor
- $J(Y_J)$ Geometry factor for bending strength (which includes root fillet stress concentration factor K_f)
- (m_t) Transverse metric module

Allowable bending gives the withstanding stress of the tooth and is determined using Eqs. (8) and (9) [17].

$$\sigma_{\text{all}} = \frac{S_t}{S_F} \frac{Y_N}{K_T K_R} \quad \text{(US units)} \quad (8)$$

$$\sigma_{\text{all}} = \frac{S_t}{S_F} \frac{Y_N}{Y_\theta Y_Z} \quad \text{(SI units)} \quad (9)$$

where

- S_t Allowable bending stress, lbf/in² (N/mm²)
- Y_N Stress cycle factor for bending stress
- $K_T (Y_\theta)$ Temperature factors
- $K_R (Y_Z)$ Reliability factors
- S_F AGMA factor of safety, a stress ratio

Similarly, theoretical contact stress is required to calculate the stresses at the time of contact which are determined using Eqs. (10) and (11) [17].

$$\sigma_c = C_P \sqrt{W^t K_o K_v K_s \frac{K_m C_f}{d_p F I}} \quad (10)$$

$$\sigma_c = Z_E \sqrt{W^t K_o K_v K_s \frac{K_H Z_R}{d_{w1} b Z_I}} \quad (11)$$

where

- $C_P (Z_E)$ Elastic coefficient, $\sqrt{\text{lbf/in}^2}$ ($\sqrt{\text{N/mm}^2}$)

- $C_f (Z_g)$ Surface condition factor
- $d_p(d_{w1})$ Pitch diameter of the pinion (in mm)
- $I (Z_I)$ Geometry factor pitting resistance

Allowable contact stress is important to know the maximum contact stress limit to prevent pitting, and is calculated using Eqs. (12) and (13) [17].

$$\sigma_{c,all} = \frac{S_c Z_N C_H}{S_H K_T K_R} \tag{12}$$

$$\sigma_{c,all} = \frac{S_c Z_N Z_W}{S_H Y_\theta Y_Z} \tag{13}$$

where

- S_c Allowable contact stress, lbf/in² (N/mm²)
- Z_N Stress cycle life factor
- $K_T (Y_\theta)$ Temperature factors
- $K_R (Y_Z)$ Reliability factors
- S_H is the AGMA factor of safety, a stress ratio

Factors such as dynamic effect, geometry, load distribution, rim thickness, temperature inside gearbox, size and reliability factors are required to determine contact and bending stress using AGMA.

Overload Factor (K_a)

The overload factor (K_o) is used for shock load eventuated during dynamic conditions. Table 3 shows the permissible values for overload factor [17].

Dynamic Effect Factor (K_v)

Dynamic effect factor (K_v) takes into consideration the effect on gear tooth when subjected to varying speed and load conditions. The dynamic factor is calculated from Eqs. (14) and (15) [17].

$$K_v = \left(\frac{A + \sqrt{V}}{A} \right)^B \quad V \text{ in ft/mm} \tag{14}$$

Table 3 Characteristic overload factor

Character of prime mover	Character of load on driven machine			
	Uniform	Light shock	Medium shock	Heavy shock
Uniform	1.00	1.25	1.50	1.75 or higher
Light shock	1.10	1.35	1.60	1.85 or higher
Medium shock	1.25	1.50	1.75	2.00 or higher
Heavy shock	1.50	1.75	2.00	2.25 or higher

Source Shigley’s Mechanical Engineering Design 9th Edition p. 758

Table 4 Overload factor values

<i>For spur gear</i>			
$Q_V = 8$	$v = 451.96$ ft/min	$A = 71.056$	$B = 0.624$
<i>For helical gear</i>			
$Q_V = 8$	$v = 160.00$ ft/min	$A = 71.056$	$B = 0.624$

$$K_V = \left(\frac{A + \sqrt{200V}}{A} \right)^B \quad V \text{ in m/s} \tag{15}$$

where A and B values are calculated from Eqs. (16) and (17),

$$A = 50 + 56(1 - B) \tag{16}$$

$$B = 0.25(12 - Q_V)^{2/3} \tag{17}$$

The quality numbers define the tolerance values for various gear sizes. For commercial gears, Q_V values vary from 3 to 7, whereas precision gears have values ranging from 8 to 12. Maximum velocity, representing the terminal points of the Q_V curve, is given by Eqs. (18) and (19).

$$(V_t)_{\max} = [A + (Q_V - 3)]^2 \text{ ft/min} \tag{18}$$

$$(V_t)_{\max} = \frac{[A + (Q_V - 3)]^2}{200} \text{ m/s} \tag{19}$$

The selected values for spur and helical gear are mentioned in Table 4.

Size Factor (K_s)

Size factor gives the aberrant material properties caused by its dimension irregularities. Lewis form factor is required and is selected from Table 5 [17].

Equations (20) and (21) are used to calculate size factor.

$$K_s = \frac{1}{k_b} = 1.192 \left(\frac{F\sqrt{Y}}{P} \right)^{0.0535} \quad (\text{US units}) \tag{20}$$

$$K_s = 0.904 (bm\sqrt{Y})^{0.0535} \quad (\text{SI units}) \tag{21}$$

where

Y Lewis form factor

m Module of gear

F Net face width of narrowest member

Table 5 Values of the Lewis form factor Y (these values are for a Normal Pressure Angle of 20° , full-depth teeth)

Number of teeth	Y	Number of teeth	Y
12	0.245	28	0.353
13	0.261	30	0.359
14	0.277	34	0.371
15	0.290	38	0.384
16	0.296	43	0.397
17	0.303	50	0.409
18	0.309	60	0.422
19	0.314	75	0.435
20	0.322	100	0.477
21	0.328	150	0.460
22	0.331	300	0.472
24	0.337	400	0.480
26	0.346	Rack	0.485

Source Shigley’s Mechanical Engineering Design 9th Edition p. 759

Table 6 Size Factor Parameters

<i>Spur gear</i>		
$F = 0.55 \text{ in.}$	$Y = 0.309$	$P_d = 12.7 \text{ in.}$
<i>Helical gear</i>		
$F = 0.905 \text{ in.}$	$Y = 0.309$	$P_d = 12.7 \text{ in.}$

P Diametral pitch

Size factor parameters selected for spur and helical gears are mentioned in Table 6.

Load Distribution Factor (K_h)

The modified load distribution factor (K_h) elucidates for the non-uniform distributed load across the line of contact. (K_h) is computed from Eq. (22) [17].

$$K_m = C_{mf} = 1 + C_{mc}(C_{pf}C_{pm} + C_{ma}C_e) \tag{22}$$

C_{mc} is calculated using Eq. (23).

$$\begin{aligned} C_{mc} & 1.0 \text{ for uncrowned teeth} \\ C_{mc} & 0.8 \text{ for crowned teeth} \end{aligned} \tag{23}$$

C_{pf} is obtained using Eq. (24).

$$C_{pf} = \frac{F}{10d} - 0.025 \quad F \leq 1 \text{ in.}$$

$$\begin{aligned}
 &= \frac{F}{10d} - 0.0375 + 0.0125F \quad 1 < F \leq 17 \text{ in.} \\
 &= \frac{F}{10d} - 0.1109 + 0.0207F \\
 &\quad - 0.000228F^2 \quad 17 < F \leq 40 \text{ in}
 \end{aligned}
 \tag{24}$$

C_{pm} is determined from Eq. (25).

$$\begin{aligned}
 C_{pm} &= 1 \text{ for straddle mounted pinion with } \frac{S_1}{S} < 0.175 \\
 &= 1 \text{ for straddle mounted pinion with } \frac{S_1}{S} \geq 0.175
 \end{aligned}
 \tag{25}$$

C_{ma} is calculated from Eq. (26).

$$C_{ma} = A + BF + CF^2
 \tag{26}$$

Values for A , B and C are obtained using Table 7.

$C_e = 0.8$ for assembly adjustments during gearing, or compatibility is refined by lapping, or both = 1 for other conditons.

The parameters considered for load distribution factor are mentioned in Table 8.

Rim Thickness Factor (K_b)

Rim thickness is not sufficient to provide reinforcement for the root. It often occurs that the bending fatigue is through the gear rim than at tooth fillet. The relation between rim thickness factors as calculated from the backup ratio is found out from Fig. 2 [17]. Tooth height is given in Eq. (28).

Table 7 A , B and C values for C_{ma}

Condition	A	B	$C \times 10^{-4}$
Open gearing	0.247000	0.0167	-0.765
Commercial, enclosed units	0.127000	0.0158	-0.930
Precision enclosed units	0.067500	0.0128	-0.926
Extra precision enclosed gear units	0.003060	0.0102	-0.822

Source Shigley’s Mechanical Engineering Design 9th Edition p. 759

Table 8 Parameters for load distribution factor

<i>Spur gear</i>				
$F = 0.55 \text{ in.}$	$d = 1.1417 \text{ in.}$	$C_{pf} = 0.013897$	$C_{ma} = 0.13568$	$K_m = 1.149577$
<i>Helical gear</i>				
$F = 0.9055 \text{ in.}$	$d = 1.5079 \text{ in.}$	$C_{pf} = 0.035$	$C_{ma} = 0.07858$	$K_m = 1.1135$

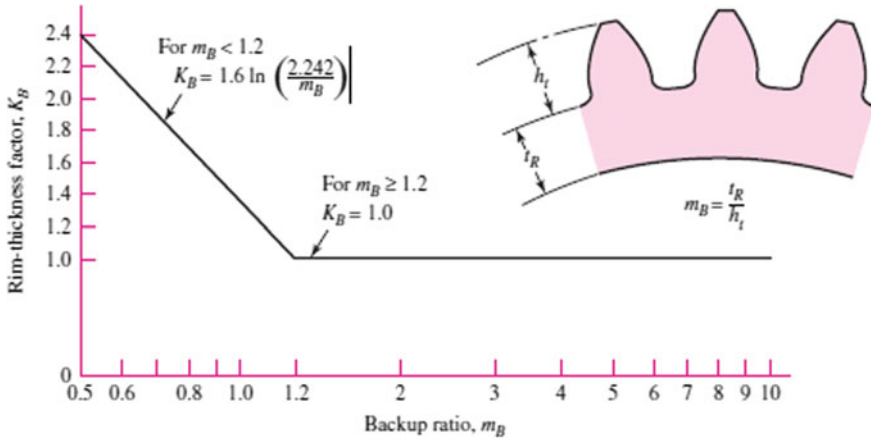


Fig. 2 Rim thickness factor. Source Shigley’s Mechanical Engineering Design 9th Edition p. 764

$$m_B = \frac{t_R}{h_t} \tag{27}$$

where

- t_R Rim thickness below the tooth
- h_t Tooth height

$$K_B = \begin{cases} 1.6 \ln \frac{2.242}{m_B} & m_B < 1.2 \\ 1 & m_B \geq 1.2 \end{cases} \tag{28}$$

where

K_B Rim thickness factor

The final parameters considered for rim thickness factor is mentioned in Table 9.

Geometry Factor (I)

AGMA standard assigns the geometry factor value depending on the choice of number of teeth as shown in Fig. 3 and helix angle in case of helical gear as shown in Fig. 4.

Table 9 Stress concentration parameters

<i>Spur gear</i>		
$t_R = 5$	$h_t = 4.5$	$m_B = 1.1$
<i>Helical gear</i>		
$t_R = 5$	$h_t = 4.5$	$m_B = 1.1$

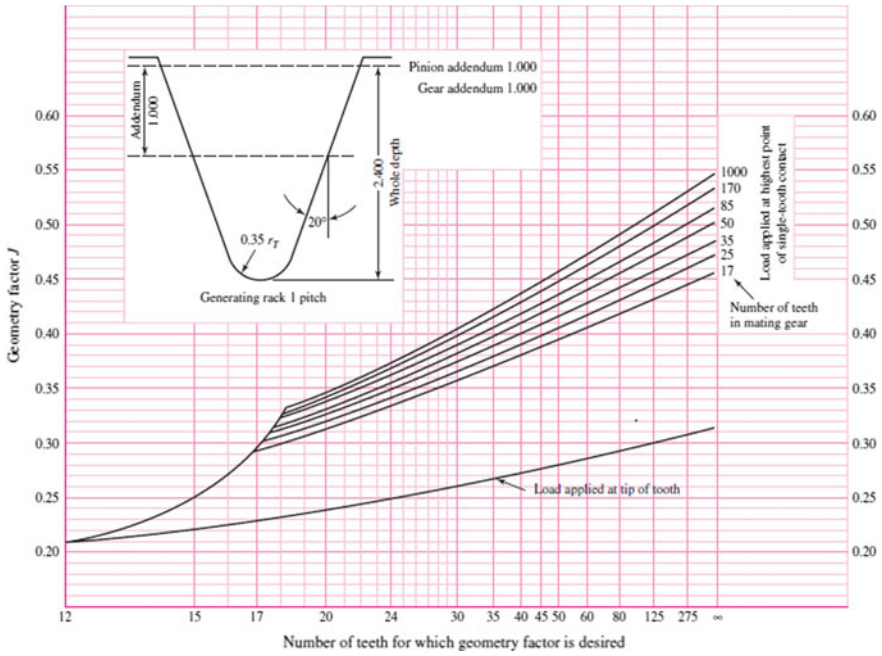


Fig. 3 Geometry factor. *Source* Shigley’s Mechanical Engineering Design 9th Edition p. 753

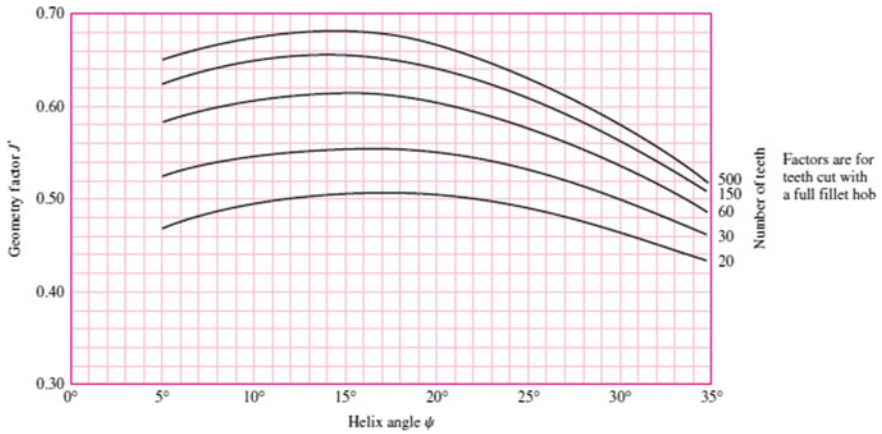


Fig. 4 Bending strength geometry factor (J). *Source* Shigley’s Mechanical Engineering Design 9th Edition p. 754

Table 10 Reliability factor

Reliability	K_r
0.9999	1.50
0.999	1.25
0.99	1.00
0.90	0.85
0.50	0.70

Source Shigley’s Mechanical Engineering Design 9th Edition p. 764

$$I = \frac{\cos \phi_t \sin \phi_t}{2m_N} \frac{m_G}{m_G + 1} \quad \text{for external gears} \quad (29)$$

where

- I Geometry factor
- ϕ_t Transverse pressure angle
- m_N Load sharing ratio
- m_G Gear ration (note: should always be greater than unity)

Temperature factor (K_t)

Temperature above 120 °C adds another Factor (K_t) to the equation, but since our temperature is well below 100°, the temperature factor turns unity.

Reliability factor (K_r)

Reliability factor deals with how reliable a system is at any given point of time. As reliability increases, so does the value of (K_r). Table 6 explains the change [15] (Table 10).

Hardness factor (C_h)

The hardness factor (C_h) is chosen in accordance with the Brinell hardness of gear material as mentioned in Fig. 5, which determines the value.

The final considered parameters for spur and helical gears are mentioned in Table 11.

4 Stress in Gears

After calculating all the paraments of the gears, the values are substituted in Eqs. (7) and (11). The Factor of safety (FOS) is determined from Eqs. (29) and (30) to diagnose whether the stresses are within the allowable limits, if not, the gear parameters are changed until the stresses are brought within allowable limits. The bending stresses have been calculated and tabulated in Tables 12 and 13.

Fig. 5 Hardness factor.
 Source Shigley's Mechanical Engineering Design 9th Edition p. 761

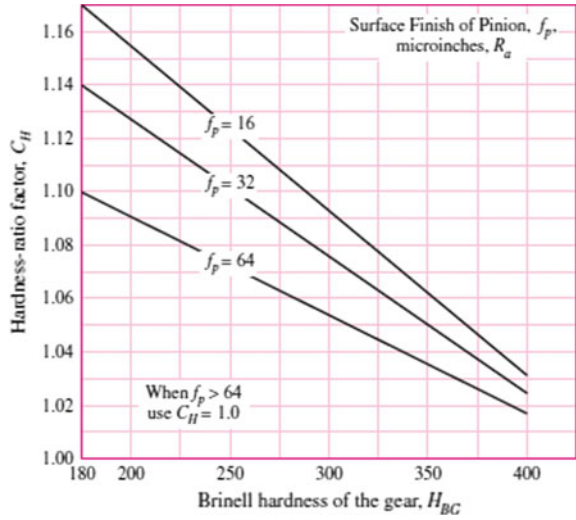


Table 11 Final parameters for helical and spur gears

Factors	Symbols	For spur	For helical
Overload factor	K_O	1	1
Dynamic effect factor	K_V	1.1774	1.178
Size factor	K_S	0.98	1.0029
Load distribution factor	K_m	1.149577	1.1135
Rim thickness factor	K_B	1.139	1.139
Bending strength factor	Y_J	0.317	0.5
Geometry factor for contact stress	I	0.12	0.10036
Temperature factor	K_T	1	1
Reliability factor	K_R	1	1
Hardness factor	C_H	1	1

Table 12 Calculated bending stress for spur and helical gear

Spur gear				
$W^t = 567.57$	$K_o = 1$	$K_m = 1.149577$	$K_b = 1.139$	$K_s = 0.98$
$K_v = 1.1777$	$P_d = 12.7$ inch	$J = 0.317$	$F = 0.55$ in.	Bending stress = 62461.7 psi

Table 13 Calculated bending stress for helical gear

Helical gear				
$W^t = 1582.19$ lbf	$K_o = 1$	$K_m = 1.1135$	$K_b = 1.139$	$K_s = 1.10029$
$J = 0.5$	$P_d = 12.7$ in.	$K_v = 1.178$	$F = 0.9055$ in.	Bending stress = 69220.87 psi

Table 14 Safe material stress for spur gear

Spur gear		
$K_t = 1$	$K_r = 1$	$Y_n = 0.97677$
$S_t = 75,000$ psi	Allowable bending stress = 73,257.75 psi	

Table 15 Safe material stress for helical gear

Helical gear		
$K_t = 1$	$K_r = 1$	$Y_n = 0.97677$
$S_t = 75,000$ psi	Allowable bending stress = 73,257.75 psi	

Table 16 Calculated contact stress for spur gear

Spur gear					
$C_p = 2300$	$W^t = 567.57$ lb	$K_o = 1$	$K_v = 1.1774$	$K_s = 0.98$	$K_m = 1.149577$
$C_f = 1$	$F = 0.55$ in.	$I = 0.12$	Calculated contact stress = 206,359.6 psi		

Table 17 Calculated contact stress for helical gear

Helical gear					
$C_p = 2300$	$W^t = 1582.119$ lbf	$K_o = 1$	$K_v = 1.178$	$K_m = 1.149$	$C_f = 1$
$F = 0.9055$ in.	$I = 0.10036$	Actual contact stress = 225,451.2 psi			

4.1 Bending Stress

Allowable safe material stress has been calculated for spur and helical gears summarized in Tables 14 and 15, respectively.

Theoretical contact stresses are calculated using Eq. (10) and formulated in Tables 16 and 17.

4.2 Calculated Contact Stress

Allowable contact stresses are calculated by using Eq. (12) and formulated in Tables 18 and 19.

Table 18 Allowable contact stress for spur gear

Spur gear		
$Z_n = 0.94843$	$C_h = 1$	$K_t = 1$
$K_r = 1$	$S_c = 275,000$ psi	Allowable contact stress 260,818.25 psi

Table 19 Allowable contact stress for helical gear

Helical gear		
$Z_n = 0.94843$	$C_h = 1$	$K_t = 1$
$K_r = 1$	$S_c = 275,000$ psi	Allowable contact stress 260,818.25 psi

4.3 Factor of Safety

Factor of safety is calculated for bending stress using Eq. (30).

$$\begin{aligned} &\text{Factor of safety } n \\ &= (\text{Maximum bending capacity})/(\text{actual bending stress}) \end{aligned} \tag{30}$$

For spur gear, $n = 2.029$

For helical gear, $n = 2.3$

For contact stress, factor of safety is calculated using Eq. (31).

$$\begin{aligned} &\text{Factor of safety } n \\ &= (\text{Maximum contact capacity})/(\text{actual contact stress}) \end{aligned} \tag{31}$$

For spur gear, $n = 1.122$

For helical gear, $n = 1.123$

4.4 Gear Optimization Using GearTrax

Camnetics’ GearTrax is a professional gear designing software having compatibility with American Gear Manufacturers Association (AGMA) equations. Software demands every technical numerical value needed for generating a gear model in Solidworks. GearTrax is a partner product as every single component is designed on it. Increased productivity, absolute documentation, assimilation of software with international standards such as ANSI, BIS, DIN, CSN, ISO, etc. GearTrax helps the designer to save time while designing. Animated gear mesh shows the working of gear, helping the designer to visualize its working and changes with varying input parameters such as different pressure angles, modules, number of teeth according to ratio as well as fluctuating outline of constant strength parabola on a single tooth. One of the major advantages of GearTrax is the feasibility of performing a large number of iterations and design optimization. Figures 6 and 9 depict the various parameters that are required to design a set of gear and pinion, while Figs. 8 and 10 show the stresses occurring at HPSTC (Fig. 7).

When the load acting on the gear shifts from tip to HPSTC loading, the induced contact and bending stresses plummet significantly, while the allowable tooth stress

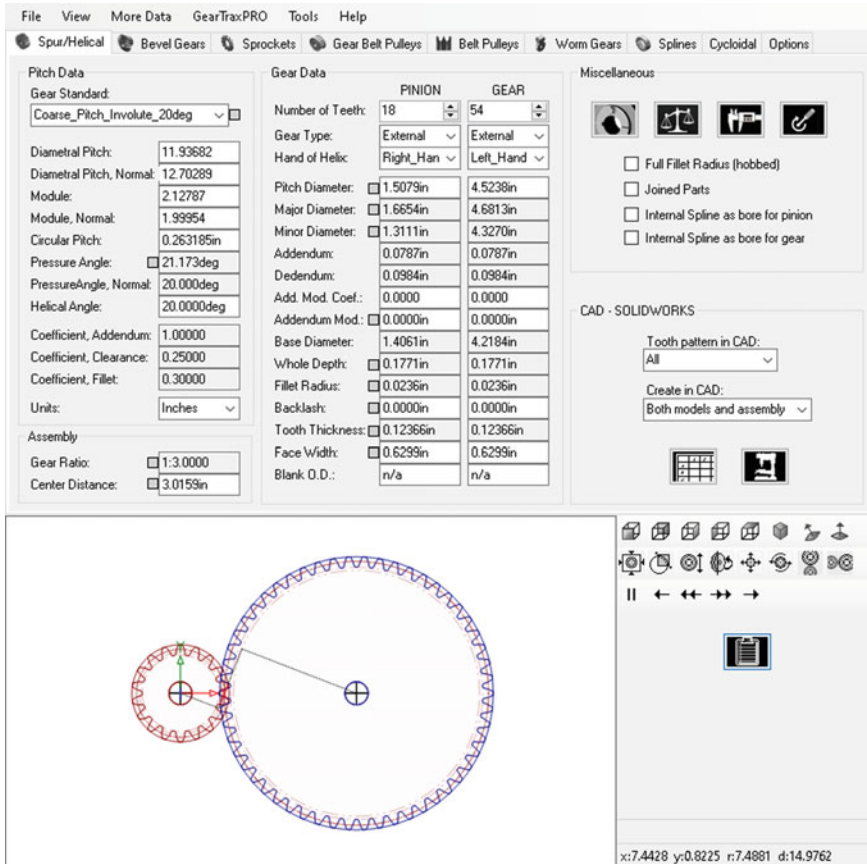


Fig. 6 Parameters for Helical gear

increases conspicuously. Figures 10 and 12 show the HPSTC values for helical and spur gears, while Figs. 11 and 13 show the tip loading values for the same.

5 Design of Shafts

There are three shafts, namely input, intermediate and output shaft. The main objective of shaft calculation is to find out the bending and torsional stresses acting on it. The first stage is to obtain bending stress on the shaft due to bearing, gear load and CVT. The later stage emphasizes on its diameter optimization using AGMA equations. The Combined DE-Goodman Eq. (32) for bending and torsion is used to calculate the shaft diameter [17].

Beam Strength of Gear Set

	PINION	GEAR
T = Torque IN LBS	397.3	1191.9
Input HP	7.6742	
REQ W = Tooth Load, LBS (along pitch line)	526.9	
RPM	1217.3900	405.7967
S = Safe Material Stress (Static) PSI	34,954.0	34,954.0
	Bronze 10,000	
V = Pitch Line Velocity Feet/Minute	480.9668	
Number of Teeth	18	54
DP = Diametral Pitch, Normal	12.70289	
PSI(s) = Helix Angle	20.0000deg	
G = Face Width	0.6299in	0.6299in
Tooth Thickness Area	0.0998in ²	0.1147in ²
W = Tooth Load Safe, LBS	709.1	879.3
Tooth Thickness PSI Capacity	7104.2	7663.4
Tooth Thickness PSI Actual	5279.2	4592.6

Fig. 7 Beam strength of helical gear

$$\frac{1}{n} = \frac{16}{\pi d^3} \left\{ \frac{1}{S_e} [4(K_f M_a)^2 + 3(K_{fs} T_a)^2]^{1/2} + \frac{1}{S_{ut}} [4(K_f M_m)^2 + 3(K_{fs} T_m)^2]^{1/2} \right\} \tag{32}$$

where

- S_e Endurance limit
- d Shaft diameter
- n Factor of safety
- K_f Stress concentration factor
- M_a Alternating bending moment
- K_{fs} Modified stress concentration factor
- T_a Alternating torsional moment
- S_{ut} Ultimate tensile strength
- M_m Mean bending moment
- T_m Mean torsional moment

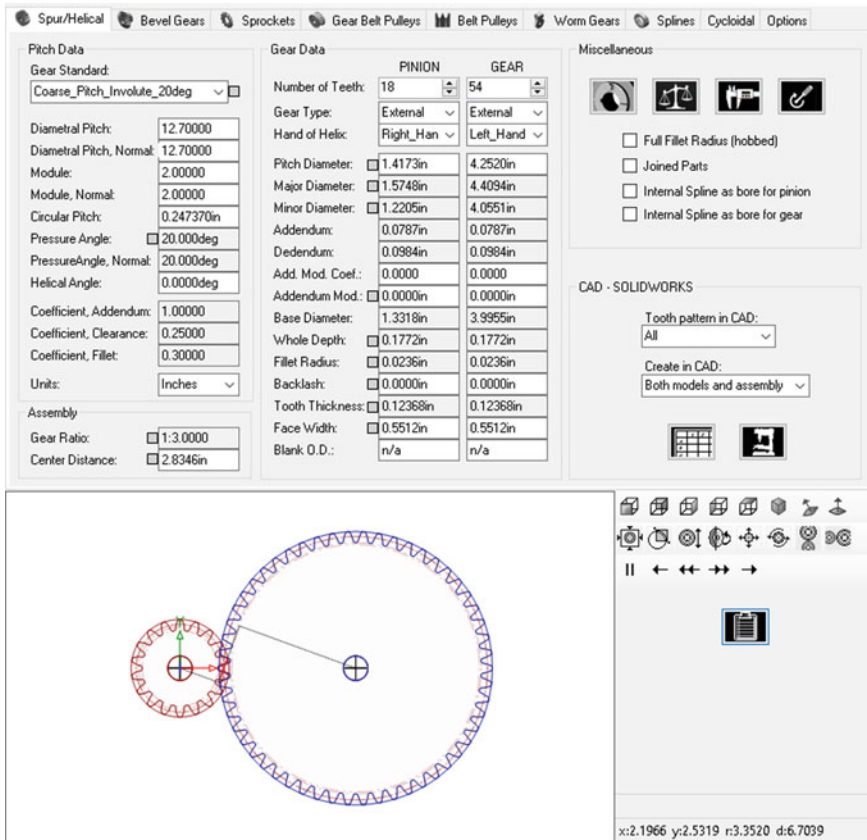


Fig. 8 Parameters for Spur gear

Various parameters such as surface finish factor, size, reliability, stress concentration, load and temperature factors are required to calculate the final diameter (d).

Surface Finish Factor (K_a)

The surface factor (K_a) is computed using Eq. (33), in which the values of a and b are to be taken from Table 20 [5].

$$K_a = a(S_{ut})^b \tag{33}$$

Size Factor (k_b)

Size factor (k_b) is calculated by using Eqs. (34) and (35) where ‘ d ’ denotes the diameter of the proposed shaft [17].

$$k_b = (d/7.62)^{-0.107} = 1.24d^{-0.107} \quad 2.79 \leq d \leq 51 \text{ mm} \tag{34}$$

Beam Strength of Gear Set		
	PINION	GEAR
T = Torque IN LBS	397.3	1191.9
Input HP	7.6742	
REQ W = Tooth Load, LBS (along pitch line)	560.6	
RPM	1217.3900	405.7967
S = Safe Material Stress (Static) PSI	68,737.0	68,737.0
	Bronze 10,000	
V = Pitch Line Velocity Feet/Minute	452.0639	
Number of Teeth	18	54
DP = Diametral Pitch, Normal	12.70000	
PSI(s) = Helix Angle	0.0000deg	
G = Face Width	0.5512in	0.5512in
Tooth Thickness Area	0.0802in ²	0.0939in ²
W = Tooth Load Safe, LBS	1,107.6	1,419.3
Tooth Thickness PSI Capacity	13818.2	15119.3
Tooth Thickness PSI Actual	6994.3	5972.1

Fig. 9 Beam strength of Spur gear

Fig. 10 Stress acting on HPSTC (helical gear)

W = Tooth Load Safe, LBS	709.2	879.4
Tooth Thickness PSI Capacity	7103.5	7662.6
Tooth Thickness PSI Actual	5276.7	4590.5

Fig. 11 Stresses acting on tip (helical gear)

W = Tooth Load Safe, LBS	411.4	514.8
Tooth Thickness PSI Capacity	4292.7	4619.4
Tooth Thickness PSI Actual	5497.1	4727.5

Fig. 12 Stress acting on HPSTC (spur gear)

W = Tooth Load Safe, LBS	643.7	824.8
Tooth Thickness PSI Capacity	7026.8	7688.4
Tooth Thickness PSI Actual	6120.2	5225.8

Fig. 13 Stresses acting on Tip (spur gear)

W = Tooth Load Safe, LBS	348.5	449.2
Tooth Thickness PSI Capacity	3991.1	4341.2
Tooth Thickness PSI Actual	6419.8	5418.3

Table 20 Surface finish factor

Surface finish	<i>a</i>	<i>b</i>
Ground	1.58	-0.085
Machined or cold-drawn	4.51	-0.265
Hot-rolled	57.7	-0.718
As forged	272	-0.995

$$k_b = 1.51d^{-0.157} \quad 51 \leq d \leq 254 \text{ mm} \tag{35}$$

Reliability Factor (*K_c*)

Reliability of the shafts (*K_c*) has to be considered for the stress calculation. This factor is selected from Table 21 [15].

Modifying Factor to Account for Stress Concentration (*K_d*)

Stress concentration factor (*K_d*) takes into account the dynamic stresses. Equation (36) shows its relation with *K_d*.

Here, *K_f* = 1.

$$K_d = \frac{1}{K_f} \tag{36}$$

Load Factor (*K_c*)

Load factor (*K_c*) takes into account various bending and axial loads occurring during its dynamic motion. Table 22 shows the values to be taken for each load.

Table 21 Reliability Factor

Reliability <i>R</i> (%)	<i>K_c</i>
50	1.000
90	0.897
95	0.868
99	0.814
99.9	0.753
99.99	0.702
99.999	0.659

Table 22 Load factor

<i>K_c</i>	1	Bending
	0.85	Axial
	0.59	Torsion

Table 23 Temperature factor

Temperature (°C)	$S_T/S_{RT} (K_t)$
20	1.000
50	1.010
100	1.020
150	1.025
200	1.020
250	1.000
300	0.975
350	0.943
400	0.900
450	0.843
500	0.768
550	0.672
600	0.549

Table 24 Shaft design parameters

Factors	Annotation	Input shaft	Intermediate shaft	Output shaft
Surface finish factor	K_a	0.723	0.723	0.723
Size factor	K_b	0.875	0.875	0.875
Reliability factor	K_c	0.814	0.814	0.814
Stress conc. factor	K_d	0.61	0.55	0.6
Load factor	K_e	0.79	0.79	0.79
Temperature factor	K_f	1.01	1.01	1.01

Temperature Factor (K_t)

Temperature encountered during operating conditions should be considered. Table 23 shows the relation between gear temperature and Temperature Factor (K_t).

Shaft and its Design Consideration Factor

The selected values of surface finish factor, size factor, reliability factor, stress concentration factor, load factor and temperature factor are represented in Table 24.

5.1 Shaft Forces Free Body Diagram and Nomenclature

For calculating the loads on input, intermediate and output shaft, the forces due to gears, CVT (Continuously Varying Transmission) and bearing support are considered. Figure 14 depicts the forces acting on the input shaft.

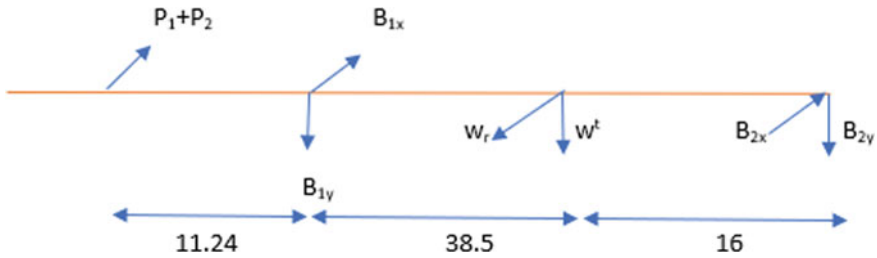


Fig. 14 Forces on input shaft

Table 25 Forces acting on input shaft

Forces		Calculated values (N)
P_1	Loads acting due to CVT	1313.1
P_2		686
W_t	Gear tangential load	2810.2
W_r	Gear radial load	1019.58
B_{1x}	Bearing forces due to first bearing	4532.3
B_{1y}		825
B_{2x}	Bearing forces due to second bearing	-2131
B_{2y}		1985.2

Table 25 shows the calculated values of all the individual force components acting on the input shaft, where P_1 and P_2 are the loads due to CVT belt tension.

5.2 Design for CVT Loads

The loads occurring due to shifting and engine torque [14] are calculated for CVT. The specification of CVT and engine [14] used in Table 26 is used to calculate belt tension.

The belt tensions T_1 , T_2 and the velocity (v) are depicted in Fig. 15.

First, Eq. (37) is used to calculate the velocity of CVT.

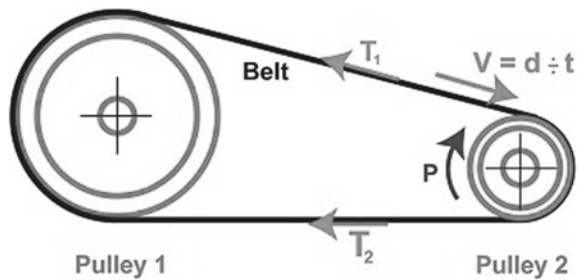
$$\begin{aligned}
 \text{Velocity}(v) &= \frac{\pi dn}{60} = \frac{3.14 * 0.144 * 1217.39}{60} \\
 &= 9.19 \text{ m/s}
 \end{aligned}
 \tag{37}$$

Equations (38) and (39) are used to formulate angle of wrap and belt tensions, respectively. CVTech (CVT) has been used for transmitting the power from engine to gearbox.

Table 26 CVT parameters

Symbol	Parameter	Value
Td_p	Travel distance (primary)	0.015 m
rp	Radius (primary)	0.0385 m
Td_s	Travel distance (secondary)	0.015 m
rs	Radius (secondary)	0.144 m
γ		8.24°
M_b	Mass of the V-belt	0.4257 kg/m (measured)
M_t	Torque at 2800 rpm	19.1 Nm
P_E	Engine power at 2800 rpm	7.6742 Hp

Fig. 15 Loads acting on CVT. *Source* V.B. Bhandari Design of Machine Elements



$$\tan(\gamma) = 0.0336/0.232$$

$$\alpha = 180 - 2(\gamma) \tag{38}$$

$$\alpha = 163.5^\circ = 2.85 \text{ rad}$$

$$\frac{T_1 - mV^2}{T_2 - mV^2} = e^{\frac{f\alpha}{\sin\theta/2}} \tag{39}$$

From Eq. (40), the difference of the two tensions of CVT is determined.

$$T_1 - T_2 = F_n = 1244.5 \text{ N}$$

$$F_n = T/(2.84/2)$$

$$F_n = 279.78 \text{ lbf}$$

$$F_n = 1244.5 \text{ N} \tag{40}$$

Solving Eqs. (39) and (40), the values of T_1 and T_2 are calculated.

$$T_1 = 1313.1 \text{ N}$$

$$T_2 = 68.6 \text{ N}$$

The tangential load on the input shaft is calculated using Eq. (41).

$$T = W^t * da/2 \tag{41}$$

$$W^t = 560.74 \text{ lbf}$$

$$f = 2494.3 \text{ N}$$

Similarly, the radial load on the input shaft is computed using Eq. (42).

$$W^r = W^t \tan \emptyset \tag{42}$$

The bearing calculations are determined by Eqs. (43) and (44).

$$\Sigma F_x = F_1 + F_2 + W_r = RB_{1x} + RB_{2x} = 2289.1 \text{ N} \tag{43}$$

$$\Sigma F_y = W^t = RB_{1y} + RB_{2y} = 2494.3 \text{ N} \tag{44}$$

Intermediate Shaft

The loads acting on the intermediate shaft are depicted in Fig. 16.

The values for intermediate shaft are calculated using Eqs. (43) and (44). Calculated values are illustrated in Table 27.

Output Shaft

Similarly, forces on the output shaft due to helical gear and bearing support are represented in Fig. 17.

The values obtained from solving the force Eqs. (43) and (44) are demonstrated in Table 28.

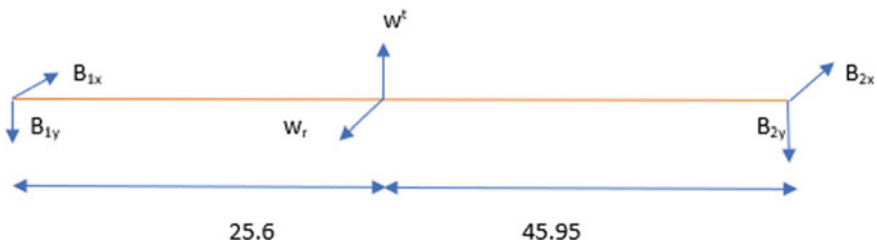


Fig. 16 Force depiction for Intermediate shaft

Table 27 Forces acting on Intermediate shaft

Forces	Calculated values (N)
W_{t1}	2166.94
W_{r1}	907.44
W_{t2}	6160.7
W_{r2}	2242.3
B_{1x}	123.77
B_{2x}	1211.09
B_{1y}	4473.36
B_{2y}	4636.64

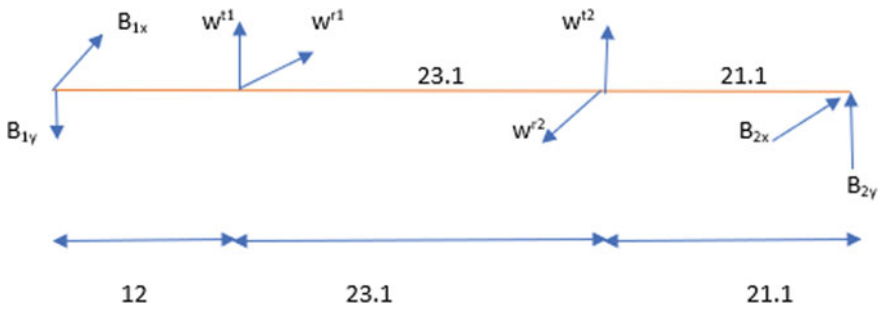


Fig. 17 Force depiction on output shaft

Table 28 Forces acting on output shaft

Forces	Calculated values (N)
W_t	6160.7
W_r	2107
B_{1x}	3956.5
B_{1y}	1353.14
B_{2x}	2204.24
B_{2y}	753.86

5.3 Optimization of Shaft

Once, all shaft forces are obtained, the optimal shaft diameter is calculated using the DE-Goodman Eq. (45) for combined bending and torsion [17].

$$\frac{1}{n} = \frac{16}{\pi d^3} \left\{ \frac{1}{S_e} [4(K_f M_a)^2 + 3(K_{fs} T_a)^2]^{1/2} + \frac{1}{S_{ut}} [4(K_f M_m)^2 + 3(K_{fs} T_m)^2]^{1/2} \right\} \quad (45)$$

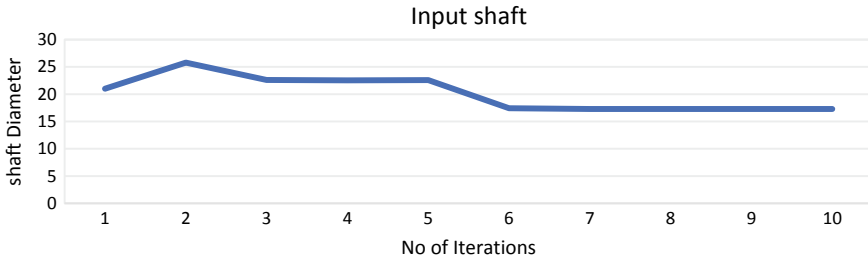


Fig. 18 Convergence graph for Input shaft

where

- S_e Endurance limit
- d Shaft diameter
- n Factor of safety
- K_f Stress concentration factor
- M_a Alternating bending moment
- K_{fs} Modified stress concentration factor
- T_a Alternating torsional moment
- S_{ut} Ultimate tensile strength
- M_m Mean bending moment
- T_m Mean torsional moment

5.4 Convergence of Shaft Diameter

A safe diameter is initially assumed, which is substituted into Eq. (45). Equation (45) yields an optimized diameter. The iteration is then continued until the value of diameter converges and no longer changes significantly. The iteration for input, intermediate and output are shown in Tables 26, 27 and 28, respectively. The converging graph is shown in Figs. 18, 19 and 20, respectively (Tables 29, 30 and 31).

6 Result and Discussions

The project targeted to design gearbox for its better optimization has been done using different tools in a highly effective manner. Design factors are calculated during dynamic loading. Complex theoretical calculations through AGMA equations provide the output of induced bending and contact stresses on the component. For safe design, induce stress capacity should be greater than actual stress on gear. HPSTC shifts the loading parameters drastically which results in substantial FOS change. Tables 32 and 33 present values for different loading conditions for spur and

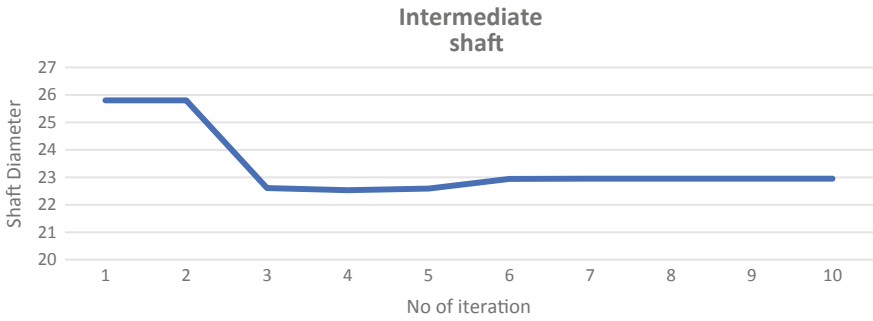


Fig. 19 Convergence graph for Intermediate shaft

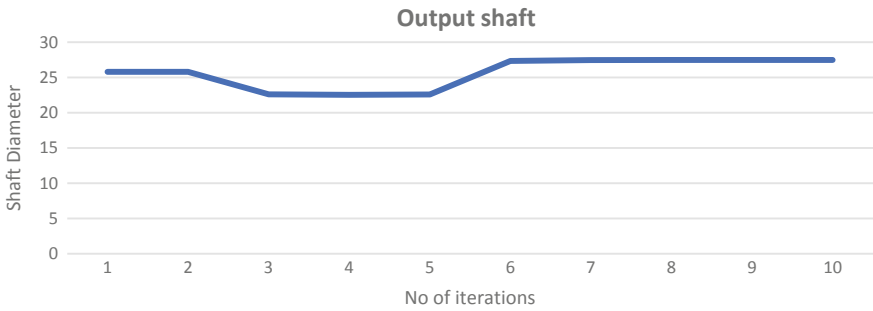


Fig. 20 Convergence graph for output shaft

Table 29 Iteration for input shaft

Iteration	Moment (Ma)	Torque TM	Dia	$K_b = 1.24 d^{-0.107}$
1	46.5	43.7	21	0.895249775
2	46.5	43.7	25.8	0.875746432
3	46.5	43.7	22.61	0.88819314
4	46.5	43.7	22.53	0.888538474
5	46.5	43.7	22.59	0.888283972
6	46.5	43.7	17.43	0.913285521
7	46.5	43.7	17.29	0.914089994
8	46.5	43.7	17.28	0.914115484
+9	46.5	43.7	17.28	0.914116291
10	46.5	43.7	17.28	0.914116317

Table 30 Iterations for intermediate shaft

Iteration	Moment (Ma)	Torque TM	Dia	$K_b = 1.24 d^{-0.107}$
1	101.15	131.1	25.8	0.875746432
2	101.15	131.1	25.8	0.875746432
3	101.15	131.1	22.61	0.88819314
4	101.15	131.1	22.53	0.888538474
5	101.15	131.1	22.59	0.888283972
6	101.15	131.1	22.94	0.886818527
7	101.15	131.1	22.95	0.886773555
8	101.15	131.1	22.95	0.886772174
9	101.15	131.1	22.95	0.886772131
10	101.15	131.1	22.95	0.88677213

Table 31 Iterations for output shaft

Iteration	Moment (Ma)	Torque TM	Dia	$K_b = 1.24 d^{-0.107}$
1	107	393.3	25.8	0.875746432
2	107	393.3	25.8	0.875746432
3	107	393.3	22.61	0.88819314
4	107	393.3	22.53	0.888538474
5	107	393.3	22.59	0.888283972
6	107	393.3	27.34	0.870324917
7	107	393.3	27.47	0.869872731
8	107	393.3	27.48	0.869861194
9	107	393.3	27.48	0.869860899
10	107	393.3	27.48	0.869860892

Table 32 Different loading points (spur gear)

Spur gear		
HPSTC loading	Allowable stress psi	Induced stress psi
Pinion	7026.8	6120.2
Gear	7688.4	5525.8
Tip loading	Allowable stress psi	Induced stress psi
Pinion	3991.1	6419.8
Gear	4341.2	5418.3

the helical gears. Bending Factor of Safety (FOS) for spur and helical gears is 2.029 and 2.3, respectively, and for contact, it is 1.122 and 1.123, respectively.

Modelling of gear is done using SOLIDWORKS [18] which is depicted in Fig. 21 for spur gear and Fig. 22 for helical gear. The Factor of Safety (FOS) computed by

Table 33 Different loading points (Helical gear)

Helical gear		
HPSTC loading	Allowable stress psi	Induced stress psi
Pinion	7103.5	5276.7
Gear	7662.6	4590.5
Tip loading	Allowable stress psi	Induced stress psi
Pinion	4292.7	5497.1
Gear	4619.4	4727.5

Fig. 21 Spur gear model

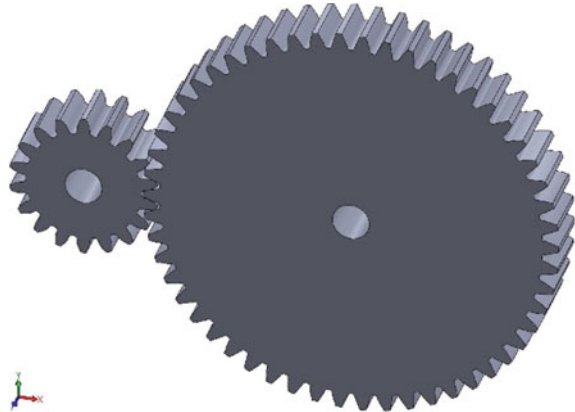
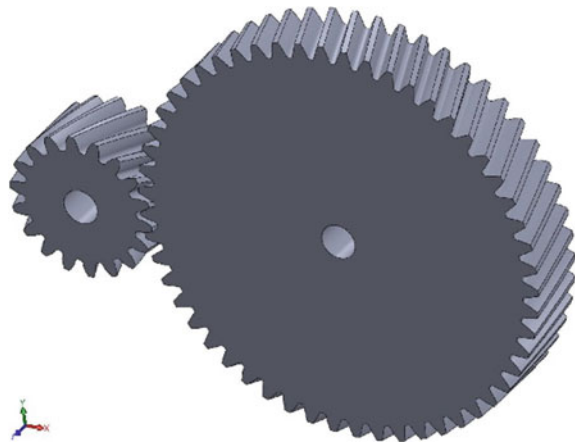


Fig. 22 Helical gear model



AGMA equations has been substantiated using ANSYS static structural [19]. The corroborated FOS is displayed in Figs. 23 and 24. Additional weight reduction of gears is possible by optimizing on the stress concentrated areas using incremental solving and analysis on each stage. However, the theory of topology optimization

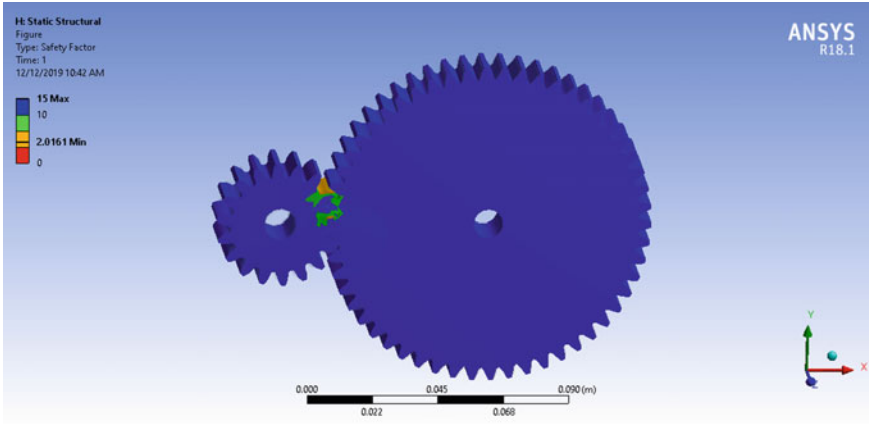


Fig. 23 FOS (Spur gear)

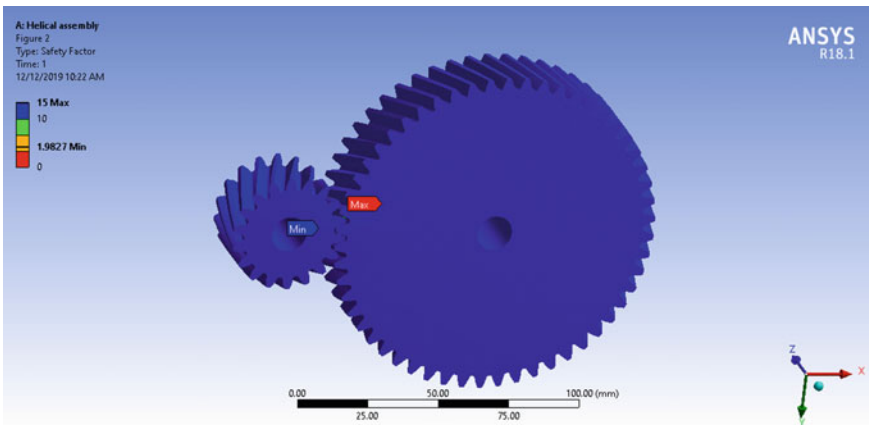


Fig. 24 FOS (Helical Gear)

cannot be inculcated into GearTrax™ while generating parameters for gear model, which puts a barrier on how much can be enhanced beforehand. Detailed failure analysis of the spur gear can be obtained through various experiments along the spur gear mesh points [16].

It is recognizable from Figs. 17, 18 and 19 that the three shafts designed have been reduced in size with all accumulated forces acting upon it according to design equation. Initial and final shaft diameters are shown in Table 34.

Table 34 Shaft optimized results

Shaft diameter		
Nomenclature	Initial shaft diameter	Optimized shaft diameter
Input	21	17.28
Intermediate	25.8	22.95
Output	25.8	27.48

7 Conclusion

As discussed, the primary task of the project to design and optimize the two-stage reduction gearbox for an All-Terrain Vehicle is fully functional and safe. Theoretical calculations and its proper culmination with software aid far better designing of the gear train set. The modus operandi of using refined software with calculated and validated data helps the designer to save time in designing with more precise iterations following industrial standards. HPSTC considerations in designing a single gear (spur/helical) drastically plummet the face width of the gear. Shaft designing is taken proper care by considering all the parameters including CVT torque and its belt tensions. The course of action followed to design gear train in this paper can be brought to design any commercial gear train set apart from automobile applications.

References

1. A. Sharma, J. Singh, A. Kumar, Optimum design and material selection of Baja vehicle. *Int. J. Curr. Eng. Technol.* **5**(3), 66–70 (2015)
2. A. Patankar, R. Kulkarni, S. Kothawade, S. Ingale, Design and development of a transmission system for an all terrain vehicle. *Int. J. Mech. Eng. Technol. (IJMET)* **7**(3), 351–359 (2016)
3. Kanase, V., Rane, D., Dongare, V., Shinde, R., Tangade, A.: Design and manufacturing of 2-stage speed reducer for a BAJA all-terrain vehicle (2017)
4. Patel, N., Gupta, T., Wankhede, A., Warudkar, V.: Design and optimization of 2-stage reduction gearbox (2017)
5. Boonmag, V., Phukaoluan, A., Wisesook, O.: Comparison of bending stress and contact stress of helical gear transmission using finite element method (2019)
6. Patil, M., Ramkumar, P., Krishna Pillai, S.: Multi-objective optimization of two stage spur gearbox using NSGA-II. SAE Technical Paper 2017-28-1939. <https://doi.org/10.4271/2017-28-1939> (2017)
7. Chetan, W., Rohal, D., Roshan, K., Versha, R., Aqleem, S., Nitin, G.: Selection, modification and analysis of power transmission and braking system of an ATV **1**(1), 2321–5747 (2013). ISSN (Print)
8. S.C. Hwang, J.H. Lee, D.H. Lee, S.H. Han, K.H. Lee, Contact stress analysis for a pair of mating gears. *Math. Comput. Model.* **57**(1–2), 40–49 (2011)
9. Ü. Atila, M. Dörterler, R. Durgut, İ. Şahin, A comprehensive investigation into the performance of optimization methods in spur gear design. *Eng. Optim.* (2019). <https://doi.org/10.1080/0305215X.2019.1634702>
10. Patel, N., Gupta, T.: Methodology for Designing a Gearbox and its Analysis (2016)

11. Eric T. Payne, *Design of an SAE Baja Racing Off-Road Vehicle Powertrain* (The University of Akron in Akron, Ohio, USA, 2015)
12. Naunheimer, H., Bertsche, B., Ryborz, J., Novak, W.: *Automotive Transmissions-Fundamentals, Selection, Design and Application*, 2nd edn (2011)
13. Ebsch, E., Kudla, J., O'Brien, C., Quick, B.: *Baja Gear Reduction* (2012)
14. https://www.briggsracing.com/sites/default/files/m19h_baja_net_power_1.pdf
15. V.B. Bhandari, *Design of Machine Elements*, 3rd edn. (Tata McGraw-Hill Education, London, 2010)
16. M.A. Muraro, F. Koda, U. Reisdorfer Jr., C.H. Silva, The influence of contact stress distribution and specific film thickness on the wear of spur gears during pitting tests. *J. Braz. Soc. Mech. Sci. Eng.* **34**(2), 135–144 (2012)
17. Richard G. Budynas, J. Keith Nisbett, *Shigley's Mechanical Engineering Design*, 9th edn. (McGraw-Hill Companies, New York, 2011)
18. SOLIDWORKS User Manual (2018)
19. ANSYS 19.0 User Manual (2019)

Analysis of Composite Leaf Springs Using Finite Element Method



S. Geetha Satya Sai, Venigalla Sailesh, S. K. Mobin,
T. Subash Chandra Bose, Y. Sai Krishna, and P. Phani Prasanthi

Abstract Composite leaf springs are extensively used in automotive industries to maximize fuel efficiency. In the present work, composite leaf springs are analyzed to find deformation and stresses by selecting different composite materials such as E glass/epoxy, carbon/epoxy, boron/epoxy, and graphite/epoxy composite. The analysis is performed by using the Finite Element Method. The interlaminar stresses generated between the leaves of composite laminate have been identified. Different combinations of composite materials have been analyzed to bring out the best composite leaf spring. The Finite Element based software Ansys is used to estimate the deformations and stresses of the composite leaf spring. The Finite Element Models are validated with the theoretical results. The present work is useful for the effective design of composite leaf springs with single fiber as well as hybrid fiber composites.

Keywords Composite leaf spring · Finite element method · ANSYS · Deformations · Interlaminar stresses

1 Introduction

Leaf springs are one of the shock absorbing members in automotive and playing an important role to give maximum cushioning effect the people irrespective of the road. These leaf springs are made by stacking different sizes of rectangular cross section plates, and these attached spring plates act as one member to take the maximum shock loads. Analysis has been carried on these leaf spring to get maximum comfort to the passengers of the public as well as private transportation.

S. Geetha Satya Sai · V. Sailesh · S. K. Mobin · T. Subash Chandra Bose · Y. Sai Krishna · P. P. Prasanthi (✉)
Department of Mechanical Engineering, P.V.P. Siddhartha Institute of Technology, Kanuru, Vijayawada, Andhra Pradesh, India
e-mail: phaniprasanthi.parvathaneni@gmail.com

© Springer Nature Singapore Pte Ltd. 2021
G. S. V. L. Narasimham et al. (eds.), *Recent Trends in Mechanical Engineering*,
Lecture Notes in Mechanical Engineering,
https://doi.org/10.1007/978-981-15-7557-0_40

Earlier, the steel leaf springs are used as shock resistance members. With the development of composite materials, the steel leaf spring is replaced by composite materials because composite materials can be designed to get the required properties.

The replacement of steel leaf springs with composite can minimize the weight in a drastic way which in terms decreases the fuel cost [1].

In the present decade, manufacturers are using composite leaf spring to the possible extent. A review of studies was presented by Ashwini and Mohan Rao on composite leaf springs and raised many issues related to the composite materials [2, 3]. Commonly used material for the composite leaf springs is glass and carbon fiber composite. Using these materials, the leaf springs were analyzed by finite element software Ansys, and static and dynamic analysis were performed to understand their behavior [4, 5].

Semielliptical and parabolic-shaped leaf springs are generally used springs in the automotive industry. In this concern, few authors studied the semielliptical and parabolic-shaped leaf springs which are made of composite materials [6].

Without any optimization of geometry and material stiffness, one cannot suggest the composite leaf springs to the transportation industry. In this view, researchers [7–9] performed studies on composite leaf spring optimization to give a clear idea of the practical usage of these members.

The analysis of the leaf springs can be carried computationally using linear and nonlinear approaches. Each method has its specific benefits, and the choice of the method adopted by the researchers will be dependent on the demand for the solution. Dipendra Kumar Roy and Kashi Nath Saha performed a nonlinear analysis of spring by idealizing the spring as a beam member [10].

The methodology of the researchers to tackle particular problems will be useful for the others in the analysis of similar structures of the same family. In this regard, the present authors review the work performed by Zhang et al. [11].

These authors performed leaf spring analysis of rotary engines to address combustion performance. In the categories of leaf springs, parallel prismatic leaf springs are analyzed for large deflection stiffness [12]. While preparing a composite leaf spring, many authors used several methods to manufacture the composite laminates. Among these, few authors suggested using textile-woven structures to make leaf springs by maintaining different architecture [13].

Still a few issues related to the composite materials are needed to be addressed. In the present work, composite leaf springs are designed and analyzed to minimize the interlaminar stresses. The interlaminar stresses cause the debonding of the layers of leaf spring which causes catastrophic failure. To avoid such failure, the composite leaf springs need to be designed by selecting the best fiber-reinforced metal composite in terms of weight, stiffness, and interlaminar stresses.

2 Finite Element Analysis of Leaf Springs

Leaf springs with four plates are considered for the analysis maintaining different lengths with equal thickness and width. The geometric details of each plate are provided below.

The geometrical model of the leaf spring is shown in Fig. 1. This model is created in Ansys workbench 18.2 software. The span length of the leaf spring is 84 mm, radius of Master Leaf is 90 mm, each leaf width is 7 mm, and the thickness is 2 mm. The created geometries are converted into the finite element model by using a medium mesh option in the software as presented in Fig. 2. The material properties of the leaf spring for the present analysis are provided in Table 1.

The analysis is performed by selecting ten different material combinations. Among these, first, the leaf springs are analyzed for E glass/epoxy composite, Carbon/epoxy composite, Boron/epoxy composite, and Graphite/epoxy composite. Later, the hybrid composites are prepared by stacking different combinations of the above-mentioned composites such as E glass/epoxy and carbon/epoxy composites (Fig. 3).

The leaf springs are analyzed by applying fixed support at the spring eye and at the bottom of the spring; a force of 100 N is applied in Y-direction.

Fig. 1 Representation of leaf spring

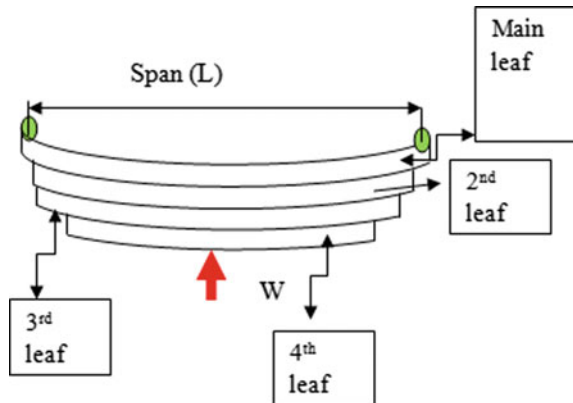


Fig. 2 Geometrical model of leaf spring

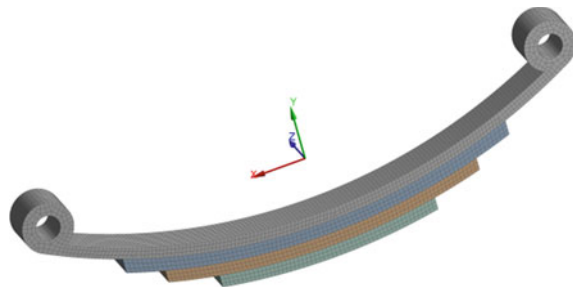
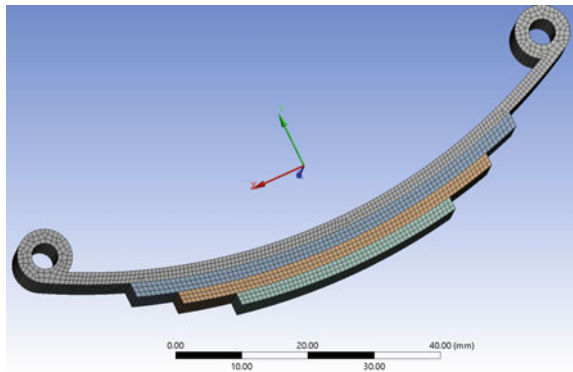


Table 1 Properties of unidirectional composite for leaf springs [14]

Material type	E glass/epoxy	Carbon/epoxy	Boron/epoxy	Graphite/epoxy
E_1 (MPa)	41e3 (0.55 vf)	147e3 (0.63 vf)	201e3	294e3
E_2 (MPa)	10.4e3	10.3e3	21.7e3	6.4e3
E_3 (MPa)	10.4e3	10.3e3	21.7e3	6.4e3
μ_{12}	0.28	0.27	0.17	0.23
μ_{21}	0.06	0.02	0.02	0.01
G_{12} (MPa)	4.3e3	7e3	5.4e3	4.9e3
ρ (g/cm ³)	1.97	1.6	2.03	1.59
Tensile strength (MPa)	1140	2280	1380	985
Compressive strength (MPa)	620	1725	1600	690

Fig. 3 Finite element mesh of leaf spring



By applying the above conditions, the composite leaf springs are studied for total deflection, Y -directional deflection, von Mises stress, interlaminar shear stresses, and factor of safety.

The analysis of leaf spring is carried out by making a composite leaf spring as per Table 2. As an example, M1 model is prepared by making all the leaves of the spring with E glass/epoxy composite, and H1 model is prepared by making a master leaf with E glass/epoxy and second leaf with Carbon/epoxy and third leaf with E glass/epoxy and the last leaf with Carbon/epoxy composite, respectively.

Validation: The leaf spring analysis and the results are validated by using conventional formulas by considering the chromium–vanadium steel springs. No. of springs: 4, load applied on the spring: 100 N, Young’s modulus (E): 206e3 MPa, allowable factor of safety: 3, spring span: 1200 mm, width: 120 mm, and allowable stresses are 460 MPa. Using the same data, the maximum stresses are estimated by using Ansys software and the results are compared to the allowable stress $\sigma = 460$ MPa. From both approaches, the allowable stresses are the same.

Table 2 Material combination taken for the analysis

Material type	Master leaf	Second leaf	Third leaf	Fourth leaf
E	E glass/epoxy	E glass/epoxy	E glass/epoxy	E glass/epoxy
C	Carbon/epoxy	Carbon/epoxy	Carbon/epoxy	Carbon/epoxy
B	Boron/epoxy	Boron/epoxy	Boron/epoxy	Boron/epoxy
G	Graphite/epoxy	Graphite/epoxy	Graphite/epoxy	Graphite/epoxy
E/C/E/C	E glass/epoxy	Carbon/epoxy	E glass/epoxy	Carbon/epoxy
E/B/E/B	E glass/epoxy	Boron/epoxy	E glass/epoxy	Boron/epoxy
E/G/E/G	E glass/epoxy	Graphite/epoxy	E glass/epoxy	Graphite/epoxy
C/B/C/B	Carbon/epoxy	Boron/epoxy	Carbon/epoxy	Boron/epoxy
C/G/C/G	Carbon/epoxy	Graphite/epoxy	Carbon/epoxy	Graphite/epoxy
B/G/B/G	Boron/epoxy	Graphite/epoxy	Boron/epoxy	Graphite/epoxy

3 Results and Discussions

Figure 4 shows the variation of total deformation of different leaf springs subjected to the same loading and boundary conditions. In the total deformation, the composite leaf spring made with E glass/epoxy composite has given the highest deformation, and for hybrid composite, E glass/epoxy combination composites' deformation is more compared to the other composite leaf springs. The deformation image is presented in Fig. 5.

Figure 6 shows the variation of von Mises stress for different composite materials. The von Mises stress is maximum for Graphite/epoxy composite and the hybrid composite of Graphite/E glass composite. The minimum stress is observed for hybrid composite with Boron and Carbon epoxy. For a case of single composite material,

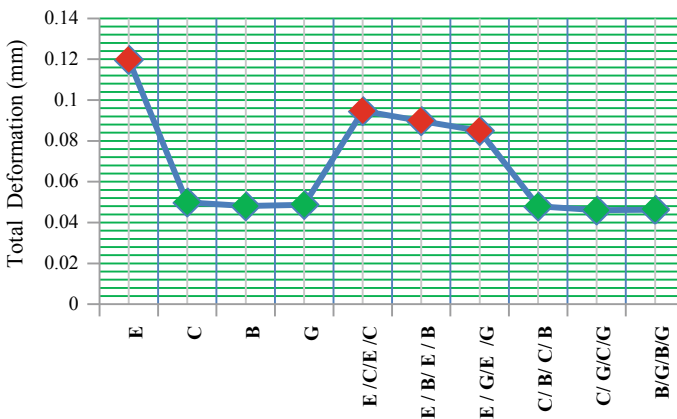


Fig. 4 Variation of total deformation

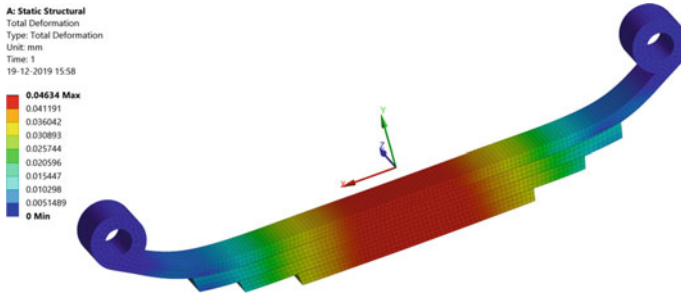


Fig. 5 Total deformation contour of composite leaf spring of B/G/B/G composite

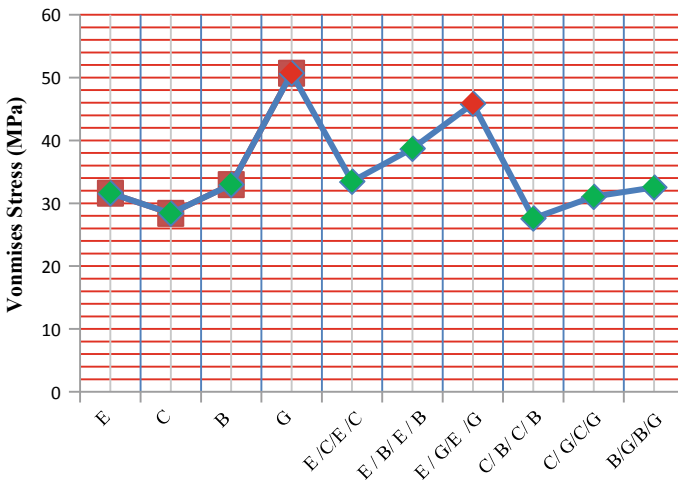


Fig. 6 Variation of von Mises stresses with respect to materials

the leaf spring with Carbon composite showed minimum von Mises stress. Figure 7 shows the variation of shear stresses. The maximum shear stress trend is the same as that of von Mises stresses. One of the intentions to carry out the present work is to address the interlaminar stresses generated between the leaves of the composite spring. For that, the shear stresses are evaluated between the interface of the main leaf and second leaf, second leaf and third leaf, and third leaf and the fourth leaf of the composite material, respectively. By these stresses, one can estimate the probability of debonding.

Once by knowing the debonding regions, preventive measures will be taken to avoid the catastrophic failure of the composite leaf springs. The interlaminar stresses are maximum between the main leaf and second leaf compared to other interfaces. The load is acting at the bottom face of the fourth leaf as mentioned in Fig. 1. These loads will be transmitted among the leaves. The magnitude of interlaminar stresses is maximum for E glass composite due to less in-plane shear modulus.

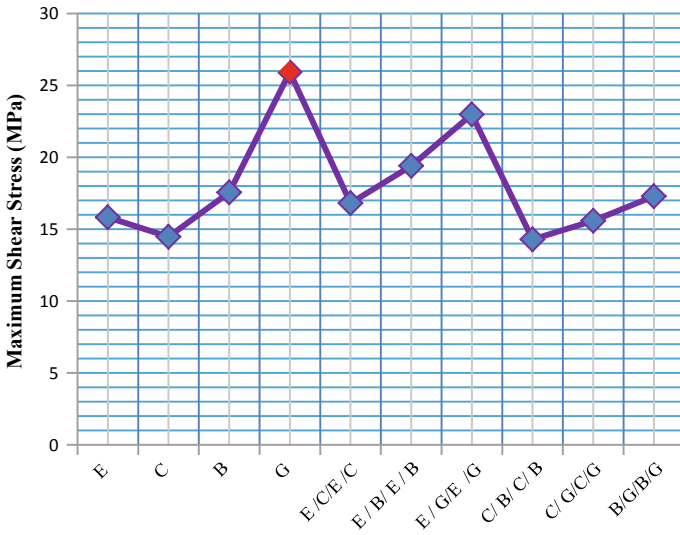


Fig. 7 Variation of Shear stresses with respect to materials

(G12) of E glass composite. This problem will be rectified by combining E glass/epoxy composite with carbon/epoxy or boron/epoxy composite.

In the case of hybrid composite, the highest magnitude is observed for carbon epoxy and boron epoxy. This is due to the mismatch effect of the properties of the respective composite Fig. 8.

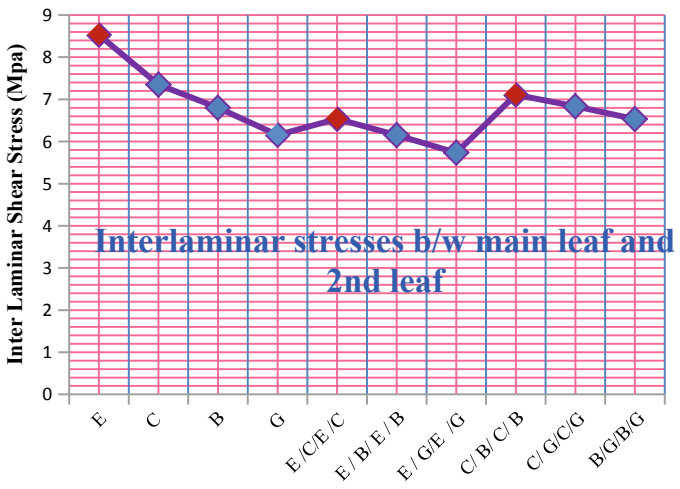


Fig. 8 Variation of Interlaminar stresses of main leaf and second leaf with respect to materials

Different behavior is observed for interlaminar stress of second leaf and third leaf of the composite. Compared to single fiber-reinforced composite, the hybrid composite made with E glass and graphite composite shows maximum magnitude due to the less in-plane shear modulus (G_{12}) of both composites Fig. 9.

Figure 10 shows the variation of interlaminar stresses between third and fourth leaves, respectively. In this case, the graphite fiber reinforced epoxy composite has got maximum stresses.

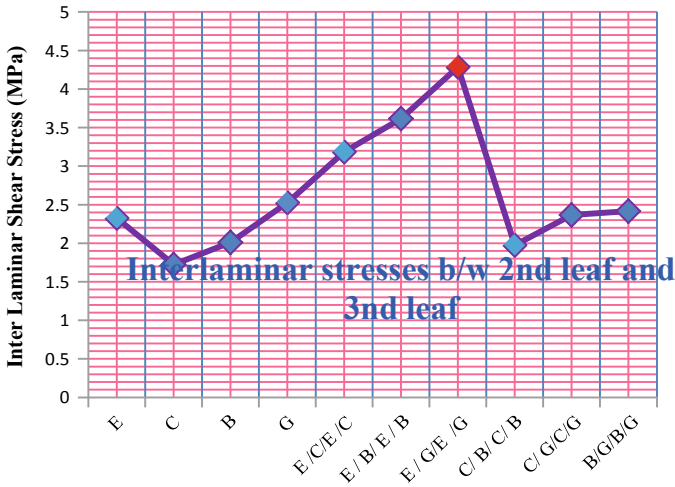


Fig. 9 Variation of Interlaminar stresses of second leaf and third leaf with respect to materials

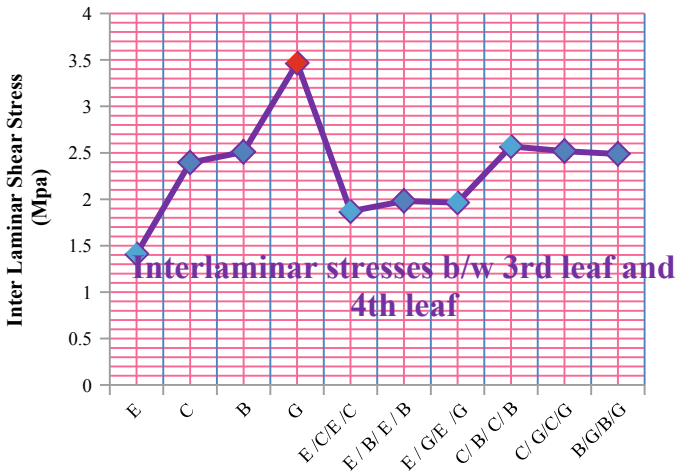


Fig. 10 Variation of Interlaminar stresses of third leaf and fourth leaf with respect to materials

4 Conclusions

The composite leaf springs are analyzed for deformations, von Mises stresses, shear stresses, and interlaminar stresses by using the finite element method. The following conclusions are extracted from the present findings.

The total deformations of the composite are more for E glass fiber epoxy reinforced composite due to the less longitudinal modulus of E glass/epoxy composite than other materials considered for the analysis.

It is recommended to use hybrid composite other than the pure E glass or graphite-epoxy composite for ensuring minimum von Mises stress.

The shear stress is more for graphite/epoxy composite spring.

The interlaminar stress is high at main leaf and second leaf interface, particularly for E glass composite.

Among all the composite leaf springs, carbon, boron fiber reinforced epoxy composite showed better performance in terms of results considered for the present study.

References

1. H. Singh, G.S. Brar, Characterization and investigation of mechanical properties of composite materials used for leaf spring. *Mater. Today Proc.* **5**, 5857–5863 (2018)
2. K. Ashwini, C.V. Mohan Rao, Design and analysis of leaf spring using various composites—an overview. *Mater. Today Proc.* **5**, 5716–5721 (2018)
3. J. Ke, Z.Y. Wu, X.Y. Chen, Z.P. Ying, A review on material selection, design method and performance investigation of composite leaf springs. *Compos. Struct.* **226**, 111277 (2019)
4. M.P. Jenarathanan, S. Ramesh Kumar, G. Venkatesh, S. Nishanthan, Analysis of leaf spring using carbon/ glass epoxy and EN45 using ANSYS: a comparison. *Mater. Today Proc.* **5**, 14512–14519 (2018)
5. T. Keerthi Vasani, S.M. Shibi, C.K. Tamilselvan, Fabrication and testing of composite leaf spring using carbon, glass and aramid fiber. *Mater. Today Proc.* **21**, 45–51 (2019)
6. P. Solanki, A.K. Kaviti, Design and computational analysis of semi-elliptical and parabolic leaf spring. *Mater. Today Proc.* **5**, 19441–19455 (2018)
7. M. Malikoutsakis, G. Savaidis, A. Savaidis, C. Ertelt, F. Schwaiger, Design, analysis and multi-disciplinary optimization of high-performance front leaf springs. *Theor. Appl. Fract. Mech.* **83**, 42–50 (2016)
8. M.M. Shokrieh, D. Rezaei, Analysis and optimization of a composite leaf spring. *Compos. Struct.* **60**, 317–325 (2003)
9. E. Sancaktar, M. Grattan, Design, analysis, and optimization of composite leaf springs for light vehicle applications. *Compos. Struct.* **44**, 195–204 (1999)
10. D.K. Roy, K.N. Saha, Nonlinear analysis of leaf springs of functionally graded materials. *Procedia Eng.* **51**, 538–543 (2013)
11. Y. Zhang, Z.X. Zuo, C.H. Yuan, D.J. Wang, Analysis on performance of leaf spring rotary engine. *Energy Procedia* **61**, 984–989 (2014)

12. D.M. Brouwer, J.P. Meijaard, J.B. Jonker, Large deflection stiffness analysis of parallel prismatic leaf-spring flexures. *Precis. Eng.* **37**(3), 505–521 (2013)
13. V. Khatkar, B.K. Behera, R.N. Manjunath, Textile structural composites for automotive leaf spring application. *Compos. Part B Eng.* **182**, 107662 (2019)
14. I.M. Danial, O. Ishai, *Engineering Mechanics of Composite Material* (Oxford University Press, Oxford, 2006)

Design of Gears Using Aluminium 6061-T6 Alloy for Formula SAE Steering System



Arnav Gupta, V. P. Yashvanth, and Lokavarapu Bhaskara Rao

Abstract Aluminium alloys have become major replacements of steel alloys for many applications due to its high strength to weight ratio and resistance to corrosion. Steering mechanism is one of the most important subsystems in an automobile that helps to control its direction of movement. In a Standard OEM (Original Equipment Manufacturer) Rack and Pinion system, generally steel alloys such as AISI 4340 and grey cast iron are used, due to higher dynamic loads and higher value of basic stress. For an efficient steering system, it is very important to take materials and properties of the gear system into consideration. This paper focuses on efficiently designing a lightweight rack and pinion steering system for an FSAE car by replacing conventional materials using aluminium 6061-T6 alloy due to its low cost and weight, taking contact stresses and bending stresses into consideration followed by verification with FEA (Finite Element Analysis) in ANSYS. In conclusion, the use of aluminium alloys in the steering system of FSAE vehicle will make it lighter and more efficient compared with standard OEM materials. The outcome of this research was use of aluminium alloys instead of conventional materials in gears based on their application.

Keywords Steering system · Rack and pinion · FSAE · Aluminium 6061-T6

A. Gupta (✉) · V. P. Yashvanth · L. B. Rao
School of Mechanical and Building Sciences, Vellore Institute of Technology,
Vandalur-Kelambakkam Road, Chennai, Tamil Nadu 600127, India
e-mail: arnavgupta98@yahoo.co.in

V. P. Yashvanth
e-mail: vp.yashvanth@gmail.com

L. B. Rao
e-mail: bhaskarbabu_20@yahoo.com

1 Introduction

FSAE is a platform that brings the world of motorsport and engineers together. The machinery and parts used require a unique combination of handling immense stresses and having a good endurance life while being lightweight. The dynamics of the entire race car rely on the delicate balance of strength to weight ratio, majorly with respect to the centre of gravity. As a result, engineers look for all possible ways of cutting down the weight on the car. The suspension and steering system is a primary example that comprises of many such crucial parts. The purpose of the subsystem is to ensure the correct response of the car while cornering and running on bumps and also to maximise the grip of the tyres in all scenarios. Most of the parts in this field vary by huge margins in every other race car, hence are made uniquely. The steering rack is one of the few parts, which is readily available in commercial market; however, they are designed for different sets of parameters such as withstanding higher loads and forces, dimensions that cannot be modified and heavier materials possessing more fatigue life leading to overdesign.

The load acting on a particular gear system plays a major role in the selection of materials. The loads acting on a formula student car are much lesser than commercial vehicles. This opens up options for using plastics such as Nylon 6-6 [1]. Non-ferrous materials show excellent corrosion resistance and are applicable for medium to low loads. Plastic gears, although having promising characteristics, can pose disadvantages due to their viscoelastic properties [2]. Aluminium alloys possess a wide range of uses based on the various series and are known for their weight reduction capabilities [3]. Modelling and simulation of steering and suspension geometries revealed the extent of forces induced on the designed parts and linkages [4].

Inferences made from the above research papers demonstrate the methodologies of weight reduction in gear systems using non-ferrous materials. Nonetheless, the research has overlooked the usage of aluminium alloys for gear systems. Based on calculations and simulations conducted for beam strength and wear strength, the use of aluminium alloys was verified [5–10].

2 Design Parameters

2.1 Material Selection

Chief design constraints of the assembly were eliminated by aluminium 6061-T6 encompassing properties of high strength to weight ratio, ease of machinability, lower material cost and abundance in the market. Aluminium 6061-T6 has the following material properties [2, 3]:

- Young's modulus (E): 68.9 GPa
- Ultimate tensile strength (σ_{ut}): 310 MPa
- Yield strength (σ_y): 275 MPa.

Rack, pinion, gearbox casing and steering stops were machined out of aluminium 6061-T6. The steering extension and shafts were made up of AISI 1060 Steel.

2.2 *Suspension and Steering Design*

According to FSAE, the teams are required to follow certain design rules and the cars should fulfil the minimum design requirements in order to participate in the competition. A few of them concerning the design of steering and suspension systems are [11]:

- Minimum wheelbase should be 1525 mm
- The rear track width should be a maximum of 75% of the front track width
- The steering system must have mechanical stops attached to restrict maximum travel of the rack
- The car should have a minimum of 25 mm jounce, 25 mm rebound and 50 mm of wheel travel.

With respect to the above rules, the suspension and steering geometries were designed. An optimum racing suspension ensures the maximum contact of the tyres with the road in all possible occasions like hard acceleration, braking and turning, with no loss of traction. The suspension geometry incorporates a number of factors such as static camber, caster, toe, scrub radius and mechanical trail. The steering geometry works on optimising the wheel lock angles, steering rack travel and turning radius. The parts of suspension system move dynamically with the changes on the road and their motion induces forces that have to be overcome by the steering to turn the wheel. Hence the process of vehicle design starts with the suspension and steering geometry. A basic suspension geometry is made followed by simulation on vehicle dynamics software [4]. For our purpose, the simulation was conducted on OptimumG Package.

An optimised result is said to have a minimal change of camber rate, toe, a desirable motion ratio, stability of the car along all three axes of rotation, that is, yaw, pitch and roll, and overall, a geometry that would generate low stress on components. After iterating lots of geometries, a double-wishbone, pull rod suspension and Ackerman steering type was finalised as shown in Figs. 1 and 2 with the parameters as illustrated in Tables 1 and 2, respectively.

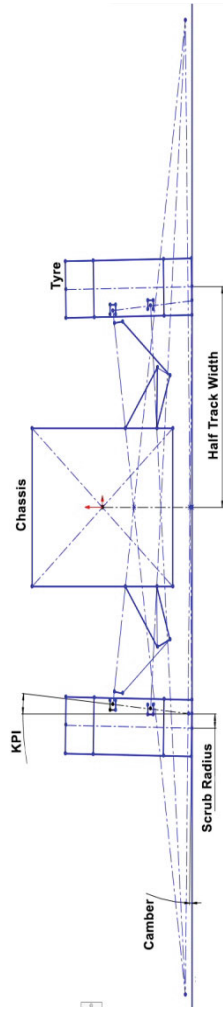


Fig. 1 Front Suspension Kinematic geometry. *Source* SolidWorks user manual

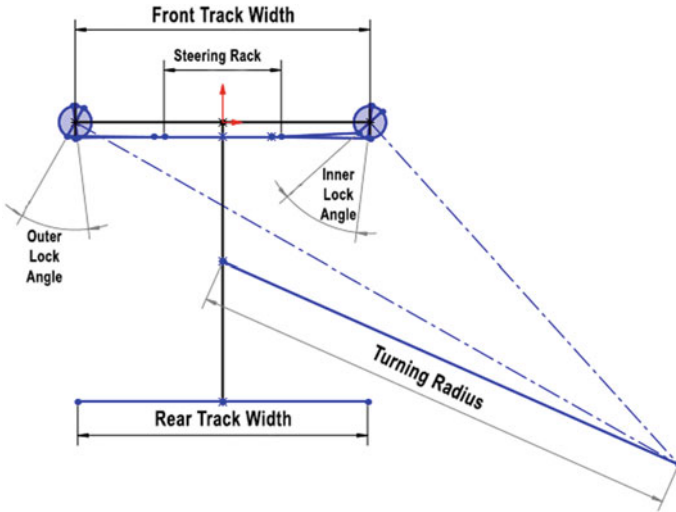


Fig. 2 Steering geometry. *Source* SolidWorks user manual

Table 1 Suspension outputs

Parameter	Value
King pin inclination	6.70 deg
Caster angle	10.39 deg
Scrub radius	30.71 mm
Mechanical trail	44.54 mm
Mass of car (with drive)	260 kg
mass% at front (with driver)	50%
Tyre diameter	457 mm

Table 2 Steering outputs

Parameter	Value
Wheelbase	1545 mm
Front track width	1180 mm
Rear track width	1160 mm
Steering arm length	76.25 mm
Ackerman angle	59.7266 deg
Angle of inside lock	40.97 deg
Angle of outside lock	36.58 deg
Turning radius of front inner wheel	1846.70 mm
Turning radius of front outer wheel	2778.59 mm
Rack travel	112 mm
Turning radius	1999.03 mm

3 Gear Type Selection

As the main task of the research is to attain weight and space optimisation, spur gear with 20° full depth involute profile was selected. This configuration allows lower face width for both gear components, no additional side thrust and a constrained volume at a reasonable cost of manufacturing. Spur gears also provide efficient power transmission and are perfectly matched towards moderate speed applications.

4 Calculations for Rack and Pinion

Parameters obtained from the kinematic diagram are as follows:

- King pin inclination (θ): 6.7 deg
- Caster angle (μ): 10.39 deg
- Scrub radius (s): 30.71 mm
- Mechanical trail (t): 44.54 mm
- Mass of car (m): 260 kg
- Inside lock angle (δ): 40.97 deg
- Turning radius (R): 1.999 m
- Steering arm length (S_L): 76.25 mm.

Total weight of the car, W_T as shown in Eq. (1)

$$W_T = 260 \times 9.81 = 2550.6 \text{ N} \quad (1)$$

4.1 Forces Due to Dynamic Conditions

Calculation of load on front axle is as follows [12]:

As weight distribution is 50% at front axle,

therefore, the weight at front axle, W_F as shown in Eq. (2)

$$W_F = 0.5 \times W_T = 1275.3 \text{ N} \quad (2)$$

Due to king pin inclination (KPI), tyre has to overcome the additional moment to turn the wheel about the tyre axis.

Therefore, moment due to KPI, M_K as shown in Eq. (3)

$$\begin{aligned} M_K &= W_F \times \sin(\theta) \times \sin(\delta) \times s = 1275.3 \times \sin(6.7) \times \sin(40.97) \times 30.71 \\ &= 2961.484 \text{ N-mm} \end{aligned} \quad (3)$$

Moment needs to overcome effects of mechanical trail.

Therefore, moment due to trail, M_{MT} as shown in Eq. (4)

$$\begin{aligned} M_{MT} &= (\text{Change in Mass Distribution}) \times t \times \sin(\mu) \times \cos(\delta) \\ &= 382.59 \times 44.54 \times \sin(10.39) \times \cos(40.97) \\ &= 2320.445 \text{ N-mm} \end{aligned} \quad (4)$$

Frictional torque is generated between tyres and ground while turning. Assuming that the vehicle is cornering with a speed of 40 kmph, the friction couple generated can be calculated as follows:

Friction couple F_C as shown in Eq. (5)

$$F_C = \frac{mv^2}{4R} = 4014.35 \text{ N} \quad (5)$$

Aligning torque due to couple, M_A as shown in Eq. (6)

$$\begin{aligned} M_A &= F_C \times \text{Tyre Radius} \times \sin(\mu) \times \sin(\delta) \\ &= 4014.35 \times 228.5 \times \sin(10.39) \times \sin(40.97) \\ &= 108465.76 \text{ N-mm} \end{aligned} \quad (6)$$

Total generated moment, M_{net} as shown in Eq. (7)

$$M_{net} = M_K + M_{MT} + M_A = 114082.16 \text{ N-mm} \quad (7)$$

4.2 Calculations of Net Load for Pinion

Tangential forces acting on pinion are given by Eq. (8),

$$M_{net} = F_T \times S_L$$

$$\text{Therefore, } F_T = 114082.16/76.25 = 1496.159 \text{ N} \quad (8)$$

Considering the service factors from design data book [13]

Application factor = $K_a = 1$

Load concentration factor = $K_m = 1.2$

Velocity factor = $K_v = 1$

Hence, the effective load is given by Eq. (9):

$$P_{\text{eff}} = (K_a \times K_m \times F_T)/K_v = (1 \times 1.2 \times 1496.159)/1 = 1795.39 \text{ N}$$

Therefore, effective load on pinion = 1800 N (approx.) (9)

4.3 Design of Pinion

For designing the pinion, the number of teeth (Z_p) and pressure angle (Φ) of the pinion were assumed to 18 and 20° , respectively. Full involute profile was taken for the teeth as mentioned above.

The material selected is Al6061-T6 alloy.

Therefore, $\sigma_y = 310 \text{ MPa}$

According to Maximum Shear Stress Theory, permissible stress (σ_p) is 0.5 times of yield strength of the material.

Therefore, σ_p is given by Eq. (10),

$$\sigma_p = 310/2 = 155 \text{ MPa} \quad (10)$$

Taking the velocity factor C_v into consideration, the permissible working stress (σ_w) is given by Eq. (11),

$$\sigma_w = \sigma_y \times C_v = 155 \times \frac{4.5}{4.5 + V} = 697.5/(4.5 + 0.05654 m) \quad (11)$$

where, v is the mean velocity of the gear and m is assumed module of the pinion.

The rack and pinion are of the same material. As pinion is the weaker element, the calculations are carried for pinion [8].

For a gear with 20° full involute teeth, Lewis form factor (y) is given by Eq. (12),

$$y = 0.154 - 0.912/Z_p = 0.1033 \quad (12)$$

From the Lewis equation,

Tangential force on pinion is given by Eq. (13) [14],

$$F_T = \sigma_w \times \pi \times m \times b \times y \quad (13)$$

where b is the face width of the pinion.

Assuming standard value for $b = 12.5 \times m$ from design data book [13],

The tangential force on the pinion is given by Eq. (14),

$$F_T = \sigma_w \times \pi \times m \times 12.5 \times m \times y = \frac{697.5 \times \pi \times m \times 12.5 \times m \times 0.10333}{4.5 + 0.05654 m} \quad (14)$$

Therefore, the tangential force on pinion is given by Eq. (15),

$$F_T = 2830.37 \times m^2 / (4.5 + 0.05654m) \text{ N} \quad (15)$$

Now, tangential force on pinion = effective load on pinion x factor of safety (16)

Let the factor of safety be 2, and is given by Eq. (16),

Therefore, the tangential force on pinion is given by Eq. (17),

$$F_T = 2830.37 \times m^2 / (4.5 + 0.05654 m) = 1800 \times 2 \quad (17)$$

Upon simplification of Eq. (17), yields the Eq. (18),

$$m^2 - 0.069115 m - 5.736157 = 0 \quad (18)$$

On solving,

$$m = 2.4298$$

Using standard value for m from design data book [13],

$$m = 2.5$$

Hence, the module of the pinion found to be 2.5 mm.

Therefore, diameter of the pinion (D_P) is given by Eq. (19),

$$\begin{aligned} D_P &= m \times Z_P \\ &= 2.5 \times 18 \\ &= 45 \text{ mm} \end{aligned} \quad (19)$$

4.4 Calculations for Rack

The length of rack will be decided based on the maximum desired motion of the pinion by the driver and as per the calculation.

Considering 95° as lock angle for steering wheel, pinion travel is given by Eq. (20),

$$\begin{aligned} \text{Pinion Travel} &= (2 \times 95 \times \pi \times D_P) / 360 \\ &= 74.6128 \text{ mm} \end{aligned} \quad (20)$$

Rack length according to steering geometry = 112 mm

Hence stops should be provided.

4.5 Pinion Parameters

Pressure angle $\Phi = 20^0$ (full involute teeth)

Number of teeth $Z_p = 18$ teeth

Module = 2.5 mm

Diameter of the pinion $D_p = 45$ mm

Addendum, m is given by Eq. (21),

$$m = 2.5 \text{ mm} \quad (21)$$

Dedendum = 1.25 m is given by Eq. (22),

$$= 3.125 \text{ mm} \quad (22)$$

Clearance = 0.2 m is given by Eq. (23),

$$= 0.625 \text{ mm} \quad (23)$$

Tooth thickness = $(\pi/2) \times m$

$$= 3.9269 \text{ mm}$$

Face width $b = 12.5 m = 32$ mm

4.6 Rack Parameters

Thickness of rack tooth is given by Eq. (24) = 3.927 mm

$$\text{Therefore, number of teeth on rack} = 112/3.927 = 29 \text{ teeth} \quad (24)$$

Therefore number of teeth on rack $Z_r = 30$ teeth (round off)

4.7 Calculation of Beam and Wear Strength

Beam strength of the pinion is calculated as follows:

Tangential force on pinion is given by Eq. (25),

$$F_T = \sigma_w \times \pi \times m \times b \times y \quad (25)$$

Lewis form factor is given by Eqs. (26 and 27),

$$y = 0.154 - 0.912 / Z_p = 0.1033 \quad (26)$$

$$b = 12.5 \times m = 32 \text{ mm} \quad (27)$$

Therefore, beam strength = $F_t = 1800 \text{ N}$

Wear strength (F_w) of the pinion is given by Eqs. (28 and 29),

$$F_w = D_p \times b \times Q \times K \quad (28)$$

where,

$$Q = 2i / (i + 1) \quad (29)$$

b = face width of the gear

D_p = diameter of the pinion, K is load stress factor is given by Eq. (30),

$$K = \left(\frac{\sin \Phi (\sigma_{-1})^2}{1.4} \right) \times \left(\frac{1}{E_p} + \frac{1}{E_g} \right) \quad (30)$$

Here, E_p and E_g are Young's modulus of pinion and gear, respectively.

Whereas σ_{-1} is endurance limit for aluminium, which is given by Eq. (31), [13]

$$\sigma_{-1} = \frac{0.4 \times \sigma_y \times ABC}{K_r} \quad (31)$$

where A , B and C are service factors as follows,

$$A = 1$$

$$B = 0.9$$

$$C = 0.7$$

K_r = reliability factor

Taking reliability as 90%

$$K_r = 0.814.$$

Therefore, $\sigma_{-1} = 85.135 \text{ MPa}$

Hence, $K = 0.05132$.

The wear strength of the pinion is given by Eq. (32),

$$\begin{aligned}
 F_w &= 45 \times (2.3 \times 2) \times 32 \times 0.05132 / (3.3) \\
 &= 103.01 \text{ N}
 \end{aligned}
 \tag{32}$$

As wear load (F_w) is much lesser than the load for beam strength ($F_T = 1800 \text{ N}$), the design is safe for the obtained gear parameters.

4.8 Calculation of Force Applied by the Driver on the Steering System

The torque on pinion is calculated by measurement of forces input by the driver from the steering wheel. Driver ergonomics tests suggest application of 100 N average force on the steering wheel. For a wheel of 300 mm diameter, torque acting is calculated as:

Steering torque is given by Eq. (33),

$$\text{steering torque} = \text{steering force} \times \text{radius of wheel} = 15000 \text{ Nmm} \tag{33}$$

Considering transmission efficiency of 90% through steering column, effective torque on pinion is given by Eq. (34),

$$\text{effective torque on pinion} = 15000 \times 0.9 = 13500 \text{ Nmm} \tag{34}$$

5 CAD Model

According to the dimensions obtained in calculations, rack and pinion gears were designed as shown in Fig. 3a, b, respectively, in SolidWorks software [15]. The gears were generated using the standard in-built toolbox present in the CAD package.

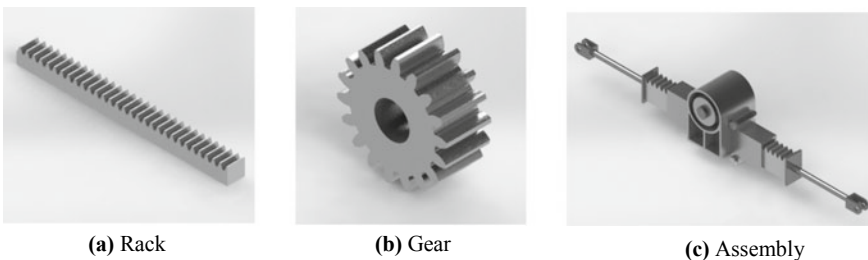


Fig. 3 a Rack. b Gear. c Assembly. *Source* SolidWorks user manual

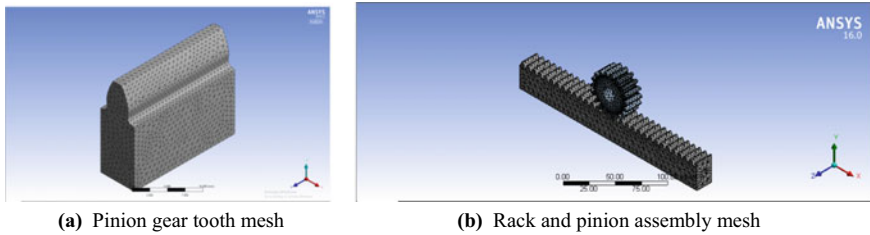


Fig. 4 **a** Pinion gear tooth mesh. **b** Rack and pinion assembly mesh. *Source* ANSYS user manual [16]

Figure 3c shows the entire assembly of the rack and pinion steering system inside the casing.

6 Finite Element Analysis

6.1 Meshing

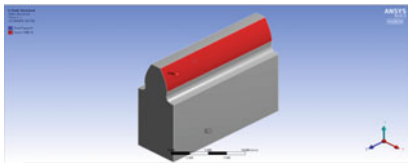
It is the process of dividing the structural elements into a number of smaller elements for computation of stress values at particular points. The entire structure was meshed using tetrahedron elements using patch conforming algorithm. Tetrahedron mesh elements were chosen because it gives more accurate results for local stress concentrations. Figure 4a, b shows the mesh of pinion tooth and the rack and pinion assembly, respectively [1, 6].

6.2 Boundary Conditions

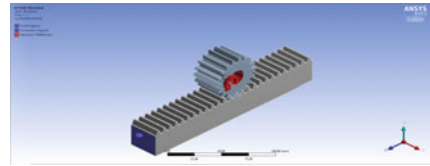
For finding the beam strength of the gear tooth, the bottom of the gear tooth was given fixed support and the tangential forces were given in terms of components on the gear tooth face as shown in Fig. 5a [5, 6]. Rack was given fixed support at both the ends and the pinion was given frictionless support and a moment of 13.5 N-m was applied on the pinion in anticlockwise direction as calculated in eq. (34). Figure 5b shows the setting up of boundary conditions for rack and pinion assembly [7, 8].

6.3 Grid Independence Study of Rack and Pinion Assembly

For the pinion gear tooth, face sizing was used to control the element sizes locally. For the rack and pinion assembly, the mesh size of the gears was decreased continuously



(a) Pinion gear tooth boundary conditions



(b) Pinion frictionless support

Fig. 5 a Pinion gear tooth boundary conditions. b Pinion frictionless support. *Source* ANSYS user manual [16]

Table 3 Grid Independence study for pinion gear tooth

Number of nodes	Equivalent (von Mises) stresses (MPa)
3354	160.08
6261	167.44
17638	198.54
17817	200.62
24323	203.06
33536	207.04
34173	207.32

Table 4 Grid Independence study for rack and pinion assembly

Number of nodes	Equivalent (von Mises) stresses (MPa)
5642	6.4758
9505	6.8463
14755	6.8534
21299	6.8893
33015	9.6032
73167	10.972
85983	11.366
109043	11.445

using body sizing and face sizing functions in Meshing Modeler until recurring values of the stresses were obtained. Tables 3 and 4 show the mesh convergence study on increasing the number of elements for pinion gear tooth and assembly, respectively.

6.4 Analysis of Von Mises Stresses and Contact Stresses

The following results were obtained using maximum distortion energy theory. For pinion gear tooth equivalent stress, equivalent strain and total deflection are shown in Fig. 6a–c, respectively. Similarly, for rack and pinion assembly, the equivalent

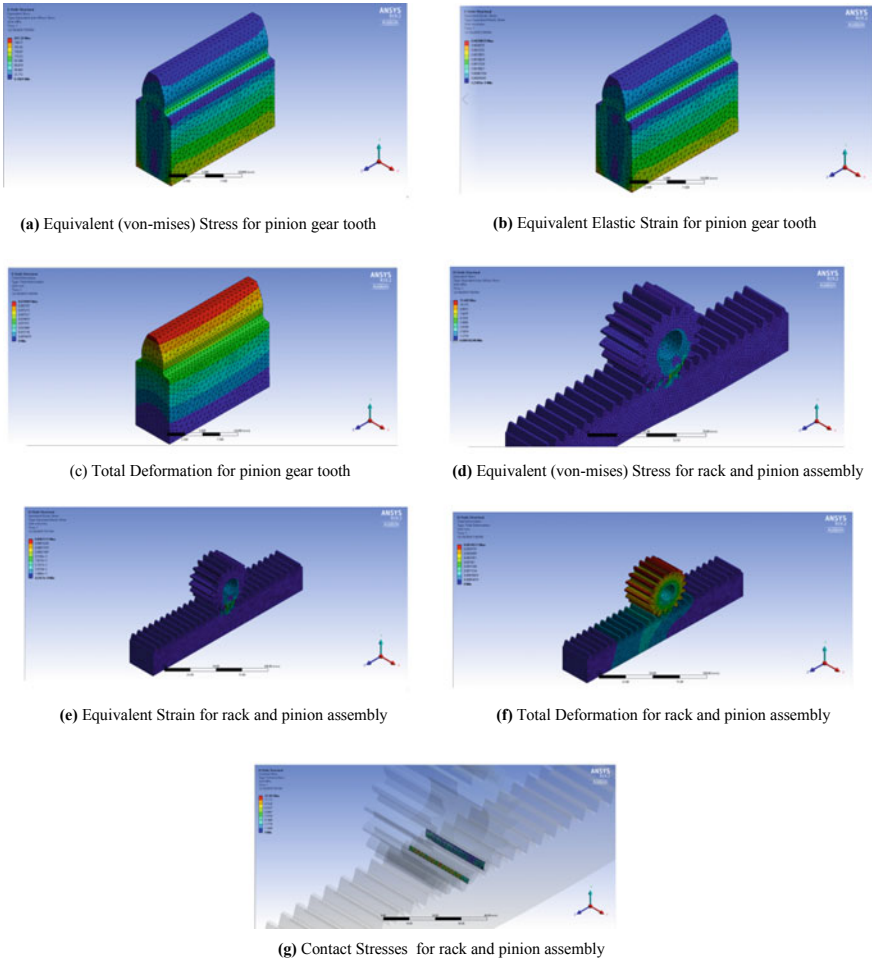


Fig. 6 **a** Equivalent (von Mises) Stress for pinion gear tooth. **b** Equivalent elastic strain for pinion gear tooth. **c** Total deformation for pinion gear tooth. **d** Equivalent (von Mises) Stress for rack and pinion assembly. **e** Equivalent Strain for rack and pinion assembly. **f** Total deformation for rack and pinion assembly. **g** Contact stresses for rack and pinion assembly. *Source* ANSYS user manual

stress, equivalent strain, total deflection and contact stresses are shown in Fig. 6d–g, respectively. The design was made based on beam and wear strength [9, 10]. From the results, it could be inferred that the stresses are way below the calculated permissible values on application of moment of 13.5 N-m on pinion.

Table 5 Structural analysis result of pinion gear tooth

Object name/state	Total deformation (mm)	Equivalent elastic strain (mm/mm)	Equivalent stress (MPa)
Minimum	0	1.2 e-05	0.7605
Maximum	0.07	0.002	207.32

Table 6 Structural Analysis result of rack and pinion assembly

Object name/state	Total deformation (mm)	Equivalent elastic strain (mm/mm)	Equivalent stress (MPa)	Contact stress (MPa)
Minimum	0	4.24 e-09	0.0001	0
Maximum	0.003	0.00017	11.445	12.501

Source ANSYS user manual

7 Result and Discussion

The theoretical calculations show the required dimensions and specifications of the rack and pinion gears. The pinion module was found to be 2.5 mm and the associated gear parameters for both the gears were calculated. The values for the beam and wear strength were also calculated. After conducting FEA for pinion gear tooth as well as rack and pinion assembly, the following results were found and are illustrated in Tables 5 and 6. The results show that the maximum value of equivalent stress and total deformation for gear tooth is 207.32 MPa and 0.07 mm, respectively. For the rack and pinion assembly, the maximum equivalent stress, maximum contact stress and total deformation are 11.445 MPa, 12.501 MPa and 0.003 mm, respectively. On comparing these results with the yield strength [3] of aluminium alloy and the beam strength and wear strength of the gears, it can be inferred that the design is safe for the given application and loads.

8 Conclusion

From the above results, we can conclude that the use of aluminium 6061-T6 alloy for making rack and pinion steering systems for an FSAE car is suitable, as it reduces weight and manufacturing costs due to its material properties and its ease of machining. Material selection was thus found to be an extremely crucial step for optimisation as per design loads. Further enhancements of aluminium gear systems can be made by heat treatment methods such as carbonitriding, austenitic nitro-carburising, induction hardening, vacuum heat treatment for better strength and improved hardness, whereas anodising can be done for a better surface finish that will increase reliability and lifetime of the component and facilitate smooth and noiseless operation.

References

1. A. Chopane, S. Gupta, A. Ajit, S. Kakroo, A. Salve, Design and analysis of plastic gears in rack and pinion steering system for formula supra car. *Mater.Today Proc.* **5**(2), 5154–5164 (2017). <https://doi.org/10.1016/j.matpr.2017.12.097>
2. Shastri, D., Ramamurthy, S., Parab, P.: Strategies for automobile gear material selection. SAE Technical Paper (2008). doi:<https://doi.org/10.4271/2008-28-0055>
3. D. Ashkenazi, How aluminum changed the world: a metallurgical revolution through technological and cultural perspectives. *Technol. Forecast. Soc. Change* **1**(143), 101–113 (2019). <https://doi.org/10.1016/j.techfore.2019.03.011>
4. Y.S. Saurabh, S. Kumar, K.K. Jain, S.K. Behera, D. Gandhi, S. Raghavendra, K. Kalita, Design of suspension system for formula student race car. *Procedia Eng.* **1**(144), 1138–1149 (2016). <https://doi.org/10.1016/j.proeng.2016.05.081>
5. K.N. Naik, D. Dolas, Static analysis bending stress on gear tooth profile by variation of gear parameters with the help of FEA. *IJERT* **3**(6), 132–136 (2014)
6. S. Ghosh, R. Ghosh, B. Patel, T. Srivastava, R.N. Barman, Structural analysis of spur gear using ANSYS workbench 14.5. *IJMET* **7**(6), 132–141 (2016)
7. U.P. Nileshta, P.C. Sunil, L.C. Gajanan, Stress analysis of spur gear by using different materials: a review. *ICIIIME* **5**(6), 355–363 (2017)
8. T.Z. Hlaing, H.H. Win, M. Thein, Design and analysis of steering gear and intermediate shaft for manual rack and pinion steering system. *IJSRP* **7**(12), 861–882 (2017)
9. M.S. Abhijit, M.M. Mirza, Contact stress analysis of spur gear by photoelastic technique and finite element analysis. *IJTARME* **3**(2), 50–54 (2014)
10. C.H. Seok, H.L. Jin, H.L. Dong, H.H. Seung, H.L. Kwon, Contact stress analysis for a pair of mating gears. *Math. Comput. Modell.* **57**(1–2), 40–49 (2013). <https://doi.org/10.1016/j.mcm.2011.06.055>
11. Formula Student Rulebook, SAE International (2017–18)
12. William, F.-M., Douglas, L.-M.: *Race Car Vehicle Dynamics*, SAE International (1994)
13. G.R. Damodaran, *PSG Design Data Book* (PSG College of Technology, Kalaikathir, Achchagam, Coimbatore, 2018)
14. R.S. Khurmi, J.K. Gupta, *A Textbook of Machine Design* (Eurasia Publishing House Pvt. Ltd, New Delhi, 2005)
15. Solidworks user manual, Version 18, 2018
16. ANSYS user manual, Version 19.2, 2019

Design and Analysis of Helical Teeth Harmonic Drive



Sekar Anand, Arunachalam Dharmalingam Srikeshav, Baskar Sharran,
and Lokavarapu Bhaskara Rao

Abstract Harmonic drives are power transmitting devices with high torque and precision. They are used in many applications for their advantage of providing high torque ratio and reduced backlash, thereby reducing the power loss in the drive. The primary objective of this project is to modify the design of the harmonic drives by introducing harmonic teeth instead of existing straight teeth. The harmonic drives were modeled using SolidWorks. Three incremental loads are applied on a tooth of each harmonic drives and the stress developed on the tooth was found out using structural analysis in ANSYS. The results showed that the stress generated on the helical tooth of the flex spline was less compared with that of the stress developed on the straight tooth. There was an increase in the stress developed as the force acting on the tooth increased.

Keywords Straight teeth flex spline · Helical teeth flex spline · Stress · Deformation · Strain

1 Introduction

Harmonic drives are devices used in many applications where high torque and precisions are required. In general, a harmonic drive consists of a circular spline, a wave generator, and a flex spline. The wave generator will be elliptical and is inserted

S. Anand (✉) · A. D. Srikeshav · B. Sharran · L. B. Rao
School of Mechanical and Building Sciences, Vellore Institute of Technology, Chennai Campus,
Vandalur-Kelambakkam Road, Chennai, Tamil Nadu 600127, India
e-mail: s.anand2016@vitstudent.ac.in

A. D. Srikeshav
e-mail: ad.srikeshav2016@vitstudent.ac.in

B. Sharran
e-mail: b.sharran2016@vitstudent.ac.in

L. B. Rao
e-mail: bhaskarbabu_20@yahoo.com

inside the flex spline due to which the flex spline will also take the shape of the wave generator that is an ellipse. The circular spline always has a greater diameter when compared with the other components of a harmonic drive. The flex spline has external teeth and the circular spline has internal teeth. The significant advantage of the harmonic drive is that there is no backlash existing in the design model, which reduces the power loss during the transmission. The space required for the drive is also less and the gear ratio of around 320:1 can be obtained. It finds applications in robotics, aerospace, rotating home television antennas to sophisticated systems for the military. Many types of research are currently going on this field as it has many advantages. FEA analysis is carried out on the harmonic drives for two materials, steel and glass/epoxy [1]. The stress and stiffness came out to be less for the composite than the steel flex spline. A method was carried out to find the load shared by the tooth [2]. In addition to that, the optimized design of the flex spline was done [3]. The flex spline root of the tooth undergoes fatigue due to circular spline. The deformation shape of the flex spline, various stress distributions at the root of the tooth in the flex spline, and the load of the bearing ball are calculated [4]. A rapid stress calculation method for short flex spline harmonic drive was formulated [5]. Also, stress and deformation analysis were carried out on short flex spline in a harmonic drive system by varying the amount of load acting on them [6]. Furthermore, in another paper, numerical stress calculation was carried out on hermitic harmonic drive flex spline [7]. Also, the stress-induced on the bottom flange of the flex spline was calculated by measuring the strain at various locations by keeping the cup stationary and rotating the cam inside the cup [8]. Ostapski et al. [9] studied the failure of the bearing supporting the generator in the harmonic drive. Dynamic simulation of the harmonic drive was established to study the intensity of the flex spline based on Finite Element Analysis [10].

2 Problem Statement

The main objective of this project is to reduce the stress that is being developed on the tooth. The design and analysis are carried out for a helical teeth-shaped harmonic drive and the stress, deformation, and strain values are compared with straight teeth harmonic drive.

3 Methodology

3.1 Modeling of Harmonic Drive

There were two harmonic drives designed, an existing design that has straight teeth and a new design that consists of helical teeth, which were modeled using SolidWorks

Table 1 Dimensions of straight teeth harmonic drive [2]

Description	Flexgear	Circular gear
Number of teeth	156	158
Pressure angle	30°	
Module	0.529 mm	
Addendum factor	0.8	0.8
Dedendum factor	1.25	0.8
Material	Steel (EN24)	
<i>Wave generator</i>		
Major axis	80.85 mm	
Minor axis	78.66 mm	

[11]. The dimension of straight teeth helical drive is shown in Table 1. The dimensions are taken from the harmonic drive catalog [13] and in the article of load shared by the number of teeth [2]. For the helical teeth harmonic drive, the same dimensions were used but helical teeth were made using the helix option provided in SolidWorks. The helix angle normally ranges between 5 and 25, [14, 15]. The pitch distance was given as 1000 mm, revolutions as 0.0199, so that the helix angle came out to be 14.71°.

The pitch circle diameter of straight teeth harmonic drive and helical teeth harmonic drive are given by Eq. (1),

$$m = D / Z_c \tag{1}$$

where

- m module
- D pitch circle diameter
- Z_c number of teeth

The values of the module and the number of teeth are taken from Table 1 and the pitch circle diameter of flex spline is calculated as follows,

$$0.529 = D / 156$$

$$D = 82.524 \text{ mm}$$

The value of D is the pitch circle diameter of the flex spline. Thus subtracting the dedendum factor (given in Table 1) from this value could yield the outer circle diameter (OD) of the flex spline. It is given by the following,

$$OD = D - \text{Dedendum factor}$$

$$OD = 82.524 - 1.25$$

$$OD = 81.274 \text{ mm}$$

Flex spline's Outer Diameter (OD) is obtained. The rim thickness of the flex spline is kept as 0.685 mm [2]. Thus, the Inner diameter (ID) of the flex spline can be found as follows,

$$ID = OD - 2 * (\text{rim thickness})$$

$$ID = 81.274 - 2 * 0.685$$

$$ID = 79.904 \text{ mm}$$

Similarly, calculations were followed to find the inner diameter of the circular spline. The thickness of the circular spline was assumed to be 20 mm. As the analysis was majorly for the tooth in flex spline, thus the assumed value will not affect the final result. The wave generator was produced as per the dimensions given in Table 1. Since our final result was focused on the stress developed on the tooth of flex spline, a slight modification was done to the flex spline model. When the wave generator is introduced into the flex spline, there will be an elongation on two sides in the flex spline. As per the Poisson ratio, there will be a contraction on the other two sides. Thus, the circular flex spline was converted into elliptical flex spline by the following

Area of circular flex spline = Area of elliptical flex spline

$$\pi \times (R_O^2 - R_I^2) = \pi \times (A_O B_O - A_I B_I) \quad (2)$$

$$B_I = B_O - \text{rim thickness} \quad (3)$$

where

R_I inner radius of the flex spline

R_O outer radius of the flex spline

A_I semimajor axis of inner ellipse

B_I semiminor axis of inner ellipse

A_O semimajor axis of outer ellipse

B_O semiminor axis of outer ellipse

Substituting the known values in Eq. (2),

$$(40.637^2 - 39.952^2) = (41.11 \times B_O) - (40.425 \times (B_O - 0.685))$$

On solving, the semimajor axis of the outer ellipse (B_O) would be 40.165 mm. By knowing B_O , B_I can be found using Eq. (3) that comes out to be 39.527 mm. Thus

from these dimensions, the flex spline was modeled using SolidWorks. The model of flex spline with straight teeth and helical teeth is seen from Fig. 1a, b. Similarly, Fig. 2a, b shows a circular spline with straight teeth and helical teeth. The model of the wave generator is seen in Fig. 3. After the assembly of these parts, the harmonic drive looks like Fig. 4.

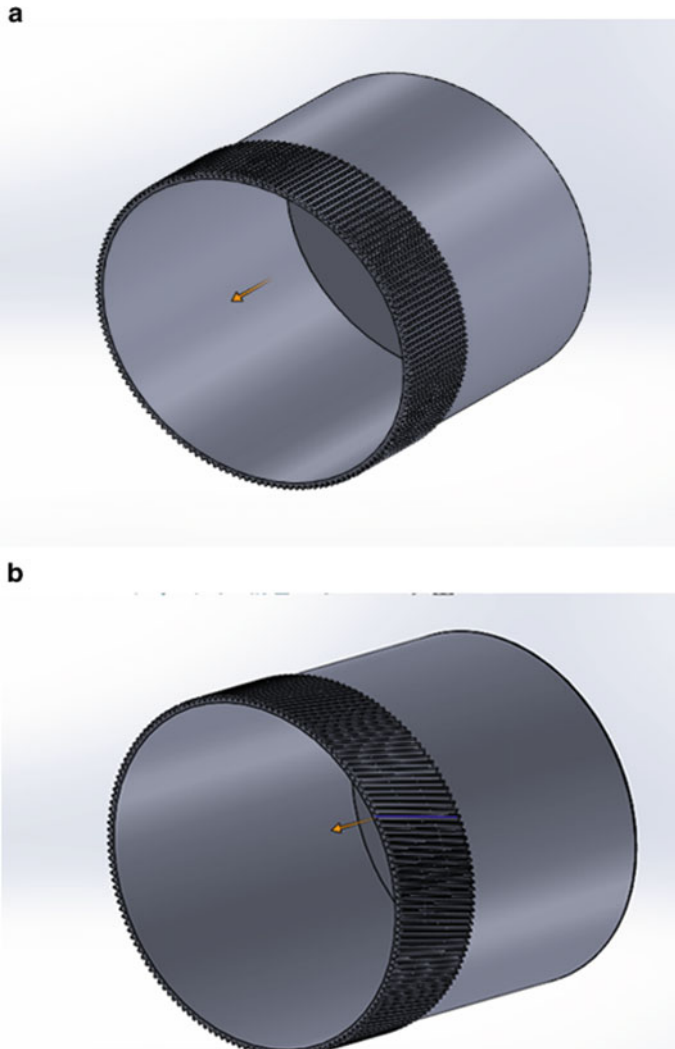


Fig. 1 a SolidWorks model of the straight teeth flex spline [11]. b SolidWorks model of the helical teeth flex spline [11]

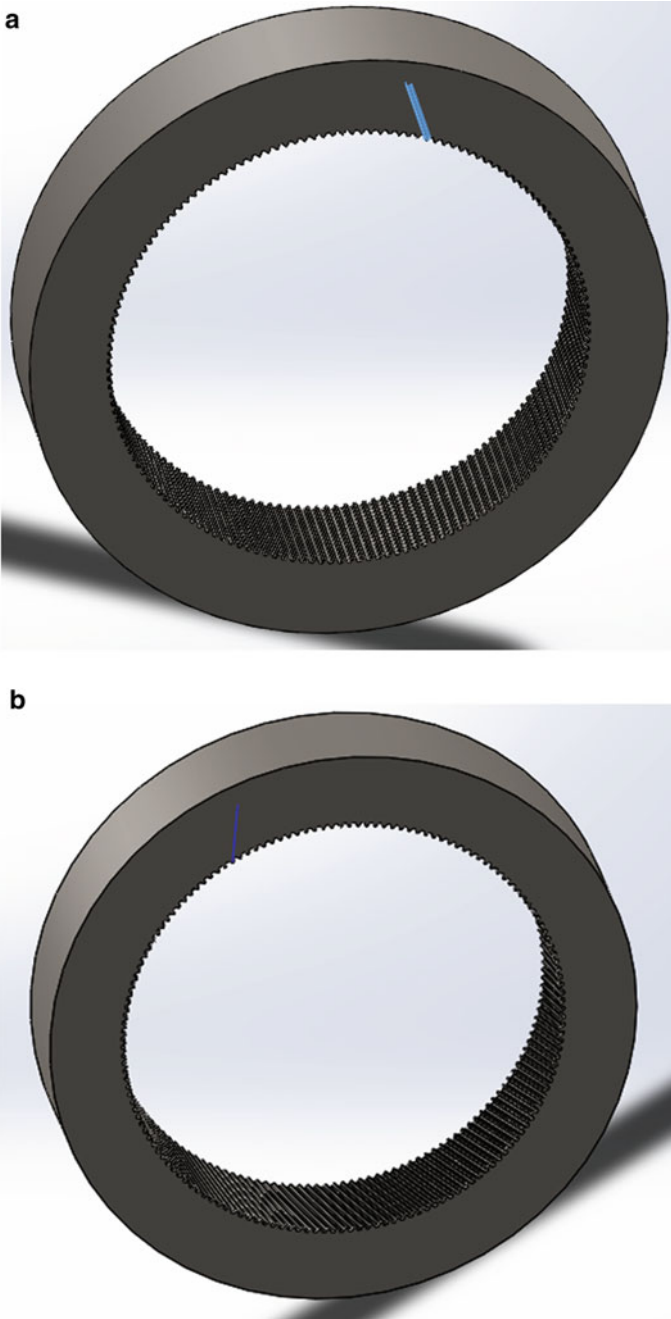


Fig. 2 a SolidWorks model of straight teeth circular spline [11]. b. SolidWorks model of helical teeth circular spline [11]

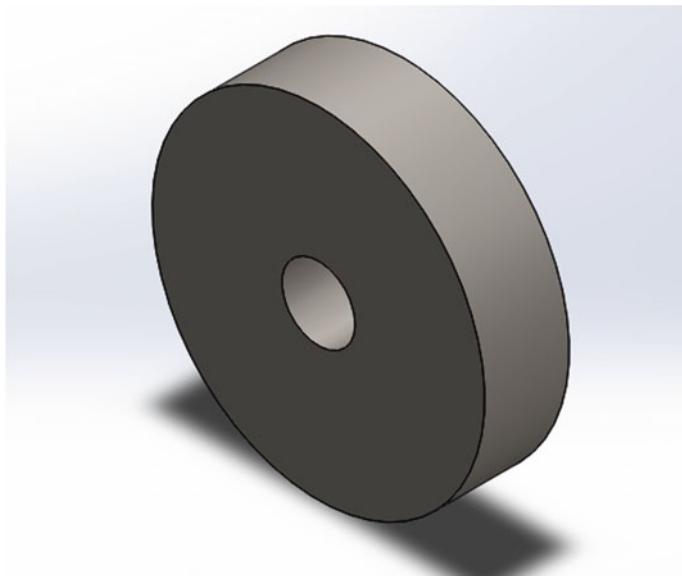


Fig. 3 SolidWorks model of wave generator [11]

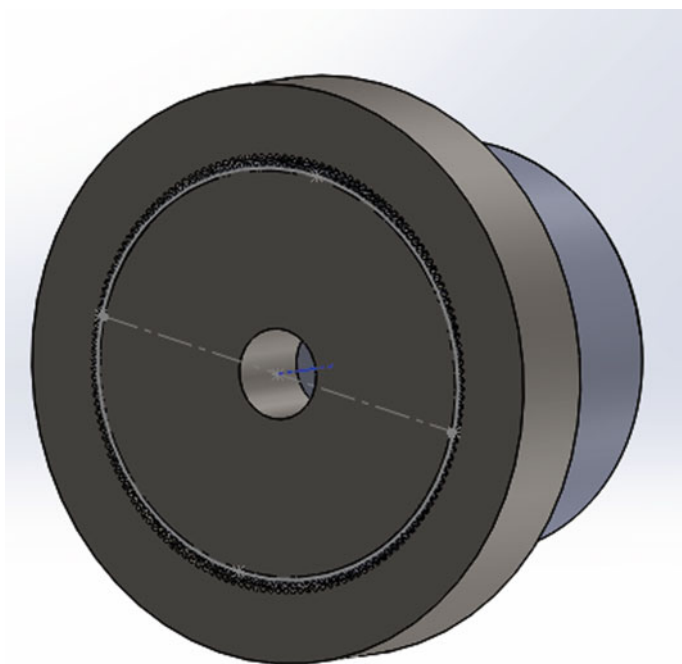


Fig. 4 SolidWorks model of assembled harmonic drive [11]

3.2 Analysis of Harmonic Drive

The modeled harmonic drive was analyzed using ANSYS [12]. Three torque values are taken according to the rating given in the catalog [5], 67, 90, and 120 Nm. The force acting on the teeth is found out using the following relation,

$$T = FR \sin \theta \quad (4)$$

where

T torque

F force

R radius of the flex spline

θ angle between force and radius

Since the force would be perpendicular to the radius, θ becomes 90° and $\sin \theta$ becomes 1. There will be a change in the forces while moving across the teeth from the dedendum to the addendum. Thus, an average force value is taken to be that of the pitch circle radius value. The value of force obtained from torque values of 67 Nm, 90 Nm, and 120 Nm will be 1623.78 N, 2181.18 N, and 2908.24 N, respectively. There will be another force due to the relation of flex spline rim after its elongation. This force value would be less compared with the torque force and hence can be neglected.

The material properties of EN24 are imported into Engineering Data in ANSYS and all the components are given similar materials. The rest of the data and options are set as default. Circular Spline is kept as fixed support throughout the analysis as shown in Fig. 5. An example is illustrated with the load of 1623.78 N acting on a single helical tooth flex is given by Fig. 6.

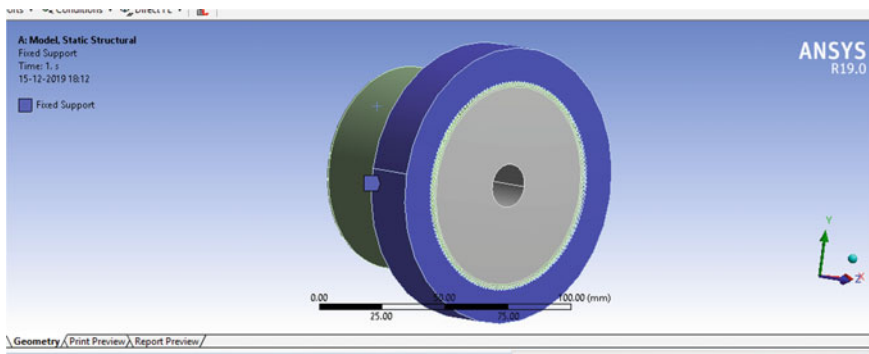


Fig. 5 Circular spline fixed support [12]

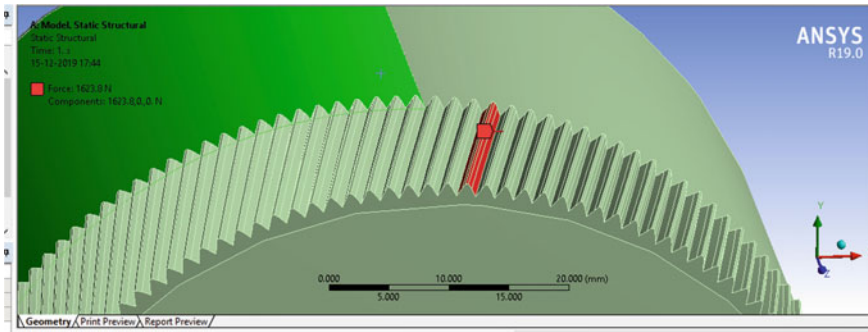


Fig. 6 Load acting on the helical tooth [12]

4 Results and Discussion

The analysis was carried out for both the harmonic drive models for the three different force values obtained from torque values. The maximum values of equivalent von Mises stress, deformation, and von Mises elastic strain values for helical teeth harmonic drive and the straight teeth harmonic drive are given from Tables 2 and 3, respectively.

The von Mises stress, deformation, and von Mises elastic strain for the load 1623.78 N on the helical tooth are seen in Fig. 7a–c, respectively.

The graphical representation of the maximum von Mises stress is given in Fig. 8a. It can be inferred that the stress values increase with an increase in the torque force values for both the harmonic drives. The increment in the stress was observed because the force that is acting upon the constant area keeps on increasing. Furthermore, for the respective torque force (67, 90, 120 Nm), there is a slight decrease in the stress

Table 2 Stress and deformation on the helical tooth

Torque (Nm)	Force (N)	Max stress (MPa)	Max deformation ($\times 10^{-4}$) (mm)	Max elastic strain ($\times 10^{-4}$)
67	1623.78	37.061	2.4	1.97
90	2181.18	49.783	3.23	2.64
120	2908.24	66.38	4.3	3.52

Table 3 Stress and deformation on the straight tooth

Torque (Nm)	Force (N)	Max stress (MPa)	Max deformation ($\times 10^{-4}$) (mm)	Max elastic strain ($\times 10^{-4}$)
67	1623.78	40.025	3.093	2.03
90	2181.18	53.76	4.01	2.8
120	2908.24	71.51	5.4	3.62

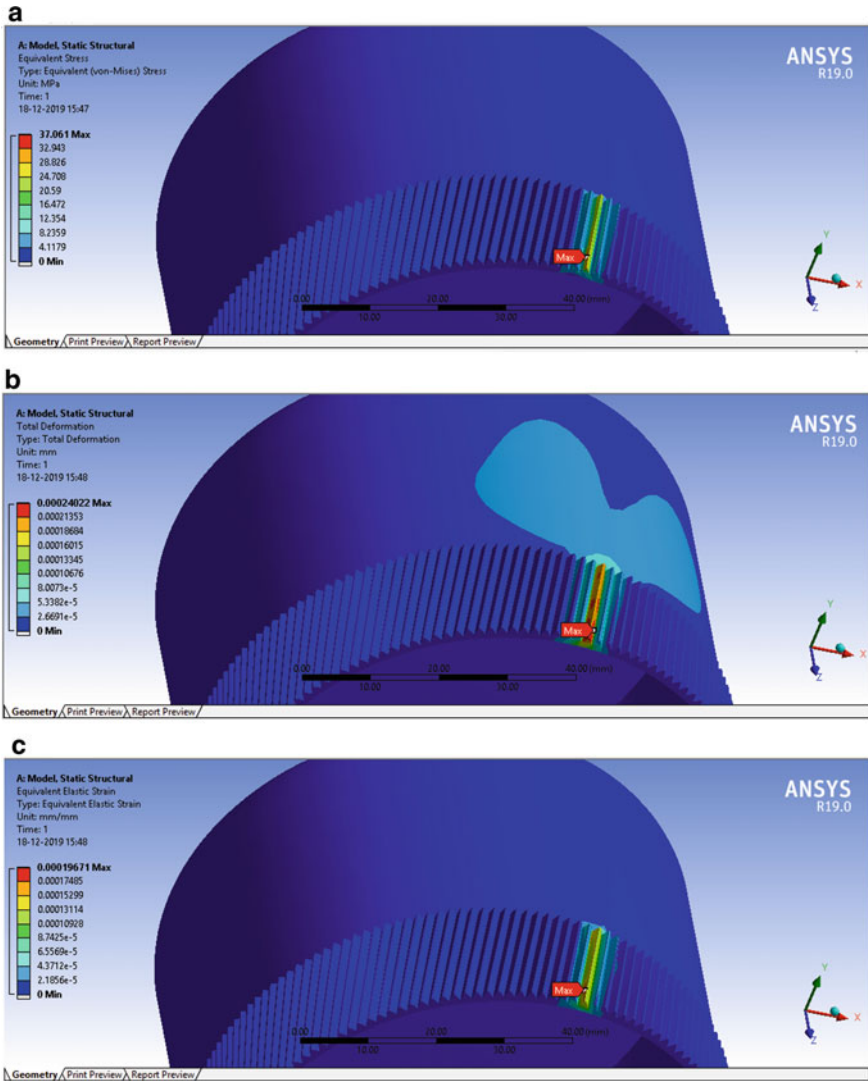


Fig. 7 a von Mises stress of the helical tooth flex spline. [12]. b Deformation of the helical tooth flex spline [12]. c von Mises elastic strain of the helical tooth flex spline. [12]

of the helical tooth (37.061, 49.783, 66.38 MPa) as compared with the stress values of the straight tooth (40.025, 53.76, 71.51 MPa). This reduction in the stresses might be because of the following reason. In straight tooth flex spline, the force acting is perpendicular to the tooth and due to which the entire load is acted upon the flex spline, whereas, in helical tooth flex spline, the force acted would be inclined and not perpendicular to the tooth. Thus, only a component of the force would be acting on the flex spline with a helical tooth, which induces less stress than that of the straight tooth.

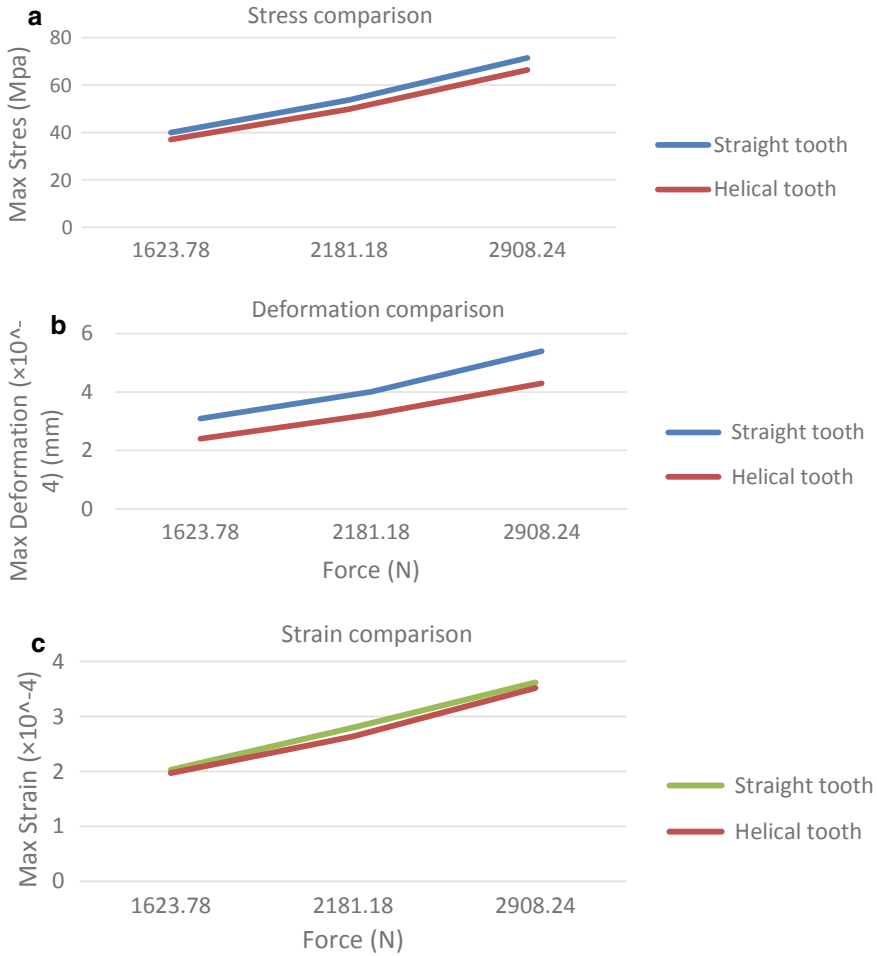


Fig. 8 a Comparison of maximum stress on the helical tooth and straight tooth for different forces. b Comparison of maximum deformation on the helical tooth and straight tooth for different forces. c Comparison of maximum strain on the helical tooth and straight tooth for different forces

However, the variation in the von Mises stress between the helical tooth and straight tooth is not drastic or significant, which implies both harmonic drives would undergo the same amount of stress for a similar torque. Also, it could be inferred that the difference between the stress values of the straight tooth and helical tooth increases with an increase in the torque force. This indicates that helical teeth harmonic drives could be a suitable option for higher torque load applications. Though the stress values acting on the straight tooth and helical tooth do not differ much, it would make a significant impact when considering fatigue. Due to less stress value, the helical teeth flex spline could have more life than the straight teeth flex spline. In the future, the fatigue analysis could be carried out because it could provide more insights

into the life of both the harmonic drives. Thus, the helical teeth could be a viable option for high torque load applications compared with straight tooth. The maximum deformation of the straight tooth and the helical tooth is represented in Fig. 8b. It can be inferred that the deformation of helical tooth and straight tooth increases with an increase in the torque load. However, for a given torque, the variation in the deformation of straight tooth and helical tooth is almost similar. Figure 8c shows the maximum strain that is induced on the helical and straight teeth. For both harmonic drives, the strain induced in the tooth increases with the torque. This increment can be attributed to the increase in the stress developed on the tooth of both harmonic drives. Similar to the deformation, the difference between the strain values of the straight tooth and helical tooth harmonic drive does vary.

5 Conclusion

In this study, a new model of the harmonic drive was developed, which has helical teeth in the flex spline and circular spline. This model was compared with the existing model of the harmonic drive in terms of stress, strain, and deformation for three incremental force values of 1623.78 N, 2181.18 N, and 2908.24 N obtained from three torque values of 67 Nm, 90 Nm, and 120 Nm, respectively. The result showed that helical teeth harmonic drive could be more preferable for high torques and could provide a better life than straight teeth harmonic drive. In the future, the fatigue analysis of the tooth can be found out to determine the exact life of the product. Furthermore, a vibration analysis could be done to check whether the designed model would be stable in operation.

References

1. S. Awasthi, R.K. Satankar, Stress deformation and stiffness analysis of two materials (steel and glass/epoxy) of flexspline using ANSYS. *Int. J. Sci. Res. Eng. Technol. (IJSRET)* **3**(3) (2014). ISSN 2278-0882
2. Vineet Sahoo, Rathindranath Maiti, Load sharing by tooth pairs in involute toothed harmonic drive with conventional wave generator cam. *Meccanica* **53**(1–2), 373–394 (2018)
3. Y.S. Hareesh, J. Varghese, Design and analysis of flex spline with involute teeth profile for harmonic drive mechanism. *Int. J. Eng. Res. Technol. (IJERT)* **4**(12) (2015)
4. M. Kikuchi, R. Nitta, Y. Kiyosawa, X.-Y. Zhang, Stress analysis of cup type strain wave gearing. *Key Eng. Mater.* **243–244**, 129–134 (2003)
5. Shuang Wang, Gedong Jiang, Xuesong Mei, Chuang Zou, Xian Zhang, Hao Zhang, A rapid stress calculation method for short flexspline harmonic drive. *Eng. Comput.* **36**(6), 1852–1867 (2009)
6. C. Zou, T. Tao, G. Jiang, X. Mei, Deformation and stress analysis of short flexgear in the harmonic drive system with load, in *IEEE International Conference on Mechatronics and Automation (ICMA)*, Takamatsu, Japan, 4–7 Aug 2013
7. J. Pacana, W. Witkowski, J. Mucha, FEM analysis of stress distribution in the Hermetic Harmonic drive flex spline. *Strength Mater.* **49**(3) (2017)

8. V. Sahoo, R. Maiti, State of stress in strain wave gear flexspline cup on insertion of drive cam—experiment and analysis, in *Proceedings of the World Congress on Engineering*, vol. 2 (WCE, London, U.K, 2016)
9. W. Ostapski, Analysis of the stress state in the harmonic drive generator-flexspline system in relation to selected structural parameters and manufacturing deviations. *Bull. Polish Acad. Sci. Tech. Sci.* **58**(4) (2010)
10. H. Dong, Z. Zhu, W. Zhou, Z. Chen, Dynamic simulation of harmonic gear drives considering tooth profiles and parameters optimization. *J. Comput.* **7**(6), 1429–1436 (2012)
11. *Introducing Solidworks*, Dassault Systems, 2015
12. ANSYS User Guide version 19
13. Harmonic Drive Reducer Catalog, https://www.harmonicdrive.net/_hd/content/documents/FB_Component.pdf
14. M.P. Boyce, in *Gas Turbine Engineering Handbook*, 4th edn (2012)
15. V.V. Gopal, L.B. Rao, Design and analysis of centrally mounted rotary fixture. *Int. J. Comput. Aided Eng. Technol.* **9**(4), 453–464 (2017)

Design and Analysis of Permanent Magnetic Gears



Kolape Poonam Gujaba, Sharmila Parashar, and Lokavarapu Bhaskara Rao

Abstract This paper is all about a design, construction, and analysis of permanent magnetic gears. The basic idea of a gearing is to convert mechanical power from one rotational speed and torque to another speed and torque. The input power that is used in most of the applications is with small revolution speed and great torque. But many applications require input power with less revolution speed and great torque. The problem is often lack of torque from the source drives. The physical size of a direct drive electrical machine able to drive a conveyer belt directly will typically be too large and expensive. A more cost-effective solution will be to place a transmission between the conveyer belt and the electrical machine. Mechanical gears are often used for such transmission purposes. The magnetic gears designed particularly for the transmission and automobile sectors, with comparison with non-magnetic gears. After completing primary design, detailed calculation is done followed by CAD modeling and analysis at the end. In increasing productivity, this can show better results.

Keywords Gear, rotor, ferromagnetic pole, deformation · Equivalent stress · Equivalent elastic strain

1 Introduction

The key concern of any transmission firm will be its ability to design and produce a high variety of gears in a short time span with high quality. Driveshaft for the conveyer

K. P. Gujaba (✉) · S. Parashar · L. B. Rao
School of Mechanical and Building Sciences, Vellore Institute of Technology, Chennai,
Vandalur-Kelambakkam Road, Chennai, Tamil Nadu 600127, India
e-mail: kolapepoonam@gmail.com

S. Parashar
e-mail: sharmila.parashar2016@vitstudent.ac.in

L. B. Rao
e-mail: bhaskarbabu_20@yahoo.com

belt must pull a relative heavy load with relative low angular velocity. Power sources for mechanical systems are often available with high speed and low torque. Examples of such a power source can be an electrical machine or a combustion engine. The problem is often lack of torque from the source drives. The physical size of a direct drive electrical machine able to drive a conveyer belt directly will typically be too large and expensive. A more cost-effective solution will be to place a transmission between the conveyer belt and the electrical machine. Mechanical gears are often used for such transmission purposes. A magnetic gear also performs as a transmission device that can transform low torque and high rotational speed to a high torque low and rotational speed [1]. Amount of magnetic material and cost are also correctly connected. To transfer torque the traditional mechanical gear uses steel teeth. The teeth of the gear wheels are physically in contact with each other which will lead to wearing of the tooth flanges. Because of the absence of physical contact in magnetic gears, no such type of wear is found in them. A fictive torsion spring effect between gear wheels will be there as magnetic gears do not have direct contact. To explain torsion spring one can imagine one wheel fixed and the other wheel is rotated a small angle. Then between the gear wheels depending on angle displacement of the second, there will be a certain torque interaction. Most of the known technologies of magnetic gears are documented through patents, and only a very few technologies are well documented in scientific papers. So, we thought we could study on permanent magnetic gears and more deep applications with design and analysis.

2 Applications

2.1 *Rolls Royce*

After many research and development, Rolls-Royce is moving toward full production of their permanent magnet tunnel thruster from their facility in Ulsteinvik, Norway. A permanent magnet azimuth thruster is also introduced at the same time in the market by the company. In a permanent magnet drive, the blades are turned by the interaction of the stator located in the rim of the thruster—that carries a number of electrical coil windings—and the rotor which is fitted with a number of very strong permanent magnets and to which the propeller blades are affixed whereas in a typical thruster the blades are turned by a gear or a motor located at the center of the thruster hub. Rolls-Royce observed that the internal footprint of their tunnel thruster without any gear or external motor is far smaller than that of typical thruster which lets them to install it farther forward or aft in a new ship which will result in provision of greater thrust moment port and starboard. Also in this system, the thrust in both the direction is the same.

The advantages may give a compelling argument, namely

1. They are very responsive—to go from full ahead RPMs to full astern RPMs it takes 6 s.
2. According to Rolls-Royce up to 50% less maintenance as very few moving parts.
3. When compared with a conventional system, 50% less noise is produced because of less moving parts.
4. Because of smaller, optimized central hub hydrodynamic efficiency is greater.
5. Torque density is high.
6. Over the entire speed, range efficiency remains higher.

3 Methodology

The basic working and need of permanent magnetic gears have been increased on an industrial scale. We found out the main difference between the traditional mechanical gears and the permanent magnetic gears. Also the different types in the magnetic gears and their design constraints, a magnetic gear also performs as a transmission device that can transform low torque and high rotational speed to a high torque low and rotational speed. The magnetic gear can achieve high efficiency, but achieving a high torque capability can be hard unless considerations regarding magnetic gear technology and design are carefully made. For the magnetic gear technology, density of torque is a very big issue.

4 Design

The main idea of developing a product design stage is to enhance the ideas of the particular product resulting in generation and evaluation. Designing is a long, iterative, complex, and eventually a more iterative process involving many steps such as:

- 1 Identifying the neediness of new product, creating ideas for a valid solution.
- 2 Refining the ideas, adding proper and complete detailing.
- 3 Evaluating the further result by testing them, preparing the complete data specification for the selected solution.
- 4 Documentation of all data such as manufacturing, drawings, and material listing.

4.1 Design Calculation

The engineering design process is the formulation of ideas, which helps an engineer to manufacture a product with a specified performance goal (Li and Melkote 1999; Teramoto et al. 1998). It includes a number of iterative processes and the process has to be tested repeatedly for ‘n’ number of times before producing the final product.

For designing, the initial data assumed were the dimension of the I-section of an axle. It was important to design the fixture. The design calculation has been carried out that is shown as below:

Formulae and calculations

module (m)

$$m = 1, p = 3.1416$$

$$m = 2, p = 6.2832$$

$$m = 4, p = 12.566$$

$$p = \text{Pi} \times \text{module} = \pi m$$

$$p = \pi m = 9.4248 (\text{Considering module} = 3)$$

Transformation to Module m from $CP = CP/\pi$

CP10 is transformed to module as shown; $m = 10/3.1416 = 3.1831$

Pressure Angle (α)

Pressure angle is an element that determines the tooth profile. It is the leaning angle of a gear tooth. The pressure angle (α) is usually set to 20° , however, 14.5° gears are mostly taken. Below are the calculations of tooth depth (h)/addendum (ha)/dedendum (hf) for a gear with module 2.

$$h = 2.25 m = 2.25 \times 2 = 4.50 m$$

$$ha = 1.00 m = 1.00 \times 2 = 2.00 m$$

$$hf = 1.25 m = 1.25 \times 2 = 2.50 m$$

Diameter of Gears (Size)

zm = reference diameter (d)

$d + 2m$ = tip diameter (da)

$d - 2.5m$ root diameter (df)

Design and Analysis Methods

Both electromagnetic and mechanical analyses are involved in the design and analysis of magnetic gears. Most of the published works have discussed about the electromagnetic design aspects. There are different design analysis approaches that have been employed such as field solution-based analytical models, reluctance network approaches, classical electric machine theory, numerical methods (finite element method).

Although analytical approaches have positivity such as time-efficient and provision of some physical insights into the electromagnetic solutions, they are still less

favorable in the design and optimization of MGs because of its limitations such as the inability to account for saturation and intricate geometries. The reluctance network approach is not that popular but it is capable of modeling the end field leakages of magnetic gears [14]. Popular numerical methods in designing and analysis of MGs like FEM used for material nonlinearity and give accurate magnetic field distribution inside the MGs. In FE analysis of electrical machines, 2D FE modeling is applied and to further reduce the complexity of the FE model geometric symmetry is used. Most of the times, stimulation of full FE models is required as concentric MGs do not exhibit periodic symmetry, which will make 2D FE modeling costly, let alone 3D FE modeling.

5 Analysis Parameters

Analysis is an important task in designing the mechanical and structural systems. Failure analysis, a depth of comprehensive study, is done to assure the complete study of the design made. It is the tool that enables a user to check whether the design is safe or not. In order to carry out the analysis, one should idealize the geometry of the structure, the actions and the support condition by means of adequate mathematical models, which roughly consist of physical properties of the design.

The analysis of the above model has been done in ANSYS16. In this mainly, the analysis is done for equivalent stress, equivalent elastic strain, and deformation. As a part of boundary condition, the base is fixed and force is applied at the centre of gravity (CG), this is because the force experienced by all the three jaws is same, and also we consider that the axle weight is concentrated at the center (CG). The force application is shown.

1. Equivalent Stress

Analysis for equivalent (von Mises) stress

Von Mises stress analysis is normally used to determine whether the design will withstand the particular condition of load given by the designer. It is considered to be the safest way of analyzing the design model as compared with the earlier times where one has to do the prototyping to determine the actual effect of the load condition. The design is said to be failed if the induced stress increases the stress of the material. The von Mises stress concept arises from the concept of distortion energy theory where according to the concept, the failure occurs when the practical distortion theory exceeds the theoretical distortion theory. The distortion theory consists of two types of energy, they are:

- 1 Actual case distortion energy
- 2 Simple tension case distortion energy.

The value according to the analysis is shown in Fig. 1, is 11.157 MPa, where the ultimate stress of the material used in the design is 650 MPa. The analysis was done using ANSYS 16.

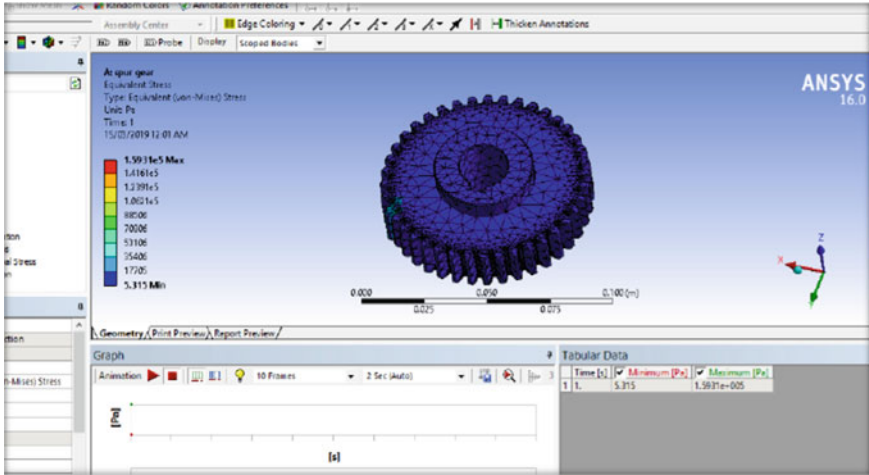


Fig. 1 Deformation analysis for static structure

Hence, the design is safe for equivalent (von Mises) stress. Now, it is further needed to be checked for equivalent strain.

2. Total Deformation

Figure 2 shows the analysis of the static structure with the axle in between which shows the axle deformation of the structure as 0.00238491 mm. Hence, the design is safe against deformation.

3. Analysis for equivalent elastic strain

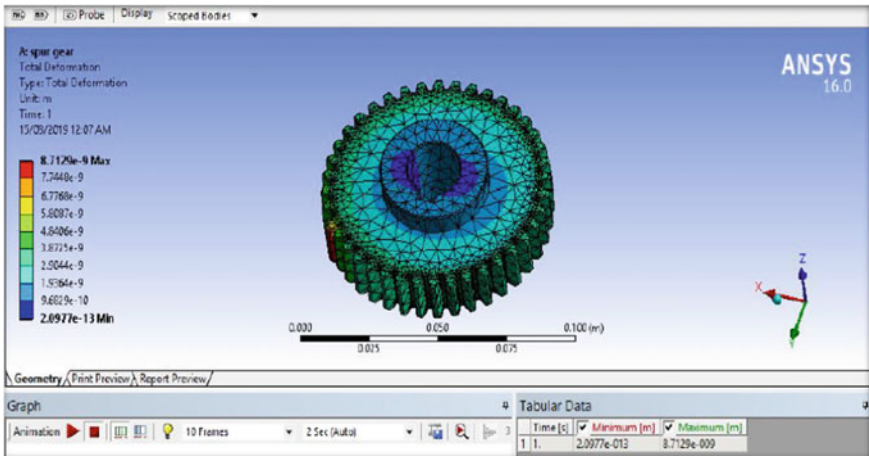


Fig. 2 Static structure analysis

Strain is nothing but the distorted body regains its shape and size when the deformation force is removed from it. The strain is nothing but the difference in change in length to the original length. But here the deformation of the body is analyzed when the strain is induced in the body as shown in Fig. 3 (analysis of equivalent strain). It is important to analyze the strain as it determines the elasticity of a body. After analysis for equivalent elastic strain for the design body was done.

4. Flux Density

The amount of electric, magnetic, and electromagnetic flux passing through a unit surface area is called as flux density. As shown in Fig. 4, the results have been obtained that show the gradual change in flux density in Tesla from 0T to 2T, respectively.

5. Torsional

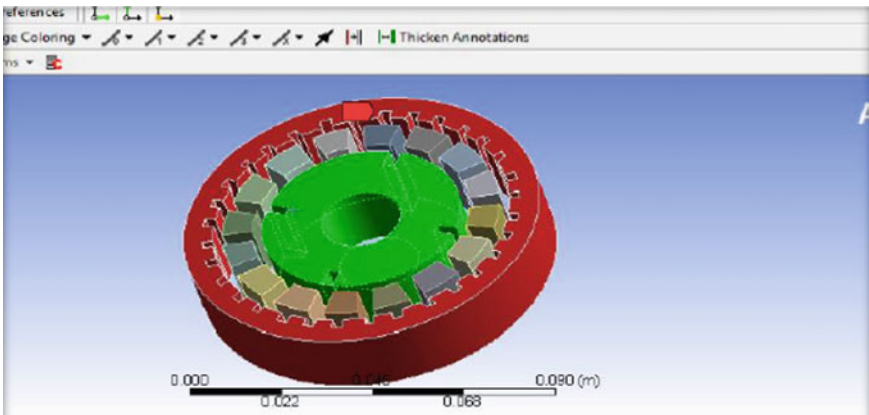


Fig. 3 Analysis of equivalent elastic strain

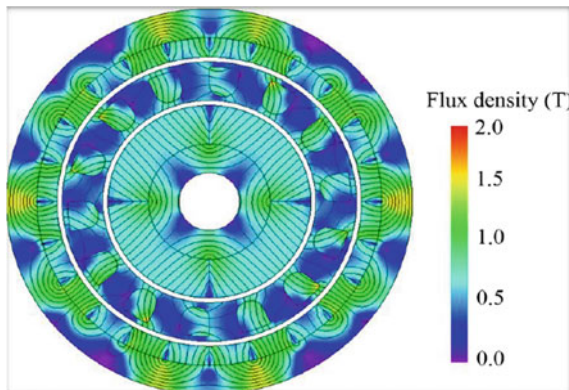


Fig. 4 Flux density

Stress related to shear is torsional stress, torsional strain can be defined as resistance to twisting by bond formation, i.e., bond twisting. Unlike the axial loads that produce an uniform, or average, stress over the cross-section of the object, a torque creates a distribution of stress over the cross-section. Just not to make anything complex, we have focused on structures with circular disc section, rotating shafts.

The torsional strain analysis was done as shown in Fig. 5.

Magnetic gears are being developed to replace mechanical gears. Mechanical gears are noisy, require lubrication and frequent maintenance. Magnetic gears are contactless. They require no lubrication when overloaded.

Operational Features with Possible Solutions

Some of the applications may face operating challenges because of the inherent overload protection characteristic of MGs. Pole slipping occurs in MGs when subjected to an overload condition that completely decouples the rotors, so until the input side reengages torque transmission is halted. To solve this issue or for quick recovery, MGs should be designed with a larger safety factor or a automatic pole-slip detection is necessary. Also, mechanical gears have higher torsional stiffness coefficient than MGs. MGs are unsuitable for servo drive applications as under rapid load change they suffer from undesired oscillations. To solve this issue, both active as well as passive methods are proposed. One among the proposed passive oscillation, suppression strategy is to add damper windings on the high speed rotor, which leads to reduction of settling time by more than 80%.

From simulation and analysis, the following results are obtained—benefits of magnetic gear key

Efficiency is increased (> 99% at full load and high part load efficiency)

- Reliability is high
- Maintenance is low
- Absence of transmission oil

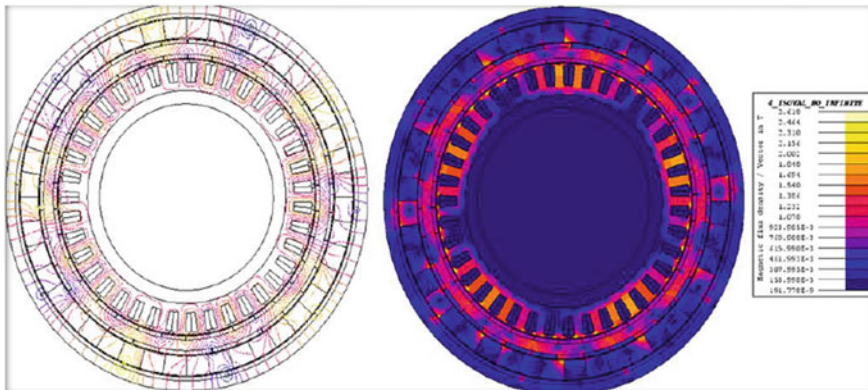


Fig. 5 Torsional strain

Table 1 Gear ratio and torque density

Gear type	Transmission rate	Torque density (kNm/m ³)
Mechanical spur gear	1.4–28,000	100–200
Multielement MG	24:1	3.96
Involute MG	3:1	1.7
Magnetic worm gear	33:1	0.74
Magnetic skew gear	1.7:1	0.15
Parallel-axis MG	4:1	11.6
Perpendicular-axis	1:1	3
Magnetic torque coupler	1:1	51.9

- In between shafts, physical isolation is present
- Transmission happens through a sealed wall
- Presence of torque fuses protection
- Very low vibration and noise production
- Drivetrain pulsations are eliminated by the compliant transmission.

Magnomatics’ magnetic gear contains two rings of permanent magnets and in between them a ring of steel pole pieces is present which acts as flux paths from all the rings of magnets and has the effect of creating harmonics in the fields produced by all the rings of magnets. Gear ratio is created by carefully selecting pole numbers that can be coupled to the harmonic field. The gear exactly behaves like mechanical epicyclical gearbox. Two of the gear elements rotate whereas one held still. In applications of gears, mostly the outer ring is held still. The transmission rate and torque density are presented in Table 1.

6 Conclusion

Magnetic gears are far better than the normal mechanical gears with some constraints

The interest for magnetic gears increases as nowadays, the goal is to use the renewable energy sources and reduce environmental pollution. There is no risk of lubricant pouring out into the water as these gears are not lubricated. In terms of environmental protection, this is a very good side of these gears.

References

1. State of the Art of Magnetic Gears, their Design, and Characteristics with Respect to EV Application by Daniel Fodorean Submitted: November 25th 2015 Reviewed: May 10th 2016 Published: October 5th 2016 <https://doi.org/10.5772/64174>. Design and characteristics of a new magnetic worm gear using permanent magnet (IEEE)
2. K. Tsurumoto, S. Kikuchi, IEEE Trans. Magn. **MAG-23**, 3622 (1988)
3. Hybrid vehicle with a magnetic planetary gear L. BAGHLI 1, E. GOUDA 2, S. MEZANI 2, A. REZZOUG 21 Department of Electrical Engineering, Université Aboubakr Belkaid, Tlemcen, Algeria (lotfi.baghli@green.uhp-nancy.fr) 2 Groupe de Recherche en Electronique et Electrotechnique de Nancy, GREEN 54506 Vandoeuvre-lès-Nancy, France
4. P.O. Rasmussen, T.O. Andersen, F.T. Joergensen, O. Nielsen, in Development of a high-performance magnetic gear. IEEE Trans. Ind. Appl. **41**(3), 764–770 (2005). (Show Context)
5. S. Mezani, K. Atallah, D. Howe, A high-performance axial-field magnetic gear. J. Appl. Phys. **99**(8), 08R303–1–08R303-3 (2006)
6. L. Shah, A. Cruden, B.W. Williams, A variable speed magnetic gear box using contra-rotating input shafts. IEEE Trans. Magn. **47**(2), 431–438 (2011)
7. K. Atallah, *Magnetic gear* (2007)
8. J. Rens, K. Atallah, *Magnetic gear* (2009)
9. J. Rens, R. Clark, S. Calverley, K. Atallah, D. Howe, Design analysis and realization of a novel magnetic harmonic gear, in *Proceedings of ICEM*, pp. 1–4 (2008)
10. J. Rens, K. Atallah, S.D. Calverley, D. Howe, A novel magnetic harmonic gear. IEEE Trans. Ind. Appl. **46**(1), 206–212 (2010)
11. A. Reinap, F. Marquez, Development of a modular linear magnetic gear as a project in the electrical engineering education, in *Proceedings of ICEM*, pp. 1–5 (2008)
12. C.-C. Huang, M.-C. Tsai, D.G. Dorrell, B.-J. Lin, Development of a magnetic planetary gearbox. IEEE Trans. Magn. **44**(3), 403–412 (2008)
13. F.T. Joergensen, T.O. Andersen, P.O. Rasmussen, The cycloid permanent magnetic gear. IEEE Trans. Ind. Appl. **44**(6), 1659–1665 (2008)
14. K. Atallah, S.D. Calverley, D. Howe, Design analysis and realization of a high-performance magnetic gear. Proc. Inst. Elect. Eng. Elect. Power Appl. **151**(2), 135–143 (2004)
15. K. Atallah, S.D. Calverley, D. Howe, High-performance magnetic gears. J. Magn. Mater. **272276**, e1727–e1729 (2004)
16. L. Shah, A. Cruden, B. W. Williams, A magnetic gear box for application with a contra-rotating tidal turbine, in *Proceedings of PEDS*, pp. 989–993 (2007)
17. L. Jian, K.T. Chau, Y. Gong, J.Z. Jiang, C. Yu, W. Li, Comparison of coaxial magnetic gears with different topologies. IEEE Trans. Magn. **45**(10), 4526–4529 (2009)
18. N.W. Frank, H.A. Toliyat, Gearing ratios of a magnetic gear for wind turbines, in *Proceedings of Electric Machines and Drives Conference*, pp. 1224–1230 (2009)
19. T. Lubin, S. Mezani, A. Rezzoug, Analytical computation of the magnetic field distribution in a magnetic gear. IEEE Trans. Magn. **46**(7), 2611–2621 (2010)
20. Vipin V. Gopal, L.B. Rao, Design and analysis of centrally mounted rotary fixture. Int. J. Comput. Aided Eng. Technol. **9**(4), 453–464. (2017)

Design and Analysis of Swing Arm Using Carbon Fiber Composite by Using Creo 2.0 and ANSYS



Pidaparthi Maheshbabu , R. Ramkumar, and Dasari Ajay 

Abstract The current research presents the first step in the design process of a cantilever composite swing arm. The aim of the project is to design and model a swing arm according to the loads applied. Presently used material for swing arm is mild steel. In this project, we are going to design swing arm for the materials, mild steel and composite material carbon fiber. For validating this design, FEA structural analysis is done on the swing arm by using different materials. Modal analysis is also done for different mode shapes to know different frequencies with respect to deformation. For validating this design, FEA structural analysis is done on the leaf spring by using different materials. Modal analysis is also done for different mode shapes to know different frequencies with respect to deformation. Creo 2.0 software is used for designing and ANSYS Workbench 16.1 is used for analysis.

Keywords Swing arm · FEA structural analysis · Modal analysis · Creo 2.0 · ANSYS workbench 16.1

1 Introduction Composites Materials

Composite materials have not been broadly utilized in the advancement of cruiser swing arms [1]. This examination explores the improvement of a composite swing

Dasari Ajay—Researcher ID: M-3638-2017.

P. Maheshbabu (✉) · D. Ajay
Department of Mechanical Engineering, Centre of Excellence in Design and Analysis, CMR
College of Engineering & Technology, Kandlakoya, Medchal Road, Hyderabad, Telangana, India
e-mail: maheshbabu.1045@gmail.com

D. Ajay
e-mail: dajay@cmrcet.org

R. Ramkumar
Mechanical Engineering, Faculty of Engineering Technology, Annamalai University,
Chidambaram, Tamilnadu, India
e-mail: rramkumarhai@gmail.com

arm with an accentuation on the basic honesty and on building up a limited component model (FEM). The engine cycle swing arm is a basic segment in the back piece of the cruiser. The writing demonstrates that swing arms should be sufficiently able to deal with different burdens experienced in the field, firm enough to expand bike reaction and security, and light enough to improve cruiser execution and lessen the back unsprung mass.

A composite material [2] (additionally called a piece material or abbreviated to composite, which is the normal name) is a material produced using at least two constituent materials with fundamentally extraordinary physical or substance properties that, when consolidated, produce a material with attributes not the same as the individual parts. The individual segments stay discrete and particular inside the completed structure. The new material might be favored for some reasons: basic models incorporate materials that are more grounded, lighter, or more affordable when contrasted with conventional materials. All the more as of late, scientists have additionally started to effectively incorporate detecting, incitation, calculation, and correspondence into composites, which are known as robotic materials. Ordinary designed composite materials incorporate mortars, concrete, reinforced plastics, for example, fiber-fortified polymer, Metal composites, ceramic composites (composite fired and metal grids). Composite materials are commonly utilized for structures, scaffolds, and structures, for example, vessel bodies, pool boards, race vehicle bodies, shower slows down, baths, stockpiling tanks, impersonation rock, and refined marble sinks and ledges. The most progressive models perform routinely on rocket and flying machine in requesting conditions. A composite material can likewise be depicted as a material made out of at least two particular stages and the interfaces between them. At a plainly visible scale, the stages are indistinct, however, at some minuscule scales, the stages are obviously independent, and each stage shows the attributes of the unadulterated material. Accentuation will be on the qualities, examination, [1] and preparing of superior basic composite materials. This unique class of composites consistently comprises of a strengthening stage and grid stage. There is driving stage is regularly a graphite, glass, earthenware, or polymer fiber, and the network is commonly a polymer, yet may likewise be clay or metal.

2 Literature Review

Roberto Saponelli et al. [3] said in topology enhancement of a cruiser swing arm under administration burdens utilizing Abaqus and Tosca in innovative work condition and idea configuration, individuals engaged with new activities regularly need to plan a totally new shape for the structure focus of the investigation. The stacking conditions and imperatives are normally known; however, the planner barely realizes how to make the geometry of the structure that meets the requirements of the project and that can be manufactured at the same time respecting the target costs.

Ashish Powar et al. [4] had expressed in the Analysis and Topological Optimization of Motorcycle Swing-Arm. This article depends on improvement of a bike

swing arm. The adjustment procedure depends on material, topological change, and approval utilizing limited component examination. The outcomes acquired from altered examination are contrasted and the assessment of the first segment. The objective of the test is to decrease the mass of the segment without bargaining the other important components. For investigation and study, a very much rumored general class 150 cc cruiser's swing arm was chosen.

Ferreira et al. [5], Department of Electromechanical Engineering, UBI. Flexural conduct of cross-breed overlaid composites. The present paper ponders the flexural conduct of hand fabricated half and half-covered composites with a hemp normal adaptable/polypropylene center and two glass fiber/polypropylene surface layers at each side of the example. At the point when contrasted and full-glass fiber glass strands strengthened polypropylene overlays, the half breed composites have efficient, biological, and reusing favorable circumstances and furthermore explicit exhaustion quality advantages. Weakness harm was estimated as far as the solidness misfortune. Disappointment locales and instruments were assessed through microscopy thinks about and a 3D numerical investigation utilizing limited component technique.

Shyam et al. [6] plan of administer arm suspension framework the representative arm suspension framework was dissected, structured, and afterward created. Because of the usage of senator arm suspension framework in vehicle padding impact will be improved. It also gives snazzy look and solace. In this manner, the improvement of burden bearing limit will be broke down at future. Consequently, this paper has proposed a recently structured suspension framework as senator arm suspension framework.

Ramesh Babu [7], design and evaluation of a bike suspension framework for variable load conditions. A Suspension framework or safeguard is a mechanical gadget intended to smooth out or soggy stun motivation and disperse motor vitality. In a vehicle, it decreases the impact of going over unpleasant ground, prompting improved ride quality, and increment in solace due to significantly diminished enhanced of aggravation the model is likewise changed by changing the thickness of a spring. Basic investigation and model is likewise changed by changing the thickness of a spring. Auxiliary investigation and model examination are done on safeguard by differing material for spring, spring steel, and beryllium copper. The investigation is finished by utilizing thinking about burdens, bicycle weight, single individual weight, and two people's weight.

3 Properties of Composites

3.1 High Strength to Weight Ratio

Fiber composites [8] are incredibly solid for their weight. By refining the overlay numerous attributes can be upgraded. A typical overlay of state 3 mm chopped strand

tangle is very adaptable contrasted with the state a 3 mm handle. In any case, it will twist far more than the employ before yielding. Firmness ought not to be mistaken for strength. A carbon fiber cover then again will have a firmness of ordinarily that of mellow steel of a similar thickness, expanded extreme quality, yet just be under 1/4 of its weight.

3.2 *Lightweight*

A standard fiberglass overlay has a particular gravity in the locale of 1.5, contrasted with alloy [9] of 2.7 or steel of 7.8. When you at that point begin seeing carbon covers, qualities can be commonly that of steel, however just a small amount of the weight. A DVD case cover was created utilizing carbon fiber to diminish the case's general weight with the goal that it could be conveyed as lodge things while voyaging, and for improved security. It was utilized by help group for the All Blacks during their 1999 Rugby World Cup battle.

3.3 *Fire Resistance*

The ability for composites to withstand fire has been steadily improving over the years. There are two types of systems to be considered:

3.3.1 *Fire Retardant*

Are self-extinguishing laminates, usually made with chlorinated resins and additives such as Antimony trioxide. These release CO₂ when burning so when the flame source is removed, the self-extinguish.

3.3.2 *Fire Resistant*

Increasingly [10] troublesome and made with any semblance of phenolic resins. These are hard to utilize, are relieved with formaldehyde, and require a hey level of postrestoring to accomplish genuine imperviousness to fire. Different materials are likewise ending up more promptly accessible to be utilized as in bloated layers, which extend and cover the surface, forestalling spread of fire. There is a paint on covering typically connected to the back of the item overlay, in addition to a flimsy fiber film to go under the Gelcoat giving the external surface a covering coat too. Fiberglass Developments Ltd produces a Fire Door as a component of our Steridor TM run. Utilization of unique phenolic pitch has enabled us to make the main completely tried

composite entryway in Australasia. Fire appraised by BRANZ to 4 h, this entryway is likewise affirmed by MAF as gathering all their hygiene prerequisites.

3.4 Electrical Properties

Fibreglass Developments Ltd produced the Insulator Support straps for the Tranz Rail main trunk electrification. The straps, although only 4 mm thick, meet the required loads of 22 kN as well as easily meeting insulation requirements.

3.5 Chemical and Weathering Resistance

Composite [11] items have great enduring properties and oppose the assault of a wide scope of synthetic concoctions. This depends as a rule on the gum utilized in assembling, however via cautious determination protection from everything except the most extraordinary conditions can be accomplished. Along these lines, composites are utilized in the production of concoction stockpiling tanks, funnels, smokestacks and channels, vessel frames, and vehicle bodies. FDL made structural boards for the development of the Auckland Marine Rescue Center. Composite boards were picked in view of their capacity to withstand salty ocean side conditions without erosion.

3.6 Color

Practically any shade of any shading can be joined into the item during assembling by pigmenting the gel coat utilized. Expenses are in this way decreased by no further completing or painting. Dissolvable colors can be utilized if a translucent item is wanted. We do not be that as it may, prescribe dim hues. These produce over the top warmth superficially which can prompt the surface falling apart and demonstrating print through, where the Resin framework fixes more and therapists, carrying the strands to the surface. In extraordinary cases, delamination can happen.

3.7 Translucency

Polyester resins are widely used to manufacture translucent moldings and sheets. Light transmission of up to 85% can be achieved.

3.8 *Design Flexibility*

Because of the versatility of composites, product design is only limited by your imagination.

3.9 *Low Thermal Conductivity*

Fibreglass Developments has been involved in the development and production of specialized meat containers, which maintain prime cuts of chilled meat at the correct temperature for Export markets. They are manufactured using the RTM process, with special reinforcing and foam inserts.

3.10 *Manufacturing Economy*

Fibreglass Developments produces several models of fuel pump covers for Fuel quip. Fibreglass is an ideal material for producing items of this type for many reasons, including being very economical.

4 *Creo 2.0*

Creo is a family or suite of structure programming supporting item plan for [12, 13] discrete producers and is created by PTC. The suite comprises of applications, each conveying an unmistakable arrangement of capacities for a client job inside item improvement. Creo keeps running on Microsoft Windows and gives applications to 3D CAD parametric component strong demonstrating, 3D direct displaying, 2D orthographic perspectives, finite element analysis and reproduction, schematic plan, specialized outlines, and survey and perception. Creo Elements/Pro and Creo Parametric contend legitimately with CATIA, Siemens NX/Solid Edge, and SolidWorks. The Creo suite of applications replaces and supplants PTC's items once known as Pro/ENGINEER, Co Create, and Product View. PTC started creating Creo in 2009, and reported it utilizing the code name Project Lightning at Planet PTC Live, in Las Vegas, in June 2010. In October 2010, PTC revealed the item name for Project Lightning to be Creo.

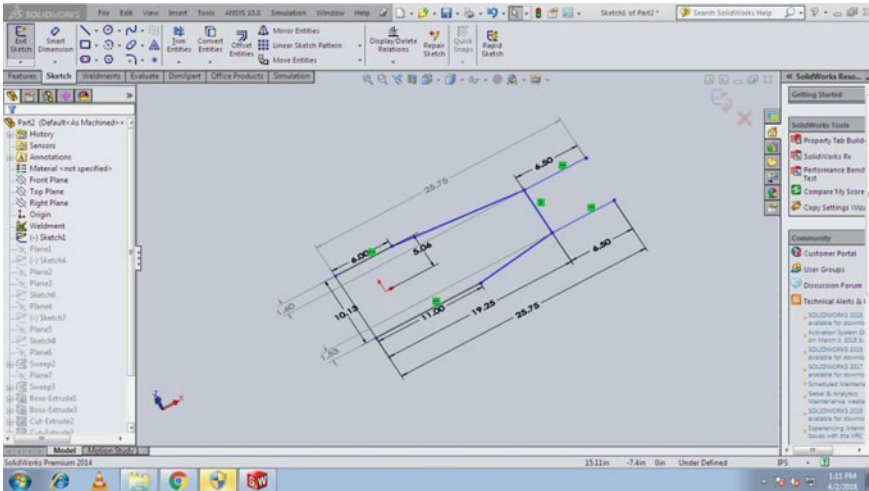


Fig. 1 2D sketch of swing arm base

5 Finite Element Analysis

ANSYS is a general-purpose finite element modeling package [14–16] for numerically solving a wide variety of mechanical problems. These problems include static/dynamic structural analysis (both linear and nonlinear), heat transfer and fluid problems as well as acoustic and electromagnetic problem

6 Dimensions of Swing Arm [17, 18]

By and large, a limited [19] component arrangement might be broken into the accompanying three phases. This is a general rule that can be utilized for setting up any limited component examination. Figures 1, 2, 3, 4, 5, 6, 7, 8, 9 and 10 indicate detailed dimensions of swing arm and Tables 1 and 2 represented material properties and structural analysis comparison. Graphs (Figs. 11 and 12) indicate material data and modal analysis for mild steel and carbon fiber.

7 Conclusion

In this paper, a Swing Arm is designed and modeled in 3D modeling software, SolidWorks. The material of Swing Arm is replaced with composite materials, carbon fiber. The advantage of using composite materials is their high strength to weight

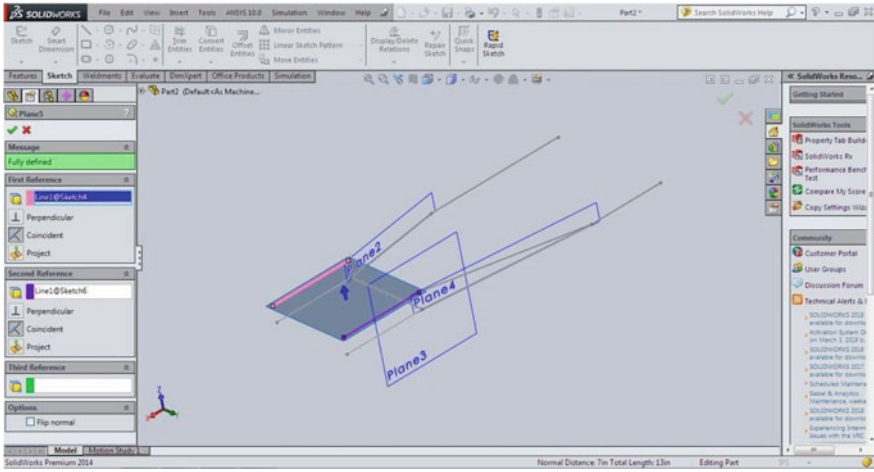


Fig. 2 Creating planes for the required inclination of pivot ends

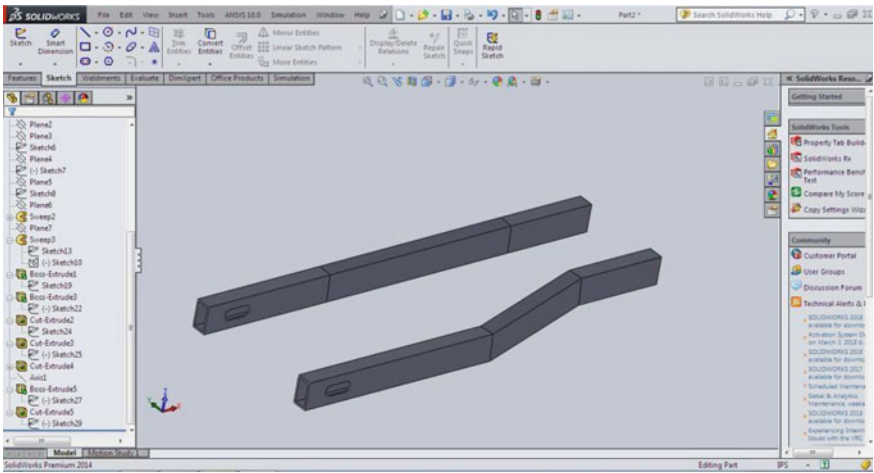


Fig. 3 Extruded model of swing arm base

ratio. By observing the structural analysis results, composite material shows the best resistance to the load applied and the stresses obtained are far less to its yield strength. The mild steel shows less deflection but the stress reaches almost the yield strength and is prone for permanent deformation. So, the carbon fiber usage is preferred for the fast-moving vehicle to withstand the heavy loads at large pace. So, it can be concluded that using carbon fiber is better than the other compared materials.

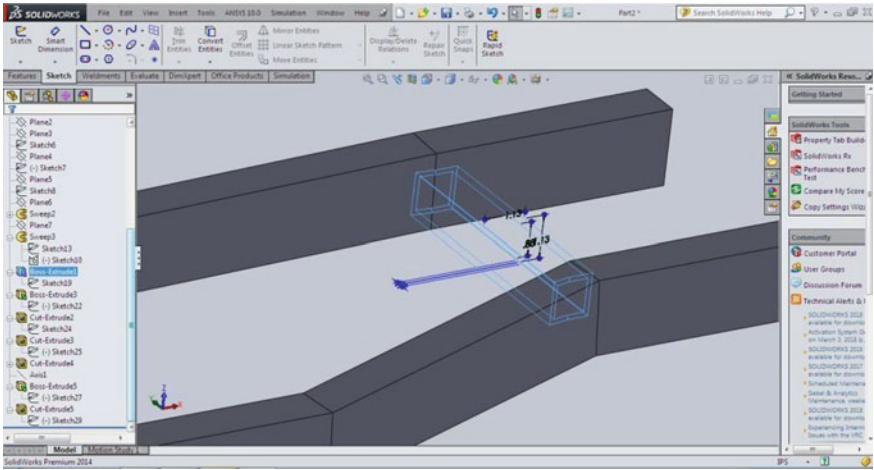


Fig. 4 Sketch of suspension mounting bar

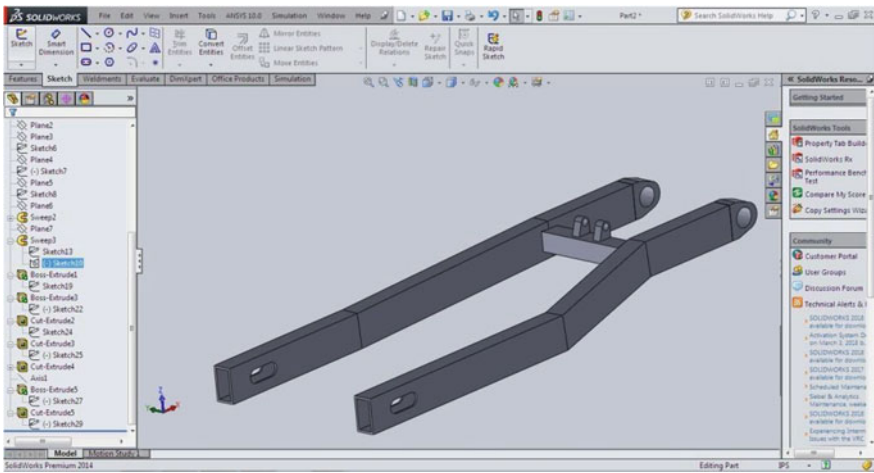


Fig. 5 Extruded model of Suspension mounting arm

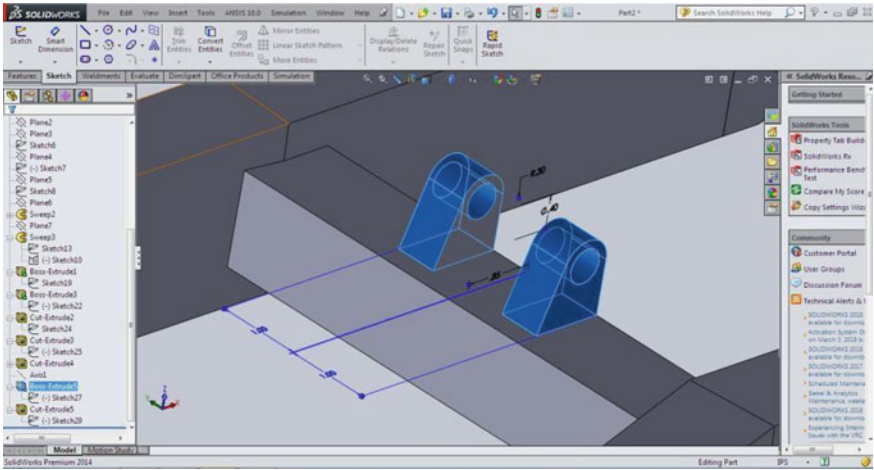


Fig. 6 Sketch and extruded model of suspension mountings

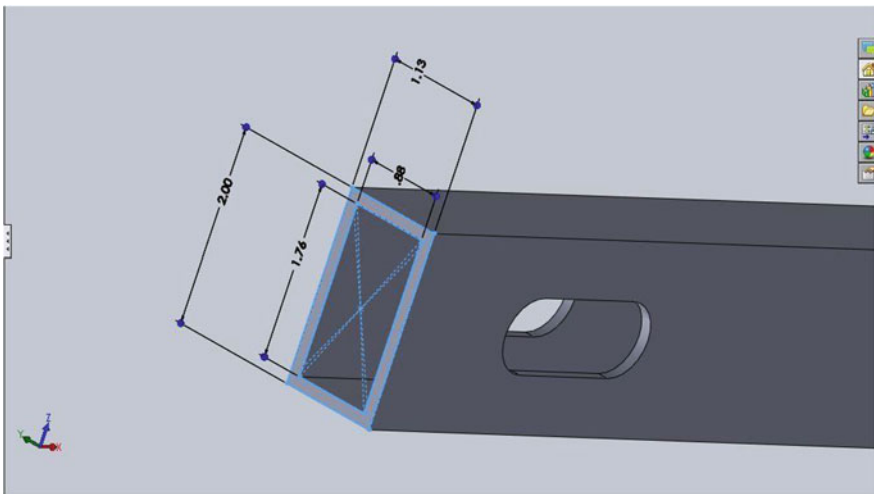


Fig. 7 Sketch for hollow section of arms

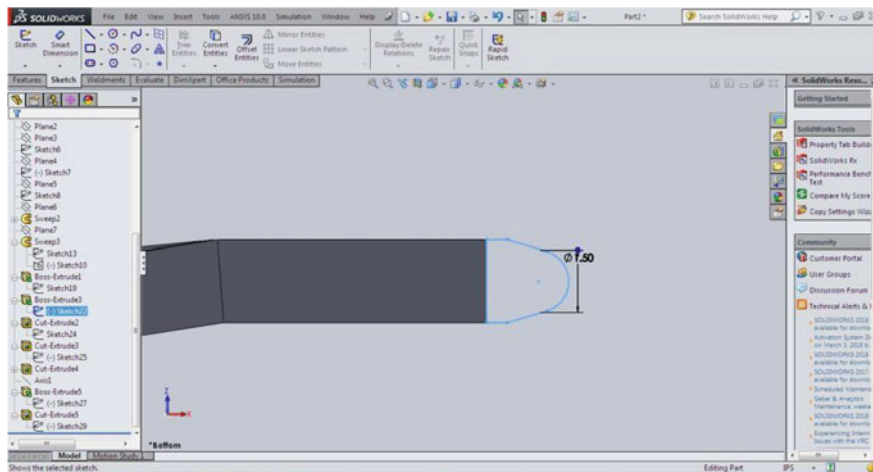


Fig. 8 Sketch of Pivot End brackets

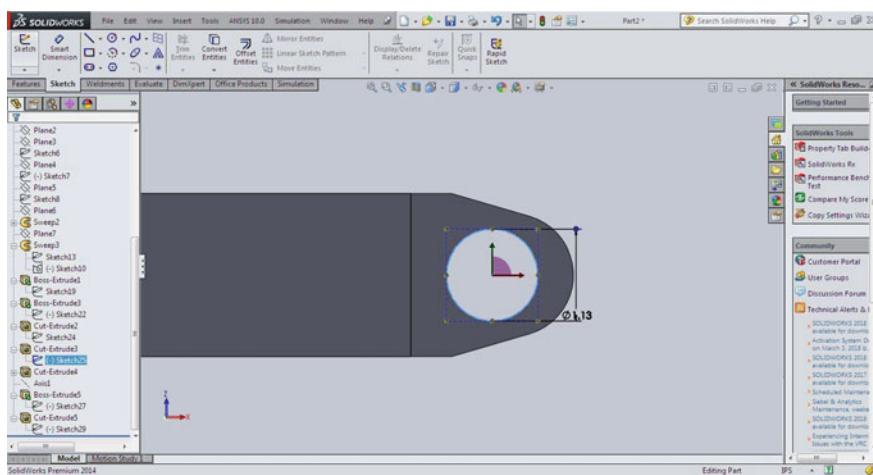


Fig. 9 Extruded model of pivot end brackets

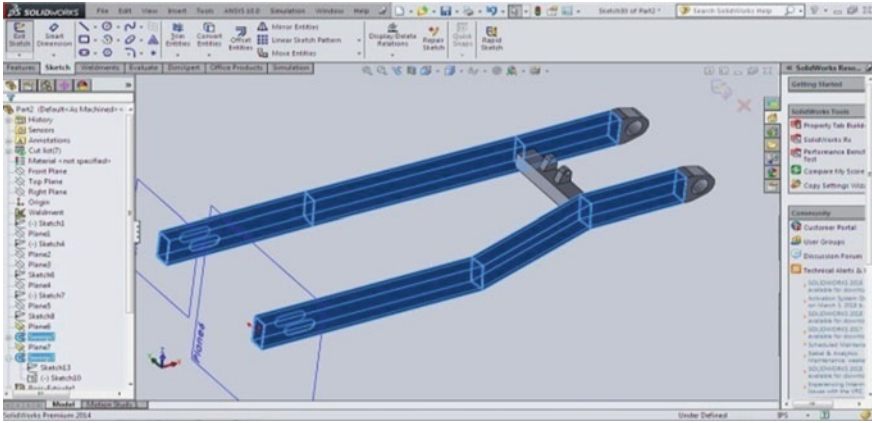


Fig. 10 Final model of swing arm

Table 1 Materials properties [9–11]

Properties	Carbon fiber	Fiber glass	Aluminum	Steel
Young’s modulus, E (GPa)	130	80	68.9	200
Density (kg/m^3)	1600	7850	2700	2689
Yield strength (GPa)	1900	2000	505	250
Ultimate tensile strength (GPa)	300	350	241	500
Strength ^(2/3) /density	9.58	6.10	2.34	5.01
Young’s modulus ^{9(1/2)} /density	0.23	0.1	0.09	0.05

Table 2 Structural analysis comparison

Material	Deformation	Stress	Strain
Mild steel	8.55	247.8	0.001811
Carbon fiber	10.26	251.7	0.00188

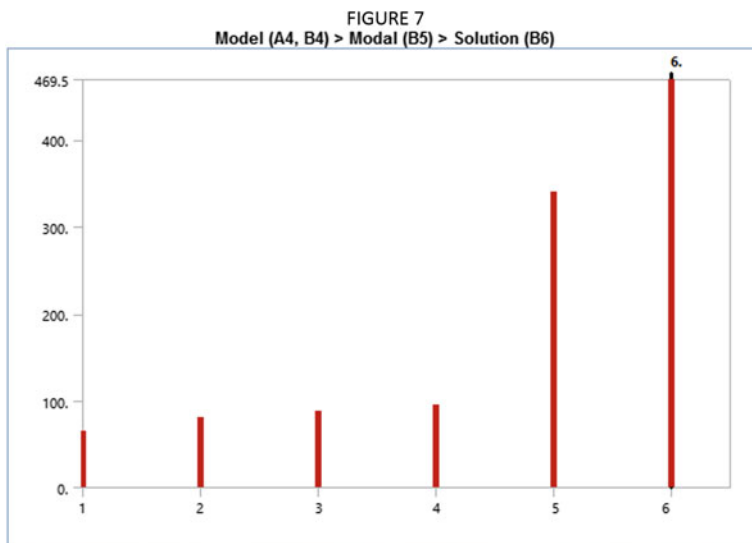


Fig. 11 Material data and modal analysis (carbon fiber)

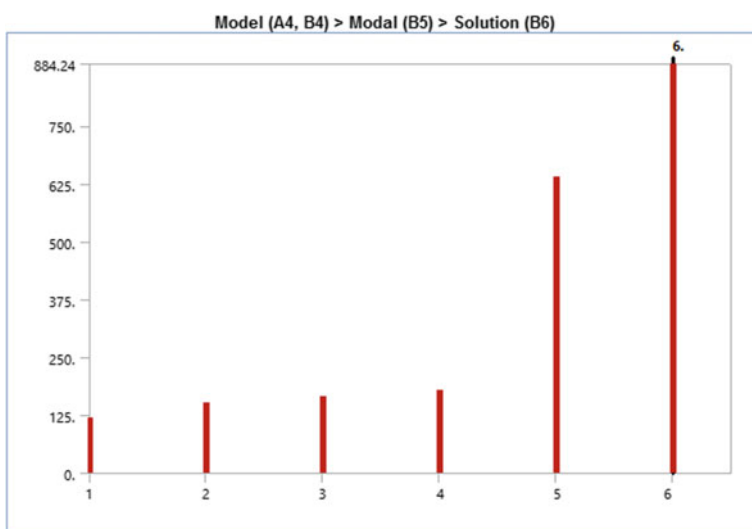


Fig. 12 Material data and modal analysis (mild steel)

References

1. S. Swathikrishnan, Design and analysis of Swingarm for performance electric motorcycle. Int. J. Innov. Technol. Explor. Eng. (IJITEE) **8**(8) (2019). ISSN 2278-3075

2. X. Wang, Static and fatigue behavior of basalt fiber-reinforced thermoplastic epoxy composites. *J. Compos. Art. Mater.* (2019)
3. R.K. Chacho, Design and experimental validation of a carbon fibre Swingarm test rig (2013)
4. Z. Song, X. Zha, Research on lightweight design of automobile lower arm based on carbon fiber materials. *World J. Eng. Technol.* **5**, 730–742 (2017). ISSN Online: 2331-4249
5. B. Smitha, F. Kienhofer, A carbon fibre swing arm design
6. S. Mallela, Dr. T. Reddy, K. Naga Manendhar Rao, Design and analysis of motor bike frame. *IJPRES* **Viii(5)** (2017)
7. M. Prem Kumar, G. Mahesh, Analysis of mono leaf spring using composite materials. *Int. J. Adv. Eng.* **1(6)**, 591–600 (2015). ISSN 2394-9260; ISSN:2394-9279
8. J.D. da Cal Ramos, *Front and Rear Swing Arm Design of an Electric Racing Motorcycle* (Instituto Superior Técnico, Universidade de Lisboa, Portugal, November 2016)
9. T.D. Jagannatha, G. Harish, Mechanical properties of carbon/glass fiber reinforced epoxy hybrid polymer composite. *IJMERR* **4(2)** (2015). ISSN 2278-0149
10. K. Meshram, G. Verma, Enhancement of mechanical property of aluminum alloy 2024: an overview. *Int. Res. J. Eng. Technol. (IRJET)*, **05(06)** (2018)
11. Dr. S. Ahamed, P.C. Shilpa, J.D. Roshan, A literature review on aluminium-6061 metal matrix composite. *Int. Res. J. Eng. Technol. (IRJET)* **06(06)** (2019)
12. K. Satyanarayana, Modelling and analysis of double sided Monoshock Swingarm. *J. Compos. Theory* (2020). ISSN 0731-6755
13. B. Smith, F. Kienhöfer, A carbon fibre Swingarm design. *R & D J. South Afr. Inst. Mech. Eng.* **31**, 1–11 (2015)
14. A. Airoldi, Design of a motorcycle composite swing-arm by means of multi-objective optimisation. *Appl. Compos. Mater.* **19**, 599–618 (2012)
15. M. Sridharan, Dr. S. Balamurugan, Design and analysis of lower control ARM. *Int. J. Innov. Res. Sci. Eng. Technol.* **5(4)** (2016). An ISO 3297: 2007 Certified Organization
16. S.H. Abdullah, Design of racing motorcycle Swingarm with shape optimisation. *IJSRD Int. J. Sci. Res. Dev.* **6(06)** (2018). ISSN (online) 2321-0613
17. Mr. K. Patil, Design and analysis of single sided swing arm for modified bike. *Int. Res. J. Eng. Technol. (IRJET)*, **06(05)** (2019)
18. A. Powar, Analysis and topological optimization of motorcycle swing-arm. *Int. J. Curr. Eng. Technol.* (2016). E-ISSN 2277-4106, P-ISSN 2347-5161
19. K. Rajesh, S. Vamshi Krishna, Ch. Sushanth, Design analysis and fabrication of composite mono leaf spring for automobile vehicle. **5(6)** (2015). E-ISSN 2277-4106, P-ISSN 2347-5161

Comparison of Kinematic Analysis of Robot Made of Conventional Theo Jansen Mechanism, Modified Theo Jansen Mechanism of PLA and Modified Theo Jansen Mechanism of Mild Steel



Keval Bhavsar, Pranav Darji, Dharmik Gohel, Jitendra Modi, and Umang Parmar

Abstract This paper presents the design analysis of an intellectual model of an autonomous surveillance robot. The principal objective is to do surveillance in the muddy or desert area or on that region where the surface is less grippy. This is the first spider robot, which will, made by Polylactic Acid (PLA) material and is having eight legs controlled by two DC servo motors. The mechanism, which is used to make those legs, is Theo Jansen mechanism, which is one of the animal walking patterns. To do the surveillance, a 360-degree rotating camera is used which is having its own working module. Arduino controls all the electronics and that Arduino takes power to run itself as well as all the other systems by 12 V DC battery. And this paper compares the performance of robots made with the same material (PLA) but, works on two different mechanisms, named as between conventional Theo Jansen mechanism and modified Theo Jansen mechanism. In addition to that, it also compares the performance of robots made with two different materials, Mild Steel (MS) and Polylactic Acid (PLA), having the same mechanism as modified Theo Jansen mechanism.

Keywords Theo Jansen mechanism · Animal walking pattern · Surveillance device · PLA material · Mild steel · Modified Theo Jansen mechanism

K. Bhavsar · P. Darji · D. Gohel (✉) · J. Modi · U. Parmar
Aditya Silver Oak Institute of Technology, Ahmedabad, Gujarat, India
e-mail: dharmikgohel67@gmail.com

K. Bhavsar
e-mail: kevalbhavsar42@gmail.com

P. Darji
e-mail: pdarji576@gmail.com

J. Modi
e-mail: jmodi655@gmail.com

U. Parmar
e-mail: umangparmar.me@socet.edu.in

1 Introduction

India is having a huge land border region and for doing surveillance we require a huge amount of manpower or a mechanical device, till now mechanical devices like wheeled robot and drones are used for surveillance. The utilization of a wheeled robot in surveillance is valid for most of the territories except those, which are less grippy. The utilization of drones is workable for the observation in the sloppy or desert territory or on that district where the surface is less grippy. however, the issue is that if the adversary's armed force sees our automaton then they will most likely shoot it or will endeavor to catch it, so, the troopers need to actually stroll in those regions to do reconnaissance. As per the research, the robot, which we have designed, is able to do surveillance in mostly all border regions and it can hide by just applying a cover. It requires only two drives motors and with the use of less number of drive motors, we can have a lesser vibration problem. The design for the legs of this robot is based on a modified version of Theo Jenson mechanism, which is basically similar to one of the creatures strolling design. The kinematic analysis of the robot is done with the aim of identifying the performance of the robot by generating graphs for various parameters. For analysis purposes, we have used the two most common software "SolidWorks 2017" and "ANSYS 2018". Polylactic Acid (PLA) is selected for making the robot as it biodegradable and Mild Steel (MS) is selected as it is one of the common materials for making a robot.

2 Literature Review

The Klann linkage gives some of the aids of more superior on foot automobiles without a number of their restrictions. It suits the technical void among the on foot devices and axel-driven wheels. While Theo Jansen mechanism uses 11 small rods, Dutch kinetic sculptor Theo Jansen has created a planar mechanism that, while utilized in tandem with many others equal to it, can stroll in a smooth ahead motion.

Qu and Durdevic [1] afford the layout and development of a conceptual prototype of a self-sufficient, self-pushed inline inspection robotic, known as Smart Spider. The primary objective is to use this form of robotic for offshore oil and gas pipeline inspection, in particular for those pipelines where the conventional intelligent pigging system could not or be difficult to be deployed. In Deepak and Pathma Sharma [2], six-legged walker is linked by using the use of a link mechanism and with the aid of coupling kinematic walkers with a separate motor for each walker. By the use of the separate motor, we are able to run every walker in the favored position like back and front, thereby we are able to capable of manipulating the walker to show left and proper motion. Swadhin Patnaik [3] gift dynamic study of a four-legged Theo Jansen linkage mechanism, the use of projection technique that effects in constraint force and equivalent Lagrange's criterion of movement essential for any evocative extension and/or optimization of this niche mechanism. Numerical simulations using

MaTX is presented in combination with the dynamic study. In Kazuma Komoda [4], the hyperlink is beneficial to mimic animal motion, they assumed that a further up-and-down motion within the linkage center provides diverse movement styles from the unique inner cycle. Amir and Nassiraei [5] gift the idea of IMD to validate how a mechanical meeting can be designed to stimulus robotic controllability, universalization, and assignment performance. N.G. Lokhande and V.B. Emche [6] present robot can step over pavements, climb staircases, or tour into areas that are presently not reachable with wheels; however, does not require microchip manipulate or multitudes of actuating gadgets. Enric Celaya [7] mounted a robust controller for a six-legged robot that allows it to stroll over grim terrains in an independent way, with restricted use of sensory information. Meenakshi Sundaram and Blair [8] discuss a ROTAB evolved for boosting the work envelope of a SIR-I robotic in a flexible production mobile. The cell carries six terminals, four of which might be served with the aid of the robotic. Bhavik Parikh et.al. [9] made a four-legged robot using the Theo Jansen mechanism to mark the pitch of the sport ground, which is an uneven terrain. The optimization was done to minimize the energy input and maximize the output. Florina Moldovan et. al. [10] present the results of kinematical Learning, established upon a ten-bar linkage designed in CAD in order to study the opportunity of using this new type of mechanism for making a walking robot. They also demonstrate the advantages of using CAD simulation tools for examining the path defined by the endpoint of the foot through walking. Servet Soyguder and Hasan Ali [11] presented a research on Design and prototype of a six-legged walking insect robot, working on cockroach leg mechanism. They used only two motors to reduce weight. Somak Sengupta and Pramod Bhatia [12] presented a Study of Applications of Jansen's Mechanism in Robot in which the belief relies on the rapid advancement of technologies like metal cutting and 3D printing, which will enable developers to easily prototype their conceptual models and also go for mass production if the prototype seems a promising one.

After doing a literature overview, many studies paper as well as patents on Theo Jansen mechanism, we located that no one had used plastic material till now in making the robotic. This looks at sets a theoretic foundation for an upcoming have a look at Theo Jansen mechanism. Till now, Theo Jansen mechanism is used only for transportation robots and walking robots. We are using this Theo Jansen mechanism for the surveillance. In all previous mechanisms, no ternary link is utilized in place of the binary link. This is the first spider robotic for you to be made by way of Polylactic Acid (PLA) fabric. As robots may be made with plastic materials and metals but till now no person had tried to examine the overall performance of robots. So we have got decided to evaluate the robots to get a perception that how the selection of material can affect the overall performance of the robot in terms of balance, speed, as well as efficiency.

3 Design and Analysis

Here, conventional Theo Jansen mechanism (Fig. 1) has 12 links includes 2 binary joints, 4 ternary joints, 4 quaternary joints. While in modified Theo Jansen mechanism (Figs. 1 and 2) has six links of which two are ternary links and four are binary links. The specification of the robot is stated in Table 1.

When we did the path analysis in SolidWorks 2017 (Fig. 3), we came to know that we are getting almost the same path when we compared it with the conventional Theo Jansen mechanism.

In displacement analysis (Fig. 4), by doing a comparison with the conventional Theo Jansen mechanism, results show a minor difference in both the graphs. In addition to this by doing a comparison between displacement graphs for both mild steel and polylactic acid material robots, results show that displacement is independent of material properties. Therefore, results, which are obtained in the graph, show that in

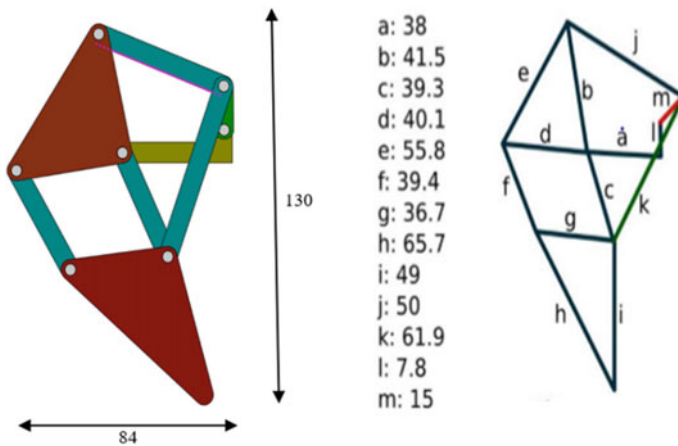


Fig. 1 Modified and conventional Theo Jansen mechanism

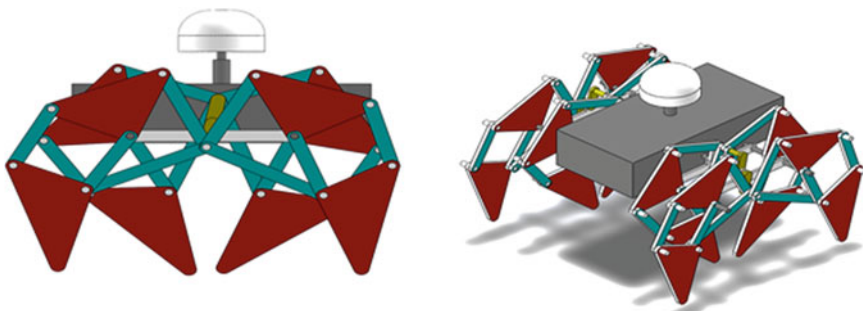


Fig. 2 Side view and isometric view of the robot

Table 1 Components of robot with specifications

Component	Specifications
Legs and body of robot	Made from Poly Lactic Acid (PLA) and mild steel
Motor	70–90 rpm, high torque
Arduino	Mega
Battery	12 V (4 unit)
Camera	Camera—360 angles motion-controlled camera module

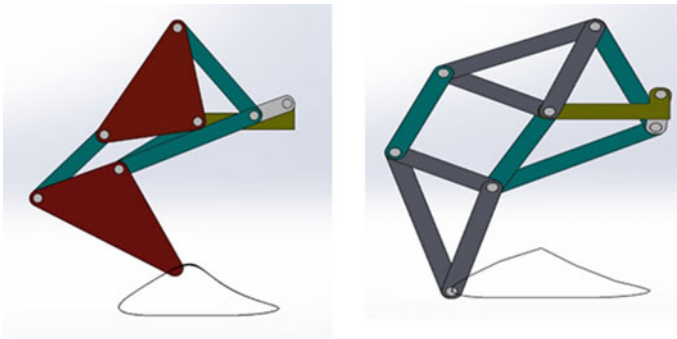


Fig. 3 Modified and conventional Theo Jansen path

the conventional number of peaks obtained per 10 s is 12 and peak value is 106 and in modified mechanism, number of peaks obtained per 10 s is 12 and the peak value is 76 mm.

Linear velocity analysis (Fig. 5) compared with conventional design, we get slightly better velocity in modified version and also, by comparison, it can be concluded that velocities for robots made with both materials are the same because of independence of velocity from material properties. Therefore, results, which are obtained in the graph, show that in conventional mechanism, number of peaks obtained per 10 s is 12 and the peak value is 393 mm/s and in modified mechanism, number of peaks obtained per 10 s is 12 and the peak value is 384 mm/s.

In acceleration analysis (Fig. 6), modified Theo Jansen mechanism, we get more acceleration in starting and then it becomes constant means that the new design is not jerky. In addition, acceleration graphs for both mild steel and polylactic acid materials, robots are compared and acceleration is also independent of material properties so results, which are obtained in the graph, show that in conventional mechanism number of peaks obtained per 10 s 12 and peak value is 12,753 mm/s² and in modified mechanism number of peaks obtained per 10 s is 12 and the peak value is 6163 mm/s².

In torque analysis (Fig. 7), modified Theo Jansen mechanism requires a maximum torque of 1.1 Newton-mm. while the convention mechanism requires 0.7 Newton-mm. From the graphs, it can be concluded that the maximum torque required for

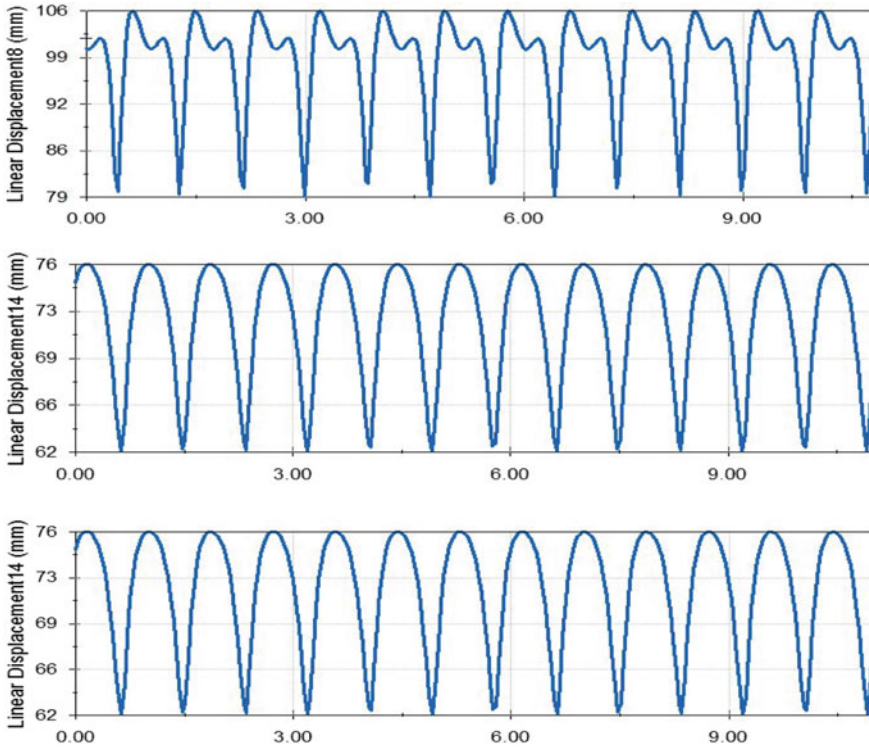


Fig. 4 Conventional, modified (PLA), and modified (MS) Theo Jansen displacement graph

the Mild Steel robot is 8 Newton-mm while in the case of Poly-lactic Acid (PLA) robot maximum torque required is 1.1 Newton-mm. This increased torque value for the Mild Steel robot is due to comparatively larger values of material properties like weight, density, inertia, etc.

Power consumption in modified Theo Jansen mechanism (Fig. 8) requires about 0.008 W to run while the convention mechanism requires 0.006 Ws. The graph also shows that the maximum power required per leg for the Mild Steel robot is 0.06 W while for Poly-lactic Acid (PLA) robot is 0.008 W. This increase in power consumption for the Mild Steel robot is due to the requirement of increased motor torque.

When we had done static structural analysis with a load of 20 N as the weight of the mounting which will be done on the robot will not exceed 2 kg in Ansys we came to know that all the results show that robot which we have designed is safe as per all aspects.

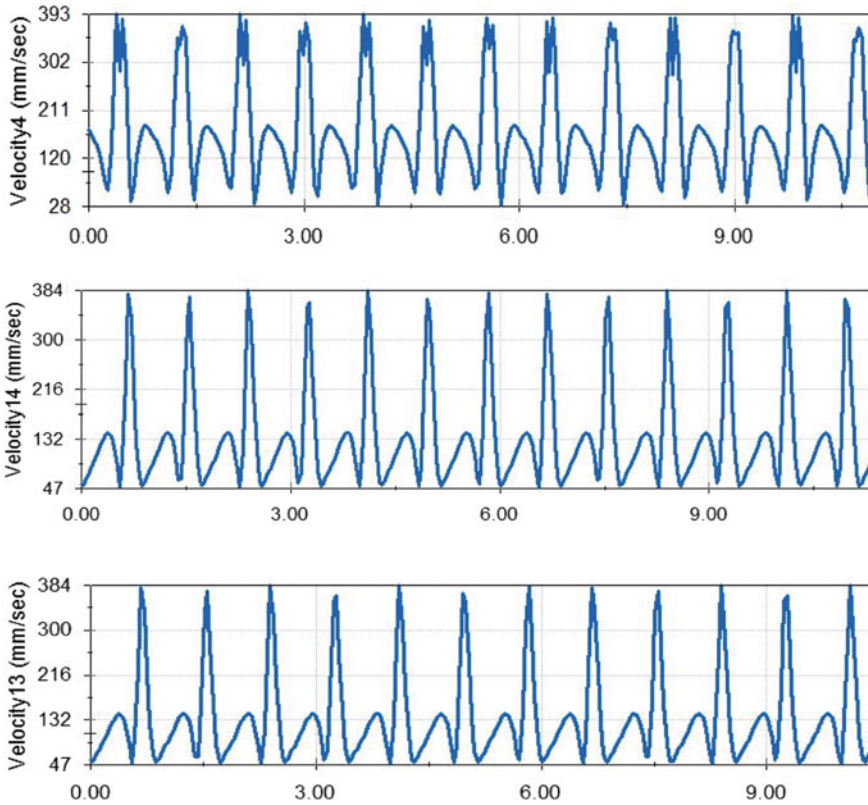


Fig. 5 Conventional, modified (PLA), and modified (MS) Theo Jansen velocity graph

4 Results and Discussion

Results of total deformation (Fig. 9) show that the total maximum deformation, which will occur in the robot (made with the same material PLA) under maximum applicable load, is comparatively higher for the robot having conventional Theo Jansen mechanism than the modified one. Moreover, if the results of total deformation compared for the robots having the same modified Theo Jansen mechanism then total deformation is more for the PLA robot than the Mild Steel robot.

Results of directional deformation (Fig. 10) show that the total maximum directional deformation that will occur in robots (made with the same material PLA) under maximum applicable load is comparatively higher for the robot having conventional Theo Jansen mechanism than the modified one. Moreover, if the results of total deformation compared for the robots having the same modified Theo Jansen Mechanism then total deformation is more for PLA robot than the Mild Steel robot as material properties play an important role.

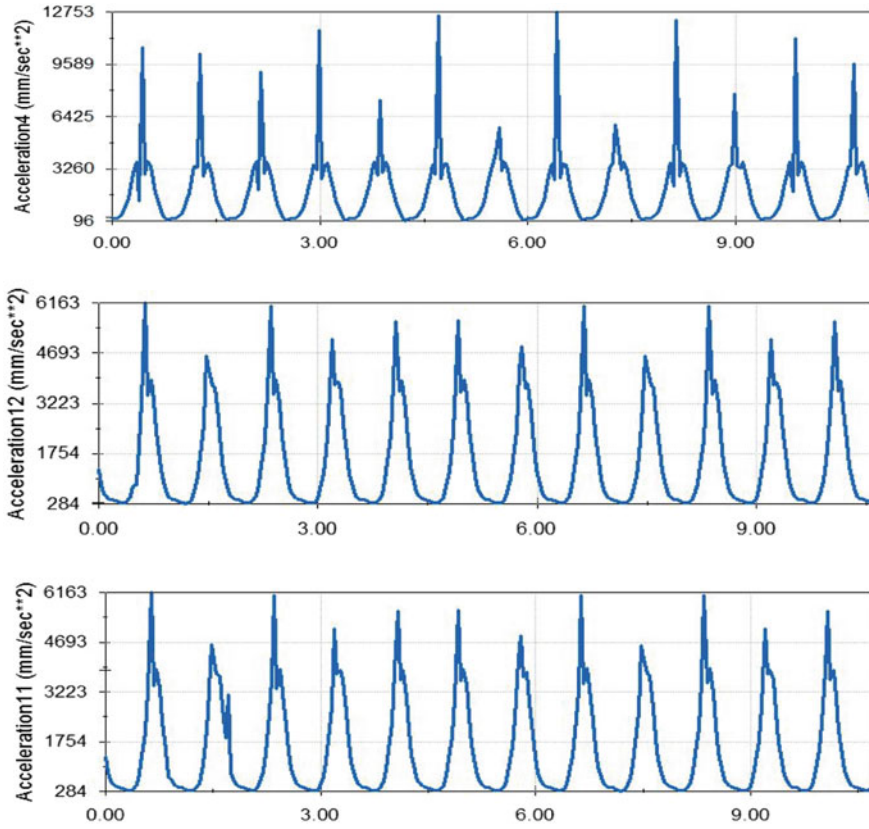


Fig. 6 Conventional, modified (PLA), and modified (MS) Theo Jansen acceleration graph

Results of equivalent elastic strain (Fig. 11) show that during analysis maximum elastic strain induced in robots of both mechanisms is the same under maximum applicable load and is very less. Moreover, if results for robots having modified Theo Jansen mechanism compared with the equivalent elastic strain is very less for Mild Steel with compare to a robot made with PLA.

Results of equivalent stress (Fig. 12) show that the total maximum stress induced in robots with two different mechanisms under maximum applicable load is the same and is less than that of allowable strength of the material (PLA). Moreover, if we compare the results of a robot having the same mechanism but made with two different materials than the stress induced in Mild Steel robot is comparatively more than that of PLA robot as material properties are concerned.

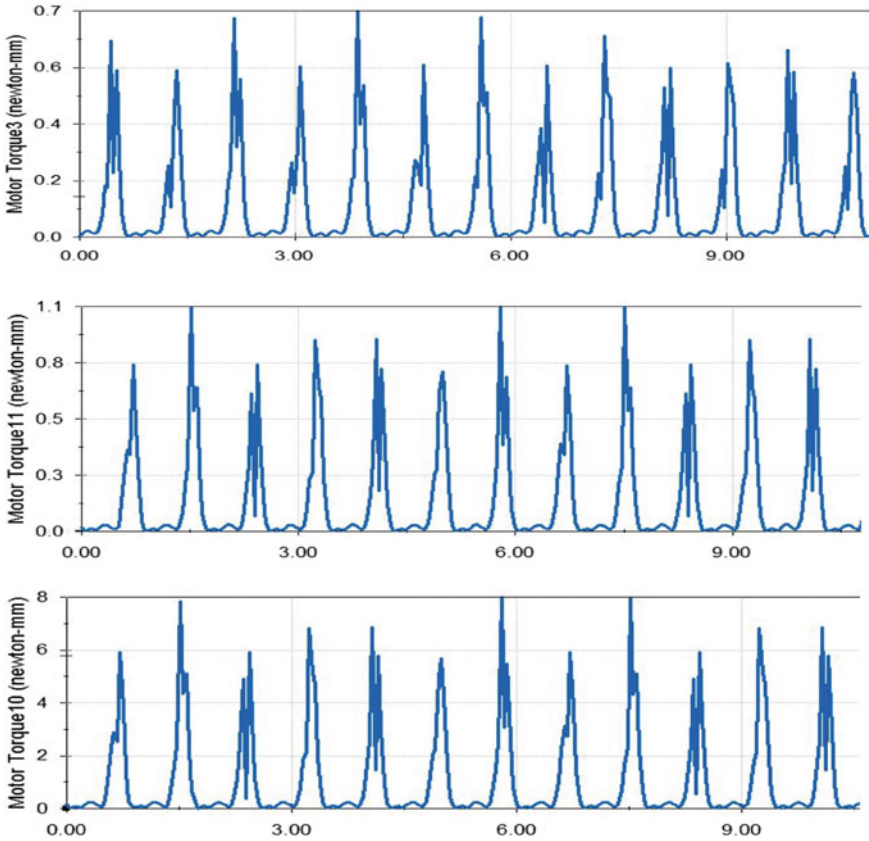


Fig. 7 Conventional, modified (PLA), and modified (MS) Theo Jansen motor torque graph

5 Conclusion

The robot uses the two different mechanisms conventional Theo Jansen mechanism and modified Theo Jansen mechanism as its walking pattern. After doing the kinematic analysis of modified Theo Jansen mechanism, we found that it is jerk free as in the conventional mechanism in each cycle, there are five points where velocity changes while in modified mechanism, in each cycle, there are three points where velocity changes, and by the use of ternary links it provides us better stability with a minor increase of input power. Also from the results of static structural analysis conclude that the deformation of robot made of conventional mechanism (PLA) > modified mechanism (PLA) > modified mechanism (Mild Steel) at 20 N. As results of equivalent stress and strain show mostly blue region, which implies that stress and strain both are in the permissible range. From all the above results, we can conclude that if strength is not concerned then Polylactic Acid (PLA) with modified Theo Jansen mechanism should be used.

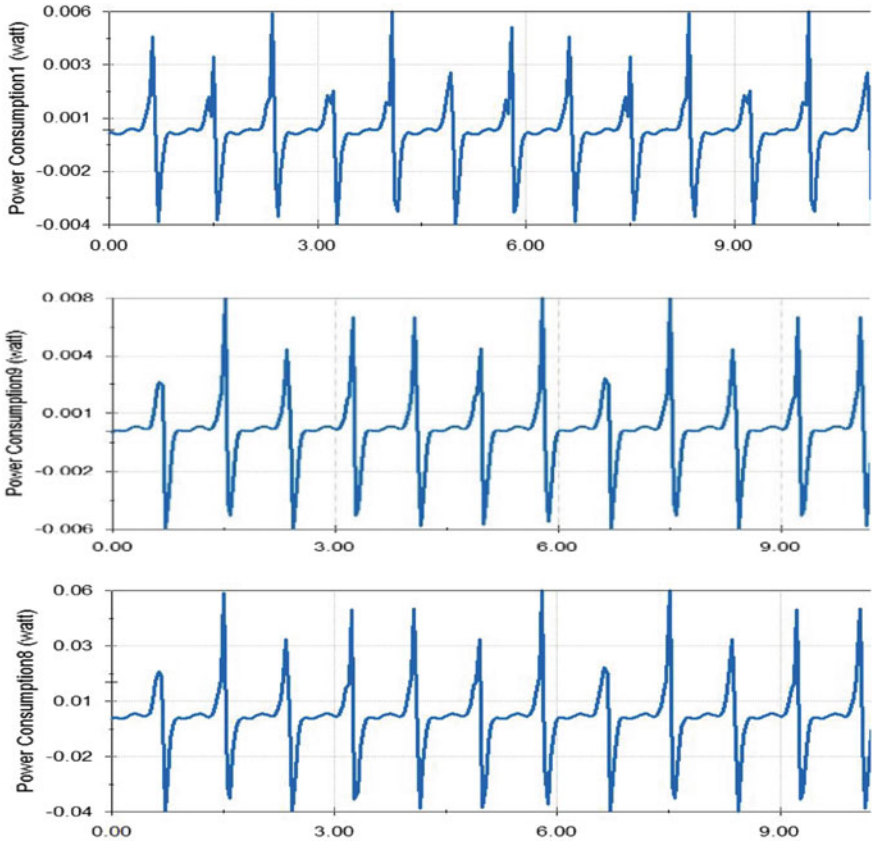


Fig. 8 Conventional, modified (PLA), and modified (MS) Theo Jansen motor power consumption graph

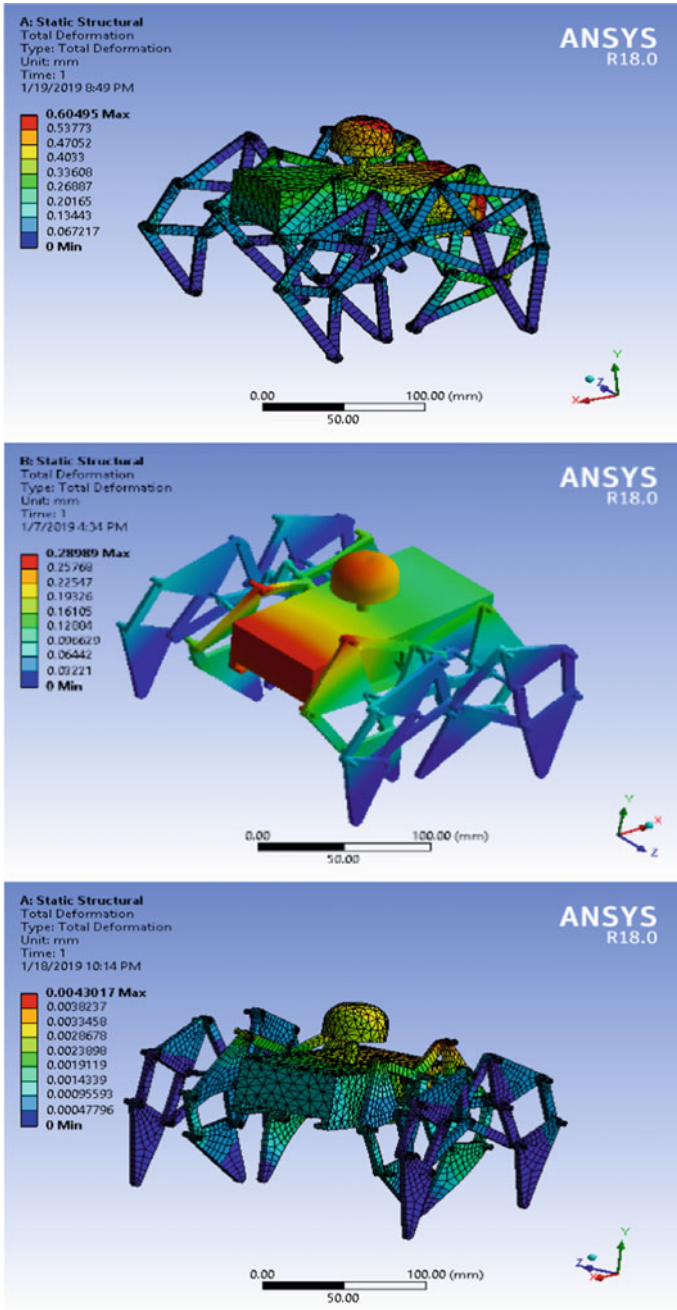


Fig. 9 Results for total deformation for robot made with conventional, modified (PLA), and modified (MS) Theo Jansen mechanism

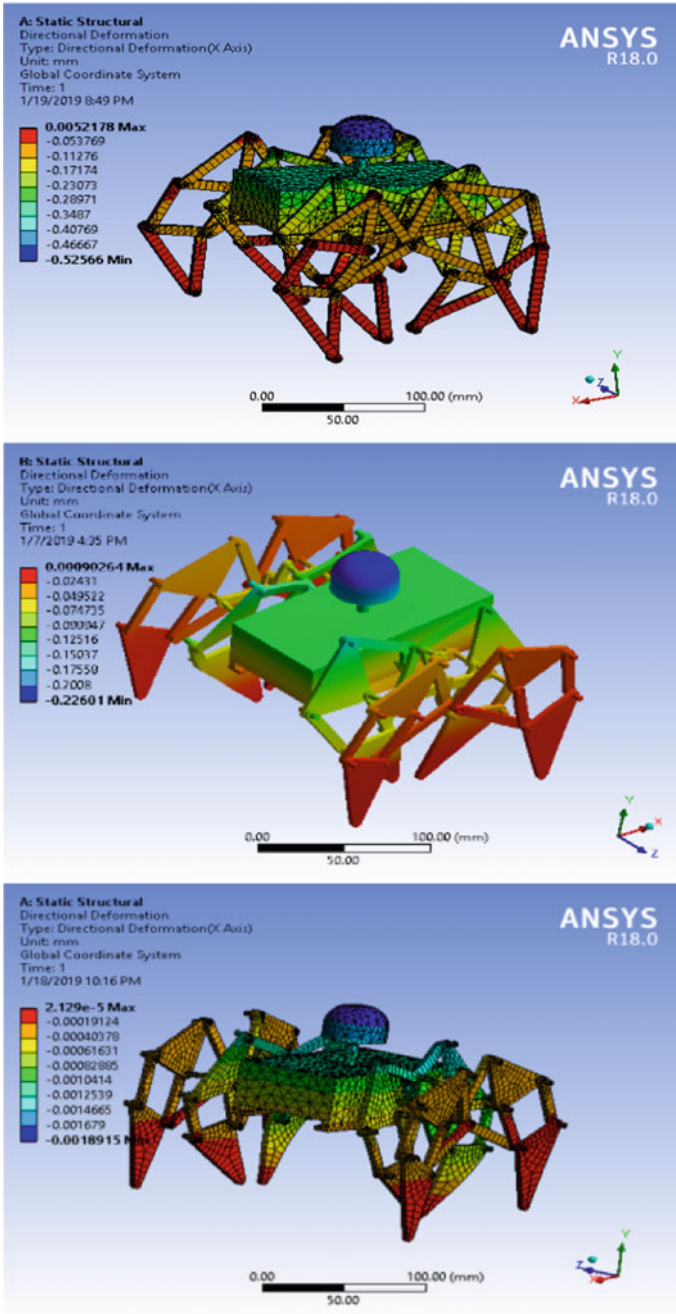


Fig. 10 Results for directional deformation for robot made with conventional, modified (PLA), and modified (MS) Theo Jansen mechanism

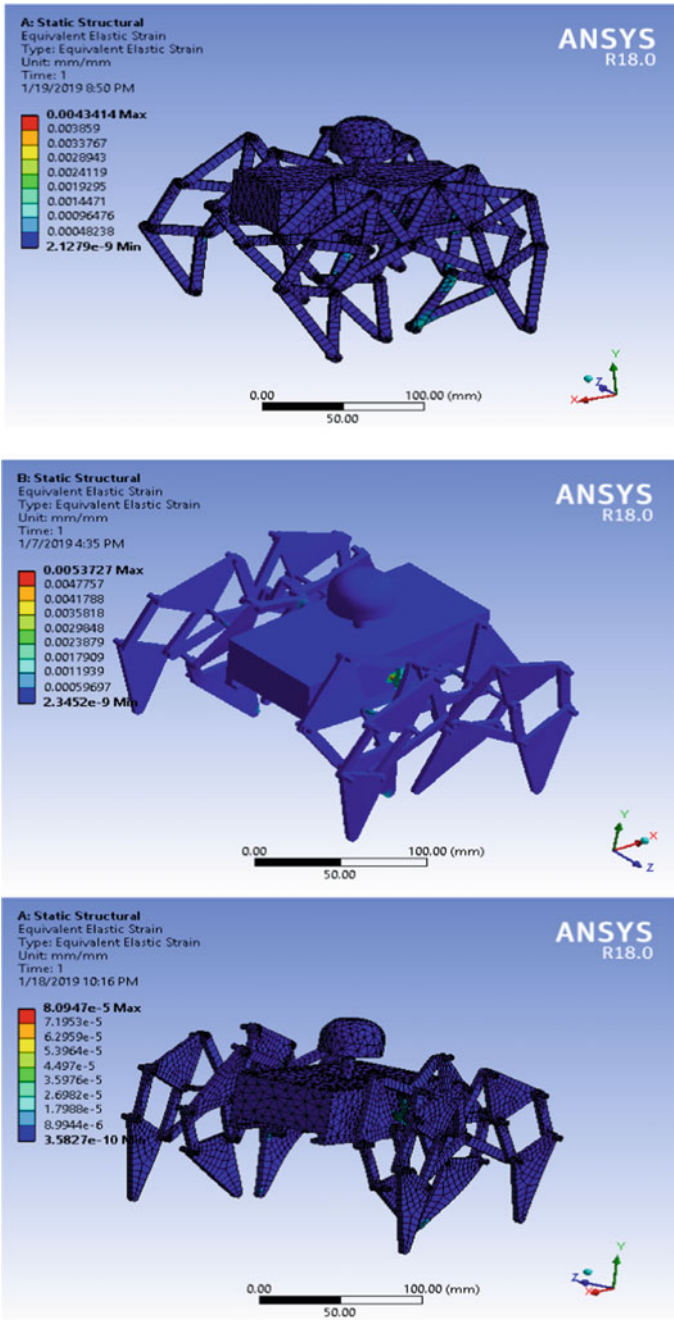


Fig. 11 Results for equivalent elastic strain for robot made with conventional, modified (PLA), and modified (MS) Theo Jansen mechanism

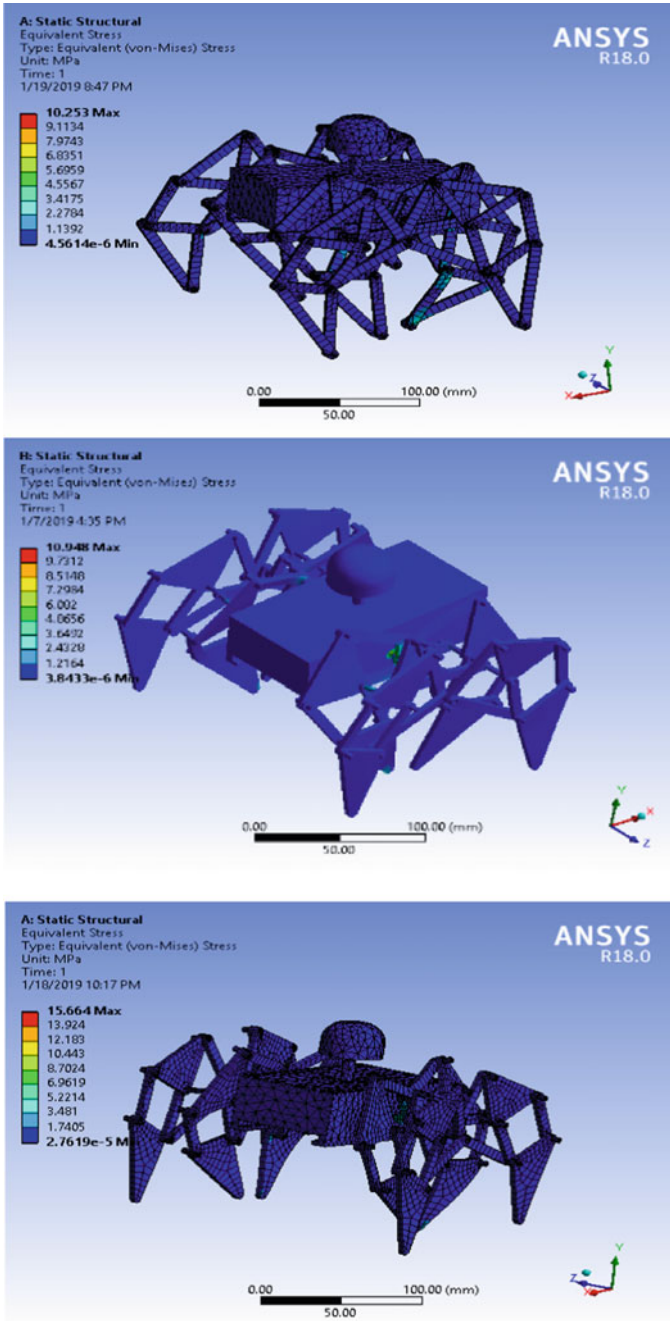


Fig. 12 Results for equivalent stress for robot made with conventional, modified (PLA), and modified (MS) Theo Jansen mechanism

Acknowledgements We would like to thank R. K. Technology who gave us an opportunity to undertake such great challenging and innovative work.

References

1. Y. Qu, P. Durdevic, Smart-spider: Autonomous self-driven in-line robot for versatile pipeline inspection. *IFAC PapersOnLine* **51**(8), 251–256 (2018)
2. D. Deepak, S. Pathma Sharma, Design and fabrication of kinematic robotic walker with left and right motion with camera. *SSRG Int. J. Mech. Eng.* **4**(4), 53–56 (2017)
3. S. Patnaik, Analysis of Theo Jansen mechanism (Strandbeest) and its comparative advantages over wheel based mine excavation system. *IOSR J. Eng.* **5**(7), 43–52 (2015)
4. H.W. Kazuma Komoda, A study of availability and extensibility of Theo Jansen mechanism toward, in *The 21st Annual Conference of the Japanese Neural Network Society* (21st) (2011)
5. A.F. Amir, K.I. Nassiraei, The concept of intelligent mechanical design for autonomous mobile robots. *J. Bionic Eng.* **4**, 217–226 (2007)
6. N.G. Lokhande, V.B. Emche, Mechanical spider by using klann mechanism. *Int. J. Mech. Eng. Comput. Appl.* **1**(5), 13–16 (2013)
7. J.P. Enric Celaya, Control of a six-legged robot walking on abrupt terrain, in *International Conference on Robotics and Automation* (Minneapolis, 1996)
8. R. Meenakshi Sundaram, L. Blair, Enhancement of robot work envelope in a flexible manufacturing cell, in *11th Annual Conference on Computers & Industrial Engineering* (1989)
9. J. Bhavik, P.N. Parekh, Design and analysis of Theo Jansen's mechanism-based ports ground (pitch) marking robot, in *Annual IEEE India Conference* (2014)
10. Moldovan F, A new type of walking robot based upon Jansen mechanism. *Adv. Mater. Res.* **463–464**, 997–1001 (2012)
11. H.A. Servet Soyguder, Design and prototype of a six-legged walking insect robot. *Ind. Robot: Int. J.* **34**(5), 412–422 (2007)
12. S. Sengupta, P. Bhatia, Study of applications of Jansen's mechanism in robot. *Int. J. Adv. Res. Innov.* **5**(3), 354–357 (2017)

Modeling of a Warfield Autonomous Robot with GPS and Digital Compass



P. V. Prasad Reddy, S. Madhava Reddy, and D. L. Tejaswini

Abstract Human life is the most valuable thing, and many lives are lost in battles. Robot uses in battles to give detailed information and live feed will help in saving lives. To perform this intelligent navigation, the Microcontroller is loaded with an efficient program written using embedded “C” language. Since all the operations of this robot can be controlled by an operator, real time situations can be analyzed and actions can be taken accordingly. System reduces fuel requirements as it can also run on solar power. It can be used for public security, monitoring.

Keywords Robot · GPS · Microcontroller · Digital compass

1 Introduction

In dangerous and inhospitable environments, even on earth, such teleported systems have gained popularity. In these cases, the low-level complexities of the robot often make it impossible for a human operator to directly control its motions [1]. These robots are compelling not for reasons of mobility but because of their autonomy, and so their ability to maintain a sense of position and to navigate without human intervention is paramount [2]. The project aims at developing an inexpensive intelligently navigable robot using GPS, GSM, and Digital Compass. The robot moves according to the GPS coordinates it receives from the user in the form of an SMS.

P. V. Prasad Reddy · S. Madhava Reddy (✉) · D. L. Tejaswini
Department of Mechanical Engineering, Mahatma Gandhi Institute of Technology, Hyderabad,
India

e-mail: smadhavareddy_mct@mgit.ac.in

P. V. Prasad Reddy

e-mail: pvprasadreddy_mct@mgit.ac.in

D. L. Tejaswini

e-mail: tejaswini19.d@gmail.com

Research into high-level questions of cognition, localization, and navigation can be performed using standard research platform that is tuned to the laboratory environment. This is one of the largest current markets for mobile robots.

The controlling device of the whole system is a Microcontroller. The Microcontroller reads the predefined formatted SMS and extracts the GPS coordinates sent by user and moves the Robot in that direction with the help of GPS and Digital compass. To perform this intelligent navigation, the Microcontroller is loaded with an efficient program written using embedded “C” language [3]. An embedded system is a combination of software and hardware to perform a dedicated task. Some of the main devices used in embedded products are Microprocessors and Microcontrollers [4].

2 Literature Review

- W. Bolton, *Instrumentation and Control Systems*, Elsevier Science and Technology Books, August 2004, explained application of various sensors and LED indicators.
- Raj Kamal, *Embedded Systems, Architecture, Programming and Design*, Tata McGraw Hill, 2nd Edition, D.V. Hall, *Microprocessor and Interfacing*, Tata McGraw Hill, Special Edition, 2006, gave principle of operation about types of microprocessors and explained programming part.
- T.S. Jayadev, *Infrared Sensors, Detectors, Electronics and Signal Processing*, explained Interfacing crystal oscillator, LCD, and other applications of sensors.
- *Micro Computer System 8086/8088 Family Architecture Programming and Design* by Liu and GA Gibson, PHI, 2nd Edition, described utilization of various micro computer systems in detail and embedded “C” language.
- *Robot Analysis and Intelligence/Asada and Slow time/Wiley Inter-Science* gave fundamentals of robot and importance of mobile robot.

3 Methodology

The microcontroller reads the predefined formatted SMS and extracts the GPS coordinates sent by user and moves the Robot in that direction with the help of GPS and Digital compass. The block diagram of Warfield Autonomous Robot using GPS and Digital Compass is shown in Figs. 1, 2, and 3.

The above schematic diagram Warfield Autonomous Robot using GPS and Digital Compass explains the interfacing section of each component with microcontroller and GPS module for the location which is to be identified according to the user requirement. Crystal oscillator is connected to thirteenth and fourteenth pins of microcontroller, and regulated power supply is also connected to microcontroller and LEDs are also connected to microcontroller through resistors.

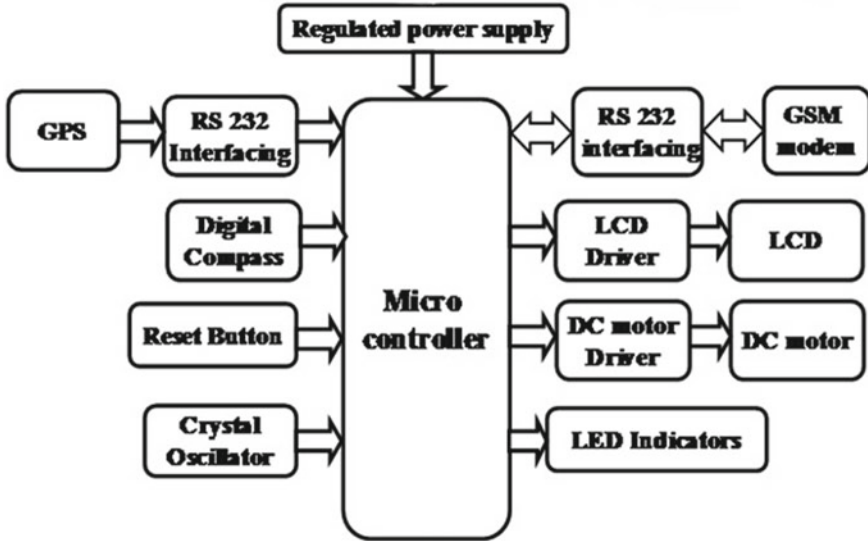


Fig. 1 Block diagram of warfield autonomous robot using digital compass and GPS

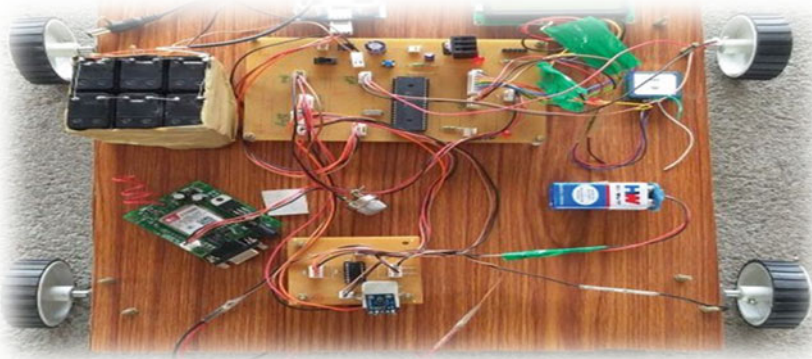


Fig. 2 Prototype of autonomous robot

3.1 Microcontroller (16F877A)

Microcontroller is a programmable device. A microcontroller has a CPU in addition to a fixed amount of RAM, ROM, I/O ports, and a timer embedded all on a single chip. The fixed amount of on-chip ROM, RAM, and number of I/O ports in microcontrollers makes them ideal for many applications in which cost and space are critical.

Autonomous Mobile Platform with artificial intelligence

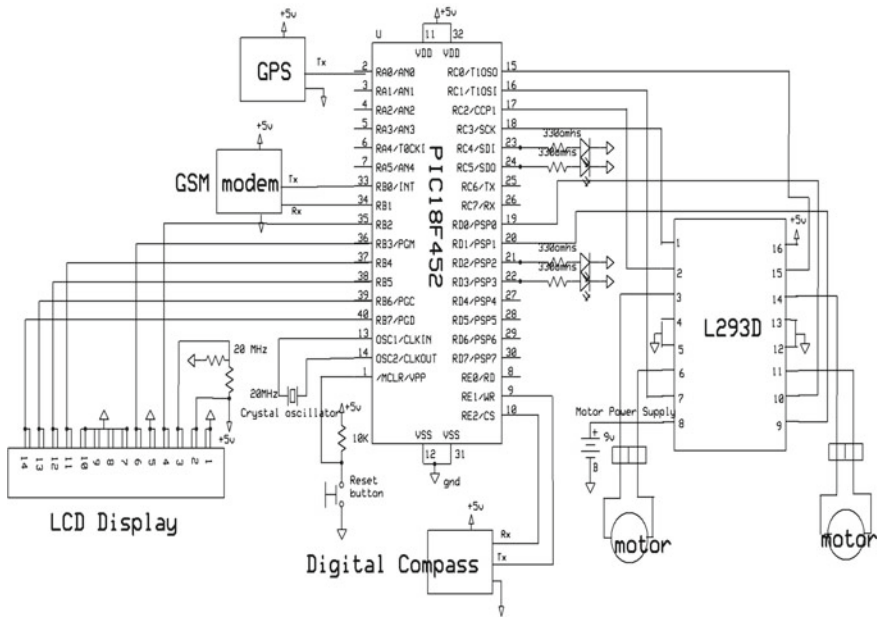


Fig. 3 Schematic diagram of warfield autonomous robot using GPS and digital compass

3.2 Crystal Oscillator

The crystal oscillator speed that can be connected to the PIC microcontroller ranges from DC to 20 MHz. Using the CCS C compiler, normally 20 MHz oscillator will be used, and the price is very cheap. The 20 MHz crystal oscillator should be connected with about 22pF capacitor.

3.3 Regulated Power Supply (RPS)

Power supply is a supply of electrical power. A device or system that supplies electrical or other types of energy to an output load or group of loads is called a power supply unit or PSU. The term is most commonly applied to electrical energy supplies, less often to mechanical ones, and rarely to others.

3.4 LED Indicator

LED indicator is used to detect the power supply which is coming from RPS to Microcontroller.

3.5 GPS Module

The Global Positioning System (GPS) is a burgeoning technology, which provides unequaled accuracy and flexibility of positioning for navigation, surveying, and GIS data capture.

3.6 Digital Compass

A compass is a navigational instrument that measures directions in a frame of reference that is stationary relative to the surface of the earth. The frame of reference defines the four cardinal directions (or points)—north, south, east, and west. Intermediate directions are also defined. Usually, a diagram called a compass rose, which shows the directions (with their names usually abbreviated to initials), is marked on the compass.

3.7 GSM Modem

GSM, which stands for Global System for Mobile communications, reigns (important) as the world's most widely used cell phone technology. Cell phones use a cell phone service carrier's GSM network by searching for cell phone towers in the nearby area. Global System for Mobile communication (GSM) is a globally accepted standard for digital cellular communication.

3.8 LCD

One of the most common devices attached to a microcontroller is an LCD display. Some of the most common LCDs connected to the many microcontrollers are 16×2 and 20×2 displays. This means 16 characters per line by two lines and 20 characters per line by two lines, respectively.

3.9 *DC Motor*

A DC motor uses electrical energy to produce mechanical energy, very typically through the interaction of magnetic fields and current-carrying conductors. The reverse process, producing electrical energy from mechanical energy, is accomplished by an alternator, generator, or dynamo. Many types of electric motors can be run as generators, and vice versa. The input of a DC motor is current/voltage, and its output is torque (speed).

3.10 *Interfacing Crystal Oscillator and Reset Button with Microcontroller*

The crystal oscillator is connected to microcontroller in such a way that two pins of oscillator are connected to the thirteenth and fourteenth pins of microcontroller; the purpose of external crystal oscillator is to speed up the execution part of instructions per cycle, and here the crystal oscillator is having 20 MHz frequency. The first pin connected to reset input pin of the microcontroller is shown in Figs. 4, 5, 6, and 7.

3.11 *Coding*

3.11.1 **Program Code**

The program code which is dumped in the microcontroller of our project is shown below.

```
#include <18F452.h>
#include <string.h>
#include <stdlib.h>
#include <math.h>
#use delay (clock=20000000)
#use rs232 (baud = 9600, xmit=PIN_B1,rcv=PIN_B0,Stream = GSM) //New
RFID Reader baudrate
#use rs232 (baud = 9600, xmit=PIN_A1,rcv=PIN_A0,stream=GPS) //Progin
#include <lcd.c>
#include <HMC6352.c>
#include <gps.c>
#include <gsm.c>
#use i2c(sda=PIN_E2, scl=PIN_E1)
#define pi 3.1415

bytedest[] = {"DP*"};
```

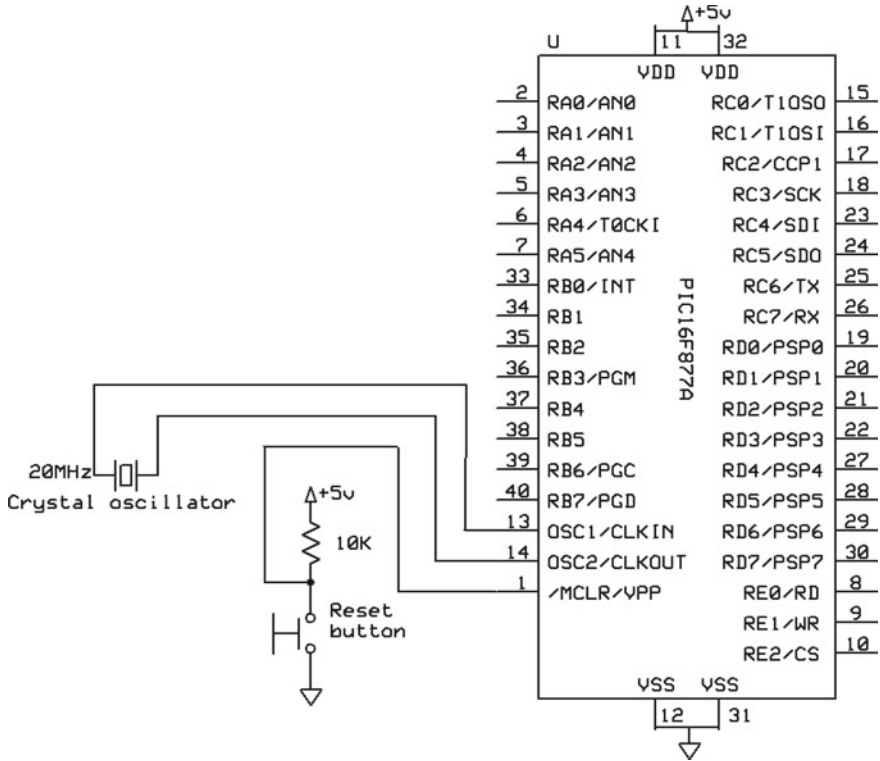


Fig. 4 Crystal oscillator and reset input interfacing with microcontroller

```

bytewru[] = { "wru" };
byte help[] = {"help"};
bytenum[18];
bytech = 0;
long i = 0;
long j = 0;
int t = 0;
intmsgsend = 0;
int count = 0;
int flag = 0;
byte data[185]; //For SMS storage

chartdata[12];
charlat[12];
charlng[12];
char plat[12];
charplng[12];
doublef_lat;
    
```

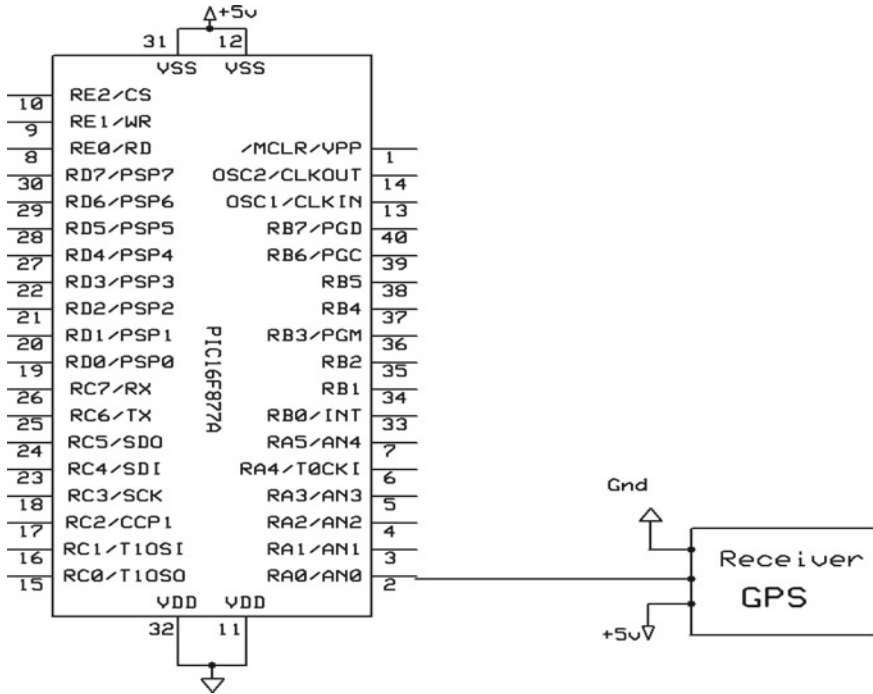


Fig. 5 GPS receiver interfacing with microcontroller

```

double lng;
double result;
double teta;
double angle;
float32 val;
double lng_old;
double lat_old;

unsigned long duty = 0;

void main()
{
int16 heading;
int16 angle;
lcd_init();
lcd_putc('\f'); //Clear LCD Display
lcd_gotoxy(1,1);
printf(lcd_putc," Autonomous ");
lcd_gotoxy(1,2);
printf(lcd_putc,"MBILE PLATFRM_II");

```

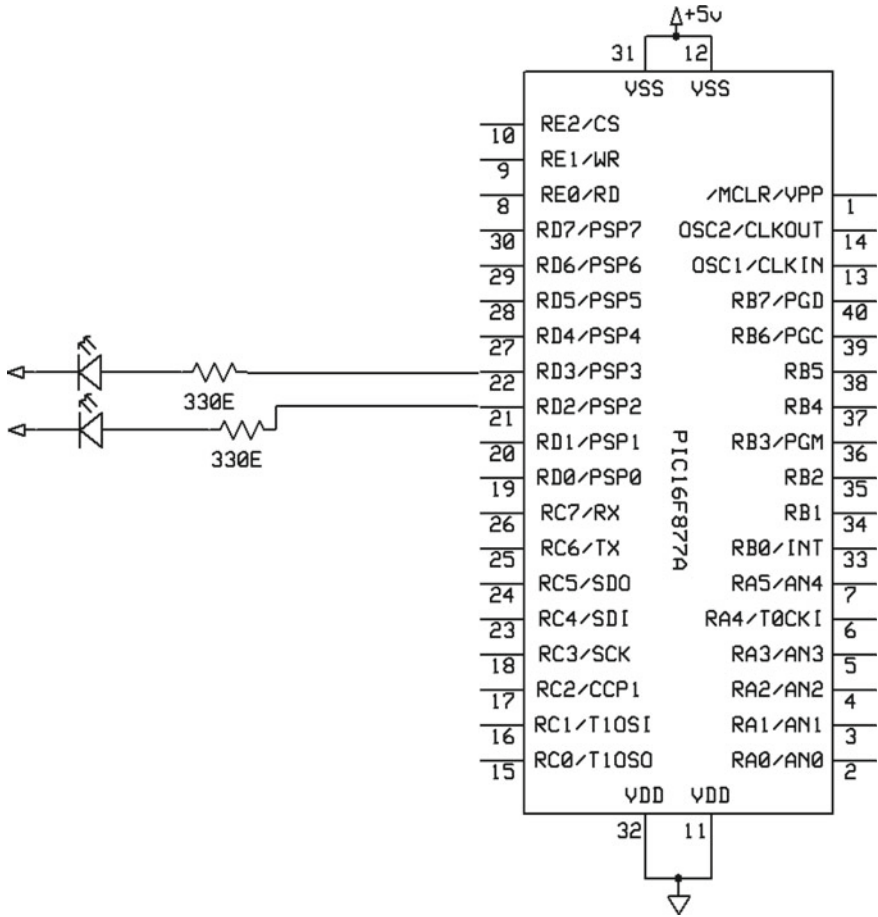


Fig. 6 LED interfacing with PIC microcontroller

```
output_high(PIN_D2);  
output_high(PIN_D3);  
output_high(PIN_C4);  
output_high(PIN_C5);  
delay_ms(500);  
output_low(PIN_D2);  
output_low(PIN_D3);  
output_low(PIN_C4);  
output_low(PIN_C5);  
delay_ms(500);  
output_high(PIN_D2);  
output_high(PIN_D3);  
output_high(PIN_C4);
```

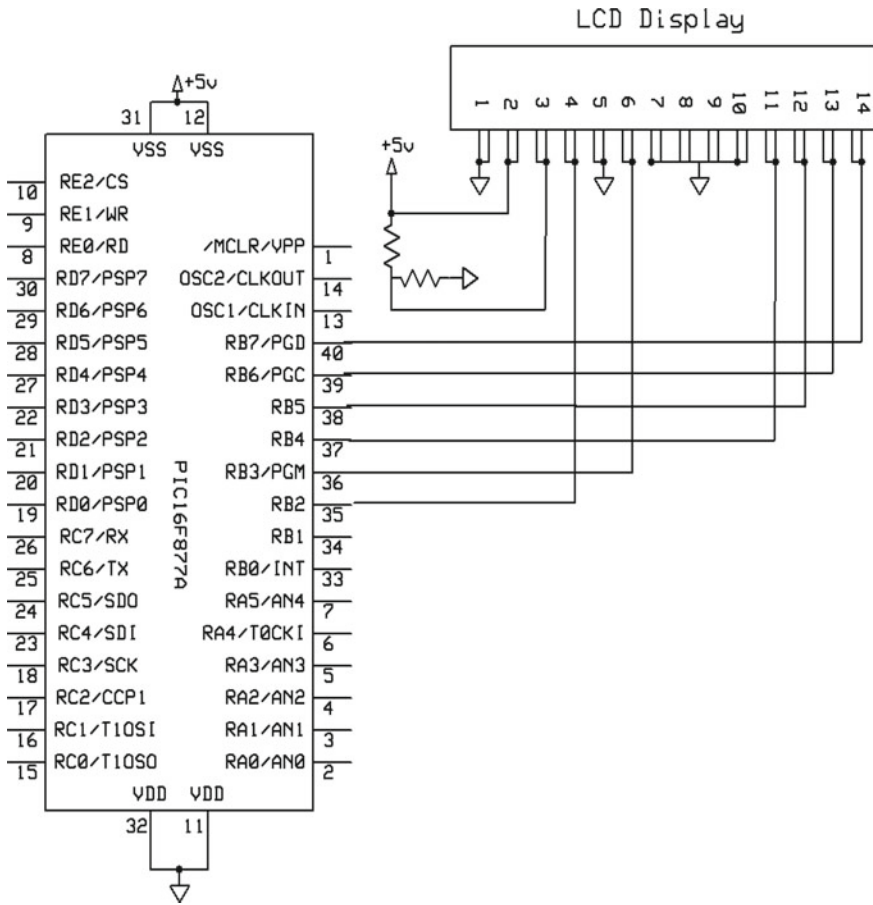


Fig. 7 LCD interfacing with microcontroller

```
output_high(PIN_C5);
delay_ms(500);
output_low(PIN_D2);
output_low(PIN_D3);
output_low(PIN_C4);
output_low(PIN_C5);
init_phone();
while(1)
{
angle = read_angle(HMC6352);
get_GPS_data();
//lcd_putc('v');
lcd_gotoxy(1,1);
```



```

printf(lcd_putc,"%s ", lat);
lcd_gotoxy(12,1);
printf(lcd_putc,"H:%lu ",angle);
lcd_gotoxy(1,2);
printf(lcd_putc,"%s", lng);
delay_ms(1000);
lcd_putc('\f');
lcd_gotoxy(1,1); // row-1, column-1
printf(lcd_putc,"please send msg");
delay_ms(1000);
count = 0; //reset data buffer
data[count] = 0;
fprintf(GSM,"AT+CMGR=1\r\n");
ch = fgetc(GSM);
data[count] = ch;
data[count] = 0; //end of string
read_sms(data);
fprintf(GSM,"AT+CMGD=1\r\n");
delay_ms(1000);
read_num(data,num);
    /*** Got the Number ***/
lcd_putc('\f');
lcd_gotoxy(1,1); // row-1, column-1
printf(lcd_putc,"Ph:%s",num);
delay_ms(3000);
if(strstr(data,dest))
    {
get_values();
result=get_gps_distance(f_lat_old,f_lng_
old,f_lat,f_lng);
lcd_gotoxy(1,2);
printf(lcd_putc,"dist: %f",result);
delay_ms(2000);
val = read_teta(f_lat_old,f_lng_old,f_lat,f_lng)
teta = rad2deg(val);
lcd_gotoxy(1,2);
printf(lcd_putc,"Angle: %F",teta);
delay_ms(1000);
lcd_gotoxy(1,2);
printf(lcd_putc,"Sending MSG...");
fprintf(GSM,"AT+CMGS=\\"%s\" \r\n",num);
delay_ms(1000);
fprintf(GSM,"Command received: ");
fprintf(GSM,"Destination: Lat: %s Long:
%s \r\n",plat,plng);

```

```

fprintf(GSM,"Angle Res.2 NORTH:
%f \r\n",teta);
fprintf(GSM,"Presentloc:Lat: %s Long:
%s \r\n",lat,lng);
delay_ms(1000);
send_sms(num);

while(1)
{
get_GPS_data();
result=get_gps_distance(f_lat_old,f_lng_
old,f_lat,f_lng);
lcd_gotoxy(1,2);
printf(lcd_putc,"dist: %f ",result);
angle = read_angle(HMC6352);
val = read_teta();
teta = rad2deg(val);
lcd_gotoxy(1,1);
printf(lcd_putc,"H:%lu ",angle);
lcd_gotoxy(8,1);
printf(lcd_putc,"A:%f ",teta);
if(angle > (teta))
{
left();
msgsend = 0;
}
else if(angle < (teta))
{
right(); msgsend = 0;
}
else if(angle <= (teta) || angle >= (teta))
{
forward();
}
if(result <= 10)
{
fprintf(GSM,"AT+CMGS=\`"%s\`\r\n",num);
delay_ms(1000);
fprintf(GSM,"Command Executed. I have Reached the Destination \r\n");
fprintf(GSM,"PresentLoc: Lat: %s Long: %s ",lat,lng);
fprintf(GSM,"Please use Google Earth to see my location.");
delay_ms(1000); send_sms(num); break;
}
}
}

```

```

else if(strstr(data,wru))
{
get_GPS_data();
fprintf(GSM,"AT+CMGS=\`%s\`\r\n",num);
delay_ms(1000);
fprintf(GSM,"Hello, I am located at ");
fprintf(GSM,"Latitude: %s Longitude:
%s ",lat,lng);
fprintf(GSM,"Please use Google Earth
to see my location.");
delay_ms(1000); send_sms(num); delay_ms(500);
}
else if(strstr(data,help))
{
fprintf(GSM,"AT+CMGS=\`%s\`\r\n",num);
delay_ms(1000);
fprintf(GSM,"Please send \`DP*latitude*longitude*\` \r\n");
fprintf(GSM,"Send \`wru\` to get my location \r\n");
delay_ms(1000); send_sms(num); delay_ms(2000);
}
delay_ms(50);
set_pwm1_duty(0);
set_pwm2_duty(0);
output_low(PIN_D2);
output_low(PIN_D3);
output_low(PIN_C4);
output_low(PIN_C5);
}
}

```

The programming and coding has been done with the use of embedded C. This program is used by the microcontroller to carry out the necessary functions using GPS and GSM technology. In turn, they help in triangulating and tracking the position of the robot.

4 Results and Discussion

The robot moves according to the GPS coordinates it receives from the user in the form of SMS. Its main advantages are low power consumption, easily operate, and fast response. GPS takes time to get the signal from satellite, when the system is switched ON. This system can be used in military areas to know the current location when there is lost in GPS signal and can also be used for location based alert ions.

Robots can be used in different fields like medical, space communication, military applications, and so on.

- Input to the system given by GPS coordinates go to $xy(1, 1)$ and go to $(1, 2)$, then robot moved to that location and using GSM module for connecting to Google earth to send location with latitude and longitude for finding live human being in warfield by using digital compass and microcontroller.
- similarly Input to the system given by GPS coordinates go to $xy(1, 1)$ and go to $(12, 1)$, then robot moved to that location and using GSM module for connecting to Google earth to send location with latitude and longitude for finding live human being by using digital compass and microcontroller.

5 Conclusion

Integrating features of all the hardware components used have been developed in it. Using highly advanced ICs with the help of growing technology, the project has been successfully implemented. Thus, the system has been successfully operated and tested. The necessary program code was written using embedded C which helps the microcontroller to meet the requirements. By using GPS, input has been given through coordinates to the robot and location was found by GSM, and then live human beings are identified as output in the warfield by using microcontroller.

References

1. T.S. Jayadev, *Infrared Sensors, Detectors, Electronics And Signal Processing*
2. *Robot Analysis and Intelligence. Asada and Slow Time* (Wiley)
3. Liu, G.A. Gibson, *Micro Computer System 8086/8088 Family Architecture Programming and Design*, 2nd edn. (PHI)
4. R. Kamal, *Embedded Systems, Architecture, Programming and Design*, 2nd edn. (Tata McGraw Hill, D.V. Hall), *Microprocessor and Interfacing*, Special edn. (Tata McGraw Hill, 2006)
5. W. Bolton, *Instrumentation and Control Systems* (Elsevier Science & Technology Books, August 2004)
6. M.J. Pont, *Embedded C*
7. K.J. Ayala, *The 8051 Microcontroller*, 3rd edn. (Cengage Learning, 2010)

Analysis of Enterprise Model Using System Dynamics: A Case of Production–Inventory System



P. S. R. K. Nageswara Rao, P. Usha Sri, and K. Vizayakumar

Abstract Enterprise modeling methodology supports capturing processes, activities, and functions of a manufacturing enterprise. Enterprise Model (EM) is the process of conceptual abstraction of enterprise functionality, business data, information channels, and triggering events. Most of the present EM modeling frameworks are open process modeling architectures which are thought of a detailed comprehensive informative data structure. The System Dynamics (SD) model captures the causal relationships among the variables and develops the feedback structure of the processes. SD analyzes and understands the dynamic behavior of the manufacturing enterprise by incorporating the time delays and draws the various policies to improve the system performance. In this paper, the integration of EM and SD methodologies to analyze qualitatively and quantitatively the process and information structures to design new policies and understand the dynamics of a manufacturing enterprise is studied.

Keywords Enterprise model · System dynamics · Manufacturing enterprise · Causal loop diagram · Policy

1 Introduction

The economic disorder of the Manufacturing Enterprises (ME) is forced to lean their manufacturing as well as management operations. In business competitiveness, customers are demanding more quality products at the lowest possible prices

P. S. R. K. Nageswara Rao (✉)

Department of Mechanical Engineering, Swami Vivekananda Institute of Technology, Secundrabad, India

e-mail: panugantisk@gmail.com

P. Usha Sri

Department of Mechanical Engineering, University College of Engineering Osmania University, Hyderabad, India

K. Vizayakumar

Department of Mechanical Engineering, Bapatla Engineering College, Bapatla, India

© Springer Nature Singapore Pte Ltd. 2021

G. S. V. L. Narasimham et al. (eds.), *Recent Trends in Mechanical Engineering*,

Lecture Notes in Mechanical Engineering,

https://doi.org/10.1007/978-981-15-7557-0_47

and excellent service options. These aspects are encouraging the MEs to establish alternative management policies and new manufacturing paradigms like CIM, lean manufacturing JIT, TQM, and networked enterprises to encounter these issues. During the last three decades, several modeling methodologies have been used for modeling, designing, and analyzing for continual performance improvements and various strategies evaluation.

Most of the modeling methodologies in the literature either are in the complete theoretical description of micro-level analysis or dealing with the complexity of the system Colquhoun [1], argued that no one technique can model in functional, resource, organizational, information and decision aspects of the system. Pidd and Woolley [2] argued that modelers should think about the nature of the system and nature of the problem prior to modeling, as some models are better suited for certain problems than others. This paper presents a modeling method EM–SD as an integrated modeling methodology for manufacturing enterprise design, analysis, and capture of the dynamics of the system. It has to meet the requirements of modeling requirements and enhance the static model to dynamic modeling.

2 System Dynamics

System Dynamics methodology is a cross-fertilization of well-known discipline, viz., feedback control theory, traditional management, and computer simulation [3]. Most of these problems are unexpected and complex in nature [4]. The decisions about these systems based on the management understanding alone perhaps prove to be counterproductive. System Dynamics methodology is a cross-fertilization of well-known disciplines, viz., feedback control theory, traditional management, and computer simulation [3]. This methodology is developed to visualize and solve the problems in a holistic manner and also to overcome the individual discipline weaknesses and to utilize their strength synergistically. In fact, other modeling methodologies usually define the problems in a static manner, but system dynamics methodology defines the problem dynamically, and it identifies the key variables in the system with respect to the time.

Causal loop diagrams are a visual representation of cause–effect relationships among the variables of the system forming the structures of feedback loops. The structure of the system represented in the SD model is based on the feedback loop which is important to understand the dynamic behavior of the system. Basically, there are two types of feedback loops in the system: (1) Positive feedback structure (2) Negative feedback structure. The third type of structure is a combination of these two which is known as the logistic structure. A positive feedback loop structure reinforces the change to its own growth or collapse. The negative feedback loop structure counteracts the change in the system, and it is characterized by goal-directed behavior. The negative feedback structure is self-governing or self-regulating and brings the system into an equilibrium state. A stock–flow diagram is to represent the flow structure of the system; it is facilitated to develop a mathematical relationship

between the system variables to analyze quantitatively the behavior of the system. The SD model depicts a stock–flow structure with four basic elements which are stocks or levels, flows or rates, converters, and connectors. It distinguishes between the physical subsystem and the information subsystem. Stocks are reservoirs; they represent accumulations or integrations that accumulate the system flows that represent the state of the system at a given point of time. The activities reflect through flows and designing a new policy for the system. The model-based analysis generates the insights to the policy structure and new policies developed intuitively to the system behavior.

3 Enterprise Model

Enterprise modeling is a generic term that represents the set of enterprise activities in detail level considering activities and processes at a global level to understand its operations. Enterprise modeling can be considered from an enterprise engineering process. Enterprise engineering is the art of understanding, specifying, defining, analyzing, and implementing the business processes for the total enterprise; then, an enterprise can achieve its objectives, be competitive, and cost-effective in the market [5]. The goal of an Enterprise Model (EM) is uniform representation and a better understanding of the enterprise, and it should fulfill the objective by either designing a new part of the enterprise for performance improvement or cost-based analysis of an existing system. Another objective is managing the complexity; generally, enterprises are complex in terms of the number of variables as well as processes, and a potential number of interactions among the enterprise objects the sudden occurrences of unexpected events that disturb operations of the system.

There are several enterprise modeling initiatives in the literature; researchers and practitioners are working parallel in developing new methodologies, tools, and methods. The major contribution in EM is CIMOSA (Computer Integrated Manufacturing Open System Architecture) developed by the AMICE consortium ESPRIT program. CIMOSA recommends modeling of manufacturing enterprise in four viewpoints viz. functional view, information view, resource view and resource view [5]. PERA (Perdue Enterprise Reference Architecture) was developed by the University of Perdue [6] which is characterized by layering and created to cover the full enterprise life cycle. GRAI/GIM methodology was developed at Bordeaux University [7, 8]. This model has four subsystems, viz., physical system, information system, decision system, and control system. ARIS [9], GERAM [10], ISO work [11], CEN ENV 40003 [12] are some of the EM architectures which are an emphasis on various viewpoints.

4 EM–SD Modeling Method

EM–SD modeling methodology has been developed to handle complex dynamic systems to meet the needs of design, analysis, and evaluation of the manufacturing systems. Enterprise models describe the enterprise functionality and enterprise behavior to the level of detail required by business users. The enterprise functionality represents actions performed in the form of functions transforming inputs into outputs over a period of time. Enterprise behavior concerns the sequence in which things are done. A model is a simplified and abstraction of [13] functional aspects describing what has to be done in terms of manufacturing and business processes related to product information, technical and necessary resource requirements. The functional view helps in understanding and describing the activities, processes, and interrelationships with information in the enterprise. An information view describes what data are used and produced by the required system. A behavioral dynamic view defining how and when shows the behavior of functions and information interacting over time. An organizational view shows the decision-making process and control flows [14]. In analyzing and designing a manufacturing system, the fundamental tasks are to identify the different variables in the organization. The relationship between the variables can describe three types of system flow: material flow, information flow, and control or decision flow.

5 Result and Discussion

This case study refers to the manufacturing enterprise production and distribution sector; products are to be shipped according to the customer order pattern. The goal of the company is to see that the products should be delivered to the customer as per the delivery schedule. The sales and marketing department receives the orders from the customers, scrutinizes, and then forwards them to the production planning and control section where they were processed and the product specifications were verified, and then the delivery schedule was charted out by negotiating with the customers. If the Inventory stock is available in the stockyard, the invoice is prepared and the products are dispatched to the concern customers. Generally, the companies are maintaining safety stock for any sudden rise of customer orders, draw from safety stock, and replenish the stock within the minimum possible duration. Most of the organizations are experiencing the dynamics in the customer order cycle. Figure 1 shows ICAM (Integrated Computer-Aided Manufacturing) graphical notations, and Fig. 2 shows the production and inventory system structure of a case study organization.

The IDEF modeling technique is a good tool to approach the analysis and modeling of manufacturing enterprise; it develops a three different nonintegrated models: IDEF0 for functional modeling helps in understanding activities and their relationships within the system, IDEF1X for information modeling helps in describing the structure of information to be required by the system, and IDEF2 for dynamic

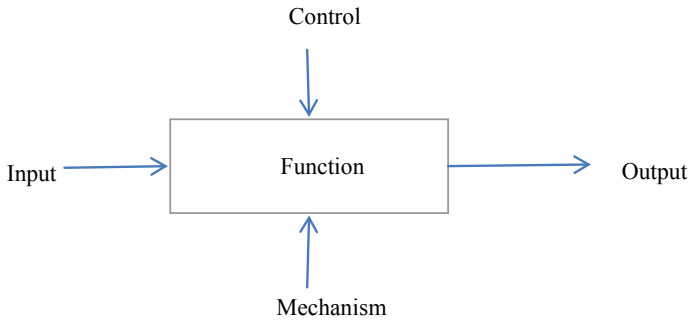


Fig. 1 Integrated computer-aided manufacturing

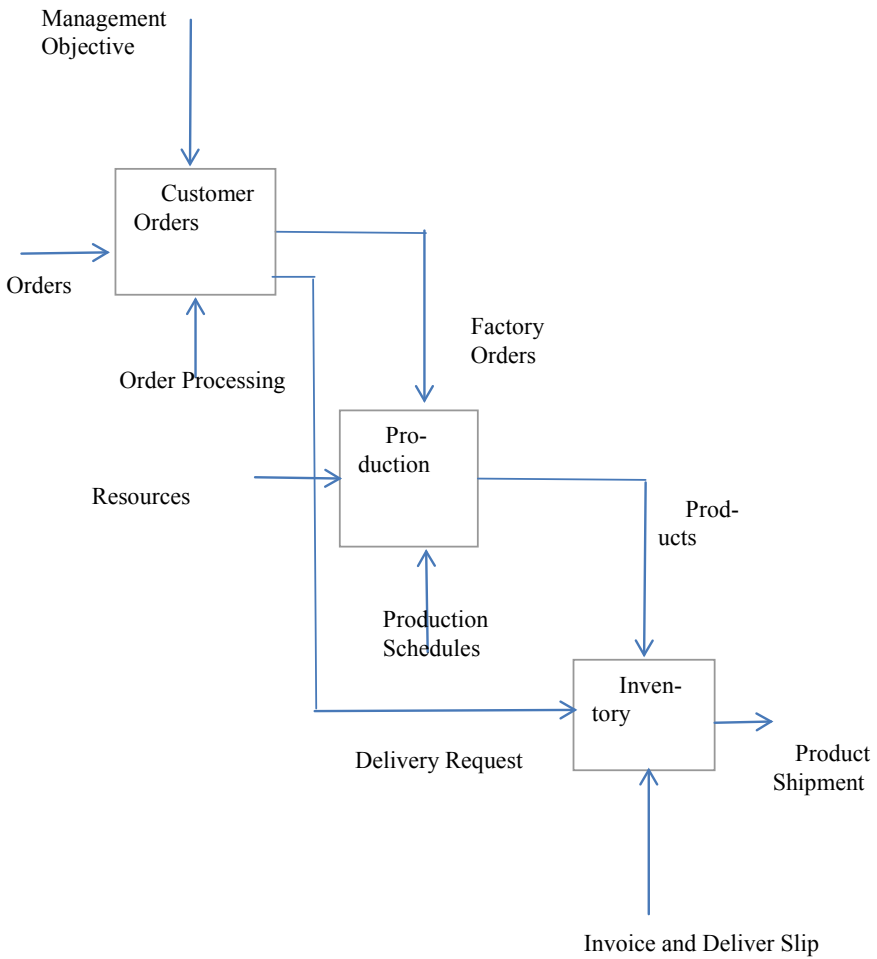


Fig. 2 The production and inventory system structure of a case study organization

modeling shows the behavior of functions and information interacting over a time. It provides a systematic approach for modeling, but there is no decision center or decision-making process in the system. The EM–SD modeling method has been developed to meet the needs of analysis, design, simulation, and policy analysis.

5.1 Casual Loop Diagram

A Causal Loop Diagram (CLD) of the Production–Inventory model is shown in Fig. 3. The basic idea behind the CLD is quickly capturing the relationships between the system variables and the dynamic hypothesis of a reference model.

CLDs are a convenient way to represent the feedback loops and generate reference mode of system behavior over a period of time. Here, there are two distinct negative feedback loops: first one controls the Inventory, and the second one controls the production rate. The first loop shows that Inventory has a counteractive effect with shipments. If shipments are high, Inventory is depleted from stock, and if inventory is high, shipments are also high. In second negative feedback loop, the production rate increases then the Inventory also increases. As Inventory increases the deficiency

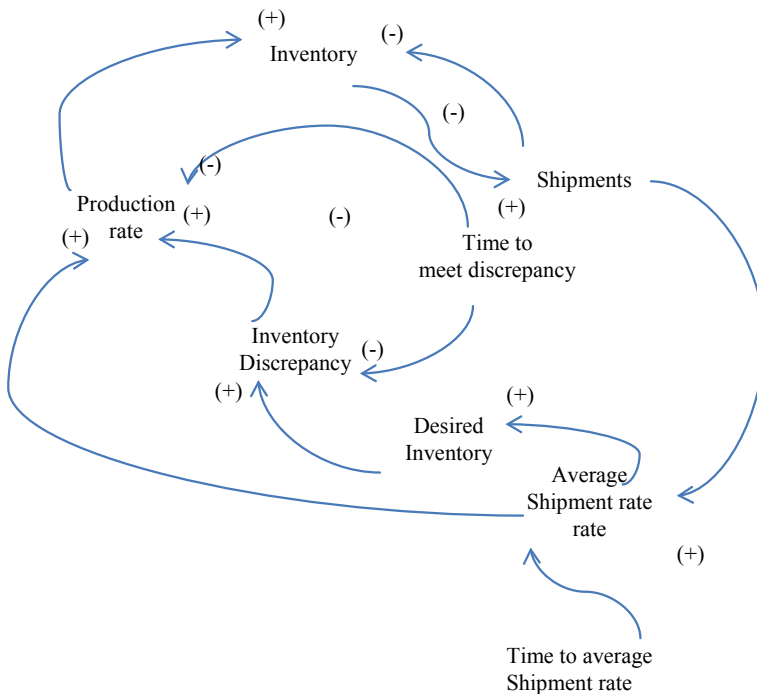


Fig. 3 Causal loop diagram

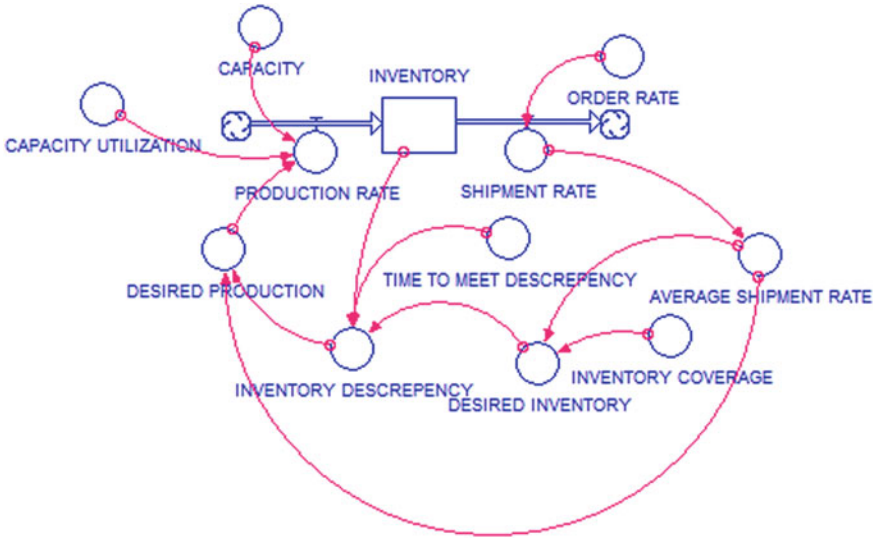


Fig. 4 Stock–flow diagram

of Inventory will decrease (Discrepancy of the Inventory is the algebraic difference between desired Inventory to the Inventory), if the discrepancy of inventory increases production rate will increase.

5.2 Stock–Flow Diagram

The stock–flow diagram shown in Fig. 4 is usually followed by the causal loop structure. The CLDs are qualitative analysis and dynamic hypotheses of the system. The stocks represent the accumulation of the state condition of the system. The stocks are altered by the flow which is changed by policies or decisions based on the condition of the system. The stock-flow diagrams represents finite differential equations, which involves the feedback loop variables, time delays and auxiliary variables of the system and simulates the dynamic behavior to analyze, derive various policy scenarios and performance improvement.

5.3 Model Analysis

For the first ten weeks, an organization is in perfect equilibrium; the customer order rate is steady for a long time. Figure 5 shows that the shipment rate is equal to the customer order rate, and the average shipment rate is equal to the production rate.

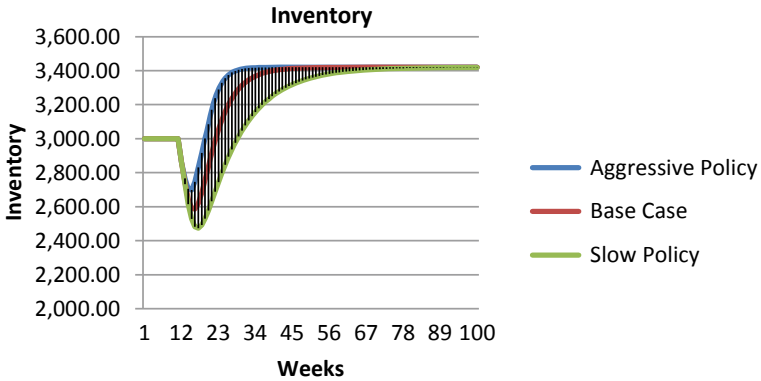


Fig. 5 Customer order rate is steady for a long time

Then, Fig. 6 shows that the desired Inventory is equal to the normal Inventory. After the tenth-week company, the customer order rate is a STEP increase permanently by 14%. Now, production rate has to enhance 140 units more than the regular production to cope up with the present order rate. The company framed a policy that three weeks of inventory has to be maintained as a safety stock. In the meantime, whatever the excess products required for dispatch should be drawn from the safety stock. The plant manager has to produce goods as per the present order rate and maintain safety stock to fulfill the company policy. In the interval between weeks 10 and 14, the shipment rate exceeds the production rate, so inventory must decline. Meanwhile, the production rate reaches equal to the shipment rate or customer order rate. This

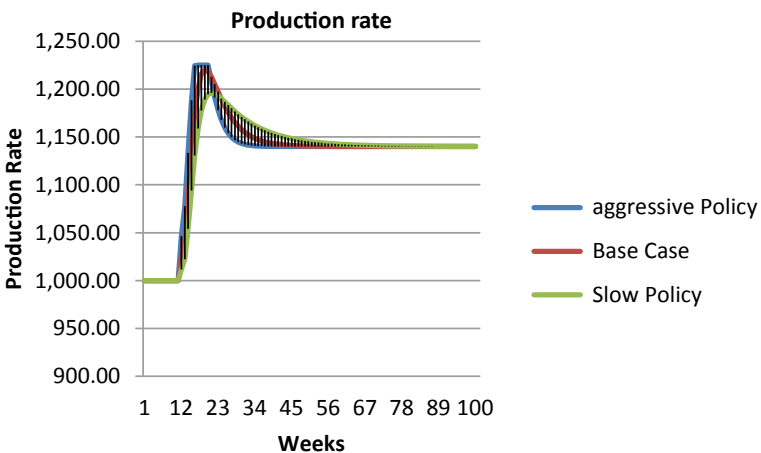


Fig. 6 Desired inventory is equal to the normal inventory

situation inventory is stable, but the company produces more until it reaches the safety stock.

5.4 Policy Design

5.4.1 Scenario 1—Aggressive Policy by Decreasing Time to Meet the Inventory Discrepancy

Under the aggressive policy, management has an option that replenishes the inventory in a short period to avoid the danger of stockouts. In this case, time to meet the Inventory discrepancy is three weeks; the production rate is gradually increased up to 24% more than the normal production rate in week 16, and Inventory is depleted to 2697 units; after that, the system is equilibrium at 32 weeks.

5.4.2 Scenario 2—Slow Policy by Increasing Time to Meet the Inventory Discrepancy

In this case, time to meet the deficiency is considered to be twelve weeks in slow policy production rate which is gradually increasing up to 19.6% in week 20, and Inventory is depleted to 2472 units; after that, system is equilibrium at week 70. The management is opting this policy where the change of production costs more than the Inventory holding costs and there are fewer chances of stock out.

6 Conclusions

This paper has presented an integrated modeling method (EM–SD) that is capable of model, design, and policy analysis of an enterprise. An IDFE0 functional model helps in understanding activities, processes, and their relationships in the system. SD methodology is developed to visualize and solve the problems in a holistic manner. The goal of this work is to present an integrated modeling method to analyze qualitatively defining the functions and develop CLDs to draw a dynamic hypothesis of an enterprise, and the stock–flow diagrams are used to analyze quantitatively. Two scenarios are developed and tested which are helpful to managers to implement according to the availability of the resource.

Appendix

Major Model equations

$$\text{INVENTORY}(t) = \text{INVENTORY}(t - \Delta t) + (\text{PRODUCTION_RATE} - \text{SHIPMENT_RATE}) * \Delta t$$

$$\text{INIT INVENTORY} = \text{ORDER_RATE} * \text{INVENTORY_COVERAGE}$$

INFLOWS :

$$\text{PRODUCTION_RATE} = \text{MIN}(\text{CAPACITY_UTILIZATION} * \text{CAPACITY}, \text{DESIRED_PRODUCTION})$$

OUTFLOWS :

$$\text{SHIPMENT_RATE} = \text{ORDER_RATE}$$

$$\text{AVERAGE_SHIPMENT_RATE} = \text{SMTH3}(\text{SHIPMENT_RATE}, 6)$$

$$\text{CAPACITY} = 1250$$

$$\text{CAPACITY_UTILIZATION} = .98$$

$$\text{DESIRED_INVENTORY} =$$

$$\text{AVERAGE_SHIPMENT_RATE} * \text{INVENTORY_COVERAGE}$$

$$\text{DESIRED_PRODUCTION} = \text{AVERAGE_SHIPMENT_RATE} + \text{INVENTORY_DESCREPENY}$$

$$\text{INVENTORY_COVERAGE} = 3$$

$$\text{INVENTORY_DESCREPENY} = (\text{DESIRED_INVENTORY} - \text{INVENTORY}) / \text{TIME_TO_MEET_DESCREPENY}$$

$$\text{ORDER_RATE} = 1000 + \text{STEP}(140, 10)$$

$$\text{TIME_TO_MEET_DESCREPENY} = 6$$

References

1. G. Colquhoun, R. Baines, R. Crossley, A state of the art review of IDEF0. *Int. J. Comput. Integr. Manuf.* **6**, 252–264 (1999)
2. M. Pidd, R.N. Woolley, A pilot study of problem structuring. *J. Oper. Res. Soc.* **31**, 1063–69 (1980)
3. J.D. Sterman, *Business Dynamics: Systems Thinking and Modeling for a Complex World* (McGraw-Hill, Boston, 2000)
4. J.W. Forrester, *Industrial Dynamics* (MIT Press, Cambridge, MA, 1961)

5. F.B. Vernadat, *Enterprise Modeling, and Integration: Principles and Applications* (Chapman & Hall, London, 1996)
6. T.J. Williams, The Purdue enterprise reference architecture. *Comput. Ind.* **24**(2–3), 141 (1997)
7. G. Documents, B. Vallespir, D. Chen, Methodologies for designing CIM systems: a survey. *Comput. Ind.* **25**(3) (1995)
8. G. Doumeings, How to decentralize decisions through the GRAI model in production management. *Comput. Ind.* **6**(1985), 501–514. (1985)
9. W.A. Scheer, *Architecture for Integrated Information Systems* (Springer, 1992)
10. IFAC-IFIP Task Force, *GERAM, Generalized Enterprise Reference Architecture, and Methodology (Version 1.5)* (IFACMP Task Force on Architecture for Enterprise Integration, 1997)
11. ISO 15704, Requirements for enterprise-reference architectures and methodologies
12. ENV 40003, Framework for enterprise modeling
13. A.M.A. Al-Ahmari, K. Ridgway, An integrated modeling method to support manufacturing systems analysis and design Architecture. *Comput. Ind.* **38**, 225–238 (1999)
14. K. Agyapong-Kodua, A. Marzano, S. Ratchev, The integrated use of enterprise and system dynamics modelling techniques in manufacturing enterprises. *Procedia CIRP* **3**, 543–548 (2012)

Comparative Analysis of Small and Large Capacity Sized On-grid, Rooftop Solar PV Systems - An LCA Approach



N. Leela Prasad , M. Shreyas , and P. Usha Sri 

Abstract Due to scarce hydrocarbon reserves in India, majorly Coal and to some extent Nuclear remain the most dependable sources of energy in near future, to meet the ever-growing demand for energy in its instant form, i.e. Electricity. Renewables such as Solar PV and Wind are relatively clean sources of electricity, but they have their own drawbacks in terms of potential, penetration, technology and the scale of deployment. But these options can supplement our energy needs to some extent. A comparative LCA study of two different capacity sized and grid-connected Solar PV systems installed on the flat rooftop of buildings located at different geographical sites within India is carried out by modelling them to run on SimaPro 9.0.0.48 LCA software with ECOINVENT 3 as database. This study covers all-important Inventory Analysis for the inputs used in terms of energy and materials, outputs resulted in terms of energy and environmental releases. The study results are expressed in the form of predefined energy metrics such as CED and EPBT. Further, this study covers the environmental impact assessment category such as GWP, and the result is presented with kWh of electricity produced by these systems as a functional unit. Further, these investigations help energy planners and policymakers to compare various power generating options and also the same option with varied capacities so that the decision on future investments in the power sector can be made in a more justifiable manner for a clean and sustainable future.

Keywords Life Cycle Assessment (LCA) · Cumulative Energy Demand (CED) · Energy Pay Back Time (EPBT) · Global Warming Potential (GWP)

N. Leela Prasad (✉)

Vignan Institute of Technology and Science, Deshmukhi, Hyderabad, Telangana, India

e-mail: nlp123@rediffmail.com

M. Shreyas

Nitte Meenakshi Institute of Technology, Belgaum, Karnataka, India

P. Usha Sri

University College of Engineering, Osmania University, Hyderabad, Telangana, India

© Springer Nature Singapore Pte Ltd. 2021

G. S. V. L. Narasimham et al. (eds.), *Recent Trends in Mechanical Engineering*,

Lecture Notes in Mechanical Engineering,

https://doi.org/10.1007/978-981-15-7557-0_48

1 Introduction

Energy makes things happen in all walks of human life, and it is usually derived from natural resources which are abundantly available on the planet earth. But many of them are non-renewable in their profile and are available in finite quantities only. The instant form of energy, i.e. Electricity is more in demand nowadays due to improved lifestyles of people across the globe. Increase in electricity demand coupled with the retirement of old generating plants makes it necessary the new investments in the generation. A pledge during COP 21 convention on climate change by India that 40 per cent of India's electric power generation capacity will be based on non-fossil fuel sources by 2030 coupled with uncertainty in conventional fuel prices complicates the choice of appropriate fuels and generation technologies. The Government of India has set a target of achieving Renewable Energy Capacity of 175 GW by the year 2022. This includes 100 GW of solar, 60 GW of Wind, 10 GW consisting of Biomass and Bagasse and 5 GW of Small Hydro. But low-carbon energy options are not scaling up fast enough to meet the rise in demand for electricity.

Therefore, sustainable utilization of various conventional resources as well as enhancing the use of unconventional energy resources is the need of the day. In order to determine the optimal mix of utilization of energy resources, all the conventional and unconventional energy sources are evaluated and compared over their life cycle based on the vital characteristics such as economic factors (resource cost, production cost, distribution cost, etc.), technical factors (availability, feasibility, maintainability and reliability of technologies), environmental factors (pollution, impacts of pollution, mitigation technologies, etc.) and social factors (rehabilitation, loss of agricultural land, etc.). In a common man's perspective, renewable energy sources are the only alternative sources of energy available, and they have zero carbon footprint. But Solar Photovoltaic based system is the one such alternative source of energy/electricity which uses renewable sunlight, and the system as a whole does have some carbon footprint. This paper explores the energy performance of two different capacity sized SPV systems and their carbon footprints over their lifetime for comparative analysis purpose.

2 Methodology

Many tools are available to assess the environmental impacts of a product, process, system or technology such as Environmental Auditing, Environmental Impact Assessment (EIA), Material Flow Auditing and Life Cycle Assessment (LCA). As Energy Generation/Conversion and Environmental Impacts have a cause and effect kind of relationship, other tools like Ecological Footprint (EF), Environmental Management System (EMS), Energy Analysis (En), Input–Output Analysis (IOA) and Net Energy Analysis (NEA) may serve the dual purpose of accounting the Energy Performance and Environmental Impacts. Some of the tools are procedural tools

usually applicable in Societal context, and others are analytical tools to support the decision-making in a commercial or business context. The decision context has many dimensions like actor, scale, complexity and uncertainty involved and object of the study as they play a key role in the selection of different tools available out there. According to Finneveden et al. [1], these tools are quite flexible and not so well defined in the sense that they can take several positions.

LCA is one such analytical tool defined according to ISO 14040 as a ‘compilation and evaluation of the inputs and outputs and the potential environmental impacts of a product system throughout its life cycle’. It has four steps: Goal and Scope Definition/Initiation, Inventory Analysis, Impact Assessment and Interpretation. Application of LCA in this study offers a methodological framework to compare two different capacity sized SPV systems with a common goal and scoping based on kWh of electricity generated as a functional unit by

- Compiling associated inventory in terms of energy and material inputs and also releases to the environment;
- Evaluating the potential impacts associated with those identified inputs and releases;
- Interpreting the results in such a manner that helps decision-makers and energy planners.

Today, there are many LCA software and databases available in the market, and the present study uses SimaPro 9.0.0.48 software [2] with ECOINVENT 3.0 [3] as a database. For evaluating system’s energy performance, a single-issue method called Cumulative Energy Demand (CED) is selected which is based on a method published by ECOINVENT version 1.01 and expanded by PRé for energy resources available in the SimaPro database. To calculate the system’s Global Warming Potential (GWP), another single-issue method IPCC 2013 is selected, which is an update of the method IPCC 2007 developed by the International Panel on Climate Change. This method lists the climate change factors of IPCC with a timeframe of 20 and 100 years.

3 LCA of Small and Large Capacity Sized On-Grid, Rooftop Solar PV Systems—A Case Study

This study covers the comparative analysis between a 100 kWp poly-Si PV system installed at KITS, Warangal, Telangana, India (Latitude: 18.1° N, Longitude: 79.5° E) and a 1.4 MWp poly-Si PV system installed at GM Institute of Technology, Davanagere, Karnataka, India (Latitude: 14.4644° N, Longitude: 75.9218° E), based on LCA methodology with 1 kWh of electricity generated by these systems as functional unit. Both systems are grid connected and installed on flat rooftops of buildings at those locations.

3.1 Inventory Analysis

The second and most important step of any study based on LCA methodology is the Inventory Analysis which covers the data collection and compilation about the material, energy inputs and emission, product outputs during the entire life cycle of a system under consideration. So, the first step in the inventory analysis is the creation of a process flow chart as shown in Fig. 1, which will serve as a master plan for the inventory data to be collected.

Material/component inputs to the system include PV modules arranged in an array and others like Inverters, Module Mounting Structure, Cable, Array Junction Box, AC Distribution Board, Lightning Arrestor and Earthing, all together termed as Balance of System (BOS). Process inputs include transport and AC power for water cleaning the modules and also for installation. Source for inventory data of about 100 kWp poly-Si PV system is Novus Green Energy Systems, Hyderabad [4], who themselves supplied and executed the project at the site, and for inventory data of about 1.4 MWp poly-Si PV system, the source is Samruddhi Renewables Solution, Bangalore [5].

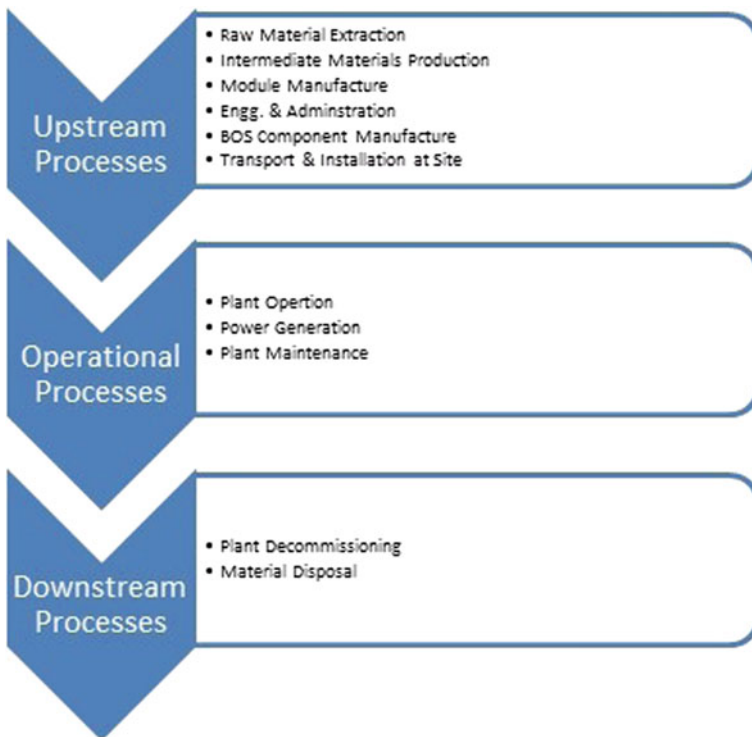


Fig. 1 Phases in the LCA chain of solar PV based electric power generation system

4 Software Modelling

World’s leading software for LCA studies SimaPro is used in this study with the world’s most consistent and transparent life cycle inventory data provider ECOINVENT as the database. Both in conjunction can analyze the life cycles of complex systems systematically. The software also facilitates the most convenient way of adding End-of-Life (EOL) scenarios to the modelled system. Additionally, Sensitivity and Uncertainty analysis studies also can be carried out.

Figures 2 and 3 are the network representations of Grid-connected, 100 kWp Rooftop, Solar PV based electric power generation system, generated after modelling and run on SimaPro software by using Cumulative Energy Demand (CED) and IPCC GWP 100a methods.

Figures 4 and 5 are the network representations of Grid-connected, 1.4 MWp Rooftop, Solar PV based electric power generation system, generated after modelling and run on SimaPro software by using Cumulative Energy Demand (CED) and IPCC GWP 100a methods.

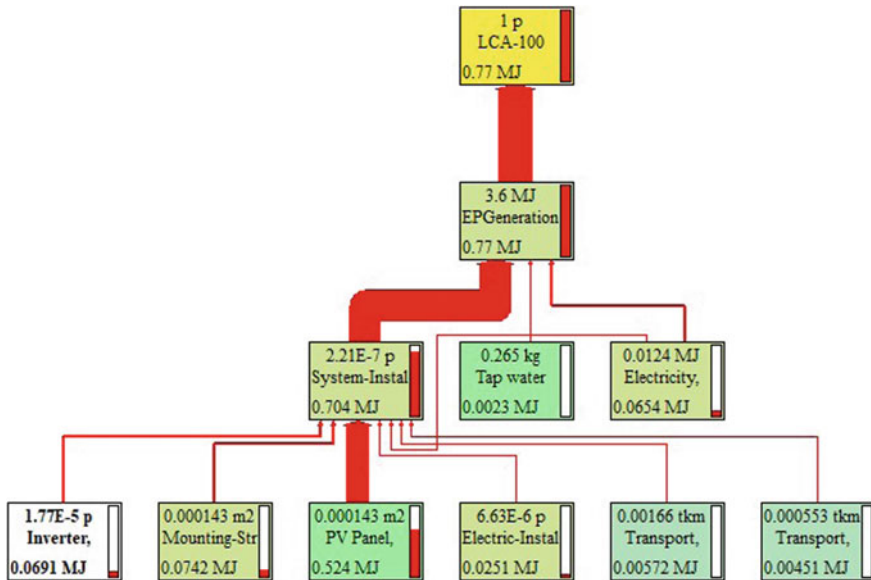


Fig. 2 Model flow chart for 100 kWp SPV system in SimaPro with cut-off value of 0%/CED method

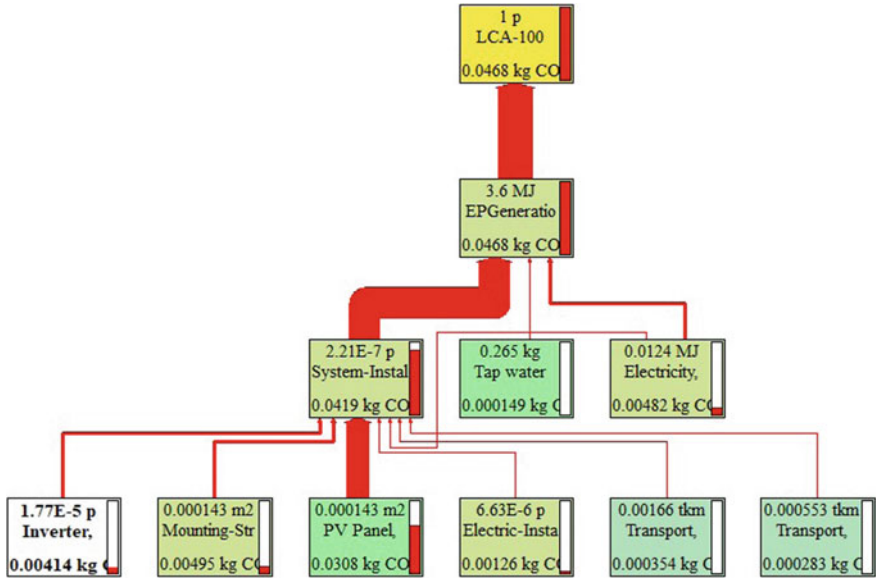


Fig. 3 Model flow chart for 100 kWp SPV system in SimaPro with cut-off value of 0%/IPCC 2013 GWP 100a method

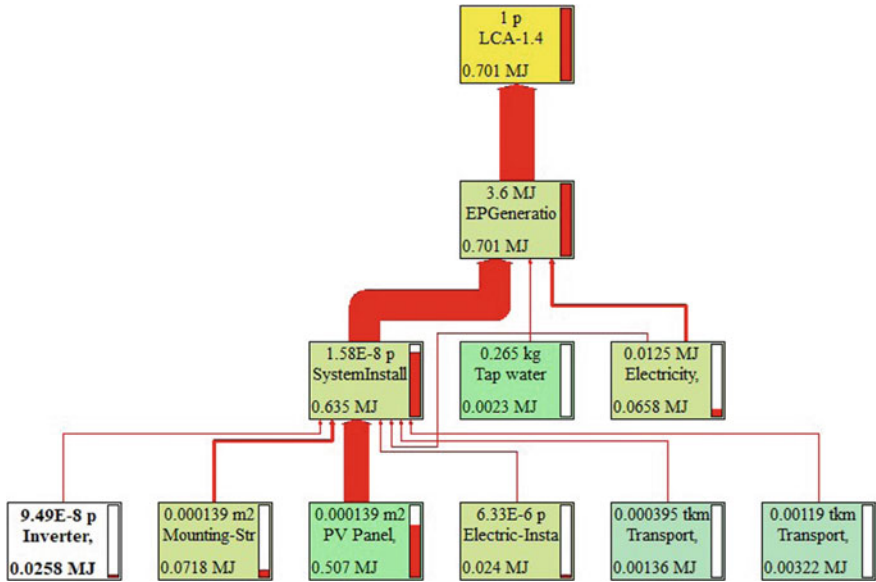


Fig. 4 Model flow chart for 1.4 MWp SPV system in SimaPro with cut-off value of 0%/CED Method

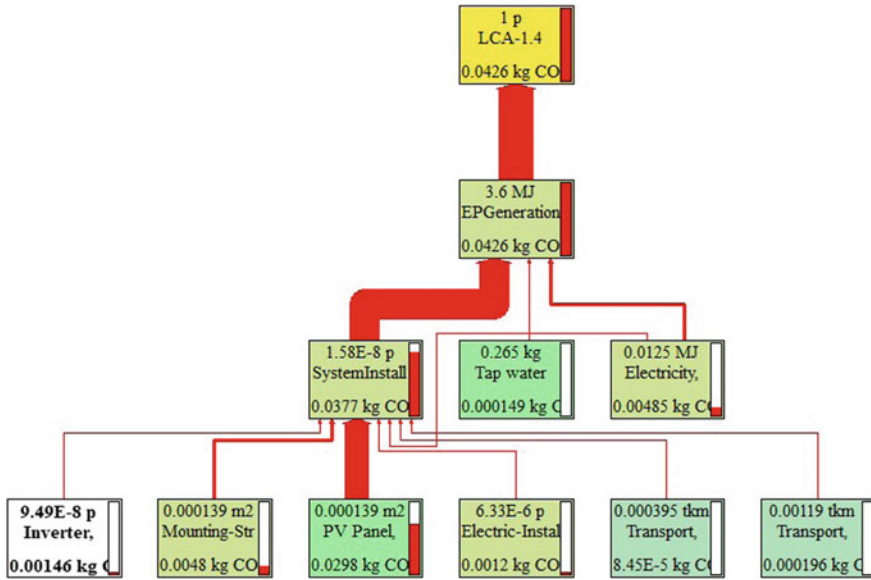


Fig. 5 Model flow chart for 1.4 MWp SPV system in SimaPro with cut-off value of 0%/IPCC 2013 GWP 100a method

5 Comparative Analysis and Results

Figures 6 and 7 are the graphical representations in the form of bar charts the comparative impact of both the systems on energy resources with characterization, weighing as indicators.

Single score results from Fig. 8 are tabulated in Table 1, for clarity and also for calculating the energy performance metrics such as CED and EPBT to carry out a comparative analysis.

For 100 kWp rated poly-Si PV system,

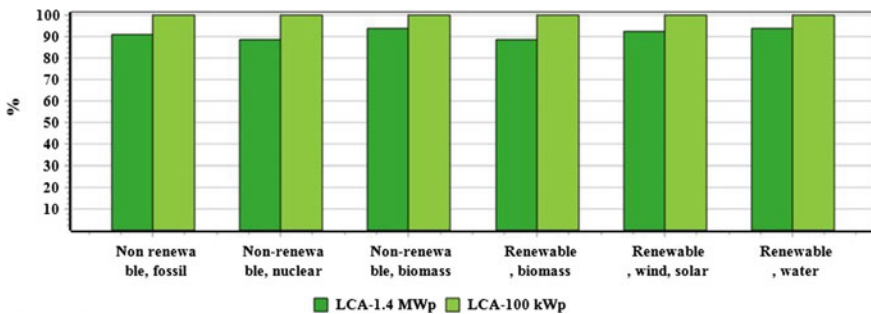


Fig. 6 Comparative CED results, method: cumulative energy demand V1.11/characterization

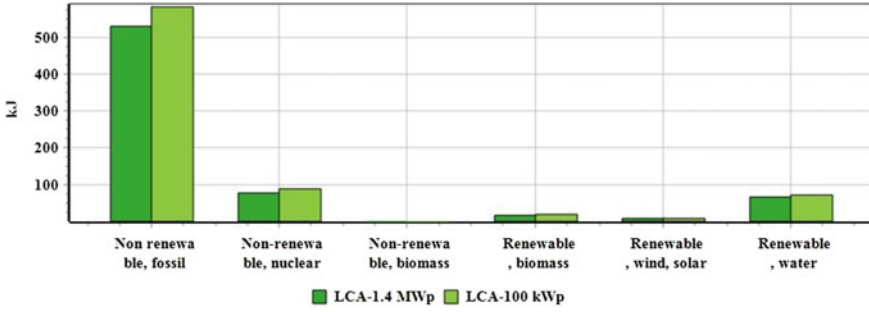


Fig. 7 Comparative CED results, method: cumulative energy demand V1.11/weighting

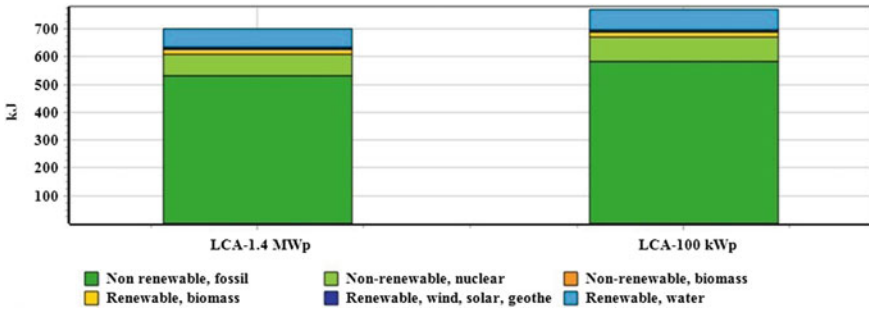


Fig. 8 Comparative CED results, method: cumulative energy demand V1.11/single score

Table 1 Impact on various energy resources by both the systems under study

Impact category	Unit	100 kWp SPV system	1.4 MWp SPV system
Non-renewable, fossil	MJ	0.5819	0.5305
Non-renewable, nuclear	MJ	0.08823	0.0783
Non-renewable, biomass	MJ	0.0001023	0.000096
Renewable, biomass	MJ	0.020036	0.017723
Renewable, wind, solar, geothermal	MJ	0.0075632	0.006984
Renewable, water	MJ	0.0721	0.067474

- Lifetime Electric Output (LEO) during 25 Years of Lifetime^{1,2}

$$= 90.3 \times 25 \times 365 \times 5.5$$

¹The average rating of a 100 kWp rated poly-Si PV system at operating conditions will be 90.3 kWp only. The average rating is taken at the lowest possible value because of PV Array loss factors like Thermal Loss Factor, Wiring Ohmic Loss, Module Quality Loss, Module Mismatch Loss, DC to AC Conversion Losses at 98.2% and Incidence Effect.

²Average sunshine is taken as 5.5 h/day throughout the year.

$$= 45, 31, 931.25 \text{ kWh}$$

- Annual Electric Output (AEO)

$$= \text{LEO}/25$$

$$= 1, 81, 277.25 \text{ kWh}(6, 52, 598.1 \text{ MJ})$$

- CED/kWh (from Fig. 2)

$$= 0.77 \text{ MJ}$$

$$\text{CED} = \text{CED/kWh} \times \text{LEO}$$

$$= 34, 89, 587.06 \text{ MJ}$$

EPBT is the time required to recover the Cumulative Energy Demand in primary energy terms that includes AC power inputs if any, during the system’s lifetime and in all its life cycle stages [6]. This term ‘EPBT’ is mostly used by energy policymakers.

- Energy Payback Time (EPBT)

$$= \text{CED}/\text{AEO}$$

$$= 34, 89, 587.06/6, 52, 598.1$$

$$= 5.34 \text{ Years}$$

Similarly, for 1.4 MWp rated poly-Si PV system,

- Lifetime Electric Output (LEO) during 25 Years of Lifetime^{3,4}

$$= 1.26 \times 25 \times 365 \times 5.5 \times 1000$$

$$= 6, 32, 36, 250 \text{ kWh}$$

- Annual Electric Output (AEO)

³The average rating of a 1.4 MWp rated poly-Si PV system at operating conditions will be 1.26 MWp only. The average rating is taken at the lowest possible value because of PV Array loss factors like Thermal Loss Factor, Wiring Ohmic Loss, Module Quality Loss, Module Mismatch Loss, DC to AC Conversion Losses at 98.2% and Incidence Effect.

⁴Average sunshine is taken as 5.5 h/day throughout the year.

$$= \text{LEO}/25$$

$$= 25, 29, 450 \text{ kWh}(91, 06, 020 \text{ MJ})$$

- CED/kWh (from Fig. 2)

$$= 0.701 \text{ MJ}$$

$$\text{CED} = \text{CED/kWh} \times \text{LEO}$$

$$= 4, 43, 28, 611.25 \text{ MJ}$$

- Energy Payback Time (EPBT)

$$= \text{CED}/\text{AEO}$$

$$= 4, 43, 28, 611.25/91, 06, 020$$

$$= 4.868 \text{ Years}$$

Characterization results from Fig. 9 are tabulated in Table 2, for clarity and also to carry out comparative analysis based on Global Warming Potential or Carbon Footprint.

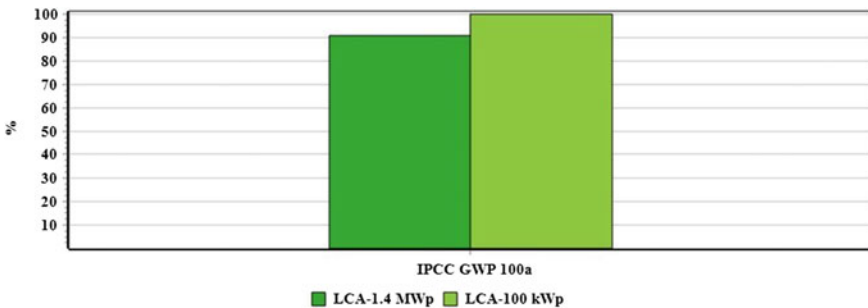


Fig. 9 Comparative GWP results, method: IPCC GWP 100a V1.03/characterization

Table 2 Global warming potential of systems under study per kWh of electricity produced

Impact category	Unit	100 kWp SPV system	1.4 MWp SPV system
GWP	kg CO ₂ eq.	0.0468	0.0426

6 Summary and Conclusions

The results of the comparative analysis presented in Tables 1 and 2 are in those expected lines such that the scaled-up system gives better energy performance in terms of lower Cumulative Energy Demand, smaller Energy Payback Times and leaves comparatively less carbon footprint. As both the systems selected in this comparative study are mounted on the flat rooftop, scaling up for better performance may not go beyond certain capacity due to available rooftop area limitation. Installing large rated system distributed over many building rooftops is not at all suggestible as increased inventory demand may offset the expected better performance. Carbon advantage of the large capacity system in this study to the tune of 4–5 gms of CO₂ eq./kWh may look so small, but it offers huge CO₂ mitigation potential over its entire lifetime. Effect of geological location on the system's performance is not explored much as both systems are sited closer and within India's geographical limits.

References

1. G. Finnveden, A. Moberg, Environmental systems analysis tools—an overview. *J. Clean. Prod.* **13**, 1165–1173 (2005)
2. Software SimaPro 9.0.0.48, PRé Consultants, Amersfoort, NL (2019)
3. ECOINVENT 3.0 Database. The Ecoinvent Centre, Swiss Centre for Life Cycle Inventories: Duebendorf, Switzerland (2015)
4. System Construction and Materials Data, Novus Green Energy Systems, Hyderabad (2015)
5. System Construction and Materials Data, Samruddhi Renewables Solution, Bengaluru (2018)
6. M. Lenzen, Life cycle energy and greenhouse gas emissions of nuclear energy: a review. *Energy Convers. Manage.* **49**, 2178–2199 (2008)

Automated Real-Time Software Based Forecasting of Climate Change Using Chlorophyll Content on Agriculture



K. Sujatha, K. S. Thivya, S. Elakkiya, V. Srividhya, NPG. Bhavani, and Bhuvaneshwari Nagarajan

Abstract The core theme of this project is to assess the economic impact of climate change on Indian agriculture. The climate change is caused due to the emission of greenhouse gases like Carbon dioxide (CO_2), Methane (CH_4), and Nitrous oxide (N_2O) from various industrial sources. Neyveli, being the source of heavy megawatt generating stations, let out flue gases which contain Carbon dioxide (CO_2), Carbon monoxide (CO), Oxides of sulfur (SO_x), Methane (CH_4), and Oxides of nitrogen (NO_x). These harmful gases are responsible for depletion of Ozone (O_3) layer which has a significant effect on year-to-year variation in weather and agricultural output and sometimes even produce acid rainfall. Considering the probable effects of climatic change on agriculture has motivated a vital change in the yield of agricultural products, livestock yields, and also changes in the food production pattern and prices. This alarming situation has motivated the researchers to propose a solution which will facilitate to identify the concentration of the constituents of the greenhouse gases, increase in atmospheric temperature, and variations in rainfall from the chlorophyll content present in the crops. This estimation of chlorophyll content can be done by extracting green colored pixels from the satellite images or images captured by the vision sensors and soil moisture sensor placed in the Indian agricultural area. These images are preprocessed for noise removal using Edge detection technique. From the preprocessed images, feature descriptors like Histogram of Gradient (HoG) are

K. Sujatha (✉)

Department of Electrical and Electronic Engineering, Dr. MGR Educational and Research Institute, Chennai, India

e-mail: drksujatha23@gmail.com

K. S. Thivya · S. Elakkiya

Department of Electronics and Communications Engineering, Dr. MGR Educational and Research Institute, Chennai, India

V. Srividhya · NPG. Bhavani

Department of Electrical and Electronic Engineering, Meenakshi College of Engineering, Chennai, India

B. Nagarajan

Abdul Kalam Research Center, Dr. MGR Educational and Research Institute, Chennai, India

© Springer Nature Singapore Pte Ltd. 2021

G. S. V. L. Narasimham et al. (eds.), *Recent Trends in Mechanical Engineering*,

Lecture Notes in Mechanical Engineering,

https://doi.org/10.1007/978-981-15-7557-0_49

extracted. The HoG values are fused with the information gathered from soil moisture sensor. The extracted features are reduced using Principal Component Analysis (PCA). The feature set is thereafter used as inputs to Artificial Neural Networks (ANN) using Feed Forward (FF) structure trained with Back Propagation Algorithm (BPA). These estimates done using data analytics will lend a helping hand to the farmers to adapt themselves to the year within annual weather shocks. It can be inferred that the estimates derived from short term are capable of predicting the short- and medium-term impacts of climate change which would direct the farmers to adapt rapidly to the changing climatic conditions. These short- and medium-term impacts of climate change are found to reduce the agricultural productivity by 4%–6% and 6%–9%, respectively. Whereas, the long term impact is drastic, decreasing the agricultural productivity by 10%–25% which makes adaptation a challenging task to the farmers in our country. Hence, it is inferred that the climate change entails significant impact on the revenue of the Indian economy until and unless the farmers can promptly identify and adjust to decreasing rainfalls and increasing atmospheric temperatures. The real challenge in the proposed method is twofold. The first challenge lies in analyzing the satellite images of the farmlands using efficient image processing algorithms to extract useful and meaningful information. This data extracted would be of a very large quantity and needs to be handled using some data analytics algorithm like BPA, whose prediction efficiency will be determined and also validated. The second challenge lies in mapping the emission of greenhouse gases with the images of the farmlands under three categories, namely Highly Productive (HP) farmlands, Medium Productive (MP) farmlands, and Less Productive (LP) farmlands and correlating the yield of farmlands with respect to emission levels of greenhouse gases in particular environment under study.

Keywords Climate change · Agriculture · Greenhouse gases · Histogram of gradient · Automated software · And back propagation algorithm

1 Introduction

Automated testing is similar to a programmer using a coding language to create programs so as to automate the manual process. In real time, testing very large systems is beyond the scope of the manual team. Hence, an automated software package or a simulation tool can be used to computerize the real-time system. The number of test beds available is less in number, so the depth of coverage is not sufficient to handle the real-time task. Increasing the size of the team for testing also complicates the situation because it increases the work overhead. Hence, an optimal solution to solve this problem is to automate the real-time environment without loss of quality which will enormously expand the capacity while sustaining the focus on testing considering the critical elements. Certain factors facilitate the choice of modeling using automated testing tools. They include the presently used testing scheme and its capacity to adjust with the automated test tools and also to

accommodate with the current trends in testing. It also initiates to indulge experts who will be using the simulated environment to design the automated testing process for a real-time system. This automated system will provide way to create a set of performance measures used for evaluation of the real-time system automated using the software package. They include repeatability in testing schemes, criticality or risk involved in real-time applications, simplicity in operations, easiness in automation, and documentation standards and requirements. It also involves training the personnel to work with the existing set of test cases and test scripts to infer the most applicable simulation package for test automation.

The testing of software can be classified into three types. They include complete manual testing, partially manual or partially automated testing, and completely automated testing. The complete manual testing is cost effective and also large-scale testing becomes difficult as it is prone to test errors and cause fatigue. The completely automated testing scheme is reliable and permits the repetitions of similar tests at an economical cost. The installation and primitive setup cost is high, but it can adapt to the changing application environment. Partially Automated or partially manual system involves a portion to be tested manually and offers redundancy by backing up automation with manual testing. The disadvantage is that it obviously does not provide as extensive benefits as either extreme solution.

Recently, in US, economists used a group of data to analyze the year-to-year variations in weather conditions across US countries to forecast the effect of weather, greenhouse gas emissions on agricultural output in a random fashion. This approach has an advantage of controlling the parameters such as the farmer quality, soil quality, climatic conditions, and greenhouse gas emissions. This panel of data with data analytics would guide the farmers to adapt themselves so that they can change the inputs or cultivation techniques to increase the yield, thereby offering a remedial measure against the natural calamities. This assessment approach would prove to be a value added approach because the impact of the climate change on the Indian people would be extremely terrible as paucity and agriculture are two salient features of the Indian economy. However, by measuring the effects of annual fluctuations, the ANN-based approach provides few features for adaptations in long run, like seasonal crop rotation rather than to exit farming.

One needs to understand the difference between the natural and enhanced greenhouse effect. In nature, the earth experiences natural greenhouse effect because of the traces of water vapor (H_2O), carbon dioxide (CO_2), methane (CH_4), and nitrous oxide (N_2O) present in the atmosphere [1–3]. These gases absorb the heat energy emitted by the sun from the surface of the earth, thereby preventing excessive solar radiation reaching the earth surface. If the natural greenhouse effect is absent, the earth surface would be 33 °C cooler. But contrary, the enhanced greenhouse effect induces excessive amount of radiation resulting from increased concentrations of greenhouse gases induced by human activities, thereby heating the surface of the planet excessively [2–5].

India being a developing country needs to battle against the effects of climate change which causes significant fall in crop yield, 15% of India's groundwater resources are damaged, and rising sea water level. In 2016, our nation recorded

its hottest day with a temperature of 510 °C at Phalodi, Rajasthan. Fossil fuel generation causes depletion of the ozone layer leading to increased pollution levels [1, 2]. The Ministry of Environment, Forest and Climate Change (MoEFCC) has suggested for few alterations to combat the pollution from coal-based thermal power plants which is bound to adversely impact Tamil Nadu Generation and Distribution Corporation (TANGEDCO) financially. Neyveli Lignite Corporation (NLC) located at Neyveli, Tamil Nadu, India, contributes to one-third of power generation, and liberates greenhouse gases which affected the agricultural produce.

Coal is the desired fuel for power generation in nations like India and China. Locally, coal is available in abundance, and continual increase in prices for natural gas and oil which is imported makes coal-fired generation of electrical power convenient. The constituents of coal have 60% of carbon content with remaining 30% of moisture content and impurities. Hence, this impure coal needs to be processed by the coal mills and electrostatic precipitator before it is used as a fuel in the thermal power plants. The fuels normally used for generation includes natural gas, diesel, nuclear, solar, hydro, and biomass power in urban and industrial areas. Nearly 54.42% of the total electric power is generated by burning coal and lignite in India. The emission of greenhouse gases are aggravated because of relatively lower calorific value, combined with high ash content due to incomplete combustion from thermal power plants in India [1–5].

The emissions include CO₂, NO_x, SO_x, air-borne inorganic particles (fly ash, carbonaceous material (soot), Suspended Particulate Matter (SPM)), and small trace of gas species from thermal power plants. Thermal power plants, using about 70% of total coal in India, are among the Large Point Sources (LPS) having significant contribution (47% each for CO₂ and SO₂) in the total LPS emissions in India. There arises a need to transform the thermal power plants in India to reduce the usage of coal per unit electricity generation (kg/kWh). Renovation with reduced coal consumption (kg/kWh) will help to reduce the greenhouse emissions. Though the quality of coal in our country remains the same, the advances in combustion technologies will lead to reduction in greenhouse gas emissions. It is approximated that 1–2% increase in heat transfer rate leading to increase in efficiency in the range of 1–2% decreases the greenhouse gas emissions per unit electricity. Carbon content present in the coal results as CO and CO₂ emissions obtained during the combustion of coal in the presence of excess air at power plants. Factors like reactivity of the coal particles, milling, air-to-fuel ratio, flame turbulence, and fuel residence time cause small amount of carbon to be left out when coal is burnt. This unburnt carbon is called as Fly Ash (FA), and the remaining goes to the Bottom Ash (BA).

2 Current Status

Coal is the prime fuel for electricity production in India, and its consumption is continually facing energy demands. Emissions of CO₂, SO₂, and Nitric-oxide (NO) from coal fired power plants from 2001–02 to 2009–10 in India. The flue gas emission

estimation is modeled theoretically by calculating the mass emission factors dependent on combustion and operating conditions of power plant. 2020–2021 gives the future values of greenhouse gas generation from 2001–2002 to 2009–2010. Different qualities of coal and combustion technologies/operating conditions are used by power plants in India [1–4]. The emissions from power plants have increased the total CO₂ emissions from 323,474.85 Gg in 2001–2002 to 498,655.78 Gg, in 2009–2010. SO₂ emissions increased from 2519.93Gg in 2001–2002 to 3840.44 Gg in 2009–2010, while NO emissions increased from 1502.07Gg to 2314.95 Gg. The emissions per unit of electricity ranges from 0.91–0.95 kg/kWh for CO₂, 6.94–7.20 g/kWh for SO₂, and 4.22–4.38 g/kWh for NO. In Indian power plants, the future emissions will be 714,976–914680 Gg CO₂, 4734–6051 Gg SO₂, and 366–469Gg NO in 2020–2021. As estimated by Planning Commission of India under “Business-as-Usual” and “Best-case-Scenario,” increase in efficiency of electricity generation by coal-fired power plants considerably decreases the greenhouse emissions. This proves to be a constructive tool for catalogue preparation for emission factors in sparse.

3 Problem Statement

Agriculture is dependent on changes in climate for the crops to be grown in a healthy manner. Research on crop yields with respect to climate change has established important awareness on varied scientific conditions. Plant and soil research indicates that the maximum yield is possible from agriculture for the given conditions. Really, it is intricate to estimate the crop yields based on varied weather conditions which occur as a result of greenhouse gas emissions from thermal power plant at Neyveli. Some studies state that increase in CO₂ enriches the crops like rice, wheat, soybeans, potatoes, and vegetables. But in reality it is not so, and their growth and yield is drastically affected by the greenhouse gas emission (CO, SO_x, CH₄, and NO_x) from the thermal power plants. A wide increase in temperature as a result of greenhouse gases extends the growing season of the crops and changes the entire life cycle of the crops like extending the growing season for paddy; it causes earlier maturity of the grains which makes it lose the quality of rice grains.

The core aim of this project is to offer a solution to farmers in the nearby regions of Neyveli, to adapt and sustain the agricultural yield for the changes in the climate and environment as a result of global warming by using the forecasting technique. Flue gases from thermal power plant constitute greenhouse gases that results in climate change in the region of Neyveli. Hence, the agricultural yield in and around this region is seriously affected. Thus, forecasting the greenhouse gases and increase in atmospheric temperature along with variations in weather conditions directs the farmers to choose seasonal crop rotation or multiple crops raising dependent on weather conditions. Neyveli (Tamil Nadu, India), being one of the important generating power plants, taking care of one-third of the power generation emits greenhouse gases which cause climate change. This variation in climate destroys the agricultural

lands and vegetation drastically in and around the region. Hence, to combat the situation, an optimal forecast of the greenhouse gases causing air pollution, increased atmospheric temperature, and decreased rainfall may help the farmers to choose seasonal crop rotation or even multiple crops growing which would give better yield dependent on the weather conditions with the help of the directions given.

4 Objective of the Proposed Work

India being a country whose focus is on agriculture, the researchers have been pondering upon solution to combat the effects of climate change. Neyveli, one important region in power generation is drastically affected by climate change due to emission of greenhouse gases which has caused increase in atmospheric temperature and decrease in rainfall. This change in the nature has affected the bio-diversity which creates a challenging environment for the farmers to fight against these changes and increase crop productivity. Hence, after an extensive survey, it is decided to monitor the farmlands using a drone which captures the images of the farmland. From these images, based on the HoG of the green intensity available pertaining to the crops along with soil moisture data, the three conditions namely HP, MP and LP conditions are predicted using ANN and this information is assimilated and appropriate action in the form of applying pesticides, or undergoing crop rotation or even suggesting multiple cropping or even farmers can take necessary steps to store the rain water for future. The HoG features are fused with the soil moisture data to improve the forecasting efficiency. This method helps to forecast the various greenhouse gases like CO₂, CO, CH₄, SO_x, NO_x, atmospheric temperature, and rainfall by capturing the images of agricultural fields using a drone or by incorporating cameras in farmlands at Neyveli where NLC is located. Images captured are preprocessed for noise removal followed by HoG feature extraction fused with soil moisture data which helps to determine the green colored pixels indicating the vegetation. These features are reduced from n-dimensions to two dimensions using PCA. Thereafter, the reduced feature set is used for training and testing the Feed Forward Neural Network (FFNN) trained with BPA. The ANN will now be able to forecast the various parameters contributing to climate change and pass on the information to farmers to take an appropriate action which would save the farmlands which is the backbone of Indian economy.

5 Research Highlights

- To assess the impact of climate change on agricultural yield (Neyveli where the thermal power plant is located).
- To forecast the greenhouse gas emissions from the images of the agricultural lands.

- To forecast the impact of climate change on increased atmospheric temperature from the images of the agricultural lands by fusing the HoG features with soil moisture data.
- To analyze the images of the agricultural lands with soil moisture content in three categories (HP, MP, and LP) along with greenhouse gases, increase in atmospheric temperature, and decrease or excessive rainfall based on chlorophyll content.
- To implement algorithms like HoG, PCA, and BPA for feature extraction, feature reduction, and forecasting the climate change.
- To automate the entire system using standard simulation software package.

6 Scientific Significance of the Proposed Work

This work focuses on the design and implementation of new automated strategy using a standard simulation package for forecasting the impact of the climate change. The change in climate poses a lot of problems on the farmers affecting the agricultural produce. The farmlands in and around Neyveli are drastically affected because of the greenhouse gas emissions from NLC due to burning of coal to generate electricity. The atmospheric concentration of greenhouse gases has increased by 30% in the last ten years. Presently, there is no well-defined method to forecast the greenhouse gas emissions and also their impact on farmlands in the region of Neyveli. Hence, through this scheme, a novel forecasting setup to monitor the agricultural fields based on the chlorophyll content present in the image, the amount of greenhouse gases, temperature, rainfall, and the remedial action the farmers need to take to save the crops in order to maximize their yield can be intimated well in advance, thereby creating an awareness to the farmers.

7 Discussion

A total of nearly 233 samples relating to the images of the agricultural fields categorized under three categories HP, MP, and LP which are affected by greenhouse gas emissions with corresponding increase in temperature and subsequent decrease in rainfall are collected. Nearly 173 samples are used for training, and remaining 60 samples are used for testing. These images may or may not be corrupted by noise. If the samples are corrupted by noise, then it is eliminated using median filter. Then, using PCA, the intensity values corresponding to green color alone is extracted and reduced. This reduced feature set is used to train and test BPA so as to predict the greenhouse gas emissions, atmospheric temperature, and decrease in rainfall. Based on these parameters sent to the farmers on their mobile, they can choose some remedial measure to save the crops and increase the productivity by combating the effects of climate change. This experimentation is done using MATLAB software. It is inferred that, for the agricultural lands in HP category, the green intensity pixels

in G-plane has a histogram count of 277. Similarly, it is inferred that, for the agricultural lands in MP and LP categories, the green intensity pixels in G-plane has a histogram count of 42 and 0, respectively. Let this value be considered as “X”. This states that the chlorophyll content is present in less quantity or totally absent in the images corresponding to MP and LP, respectively. To support this concept strongly, the soil moisture data obtained from three categories of farmlands are modified using the additive rule. The features are then used for training the FFNN with BPA.

8 Conclusion

The chlorophyll content estimated from the vegetation by extracting green colored pixels from the satellite images of the Indian Agricultural Area and the soil moisture level for each type of vegetation will then be analyzed for the impact on climate change for agriculture. The analysis will be done by introducing the chlorophyll content and the soil moisture level as the inputs to the ANN using FF with BPA. Hence, the proposed system will incorporate the data analytics and its different regression models to bring out various correlations and trends in the agriculture with respect to the climate change. Based on this analysis, the farmers will be notified via SMS about the type of crops that are favorable for yielding at a particular period of the year.

References

1. A. Gattinger, J. Jawtusich, A. Muller (FIBL), Mitigating greenhouse gases in agriculture-A challenge and opportunity for agriculture policies. DiakonischesWerk der EKD e.V, Nov 2011
2. T. Gunda, J.T. Bazuin, J. Nay, K.L. Yeung, Impact of seasonal forecast use on agricultural income in a system with varying crop costs and returns: an empirically-grounded simulation. *Environ. Res. Lett.* **12**(3), 034001 (2017)
3. M.D. Frías, M. Iturbide, R. Manzananas, J.M. Gutiérrez, An R package to visualize and communicate uncertainty in seasonal climate prediction. *Environ. Modell. Softw.* **1**(99), 101–110 (2018)
4. C. Clement Atzberger, Advances in remote sensing of agriculture: context description, existing operational monitoring systems and major information needs. *Remote Sens.* **5**, 949–981 (2013)
5. M. Meroni, C. Atzberger, C. Vancutsem, N. Gobron, F. Baret, R. Lacaze, H. Eerens, O. Leo, Evaluation of agreement between space remote sensing SPOT-VEGETATION fAPAR time series. *IEEE Trans. Geosci. Remote Sens.* **51**(4), 1951–1962 (2012)

Studies on Drop Test of a Helmeted Head Form with and Without Chinstrap Using LS-Dyna



Madipalli Manisha, Suresh Lonka, R. Dhanasekaran,
and S. Sreenatha Reddy

Abstract The aim of this research is to study the behavior of human head during the event of impact while wearing a helmet with and without locking the chinstrap. While many accidents are reported due to the negligence of wearing a helmet, there are also a few cases where not locking the chinstrap of the helmet led to major loss of lives. There is no much information about the threat level caused due to negligence of locking the chinstrap while wearing a helmet. This paper investigates the significance of locking the chinstrap, and compares the results of impact on head in both cases. The dimensions of a commercially available helmet are considered, and a head is designed to fit into the helmet. Numerical simulation, i.e., Impact test is carried out with the presence of chinstrap and in the absence of chinstrap using computer-aided engineering simulation solver LS-Dyna. The FEA model preparation and meshing is carried out using Hypermesh. Finally, comparisons are made on the impact of injured head. Results are plotted using Hyperview software. The impact forces during drop test of the helmeted form with a chinstrap were found to be minimal when compared to the forces without a chinstrap. The stresses on the chin region were major in case 2 in contrast with case 1 stresses. Energy plots were similar in both the scenarios, which ensure that drop test behavior is proper. The significance of chinstrap of helmet is immense while driving a two-wheeler. Numerical simulation also proves the importance of the chinstrap. Wearing a helmet with locked chinstrap results in minimal injuries to the victim rather than long-term diseases and death.

Keywords Helmets · Head injuries · Chinstrap · Drop test · Hypermesh · LS-Dyna · Hyperview

M. Manisha (✉) · S. Lonka
Medical Technology and Health Care, Cyient, Lanco Hills, Hyderabad, Telangana, India
e-mail: madipallimanisha1197@gmail.com

S. Lonka
e-mail: sureshlonka@gmail.com

R. Dhanasekaran · S. Sreenatha Reddy
Department of Mechanical Engineering, Guru Nanak Institute of Technology, Hyderabad,
Telangana, India
e-mail: dhanagni@gmail.com

1 Introduction

A two-wheeler is the most often used vehicle by most of the population globally. One of the reasons that escalates the use of a motorcycle is the income of a person. The maintenance of a two-wheeler is budget friendly. It also reduces time and avoids certain extent of traffic congestion, but two-wheeler driving is also prone to many accidents. When compared to all other means of transportation, only bicycles and motorcycle do not possess any protective equipment like seat belts, airbags, etc., [1]. Therefore, the use of helmets was instigated to protect the head against injuries, though the initial purpose of introducing a helmet was not meant for a motorcyclist.

The primary necessary to design a helmet was to protect heads of soldiers during battles. Helmets were discarded around the thirteenth century as their purpose of protecting the head against musket rounds was not that effective when compared to their efficiency to protect against arrows and swords [2]. They were reintroduced during World War 1 and their use continued simultaneously by making several design changes for comfort, protection, heat retention, etc. With the invention of motorcycle in nineteenth century, crash helmets were utilized as shields for head against skull fractures and brain injuries during traffic accidents [3].

Among the total road user fatal accidents, motorcyclist comprises the major proportion. Lakhs of people are losing lives in road crashes and about millions are getting injured which affects the health care system economically. Most of the two-wheeler fatalities were due to the lack of use of helmets. According to estimation by the National Highway Traffic Safety Administration (NHTSA), the overall risk of death in an accident reduces by 29% with the use of a helmet and the risk of brain injury takes the edge of 67% [4]. Many research studies depict that use of helmets reduce the rate of mortality and traumatic brain injury after a motorcycle collision [5]. Average hospital expenses for TBI patients are 13 times greater than those without TBI [6], and severe TBI patients average 55 days of acute rehabilitation [7].

Even though it is a universal fact, however, most of the people are likely to drive a motorcycle without a helmet. Education also plays a prominent role in this issue. As few reports depict those owners of licensed two wheelers in the past who were educated and possess high income were probable to wear a helmet [8] than those without college education.

The present study focusses on the significance of chinstrap of a helmet. During an accident, if a human head is blown to an impact on the chin, there is high possibility that the helmet disengages from the head and leads to severe injury to the head. Numerical analysis is performed to understand the damage level to the head. Comparisons are made on the results of a human head wearing a helmet with chinstrap locked and without chinstrap being locked.

2 Experimental Details

A human head, helmet with chinstrap, and helmet without chinstrap are considered for carrying out numerical simulation. The details of the components considered are discussed below.

2.1 Human Head

Human head is not in a stable position as it is supported by neck (which is free to move in three degrees of freedom) and experiences rotational forces and acceleration/deceleration [9]. The impact in an accident is due to the involvement of high masses and high velocities [2]. To reduce the effect, impact force should be distributed and absorbed. For this purpose, a helmet is mandatory to reduce the impact on the head. Wearing a helmet in a proper position plays a vital role.

The possibility of injury to a human head due to an impact load is exorbitantly high [13]. Many cases have been reported since many years especially during road crashes. Motorcycle collision not only leads to death but sometimes leads to long-term illness, which includes cranium damages, cervical spine issues, bone and non-bone damages, effect to spinal cord, etc. Analysis discloses that a substantial proportion of non-helmeted riders were affected by traumatic brain injury and perished when compared to riders with helmet. Few research databases show that cervical spine injury was considerably less likely in helmeted riders than non-helmeted riders [10].

2.2 Helmet

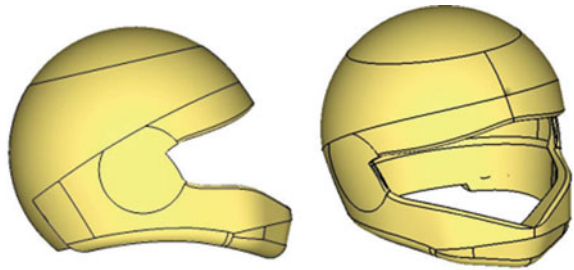
A helmet consists of two major parts, one being the hard outer shell to protect head against objects that cause injury and the other being the energy absorbing liner. A helmet protects the head of a motorcyclist against skull fractures, cranial impacts, and other head-related injuries during an accident. The purpose of wearing a protective helmet is to reduce the impact energy on the head by diminishing the severity of injury. Many modern helmets are developed fulfilling all the major criteria required to safeguard a rider's head. Helmet available in various models is shown in Fig. 1.

For the current study, a simple bell helmet is considered and modeled using Unigraphics software. The dimensions of commercially available helmet are considered as shown in Fig. 2.

Fig. 1 Helmet model



Fig. 2 Helmet design model



2.3 Chinstrap

A potentially exposed region of the head even after wearing a helmet is the chin and jaw area. Therefore, chin and jaw are more vulnerable to injury from impact forces [11]. Chinstraps project outward from opposite ends of a helmet, and are locked just beneath the chin to secure the helmet tightly to the rider’s head. Law enforcement agencies have made mandatory to wear a helmet in most of the countries. This is the reason few people are forced to wear a helmet rather than their conscious about health. People are more deviated to buy cheap quality helmets and helmets without chinstraps though these do not safeguard the head as much as a helmet with hard outer core and a chinstrap. Chinstraps play a prominent role in proper positioning of helmet. Chinstraps are flexible and resilient as shown in Fig. 3 [11].

Fig. 3 Chinstrap



3 Methodology

Numerical Modeling: Numerical analysis is carried out by performing Drop test for the helmeted head. The speed of falling object varies with time. According to the Law of conservation of energy principle, the potential energy of the object before falling should be equal to the kinetic energy when it hits the ground. From balancing the equations of potential energy and kinetic energy, the velocity of the object can be determined. We know that

$$PE = mgh \quad \text{and} \quad KE = 1/2mv^2$$

where

- m mass
- g acceleration due to gravity (9810 mm/s²)
- h height
- v velocity

From balancing the above equations, we get

$$v = \sqrt{2gh}$$

The height of the drop considered for current analysis is 1500 mm.

Therefore, $v = 5424.94$ mm/s.

The obtained velocity is assigned to the helmeted head form, and drop test is performed.

The advanced nonlinear computer-aided engineering solver LS-DYNA [11] was used for the Numerical simulation, and Hypermesh was used for the preprocessing of the FEA model. Primary and most significant phase in preprocessing of an FEA model is Meshing. Meshing involves discretization of the body into finite number of elements constituting nodes. Each element correlates the behavior of the body. Meshing is done using Hypermesh software. Tetra mesh is considered for all the parts except for the rigid wall. Quad mesh is considered for rigid wall.

3.1 Human Head

A human head consists of many parts which include a skull surrounded by the fleshy outer portion, brain, neck, and seven cervical vertebrae. To carry out finite element analysis of a helmeted head form, a human head is modeled as per the dimensions in Fig. 4. For simulation purpose, the human head is approximated. All the parts of a human head are not considered; a skull is modeled, and the relevant properties are assigned.

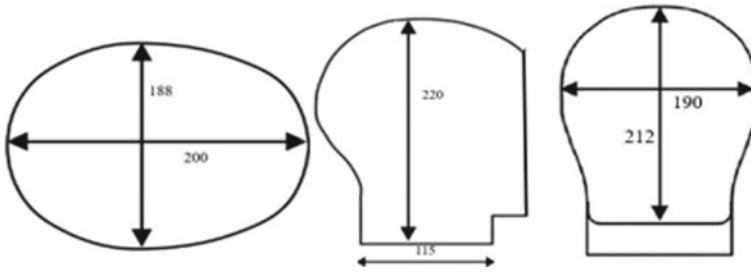


Fig. 4 Geometry of head model (dimensions in mm)

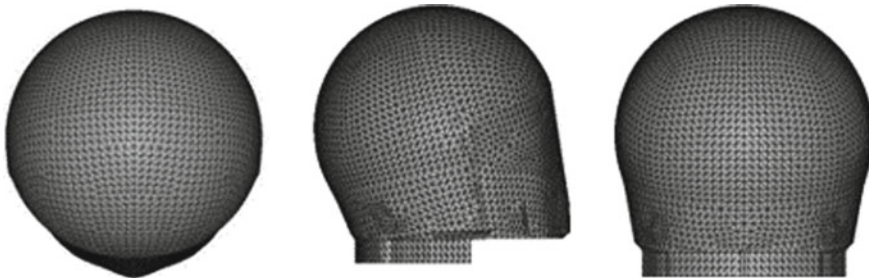


Fig. 5 Skull model

The meshed model of a skull as shown in Fig. 5 consists of 9985 nodes and 45,494 solid tetra elements and possesses a mass of 3.93 kg.

3.2 *Helmet*

A full face covering bell helmet shown in Fig. 6 is considered for simulation purpose. The same helmet is used in both the cases, once with a chinstrap and in the other simulation the chinstrap is detached from the helmet. The helmet contains 8474 nodes, 28,864 solid tetra elements, and has a mass of 1.2 kg. Figure 7 shows the Meshed model of helmet with (left) and without (right) chinstrap.

3.3 *Chinstrap*

In the present study, chinstrap is also approximated as 1 mm thick band containing 444 nodes and 962 solid tetra elements. Figure 8 shows the chinstrap model.

Fig. 6 Helmet model

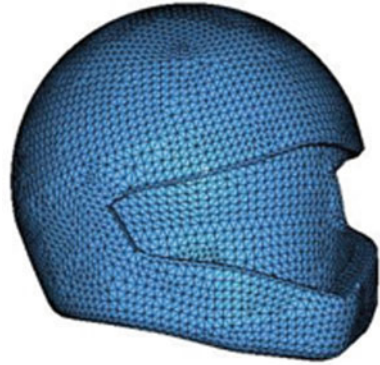


Fig. 7 Meshed model of helmet with (left) and without (right) chinstrap

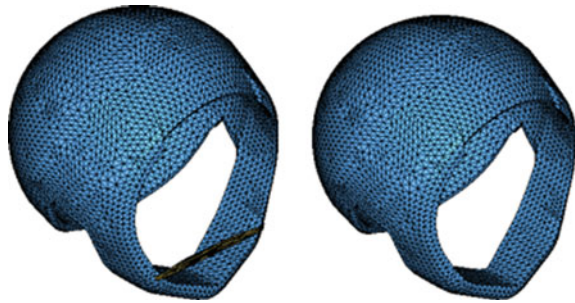


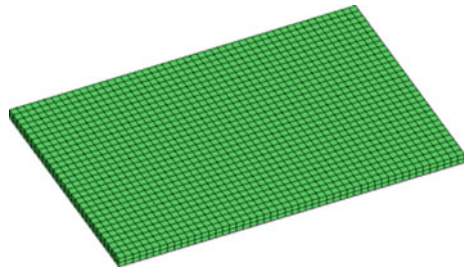
Fig. 8 Chinstrap model



3.4 Surface of Impact

A rigid wall shown in Fig. 9 is modeled representing the ground to drop the helmeted head form. This surface is used for the impact of the helmet. The wall consists of 4743 nodes and 3000 solid quad elements.

Fig. 9 Rigid wall



3.5 Finite Element Model

The pre-finite element model is prepared in Hypermesh software. Drop test is performed using LS-Dyna simulation solver. The post FE model is viewed in hyperworks software for failure regions and stresses. The size of the elements used is 5 mm. The helmet and human head are given automatic surface contacts, and nodes are merged at the interface of chinstrap and the helmet. The entire model is impacted against the rigid wall with a velocity of 5424.94 mm/s in Y-direction. Figure 10 shows the Meshed model with (left) and without (right) helmet.

The elastic material model is assumed, and the details of the material properties of the helmet, skull, and chinstrap are shown in Table 1.

4 Results and Discussion

Major objective of our study is to prove numerically the significance of tightening the chinstrap along with wearing a helmet for complete safety of motorcyclist during unexpected accidents. Effectively fastened chinstrap adequately holds the helmet onto the head preventing it from rolling off during major road crashes. Though there are many research journals depicting the significance of helmets and studies showing accident databases, there is no much information about the importance of the chinstrap and the role that possess during a motorcycle collision. Our research study has proved numerically with the aid of simulation that the impact at chin location is minor in the case where chinstrap is locked to the helmeted head than with the one without locking chinstrap. If the chinstrap is locked accurately, it prevents the

Fig. 10 Meshed model with (left) and without (right) helmet

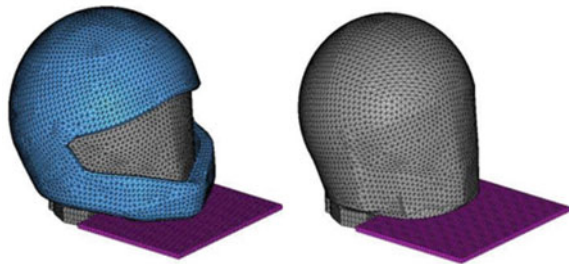
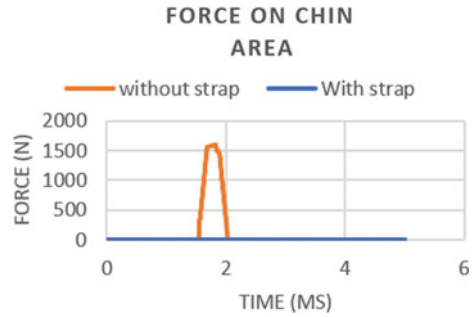


Table 1 Material properties

S. No.	Component	Density (g/cc)	Young's modulus (MPa)	Poisson's ratio
1	Helmet	0.1	2300	0.3
2	Human Head	0.9	1500	0.32
3	Chinstrap	0.87	1500	0.3

Fig. 11 Force plots

helmeted head from bouncing out of the helmet and prevents from major injuries to a large extent. While using a helmeted head without locking chinstrap, the chances of head bouncing out of the helmet are very high and it results in substantial damage to skull.

4.1 Force on Skull Due to Impact with Wall

Forces on skull due to impact with wall are compared for both the scenarios, i.e., helmet with and without chinstrap are shown in Fig. 11. It is obvious from the numerical results that there is no force observed in the case where helmet is secured using a chinstrap. In contrast, for the second scenario where the chinstrap is not considered, the impact force observed on skull is above 1500 N. This would result in severe damage to the motorcyclist. The abscissa represents the time in milliseconds, whereas the ordinate denotes impact force (in Newton) resulting on the chin.

4.2 Energy Plots

Energy plots are used to validate the behavior of impact. The energy plots (shown in Fig. 12) for current study are derived from LS pre-post software. During the event of drop, potential energy will be thus converted to kinetic energy. As the helmeted head form comes in contact to the rigid wall, the kinetic energy reduces and gets converted to work and internal energy. Reduction in kinetic energy results in increase of internal energy and work [12]. Total energy remains constant. Plot behavior remained similar for both the locked and unlocked chinstrap impact test results.

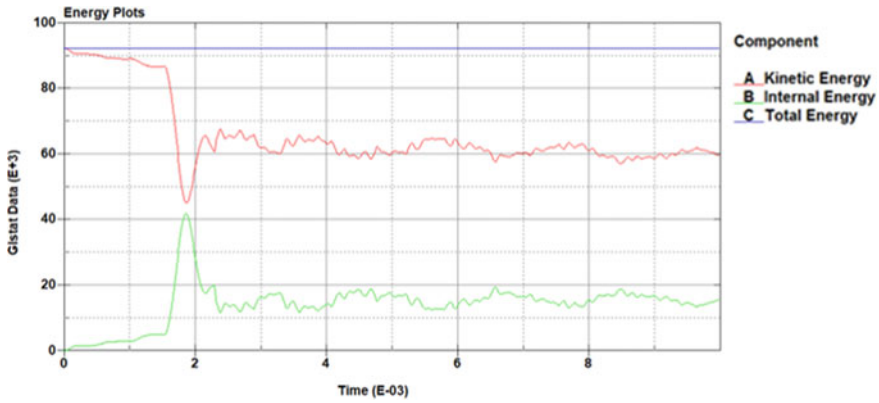


Fig. 12 Energy plots

4.3 Behavior of Skull with and Without Using Chinstrap

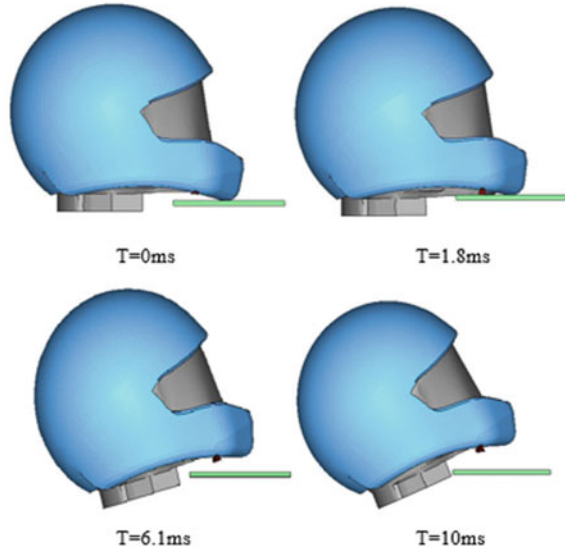
During the simulation, the position of the helmet and the skull keeps varying with time. The time at which the skull hits the ground is the crucial one. Once the skull impacts the ground, high forces are observed. At a certain time, when kinetic energy reduces drastically, the component rebounds. This is called rebound time and at this point stresses are maximum [12]. All the results of the impact are to be noted at this particular time. The behavior of skull at different time intervals is plotted for two cases.

Behavior during impact with chinstrap In this case, the chinstrap holds the chin area tightly and restricts it from bouncing out of helmet during impact. Due to direct impact of helmet with wall, helmet bounces back in reaction. If head is not adequately locked using chinstrap, the chances of head trying to fall out of helmet will be very high and which in turn may lead to direct contact of chin area with external objects. As the bodies are already moving at high velocity due to crash, this will lead to extreme damage of head as it hits the wall. Figure 13 shows the different positions of helmet with chinstrap at different time intervals during impact.

Observations:

- At time $t = 0$ ms, position of helmeted head remains stable.
- At time $t = 1.8$ ms, the skull reached the ground but does not impact with the wall majorly due to the presence of chinstrap.
- At time $t = 6.1$ ms, the helmeted head loses its balance, but the skull does not detach with the helmet as the chinstrap possesses elastic behavior and retains its position pushing the head inward.
- At $t = 10$ ms, the position remains unstable.

Fig. 13 Different positions of helmet with chinstrap at different time intervals during impact



Behavior during impact without chinstrap In this case, due to absence of chinstrap at the chin area, the head easily bounces out of helmet during impact and therefore collides with wall. As the helmet directly hits the wall, it starts bouncing back in reaction. During this motion, the head inside the helmet starts coming out of helmet as there is no restriction available on it other than contact with the helmet's inner surface. Immediately as the head comes out of helmet, it hits the wall and results in high contact forces leading to fracture of the skull. Sometimes not locking the chinstrap may even lead to loss of lives. Figure 14 shows the different positions of helmet without chinstrap at different time intervals during impact.

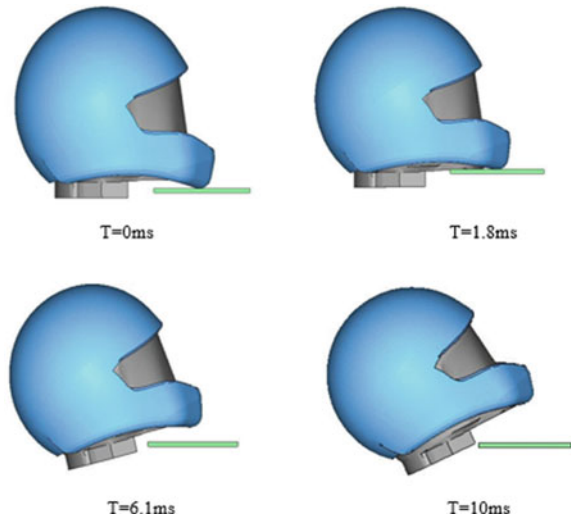
Observations:

- At time $t = 0$ ms, position of helmeted head remains stable.
- At time $t = 1.8$ ms, the skull reaches the ground and hits the wall with high impact. At time $t = 6.1$ ms, the helmeted head loses its balance and the skull starts detaching from the helmet. This may result in multiple blows on the head increasing the severity of the accident.
- At $t = 10$ ms, the helmeted head is in unstable position.

4.4 Stress Distribution on Chin Region

As the skull hits the wall with high velocity, stresses will be developed in the region where impact is major. Von Mises stresses distribution is plotted for both the cases using Hyperview software.

Fig. 14 Different positions of helmet without chinstrap at different time intervals during impact



Stress distribution on chin region without chinstrap Stresses in skull without chinstrap (shown in Fig. 15) are distributed along the width of chin. Von Mises stress of 97.16 MPa is observed on the chin region when the chinstrap is not locked to secure the helmet. During collision of helmet with wall, helmet immediately bounces in upward direction. Due to absence of chinstrap, there is no restriction to the head and hence the head moves outward and hits the wall resulting in damage to the chin region. The same is reflected in the stress pattern due to contact force generated by the collision with wall.

Stress distribution on chin region with chinstrap Stress distribution with chinstrap (shown in Fig. 16) is minimal and can be ignored as it is at localized region due to chinstrap contact with skull. Thus, by wearing chinstrap, damage on skull is minimal and it assures better safety to the rider. Head is protected from the impact to a larger extent as locked chinstrap firmly holds the skull inside the helmet. The chinstrap does not allow the chin region to come directly in contact with wall during

Fig. 15 Von Mises stress plot on skull without chinstrap

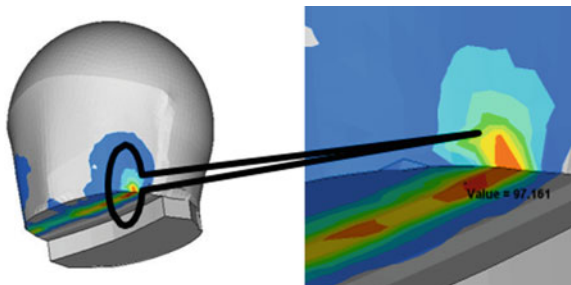


Fig. 16 Von Mises stress plot on skull with chinstrap

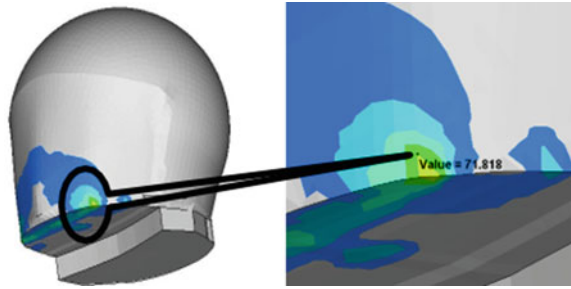


Table 2 Results comparison

S. No.	Case	Von Mises stress (MPa)	Impact force (N)
1	With chinstrap	71.81	–
2	Without chinstrap	97.16	1561

impact and avoids major damage. Thus, in many cases, locked chinstrap can be a life savior.

Table 2 represents the values of von Mises stress and Impact force.

5 Conclusion

In conclusion, this study has depicted the behavior of drop test of helmeted head using LS-DYNA. The aim of the research is achieved by studying the behavior of human helmeted head during the event of impact with and without locking the chinstrap. This paper successfully investigated the significance of locking the chinstrap numerically, and compared the results of impact on head in both the cases. Wearing helmet during driving is of high importance for human safety, but along with helmet, tightening chinstrap is also equally important. In many cases, even after wearing the helmet, due to certain type of accidents, the helmet rolls away from head and results in severe damage to the rider as the impact is unanticipated. To avoid such fortuitous dangerous situation, a chinstrap should be locked to prevent major injuries. Locking chinstrap while using helmet is similar to wearing seat belt in a car which prevents the passenger from falling away from the seat during accidents. It is necessary to extend further studies on helmet and chinstrap with varying material properties to ensure good quality of the helmet.

The following points can be concluded from the research findings:

1. The contact force between skull and rigid wall is plotted, and the force on chin area is major (1500 N approx.) for skull without chinstrap, whereas it is negligible in the other case.
2. Validation of the drop behavior was done using Energy plots.
3. Behavior of helmeted head is studied for both the cases.
4. The maximum stress was found to be 97.161 MPa for the helmeted head without locking chinstrap and the minimum was due to contact stresses and was found to be 71.818 MPa for skull locked with chinstrap.
5. Stress distribution pattern extended from region of impact was found to be reasonable as peak stresses were observed at the area of collision with impact surface.

References

1. S.P. Babu, C. Srinivas, Design and finite element analysis of helmeted head form in impact. *Int. J. Adv. Sci. Technol.* **93**, 15–24 (2016)
2. H.P. Lee, S.W. Gong, Finite element analysis for the evaluation of protective functions of helmets against ballistic impact. *Comput. Methods Biomech. Biomed. Eng.* **13**(5), 537–550 (2010)
3. F.A.O. Fernandes, R.J.A. De Sousa, Motorcycle helmets—a state of the art review. *J. Accid. Anal. Prev.* **56**, 1–21 (2013)
4. P.K. Sisimwo, G.M. Onchiri, Epidemiology of head injuries and helmet use among motorcycle crash injury: a quantitative analysis from a local hospital in Western Kenya. *Pan Afr. Med. J.* **31**, 1–6 (2018)
5. J.G. Crompton, C. Bone, T. Oyetunji, K.M. Pollack, O. Bolorunduro, C. Villegas, K. Stevens, E.E. Cornwell III, D.T. Efron, E.R. Haut, A.H. Haider, Motorcycle helmets associated with lower risk of cervical spine injury: debunking the myth. *J. Am. Coll. Surg.* **212**(3), 295–300 (2011)
6. L.J. Cook, T. Kerns, C. Burch, A. Thomas, E. Bell, *Motorcycle Helmet Use and Head and Facial Injuries: Crash Outcomes in Codes-Linked Data* (National Highway Traffic Safety Administration, US Department of Transportation, Washington, 2009)
7. J.A. Whitlock, B.B. Hamilton, Functional outcome after rehabilitation for severe traumatic brain injury. *Arch. Phys. Med. Rehabil.* **76**, 1103–1112 (1995)
8. J.M.R. Hernández, F.A.C. Tovar, L.K.A. Ruiz, Factors associated with the use of motorcycle helmets in two Colombian cities. *Cienc saude coletiva* **21**(12), 3793–3801 (2016)
9. P.K. Pinnoji, P. Mahajan, Finite element modelling of helmeted head impact under frontal loading. *Sadhana* **32**, 445–458 (2007)
10. M.D. Singleton, Differential protective effects of motorcycle helmets against head injury. *Traffic Inj. Prev.* **19–18**(4), 387–392 (2017)
11. LS-Dyna, Keyword User's Manual, *Livermore Software Technology Corporation*, vol. 1. (California, 2007)
12. P. Jain, R. Oswal, A. Khisty, Study of drop test parameters using design of experiments, in *15th International LS-DYNA User's Conference*
13. D. Mohotti, P.L.N. Fernando, A. Zaghoul, Evaluation of possible head injuries ensuing a cricket ball impact. *Comput. Methods Programs Biomed.* **158**, 193–205 (2018)

Design and Implementation of SEPIC Converter Based Nine-Level MLI Fed IM with PI, FLC, and ANN Controller



S. Karthikeyan, K. Lakshmi, and S. Gobhinath

Abstract In recent year, the field of power converters has experienced a large growth due to confluence of several factors. Moreover, these advances in semiconductor fabrication technology have made it possible to significantly improve the voltage and current handling capabilities and the switching speeds of power semiconductor devices, which make up the converter to design for many applications. Whereas industrial sectors are facing many difficulties to convert the fixed voltage into variable voltage. For that reason, a DC-to-DC conversion process is established from conventional methods like voltage divider, potentiometer to get output voltage less than the input supply; in that case, this will lead to power losses. The DC-to-DC converter topologies can be divided into two major types, depending on whether or not they have galvanic isolation between the input supply and the output circuitry. DC-to-DC converters are used in portable electronic devices such as mobile application and laptop computers, which are supplied with power from batteries primarily. Such electronic devices often contain several sub-circuits, each with its own voltage level requirement different from that supplied by the battery or an external supply. Additionally, the battery voltage declines as its stored energy is drained. Switched DC-to-DC converters offers a method to increase voltage from a partially lowered battery voltage, thereby saving space instead of using multiple batteries to accomplish the same thing. This research work is focused on a performance analysis of SEPIC converter fed nine-level inverter with artificial neural network for induction motor; the performance analysis is carried out for Boost–SEPIC converter fed multi-level inverter IM drive system. Comparison is made with PI, Fuzzy logic, and ANN controllers. The simulation and experimental results validate the various time domain parameters.

S. Karthikeyan (✉) · K. Lakshmi · S. Gobhinath
Department of Electrical and Electronics Engineering, Sri Krishna College of Engineering and Technology, Coimbatore, India
e-mail: karthitamilsona@gmail.com

K. Lakshmi
e-mail: klakshmi01@gmail.com

S. Gobhinath
e-mail: gobhinaths@skcet.ac.in

Keywords DC-to-DC converters · SEPIC converter · Boost–SEPIC converter · PI · Fuzzy logic · ANN controllers

1 Introduction

The nonuniform irradiation of a photovoltaic (PV) source, consisting of series-connected modules with bypass diodes, results in multiple peaks in the power–voltage characteristics. This makes the maximum power point tracking (MPPT) difficult because the conventional MPPT algorithms can only deal with single power peak characteristics. This research proposed a novel distributed MPPT (DMPPT) scheme based on an interleaved single-ended primary-inductor converter (SEPIC) configuration for compensating the mismatch in characteristics of series-connected PV modules [1].

Solar irradiation and load resistance, a fast-converging maximum power point tracking (MPPT) system is required to ensure the photovoltaic (PV) system response rapidly with minimum power losses. Traditionally, maximum power point (MPP) locus was used to provide such a fast response. However, the algorithm requires extra control loop or intermittent disconnection of the PV module. Hence, this system is a simpler fast-converging MPPT technique, which excludes the extra control loop and intermittent disconnection. In the proposed algorithm, the relationship between the load line and the I – V curve is used with trigonometry rule to obtain the fast response [2].

A perturb and observe algorithm based on both the power–current characteristic of a photovoltaic (PV) panel and the sliding-mode control of the input inductor current of an associated converter is investigated in a static application. A single-ended primary-inductor converter (SEPIC) charging a battery from a PV generator illustrates the procedure whose effectiveness is proved with experimental results. The reported technique is appropriate for distributed maximum power point tracking of PV systems with output series connected DC–DC switching converters. In these systems, each converter is supplied by an independent PV panel at the input port, whereas its output port is connected in series with the output ports of the other converters [3]. The investigation of energy transmission process of the SEPIC converter in each of its operating modes are observed and analysed.

In this converter, the continuous conduction mode (CCM) is classified into two: complete inductor supply mode (CISM) and incomplete inductor supply mode (IISM). The discontinuous CM (DCM) of the converter just contains an interval of IISM. The equivalent critical inductances between CISM–IISM and CCM–DCM are calculated in this study. In addition, for a specific range of input voltage and load resistance, the minimum and maximum values of the equivalent critical inductances are obtained [4].

Khateb et al. [5] stated a fuzzy logic controller (FLC) based single-ended primary-inductor converter (SEPIC) for maximum power point tracking (MPPT) operation of

a photovoltaic (PV) system. The FLC proposed presents that the convergent distribution of the membership function offers faster response than the symmetrically distributed membership functions. The fuzzy controller for the SEPIC MPPT scheme shows high precision in current transition and keeps the voltage without any changes, in the variable load case, represented in small steady-state error and small overshoot. The proposed scheme ensures optimal use of PV array and proves its efficacy in variable load conditions, unity, and lagging power factor at the inverter output (load) side. The real-time implementation of the MPPT SEPIC converter is done by a digital signal processor (DSP) [5]. In multilevel inverter fed induction motor drive, the artificial neural network controller (ANN) is employed to improve the overall dynamic time response. The Induction motor is fed from seven-level inverter to reduce total harmonic distortion (THD) and steady-state error. The single-ended primary-inductor converter (SEPIC) is mainly used for better isolation. It is implemented in hardware using PIC16F84, tested, and the consequences are conferred [6]. The proposed topologies present low switch voltage and high efficiency for low input voltage and high output voltage applications. The configurations with magnetic coupling and without magnetic coupling are presented and analyzed. The magnetic coupling allows the increase of the static gain maintaining a reduced switch voltage. The theoretical analysis and experimental results show that both structures are suitable for high static gain applications as a renewable power sources with low DC output voltage [7].

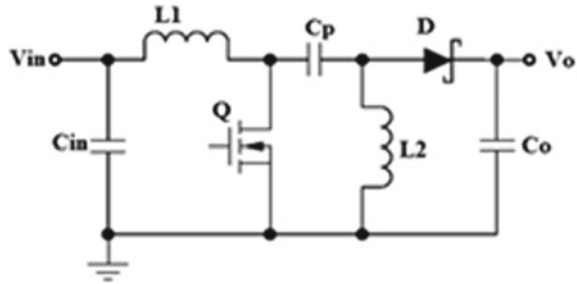
2 Proposed System Details

Based on the literature review, it is tacit that the design of control techniques for the SEPIC converters should have some more improvement in their design and dynamic performance; to overcome this issue, the research work is proposed to design a controller part using PI controller, Fuzzy logic controller, and ANN controller. A nine-level inverter topology, configured by Boost–SEPIC converter with different controllers, is proposed. The nine-level inverter contains only six power electronic switches, which simplifies the circuit configuration.

The important objective of the present research work is that the two-stage voltage step-up using Boost and SEPIC Converters are implemented for the proposed system. The Closed loop performance of Boost to SEPIC based nine level inverter fed IM drive system with different controllers were analyzed in terms of Rise time, Peak time, settling time, and Harmonic Performance is presented.

The proposed work is to extend and prove the contemporary DC-to-DC converter with nonlinear controllers that have the better steady-state performance under different test conditions; parameter such as input voltage, output power, and the load disturbances can be reduced. Better power transfer gain, current regulations can be achieved with this converter. The motivation of the work is planned due to the aspiration of achieving recital investigation using different DC to DC converters thus Buck converter, Boost converter, Buck-Boost converter, CUK converter and to

Fig. 1 Basic circuit diagram for SEPIC converter



verify with the proposed SEPIC converter fed Multilevel inverter fed induction motor drives.

The single-ended primary-inductor converter (SEPIC) is a DC/DC converter topology that provides a positive regulated output voltage from an input voltage that varies from above to below the output voltage. The coupled inductor not only provides a smaller footprint but also, to get the same inductor ripple current, requires only half the inductance required for a SEPIC with two separate inductors.

Figure 1 shows a simple circuit diagram of a SEPIC converter, consisting of an input capacitor C_{in} , an output capacitor C_o , coupled inductors L_1 and L_2 , an AC coupling capacitor C_p , a power FET Q , and a diode D . It is important to analyze the circuit at DC when Q is off and not switching. During steady-state CCM, pulse-width modulation (PWM) operation, and neglecting ripple voltage, capacitor C_p is charged to the input voltage, V_{in} . When Q is off, the voltage across L_2 must be V_o . Since C_{in} is charged to V_{in} , when Q is off the voltage across Q is $V_{in} + V_o$, so the voltage across L_1 is V_o . When Q is on, capacitor C_p , charged to V_{in} , is connected in parallel with L_2 , so the voltage across L_2 is $-V_{in}$.

The currents flowing through various circuit components are shown in Figure. When Q is on, energy is being stored in L_1 from the input and in L_2 from C_p . When Q turns off, the current through L_1 flows through C_p and D , and into C_o and the load. Both C_o and C_p get recharged so that they can provide the load current and charge L_2 , respectively, when Q turns back on.

Duty cycle of Boost-SEPIC converter can be determined by

$$D = \frac{V_o + V_{FWD}}{V_{in} + V_o + V_{FWD}} \quad (1)$$

where V_{FWD} is the forward voltage drop.

Figure 2 shows the block diagram of Boost to SEPIC Converter fed nine-level inverter with PI, FLC, and ANN Controller. PV array converts solar energy into electrical energy and has output of 54 V. The Boost converter boosts up to 70 V. SEPIC converter boosts up to 98 V DC. PWM Gate pulses trigger nine-level Inverter MOSFET switches at a frequency of 50 Hz. Nine-level Inverter converts boosted 98 V DC voltage into 200 V 1 \emptyset AC. The Inverter output voltage is applied to run the Induction Motor. The Motor Speed and Torque are measured.

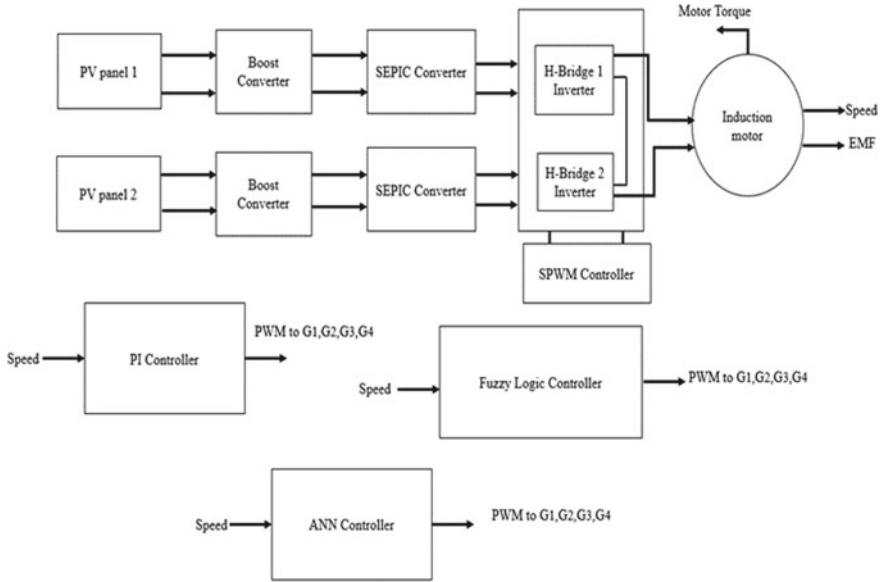


Fig. 2 Block diagram of boost to SEPIC converter FED nine-level MLI with PI, FLC, and ANN controller for IM

3 Results and Discussion

3.1 Analysis of Input Parameters

The photovoltaic system is modeled and integrated in MATLAB/SIMULINK. The harvested PV voltage is shown in Fig. 3, and its harvested voltage is 58 V. The output voltage from the Boost converter is shown in Fig. 4.

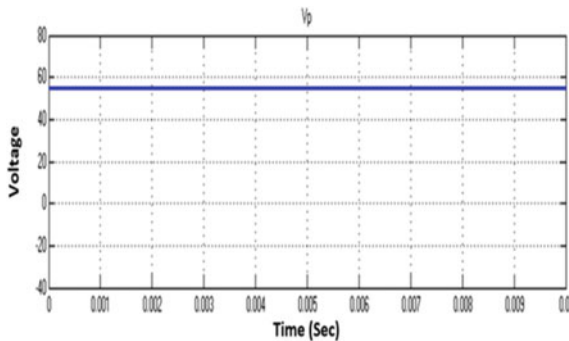


Fig. 3 Harvested PV voltage

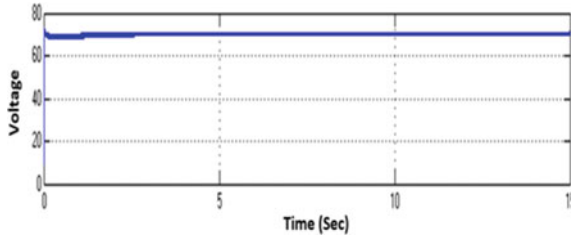


Fig. 4 Output voltage of the boost converter

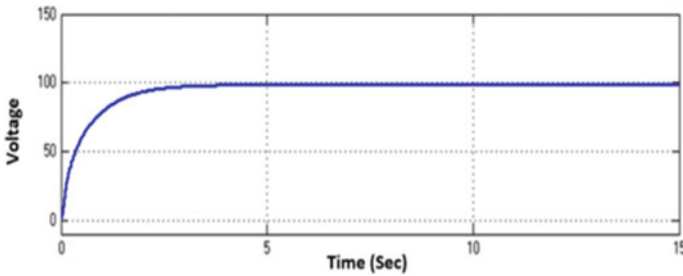


Fig. 5 Output voltage of the SEPIC converter

The output voltage from the SEPIC converter is shown in Fig. 5, and it is nearly double the voltage harvested from the PV system (Fig. 6 and Table 1).

The analysis of Boost–SEPIC converter fed nine-level MLI fed induction motor is carried out with FLC controller. The yielded results are tabulated in Table 2. From the obtained result for boost to SEPIC converter fed nine-level MLI with FLC controller yield, results for various time domain parameters are listed below, and the boost to SEPIC converter with FLC controller yields 18.00% of THD; this shows that the

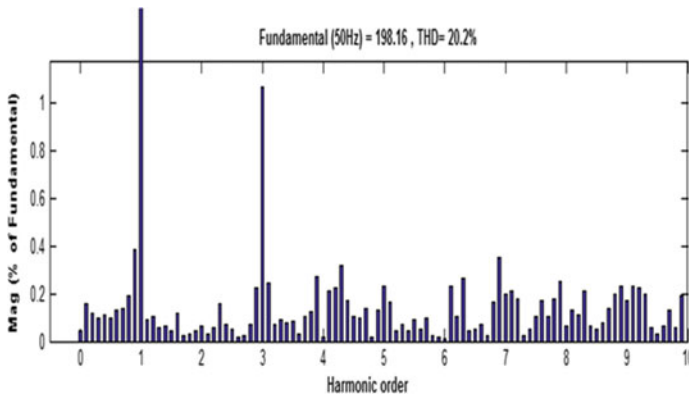


Fig. 6 Total harmonic distortion for boost–SEPIC fed nine-level MLI with PI controller

Table 1 Comparison of time domain parameters for closed loop boost–SEPIC based MLI for induction motor drive

Controller	Rise time T_r (s)	Peak time T_p (s)	Settling time T_s (s)
PI	0.8	1.4	3.9

Table 2 Simulation results of various time domain parameters for boost–SEPIC converter based nine-level MLI with FLC controller

Controller	Rise time T_r (s)	Peak time T_p (s)	Settling time T_s (s)
FLC	0.5	1.2	3.5

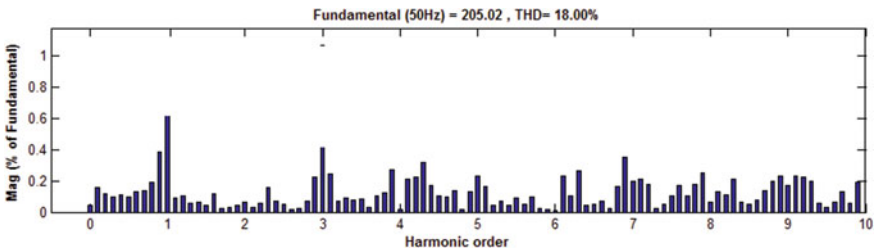


Fig. 7 Total harmonic distortion for boost–SEPIC fed nine-level MLI with FLC controller

there is an improvement over the boost to SEPIC with PI controller as shown in Fig. 7.

The analysis of Boost–SEPIC converter fed nine-level MLI fed induction motor is carried out with ANN controller. The yielded results are tabulated in Table 3. From the obtained result for Boost–SEPIC converter fed nine-level MLI with ANN controller yield, results for various time domain parameters are listed below, and ANN controller with boost to SEPIC converter fed nine-level MLI yields 7.94% of THD as shown in Fig. 8 and Table 4.

From the comparison, it is clear that boost to SEPIC with ANN is suitable choice based on parameters obtained. The boost to SEPIC converter with ANN controller has yielded a 7.94% of THD.

Table 3 Simulation results of various time domain parameters for boost–SEPIC converter fed nine-level MLI with ANN controller

Controller	Rise time T_r (s)	Peak time T_p (s)	Settling time T_s (s)
ANN	0.4	0.51	1

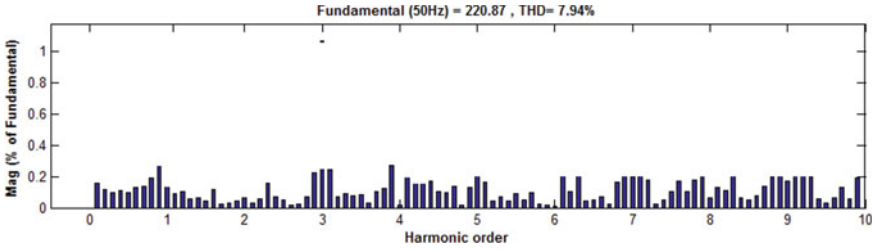


Fig. 8 Total harmonic distortion for boost-SEPIC fed nine-level MLI with ANN controller

Table 4 Comparison of time domain parameters for closed loop boost-SEPIC fed nine-level MLI for induction motor drive

Controller	Rise time T_r (s)	Peak time T_p (s)	Settling time T_s (s)	THD (%)
PI	0.8	1.4	3.9	20.20
FLC	0.5	1.2	3.5	18.00
ANN	0.4	0.51	1	7.94

3.2 Experimental Result of Boost to SEPIC Fed Nine-Level MLI with ANN Controller

The hardware of boost to SEPIC fed nine-level MLI with ANN controller for IM drives is fabricated and tested in laboratory using the following components which are listed in Table 5.

The hardware block diagram consists of Transformer, a Rectifier, inductors, capacitors, boost converter and SEPIC converter IM motor, driving, pulse generating & controlling circuits as shown in Figs. 9 and 10.

Figure 11 shows the output voltage of SEPIC converter where this is the second stage of conversion in which the input voltage is once again boost, and obtained output voltage of 98 V is fed to the multilevel inverter; the x -axis represents the time in seconds, and the y -axis represents the voltage measured through CRO which is 98 V.

Table 5 Components and model and their count

S. No.	Component	Model	Count
1.	MOSFET	IRF840	10
2.	Diode	1N4007	4
3.	MOSFET driver	IR2110	4
4.	Transformer	MINI/12 V	3
5.	Single phase induction motor	0.5 HP	1
6.	Inductor	2.5 μ H	1
7.	Capacitors	1600 μ F	2
8.	Processor controller	PIC16F84A	1

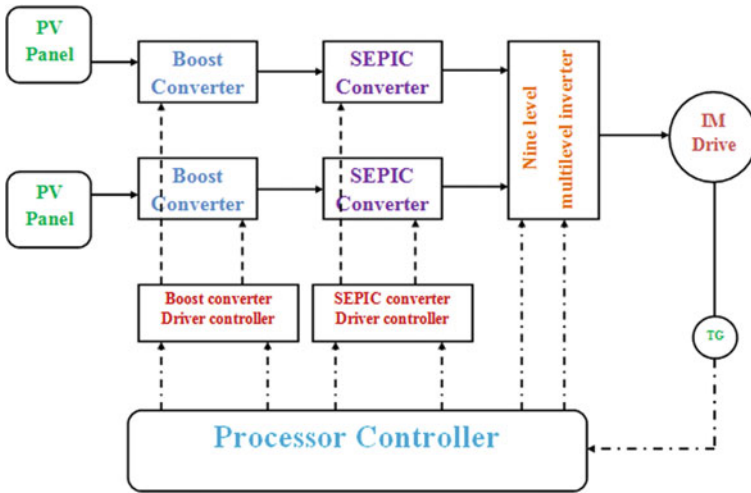


Fig. 9 Block diagram of hardware setup

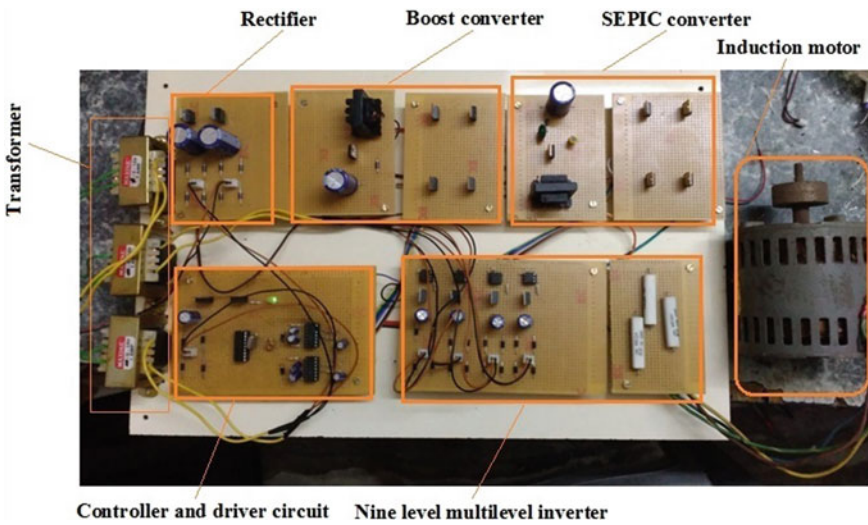


Fig. 10 Top view of hardware setup

In Fig. 12 shows the output voltage of MLI where this is the voltage is fed from SEPIC converter and conversion from DC to AC with nine level output wave form obtained an output voltage of 220 V which is suitable for lighting load and the disadvantage of the output voltage is not pure sinusoidal. The x -axis represents the time in seconds, and the y -axis represents the voltage measured through CRO which is 220 V.



Fig. 11 Output voltage of SEPIC converter

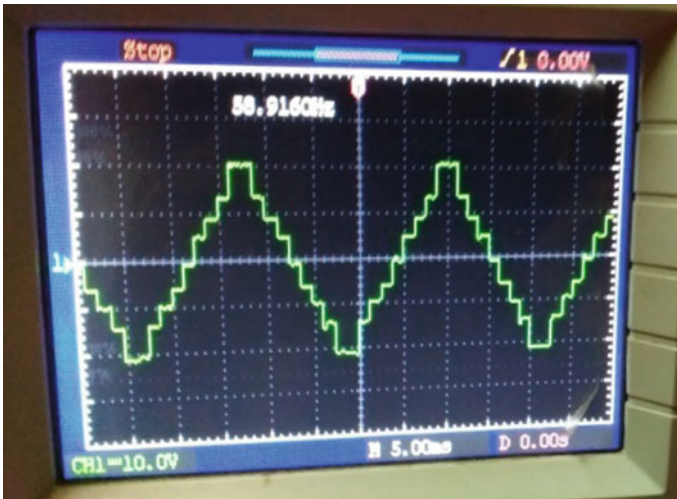


Fig. 12 Nine-level output voltage waveform of MLI

4 Conclusion

The comparison is made with Boost-SEPIC converter fed nine-level MLI with various controllers like PI, FLC, and ANN controller. Boost-SEPIC converter fed nine-level MLI with PI controller and FLC controller yields 20.20% and 18.00% of THD, respectively. This shows that there is an improvement over the Boost-SEPIC converter with FLC controller. Further, the research extended with ANN controller boost to SEPIC converter fed nine-level MLI with ANN controller yields 7.94% of


THD. The result shows that boost–SEPIC converter fed nine-level MLI for IM drive with ANN controller is the best choice.

References

1. N. Pragallapati, V. Agarwal, Distributed PV power extraction based on a modified interleaved SEPIC for non uniform irradiation conditions. *IEEE J. photovol.* **5**(5) (September, 2015)
2. T.K. Soon, S. Mekhilef, A fast-converging MPPT technique for photovoltaic system under fast-varying solar irradiation and load resistance. *IEEE Trans. Ind. Inf.* **11**(1) (2014)
3. C. Cabal, L. Martínez-Salamero, L. Séguier, C. Alonso, F. Guinjoan, Maximum power point tracking based on sliding mode control for output-series connected converters in photovoltaic systems. *IET Power Electron.* **7**(4) (April, 2014)
4. E. Babaei, M.E.S. Mahmoodieh, Analysis and investigation of energy transmission process in different operating modes of SEPIC converter. *IET Power Electron.* **7**(4) (April, 2014)
5. A. El Khateb, N. Abd Rahim, J. Selvaraj, M.N. Uddin, Fuzzy-logic-controller-based SEPIC converter for maximum power point tracking. *IEEE Trans. Ind. Appl.* **50**(4) (July–August, 2014)
6. P. Ramesh, C. Sharmeela, B. Prabakaran, S. Rajkumar, ANN controlled SEPIC cascaded with multi level inverter fed induction motor drive. *IEEE Comp. Power, Energy Inf. Commun. (ICCPEIC)* (20–21 April, 2016)
7. R. Gules, W.M. Dos Santos, F.A. Dos Reis, E.F.R. Romanelli, A.A. Badin, A modified SEPIC converter with high static gain for renewable applications. *IEEE Trans. Power Electron.* **29**(11) (November, 2014)

Preparation and Experimental Evaluation of Membrane Electrode Assembly of Proton Exchange Membrane Fuel Cell



Syed Aslam , Md. Masood, and Sudheer Prem Kumar

Abstract The present paper deals with the preparation and experimental evaluation of membrane electrode assemblies (MEAs) of proton exchange membrane fuel cells (PEMFCs). For MEAs fabrication, the electrodes (anodes and cathodes) were prepared using 10% by wt. Platinized carbon on backing paper and Nafion 112 membranes. The prepared MEAs were assembled in single cells and tested on the fuel cell test bench. The MEAs were tested at 70 °C, with the hydrogen gas humidified and air/oxygen unhumidified at 1 barg operation. The results were evaluated for its V-I characteristic under the above-mentioned conditions. The maximum current density for cell-1 of 200 mA/cm² is achieved for H₂/Air operation. The maximum current density for same cell-1 of 450 mA/cm² is achieved for H₂/O₂ operation. Future work will be focused on the modeling and simulation of PEMFCs with various gas flow field designs and their experimental validation to optimize the performance of the cells and stacks.

Keywords PEMFC · Hydrogen fuel · Zero-emission vehicle · Automotive application

S. Aslam (✉)

Department of Mechanical Engineering, Jawaharlal Nehru Technological University, Hyderabad, Telangana, India

e-mail: saslammehdi@gmail.com

Md. Masood

Islamia Engineering College, Hyderabad, Telangana, India

e-mail: drmasoodliet@gmail.com

S. P. Kumar

Department of Mechanical Engineering, Jawaharlal Nehru Technological University, Hyderabad, Telangana, India

e-mail: bsudheerpk@jntuh.ac.in

© Springer Nature Singapore Pte Ltd. 2021

G. S. V. L. Narasimham et al. (eds.), *Recent Trends in Mechanical Engineering*,

Lecture Notes in Mechanical Engineering,

https://doi.org/10.1007/978-981-15-7557-0_52

1 Introduction

A fuel cell uses the chemical energy of hydrogen or another fuel to cleanly and efficiently produce electricity. If hydrogen is the fuel, electricity, water, and heat are the only products. They can be used in a wide range of applications, including transportation, material handling, stationary, portable, and emergency backup power applications.

Fuel cells have several benefits over conventional combustion-based technologies currently used in many power plants and passenger vehicles. They can operate at higher efficiencies than combustion engines and can convert the chemical energy in the fuel to electrical energy with efficiencies of up to 60%. Fuel cells have lower emissions than combustion engines [1].

Proton Exchange Membrane Fuel Cell (PEMFC) also known as hydrogen fuel cell is one of the most popular fuel cell types being developed for the above-mentioned applications, which uses hydrogen as fuel and emit only water. There are no carbon dioxide emissions and no air pollutants that create smog and cause health problems at the point of operation.

Also, they are quiet during operation as they have fewer moving parts. Advancements in zero-emission fuel cells could make the technology cheap enough to replace traditional gasoline engines in vehicles, according to a study. Researchers from the University of Waterloo in Canada developed a new fuel cell that lasts at least 10 times longer than current technology [2].

Hydrogen fuel cell vehicles are the future said Wan Gang, a Vice Chairman of China's national advisory body for policy making [3]. Storing energy in hydrogen is 20 times more effective using platinum-nickel alloy catalyst. The researchers therefore tested the same catalyst with hollow nanocages for 50,000 'laps' in the fuel cell and saw a negligible decrease in activity [4].

The global fuel cells market size are projected to reach USD 1059 million by 2024 from an estimated value of USD 342 million in 2019, growing at a CAGR of 25.4% during the forecast period. The growth is attributed to the rising demand for clean energy generation in developed regions, increased use of fuel cell-based vehicles, booming power sector, and augmented power generation capacities globally [5].

1.1 How Fuel Cells Work

Fuel cells work similar to batteries, but they do not run down or need recharging. They produce electricity, heat, and water as long as fuel is supplied. A fuel cell consists of two electrodes—a negative electrode (or anode) and a positive electrode (or cathode)—sandwiched around an electrolyte. A fuel, such as hydrogen, is fed to the anode, and oxygen/air is fed to the cathode.

In a PEMFC as shown in Fig. 1, a catalyst at the anode separates hydrogen molecules into protons and electrons, which take different paths to the cathode. The

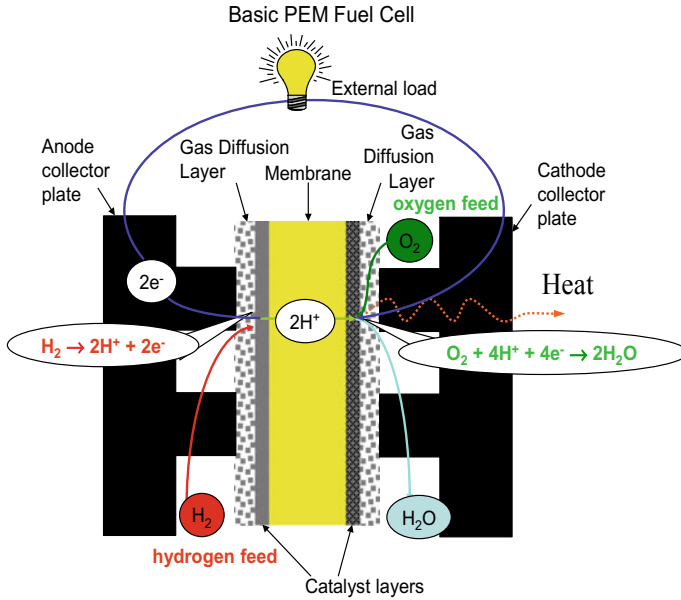


Fig. 1 Shows schematic of polymer electrolyte membrane fuel cell

electrons go through an external circuit, creating a flow of electricity. The protons migrate through the electrolyte to the cathode, where they unite with oxygen and the electrons to produce water and heat.

2 Materials

2.1 Catalyst

Platinum and Platinum Ruthenium Alloy are the most effective catalysts for oxidation and reduction reactions in a Proton Exchange Membrane Fuel Cell (PEMFC).

2.2 Electrodes

Anode and Cathode Gas Diffusion Electrodes (GDE) for an electrochemical device consist of catalyst loaded onto a GDL. The most commonly used catalysts include carbon-supported Platinum and Platinum/Ruthenium for the utilization of PEMFC. Electrodes for a fuel cell applications are generally hydrophobic to reduce flooding issue during fuel cell operation.

2.3 Gas Diffusion Layers

Gas diffusion layers are key components in various types of fuel cells. In fuel cells, this thin, porous sheet must provide high electrical and thermal conductivity in addition to controlling the proper flow of reactant gases (hydrogen and air) and managing the water transport out of the Membrane Electrode Assembly (MEA). They provide enough mechanical strength to hold the MEA. They are made of carbon fiber and made as carbon cloth or toray paper.

2.4 Membrane Electrode Assemblies (MEAs)

Catalysts on each side of electrodes enable reactions and the membrane allows protons to pass through while keeping the gases separate. In this way, cell potential is maintained and current is drawn from the cell producing electricity. A typical MEA is composed of a proton exchange membrane, two catalyst layers, and two Gas Diffusion Layers (GDL).

An alternative version of a membrane electrode assembly is the three-layer MEA which is composed of a proton exchange membrane with catalyst layers applied to both sides, anode and cathode. An alternative name for this type of MEA is a Catalyst Coated Membrane (CCM).

2.5 Bipolar Plates

Each individual MEA produces less than 1 V under typical operating conditions, but most applications require higher voltages. Therefore, multiple MEAs are usually connected in series by stacking them on top of each other.

These plates, which may be made of metal, carbon, or composites, provide electrical conduction between cells, as well as providing physical strength to the stack. The surfaces of the plates typically contain a “flow field,” which is a set of channels machined or stamped into the plate to allow gases to flow over the MEA. Figure 2 shows four different types of flow channels in graphite plates.

3 Method of Fabrication of Electrode and MEA

The toray carbon paper is hydrophobed with PTFE emulsion and sintered in an oven at a temperature of 340 °C. A Micro Porous Layer (MPL) is formed on to toray carbon paper containing PTFE and carbon (Vulcan XC-72R) using spraying technique and

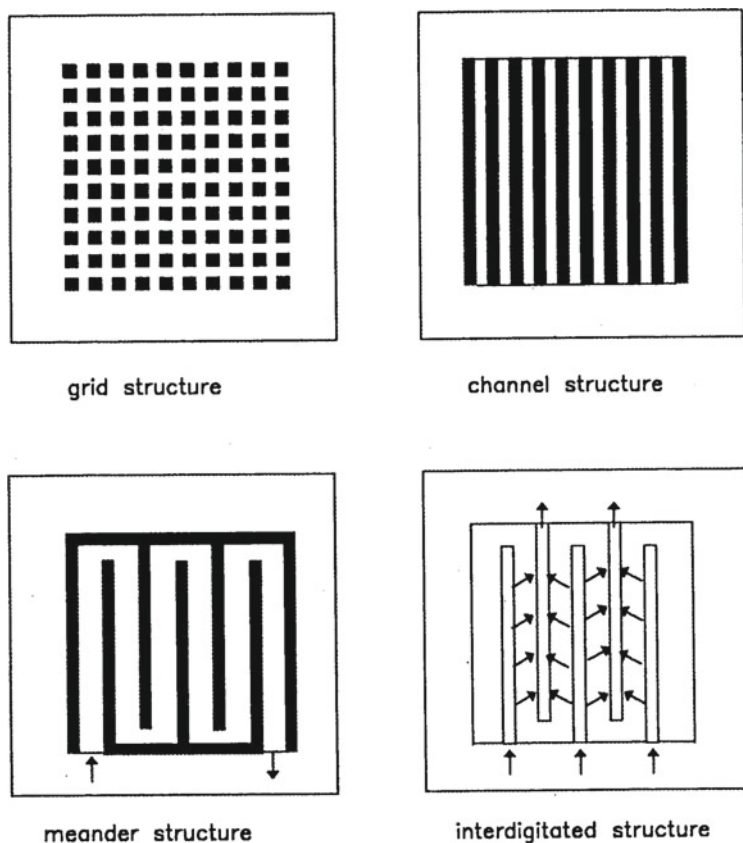


Fig. 2 Principles of the different flow field structures

sintered in an oven at 335 °C which is known as GDL. Thickness of this MPL is 30–40 μm .

The catalyst layer is screen printed on the GDL forming electrodes (Anodes and Cathodes) and sinter at 135 °C in an oven under the inert gas atmosphere. The thickness of catalyst layer is 10–15 μm .

After the electrodes (Anode/Cathode) are sintered, membrane electrode assembly was fabricated. The procedure for making MEA as follows.

Nafion[®] 112 (50 μm) thick membrane as an electrolyte was sandwiched between anode and cathode and assembled in avsteel plates and mounted in a hydraulic press and hot pressed at 135–140 °C at 200 kg/cm^2 pressure holding for 2 min. Figure 3 shows fabrication procedure for membrane electrode assemblies.



Fig. 3 Shows fabrication procedure for membrane electrode assemblies

4 Result and Discussion

The fabricated membrane electrode assemblies were tested as single cells by assembling them in respective hardware and measurements were carried out using fuel cell test bench and dc electric bulbs/multimeter as load.

Fuel cell test station consists of a gas handling sub-unit (Hydrogen, Oxygen and Air Cylinders with two-stage regulators), shut-off valves, pressure gauges, Check valves, pressure release valves, needle valves, rotameters (mass flow controllers), and humidifiers for the reactant gases. All the tube fittings and piping required for the fabrication of test station is of 1/4" size.

Three gas lines each one for hydrogen, oxygen, and air constitute the test station. Check valves and pressure release valves mounted on the test station are incorporated for safety purpose. At a time three single cells can be tested on the fuel cell test station.

Totally 4 MEAs were prepared in the batch under identical conditions out of which two single cells (Cell-1 and Cell-2) were assembled in individual single cell hardware and tested for 15 days on daily start and stop basis (10 AM to 4.30 PM) on the test bench. The performance of the cells improved on the second day. The data was collected and the polarization curves were drawn for the cells.

Figure 4 shows polarization characteristic curves V-I of single cells (Cell-1 and Cell-2) operated on H₂/air and Fig. 5 shows polarization characteristic curves V-I of same single cells (Cell-1 and Cell-2) operated on H₂/O₂ on the fuel cell test station.

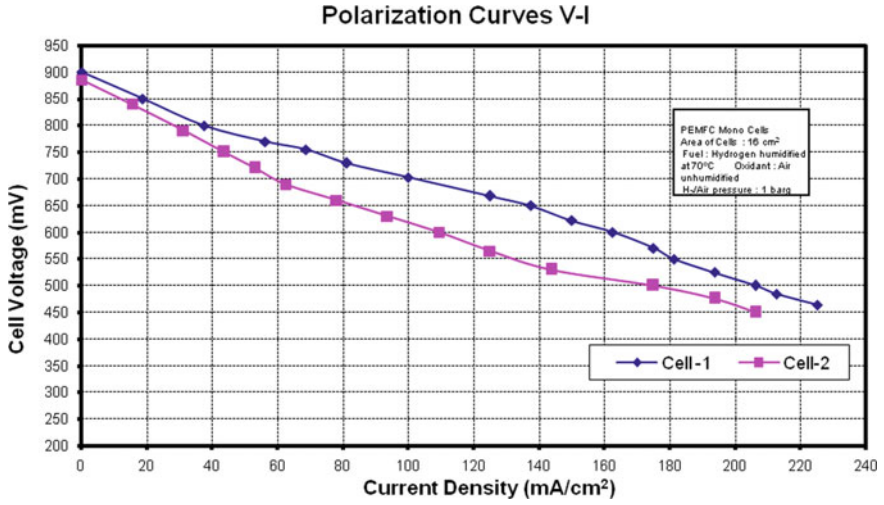


Fig. 4 Shows single cells polarization curves H₂/air operation

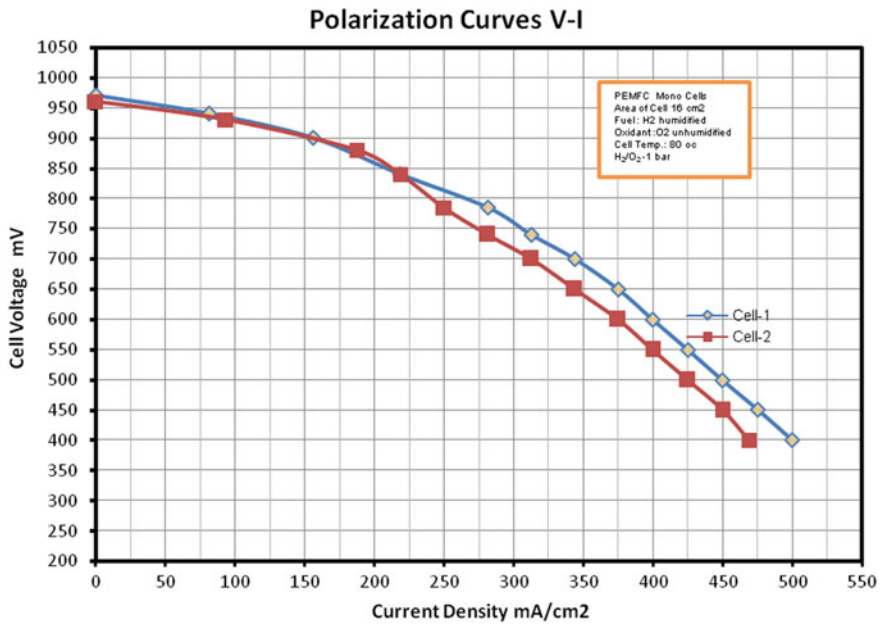


Fig. 5 Shows single cells polarization curves for H₂/O₂ operation

The maximum current density for cell-1 of 200 mA/cm² was achieved for H₂/Air operation. The maximum current density for same cell-1 of 450 mA/cm² was achieved for H₂/O₂ operation. The cells were operated for more than 2 weeks and remained stable with very little fall in the performance.

5 Conclusion

The present paper dealt with the preparation and experimental evaluation of Membrane Electrode Assemblies (MEAs) of Proton Exchange Membrane Fuel Cells (PEMFCs).

For MEAs fabrication the electrodes (anodes and cathodes) were prepared using 10% by wt. Platinized carbon on backing paper and Nafion 112 membranes. The prepared MEAs were assembled in single cells and tested on the fuel cell test bench. The MEAs were tested at 70 °C, with the hydrogen gas humidified and air/oxygen unhumidified at 1 barg operation.

The results were evaluated for its V-I characteristic under the above-mentioned conditions. The maximum current density for cell-1 of 200 mA/cm² is achieved for H₂/Air operation. The maximum current density for same cell-1 of 450 mA/cm² is achieved for H₂/O₂ operation.

Future work will be focused on the modeling and simulation of PEMFCs with various gas flow field designs and their experimental validation to optimize the performance of the cells and stacks.

Acknowledgments The author wishes to express sincere thanks to Mr. K. T. Mahi Secretary, SNIST and Dr. P. Narasimha Reddy Director, SNIST for their support and encouragement during AICTE project work.

References

1. <http://www.energy.gov/eere/fuelcells/fuel-cells>
2. PTI, May 08, 2019, Newsletter
3. Bloomberg Television interview in Beijing, China
4. Science Daily 11-23-19
5. Fuel Cells Market Size, Share, Industry Analysis to 2024| Markets and Markets

Relative Importance Analysis of Factors Influencing Sea Port Service Quality



S. Hemalatha , Lingaraju Dumpala, and B. Balakrishna

Abstract In any competitive business environment customer satisfaction is more important to manage and improve their business. Nowadays sea ports are playing key role in any country economy and development. The main view of this work is to examine the impact of service quality of sea port on customer satisfaction of sea port. The literature review deals with the attributes that affect the service quality of sea ports. To check the relationship among sea port service quality and its customer satisfaction a confirmatory factor analysis, along with multiple regression is conducted. It is also concluded that PSQ is a seven-dimensional construct and identified that PSQ and customer satisfaction are related positively. Finally Relative Importance Analysis (RIA) is applied to obtain the weights and ranks of each criterion. The proposed model was tested with a survey of 180 members of the Indian Ports Association (IPA).

Keywords Relative importance analysis · Sea ports · Service quality · Attributes

1 Introduction

Ports play the role of nodes for both inbound and outbound logistics processes, i.e. platforms where logistics-related activities occur, and are also important national economic contributors. In this context, sea ports are not only where cargoes are loaded/discharged onto/from vessels but also distribution centres where value-added services such as labelling, packaging and cross-docking are provided.

S. Hemalatha (✉) · L. Dumpala

Department of Mechanical Engineering, Raghu Institute of Technology, Modavalasa, Andhra Pradesh, India

e-mail: somu_hemalatha@yahoo.co.in

L. Dumpala

e-mail: dlraju@gmail.com

L. Dumpala · B. Balakrishna

Department of Mechanical Engineering, JNTUCEK, JNTUK, Kakinada, Andhra Pradesh, India

e-mail: balakrishnajntu06@gmail.com

© Springer Nature Singapore Pte Ltd. 2021

G. S. V. L. Narasimham et al. (eds.), *Recent Trends in Mechanical Engineering*,

Lecture Notes in Mechanical Engineering,

https://doi.org/10.1007/978-981-15-7557-0_53

Other well-developed researches about ports in the existing literature include the measurement of port efficiency and port choice in a logistics and supply chain context. However, research on what constitutes Port Service Quality (PSQ) and its impacts on the satisfaction of port customers, such as shipping lines and cargo owners, is not well investigated in the contemporary literature. In this paper, we propose and validate a conceptual model of PSQ and examine the causal relationship between PSQ and customer satisfaction. The paper is organized as follows. First, a literature review is provided followed by the proposed conceptual model of PSQ with factors and explaining variables. Methodologies are described next, followed by analyses and discussions on study findings. Finally, concluding comments, including academic and management implications and future research directions are outlined.

2 Literature Review

Ugboma et al. [1] identified the key determinants of service quality and determined the quality of service offered by two ports in Nigeria using the SERVQUAL model. Miremadi et al. [2] identified and assessed the key determinants of service quality and determined the quality of service offered. Lu et al. [3] evaluated container service equality attributes by internal-consistency reliability, factor analysis, cluster analysis, importance-satisfaction analysis, and analysis of variance methods. Also suggested that reliability attribute plays an important role in PSQ. Kolanović et al. [4] presented a customer-based port service quality model based on empirical study and tested its reliability on a selected sample. The proposed model is defined by five factors and fits satisfactorily into the obtained poll questionnaire results. Yeo et al. [5] considered five factors, namely, process, outcomes, process, management and social responsibility to measure service quality of Korean container ports. Partial least squares structural equation modelling (PLS-SEM) was conducted to confirm the PSQ dimensions and to examine their relationship with customer satisfaction. Thai [6] found that PSQ is a four-dimensional construct, namely, outcomes, management, process and image and social responsibility all have significant positive impact on customer satisfaction. Viet [7] recognized five variables resources, capacities, process of services, management capacities, image and reputation on the port service quality. Sayareh et al. [8] evaluated the service quality of container terminal in Bandar Abbas Port by using SERVQUAL model.

3 Methodology

Confirmatory Factor Analysis (CFA) is a powerful statistical technique to verify the factor structure of a set of observed variables. CFA allows testing the hypothesis that a relationship between observed variables and their underlying latent constructs exists.

The data were collected by delivering the questionnaire to 180 respondents of various working positions (Managers, Sr. Managers, Chief Managers, Asst general managers, Deputy General Managers) of twelve 12 major Indian container terminals. They were requested to fill a questionnaire that contained measures of the concerned performance dimension.

3.1 Conceptual Framework and Measures

The conceptual framework for this research and summary of measures are presented in Table 1.

3.2 Hypotheses

The hypotheses regarding sea port service quality are presented in the study's research questions and are given below.

Research Question: What are the customer requirements of sea port service quality?

From review of the literature, the following hypotheses are introduced:

- Ha Items relating to PAF constitute customer requirements of PSQ.
- Hb Items relating to PRF constitute customer requirements of PSQ.
- Hc Items relating to PFF constitute customer requirements of PSQ.
- Hd Items relating to PIF constitute customer requirements of PSQ.
- He Items relating to PLF constitute customer requirements of PSQ.
- Hf Items relating to PEF constitute customer requirements of PSQ.
- Hg Items relating to PSF constitute customer requirements of PSQ (Fig. 1).

3.3 Reliability Analysis

The study tested the measurement properties of the constructs (latent variables) through confirmatory factor analysis using the data collected from the survey questionnaire shown in Appendix-A. CFA was used to evaluate how well the measurement items reflect latent variables in the hypothesized structure. Average Variance Extracted (AVE) of Squared Multiple Correlation (SMC), Composite Reliability (CR) of latent variables is presented in Table 2.

Average variance extracted of each latent variable was more than 0.7 which showed that latent variables had reliability and convergence validity.

Table 1 Constructs and measurement items

Sea port service quality factors	Measures	Code
Port accessibility factors (PAF)	Container damage low-frequency rate	PAF 1
	Ports good connections to the main road	PAF 2
	Ports good railway connections to the main line	PAF 3
	Ports good connections with hinter land	PAF 4
Port reliability factors (PRF)	Berth availability immediately upon vessel's arrival at port	PRF 1
	Vessels loading/discharging operations in compliance with contracts	PRF 2
Port functionality factors (PFF)	Port service availability 24/365	PFF 1
	Container railway delivery with no delays attributable to unforeseen queuing at terminal	PFF 2
	Complete and correct container information availability at port at any time	PFF 3
	Intermodal transport system in operation at port	PFF 4
Port information availability factors (PIF)	High level of information integration between stakeholders	PIF 1
	Port information availability on the intimae	PIF 2
Port flexibility factors (PLF)	Online port service availability for customers on website	PLF 1
	Accurate/complete container/vessel documents	PLF 2
	Adequate number of berths at port	PLF 3
Port environmental management factors (PEF)	Environmental quality	PEF 1
	Use of energy and resources	PEF 2
	Waste handling	PEF 3
Port overall satisfaction factors (PSF)	Satisfaction with the facilities, equipment and infrastructure	PSF 1
	Satisfaction with the management and employees	PSF 2

3.4 Goodness of Fit Indices

Fit indices of the conceptual model obtained through CFA are shown in Table 3.

The chi-square tests the hypothesis that the model is consistent with the pattern of co-variation among the observed variables. In the case of the chi-square statistic, smaller rather than larger values indicate a good fit.

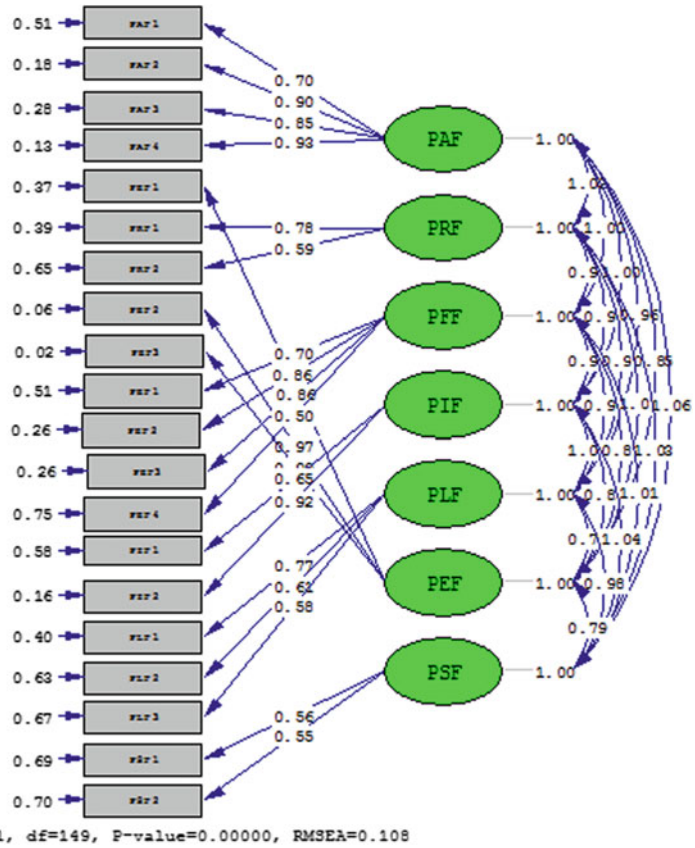


Fig. 1 PSQ and customer satisfaction measurement using CFA

3.5 Relative Weights of Service Quality Factors

Twenty (20) key variables were identified in the literature review which mostly affect the port service quality were presented. On each of the 20 variables, respondents were asked to indicate the extent to which that variable influences port service quality, based on a five-point scale were: 1-highly insignificant, 2-Insignificant, 3-Neither, 4-Significant, and 5-highly significant. In order to empirically establish the factors accounting for port service quality to give an understanding as to the extent to which each factor contributes to port service quality, both by itself and in combination of the other factors, the Relative Importance Index (RII) was employed:

$$RII = \sum W / (A * N),$$

Table 2 Reliability and validity analytical results of measurement model

Latent variable	Item	Standardized factor loadings	SMC	AVE	Composite reliability (CR)
PAF	PAF1	0.75	0.56	0.754	0.924
	PAF2	0.92	0.85		
	PAF3	0.85	0.72		
	PAF4	0.94	0.89		
PRF	PRF1	0.80	0.64	0.525	0.740
	PRF2	0.64	0.41		
PFF	PFF1	0.78	0.60	0.625	0.902
	PFF2	0.88	0.78		
	PFF3	0.87	0.77		
	PFF4	0.60	0.35		
PIF	PIF1	0.61	0.38	0.619	0.841
	PIF2	0.93	0.87		
PLF	PLF1	0.66	0.44	0.445	0.741
	PLF2	0.66	0.43		
	PLF3	0.68	0.46		
PEF	PEF1	0.79	0.63	0.848	0.819
	PEF2	0.97	0.95		
	PEF3	0.99	0.98		
PSF	PSF1	0.70	0.49	0.450	0.620
	PSF2	0.64	0.41		

Table 3 Fit indices of structure model

Indicators	Propriety indicators	Ideal figures	Research findings
Absolute propriety indicators	$\chi^2/d \cdot f$	1.0–3.0	2.988
	GFI	>0.90	0.80
	AGFI	>0.90	0.72
	SRMR	≤0.05	0.073
	RMSEA	≤0.08	0.11
Relative propriety indicators	NNFI	≥0.90	0.96
	NFI	≥0.90	0.96
	CFI	≥0.90	0.97

where *W*—weighting given to each statement by the respondents and ranges from 1 to 5; *A*—Higher response integer (5); and *N*—total number of respondents (Table 4).

From the above table, it is observed that reliability factor ranked as one (0.6872), functionality as two (0.6619), overall satisfaction as three (0.6577), environmental

Table 4 Relative importance indices

Factors	1	2	3	4	5	W	RII	AVG	Rank
PAF1	16	34	40	41	49	613	0.6811	0.6247	VI
PAF2	26	32	44	40	38	572	0.6355		
PAF3	33	41	31	41	34	542	0.6022		
PAF4	46	22	46	36	30	522	0.58		
PRF1	31	18	35	35	61	617	0.6855	0.6872	I
PRF2	18	29	39	43	51	620	0.6888		
PFF1	28	41	31	35	45	568	0.6311	0.6619	II
PFF2	13	32	51	46	38	604	0.6711		
PFF3	36	20	50	37	37	559	0.6211		
PFF4	27	11	37	33	72	652	0.7244		
PIF1	52	26	40	35	27	499	0.5544	0.6022	VII
PIF2	23	41	34	32	50	585	0.65		
PLF1	61	30	31	35	23	469	0.5211	0.6307	V
PLF2	33	20	30	37	60	611	0.6788		
PLF3	15	27	45	46	47	623	0.6922		
PEF1	44	25	30	37	44	552	0.6133	0.6496	IV
PEF2	30	23	34	42	51	601	0.6677		
PEF3	33	19	34	42	52	601	0.6677		
PSF1	18	43	48	27	44	576	0.64	0.6577	III
PSF2	27	26	36	34	57	608	0.6755		

management as four (0.6496), flexibility as five (0.6307) and accessibility as six (0.6247).

4 Results and Discussion

In this study, confirmatory factor analysis is used to verify the items of customer requirements of sea port service quality. The model identified twenty items under seven customer requirements of the sea port service quality. The factor loadings of the items are above 0.7 indicates the significance of these items for the requirements of sea port service quality. From the fit indices results, it is observed that the value of $\chi^2/d \cdot f$ is 2.988 which indicates the close fit of the model. The indices GFI and AGFI can be thought of as being roughly analogous to the multiple R^2 and adjusted R^2 as in multiple regressions. As to the propriety of model, GFI value was 0.80, AGFI was 0.72, CFI was 0.97 indicates the moderately close fit. Further, the values of RMSEA (0.11) and SRMR (0.073) obtained in the study indicates the satisfactory fitness of the model. Therefore, the measurement model of customer requirements

of sea port service quality suggests a reasonably acceptable fit to the data as there were enough evidences to accept all the propositions (Ha, Hb Hc Hd He Hf and Hg) supported. Hence, the items shown in Table 1 confirm the customer requirements of sea port service quality.

5 Concluding Remarks

In this research, a seven-factor model with 20 items of customer prerequisites of sea port service quality is recommended through confirmatory factor analysis. The present findings give confirmation to support that this is a valid instrument to determine customer prerequisites of sea port service quality. In the present study, reliability factor is identified as most effective factor that influences the sea port service quality.

Appendix-A

Kindly indicate the status of the performance enablers in respect of your organization through the following fuzzy linguistic variables.

(1-highly insignificant, 2-Insignificant, 3-Neither, 4-Significant and 5-highly significant).

Questionnaire

S.No	Performance enablers	Linguistic variable
1.	Container damage low-frequency rate	
2.	Ports good connections to the main road	
3.	Ports good railway connections to the main line	
4.	Ports good connections with hinter land	
5.	Berth availability immediately upon vessel’s arrival at port	
6.	Vessels loading/discharging operations in compliance with contracts	
7.	Port service availability 24/365	
8.	Container railway delivery with no delays attributable to unforeseen queuing at terminal	
9.	Complete and correct container information availability at port at any time	
10.	Intermodal transport system in operation at port	
11.	High level of information integration between stakeholders	
12.	Port information availability on the intimae	
13.	Online port service availability for customers on website	
14.	Accurate/complete container/vessel documents	

(continued)

(continued)

S.No	Performance enablers	Linguistic variable
15.	Adequate number of berths at port	
16.	Environmental quality	
17.	Use of energy and resources	
18.	Waste handling	
19.	Satisfaction with the facilities, equipment and infrastructure	
20.	Satisfaction with the management and employees	

Name of the Respondent: Mr./Mrs./Miss:

Designation:

Contact Number:

References

1. C. Ugboma, C. Ibe, I.C. Ogwude, Service quality measurements in ports of a developing economy: Nigerian ports survey managing service quality. *Int. J.* **14**(6), 487–495 (2004)
2. A. Miremadi, S. Ghalamkari, F. Sadeh, Proc. Customer satisfaction in port industry (a case study of Iranian shipping). In: *International Conference on Sociality and Economics Development*, Vol. 10, pp. 58–62. IPEDR IACSIT Press, Singapore (2011)
3. J. Lu, X. Gong, L. Wang, An empirical study of container terminal's service attributes. *J. Serv. Sci. Manage.* **4**(1), 97–109 (2011)
4. K. Kolanović, C. Dundović, A. Jugović, Customer-based port service quality model. *Distrib. Logist. Rev.* **23**(6), 495–502 (2011)
5. G.T. Yeo, V.V. Thai, S.Y. Roh, An analysis of port service quality and customer satisfaction: the case of korean container ports. *Asian J. Shipp. Logist.* **31**(4), 437–447 (2015)
6. V.V. Thai, The impact of port service quality on customer satisfaction: The case of Singapore. *Marit. Econ. Logist.* **18**(4), 458–475 (2016)
7. N.H. Viet, Service quality at the seaport system of saigon newport corporation. *Int. J. Mark. Stud.* **7**(6), 145–154 (2015)
8. J. Sayareh, S. Iranshahi, N. Golfakhrabadi, Service quality evaluation and ranking of container terminal operators. *Asian J. Shipp. Logist.* **32**(4), 203–212 (2016)

Photovoltaic/Thermal (PV/T) System Performance Effects Using Conventional/Modern Cooling Techniques with and Without PCM



D. Kameswara Rao, K. Sudhakar Reddy, and V. V. Subba Rao

Abstract The PV panel electrical efficiency depends upon panel material and its operating temperature. Photovoltaic cell electrical generation will drop with rise in temperature, so cooling is required to increase the PV panel electrical efficiency. Photovoltaic Thermal (PVT) system is a technology in which thermal system implants behind PV panel which removes heat of photovoltaic panel and cools the panel. Photovoltaic thermal control is technically feasible using phase change materials (passive method cooling), if some issues like thermal conductivity, high nucleation rate, and high PCM life cycle are properly addressed. Phase change material major drawbacks are their poor thermal conductivity and large undercooling. The PVT-PCM systems were established to propose more thermal storage potential about 30–43% than the conventional PVT water system, along with more time of thermal availability and output escalation around 8–12%. The PV panel back surface is attached with the aluminum container inside PCM with different (geometric, spherical, and fins) configurations. This paper presents the study of research gap and to adopt the better cooling techniques to enhance the best panel efficiency under all conditions by lowering the PV panel temperature.

Keywords Phase change material · PVT · Fins · Thermal systems · Passive method

1 Introduction

The present current energy demand and continuous growth of renewable energy sources mainly solar energy was demanded for a raise in efficiency of photovoltaic. Photovoltaic Thermal (PVT) systems were designed for solar cogeneration to

D. Kameswara Rao (✉) · K. Sudhakar Reddy
Department of Mechanical Engineering, Mahatma Gandhi Institute of Technology, Hyderabad,
India
e-mail: kameshd@rediffmail.com

V. V. Subba Rao
University College of Engineering, JNT University, Kakinada, Andhra Pradesh, India

© Springer Nature Singapore Pte Ltd. 2021
G. S. V. L. Narasimham et al. (eds.), *Recent Trends in Mechanical Engineering*,
Lecture Notes in Mechanical Engineering,
https://doi.org/10.1007/978-981-15-7557-0_54

combine both PV module and thermal instruments to form as hybrid to get the benefits of both electricity and heat. Besides the efficiency solar (PVT) energy claims less greenhouse gas emissions from burning of the fossil fuels. PVT systems overall efficiency can be increased by decreasing the panel temperature with different cooling methods. Photovoltaic/Thermal (PV/T) system enhances the electrical and thermal benefits, thereby increasing the overall efficiency. The instantaneous PVT collector thermal efficiency is determined by standard Eq. (1).

$$\eta_{\text{thermal}} = mC_p(T_o - T_i)/(A \cdot G) \quad (1)$$

where “ m ” is the flow rate (kg/s), “ C_p ” is specific heat (kJ/kg/k), “ T_o ”, “ T_i ” are outlet, inlet fluid (medium) temperature, A is collector surface area (m^2) and G is the total radiance received on the plan of the collector (W/m^2). The PVT system maintains constant cell temperature by various cooling methods that provide the thermal and electrical power, will be able to increase the systems overall efficiency with reduced photovoltaic cell area along with installation cost and also increases the life of the solar panel. Many researchers stated that solar cells efficiency decrease by 0.4–0.5% per every degree rise in cell temperature and a decrease in solar cell efficiency varies mainly with cell material. Chow [1] have done experiments and stated that a 10 °C rise in temperature can cause a reduction of 5% in the PV panel efficiency. Philipps and Warmuth [2] reported PV panel temperature increment will result decrease in power output and conversion efficiency. Wu et al. [3] stated increment in mass flow rate gives the better thermal efficiency with reduced solar cell temperature. Nizetic et al. [4] developed the model of PV panel with an active cooling water technique that consists of solar panel with water on either side to reduce panel temperature by absorbing thermal energy at different flow conditions. He also conducted recent experimental investigations, cooling of photovoltaic panel using water spray technique and found increment in electrical efficiency was 16% of PV panel and PV panel temperature was dropped from 23 to 24 °C as compared to 54 °C of non-cooled conventional PV panel. PV panel temperature can be reduced by increasing the solar panel cooling by natural convection or forced convection or reducing the surplus heat with new solar panel architecture. Phase change materials with solar panel will remove the excess heat efficiently. PCM is material that changes their phase during temperature change. Phase change material completely melts when excess heat absorbed due to the increment of solar panel temperature and it solidifies after a decrease in panel temperature. Researchers’ studies show that PCM can be successfully integrated with all the solar thermal/PVT devices to enhance electrical and thermal energy that reduce the requirement of conventional fuels like oil, coal, etc. and also help in reducing greenhouse gasses.

2 Factors Influence the Performance of Photovoltaics

Most of the PV panel suffers from efficiency reduction mainly due to increase in cell temperature which causes to reduce its power output. Solar cells temperature depend on various parameters like conduction, convection, and radiation effects due to degree of orientation along with wind direction and speed, received radiation, ambient temperature, solar cell materials, mass flow rate, packing factor, and glazing factor. In PVT hybrid system designing important parameter was mass flow rate. Variations of mass flow rate affect the convective heat transfer coefficient. PVT system overall efficiency will be enhanced with high convective coefficient. From the researchers' studies, it was understood that an optimum mass flow rate of PVT system will produce maximum electrical and thermal efficiency. Miles et al. [5] presented a paper regarding the overview of the different solar cell materials and their best efficiencies. They are silicon solar cells, III–V group solar cells, and dye-sensitized solar cells. Silicon solar (crystalline silicon) cell ideal efficiency is 24.72% and commercial module efficiency is 18%. III–V group solar cells having 25.0% PV conversion efficiency on single-junction solar cells.

3 PVT Collectors and Panel Cooling

The PVT collectors mainly categorized according to the kind of working fluid as PVT Water and PVT-Air systems were shown in Fig. 1.

3.1 PVT-Air Collectors

Air collectors are mainly classified on the basis of airflow patterns. These are classified with respect to the flow of air on either side of absorber, above absorber plate, and below the absorber in single and double pass. Convection heat transfer for PVT panel front and backside can be calculated by Natural and forced convection. The Total Heat Convection

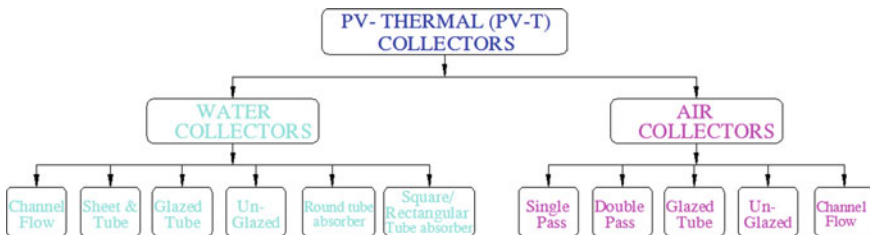


Fig. 1 Typical classification of PV–thermal collector types

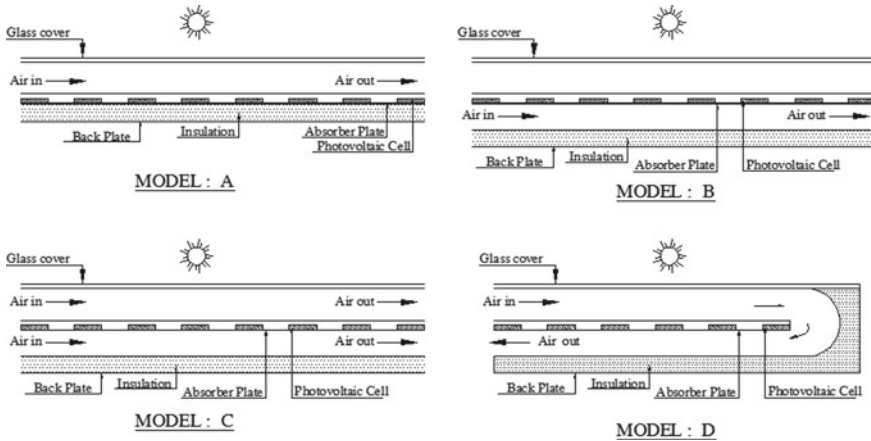


Fig. 2 Schematics of the various types of PVT-air collector models

$$Q_{conv} = Q_n + Q_f = (h_{free} + h_{forced}) \cdot A \cdot (T_{PVT} - T_{amb}),$$

where Q_n and Q_f are heat losses due to natural, forced convection, and h_{free} and h_{forced} forced and free convection coefficients, “A” area of collector, T_{PVT} , T_{amb} are PV Panel temperature and Ambient air temperatures, respectively.

Natural convection Heat transfer (Q_n): According to Newton’s law of cooling Natural convection heat losses given by $Q_n = h_{free} \cdot A \cdot (T_{PVT} - T_{amb})$.

Forced convection Heat transfer (Q_n): According to Newton’s law of cooling Forced convection heat losses given by $Q_f = h_{forced} \cdot A \cdot (T_{PVT} - T_{amb})$.

Among the air-based PVT systems, Hegazy [6] proposed and investigated four basic modes, with air flowing either above absorber (Model A) or below it (Model B) and in Model C with single pass on either side of absorber or Model D with double pass as mentioned in Fig. 2.

Tiwari and Sodha [7] calculated Hybrid PVT-AIR collector overall performance with different modulated configurations with glazed and unglazed and with or without tedlar as shown in Fig. 3. Enhancement of efficiency was found in Model IV of glazed hybrid PVT system without tedlar used for different applications, namely, space heating, water heating illumination, and lighting. Solanki and Dubey [8] examined the Air PVT collectors models in indoor testing and simulation. When the inlet temperature and the irradiation rate was 38 °C and 600 W/m², respectively. They got the electrical, thermal efficiencies of 8.4% and 42%, respectively.

3.2 PVT Water Collectors

PVT water collectors are differentiated according to water flow pattern which is a sheet and tube, types of absorber, and channel free flow. PVT panel cooling with water

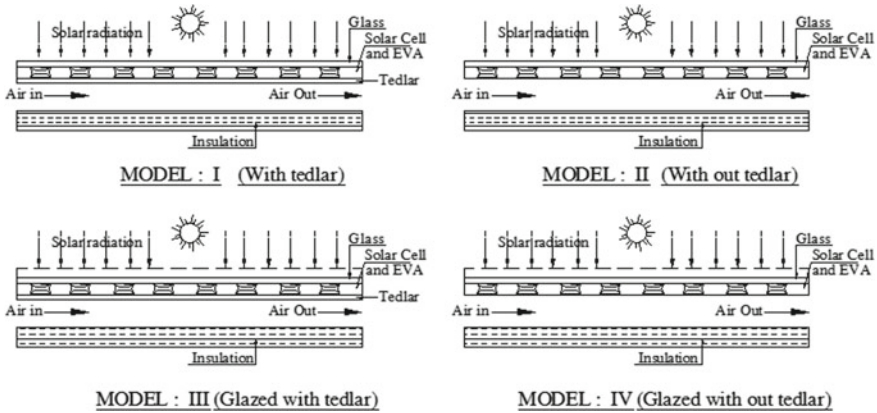


Fig. 3 Glazed and unglazed PVT-air heater with Tedlar and without Tedlar

can be classified as passive cooling and active cooling. Water-based passive cooling, found effective, provides a good thermal contact in the PVT system without using pumps and removes excess heat continuously or utilized elsewhere. Water-based active cooling improves PV Panel performance as water flow velocity increased. The advantage of active water cooling was higher heat transfer, compared to both natural and forced convection of air. The disadvantages of this system are higher investment due to the use of pumps, higher maintenance cost compared to natural and forced convection, and less life due to corrosion and leakage of fluid. Nizetic et al. [5] developed experimental investigations of water spray cooling technique of PV panel and got incremental electrical efficiency about 16.3% and temperature was dropped about 25 °C as compared to 55 °C of conventional non-cooled panel.

In the work Chow et al. developed the new PVT water collector with the principle of thermosiphon to reduce the cost of pumping power. Figures 4a, b shows the cross section views of three adjacent water tubing in a sheet and tube PVT collector and several integrated flat box absorber modules of PVT collector, respectively.

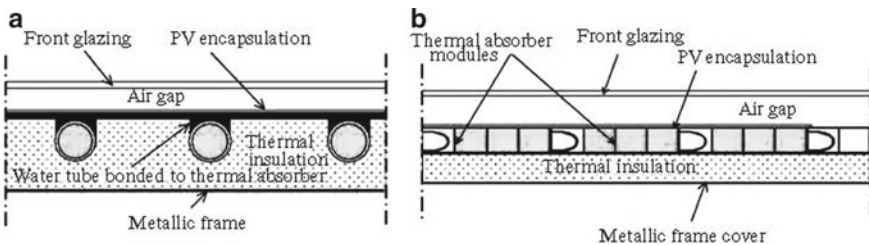


Fig. 4 a C/S view of three adjacent water tubing, b C/S view of PVT collector showing several sheet and tube PVT collector (from SCIJ Ref. [15]) integrated flat box absorber modules

3.3 *Thermoelectric Cooling*

Thermoelectric cooling is based on converting additional heat generated by the panel into electricity based on Peltier effect. This process may elevate the electricity efficiency of PV panel by 8–23%. The advantages of Thermoelectric cooling are Compact in size, no moving parts and Low Maintenance cost. The disadvantages of this system were more electrical consumption besides that heat transfer rate depends on ambient conditions, no heat storage capacity, and Low reliability.

3.4 *Cooling Using PCM*

PCM is kept behind the PV Panel to absorb the heat and it maintains constant temperature of PV panel during phase change and stores only heat energy. The PCM latent heat is utilized to maintain the PV panel at a fairly constant temperature. The stored heat capacity can be used later for space heating, water heating, and other purposes; however, the initial investment with these systems is quite high. PCM stored heat will increase the systems overall efficiency without any electricity consumption. Researcher studies confirmed the PVT-PCM system, PCM encapsulation into honeycomb structure will increase heat conduction with increase in electrical efficiency of 15–23% while comparing with normal PV panel.

4 PVT System Thermal Management Solution Using PCM

Thermal management in PVT can be maintained as passive mode and active mode. Passive mode means using Fins, PCM (Latent melting) does not require any electrical and mechanical power, whereas active mode of PVT cooling which uses air, oil, and water (Sensible media) requires power, in which leakage, maintenance, and pumping is a big problem. The process of transformation of heat from a substance/materials as long as no change in its existing phase happens by mean of using sensible heat. When phase change of material occurs, the material (PCM) does not acquire sensible heat, i.e., heat supply from external source, rather it undergoes endothermic process by absorbing the surrounding heat. Phase change material melting period determined by the thermal conductivity and PCM volume.

Phase change material utilizes latent heat storage, which exchange some part of heat energy as latent heat with a minor change in temperature involving phase transformation. The PCMS temperatures of phase transition differ considerably with material thermal properties, material type, and chemical structure. PVT system using PCM initiates thermal energy storage devices, the wasted heat during working of PV modules for short term applications. PCM provides better solution to a TES system that provides better heat storage potential with minor volume. Main advantage of

PCM is that it provides better storage capacity of 6–15 times more energy per unit volume than the sensible heat storage materials. PCM offers a best solution, on one side it will act as thermal energy storage device and on another side, these PCM offer availability of heat for extended period during night time. Due to global warming and energy crisis in present, researchers have done a great work on PV thermal energy storage where PCM's came out as most reliable/promising alternative.

4.1 Classification of PCM

PCM can be classified in different ways, i.e., based on their phase transition, melting temperature such as low temp PCM (15 °C), medium temp PCM (15–90 °C), high temperature PCMs (above 90 °C), and their material compositions are shown in Fig. 5a–c. Based on their mode of phase transition, PCMs are Gas–Liquid, Solid–Solid, Solid–Liquid, and Solid–Gas. PCMs can also be classified based on chemical identity as organic, inorganic, and eutectic. The application of PCMs with Solid–Gas or Liquid–Gas phase transition is limited in TES and PVT-PCM system because of high volume changes associated with phase transition.

A variety of phase change materials (organic, inorganic, and eutectic) are available in a different temperature range, finding all the properties in single PCM for a model thermal storage media are difficult. Organic material paraffin wax is a soft colorless solid which is a mixture of high molecular weight straight chain n-alkenes with melting point above 36 °C and the heat of fusion from 200 to 220 kJ/kg. Paraffin waxes are recyclable, non-reactive (non-corrosive), and non-toxic materials having good latent heat and self-nucleating property. They freeze without much undercooling, melt congruently, and do not separate on solidification (Table 1).

4.2 Selection of PCM for PV Thermal Systems

Nowadays efforts have been engaged in innovative methods of passive cooling with the use of phase change material. Research work initiation was going to get a better PVT-PCM model with mixing of different PCM at different proportions with variety of geometrical fins along with nanomaterials. Solar energy efficiency depends on the efficiency of thermal storage technology due to unpredictable and intermittent solar energy. PCM stores best heat accumulation per unit volume by combination of sensible heat and latent heat storages. Most of the PCM absorbs heat during its phase change during a cycle from solid phase to liquid phase during day time and releases heat at night time. This technology enhances the overall efficiency of solar thermal PV system. Hasan and Sumathy [9] and others obtained separately table of properties in Table 2 as preferred suitable PCM for PV applications.

The main concern in PV-PCM system is the thermal conductivity. The PV systems with PCMs with elevated thermal conductivity will boost the systems heat transfer in

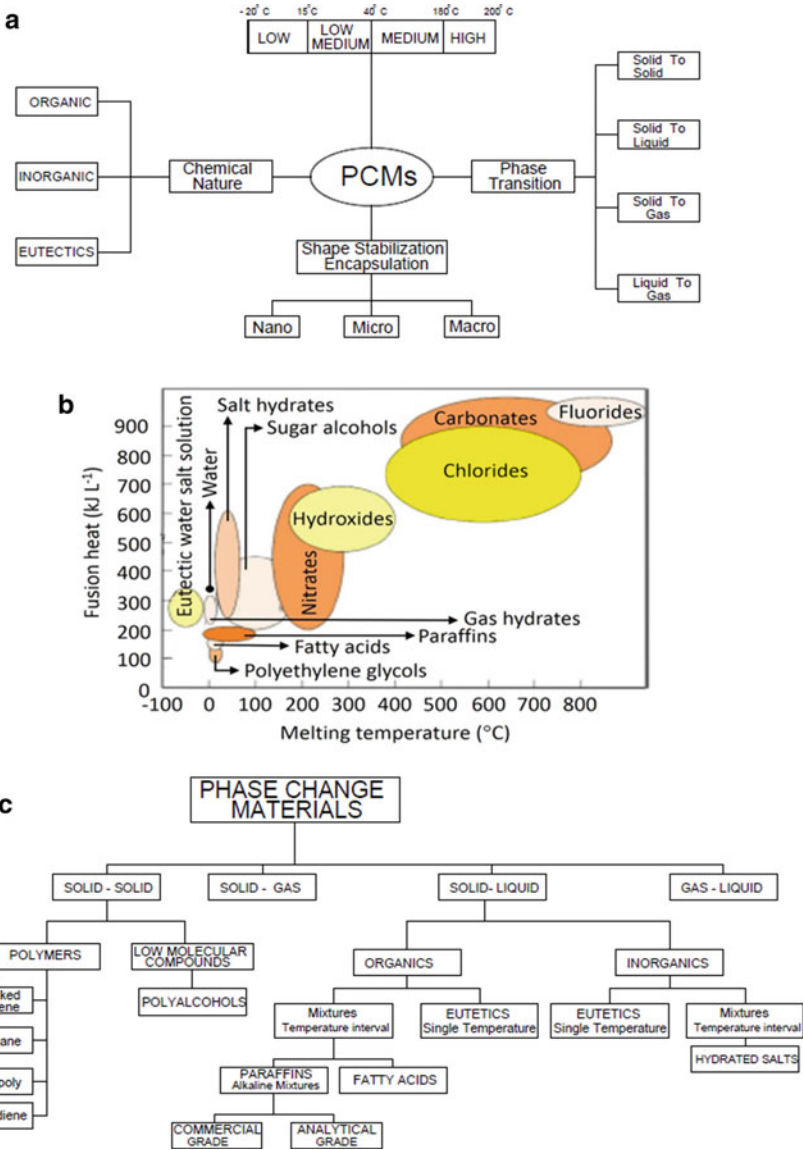


Fig. 5 a PCM classification (from Scopus journals), b PCM classification based on temperature (from Scopus journals), c PCM classification (based on phase change)

Table 1 Comparative merits and demerits of organic PCM, inorganic PCM, and eutectics (from Scopus indexed journals)

PCM types	Merits	Demerits
Organic	<ul style="list-style-type: none"> • Available in extensive range of temperature • Better rate of fusion heat • Self-nucleating property • Congruent melting 	<ul style="list-style-type: none"> • Less volumetric rate of latent heat storage capacity • Low thermal conductivity • Huge volume change on phase transition • Flammable
Inorganic	<ul style="list-style-type: none"> • High heat of fusion • High thermal conductivity • Better volumetric latent heat storage • Sharp melting point • Non-flammable 	<ul style="list-style-type: none"> • Supercooling • Quick phase separation • Lack of thermal stability • Incongruent melting • Corrosiveness
Eutectics	<ul style="list-style-type: none"> • Sharp melting point • Lack of thermophysical properties • High volumetric heat storage density 	

Table 2 Desirable properties required for PCM selection in PVT application

S. No	Properties	Required	Advantages
1.	Thermal	<ul style="list-style-type: none"> • High latent heat • High thermal conductivity • Phase change reversal • High heat capacity • Phase change temperature range • Fixed melting point 	<ul style="list-style-type: none"> • Maximum heat absorption • Heat removal rate is more • Diurnal response • Minimum sensible heating • Phase transition confirmation • Consistency in behavior
2.	Physical	<ul style="list-style-type: none"> • High density and specific heat • Phase transition with small volume • Desirable phase equilibrium 	<ul style="list-style-type: none"> • To ensure low suppression • Avoid over design • Stable thermal storage
3.	Chemical	<ul style="list-style-type: none"> • Non-corrosive • Non-explosive, flammable, and toxic • Chemical stability • Congruent melting 	<ul style="list-style-type: none"> • More container life • To Better safety • Long PCM lifecycle • Optimum thermal gradient
4.	Kinetic	<ul style="list-style-type: none"> • High nucleation rate • No super cooling • High-crystal growth rate 	<ul style="list-style-type: none"> • To avoid super cooling • Easy to freeze • Better solidification to meet heat recovery requirement
5.	Environmental	<ul style="list-style-type: none"> • Reusable/Recyclable • Odor free 	<ul style="list-style-type: none"> • Ease to dispose off • Comfortable for dwelling places
6.	Economic	<ul style="list-style-type: none"> • Low cost • Abundant • Cost effective 	<ul style="list-style-type: none"> • Better market penetration • Easy availability • Economic viability

less time. Research of numerical investigations mentioned that 10% increase in PCM thermal conductivity in PVT-PCM system can improve the hybrid system output by 3–4%. Besides all the properties physical stability, environmental (reusable) are important characteristics along with thermal conductivity. Selection of best PCM for PVT-PCM system is difficult to improve Overall system efficiency, while selecting the material properties of high thermal conductivity and specific heat at all Phase changes. The selection of PCM depends on availability at low cost in large quantities with better stability of chemical and physical characteristics and also non-corrosive to construction materials. PCM with high density along with more nucleation rate with limited volume change in phase change also plays a vital role in PCM selection.

4.2.1 Phase Change Materials Composites

During the PCM usage after heating, it may convert into liquid form may possess a leakage problem. An alternate method to overcome the leakage problem of liquid PCM is making its composite with high density polyethylene and by absorbing it in porous materials like ceramic granules, wood fiberboard, and tiles. In composite, PCM is finely circulated in polyethylene/other porous matrices, which controls flow of liquid PCM, and therefore can be cut in different shapes easily without any leakages. Kumar et al. [10] studied on composites of less conductivity PCM by combining with graphite material of high conductivity.

4.3 Salt Hydrates for PCM Cooling

Salt hydrate is a potential applicant for cooling photovoltaic panels in terms of high conductivity, large capacity for heat storage, and expansion of volumetric volume, but they suffer from large subcooling that causes stiffness problems at night, especially in the summer when the need for thermal regulation of photovoltaic panels is highest. Organic PCM, on the other hand, suffers with low thermal capacity with oversized expansions. Performance improvements were observed using organic PCMs low thermal conductivity, however, in any of the systems studied, good initiation on working of salt hydrates with less cost than organic PCM with good thermal conductivity.

4.4 Nanomaterials and Fins for PCM Cooling Enhancement

The PCM performance can be increased by composing high thermal conductivity material into the PCM generally the materials are graphite, nanomaterials, ceramic compounds, and foam. Researchers have been studied more about graphite as heat transfer enhancer in PCM due to its less density, good heat conductivity, and better

chemical resistance. There are different types of graphite, such as natural graphite flakes, nanographite, and expanded grapheme. Sun et al. [11] experimentally investigated the feasibility of using graphite with metal foam to elevate the heat transfer capability of salt hydrides and results were shown the rate of heat transfer was increased in all charging and discharging phases. Another technique is insertion of fins, cylindrical, or spherical geometry into the PCM to obtain solidification or melting time reduction to increase the heat transfer from surface. PCMs heat transfer rate can be enhanced by the use of capsules or finned tubes to reduce the heat transfer distance. The encapsulation of PCM is divided into micro-, macro- and nanoencapsulation. The macro-encapsulation is done with PCM ranges several mm to several cm filled in container made with plastic or metal. PCM micro-encapsulation is the encapsulation of solid or liquid particles of diameter $1 \mu\text{m}$ to 1mm with a solid shell, the nanoencapsulation capsules are less than $1 \mu\text{m}$. This encapsulation can be done by a physical process or chemical process by spray drying, centrifugal bed process, or coating process with different technical approaches.

5 Result and Discussion

This section highlights the updated literature and research studies. The objective is to find the research gaps and to improve the current status of growth in PVT technology. Researchers were developed various cooling techniques to cool the solar panels wherein, implementation of PCM was found best method to retain the solar panel efficiency with reduced panel overheating with better energy converse on efficiency along with increase of solar panel life. From the literature review, it was found most of the works are focused on active and passive cooling systems using water, airflow circulation. But passive cooling systems will not maintain the cell temperature to a certain level. An active system suffers from extra equipment and cost of circulating fluid. The following Table 3 gives the method of cooling, its advantages, and limitations.

Japs et al. [12] declared PVT-PCM will give better efficiency [12] than the solar panel without using phase change material and tests were conducted for 25 days and more with graphite PCM. They observed that PVT-PCM system results were positive with Maximum temperature in forenoon and negative during remaining test duration. Temperature are only positive and were negative for the rest of remaining test duration of test. Smith et al. [13] confirmed PVT-PCMs were most beneficial, where low inter-seasonal climatic variations and high radiation area. He stated that increased energy was around 6% along with payback period of 25 years. Malvi et al. [14] confirmed in their PCMs numerical studies, increase in thermal conductivity by 10% the system can enhance the PV output of 3%. PCM container with fins will further increase the systems overall efficiency. Hussien et al. [15] reported that by active cooling of PVT panel, the temperature was dropped to 9°C , with raise in electrical efficiency of 9.8% at optimum rate of mass flow at 0.2kg/sec and thermal efficiency to 12.3%.

Atkin and Farid [16] conducted an experimental analysis and modeling with MATLAB of PV-PCM system in which graphite embedded with aluminum fins in PCM (paraffin wax) under four cases and got the highest efficiency of 12.9%. PV-PCM simulation with micro-encapsulation in which MEPCM system was attached at the back of PV panel and PV panel was floated on water surface got an enhancement of electrical efficiency 2.0%. Deng et al. [17] and others gave the results thermal efficiency of water-based PVT without PCM was high compared to thermal

Table 3 Cooling methods advantages and disadvantages (from Scopus journals)

S. No	Cooling method	Attained PV panel temperature	Advantages	Limitations
1.	Natural ventilation	45–75 °C	<ul style="list-style-type: none"> • No maintenance • No Electricity requirement • Low initial cost • Longer life 	<ul style="list-style-type: none"> • Less heat transfer rate and conductivity • More PV panel temperature variations • Extracted heat Utilization is very less • Depends on atom air temperature and wind movement
2.	Forced ventilation	20–30 °C	<ul style="list-style-type: none"> • More heat transfer rate compared to natural ventilation • Higher temperature reduction than natural convection 	<ul style="list-style-type: none"> • High initial and installation cost • Consumes more power and more noisy
3.	Active water cooling	Up to 25 °C	<ul style="list-style-type: none"> • Can be maintained PV panel temperature Effectively • Good heat transfer rate 	<ul style="list-style-type: none"> • High initial cost and maintenance cost • Required pumping power is more and noisy system
4.	Thermo electric cooling	N A cooling is not important.	<ul style="list-style-type: none"> • Low maintenance cost • Low initial cost and less noisy • Compact size • Easy to integrate 	<ul style="list-style-type: none"> • Ambient temperature influenced cooling performance • More Electrical consumption • Very effective heat removal is required
5.	Heat pipe cooling		<ul style="list-style-type: none"> • Passive heat exchange • Low cost • Integration is easy 	<ul style="list-style-type: none"> • Low heat transfer rates • Wind speed and direction influenced

(continued)

Table 3 (continued)

S. No	Cooling method	Attained PV panel temperature	Advantages	Limitations
6.	PCM	22–32 °C	<ul style="list-style-type: none"> • No maintenance and electricity cost • PV panel temperature can be delayed • Temperature can be maintained constantly for long time • Heat removed can be reused effectively • Supplies heat on demand • No noise issues 	<ul style="list-style-type: none"> • High initial cost. • Material stability and life is an issue • Containment is a concern • Some PCM are toxic and flammable • Disposal issue after completion of cycle

efficiency of water-based PVT-PCM because increase in temperature of water in PVT system is higher compared to PVT-PCM system at same solar concentration. Researchers can get better optimization of PVT-PCM system by developing a mathematical and numerical model for convectional PV panel, water-based PVT, and PVT-PCM systems based on energy balance of different components (with different materials) at different flow rates conditions by considering some assumption into account. Research studies shown that using PCM (Passive heat exchange method) in PVT cooling having so many advantages like high heat transfer rates, high heat storage capacity (due to latent heating) along with noiseless isothermal heat removal without noise and electricity need. Besides the disadvantages of PCM are corrosive, toxic, inflammable, and high PCM cost with disposal issues after completion of life cycle.

6 Conclusions

The emerging issue of energy efficiency is encouraging research in PCMs field over the last decade. A comprehensive review of cooling techniques for PVT systems was discussed in this paper using different conventional/modern cooling methods including PCMs are presented to find the research gaps and to identify the status to suggest a possible solution. The Recent PVT systems merits and demerits with different control parameters were studied in this paper. Earlier studies shown that the natural ventilation-based cooling is the most ineffective method while forced water and air-cooling techniques are being used around the world for PV panel cooling even though pumping cost included. From research literature shown that the thermal and electrical efficiencies were increased from 25 to 28% and 6.7 to 8.1%, respectively,

based on the broad review the conclusions of PCM implementation in real system and its benefits, studied to access the market potential. Researchers' studies found that PV panel cooling results better (lesser) payback in energy and greenhouse gas time. Many researchers concluded overall efficiency of PVT panel can be increased several times by using with heat sinks and conductivity enhancers. It was also found that PCM material use and PCM using technologies are to be more optimized in terms of arrangement of PCM, fins, heat pipes, macro- and micro-encapsulation, and adding nanoparticles with high thermal conductivity in PCM for better enhancement of thermal conductivity. Even though it was not economically viable 13 years of payback period, but recommended for good environmental issues. Numerical research investigations were mentioned that 10% increase in PCM thermal conductivity in PVT-PCM system can improve the hybrid system output by 3–4%. Phase change material selection for cooling the PV panel depends on ambient temperature and year round climatic conditions. PV Panel temperature can be maintained easily when PCM melting temperature above 30 °C than compared to low PCM (<25 °C). PCM above 30 °C avoids formation of hot spots, below 30 °C problems with complete solidification at night. Selection of the PV cell material and PCM material plays a vital role in overall efficiency of PVT system. PCM usage after end of cycle disposal of PCM is a major problem along with its corrosiveness to component and its inflammability. PVT cooling techniques with Novel materials can be developed to meet the global challenges with high thermal conductivity for efficient heat removal from systems. Future trends in the area of PCMs will mostly related to use of nano and bio-based materials which offer different possibilities in the design of advanced composites with superior properties to the traditional materials. The performance of cooling in the PV Panel with micro-encapsulated PCM can give better results at certain temperature range. Researcher has to develop the highly efficient PCMs which are stable for more cycles over wide variety of temperature ranges are being suitable for TES and PVT systems.

References

1. T.T. Chow, A review on photovoltaic/thermal hybrid solar technology. *Appl. Energy* **87**(2), 365–379 (2010)
2. S. Philipps, W. Warmuth, Photovoltaics report. Fraunhofer Institute for Solar Energy Systems (2016)
3. S.-Y. Wu, Q.-L. Zhang, L. Xiao, F.-H. Guo, A heat pipe photovoltaic/thermal (PV/T) hybrid system and its performance evaluation. *Energy Build.* **43**, 3558–3567 (2011)
4. S. Nizetic, D. Coko, A. Yadav, F.G. Cabo, Water spray cooling technique applied on a photovoltaic panel: the performance response. *Energy Convers. Manage.* **108**, 287–296 (2016)
5. R.W. Miles, K.M. Hynes, I. Forbes, Photovoltaic solar cells: an overview of state of the-art cell development and environment. *Prog. Cryst. Growth Charact. Mater.* **51**, 1–42 (2005)
6. A.A. Hegazy, Comparative study of the performances of four photovoltaic/thermal solar air collectors. *Energy Convers. Manage.* **41**, 861–881 (2000)
7. M.S. Tiwari, Sodha, Parametric study of various configurations of hybrid PV/thermal air collector: experimental validation of theoretical model. *Sol. Energy Mater. Sol. Cells* **91**, 17–28 (2007)

8. S.C. Solanki, S. Dubey, A. Tiwari, Indoor simulation and testing of photovoltaic thermal (PV/T) air collectors. *Appl. Energy* **86**, 2421–2428 (2009)
9. M.A. Hasan, K. Sumathy, Photovoltaic thermal module concepts and their performance analysis: a review. *Renew. Sustain. Energy Rev.* **14**, 1845–1859 (2010)
10. R. Kumar, M.K. Misra, K. Rohitash, other published a review paper on, Phase change materials: technology status and potential defence applications. *Def. Sci. J.* **61**(6), 576–582 (November, 2011). <https://doi.org/10.14429/dsj.61.363>
11. X. Sun, T.J. Silverman, Z. Zhou, M.R. Khan, P. Bermel, M.A. Alam, Optics-Based approach to thermal management of photovoltaics: selective-spectral and radiative cooling. *IEEE J. Photovolt.* **7**, 566–574 (2017)
12. E. Japs, S. Peters, G. Sonnenrein, S. Krauter, Energy-economic comparison of photovoltaic modules equipped with a layer of conventional and improved phase change material. In: *Proceedings of the 40th IEEE Photovoltaic Specialist Conference (PVSC)*, Denver CO (USA), pp. 1348–1352 (2014)
13. C.J. Smith, P.M. Forster, R. Crook, Global analysis of photovoltaic energy output enhanced by phase change material cooling. *Appl. Energy* **126**, 21–28 (2014)
14. C.S. Malvi, D.W. Hardy, R. Crook, Energy balance model of combined photovoltaic solar-thermal system incorporating phase change material. *Sol. Energy* **85**, 1440–1446 (2011)
15. H.A. Hussien, A.H. Numan, A.R. Abdulmunem, Improving of the photovoltaic/thermal system performance using water cooling technique. *Mater. Sci. Eng.* **78**, 1–9 (2015)
16. P. Atkin, M.M. Farid, Improving the efficiency of photovoltaic cells using PCM infused graphite and aluminium fins. *Sol. Energy* **114**, 217–228 (2015)
17. Y. Deng, Z. Quan, Y. Zhao, L. Wang, Z. Liu, Experimental research on the performance of household-type photovoltaic-thermal system based on micro heat pipe array in Beijing. *Energy Convers. Manage.* **106**, 1039–1047 (2015)



D. Kameswara Rao received the B.Tech in Mechanical Engineering and M.Tech (Energy System) from JNTU College of Engineering Hyderabad, India. He is pursuing his Ph.D on solar panels and PCM from JNTU College of Engineering, Kakinada, India. He published Six international papers in reputed journals and presented two papers in International Conferences. He is working as academician in Mahatma Gandhi Institute of technology, Gandipet, Hyderabad.

Studies on Emergency Alert for Women with Smart Dollar



R. Dhanasekaran, S. Sreenatha Reddy, Mohammed Sirajuddin, Harisaiteja Nanaboina, and I. Jahnavi

Abstract The main motto of this research is to save the woman from kidnappings, rapes, and harassment. There is no safety for women anywhere. Nowadays these rapes and kidnappings were happening more and more all over the world. Government of India is also coming forward to reduce these issues. Recently government has introduced a new application for the safety of women, i.e., 112 India app. This app is completely meant for women's safety. But apps cannot save the women all the time, devices are far better than apps. Many devices are introduced, like safe lets, pepper spray gun, lipstick flashlight, safety rods, safety smart pendants, etc. Safe lets and safety smart pendants don't harm the opponent but intimate to the cops, friends, and family. Pepper spray, safety rods, all these devices just help to defend the opponent but will not give any information to the police and family. In this way every device has only one or two advantages. So this research work will combine all advantages into one device. The device contains micro-camera, which captures images and records the video. GPRS which gives the information about the location of the woman. Button which activates the device by pressing and transmitter helps to transfer the captured pictures and videos to the nearby police station and to the family members. So this research work will surely help every woman.

Keywords Hidden camera · GPS terminology · Women security · Application · Emergency · SOS emergency helpline

R. Dhanasekaran · S. Sreenatha Reddy
Department of Mechanical Engineering, Guru Nanak Institute of Technology, Hyderabad, India

M. Sirajuddin (✉) · H. Nanaboina
Department of Computer Science and Engineering, Guru Nanak Institute of Technology, Hyderabad, India
e-mail: mohammedsiraj77@gmail.com

H. Nanaboina
e-mail: nharisaiteja@gmail.com

I. Jahnavi
Department of Electronics and Communication Engineering, Guru Nanak Institute of Technology, Hyderabad, India
e-mail: jahnaviimmadi@gmail.com

1 Introduction

Nowadays women harassment takes place in many places. The central theme of this device is to protect women from critical situations. Mahatma Gandhi said, “The day a woman can walk freely on the roads at night, that day we can say that India has achieved independence” [1]. Many rules, regulations, and acts were passed for women safety but there is of no use. Rules and regulations will never help to change the people mindset. In India, there is a development in every aspect from past 10 years but no development in the women’s safety. Every women think twice or thrice while stepping out of the home. This is the present status of our country [2]. We should feel ashamed about this condition in our country. Because in Vedas, women were treated as goddesses but now these goddesses are in dangerous condition. Even though there are many achievements in our country, all those will be faded if there is no safety for women because they are the major contributors for a country’s development and growth. Every day at least there is one news regarding the crimes against women. Gradually this became daily news for everyone. The crimes against cannot be explained like rapes, kidnappings, harassment, acid attacks, etc. Not only outside the home but also in home there no safety for women, i.e., domestic violence and gender discrimination. The only creature in the world that are facing these many problems. The very recent crime against women is Disha case. Police played a good job in punishing the criminals but not in saving her. Slowly the government is coming forward to save women by appointing some police teams only for women safety, apps, passed some new rules [3]. This research work is completely for women’s safety. Through this research, we are going to produce a device that can save the women from dangerous situations. This device is user friendly and it is placed in the dollar so in undependable situations, if the women press the dollar and shout the word “Help me” for three times then the device will activate and using the SOS communication, photos, location, and video will be shared to family friends and nearby police stations through smartphone which is connected to the device. We can also say that this device is easy to carry and having featured gadgets inside which helps women to send her live location with the pictures, videos, and voice recording by these things we can exactly know the situation of the victim which is not yet designed before in any other gadget. Let us take an example of women working at late nights and alone she need to reach home then with the help of vehicle or by walk she is going then if suddenly someone attacks her with the help of this device she gets a loud siren in her mobile which alerts the nearby people and the pictures, videos, and the voice recordings are sent to the police, family, and friends. Then the police reach the destination by seeing her live location. Then the woman will be saved as soon as possible [4].

2 Smart Device to Alert Cops

There are many online applications and also devices for women safety. The government of India is also working to avoid this type of activities and implemented acts to punish the responsible and give justice to victims. In case of critical situation, women cannot use their mobiles and call the cops for help. So this device helps women to alert cops, friends, and also family members. By pressing the button or shouting "HELP ME" three times the device gets activated. The local area police station gets the notification and this notification is forwarded to higher authority like CID or CBI [5]. Then after receiving the notification cops reach victims as soon as possible. These notifications are video clips, audio clips, photos, and live location of the victim by cross checking the above notifications police get alert and they immediately take required action and woman will be saved.

3 Methodology

The major use of this device is to save women in dangerous situations in which communication is not possible. Device is placed in the dollar and it gets activated by pressing button or by shouting "HELP ME" three times the internal parts get activated and work on their respective functions. After the completion of the functions, the video clip and audio clip are sent as the emergency notification to police, family, and friends. This device has two methods to get activated. The first thing is to activate by pressing the button and another is by shouting "HELP ME" three times then the device gets activated and then the siren is activated in the victims' mobile which alerts the nearby people with loud noise. The following Fig. 1 represents the main theme of this device and shows how the notification reaches from the victim to police, family, and friends [6]. In the Fig. 1, we can able to see the women can send her emergency alert to police, family, and friends as soon as she activates the device which is placed right in her dollar. After getting the notification through the SOS communication police will reach the destination as soon as possible.

3.1 Hardware Device

Women basically like the jewelry. Basing on that this device is designed in a dollar which is not an ordinary one. We can also call this device as smart device. This is totally a smart device which helps women and also looks attractive. This device gets activated by pressing the button or by shouting "HELP ME" which is inbuilt in the dollar. After getting activated the device starts taking pictures with the help of the small micro-camera which is located in front of dollar which is helpful to take pictures of the opponent. These pictures are transferred to mobile and then to police

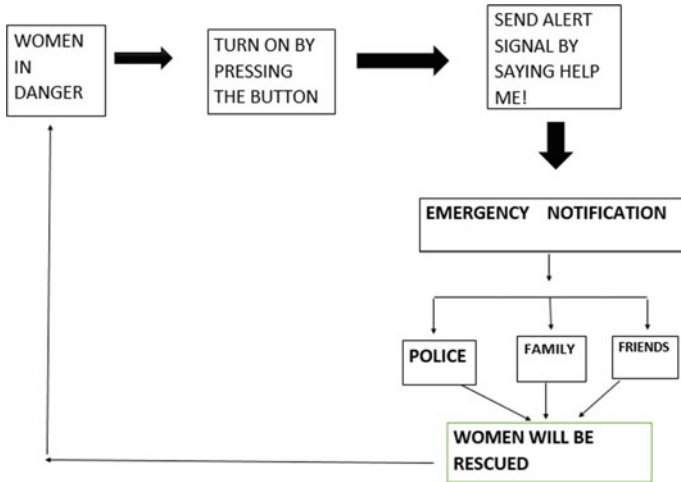


Fig. 1 Main theme of the device

with the help of the application. After activation of device the mobile phone which is connected to the device starts siren (alarm) which gives warning sign loudly to nearby people this feature is added because if someone is near by the victim she may get help from them quickly. GPS terminology which is already inbuilt in smartphones, this terminology is used to send the live location of the victim to police, family, and friends, which helps them to locate victim easily and with the help of the application we can also see the victims' live location. SOS emergency helpline, this feature is kept inbuilt in the application which is connected to the device. This helpline uses the terminology of the network instead of not having the Internet connection also the pictures, videos, and live location is sent to the emergency helpline called police.

3.2 Android Application

The following Fig. 2 represents the whole working of the device. When you click the button of the device, they start working on their own and the android application grasps all the files from the device like pictures and videos. By observing to the Fig. 2, we can able to understand the working of the device after the woman turning on the device by pressing the button or by saying "Help me" three times then the internal workings are activated as the hidden camera takes pictures and videos next the voice recorder recognizes the voice and records the few seconds audio to help the police for investigation and these messages reach to mobile consisting app that is then transferred to police, family, and friends. Through SOS communication the messages reach quickly to them and reach the destination as soon as possible by seeing the live location of the woman.

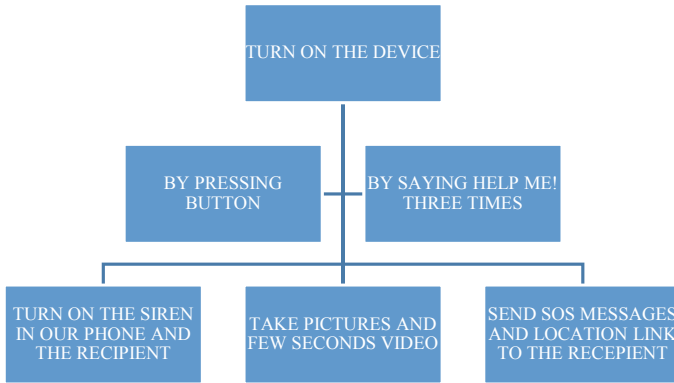


Fig. 2 Working of smart device

4 Discussion

4.1 SOS Message

SOS is an international emergency helpline. This communication is helpful in a situation when woman was unable to contact with the police and family. Using SOS communication, messages can be sent in the absence of network. This emergency message consists of our current location tracked by Global Positioning System (UBLOX) and sent to GSM module in which our location and our default emergency message are sent to our pre-stored contacts and police and a call is connected to the police with a recorded voice to seek help.

4.2 Hidden Camera

Hidden camera detector is a radio frequency receiver, which picks up electromagnetic signals that are broadcasted from electronic devices such as spy camera as shown in Fig. 3. By moving this detector, we are able to take pictures and videos. With the help of a hidden camera, we can take the opponent pictures without knowing to him easily.

4.3 Video Recorder

The video recorder is activated when woman press button or shout “HELP ME” it gets activated and records the whole incident and it is useful for the police to find

Fig. 3 Hidden camera

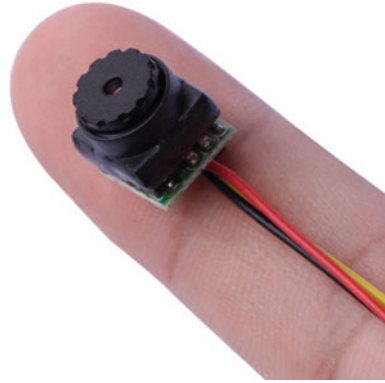


Fig. 4 Condenser microphone



the crime investigation. The plus point of this video recorder is that opposite person will never get to know about the recording of this hidden camera.

4.4 Voice Recorder

The video recorder is activated when woman press button or shout “HELP ME” it gets activated and records the whole incident and it is useful for the police to find the crime investigation as shown in Fig. 4. The plus point of this video recorder is that opposite person will never get to know about the recording of this hidden camera.

5 Conclusion

With the help of this device, we can find the criminal very easily and save women from dangerous situation. Nowadays there are many devices for the safety of women like wrist bands, locketts, etc., our device differs that it is less weight to carry and

the components used in the device are very featured basing on the new generation with all the before gadgets doesn't have this features. Our main theme is to make this device for women safety and help them in the situations where they don't have an option to contact police, family, and friends. When women feel that they are in emergency situation, for example, traveling at night after office hours and suddenly some situation occurs like someone attacks her in case if she is unable to take her mobile and contact police at that time she can use our device which is connected to the mobile when she turns on the device automatically the device starts working on their functions and grab the pictures, videos, and voice recordings are sent to the police, family, and friends with the help of SOS communication present in their own mobile. This device also works if the victim's phone doesn't have the network in their mobile. Then the police cross check all the pictures, videos, and voice recordings if they see that there is something emergency then the police immediately see the live location and reach the right location to save the woman.

We finally conclude that with the help of this device we can save many women lives. Our main goal is to help women and make them feel secured with the help of this device.

References

1. S. Dhanasekaran, V. Vasudevan, Smart agent system for efficiently monitoring and preventing kidnap activity. *J. Excell. Comput. Sci. Eng.* **4**(2), 1–4 (2018)
2. T. Dey, U. Bhattacharjee, S. Mukherjee, T. Paul, R. Ghoshhajra, Advanced women security app-We R Safe. *Rev. Comput. Sci. Stud.* **4**(2), 47–51 (2017)
3. D. Uma, V. Vishakha, R. Ravina, B. Rinku, An android application for women safety on voice recognition. *Int. J. Comput. Sci. Mob. Comput.* **4**(3), 216–220 (2015)
4. P. Dhiviyabharathi, M. Elamathi, V. Elakiya, V.N. Arumbu, SCIWARS Android app for women safety. *Int. J. Res. Sci. Eng. Technol.* **4**(11), 284–289 (2015)
5. S. Mandapati, S. Pamidi, S. Ambati, A mobile based women safety application-I Safe Apps. *Int. Organ. Sci. Res. J. Comput. Sci. Eng.* **17**(1), 29–34 (January–February, 2015)
6. K. Sharma, M. Anand, Android application for women security system. *Int. J. Adv. Res. Comput. Sci. Eng. Technol.* **5**(3), 725–729 (2016)

A Comparative Analysis of Multi-criteria Decision-Making Techniques to Optimize the Process Parameters in Electro Discharge Machine



J. Anitha and Raja Das

Abstract In today's tremendous competitive market, industrial produce should possess high precision and quality and should be manufactured in minimal time. To obtain these objectives, the input parameters are controlled to attain the desired output depending on the conditions. The process parameters play a substantial role in defining the material removal rate as well as the surface quality. Based on its features, Electro Discharge Machine (EDM) is a striking alternative in the manufacturing industry. The effect of four process parameters (i.e.,) Voltage, Pulse-on-time, Current, Duty Cycle on the performance measures Material Removal Rate (MRR) and Surface Roughness (Ra) are studied based on the experimental results. Multi-Criteria Decision-Making (MCDM) approaches support a decision-maker to pick the best substitute from a set of substitutes where the objectives are differing in nature. To establish the relative importance of the performance measures, entropy method is employed. The weights obtained using entropy method are MRR is 0.34 and for Ra is 0.66. Further, MCDM techniques, namely, MOORA, MULTIMOORA, and TOPSIS are used to attain the optimum process parameters. The optimum values are Pulse-on-time 100 μ s, Voltage 50 V, Current 15 A, and Duty Cycle 50.

Keywords EDM · Surface roughness · Material removal rate · Multi-criteria decision-making methods-MOORA · MULTIMOORA · TOPSIS

1 Introduction

Electro Discharge Machine (EDM) is a non-traditional machining procedure with high potential and can be used successfully in modern industries because of wide range of applications. It is a process which is employed extensively after milling,

J. Anitha (✉)
New Jersey City University, New Jersey, USA
e-mail: anithajandhyala@gmail.com

R. Das
Vellore Institute of Technology, Vellore, India

grinding, and turning. Rigid materials which are quite tough to machine like the titanium alloys, nickel alloys, and hardened steel can be used in this process. EDM process is quite complex, as it is affected by many parameters. To choose higher values of Material Removal Rate with a decent surface finish is quite a difficult task. For higher productivity, MRR should be maximum and for better quality Surface Roughness should be minimum. These two performance measures are contradictory in nature.

A lot of problems in engineering include simultaneous optimization, with differing objectives. Such problems are recognized as Multi-objective optimization problems. The methods to resolve these multi-objective problems according to Jaimes et al. [1] is Multi-Criteria Decision-Making (MCDM). Brauers and Zavadskas [2] first introduced MOORA technique for privatization in transition economy. Brauers et al. solved road design alternatives [3] and contractors ranking [4] using MOORA method. Chakraborty [5] used MOORA method to obtain the solutions of problems in manufacturing industry. MOORA along with standard deviation was employed by Joseph and William [6] to optimize gas metal welding process parameters. Muniappan et al. [7] applied Standard deviation along with MOORA to improve WEDM input parameters. Brauers [8] used MULTIMOORA for application of arms procurement method. Brauers WKM [9] applied this method for a stakeholder society. Karcka et al. [10] employed MULTIMOORA for ranking heating losses in a building.

TOPSIS is a MADM method, presented by Hwang and Yoon [11]. Gadakh [12] used this method to regulate the best parametric combination in WEDM process. Chu [13, 14] changed a vague MADM problem into a crisp one and further applied this method. Chen [15] employed TOPSIS technique for group decision-making in fuzzy condition. Nayak and Mahapatra [16] applied TOPSIS and AHP for optimizing WEDM process parameters. Rao [17] employed this method to several applications like material selection, machinability valuation, and assessment of product design.

Based on the above literature, a considerable amount of work has been done using different MCDM methods, but the relative position of output measures is not considered in most of the papers. The novelty of this paper is to find the relative importance of performance measures like MRR and Ra is found from experimental data using entropy method. In this study, entropy method along with MOORA, MULTIMOORA, TOPSIS methods are used to optimize the input parameters. Entropy technique is used to determine the relative importance of output measures. Later different MCDM methods which are quite simple and easy to calculate are used to choose the best alternative.

2 Experimental Details

- Processing Machine: The experiment is conducted on Electronica Electra plus PS 50ZNC Processing Machine.
- Work-piece material: AISI D2 steel in rectangular shape, thickness of 4 mm, and density 7.7 g/cc (negative polarity).

Table 1 Experimental values of MRR and Ra

Run	I_p	Ton	τ	V	MRR	Ra
1	15	50	83	50	29.163	8.43
2	5	50	50	50	5.18	5.01
3	5	100	83	40	5.245	5.03
4	10	75	83	45	9.356	7.13
5	15	100	83	50	33.11	9.01
6	5	50	83	40	8.872	4.71
7	15	100	50	50	51.09	8.1
8	5	100	50	40	4.349	4.89
9	15	100	50	40	51.004	10.93
10	5	100	83	50	6.972	5.7
11	10	50	75	45	8.074	8.301
12	5	50	83	50	14.12	5.19
13	10	50	75	40	8.14	8.497
14	5	50	50	40	4.606	4.59
15	15	50	50	40	29.737	10.49
16	10	75	50	45	9.25	5.92
17	10	75	75	45	8.796	8.403
18	15	50	50	50	33.103	7.43

- Electrode material: Electrolytic copper 30 mm diameter (positive polarity).
- Di-electric Fluid: A viable grade EDM oil which has a specific gravity of 0.76 and freezing point of 94 °C.
- Flushing technique: Side flushing technique with 0.3 kg f/cm² pressure.

The four process parameters and the experimental results are presented in Table 1.

3 Optimization Techniques

3.1 Entropy Method

For the decision matrix $X = [x_{ij}]_{m \times n}$, the entropy for the i th value is defined as (1)

$$H_i = -1/\ln(m) \sum_{j=1}^n x_{ij} \ln(x_{ij}) \tag{1}$$

for $i = 1, 2, \dots, m$.

The entropy weight for i th indicator is given by (2)

$$w_i = \frac{1 - H_i}{\sum_{i=1}^m 1 - H_i} \tag{2}$$

where $0 \leq w_i \leq 1$ and $\sum_{i=1}^m w_i = 1$.

3.2 MOORA Method

MOORA is one of the MCDM technique which is used to pick the finest alternate from number of alternates. This method was first presented by Brauers [9] to solve complex decision-making problems in the industrial sector. This technique [2, 18–21] commences with a decision matrix that represents various substitutes and objectives.

- Step 1: Describing the problem and defining the objectives is the key step. In the present work, MRR must be maximized and Ra must be minimized.
- Step 2: Create a decision matrix using the experimental values of output measures. In Eq. (3)

$$X = \begin{bmatrix} x_{11} & x_{12} & \cdots & x_{1n} \\ x_{21} & x_{22} & \cdots & x_{2n} \\ \cdot & \cdot & \cdot & \cdot \\ \cdot & \cdot & \cdot & \cdot \\ x_{m1} & x_{m2} & \cdots & x_{mn} \end{bmatrix} \tag{3}$$

- Step 3: The performance of the i th alternate on j th feature is normalized using Eq. (4)

$$x_{ij}^* = \frac{x_{ij}}{\sqrt{\sum_{i=1}^m x_{ij}^2}} \tag{4}$$

where j ranges between 1 and n .

- Step 4: In the multi-objective optimization process, these normalized values are added if it is a case of maximization and subtracted if it is a case of minimization. Hence the optimized values are calculated using the Eq. (5)

$$y_i = \sum_{j=1}^g x_{ij}^* - \sum_{j=g+1}^n x_{ij}^* \tag{5}$$

where g are features which should be maximized, and $(n - g)$ features which should be minimized.

Step 5: To give more significance to features, it is multiplied with corresponding weight. The optimized problem is calculated using Eq. (6)

$$y_i = \sum_{j=1}^g w_j x_{ij}^* - \sum_{j=g+1}^n w_j x_{ij}^* \tag{6}$$

where w_j is the weight of the j th factor, which is found using entropy method.

Step 6: The y_i values can be either positive or negative based on the maximizing and minimizing features in the decision matrix. Rank the values from highest to the lowest. The best alternative is the highest value, and the worst value is the least y_i .

3.3 The Full Multiplicative Form (MULTIMOORA)

Miller and Starr developed this method. The formula is given as

$$U_i = \frac{A_i}{B_i} \tag{7}$$

where $A_i = \prod_{j=1}^g x_{ij}$ and $B_i = \sum_{j=g+1}^n x_{ij}$
 where g and $(n - g)$ are the measures that should be maximized and minimized given to Brauers [22].

3.4 TOPSIS Method

Hwang and Yoon [11] presented this method and it is found to be effective and has practical application.

Step 1: Calculate the normalized values using

$$r_{ij} = \frac{x_{ij}}{\sqrt{\sum_{i=1}^m x_{ij}^2}} \tag{8}$$

x_{ij} is the real value and r_{ij} are the normalized decision values.

Step 2: Compute the relative importance(weight) for the output values. Entropy method is applied to determine the importance of output measures.

Step 3: Calculate the weighted normalized decision values with the formula.

$$V_{ij} = w_j \times r_{ij} \tag{9}$$

w_j is the weight of the j th attribute.

Step 4: Find the positive and negative ideal alternative

$$V^+ = (v_1^+, v_2^+, v_3^+, \dots, v_n^+) \text{ is for highest values} \tag{10}$$

$$V^- = (v_1^-, v_2^-, v_3^-, \dots, v_n^-) \text{ is for lowest values} \tag{11}$$

Step 5: Separation of each value from the positive and negative ideal alternate are computed as

$$S_i^+ = \sqrt{\sum_{j=1}^m (V_{ij} - V_j^+)^2} \tag{12}$$

$$S_i^- = \sqrt{\sum_{j=1}^m (V_{ij} - V_j^-)^2} \tag{13}$$

Step 6: The comparative closeness coefficient for each alternate (CCi) is calculated. Rank the values from highest to lowest.

$$CCi = \frac{S_i^-}{S_i^+ + S_i^-} \tag{14}$$

4 Results and Discussion

4.1 Weights

Entropy weights are calculated in the first step using Eqs. (1) and (2). Tables 2 and 3 present the computation of the entropy weights. The weights obtained for Material Removal Rate are 0.34 and for Surface Roughness are 0.66.

Table 2 Entropy weight calculation

Material removal rate		Surface roughness	
X_{ij}	$X_{ij} \ln(X_{ij})$	X_{ij}	$X_{ij} \ln(X_{ij})$
0.2925	-0.3596	0.2697	-0.35342
0.0520	-0.1536	0.1603	-0.29344
0.0526	-0.1549	0.1609	-0.29397
0.0938	-0.2220	0.2281	-0.33712
0.3321	-0.3661	0.2882	-0.35856
0.0890	-0.2153	0.1507	-0.28517
0.5124	-0.3426	0.2591	-0.34993
0.0436	-0.1366	0.1564	-0.2902
0.5115	-0.3429	0.3496	-0.36742
0.0699	-0.1860	0.1823	-0.31032
0.0810	-0.2035	0.2655	-0.35211
0.1416	-0.2768	0.1660	-0.29812
0.0816	-0.2045	0.2718	-0.35408
0.0462	-0.1420	0.1468	-0.28169
0.2982	-0.3608	0.3356	-0.36642
0.0928	-0.2206	0.1894	-0.31513
0.0882	-0.2142	0.2688	-0.35315
0.3320	-0.3661	0.2377	-0.34151

Table 3 Weights using entropy method

Values	MRR	Ra
H_i	1.5459	2.0419
w_i	0.34	0.66

Table 4 MOORA Method

MRR		Ra		Max-min	Rank
X_{ij}	$w_i X_{ij}$	X_{ij}	$w_i X_{ij}$		
0.2925	0.0994	0.2697	0.1780	-0.0785	7
0.0520	0.0177	0.1603	0.1058	-0.0881	9
0.0526	0.0179	0.1609	0.1062	-0.0883	10
0.0938	0.0319	0.2281	0.1505	-0.1186	14
0.3321	0.1129	0.2882	0.1902	-0.0773	6
0.0890	0.0303	0.1507	0.0994	-0.0692	5
0.5124	0.1742	0.2591	0.1710	0.0032	1
0.0436	0.0148	0.1564	0.1032	-0.0884	11
0.5115	0.1739	0.3496	0.2308	-0.0568	3
0.0699	0.0238	0.1823	0.1203	-0.0966	13
0.0810	0.0275	0.2655	0.1753	-0.1477	17
0.1416	0.0481	0.1660	0.1096	-0.0614	4
0.0816	0.0278	0.2718	0.1794	-0.1516	18
0.0462	0.0157	0.1468	0.0969	-0.0812	8
0.2982	0.1014	0.3356	0.2215	-0.1201	15
0.0928	0.0315	0.1894	0.1250	-0.0934	12
0.0882	0.0300	0.2688	0.1774	-0.1474	16
0.3320	0.1129	0.2377	0.1569	-0.0440	2

4.2 Solutions Using Different Methods

4.2.1 MOORA Results

The normalized decision matrix is found using Eq. (4). Table 4 depicts the ranking using MOORA method, and the calculation is done using Eq. (6). From the table it is evident the first rank is given to run 7 and the worst rank is given to run 13.

4.2.2 MULTIMOORA Results

Using Eq. (7) the values are calculated in MULTIMOORA method and ranks obtained are shown in Table 5. Based on the results run 7 is given the best rank and the worst rank is given to run 8.

Table 5 MULTIMOORA method

MRR	Ra	$U_i = \frac{A_i}{B_i}$	Rank
29.163	8.43	3.4594	5
5.18	5.01	1.0339	14
5.245	5.03	1.0427	13
9.356	7.13	1.3122	10
33.11	9.01	3.6748	4
8.872	4.71	1.8837	8
51.09	8.1	6.3074	1
4.349	4.89	0.8894	18
51.004	10.93	4.6664	2
6.972	5.7	1.2232	11
8.074	8.301	0.9727	16
14.12	5.19	2.7206	7
8.14	8.497	0.9580	17
4.606	4.59	1.0035	15
29.737	10.49	2.8348	6
9.25	5.92	1.5625	9
8.796	8.403	1.0468	13
33.103	7.43	4.4553	3

4.2.3 TOPSIS Results

Table 6 shows the results using TOPSIS method. The positive and negative ideal values are computed using Eqs. (10) and (11). The parting of each value from positive and negative ideal is done using Eqs. (12) and (13). The relative closeness coefficient is computed using Eq. (14). Based on this method run 7 is given the best rank and the worst rank to run 14.

4.3 Comparing the MCDM Methods

Table 7 shows the ranking of results using three different MCDM methods and plotted in Fig. 1.

Spearman’s rank correlation is used to determine the correlation between the MCDM methods. The results are presented in Table 8. The correlation coefficient amid MOORA and MULTIMOORA is higher than others (0.71).

Table 6 TOPSIS method

$w_i X_{ij}$ (MRR)	$w_i X_{ij}$ (Ra)	Si ⁺	Si ⁻	C_i	Rank
0.0994	0.1780	0.0748	0.0811	0.5203	5
0.0177	0.1058	0.1565	0.0089	0.0537	15
0.0179	0.1062	0.1563	0.0093	0.0562	14
0.0319	0.1505	0.1423	0.0536	0.2738	10
0.1129	0.1902	0.0613	0.0933	0.6036	4
0.0303	0.0994	0.1439	0.0025	0.0174	17
0.1742	0.1710	0.0000	0.0741	0.9998	1
0.0148	0.1032	0.1594	0.0063	0.0383	16
0.1739	0.2308	0.0003	0.1339	0.9979	2
0.0238	0.1203	0.1504	0.0234	0.1348	12
0.0275	0.1753	0.1467	0.0784	0.3482	9
0.0481	0.1096	0.1261	0.0127	0.0914	13
0.0278	0.1794	0.1464	0.0825	0.3603	7
0.0157	0.0969	0.1585	0.0000	0.0001	18
0.1014	0.2215	0.0728	0.1246	0.6312	3
0.0315	0.1250	0.1427	0.0281	0.1645	11
0.0300	0.1774	0.1442	0.0805	0.3583	8
0.1129	0.1569	0.0613	0.0600	0.4944	6

5 Conclusion

In this study, the optimum values of input parameters are selected using three different MCDM methods. The relative importance of performance measures is calculated using entropy method. Eighteen different combinations of process parameters were considered. The different alternatives were analyzed and ranked using MOORA, MULTIMOORA, and TOPSIS methods. Later, Spearman's rank correlation is applied to compare the association between different MCDM methods, and the outcomes exhibited a good correlation among the methods.

Table 7 Ranking of alternatives using different methods

Run	MOORA	MULTIMOORA	TOPSIS
1	7	5	5
2	9	14	15
3	10	13	14
4	14	10	10
5	6	4	4
6	5	8	17
7	1	1	1
8	11	18	16
9	3	2	2
10	13	11	12
11	17	16	9
12	4	7	13
13	18	17	7
14	8	15	18
15	15	6	3
16	12	9	11
17	16	13	8
18	2	3	6

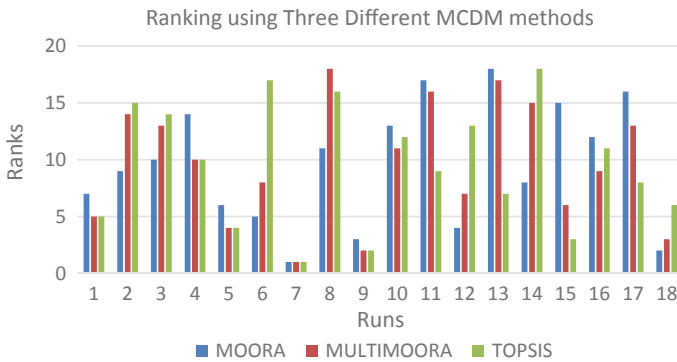


Fig. 1 Ranking using three different MCDM methods

Table 8 Correlation between different MCDM methods

MCDM Methods	MOORA	MULTIMOORA	TOPSIS
MOORA	–	0.71	0.13
MULTIMOORA	–	–	0.66
TOPSIS	–	–	–

References

1. A.L. Jaimes, S.Z. Martinez, C.A.C. Coello, An introduction to multi-objective optimization techniques, in *Optimization in Polymer processing*, ed. by A. Gaspar-Cunha, J.A. Covas (Nova Science Publishers, New York, 2011), pp. 29–57
2. W.K.M. Brauers, E.K. Zavadskas, The MOORA method and its applications to privatization in some transition economy. *Control Cybern.* **35**, 445–469 (2006)
3. W.K.M. Brauers, E.K. Zavadskas, F. Pedschus, Z. Turkis, Multi-objective decision making for road design. *Transport* **23**, 183–193 (2008)
4. W.K.M. Brauers, E.K. Zavadskas, Turkis, T. Viutiene, Multi-objective contractors ranking by applying the MOORA method. *J. Bus. Econ. Manage.* **9**, 245–255 (2008a)
5. S. Chakraborty, Applications of the MOORA method for decision making in manufacturing environment. *Int. J. Adv. Manuf. Technol.* **54**(9–12), 1155–1166 (2011)
6. J. Achebo, W.E. Odinikuku, Optimization of gas metal arc welding process parameters using standard deviation and MOORA. *J. Miner. Mater. Charact. Eng.* **2**, 298–308 (2015)
7. A. Muniappan, J.A. Raj, V. Jaykumar, R.S. Prakash, R. Sathyaraj, Optimization of WEDM process parameters using standard deviation and MOORA method. In: *2nd International conference on advances in Mechanical Engineering (ICAME)* (2018)
8. W.K.M. Brauers, The multiplicative representation for multiple objectives optimization with an application for arms procurement. *Nav. Res. Log.* **49**, 327–340 (2002)
9. W.K.M. Brauers, *Optimization Methods for a Stakeholder Society. A Revolution in Economic Thinking by Multiobjective Optimization: Non-convex Optimization and Its Applications*. Kluwer Academic Publishers, Boston, USA (2004)
10. M. Karcka, W.K.M. Brauers, E.K. Zavadskas, Ranking heating losses in a building by applying the MULTIMOORA. *Eng. Econ.* **21**(4), 352–359 (2010)
11. C.L. Hwang, K. Yoon, *Multiple attribute decision making, a state-of-the-art survey* (Springer, New York, 1981)
12. V.S. Gadakh, Parametric optimization of wire electric discharge machining using TOPSIS method. *Adv. Prod. Eng. Manage.* **7**(4), 157–164 (2012)
13. T.C. Chu, Facility location selection using fuzzy TOPSIS under group decisions. *Int. J. Uncertain. (Fuzziness and Knowledge-Based Systems)* **10**, 687–701 (2002)
14. T.C. Chu, Selecting plant location via a fuzzy TOPSIS approach. *Int. J. Adv. Manuf. Technol.* **20**, 859–864 (2002)
15. C.T. Chen, Extension of the TOPSIS for group decision-making under fuzzy environment. *Fuzzy Sets Syst.* 1141–1149 (2000)
16. B.B. Nayak, S.S. Mahapatra, Multi-response optimization of WEDM process parameters using the AHP and TOPSIS method. *Int. J. Theor. Appl. Res. Mech. Eng.* **2**(3), 109–115 (2013)
17. R.V. Rao, *Decision making in the manufacturing environment using graph theory and fuzzy multiple attribute decision making methods* (Springer, London, 2007)
18. W.K.M. Brauers, E.K. Zavadskas, Multi-objective optimization with discrete alternatives on the basis of ratio analysis. *Intellect. Econ.* **2**(6), 30–41 (2009)
19. W.K.M. Brauers, E.K. Zavadskas, Robustness of the multiobjective MOORA method with a test for the facilities sector. *Technol. Econ. Dev. Econ. Balt. J. Sustain.* **15**(2), 352–375 (2009)
20. D. Kalibatás, Z. Turskis, Multicriteria evaluation of inner climate by using MOORA method. *Inf. Technol. Con.* **37**, 79–83 (2008)
21. F.A. Lootsma, *Multicriteria decision analysis via ratio and difference judgement* (Springer, London, 1999)
22. W.K.M. Brauers, E.K. Zavadskas, Robustness of MULTIMOORA; a method for multi-objective optimization. *Informatica* **23**(1), 1–25 (2012)

Studies on Customized Compression Bandage Materials for Healing Injured Part



S. Sreenatha Reddy, R. Dhanasekaran, M. Srihari, Sirgripet Sai Kiran, S. Kalyan, and T. Anvesh Kumar

Abstract Aim of the paper is to cure the swelling of a body part with the help of compression bandages which are made with different fibers. Some of the natural and synthetic fiber materials are used for compression bandages that is cotton, viscose, Lycra, polyester, nylon, and latex. The main property of compression bandage is its flexibility. Compression bandage is mainly used for curing the Venous Leg Ulcers. Swelling is caused due to the clotting of the blood in body part; in order to heal the clot effectively compression bandage is used. Compression bandage assist veins to transfer the de-oxygenated blood to the ventricle by providing pressure to the part which is swollen. The present problem faced by using the compression bandage is severe pain at the injured area due to the fluctuated pressure applied by the clinician. Even skilled clinician applies the compression bandage but it gets severe pain to the patient caused by the uneven pressure applied. Uneven distribution of the pressure may also leads the swelling to chronic stage. In order to reduce the problems faced due to fluctuating pressure, sensor is used in combination with compression bandage. So that the semi-skilled nurse can also apply the bandage effectively and efficiently. This paper concentrates on bandages which are arranged in combination with sensor in order to minimize the problems faced due to uneven pressure.

Keywords Compression bandage · Viscose · Lycra · Pressure sensor · Oedema (blood clot)

S. Sreenatha Reddy · R. Dhanasekaran · M. Srihari · S. Sai Kiran (✉) · S. Kalyan · T. Anvesh Kumar

Department of Mechanical Engineering, Guru Nanak Institute of Technology, Hyderabad, Telangana, India

e-mail: sirgripet.saikiran@gmail.com

S. Kalyan

e-mail: kalyansamala46@gmail.com

T. Anvesh Kumar

e-mail: anveshthokala818@gmail.com

© Springer Nature Singapore Pte Ltd. 2021

G. S. V. L. Narasimham et al. (eds.), *Recent Trends in Mechanical Engineering*,

Lecture Notes in Mechanical Engineering,

https://doi.org/10.1007/978-981-15-7557-0_57

1 Introduction

Swelling is a puffiness obtained due to the accumulation of blood in the body tissues. It may occur at any part of the body. Swelling or edema is cured using the compression bandage which is effective in healing. Swelling causes due to the blood clot in the injured part. And to cure the swollen part the compression bandages were used with definite shapes and structures depending on the swollen area. Acute swelling can be cured naturally by home remedies. For effective treatment the compression bandages are made of natural fibers and synthetic fibers. While using these combinations of fibers it gives quick healing to the swollen area. The natural fibers are available cheaply and it won't harm environment which means that those are biodegradable.

The healing of the swollen part depends on the circumference of the limb, i.e., shape of the limb indirectly affect the rate of healing and shape of limb may not be in exact circular but it is like in elliptical shape. For these reason, the pressure induced in the limb is uneven for elliptical shape [1]. The pressure induced between the limb and bandage while wrapping leads to cure the thrombosis and pass the blood through veins to heart.

These are the types of swelling/edema. They are Peripheral edema, Pulmonary edema, Cerebral edema, and Macular edema.

2 Literature Review

A bandage is a material used for supporting a medical splint as well as to restrict the body part. Bandaging is a process of protecting an injured part from contaminants or bacteria present in environment. It is also used for providing support to bruised part. [2] Compression bandages are used for curing Venous leg ulcers, lymphorrhoea, imbalance in limb shapes, swollen limbs, etc. some of the types of compression bandages are short-stretch bandage (non-elastic) and long-stretch bandage (elastic). The bandages which have extensibility less than 100% are called short-stretch bandages and having extensibility more than 100% are called long-stretch bandages [2]. Depending on the pressure bandages are classified as follows.

1. Light compression bandages (14–17) mm of Hg
2. Moderate compression bandages (18–24) mm of Hg
3. High compression bandages (25–35) mm of Hg
4. 3D-Spacer compression bandages (up to 60) mm of Hg.

The following materials are used in fabrication of bandages wool, jute, nylon/spandex, cotton gauze, viscose, polyamide, elastomeric yarns, polyester, polypropylene, polyurethane forms, spun or filament yarns, etc.

These are mechanical properties required for compression bandage (as shown in Table 1) are elasticity, durability, rigidity, stiffness, reliability, and fabric fatigue.

Table 1 Materials and their properties

Materials/properties	Elasticity	Stiffness	Resilience	Absorbency	Durability	Melting point (0c)
Cotton						149
Jute						170
Wool						No MP
Nylon						269
Polyester						295
Viscose						>150
Elastomeric yarns						>70
Polymide						250

	It indicates that it has a specific property
	It indicates that it has no specific property
	It indicates that it has low capability in that property

2.1 Behavior of Cotton, Viscose, and Lycra

The color of cotton may be white, yellow, bluish-white. The tensile strength of cotton may be 3.5 gm/den. The strength of cotton is greatly affected by its moisture. The wet strength of cotton is 22% higher than the dry strength. If 2% extension is done it has its elastic recovery of 75% and if 5% extension is done then it has an elastic recovery of 45%. Age of the cotton does not affect its strength if it is stored carefully. If cotton is exposed to sunlight it will lose its strength slowly and it will be turned into yellow. If cotton is heated under a temperature of 1200 °C there by it starts to change its color into yellow and if heat is increased up to 2400 °C then it will be completely burnt in air. Fabrics made of cotton are free from laundering.

Viscose is a natural fiber which is extracted from cellulosic fiber which comes from wood pulp, agricultural products, and cotton. Composition of NaOH and other chemicals with cellulosic fiber gives the viscose fiber. When compared to other fibers, viscose is greatly affected by its moisture and thus quality of the bandage will be reduced. Its properties can be increased by adding different compositions to the viscose. Some of the properties are strength, elasticity, and water resistant.

Lycra is a synthetic fiber which has a good elasticity property up to 500% without any failure. It can resist over a heat of 1490 °C. It has melting point of above 2600 °C. It has a poor capability of resistance to bleaching.

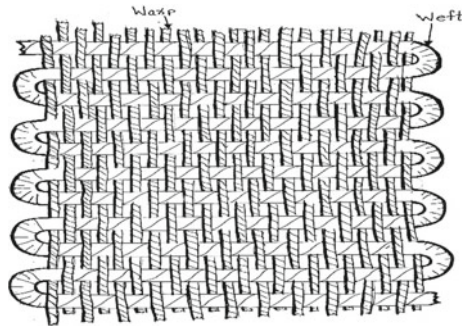
3 Methodology

Fabrication process is two types mainly woven and non-woven [8].

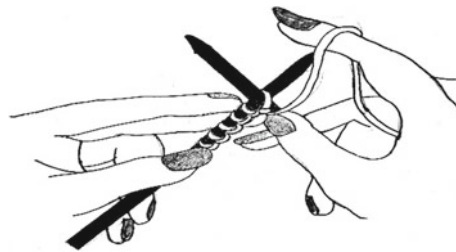
The following are the woven techniques (shown in Fig. 1):

- Weaving
- Knitting
- Electrospinning
- Embroidery technique.

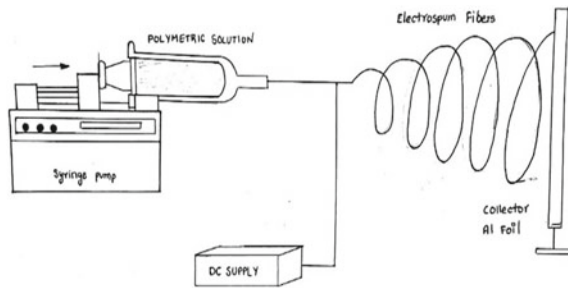
Fig. 1 Fabrication processes



(a) Weaving



(b) Knitting



(c) Electro spinning

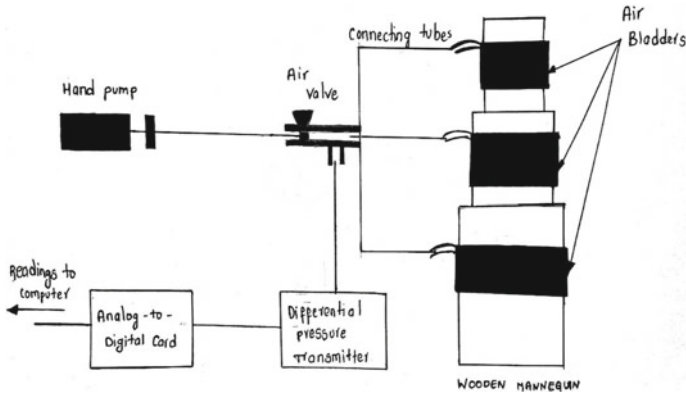


Fig. 2 Pressure interface measurement setup

3.1 Interface Pressure Measurement Using Wooden Leg

The pressure is developed between the bandage and prototype surface as shown in Fig. 2. Pneumatic principle is used on prototype, i.e., air bladders are used for increasing the pressure in the bandage, i.e., firstly air bladders are fitted on the wooden leg and then bandages are fixed on the air bladders. Tubes are connected in between the air bladders and air valve in order to supply the air for bladders as shown in Fig. 2. In order to determine the interface pressure firstly the initial pressure is noted and then pneumatic pressure is applied and then final pressure is noted and the difference between the initial and final pressure gives the interface pressure [3].

3.2 Effect of Bandage Thickness on Interface Pressure

Generally, Bandage thickness is not considered by clinician in order to apply the CB. If thickness is considered the interface pressure will be accurate and if thickness is not considered the interface pressure will be approximate. Both the pressures are compared in order to estimate the sub-bandage pressure. In advanced techniques finite element analysis is used, in order to estimate the pressure of compression bandages with limb. In order to estimate the theoretical pressure De Bruyne and Dvorak have used trigonometric equations and Thomas used Laplace law to estimate the theoretical pressure [4]. It states that “the pressure exerted in the compression bandage is directly proportional to tension in the compression bandage and no. of layers and inversely proportional to circumference area and width”.

3.3 *Effect of Thread Density on Compression Bandage*

Thread density means that no. of threads per unit length on a garment. If thread density is more, then the rate of pressure reduction will be less [6]. An experiment was conducted to know the rate of variation of pressure over thread density. Two different bandages were taken which are fabricated by knitting technique and having different thread densities. These bandages are used to test the fluctuations of pressure over time. It was found that bandages made of viscose and cotton have more rate of pressure reduction and bandages consisting of elastomeric yarns have less rate of pressure reduction [6].

3.4 *Effect of Cyclic Loads on Compression Bandage*

Bandages made of cotton, viscose, and elastomeric yarns were taken for determining the stress over time under repeated loads. Tests were conducted on Roell universal testing machine and height of ± 5 mm is given for load and a frequency of one cycle per second is carried out throughout the test. The stress developed at 5 mm extension was considered for analyzing the stress variation and it was found that bandages made of cotton and viscose yarns have more stress reduction over time and bandages consisting of elastomeric yarns have less stress reduction over time [6].

3.5 *Tension Test Conducted on Testometric Instrument*

Tension test is conducted on the cotton bandage and pressure is obtained by Laplace equation according to ankle position and mid-calf position. Load is applied based on the layers (two or three layers). An extension of 70% and load of 13 N is applied and found that 47.91 mm of Hg of pressure is found in two layers and 71.87 mm of Hg of pressure in three layers in ankle position, respectively, whereas 31.51 mm of Hg of pressure is found in two layers and 47.25 mm of Hg of pressure is found in three layers in mid-calf position, respectively [7].

Laplace law equation

$$P(\text{mm of Hg}) = \frac{T(N) \times n}{R(m) \times W(m)} \times 0.0075$$

It states that the pressure is directly proportional to tension in the bandage and number of layers and it also states that pressure is inversely proportional to radius of limb and width of the bandage.

4 Discussion

We propose creep bandage which is manufactured in combination with sensors which helps in indicating perfect pressures. A sensor is a device which detects the parameters like pressure, temperature, etc. It converts parameters into electrical signals and displays numerical values on the monitor which are in the form of waves. In biomedical applications, the pressure sensors are used to detect the pressure between the body and bandage. Sensors are used in order to observe the safety of parameters (pressure, temperature, etc.). Different sensors are used in biomedical such as breath analyzers, respiration pulse oximeters, blood pressure sensing devices etc. Some of the advantages by using the sensors are it will be highly accurate, and the system is simple in analyzing and it will be cheaply available in market [5].

Since pressure is not applied evenly on the body part even though pressure is applied by experts. If it is not applied perfectly, it may lead to increase the swell or the rate of healing may be decreased depending on the pressure applied. So, in this paper pressure sensor is used in combination with compression bandage in order to warn the pressure applied [5].

Bandages made of cotton, viscose, and elastomeric yarns are having less stress reduction. Thread density means that no. of threads per unit length on a garment. If thread density is more, then the rate of pressure reduction will be less. If thickness is considered the interface pressure will be accurate and if thickness is not considered the interface pressure will be approximate. So if pressure sensor is used in combination with compression bandage in order to warn the pressure applied.

5 Conclusion

Compression bandage acts as a main role in treating the swollen limbs and it can be used to reduce a swollen area which depends on interface pressure induced between the bandage and swollen part. Proper skill is required in order to apply the pressure on the swollen part. Different compositions of the fibers are used in fabrication of compression bandage for immediate healing, for example, Natural and synthetic fibers with some chemical composition. It can be used for curing the acute and chronic diseases. Compression bandage cures swollen limbs based on bandage properties and its behavior. the compression bandages are effectively used to reduce the swollen limbs. Theoretical pressure at different positions (ankle, knee and mid-calf) can be calculated by using Laplace equation. Thickness of the bandage should be considered for accurate pressures. In order to reduce the pressure reduction more thread density should be given. For more accuracy, compression bandage consisting of elastomeric yarns with high-thread density is used with sensors for indicating pressure ranges.

References

1. M. Todd (2011) Compression bandaging, types and skills used in practical applications. *J. Br. J. Nurs.* **20**, 681–682, 684, 686–687 (2011)
2. S. Rajendran, S.C. Anand, Advanced textiles for wound compression. *J. Adv. Text. Wound Care*, 153–178 (2009)
3. B. Kumar, A. Das, R. Alagirusamy, Effect of materials and structure of compression bandage on interface pressure variation over time. *J. Phlebol.* **26**, 376–385 (2014)
4. J. Al Khaburi, A. Abbas, E.A. Dehghani-sanji, J.H. Nelson, Effect of bandage thickness on interface pressure applied by compression bandages. *J. Med. Eng. Phys.* **34**, 378–385 (2012)
5. Y. Xiong, X. Tao, Compression bandage for medical therapy and sports. *J. Polymers.* **10**, 663 (2018)
6. B. Kumar, A. Das, R. Alagirusamy, Study of the effect of composition and construction of materials on sub-bandage pressure during dynamic loading of a limb in vitro. *J. Biorhelo.* **50**, 83–94 (2013)
7. A.R. Aboalasaad, B.K. Sirková, Z. Ahmad, Influence of tensile stress on woven compression bandage structure and porosity. *AUTEX Res. J.* (2019)
8. E. Ramazan, Advances in fabric structures for wound care. *J. Adv. Text. Wound Care* 509–540 (2019)

Investigation on Effect of Industrial Waste on Tribological Properties of Polymer Composites



V. L. Raja, K. Muralidharan, S. Lakshman Kumar, and K. Shanmugavel

Abstract Particulate-filled polymer composites for various industrial and domestic tribological applications have become a domain of interest for researchers in recent times. Conventional fillers have been replaced by by-products and nano-sized fillers and the performance enhancement of the composites is being evaluated. In this study, fly ash, a by-product of coal combustion process, was used as filler from the perspective of reusing waste material that otherwise would cause pollution due to landfilling. It was reinforced into the Nylon 66 matrix in various weight fractions of 5, 10, 15, 20, and 25%. The wear tests were conducted at three sliding velocities of 2, 4, and 6 m/s at three normal loads of 25, 50, and 75 N; and at a constant sliding distance of 5000 m. Scanning electron microscopic observations were used to understand the wear mechanisms.

Keywords Nylon · Fly ash · Wear · Particulate reinforcement

1 Introduction

Nylon 66 has been preferred as an alternate material for metals in various engineering and domestic applications such as gears, friction pads, and sleeve bushes. Various researches have been carried out on replacing the metal parts with particulate-reinforced Nylon 66 composites for applications that involve tribological environment.

While studying the effect of varying injection parameters on the tribological properties of Nylon 66, Apichartpattanasiri et al. [1] found that at high slip ratio, the effect of processing parameters was different in initial stages but was same in

V. L. Raja (✉)

Department of Mechanical Engineering, Muthayammal Engineering College, Rasipuram,
Tamil Nadu 637408, India
e-mail: vlraja73@gmail.com

K. Muralidharan · S. Lakshman Kumar · K. Shanmugavel

Department of Mechanical Engineering, Sona College of Technology, Salem, Tamil Nadu
636005, India

© Springer Nature Singapore Pte Ltd. 2021

G. S. V. L. Narasimham et al. (eds.), *Recent Trends in Mechanical Engineering*,
Lecture Notes in Mechanical Engineering,
https://doi.org/10.1007/978-981-15-7557-0_58

695

the final stages. But it was insignificant at low slip ratios. Suresha et al. [2] used graphites, nanoclay, and short carbon fiber as reinforcement in Nylon 66 to enhance the properties of the matrix. Ravi Kumar et al. [3] found that when nanoclay and short carbon fiber were mixed in Nylon 66 and polypropylene blends, the wear volume and specific wear also increased. Yu et al. [4] found that rubber mixed with polyamide 66 reduced the wear rate at various normal loads and the main mechanisms involved were microplothing and plastic deformation.

Fly ash is becoming a significant filler used in all types of matrixes. When fly ash was reinforced along with graphite by Venkat Prasat et al. [5], aluminum matrix showed enhanced wear resistance. Fly ash increased the mechanical and heat-resistant properties of Nylon 6 and the increase was found to be more when large-sized particles were used by Bose and Mahanwar [6]. But Sharma and Mahanwar [7] in their study found that small-sized fly ash particles were more effective than large-sized particles in enhancing mechanical and electrical properties of recycled polyethylene terephthalate (RPET) matrix. In a study, Chauhan et al. [8] found that wear resistance of vinyl ester increased by the addition of fly ash. Veeresh Kumar et al. [9] found that to achieve maximum wear resistance, proper interfacial adhesion between the matrix and the particulates is essential. Chand and Vashishtha [10] found that thermal stability of polypropylene/polymethyl methacrylate (PP/PMMA) blend increased when fly ash was incorporated in it. Parvaiz et al. [11] found the tensile modulus of polyetheretherketone (PEEK) had increased on the addition of fly ash.

From the literature review, it is evident that studies on wear characteristics of fly ash-filled Nylon 66 are scarce. In this study, an attempt has been made to find out the wear properties of Nylon 66 reinforced with fly ash.

2 Experimental Procedures

The materials used and the sample preparation are explained elsewhere [12, 13]. The experimental procedures, preparation of the samples for the tests, the formulas used for output calculation were same as explained in previous studies [13] except the test parameters. The tests were performed at three sliding velocities of 2, 4, and 6 m/s and at three normal loads of 25, 50, and 75 N. The sliding distance was kept constant as 5000 m for all tests.

3 Result and Discussion

3.1 Effect of Filler Concentration

Figures 1, 2, 3, 4, 5, and 6 show the effect of fly ash concentration on the wear rate of the composites at various loads and various speeds. The wear rate of the unfilled

Fig. 1 Effect of filler concentration on specific wear rate at 25 N normal load

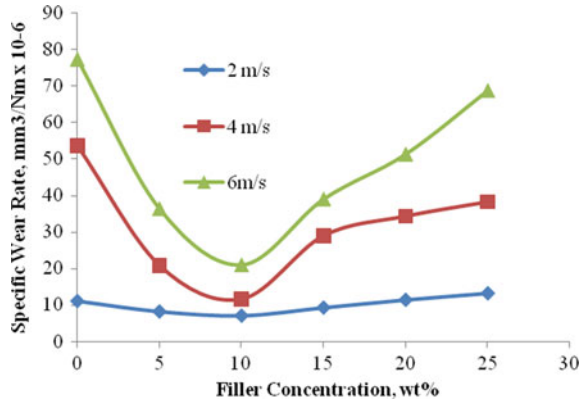


Fig. 2 Effect of filler concentration on specific wear rate at 50 N normal load

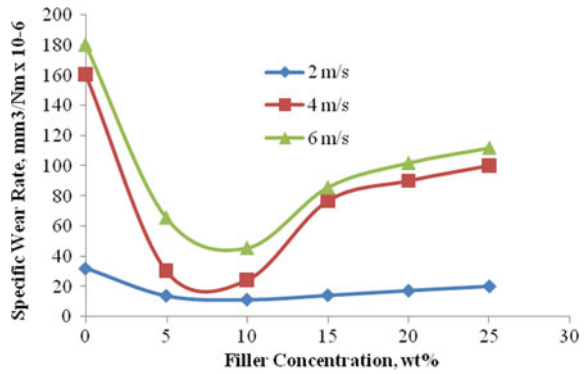
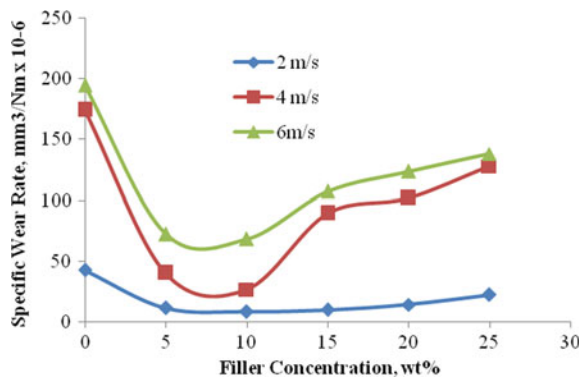


Fig. 3 Effect of filler concentration on specific wear rate at 75 N normal load



Nylon is higher than the other composites in all tested parameters. The wear rate decreases for the addition of 5% wt. fraction of fly ash and it further decreases with further addition of fly ash up to 10% wt. fraction. But as the filler concentration

Fig. 4 Effect of filler concentration on specific wear rate at 2 m/s sliding velocity

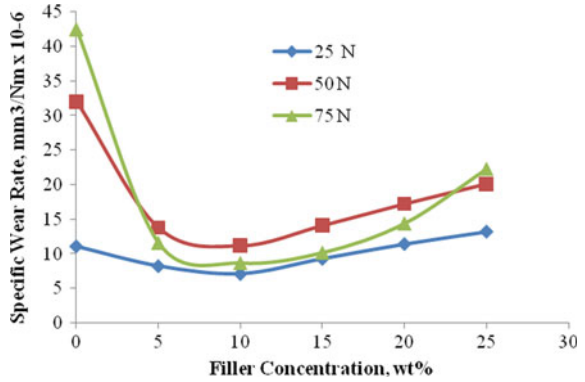


Fig. 5 Effect of filler concentration on specific wear rate at 4 m/s sliding velocity

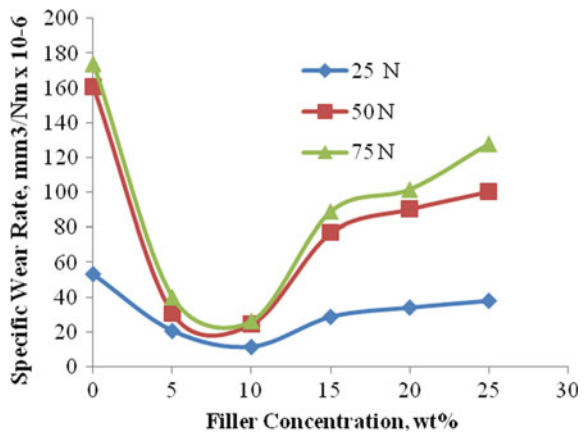
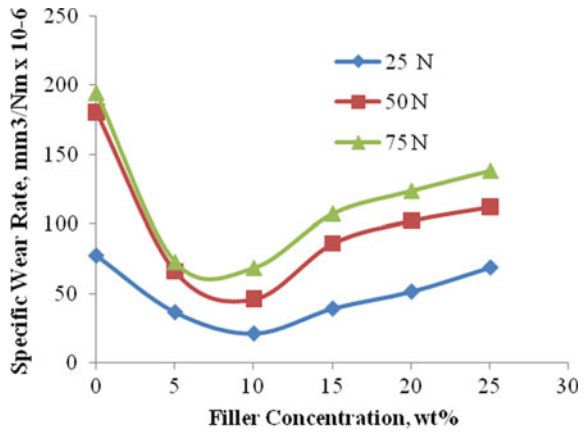


Fig. 6 Effect of filler concentration on specific wear rate at 6 m/s sliding velocity



is increased further, the wear rate starts to increase. Hence 10% weight fraction is the optimum level of reinforcement of the pure nylon. Since the wear rate of pure Nylon is higher than fly ash filled Nylon, it is obvious that the fly ash is reducing the wear rate of Nylon. But, the reinforcement of fly ash is inefficient after 10% weight fraction due to various reasons such as agglomeration of reinforced particles [14], high load, and high velocity which creates the crack propagation easily.

The nonlinearity that is seen in the graphical images is due to the various factors that influence the wear phenomenon in materials. The difference between the wear rates at low normal load and low sliding velocity is significantly higher than the wear rates at high normal loads and high sliding velocities. The phenomenon could be understood by analyzing the effect of load and sliding velocity on the wear rate separately.

3.2 Effect of Normal Load

Figures 7, 8, and 9 show the effect of normal load on the wear rate of the composites at different sliding velocities. The common behavior of the composites that could be noted from the graphs is that the wear rate increases with the increase in load, except for few composites at low sliding velocity. Similar behavior of polymer composites is found in literature [15]. While sliding at low velocity and low load, the material is not removed entirely but it is displaced toward the circumference of the pin and ridges are formed. The heat generated in these testing conditions or the friction force acting on the pin is not enough to pull out the reinforcement from the matrix. But again, at high sliding velocity combined with high normal load, the wear rate goes on increasing with the increase in load. However, while comparing the increase of wear rate from lower load to intermediate load and from intermediate load to higher load, it found that it is comparatively less. This behavior could be attributed to the principle of transfer film formation. Also it is seen that the wear rate of pure Nylon is entirely higher than that of fly ash-filled Nylon composites. Also at higher sliding

Fig. 7 Effect of normal load on specific wear rate at 2 m/s sliding velocity

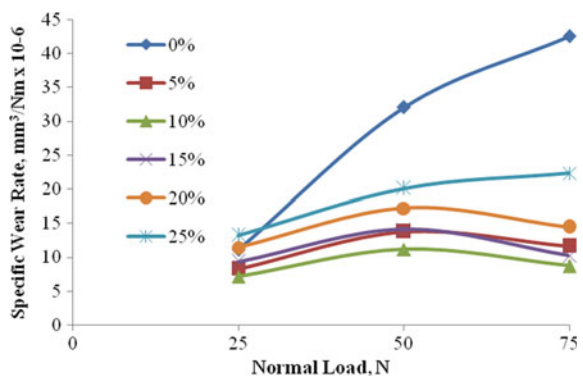


Fig. 8 Effect of normal load on specific wear rate at 4 m/s sliding velocity

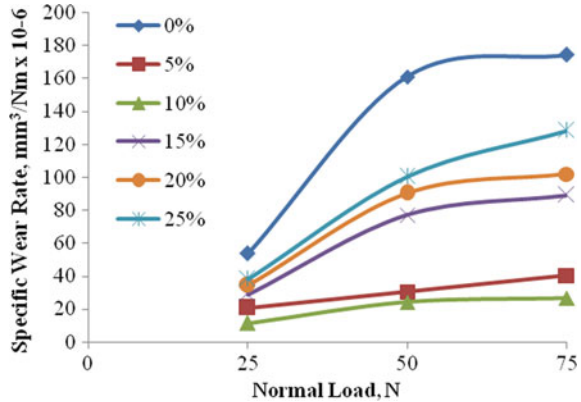
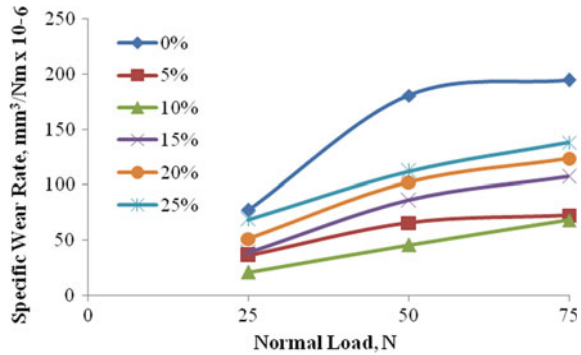


Fig. 9 Effect of normal load on specific wear rate at 6 m/s sliding velocity



velocities, the effect of load on pure Nylon is very high, such that its wear rate increases drastically with the increase in load. This is due to Nylon being a poor conductor of heat [16]. However, in the fly ash-filled Nylon composites, the wear rate increases gradually. This is due to the ability of fly ash particles to increase the heat-withstanding ability of the matrix, which in turn reduces the wear rate [12].

3.3 Effect of Sliding Velocity

Figures 10, 11 and 12 show the behavior of the wear rate of composites with respect to the sliding velocity at different normal loads. From the graphs, the effect of velocity is found to be more than that of the load on the composites. This is evident from the fact that the wear rate increases with the increase in velocity, in all the composites, unlike in the wear rate versus normal load graphs where some of the composites exhibit a behavior of reduction in wear rate with the additional increase in load. The second observation that could be made from the graphical images is that the wear rates of

Fig. 10 Effect of sliding velocity on specific wear rate at normal load 25N

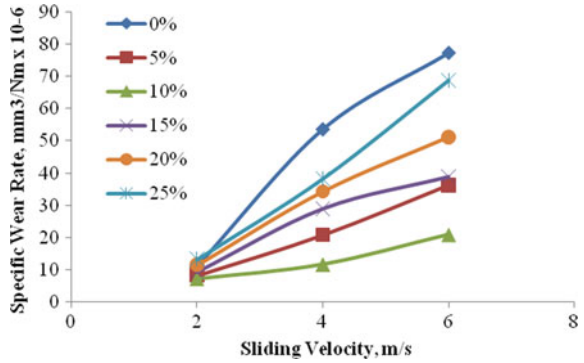


Fig. 11 Effect of sliding velocity on specific wear rate at normal load 50N

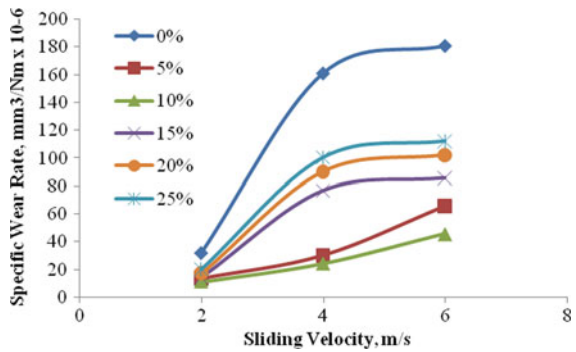
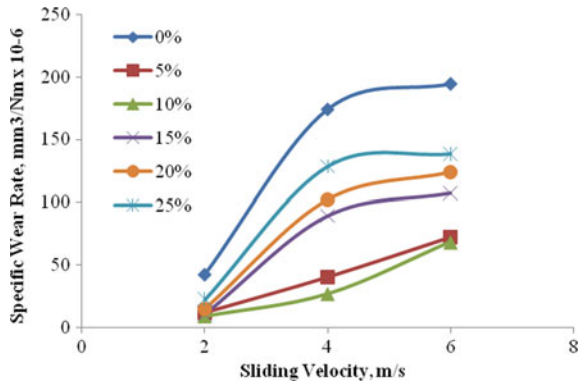


Fig. 12 Effect of sliding velocity on specific wear rate at normal load 75N



composites with 5 and 10% wt. fraction of fly ash is lesser than other composites, which lie entirely in higher zone. This is due to the breakup of matrix material when the heat generated is high due to the high normal load and high sliding velocity. At this level of heat generation, the matrix material could not hold the reinforcement and due to its high melting, it releases the material and subsequently high wear rate

is found. In the previous study, at lower normal load and sliding velocity, it was found that 15% wt. fraction reinforcement improved the wear resistance of Nylon higher than other proportions of reinforcement. This behavior could be attributed to the formation of transfer film on the sliding surface [17], which depends on many factors such as filler type, their amount of concentration in the matrix, velocity and load applied, and heat generated due to these variables. The transfer films play an important role in the decrease of wear rate, but it is not clear why transfer films are selectively formed [18].

4 Conclusion

Nylon 66 was reinforced with fly ash in different weight fractions from 5 to 25% in steps of 5%. The wear tests were conducted at three velocities and three normal loads keeping the sliding distance constant

1. Nylon reinforced with 10% weight fraction of fly ash showed high increase in wear resistance compared to all other composites in all testing conditions. Hence, 10% weight fraction was found to be the optimum filler weight percentage.
2. Wear resistance of 10% fly ash-filled Nylon was increased by a minimum of 60% to a maximum of 95% compared to that of pure Nylon.
3. At 2 m/s velocity and 25 N normal load, filler concentration did not have significant impact on the wear rate. The wear rates of the composites were more or less same.
4. Increase in load increased the wear rate, except for few composites at low sliding velocity.
5. Increase in the sliding velocity increased the wear rate for all composites.
6. Increase in wear rate with the increase in velocity was more than that with the increase in load.

References

1. S. Apichartpattanasiri, J.N. Hay, S.N. Kukureka, A study of the tribological behaviour of polyamide 66 with varying injection-moulding parameters. *Wear* **251**, 1557–1566 (2001)
2. B. Suresha, B.N. Ravi Kumar, M. Venkataramareddy, T. Jayaraju, Role of micro/nano fillers on mechanical and tribological properties of polyamide 66/polypropylene composites. *Mater. Des.* **3**, 1993–2000 (2010)
3. B.N. Ravi Kumar, B. Suresha, M. Venkataramareddy, Effect of particulate fillers on mechanical and abrasive wear behavior of polyamide 66/polypropylene nanocomposites. *Mater. Des.* **30**, 3852–3858 (2009)
4. S. Yu, H. Hua, J. Yin, Effect of rubber on tribological behaviors of polyamide 66 under dry and water lubricated sliding. *Wear* **265**, 361–366 (2008)

5. S. Venkat Prasat, N. Radhika, B. Anandavel, L. Arun, N. Praveen, Influence of parameters on the dry sliding wear behavior of aluminium/fly ash/graphite hybrid metal matrix composites. *Eur. J. Sci. Res.* **53**, 280–290 (2011)
6. K. Sathish Kumar, R. Dhanasekaran, G. Venkatachalam, A. Kumaravel, Microstructure, hardness and tensile properties of Al 7%, Si 0.35%, Mg aluminum alloy. *Int. J. Adv. Technol. Eng. Sci.* **03**(01), 1235–1239 (2015)
7. A.K. Sharma, P.A. Mahanwar, Effect of particle size of fly ash on recycled poly(ethylene terephthalate)/fly ash composites. *Int. J. Plast. Tech.* **14**, 53–64 (2010)
8. S.R. Chauhan, A. Kumar, I. Singh, P. Kumar, Effect of fly ash content on friction and dry sliding wear behavior of glass fiber reinforced polymer composites—a Taguchi approach. *J. Miner. Mater. Charact. Eng.* **9**, 365–387 (2010)
9. G.B. Veeresh Kumar, C.S.P. Rao, N. Selvaraj, Mechanical and tribological behavior of particulate reinforced aluminum metal matrix composites—a review. *J. Miner. Mater. Charact. Eng.* **10**, 59–91 (2011)
10. N. Chand, S.R. Vashishtha, Development, structure and strength properties of PP/PMMA/FA blends'. *Bull. Mater. Sci.* **23**, 103–107 (2000)
11. M.R. Parvaiz, S. Mohanty, S.K. Nayak, P.A. Mahanwar, Polyetheretherketone (PEEK) composites reinforced with fly ash and mica. *J. Miner. Mater. Charact. Eng.* **9**, 25–41 (2010)
12. V.L. Raja, A. Kumaravel, M. Ramesh, A. Karthikeyan (2013) Effective utilization of industrial waste (fly ash) to enhance the properties of polymer composites for mechanical components. *J. Ind. Pollut. Control* **29**(1), 65–71 (2013)
13. V.L. Raja, A. Kumaravel, Comparative study on the wear properties of fly ash and silica fume filled nylon composites. *App. Mech. Mat.* **592–594**, 1277–1284 (2014)
14. V.L. Raja, A. Kumaravel, Studies on physical and mechanical properties of silica fume filled polymer composites for mechanical components. *Polym. Polym. Comp.* **23**(6), 427–434 (2015)
15. B.R. Raju, R.P. Swamy, B. Suresha, K.N. Bharath, The effect of silicon dioxide filler on the wear resistance of glass fabric reinforced epoxy composites. *Adv. Polym. Sci. Tech.* **2**, 51–57 (2012)
16. J. Li, Y.C. Xia, The friction and wear properties of thermoplastic PA6 composites filled with carbon fiber. *J. Thermplast. Comp. Mater.* **23**, 337–349 (2010)
17. J. Srinath, R. Gnanamoorthy, Effect of nanoclay reinforcement on tensile and tribo behaviour of Nylon 6. *J. Mater. Sci.* **40**, 2897–2901 (2005)
18. S. Bahadur, The development of transfer layers and their role in polymer tribology. *Wear* **245**, 92–99 (2000)

Computational Analysis of Concentrating Solar Boiler Uses with and Without Graphene Coating



Mohammad Arif Hussain, S. Nagakalyan, and M. Prakashbabu

Abstract This paper presents an enhanced thermal conductivity for composite wall of solar boiler by using the heat-transfer characteristic of a graphene coating. Utilizing the arrangement of reflective mirrors, the sun beams are made to focus on the reflective mirrors. The light beams which produce heat falls on these reflectors get reflected and consumed by the engrossing material that is set toward the looking of reflectors. The modeled plant layout which is expected to manufacture is a semi-round about design in which a semicircularly orchestrated reflectors are made to concentrate on a solar boiler. Results verified from transient analysis, that thermal conductivity of solar boiler without coating and with coating of a graphene. This investigation gives an exploratory reference to the utilization of graphene covering in against/deicing.

Keywords Solar tower · Copper vessel · Graphene coating · Thermal conductivity

1 Introduction

Innovations in concentrating solar thermal electricity (CSTE) can create power on demand when conveyed with thermal vitality stockpiling, giving a dispatchable well-spring of sustainable power source. [1]. The four fundamental business CST advancements are recognized by the way they center the sun's beams and the innovation used to get the sun-based vitality. Parabolic-trough collector (PT), solar tower (ST), linear Fresnel (LF), and parabolic dish (PD) [2]. Two types of CSTE are innovated till now, those are medium-CSTE Innovation and High-CSTE Innvoation [3, 4]. Till date every inventors are concentrating on tower receivers shapes only. But they are preferring tower material that used copper and other materials. This Computational

M. A. Hussain

Department of Mechanical Engineering, K L University, Vijayawada, Andhra Pradesh, India

S. Nagakalyan (✉) · M. Prakashbabu

Department of Mechanical Engineering, Guru Nanak Institutions Technical Campus, Hyderabad, Telangana, India

e-mail: kalyan502@gmail.com

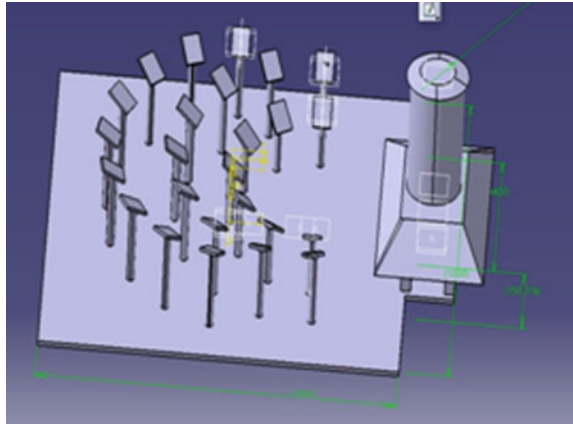
© Springer Nature Singapore Pte Ltd. 2021

G. S. V. L. Narasimham et al. (eds.), *Recent Trends in Mechanical Engineering*,

Lecture Notes in Mechanical Engineering,

https://doi.org/10.1007/978-981-15-7557-0_59

Fig. 1 Model of concentrated solar energy field



analysis represent Graphene and copper combination of material uses in tower, and investigated how it behaves.

2 Computational Analysis

2.1 Modeling

The prototype model consist of several parts those are platform, reepers, mirrors, vessel, and tower. The platform or the base we used is a wooden one, whose thickness is 12 mm and length, width are 1000 mm \times 1000 mm i.e., 1 m². Mirrors are the main part of the prototype. We used mirrors as reflectors because these are the best source for reflection. The size of the reflector we considered is 75 mm \times 75 mm. A copper vessel (with and without coating of grapheme) of 1 L. capacity has been used as an absorber as well as a boiler. The dimensions of the boiler (or) absorber are 190 mm \times 80 mm dia. Reepers are used as the support structure to the reflector. These are made into different sizes as per the field radius calculations. The sizes we took are 50, 61, 73, 84, 92, 105, 113 mm. Shown in Fig. 1.

2.2 Boundary Conditions

Expected limit conditions are the working pressure of the solar receiver and is the Ambient one. It is assumed that the fluid (air) is under steady-state flow condition, and the blower of the volumetric collector delivers a stream rate whose worth is assessed for each semi-consistent state condition (0.198–0.310 kg/s). The gravitational power can be ignored because of the low thickness of the liquid and its constrained stream.

Table 1 Cases considered in the assessment of the breeze impact and the arrival air impact

Wind velocity (m/s)	Wind direction ^(o)	Arrival air velocity (m/s)	Arrival air temperature (°K)
0	–	1.34, 0.64	300, 400, 500, 600
1.5	45, 90	1.34	300
3.5	0, 20	1.34	300, 400, 500, 600
	45	1.34, 0.64	300, 400, 500, 600
	70, 90	1.34	300
5.5	45, 90	1.34	300
7	0, 20	1.34	300
	45	1.34	300, 400, 500, 600
	70, 90	1.34	300
	45, 90	1.34	300

This presumption has been contemplated by the reproduction of two cases with a breeze speed of zero and 1.5 m/s, considering lightness impacts. These outcomes were contrasted and those assessed without the gravity impact, acquiring a most extreme deviation lower than 1.2% for the outlet temperature of the cup. Subsequently, the impact of the gravitational power isn't noteworthy for this situation. The thermophysical properties of the air stream have been characterized for dry air at barometrical weight and the properties of the strong materials were considered at the temperature scope of the chose relentless states. This data was provided by the information sheets of every material as appeared in Table 1 [5].

Wind impact has been considered for the lateral side of the encompassing air subdomain. The velocity inlet state of the breeze (lateral side of the encompassing air subdomain) incorporates the surrounding temperature and the segments of the speed vector as indicated by the Cartesian facilitate framework. These qualities have been assessed from the velocity and the breeze heading estimated for the approval procedure, and, then again, they were set considering the conditions characterized in Table 1.

Table 2 Material properties

Material type	Volume (m ³)	Mass (kg)	Density (kg/m ³)	Thermal conductivity
Copper alloy	5.3376×10^{-5}	0.44302	8300.9	$385 \text{ W m}^{-1} \text{ K}^{-1}$
Graphene	5.0926×10^{-5}	0.11204	300	$5300 \text{ W m}^{-1} \text{ K}^{-1}$
Water liquid	9.5002×10^{-4}	0.94831	1000	$598 \text{ mW m}^{-1} \text{ K}^{-1}$

3 Material Properties

3.1 Copper

The two main characteristics of copper that make it invaluable for humanity are its electrical and thermal conductivity, but it is the unique combination of these and other characteristics that makes copper so flexible.

Copper is a good heat conductor (about 30 times better than inoxidable steel and 1.5 times better than aluminum). This leads to applications where rapid heat transfer is required, such as heat exchangers in air conditioning units, vehicle radiators, computer heat sinks, heat sealing machines and televisions, and water-cooled furnace components.

3.2 Graphene

Graphene is a carbon allotrope (form) consisting of a single layer of carbon atoms arranged in a hexagonal lattice.

Thermal conductivity Thermal transport in graphene is an active area of research that has attracted attention due to the potential for thermal management applications Early measurements of the thermal conductivity of the suspended graphene reported an exceptionally high thermal conductivity of approximately $5300 \text{ W m}^{-1} \text{ K}^{-1}$ compared to the thermal conductivity of approximately $2000 \text{ W m}^{-1} \text{ K}^{-1}$ pyrolytic graphite at room temperature. When single-layer graphene is based on an amorphous material, the thermal conductivity is reduced to approximately $500\text{--}600 \text{ W m}^{-1} \text{ K}^{-1}$ at room temperature as a result of the dispersion of graphene lattice waves by the substrate. Table 2 shows the density, thermal conductivity of copper, grapheme, and water.

3.3 Transient Thermal Analysis of a Vessel [6]

The final point of the study is to know the limit of this concentrated solar energy vitality field consisting of 60 reflectors, for example, to examine the measure of heat

Table 3 Temperature readings of beneficiary copper without graphene covering, with grapheme and ambient temperature

Duration	Time (s)	Ambient temperature T_1 (°C)	Concentrating temperature at concentrator temperature T_2 (°C)
9:00 AM	0	29	63
9:30 AM	3600	25	72
10:0 AM	5400	28	91
10:30 AM	7200	32	103
11:00 AM	9000	35	107
11:30 AM	10,800	37	110
12:00 PM	12,600	40	112
12:30 PM	14,400	43	115
1:00 PM	16,200	45	120
1:30 PM	18,000	45	124
2:00 PM	19,800	43	128
2:30 PM	21,600	41	130
3:00 PM	23,400	39	126
3:30 PM	25,200	38	124
4:00 PM	27,000	34	118

that is designed to be protected. Simulated time to time-temperature readings using a Transient Thermal Analysis. The perceptions are recorded in the beneath Table 3. This Table 3 indicates ambient temperature and concentrated temperature of receiver.

Convection Coefficient = 12 W/m² °C.

The copper vessel transient analysis was done with above inputs the end result was shown in Fig. 2.

Figure 3 shows maximum temperature 124.27 °C at 2.30 PM minimum 63 °C at 9 AM.

The copper vessel with graphene coating transient analysis was done with above inputs and the end result was shown in Fig. 3.

Figure 3 shows maximum temperature 127.1 °C at 3.00 PM minimum 63 °C at 9 AM.

Thermal Conductivity is Thermal transport in graphene is a lively area of studies which has attracted attention because of the potential for thermal control applications. Early measurements of the thermal conductivity of suspended graphene reported an exceedingly large thermal conductivity of about 5300 Wm⁻¹K⁻¹, compared with the thermal conductivity of pyrolytic graphite of about 2000 Wm⁻¹K⁻¹ at room temperature.

The thermal conductivity of Copper of about 1450 Wm⁻¹K⁻¹ at room temperature. Tables 4 and 5 represent Conductivity rate with and without coating of grapheme in vessel [7, 8].

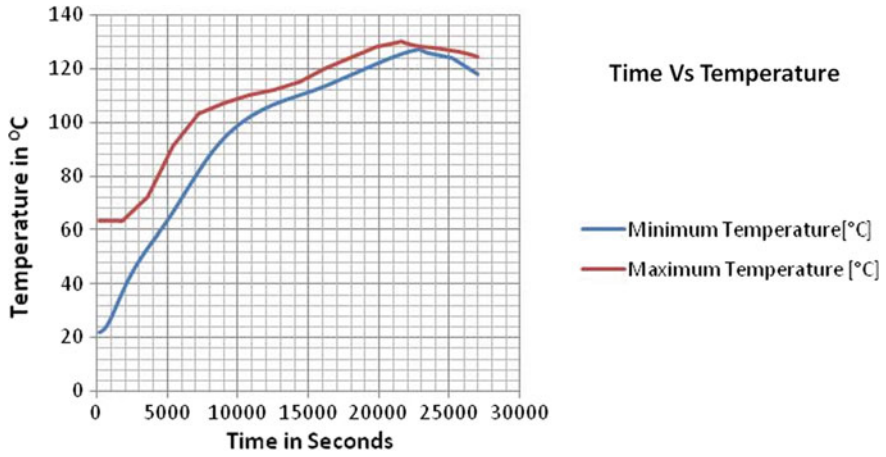


Fig. 2 Temperature variation in copper vessel transient analysis with respect to time

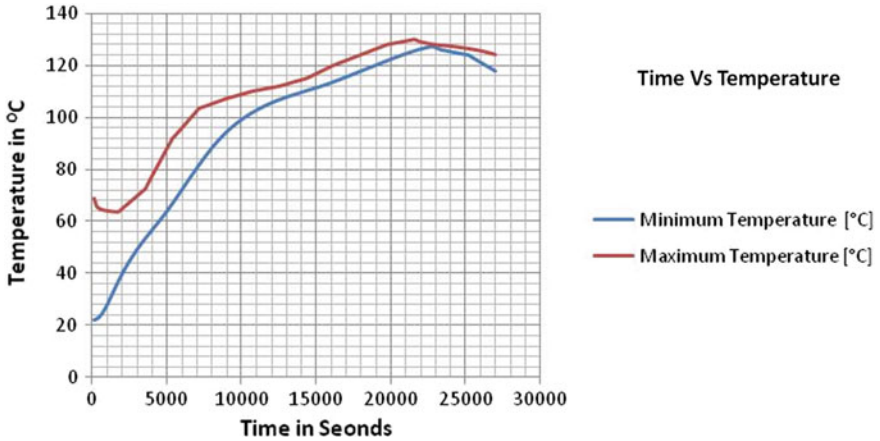


Fig. 3 Temperature variation in vessel with respect to time

4 Result and Discussion

The estimations of copper without graphene, utilizing the parameters characterized in the previous chapters, this work introduces a foreseen everyday execution of Concentrated solar power. The base temperature acquired at outside of kettle is 63 °C, the base temperature got inside the kettle is 29 °C, and the base temperature of water inside the evaporator is 25 °C. The pressure acquired in the kettle is beneath 1 kg per cm square. The maximum temperature obtained outside of kettle is 130 °C, the most extreme temperature acquired inside the kettle is 63 °C and the greatest

Table 4 Heat transfer and thermal conductivity of receiver without graphene coating

	Heat transfer	Conduction rate
9:00 AM	0.19	195.62
9:30 AM	0.26	267.69
10:00 AM	0.43	432.43
10:30 AM	0.47	473.61
11:00 AM	0.46	463.32
11:30 AM	0.43	432.43
12:00 PM	0.42	422.13
12:30 PM	0.46	463.32
1:00 PM	0.53	535.39
1:30 PM	0.58	586.87
2:00 PM	0.65	658.94
2:30 PM	0.70	700.12
3:00 PM	0.78	782.49
3:30 PM	0.77	772.2
4:00 PM	0.72	720.72

Table 5 Heat transfer and thermal conductivity of receiver with graphene coating

	Heat transfer	Conduction rate
9:00 AM	0.26	267.69
9:30 AM	0.33	339.76
10:00 AM	0.50	504.50
10:30 AM	0.56	566.28
11:00 AM	0.57	576.57
11:30 AM	0.57	566.28
12:00 PM	0.57	566.28
12:30 PM	0.57	576.57
1:00 PM	0.57	607.46
1:30 PM	0.60	628.05
2:00 PM	0.62	720.72
2:30 PM	0.62	772.20
3:00 PM	0.72	761.90
3:30 PM	0.77	761.90
4:00 PM	0.76	731.01

temperature of water inside the evaporator is 45 °C. The pressure obtained in the vessel is underneath 1 kg per cm square.

The estimations of copper with graphene, a base temperature acquired at outside of kettle is 63 °C, the base temperature got inside the vessel is 44 °C, and the base

temperature of water inside the evaporator is 25 °C. The pressure acquired in the kettle is beneath 1 kg per cm square. The most extreme temperature acquired outside of kettle is 130 °C, the greatest temperature got inside the evaporator is 72 °C, and the greatest temperature of water inside the vessel is 55 °C. The pressure obtained in the evaporator is beneath 1 kg per cm square.

5 Conclusion

The solar tower power plant designed in this work is theoretically equipped for creating steam. Compelling assimilation of reflected light happens with assistance of graphene covering on the copper chamber. Thermal conduction in kettle is increasingly due to the graphene covered copper vessel, which is utilized as boiler. So at long last this work can finished up graphene covering improves thermal efficiency of boiler. Future enhancements for the sun are following heliostat and ingestion territory on the collector. Hence, the outcomes are taken as sensible and instinctive for this application.

References

1. J.A. Cabrera, M.J. Cuesta, M. Pérez, Concentrating solar power: current state and sector actors. CIEMAT Tech Report (2006)
2. J.A. Duffie, W.A. Beckman, Solar engineering of thermal processes. Wiley, New York International Energy Agency (2014) Technology roadmap: solar thermal electricity (1980)
3. A. Kassem, K. Al-Haddad, D. Komljenovic, A. Schiffauerova, A value tree for identification of evaluation criteria for solar thermal power technologies in developing countries. Sustain. Energy Technol. Assess. (2016)
4. J.T. Masters, *Tower-Tracking Heliostat Array*. A thesis. Cal Poly San Luis Obispo (2011)
5. J.M. Chavez, *Development and Testing of Advanced Central Receivers*. Sandia National Labs Report (1996)
6. P.K. Falcone, *A Handbook for Solar Central Receiver Design*. Livermore: Sandia National Laboratories (1986)
7. Renewable Resource Data Center, NREL. National Solar Radiation Database
8. G.N. Tiwari, *Solar Energy: Fundamentals, Design, Modeling, and Applications* (Narosa Publishing House, New Delhi, 2002)